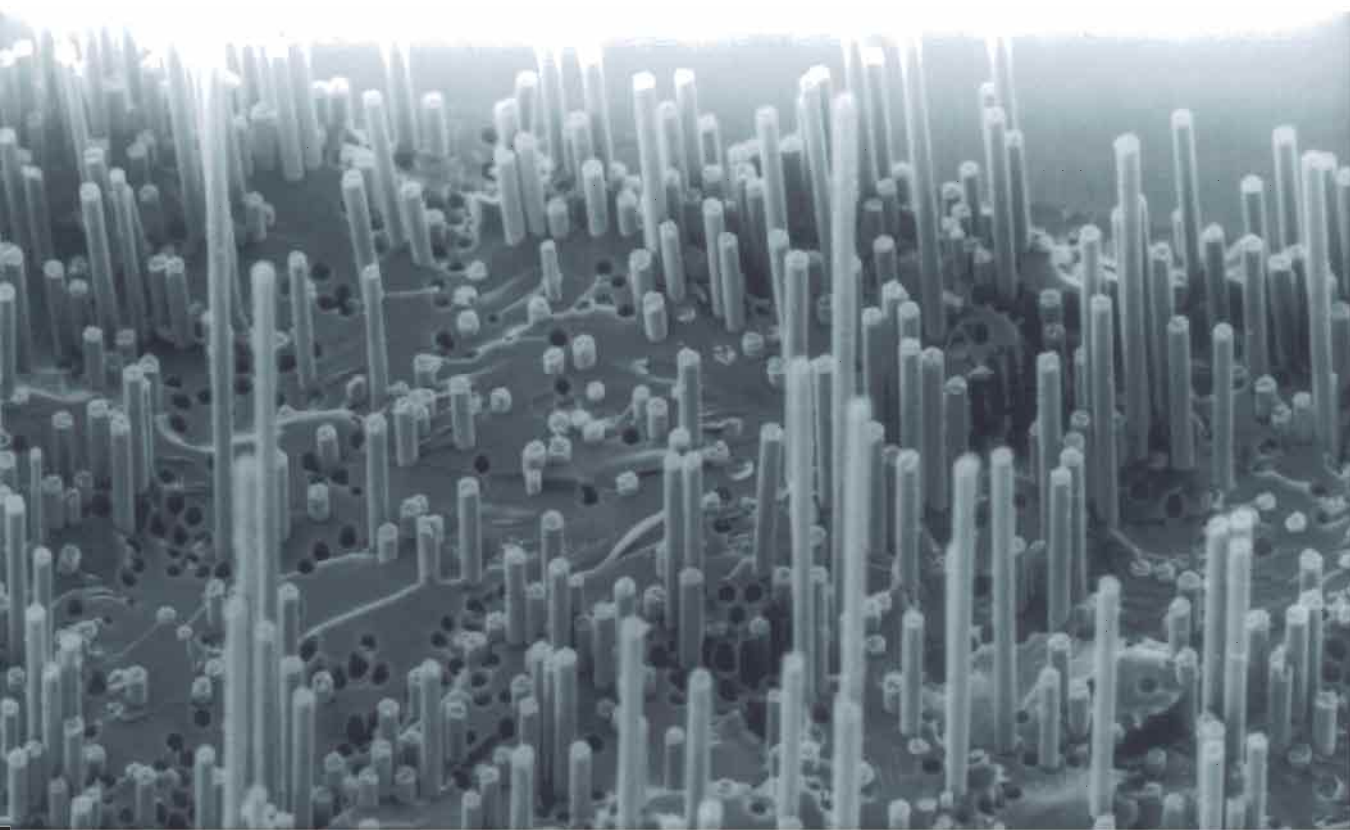


ENGINEERED INTERFACES IN FIBER REINFORCED COMPOSITES

JANG-KYO KIM & YIU-WING MAI



ENGINEERED
INTERFACES IN
FIBER REINFORCED
COMPOSITES

ENGINEERED INTERFACES IN FIBER REINFORCED COMPOSITES

Jang-Kyo Kim

Department of Mechanical Engineering
Hong Kong University of Science and Technology
Clear Water Bay, Hong Kong

Yiu-Wing Mai

Centre for Advanced Materials Technology and
Department of Mechanical & Mechatronic Engineering
University of Sydney, NSW 2006, Australia



1998

ELSEVIER

Amsterdam · Lausanne · New York · Oxford · Shannon · Singapore · Tokyo

ELSEVIER SCIENCE Ltd
The Boulevard, Langford Lane
Kidlington, Oxford OX5 1GB, U.K.

Library of Congress Cataloging-in-Publication Data

Kim, Jang-Kyo.

Engineered interfaces in fiber reinforced composites / Jang-Kyo

Kim and Yiu-Wing, Mai. -- 1st ed.

p. cm.

Includes index.

ISBN 0-08-042695-6 (hardcover)

1. Fibrous composites. I. Mai, Y. W., 1946- . II. Title.

TA418.9.C6K55 1998

620.1'18--DC21

97-52002

CIP

First edition 1998

ISBN 0-08-042695-6

© 1998 Elsevier Science Ltd

All rights reserved. No part of this publication may be reproduced, stored in a retrieval system or transmitted in any form or by any means: electronic, electrostatic, magnetic tape, mechanical photocopying, recording or otherwise, without permission in writing from the publishers.

Ⓢ The paper used in this publication meets the requirements of ANSI/NISO Z39.48-1992 (Permanence of Paper).

Printed in The Netherlands

FOREWORD

It is a pleasure to write the foreword to this book. This work emphasizes for the first time in one volume how interfaces in fibrous composites can be defined, measured, improved and optimized. Many practitioners of composites technology will find in this book the information they have been seeking to match fiber and matrix at the interface, thereby obtaining the best mix of properties in the final application.

Composites engineering is a relatively young field in which the test methods and measurement techniques are not yet fully developed. Even more important, the ideas linking the properties of composites to the interface structure are still emerging. This book not only reviews the historic and pragmatic methods for studying composites; but it also presents the most recent theories and fundamental tests of interface properties. This allows the reader to find the true framework of theory to fit his/her observations.

The fact that two brittle materials can be brought together to give a tough product is the proof that interfaces are critical to composite properties. However, the complexities of this process depend on the raw materials, on the surface chemistry of the components, on the fabrication procedures, on the chemistry of hardening, and on the damage and corrosion sustained in use. A wide view of material science, chemistry, mechanics, process engineering and applications experience is necessary to focus successfully on the role of the interface. The authors have demonstrated such a global view in this volume.

I have known Professor Mai for over 20 years. He is a foremost authority on fracture mechanics of composite materials, having studied polymer composites, cement, ceramic and natural composite systems, in the US, Britain, Australia and Hong Kong. In particular, he has made memorable contributions to the understanding of cracks and to the crack-inhibiting effects seen in fibrous composites. He has previously coauthored two books on fracture. Professor Kim originally worked in the composites industry and has returned during the past 10 years to study interface mechanisms more closely. He is currently working in the Hong Kong University of Science & Technology.

In summary, the topic of engineered interfaces in composites is an important one, critical to the advance of the composites industry. Many practitioners from a range of disciplines are seeking the information which can be found in this book. The authors display the wide experience and theoretical knowledge necessary to provide a critical view of the subject. I strongly recommend this volume to the composite expert and student alike.

*Kevin Kendall
Keele University, UK
May 1997*

PREFACE

The study and application of composite materials are a truly interdisciplinary endeavor that has been enriched by contributions from chemistry, physics, materials science, mechanics and manufacturing engineering. The understanding of the interface (or interphase) in composites is the central point of this interdisciplinary effort. From the early development of composite materials of various nature, the optimization of the interface has been of major importance. While there are many reference books available on composite materials, few of them deal specifically with the science and mechanics of the interface of fiber reinforced composites. Further, many recent advances devoted solely to research in composite interfaces are scattered in different published literature and have yet to be assembled in a readily accessible form. To this end this book is an attempt to bring together recent developments in the field, both from the materials science and mechanics perspective, in a single convenient volume.

The central theme of this book is tailoring the interface properties to optimize the mechanical performance and structural integrity of composites with enhanced strength/stiffness and fracture toughness (or specific fracture resistance). It deals mainly with interfaces in advanced composites made from high performance fibers, such as glass, carbon, aramid, ultrahigh modulus polyethylene and some inorganic (e.g. B/W, Al_2O_3 , SiC) fibers, and matrix materials encompassing polymers, metals/alloys and ceramics. The book is intended to provide a comprehensive treatment of composite interfaces in such a way that it should be of interest to materials scientists, technologists and practising engineers, as well as graduate students and their supervisors in advanced composites. We hope that this book will also serve as a valuable source of reference to all those involved in the design and research of composite interfaces.

The book contains eight chapters of discussions on microstructure–property relationships with underlying fundamental mechanics principles. In Chapter 1, an introduction is given to the nature and definition of interfaces in fiber reinforced composites. Chapter 2 is devoted to the mechanisms of adhesion which are specific to each fiber–matrix system, and the physico-chemical characterization of the interface with regard to the origin of adhesion. The experimental techniques that have been developed to assess the fiber–matrix interface bond quality on a microscopic scale are presented in Chapter 3, along with the techniques of measuring interlaminar/intralaminar strengths and fracture toughness using bulk composite laminates. The applicability and limitations associated with loading geometry and interpretation of test data are compared. Chapter 4 presents comprehensive theoretical analyses based on shear-lag models of the single fiber composite tests, with particular emphasis being placed on the interface debond

process and the nature of the fiber–matrix interface bonding. Chapter 5 is devoted to reviewing current techniques of fiber surface treatments which have been devised to improve the bond strength and the fiber–matrix compatibility/stability during the manufacturing processes of composites. The microfailure mechanisms and their associated theories of fracture toughness of composites are discussed in Chapter 6. The role of the interface and its effects on the mechanical performance of fiber composites are addressed from several viewpoints. Recent research efforts to augment the transverse and interlaminar fracture toughness by means of controlled interfaces are presented in Chapters 7 and 8. Three concepts of engineered interfaces are put forward to explain the results obtained from fiber coatings. Among those with special interest from the composite designer’s perspective are the effects of residual stresses arising from differential shrinkage between the composite constituents, tough matrix materials, interleaves as delamination arresters and three-dimensional fiber preforms.

We are grateful for assistance from many sources in the preparation of this book. We acknowledge the invaluable contributions of many individuals with whom we had the privilege and delight to work together: in particular the past and present colleagues at the University of Sydney and the Hong Kong University of Science & Technology, including C.A. Baillie, F. Castino, B. Cotterell, K.A. Dransfield, S.L. Gao, Y.C. Gao, M.I. Hakeem, B.J. Kennedy, M.G. Lau, L.M. Leung, H.Y. Liu, R. Lord, I.M. Low, S.V. Lu, D.B. Mackay, L. Ye and L.M. Zhou. The generous financial support provided by many organizations, most notably the Australian Research Council and the Hong Kong Research Grant Council, for performing the research recorded in this book is greatly appreciated. Thanks are also due to all those who have allowed us to reproduce photographs and diagrams from their published work and to their publishers for the permission to use them.

Special thanks are also due to our technical writer Dr. Virginia Unkefer of the Hong Kong University of Science & Technology for her help without which this book would never have eventuated. Finally, we can never thank sufficiently our family members, Hyang and Jong-Rin Kim, and Louisa Mai, for their patience and understanding of our pressure to undertake and complete such a time-consuming task.

Jang-Kyo Kim
Clear Water Bay, Hong Kong
May 1997

Yiu-Wing Mai
Sydney, Australia
May 1997

CONTENTS

Foreword v

Preface vii

Chapter 1. Introduction 1

References 4

Chapter 2. Characterization of Interface Properties 5

- 2.1. Introduction 5
 - 2.2. Theories of Adhesion and Types of Bonding 5
 - 2.2.1. Adsorption and Wetting 7
 - 2.2.2. Interdiffusion 12
 - 2.2.3. Electrostatic Attraction 13
 - 2.2.4. Chemical Bonding 14
 - 2.2.5. Reaction Bonding 14
 - 2.2.6. Mechanical Bonding 16
 - 2.3. Physico-chemical Characterization of Interfaces 17
 - 2.3.1. Introduction 17
 - 2.3.2. Infrared (IR) and Fourier Transform Infrared (FTIR) Spectroscopy 18
 - 2.3.3. Laser Raman Spectroscopy 21
 - 2.3.4. X-Ray Photoelectron Spectroscopy (XPS) 24
 - 2.3.5. Auger Electron Spectroscopy (AES) 26
 - 2.3.6. Secondary Ion Mass Spectroscopy (SIMS) 29
 - 2.3.7. Ion Scattering Spectroscopy (ISS) 30
 - 2.3.8. Solid State Nuclear Magnetic Resonance (NMR) Spectroscopy 31
 - 2.3.9. Wide-Angle X-Ray Scattering (WAXS) 32
 - 2.3.10. Small-Angle Light Scattering (SALS) and Small-Angle X-ray Scattering (SAXS) 33
 - 2.3.11. Measurement of Contact Angle 34
- References 38

Chapter 3. Measurements of Interface/Interlaminar Properties 43

- 3.1. Introduction 43
- 3.2. The Mechanical Properties of Fiber–Matrix Interfaces 44

3.2.1.	Introduction	44
3.2.2.	Single Fiber Compression Test	44
3.2.3.	Fiber Fragmentation Test	45
3.2.4.	Fiber Pull-out Test	51
3.2.5.	Microindentation (or Fiber Push-out) Test	56
3.2.6.	Slice Compression Test	58
3.2.7.	Comparison of Microcomposite Tests and Experimental Data	59
3.3.	Interlaminar/Intralaminar Properties	61
3.3.1.	Introduction	61
3.3.2.	Short Beam Shear Test	62
3.3.3.	Iosipescu Shear Test	66
3.3.4.	$[\pm 45^\circ]_s$ Tensile Test	69
3.3.5.	$[10^\circ]$ Off-axis Tensile Test	70
3.3.6.	Rail Shear Test	71
3.3.7.	In-plane Lap-shear Test	72
3.3.8.	Transverse Tensile Test	72
3.4.	Interlaminar Fracture Toughness	74
3.4.1.	Delamination	74
3.4.2.	Mode I Interlaminar Fracture Tests (IFT)	76
3.4.3.	Mode II Interlaminar Fracture Tests	81
3.4.4.	Mode I Edge Delamination Tests	83
	References	85

Chapter 4. Micromechanics of Stress Transfer Across the Interface 93

4.1.	Introduction	93
4.2.	Fiber Fragmentation Test	94
4.2.1.	Introduction	94
4.2.2.	Early Shear-Lag Models	97
4.2.3.	An Improved Model based on a Fracture Mechanics Approach	101
4.2.4.	An Improved Model based on a Shear Strength Criterion	110
4.3.	Fiber Pull-Out Test	125
4.3.1.	Introduction	125
4.3.2.	Solutions for Stress Distributions	128
4.3.3.	Interface Debond Criterion and Partial Debond Stress	131
4.3.4.	Instability of Debond Process	135
4.3.5.	Characterization of Interface Properties	138
4.3.6.	Multiple Fiber Composite Model	139
4.3.7.	Two-way Debonding Phenomenon	147
4.4.	Fiber Push-out	150
4.4.1.	Solutions for Stress Distributions	150
4.4.2.	Debond Criterion and Debond Stresses	152
4.4.3.	Comparisons between Fiber Pull-out and Fiber Push-out	154
4.5.	Cyclic Loading in Fiber Pull-out and Fiber Push-out	156
4.5.1.	Introduction	156

- 4.5.2. Relative Displacements and Degradation Function 157
- 4.5.3. Degradation of Interface Frictional Properties 161
- References 164

Chapter 5. Surface Treatments of Fibers and Effects on Composite Properties 171

- 5.1. Introduction 171
- 5.2. Glass Fibers and Silane Coupling Agents 172
 - 5.2.1. Structure and Properties of Glass Fibers 172
 - 5.2.2. Silane Treatments of Glass Fibers 174
- 5.3. Carbon Fibers 183
 - 5.3.1. Structure and Properties of Carbon Fibers 183
 - 5.3.2. Surface Treatments of Carbon Fibers 186
- 5.4. Polymeric Fibers 196
 - 5.4.1. Aramid Fibers 196
 - 5.4.2. Ultrahigh Modulus Polyethylene (UHMPE) Fibers 201
- 5.5. Inorganic Fibers 205
 - 5.5.1. Introduction 205
 - 5.5.2. Selection of Coating Materials and Coating Techniques 206
 - 5.5.3. Carbon Fibers 210
 - 5.5.4. Boron Fibers 214
 - 5.5.5. Silicon Carbide (SiC) Fibers 216
 - 5.5.6. Alumina (Al_2O_3) Fibers 223
 - References 228

Chapter 6. Interface Mechanics and Fracture Toughness Theories 239

- 6.1. Interface-related Fracture Toughness Theories 239
 - 6.1.1. Introduction 239
 - 6.1.2. Fiber–Matrix Interface Debonding in Mode II Shear 242
 - 6.1.3. Post-debond Friction 243
 - 6.1.4. Stress Redistribution 243
 - 6.1.5. Fiber Pull-out 243
 - 6.1.6. Total Fracture Toughness Theories 245
 - 6.1.7. Fracture of Ductile Fibers and Ductile Matrices 247
- 6.2. Toughness Theories for Short and Randomly Oriented Fiber Composites 247
 - 6.2.1. Introduction 247
 - 6.2.2. Fiber Pull-out Dominant Fracture Mechanisms 248
 - 6.2.3. Matrix Dominant Fracture Mechanisms 250
 - 6.2.4. Total Fracture Toughness Theory 252
- 6.3. Fracture Toughness Maps 254
 - 6.3.1. Continuous Fiber Composites 255
 - 6.3.2. Short Fiber Composites 255
- 6.4. Crack–Interface Interactions 257

- 6.4.1. Tensile Debonding Phenomenon 257
- 6.4.2. Transverse Cracking versus Longitudinal Splitting 260
- 6.4.3. Crack Growth Resistance (R-curve) Behavior
in Transverse Fracture 268
References 273

Chapter 7. Improvement of Transverse Fracture Toughness with Interface Control 279

- 7.1. Introduction 279
- 7.2. Fiber Coating and Intermittent Bonding Concept – Experimental
Studies 281
 - 7.2.1. Intermittent Bonding Concept 282
 - 7.2.2. Fiber Coating for Improved Energy Absorption Capability 285
 - 7.2.3. Fiber Coating Techniques 293
- 7.3. Theoretical Studies of Interphase and Three Engineered
Interphase Concepts 295
 - 7.3.1. Theoretical Studies of Interphase 296
 - 7.3.2. Engineered Interface Concepts with Fiber Coating 300
- 7.4. Control of Laminar Interfaces-Delamination Promoters 306
- 7.5. Residual Stresses 308
 - 7.5.1. Origin of Residual Stresses 308
 - 7.5.2. Control of Residual Stresses 315
- References 320

Chapter 8. Improvement of Interlaminar Fracture Toughness with Interface Control 329

- 8.1. Introduction 329
- 8.2. Effects of Matrix Materials on Interlaminar Fracture Resistance 330
 - 8.2.1. Introduction 330
 - 8.2.2. Correlations between Matrix Properties and Composite Interlaminar
Properties 332
 - 8.2.3. Impact Resistance and Tolerance of Fiber Composites with Tough
Matrices 339
- 8.3. Delamination Resisters 342
 - 8.3.1. Mechanics of Free-edge Delamination 342
 - 8.3.2. Interleaving Techniques 345
- 8.4. Three-dimensional Textile Composites Concept 351
 - 8.4.1. Introduction 351
 - 8.4.2. Improvement of Interlaminar Fracture Toughness 354
 - 8.4.3. Impact Response of Stitched Composites 357
- References 360

Appendices	367
List of Symbols and Abbreviations	371
Author Index	377
Subject Index	391

Chapter 1

INTRODUCTION

Fiber composite technology is based on taking advantage of the high strength and high stiffness of fibers, which are combined with matrix materials of similar/dissimilar natures in various ways, creating inevitable interfaces. In fiber composites, both the fiber and the matrix retain their original physical and chemical identities, yet together they produce a combination of mechanical properties that cannot be achieved with either of the constituents acting alone, due to the presence of an interface between these two constituents. The growing number of uses for fiber reinforced composites in many engineering applications has made the issue of *interface* (or more properly termed, *interphase* (Drzal et al., 1983)) a major focus of interest in the design and manufacture of composite components.

A classic definition of the *interface* in fiber composites is a surface formed by a common boundary of reinforcing fiber and matrix that is in contact with and maintains the bond in between for the transfer of loads. It has physical and mechanical properties that are unique from those of the fiber or the matrix. In contrast, the *interphase* is the geometrical surface of the classic fiber–matrix contact as well as the region of finite volume extending therefrom, wherein the chemical, physical and mechanical properties vary either continuously or in a stepwise manner between those of the bulk fiber and matrix material. In other words, the interphase exists from some point in the fiber through the actual interface into the matrix, embracing all the volume altered during the consolidation or fabrication process from the original fiber and matrix materials. Therefore, the earlier definition of Metcalfe (1974) for interface can be used for interphase as well: “An interface is the region of significantly changed chemical composition that constitutes the bond between the matrix and reinforcement”. Fig. 1.1 schematically illustrates the concept of the interphase according to Drzal et al. (1983). Also shown in Fig. 1.1 are the various processing conditions that are imposed on the interphase to allow chemical reactions to take place and volumetric changes and residual stresses to be generated. It is the latter definition of interface that is in general use in this book. However, for analytical purposes in micromechanics the interface is still conveniently considered to be infinitely thin and the properties of the mating fiber and matrix are isotropic and homogeneous.

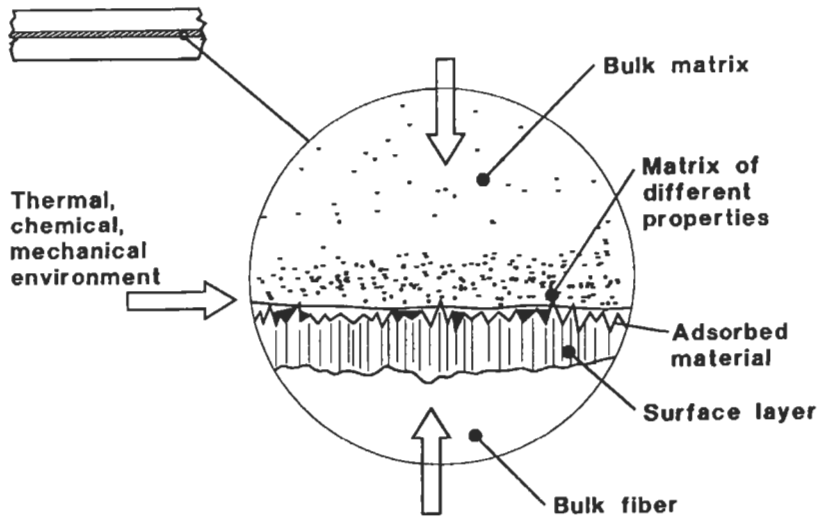


Fig. 1.1. Schematic illustration of the components of the three-dimensional interphase between fiber and matrix. After Drzal et al. (1983).

The issue of understanding the composition and properties of interfaces in fiber composite materials is still evolving despite the fact that there have been a great number of publications devoted to research in this field. Part of the reason for this evolution is the interdisciplinary nature of the subject. In addition to a number of multi-disciplinary conferences held in the past 30 years on adhesion science in general, several international conferences dealing solely with the fiber-matrix interfaces, such as the *International Conference on Composite Interfaces (ICCI)* and *Interfacial Phenomenon in Composite Materials (IPCM)*, have been held since 1986. These conferences have provided a centralized forum not only to discuss and identify the important problems of the subject, but also to disseminate important research results from various sources. They are thus leading the scattered research and development efforts in a sensible direction, as well as helping to make significant contributions toward the improvement of our fundamental understanding of interfaces in polymer, metal and ceramic matrices composites.

Nevertheless, recent advances in research in this multi-disciplinary field have not yet been collected together. While there are plenty of reference books available on composite materials in general, few of them are devoted specifically to composite interface science and mechanics. It is hoped that this book adds to the research effort by bringing recent developments in the field together in one convenient single volume. It is intended to create a comprehensive reference work from both the materials science and mechanics perspectives.

It is well known that the properties of an interface are governed largely by the chemical/morphological nature and physical/thermodynamic compatibility between the two constituents and most often limit the overall performance of the bulk

composite. There is now a considerable amount of evidential data regarding the influences of interfaces on fracture toughness in both transverse and interlaminar fractures, and strength and stiffness of fiber composites in various failure modes and loading configurations (Kim and Mai, 1991; Drzal and Madhukar, 1993), although the relationship between documented material properties and the actual performances of composites is still in question. It follows therefore that a thorough knowledge of the microstructure–property relationship at the interface region is an essential key to the successful design and proper use of composite materials. Further, the interface properties are becoming gradually accepted as design and process variables to be tailored for particular end applications (Kim and Mai, 1993). Although there is no simple quantitative relation known for interface optimization of a given combination of fiber and matrix, various chemical–physical and thermodynamic–mechanical principles along with previous experience are invaluable sources of information to design the interface qualitatively. A number of potential solutions have been suggested to improve specific properties of the composites, particularly the interface bond quality for efficient stress transfer and the fracture resistance/damage tolerance of inherently brittle composites without sacrificing other important mechanical properties.

This book is concerned mainly with interfaces in advanced composites made from high performance fibers, such as glass, carbon, aramid and some other organic (e.g. ultrahigh molecular weight (UHMW) polyethylene) and inorganic (e.g. B/W, Al_2O_3 , SiC) fibers and useful matrix materials encompassing polymer, metals/alloys and ceramics. To control the interface properly and thereby to provide the composite with improved mechanical performance and structural integrity, it is essential to understand the mechanisms of adhesion which are specific to each fiber–matrix system, and the physico-chemical characterization of the interface with regard to the origin of adhesion. This is the focus of Chapter 2. A number of theoretical and experimental methods developed to assess the quality of the interface bond are summarized. Several common experimental techniques that have been developed to assess the fiber–matrix interface bond quality on a microscopic scale of the so-called ‘single fiber microcomposite test’, are presented in Chapter 3 along with the interlaminar/intralaminar strengths and fracture toughness of various failure modes using composite laminates. Their applicability and limitations are critically discussed with regard to the loading geometry and interpretation of the test data based on the underlying mechanics. A proper load transfer across the interface region is also of particular importance in composites technology. Chapter 4 considers from the load transfer and fracture mechanics angles, extensive and in-depth theoretical analyses based on a shear-lag model for the single fiber composite test with different loading geometry. Of special interest are the stress states in the composite constituents and debond process along the interface depending on the nature of the interface bond. This is followed in Chapter 5 by comparisons of the theories with experimental results of several different composite systems. Particular emphasis is placed on the various techniques of surface treatments on a range of technologically important fibers to improve bond strength as well as to enhance fiber–matrix compatibility and stability during processing or fabrication of the

composites. A review of the microfailure mechanisms and their associated theories of fracture toughness of fiber composites in Chapter 6 identifies that a high bond strength does not necessarily lead to a high fracture toughness. Instead a compromise always has to be made in the bond strength to optimize the strength and toughness. The role of the interface and its effects on the overall performance of composites is addressed from several viewpoints. Novel methods to improve the transverse fracture toughness of composites by means of controlled interfaces are presented in Chapter 7. The effects of residual stresses arising from the thermal mismatch between the fiber and matrix and the shrinkage of the matrix material upon cooling from the processing temperature are specifically discussed. Recent advances in efforts to improve the interlaminar fracture toughness are also critically reviewed in Chapter 8.

References

- Drzal, L.T., Rich, M.J. and Lloyd, P.F. (1983). Adhesion of graphite fibers to epoxy matrices. part I. The role of fiber surface treatment. *J. Adhesion* **16**, 1–30.
- Drzal, L.T. and Madhukar, M. (1993). Fiber–matrix adhesion and its relationship to composite mechanical properties. *J. Mater. Sci.* **28**, 569–610.
- Kim, J.K. and Mai, Y.W. (1991). High strength, high fracture toughness fiber composites with interface control—a review. *Composites Sci. Technol.* **41**, 333–378.
- Kim, J.K. and Mai, Y.W. (1993). Interfaces in composites. in *Structure and Properties of Fiber Composites*, Materials Science and Technology, Series Vol. 13, (T.W. Chou ed.), VCH Publishers, Weinheim, Germany, pp. 239–289.
- Metcalf, A.G. (1974). Physical–chemical aspects of the interface. In *Interfaces in Metal Matrix Composites*, Composite Materials. Vol. 1. (A.G. Metcalf ed.), New York, Academic Press, pp. 65–123.

Chapter 2

CHARACTERIZATION OF INTERFACES

2.1. Introduction

The physico-chemical aspect of composite interfaces is a difficult subject and our understanding of this feature is still far from complete. Two important topics will be reviewed in this chapter. They are the theory of bonding at the fiber–matrix interface and the analytical techniques to characterize the interface. The nature or origin of the bonding between the fiber and matrix is discussed in terms of the theories of adhesion with associated mechanisms of bonding. Examples of specific fiber–matrix systems are provided along with their corresponding mechanisms of adhesion. Various physico-chemical analytical techniques, which have been devised to characterize the surface properties of fibers and composite interfaces, are also extensively reviewed with corresponding analytical models for evaluation of the experimental data. Advantages and limitations of each method are also presented.

Proper characterization of composite interfaces, whether it is for chemical, physical or mechanical properties, is extremely difficult because most interfaces with which we are concerned are buried inside the material. Furthermore, the microscopic and often nanoscopic nature of interfaces in most useful advanced fiber composites requires the characterization and measurement techniques to be of ultrahigh magnification and resolution for sensible and accurate solutions. In addition, experiments have to be carried out in a well-controlled environment using sophisticated testing conditions (e.g. in a high vacuum chamber). There are many difficulties often encountered in the physico-chemical analyses of surfaces.

2.2. Theories of adhesion and types of bonding

The nature of bonding is not only dependent on the atomic arrangement, molecular conformation and chemical constitution of the fiber and matrix, but also on the morphological properties of the fiber and the diffusivity of elements in each constituent. It follows therefore that the interface is specific to each fiber–matrix system (Kim and Mai, 1991). Adhesion in general can be attributed to mechanisms including, but not restricted to, adsorption and wetting, electrostatic attraction,

chemical bonding, reaction bonding, and exchange reaction bonding (Kim and Mai, 1993), which are schematically shown in Fig. 2.1 and discussed in the following sections. In addition to the major mechanisms, hydrogen bonding, van der Waals forces and other low energy forces may also be involved. All these mechanisms take place at the interface region either in isolation, or, most likely, in combination to produce the final bond. Reviews on these major mechanisms can be found in many references including Scola (1974), Wake (1978), Kinloch (1980, 1982), Hull (1981), Adamson (1982) and Kinloch et al. (1992) for polymer matrix composites; Metcalfe (1974) for metal matrix composites (MMCs); and Naslain (1993) for ceramic matrix composites (CMCs). More recently, mechanisms and mechanics modeling of interfaces in cementitious composites have received a lot of attention (see for example, Maso, 1993; Cotterell and Mai, 1996).

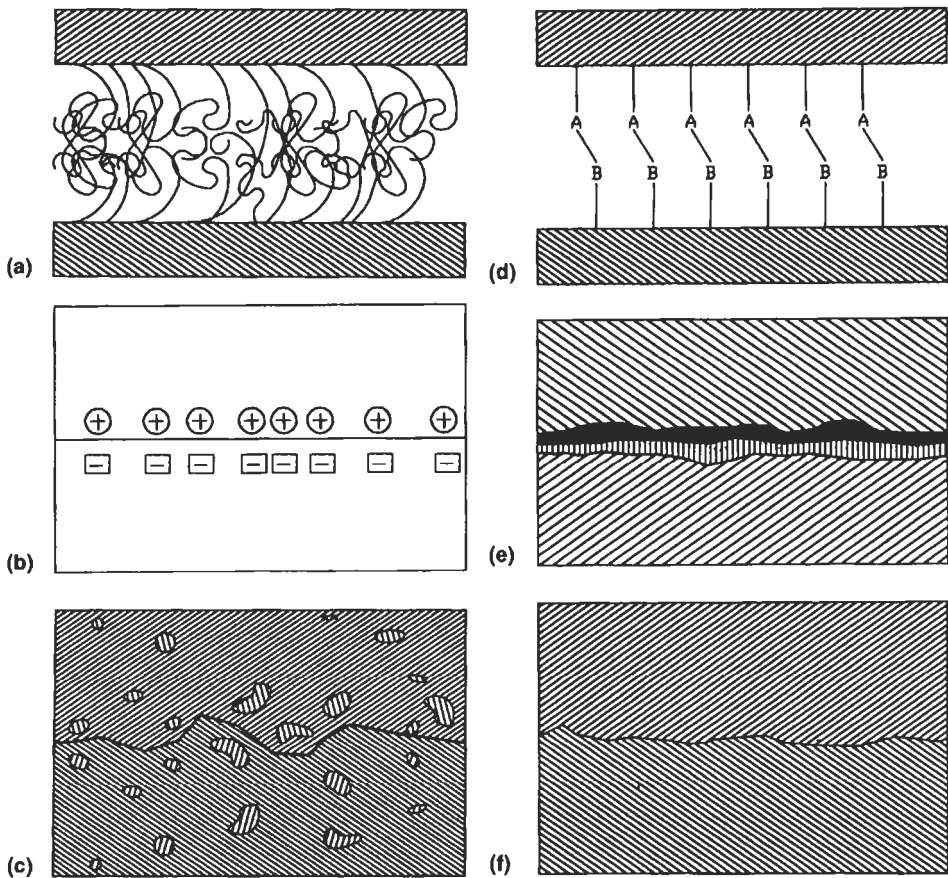


Fig. 2.1. Interface bonds formed (a) by molecular entanglement; (b) by electrostatic attraction; (c) by interdiffusion of elements; (d) by chemical reaction between groups A on one surface and groups B on the other surface; (e) by chemical reaction following forming of a new compound(s), particularly in MMCs; (f) by mechanical interlocking. After Hull (1981) and Naslain (1993).

2.2.1. Adsorption and wetting

Good wetting of fibers by matrix material during the impregnation stages of fabrication is a prerequisite to proper consolidation of composites, particularly for composites based on polymer resins and molten metals. It is well understood that physical adsorption of gas molecules to solid surfaces is ascribed to the attraction arising from the quantum mechanical effect due to the valence electrons present in the constituents as a free gas. The physical attraction between electrically neutral bodies is best described by the wetting of solid surfaces by liquids. Bonding due to wetting involves very short-range interactions of electrons on an atomic scale which develop only when the atoms of the constituents approach within a few atomic diameters or are in contact with each other.

Wetting can be quantitatively expressed in terms of the thermodynamic work of adhesion, W_A , of a liquid to a solid using the Dupre equation

$$W_A = \gamma_1 + \gamma_2 - \gamma_{12} \quad (2.1)$$

W_A represents a physical bond resulting from highly localized intermolecular dispersion forces. It is equal to the sum of the surface free energies of the liquid, γ_1 , and the solid, γ_2 , less the interfacial free energy, γ_{12} . It follows that Eq. (2.1) can be related to a model of a liquid drop on a solid shown in Fig. 2.2. Resolution of forces in the horizontal direction at the point A where the three phases are in contact yields Young's equation

$$\gamma_{SV} = \gamma_{SL} + \gamma_{LV} \cos \theta \quad (2.2)$$

where γ_{SV} , γ_{SL} and γ_{LV} are the surface free energies of the solid–vapor, solid–liquid and liquid–vapor interfaces, respectively, and θ is the contact angle. Liquids that form contact angles greater and less than 90° are respectively called ‘non-wetting’ and ‘wetting’. If the liquid does not form a droplet, i.e. $\theta = 0^\circ$, it is termed ‘spreading’ and the relationship given by Eq. (2.2) becomes invalid. In this case, the equilibrium is expressed by an inequality

$$\gamma_{SV} - \gamma_{SL} > \gamma_{LV} \quad (2.3)$$

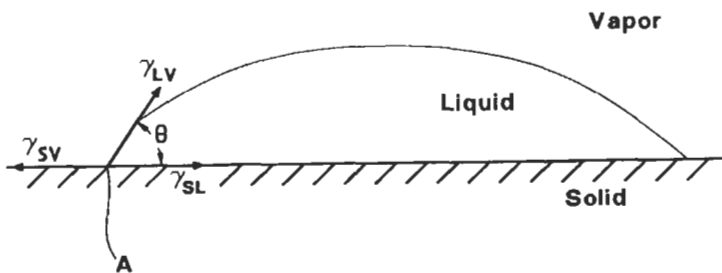


Fig. 2.2. Contact angle, θ , and surface energies, γ_{LV} , γ_{SL} and γ_{SV} , for a liquid drop on a solid surface.

The surface energy of a solid (i.e. reinforcement in composites), γ_{SV} , must be greater than that of a liquid (i.e. matrix resin), γ_{LV} , for proper wetting to take place. Table 2.1 gives values of surface energies for some fibers and polymer matrix materials. Thus, glass and carbon fibers can be readily wetted by thermoset resins like epoxy and polyester resins at room temperature unless the viscosity of the resin is too high (Hull, 1981), and by some thermoplastic resins (e.g. Nylon 6.6, PET, PMMA and PS). In contrast, it is difficult to wet polyethylene fibers (of surface energy approximately 31 mJ/m^2) with any of these resins unless the fibers are surface treated. For the same reason, carbon fibers are often coated with Ti-B (Amateau, 1976) using a chemical vapor deposition process to allow wetting by an aluminum matrix.

Combining Eqs. (2.1) and (2.2) yields the familiar Young–Dupre equation

$$W_A = \gamma_{LV}(1 + \cos \theta) . \quad (2.4)$$

The values of W_A reflect directly the significance of energetics between the liquid and solid phases, i.e. the higher the work of adhesion the stronger the interactions. W_A can be determined in experiments by measuring the surface energy of the liquid, γ_{LV} , and the contact angle, θ . Details of the measurement techniques of the contact angle are discussed in Section 2.3.11.

It should be noted that, in the above equations, the effects of adsorption of vapor or gas on the solid surfaces are completely neglected. The amount of adsorption can be quite large, and may approach or exceed the point of monolayer formation at saturation. The spreading pressure, π_s , which is the amount of the reduction in surface energy on the solid surface due to the adsorption of vapor in equilibrium, is given by (Adamson, 1982)

$$\pi_s = \gamma_s - \gamma_{SV} . \quad (2.5)$$

The subscript s indicates the hypothetical case of a solid in contact with a vacuum. The importance of impure surfaces is well recognized in areas like brazing where the difficulty of brazing aluminum is associated with the presence of an oxide film on the surface. Therefore, Eq. (2.5) can be substituted in Eqs. (2.1) and (2.2) by introducing the spreading pressure. The Young–Dupre equation is then modified to

$$W_A = \gamma_{LV}(1 + \cos \theta) + \pi_s . \quad (2.6)$$

Although the discussion of wettability presented above has focused on the thermodynamics between the fiber surface and the liquid resin, real composite systems consist of an extremely large number of small diameter fibers embedded in a matrix. Adding to the issue of proper wetting of fiber surfaces by the resin, a key to creating good adhesion at the fiber–matrix interface is infiltration of the resin into the fiber tow during the fabrication process. The minute gaps present between the fibers can create very large capillary forces, which are often characterized by a pressure drop due to the surface energy acting in the small capillaries. If the liquid

Table 2.1
Surface energies of solids, γ_{SV} , and liquids, γ_{LV} , including some fibers, matrix materials and composites

Solids	γ_{SV} (mJ/m ²)	γ_{LV} (mJ/m ²)	References ^a
E-glass fibers			
Heat + rinsed in H ₂ O	63.0		1
0.3% silane A-174	42.9		1
0.3% silane A-153	33.2		1
Silicone resin coated	15.8		1
5% PVA resin coated	35.1		1
0.1% q-MPS silane	46.0		1
0.3% q-MPS silane	42.3		1
0.5% q-MPS silane	40.8		1
0.8% q-MPS silane	39.5		1
1.1% q-MPS silane	40.0		1
1.5% q-MPS silane	40.8		1
2.0% q-MPS silane	43.7		1
Quartz particles			
No treatment	64		1
0.5% A-1000 treatment	41.77		1
1.0% A-1000 treatment	44.74		1
2.0% A-1000 treatment	46.47		1
0.5% Z-6032 treatment	41.7		1
1.0% Z-6032 treatment	38.9		1
2.0% Z-6032 treatment	38.0		1
Hercules AS-4 Carbon fiber	39.4		2
Pitch-based PRD-172 carbon fibers			
LM untreated	33.8		3
LM PTC treated	52.5		3
IM untreated	32.7		3
IM PTC treated	44.5		3
HM untreated	36.6		3
HM PTC treated	49.4		3
Thornel T-300 carbon fiber	36.08		4
Teflon fiber	16.09		4
Fiber-reinforced polymer matrix composites			
UD carbon fiber-epoxy matrix			
UD carbon fiber-PEEK matrix	48.8		5
UD carbon fiber-polyamide (PA) matrix	42.2		5
UD Kevlar fiber-polyamide (PA) matrix	42.0		5
Woven carbon fabric-polyetherimide (PEI) matrix	42.3		5
Woven carbon fabric-polyimide (PI) matrix	40.7		5
UD carbon fiber-polyphenylene sulphide (PPS)	41.9		5
	37.8		5

Table 2.1 (contd.)

Liquids	γ_{sv} (mJ/m ²)	γ_{LV} (mJ/m ²)	References ^a
Polyester		40.4	1
DER 330 epoxy		39.33	1
Polypropylene (PP)		29.8	2
Nylon 6,6 polyamide (PA)		46.5	2
Polyethylene terephthalate (PET)		44.6	2
Polymethyl methacrylate (PMMA)		41.1	2
Polystyrene (PS)		40.7	2
High density polyethylene (HDPE)		35.7	2
Polycarbonate (PC, Lexan 101)		33.5	2
Polysulfone (PSU, Udel P-1700)		30.71	2
NPDGE epoxy		36.33	4
HMDS silicone oil		16.33	4
Glycerol		63.4	5
Formamide		58.2	5
Water		72.6	5
Methylene iodide		48.6	5
1-bromonaphthalene		44.6	5
Polyglycol E-200		43.5	5
Dimethyle sulfoxide		43.3	5
Iodoethanol		44.9	5

^aRef 1: Gutowski, 1988.

Ref 2: Gutowski, 1990.

Ref 3: Gilbert et al., 1990.

Ref 4: Lee et al., 1988.

Ref 5: Kinloch et al., 1992.

LM = low modulus

IM = intermediate modulus

HM = high modulus

UD = unidirectional

NPDGE = Neopentyl diglycidyl ether

HMDS = Hexamethyl disiloxane

wets the wall of the capillary, the liquid surface is thereby constrained to lie parallel with the wall, and the complete surface must be concave in shape, as shown in Fig. 2.3. The driving force for infiltration, ΔP , is a direct function of the surface tension of the liquid, γ_{LV} , and inversely related to the effective radius of the capillary, r_c

$$\Delta P = \Delta \rho g h = \frac{2\gamma_{LV} \cos \theta}{r_c} \quad (2.7)$$

where $\Delta \rho$ is the difference in density between the liquid and gas phases, g the acceleration due to gravity, and h the height of the meniscus above the flat liquid surface for which ΔP must be zero. Again it is clear that the contact angle is one of the most important parameters controlling the capillary forces that are present only when $\theta < 90^\circ$.

The surface free energies of the separate phases may also be considered in terms of distinctive additive components

$$\gamma = \gamma^d + \gamma^p \quad (2.8)$$

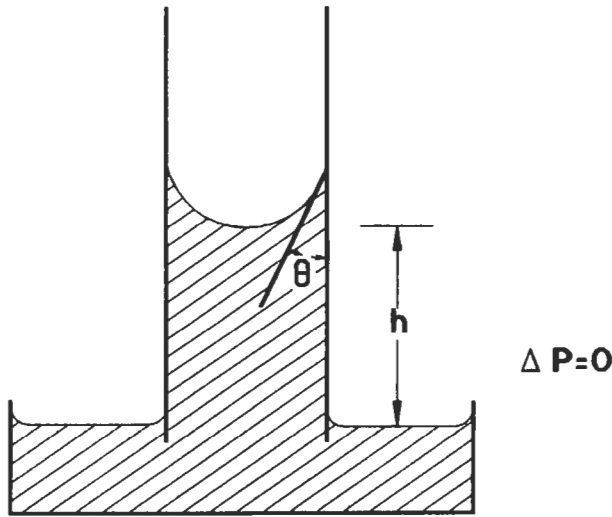


Fig. 2.3. Capillary rise, showing the contact angle, θ , and height of meniscus, h .

where γ^d represents the contribution due to London dispersion forces, which are common to all materials, and γ^p relates to the polar contribution largely consisting of hydrogen bonding and dipole-dipole interactions. When there is negligible adsorption of the liquid-vapor phase onto the solid surface (i.e. $\gamma_{SV} = \gamma_s$) and a liquid adsorbs its own (i.e. $\gamma_{LV} = \gamma_L$), the surface tension at the solid/liquid interface is given by (Owen and Wendt, 1969)

$$\gamma_{SL} = \gamma_L + \gamma_S - (\gamma_S^d \gamma_L^d)^{1/2} - (\gamma_S^p \gamma_L^p)^{1/2} \quad (2.9)$$

The above equation can be used to determine the total surface tension of a low energy solid from a single contact angle measurement (Neumann et al., 1974). If the liquid is chemically inert with respect to the solid

$$\gamma_{SL} = \frac{[(\gamma_{SV})^{1/2} - (\gamma_{LV})^{1/2}]^2}{[1 - 0.015(\gamma_{SV}\gamma_{LV})^{1/2}]} \quad (2.10)$$

Combining Eq. (2.10) with Eq. (2.2) leads to

$$\cos \theta = \frac{(0.015\gamma_{SV} - 2)(\gamma_{SV}\gamma_{LV})^{1/2} + \gamma_{LV}}{\gamma_{LV}[0.015(\gamma_{SV}\gamma_{LV})^{1/2} - 1]} \quad (2.11)$$

from which γ_{SV} can be derived for different values of the contact angle obtained for a liquid of given γ_{LV} (Neumann et al., 1980).

2.2.2. Interdiffusion

A bond between two surfaces may be formed by the interdiffusion of atoms or molecules across the interface. A fundamental feature of the interdiffusion mechanism is that there must exist a thermodynamic equilibrium between the two constituents. The bond strength in polymer matrix composites will depend on the amount of molecular entanglement, the number of molecules involved and the strength of the bonding between the molecules. Interdiffusion may be promoted by the presence of solvents and the amount of diffusion will depend on the molecular conformation, the constituents involved, and the ease of molecular motion. For example, bonding between glass fibers and polymer resins through silane coupling agents by a process other than chemical bonding can be explained by interdiffusion and the interpenetrating network (IPN) formation in the interface region (Plueddemann, 1974; Ishida and Koenig, 1978; Plueddemann and Stark, 1980) as illustrated in Fig. 2.4. A thin layer of epoxy matrix revealed on the fracture surface of the carbon fiber by using a scanning Auger microscope (Cazeneuve et al. 1990) is concrete evidence of interdiffusion.

The interface region thus formed has a substantial thickness, and its chemical, physical and mechanical properties are different from those of either the bulk fiber and the matrix (i.e., the interphase as opposed to the interface of zero thickness). The interphase is found to be significantly softer than the bulk matrix material in polymer matrix composites (Williams et al., 1990; Tsai et al., 1990). For example,

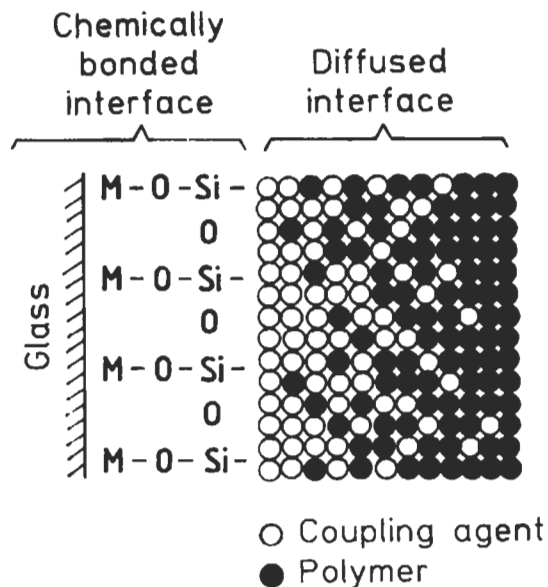


Fig. 2.4. A schematic model for interdiffusion and IPN in a silane-treated glass fiber-polymer matrix composite. After Plueddemann (1988).

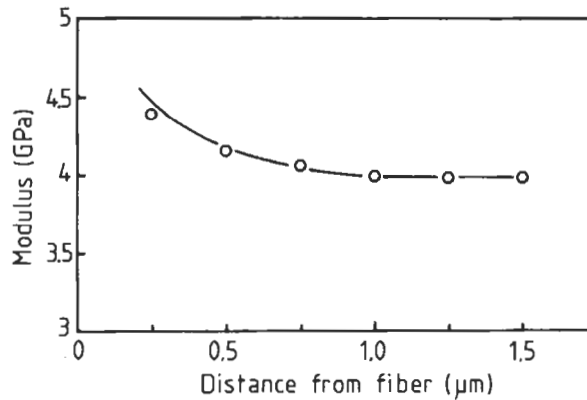


Fig. 2.5. Modulus data as a function of distance from the fiber surface of a carbon fiber–epoxy matrix composite which are measured from nanoindentation experiments. After Williams et al. (1990).

the average modulus of the interphase of a thickness of approximately 500 nm formed between a single carbon fiber and epoxy matrix is about one-quarter of that in the bulk matrix. However, the presence of a stiff fiber mitigates the effect of a soft interphase, increasing the effective modulus of the interphase beyond that of the bulk matrix in close vicinity of the fiber (Garton and Daly, 1985; Thomason 1990; Tsai et al., 1990; Williams et al., 1990). Fig. 2.5 shows typical Young's modulus data obtained from nanoindentation experiments on a carbon fiber–epoxy system where the Young's modulus of the bulk matrix material is 3.8 GPa.

In MMCs, interdiffusion also plays an important role in promoting reaction between elements of each constituent at the interface region. The special type of interdiffusion that takes place in conjunction with chemical reaction in MMCs is called an exchange reaction, which is described in Section 2.2.5. However, interdiffusion in MMCs may not be always beneficial because undesirable compounds are often formed, particularly when the oxide films present on the fibers are completely disrupted under extremely high temperature and pressure in a solid state process (Metcalf, 1974). To prevent or at least reduce the interaction, it is necessary to apply an effective diffusion barrier in the form of a coating on the fiber, or alloying elements in the matrix, to be discussed in Chapter 5. The selection of an appropriate diffusion barrier relies on a detailed knowledge of the nature of the interaction taking place at the interface region, which is specific to each fiber–matrix system.

2.2.3. Electrostatic attraction

A difference in electrostatic charge between constituents at the interface may contribute to the force of attraction bonding. The strength of the interface will depend on the charge density. Although this attraction is unlikely to make a major contribution to the final bond strength of the interface, it could be important when the fiber surface is treated with some coupling agent. This type of bonding will explain why silane finishes are especially effective for certain acidic or neutral

reinforcements like glass, silica, and alumina, but are less effective with alkaline surfaces like magnesium, asbestos, and calcium carbonate (Plueddemann, 1974).

2.2.4. Chemical bonding

Chemical bonding is the oldest and best known of all bonding theories. Physical adsorption mechanisms discussed in Section 2.2.2 depend on van der Waal forces or the acid-based interaction, while chemical bonding mechanism is based on the primary bond at the interface. A chemical reaction at the interface is of particular interest in the study of polymer matrix composites because it offers a major explanation for the use of silane coupling agents on glass fibers embedded in thermoset and amorphous thermoplastic matrices. Surface oxidative treatments of carbon fibers have been known for many years to promote chemical bonding with many different polymer resins. Recent work (Buxton and Baillie, 1995) has shown that the adhesion is a two-part process: the first part is the removal of a weak layer of a graphitic-like structure from the fiber surface particularly at low levels of treatment; and the second part is chemical bonding at the acidic sites. However, much further work is still needed to verify this hypothesis.

In this mechanism of adhesion, a bond is formed between a chemical group on the fiber surface and another compatible chemical group in the matrix, the formation of which results from usual thermally activated chemical reactions. For example, a silane group in an aqueous solution of a silane coupling agent reacts with a hydroxyl group of the glass fiber surface, while a group like vinyl on the other end will react with the epoxide group in the matrix. The chemical compositions of the bulk fiber and of the surface for several widely used fiber systems are given in Table 2.2. It is interesting to note that except for glass fibers, the chemical composition of the surface does not resemble that of the bulk fiber, and oxygen is common to all fiber surfaces. Further details regarding the types of surface treatments commonly applied to a variety of organic and inorganic fibers and their effects on the properties of the interfaces and bulk composites are given in Chapter 5.

2.2.5. Reaction bonding

Other than in polymer matrix composites, the chemical reaction between elements of constituents takes place in different ways. Reaction occurs to form a new compound(s) at the interface region in MMCs, particularly those manufactured by a molten metal infiltration process. Reaction involves transfer of atoms from one or both of the constituents to the reaction site near the interface and these transfer processes are diffusion controlled. Depending on the composite constituents, the atoms of the fiber surface diffuse through the reaction site, (for example, in the boron fiber–titanium matrix system, this causes a significant volume contraction due to void formation in the center of the fiber or at the fiber–compound interface (Blackburn et al., 1966)), or the matrix atoms diffuse through the reaction product. Continued reaction to form a new compound at the interface region is generally harmful to the mechanical properties of composites.

Table 2.2
Elemental composition of fibers^a

Fiber	Bulk	Surface analysis	Probable functional group
E-glass	Si, O, Al, Ca, Mg, B, F, Fe, Na	S, O, Al	-Si-OH, -Si-O-Si
Carbon	C, O, N, H, metal impurities	C, O, H	-COOH, C-OH, C=O
Boron (B/W core)	W ₂ B ₅ , WB ₄ (inner core), B (outer core)	B ₂ O ₃ as methyl borate	B-OH, B-O-B
Silicon carbide (SiC/W core)	Si, W (inner core), C (outer core), O, N	Si, C	Si-O-Si, Si-OH

^aAfter Sclar (1974)

Special cases of reaction bonding include the exchange reaction bond and the oxide bond. The exchange reaction bond occurs when a second element in the constituents begins to exchange lattice sites with the elements in the reaction product in thermodynamic equilibrium (Rudy, 1969). A good example of an exchange reaction is one that takes place between a titanium-aluminum alloy with boron fibers. The boride compound is initially formed at the interface region in an early stage of the process composed of both elements. This is followed by an exchange reaction between the titanium in the matrix and the aluminum in the boride. The exchange reaction causes the composition of the matrix adjacent to the compound to suffer a loss of titanium, which is now embedded in the compound. This eventually slows down the overall reaction rate.

The oxide bond occurs between the oxide films present in the matching surfaces of fiber and matrix. The reaction bond makes a major contribution to the final bond strength of the interface for some MMCs, depending on the fiber-matrix combination (which determines the diffusivity of elements from one constituent to another) and the processing conditions (particularly temperature and exposure time). A general scheme for the classification of interfaces in MMCs can be made based on the chemical reaction occurring between fiber and matrix according to Metcalfe (1974). Table 2.3 gives examples of each type. In class I, the fiber and matrix are mutually non-reactive and insoluble with each other; in class II, the fiber and matrix are mutually non-reactive but soluble in each other; and in class III, the fiber and matrix react to form compound(s) at the interface. There are no clear-cut definitions between the different classes, but the grouping provides a systematic division to evaluate their characteristics. For pseudoclass I composites that include B-Al, stainless steel-Al and SiC-Al systems, hardly any interaction occurs in solid state diffusion bonding, but a reaction does occur when the Al matrix is melted for liquid infiltration.

In general, in most CMCs, chemical reaction hardly occurs between fiber (or whisker) and matrix. However, an extremely thin amorphous film can be formed,

Table 2.3
Classification of fiber-metal matrix composite systems^a

Class I	Class II	Class III
W-Cu	W-Cu(Cr) eutectics	W-Cu(Ti)
Al ₂ O ₃ -Cu	W-Nb	C-Al (> 700 °C)
Al ₂ O ₃ -Ag	C-Ni	Al ₂ O ₃ -Ti
BN coated B	W-Ni	B-Ti
B-Mg		SiC-Ti
B-Al		SiO ₂ -Al
Stainless steel-Al		
SiC-Al		

^aAfter Metcalfe (1974)

originating from the oxide present on the fiber surface, due to the limited fiber-matrix reaction, e.g., between alumina whisker and zirconia matrix (Becher and Tiegs, 1987), or resulting from the decomposition of the metastable SiC fibers in SiC matrix (Naslain, 1993). The reaction compound thereby formed normally has a low fracture energy and is soft compared to the fiber or matrix. It acts as a compliant layer for the relaxation of residual thermal stresses and promotes longitudinal splitting along the fiber length.

2.2.6. Mechanical bonding

Mechanical bonds involve solely mechanical interlocking at the fiber surface. Mechanical anchoring promoted by surface oxidation treatments, which produce a large number of pits, corrugations and large surface area of the carbon fiber, is known to be a significant mechanism of bonding in carbon fiber-polymer matrix composites (see Chapter 5). The strength of this type of interface is unlikely to be very high in transverse tension unless there are a large number of re-entrant angles on the fiber surface, but the strength in longitudinal shear may be significant depending on the degree of roughness.

In addition to the simple geometrical aspects of mechanical bonding, there are many different types of internal stresses present in composite materials that arise from shrinkage of the matrix material and the differential thermal expansion between fiber and matrix upon cooling from the processing temperature. Among these stresses, the residual clamping stress acting normal to the fiber direction renders a synergistic benefit on top of the mechanical anchoring discussed above. These mechanisms provide major bonding at the interface of many CMCs and play a decisive role in controlling their fracture resistance and R-curve behavior. Further details of these residual stresses are discussed in Chapter 7.

2.3. Physico-chemical characterization of interfaces

2.3.1. Introduction

Composite interfaces exist in a variety of forms of differing materials. A convenient way to characterize composite interfaces embedded within the bulk material is to analyze the surfaces of the composite constituents before they are combined together, or the surfaces created by fracture. Surface layers represent only a small portion of the total volume of bulk material. The structure and composition of the local surface often differ from the bulk material, yet they can provide critical information in predicting the overall properties and performance. The basic unknown parameters in physico-chemical surface analysis are the chemical composition, depth, purity and the distribution of specific constituents and their atomic/microscopic structures, which constitute the interfaces. Many factors such as process variables, contaminants, surface treatments and exposure to environmental conditions must be considered in the analysis.

When a solid surface is irradiated with a beam of photons, electrons or ions, species are generated in various combinations. An analytical method for surface characterization consists of using a particular type of probe beam and detecting a particular type of generated species. In spectroscopy, the intensity or efficiency of the phenomenon of species generation is studied as a function of the energy of the species generated at a constant probe beam energy, or vice versa. Most spectroscopic techniques are capable of analyzing surface composition, and some also allow an estimation of the chemical state of the atoms. However, it may be difficult to isolate the contributions of each surface layer of the material being probed to these properties. Since most surface analysis techniques probe only the top dozen atomic layers, it is important not to contaminate this region. For this reason and particularly to reduce gas adsorption, a vacuum always has to be used in conjunction with these techniques. The emergence of ultrahigh vacuum systems of less than 10^{-6} Pa (or 7.5×10^{-9} Torr), due to rapid technological advances in recent years, has accelerated the development of sophisticated techniques utilizing electrons, atoms and ions. Amongst the currently available characterization techniques, the most useful ones for composite interfaces are: infrared (IR) and Fourier transform infrared (FTIR) spectroscopy, laser Raman spectroscopy, X-ray photoelectron spectroscopy (XPS), Auger electron spectroscopy (AES), secondary ion mass spectroscopy (SIMS), ion scattering spectroscopy (ISS), solid state nuclear magnetic resonance (NMR) spectroscopy, wide-angle X-ray scattering (WAXS), small-angle X-ray scattering (SAXS) and the measurement of the contact angle. A selected list of these techniques is presented in Table 2.4 along with their atomic processes and the information they provide. Each technique has its own complexity, definite applications and limitations. Often the information sought cannot be provided by a single technique. This has resulted in the design of equipment that utilizes two or more techniques and obtains different sets of data from the same surface of the sample (e.g. ISS/SIMS two-in-one and XPS/AES/SIMS three-in-one equipment). Adamson (1982), Lee (1989), Castle and Watts (1988) and Ishida (1994)

have presented excellent reviews of most of these techniques, with Ishida (1994) being particularly informative for characterization of composite materials.

In addition to surface analytical techniques, microscopy, such as scanning electron microscopy (SEM), transmission electron microscopy (TEM), scanning tunneling microscopy (STM) and atomic force microscopy (AFM), also provide invaluable information regarding the surface morphology, physico-chemical interaction at the fiber–matrix interface region, surface depth profile and concentration of elements. It is beyond the scope of this book to present details of all these microscopic techniques.

2.3.2. Infrared and Fourier transform infrared spectroscopy

IR spectroscopy, one of the few surface analytical techniques not requiring a vacuum, provides a large amount of molecular information. The absorption versus frequency characteristics are obtained when a beam of IR radiation is transmitted through a specimen. IR is absorbed when a dipole vibrates naturally at the same frequency as the absorber, and the pattern of vibration is unique for a given molecule. Therefore, the components or groups of atoms that are absorbed into the IR at specific frequencies can be determined, allowing identification of the molecular structure.

The FTIR technique uses a moving mirror in an interferometer to produce an optical transformation of the IR signal as shown in Fig. 2.6. During this operation, the source radiation is split into two: one half is reflected into the fixed mirror and the other half transmitted to the moving mirror. If the mirrors are placed equidistant from the beam splitter, their beams will be in phase and reinforce each other. In contrast, the beams that are out of phase interfere destructively. An interferogram is produced from the equations involving the wavelength of the radiation, and a Fourier analysis is conducted to determine the relation between the intensity and frequency. FTIR can be used to analyze gases, liquids and solids with minimal preparation and little time. This technique has been extensively applied to the study

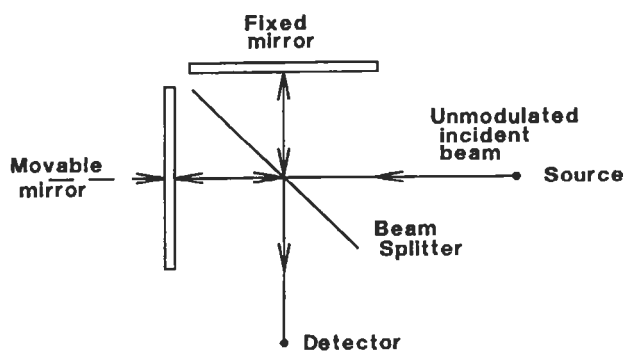


Fig. 2.6. Schematic diagram of an interferometry used in the FTIR spectroscopy. After Lee (1989).

Table 2.4
Techniques for studying surface structures and composition^a

Technique	Atomic process and type of information
<i>Microscopy</i>	
Scanning electron microscopy (SEM)	An analytical SEM consists of electron optics, comprehensive signal detection facilities, and a high-vacuum environment. When the primary electron beam is targeted at the specimen, a portion of the electrons is backscattered from the upper surface of the specimen. The electrons in the specimen can also be excited and emitted from the upper surface which are called secondary electrons. Both backscattered and secondary electrons carry the morphological information from the specimen surface. The microscope collects these electrons and transmits the signals to a cathode ray tube where the signals are scanned synchronously, providing morphological information on the specimen surface. Environmental SEMs are a special type of SEM that work under controlled environmental conditions and require no conductive coating on the specimen with the pressure in the sample chamber only 1 or 2 orders magnitude lower than the atmosphere.
Transmission electron microscopy (TEM)	TEM is composed of comprehensive electron optics, a projection system, and a high-vacuum environment. When a portion of high voltage primary electrons is transmitted through an ultrathin sample, they can be unscattered and scattered to carry the microstructural information of the specimen. The microscopes collect the electrons with a comprehensive detection system and project the microstructural images onto a fluorescent screen. The ultimate voltage for a TEM can generally be from 10 to 1000 keV, depending on the requirement of resolving power and specimen thickness.
Scanning tunneling microscopy (STM)	The STM, like other scanning probe microscopes, relies on the scanning of a sharp tip over a sample surface. When the tip and sample are very close so that the electron clouds of tip and sample atoms overlap, a tunneling current can be established through voltage differences applied between the two electrodes. When a raster scan is made, the relative height coordinate z as a function of the raster coordinate x and y reflects the surface topography of the sample. The STM is limited to conducting materials as it is based on the flow of electrons.
Atomic force microscopy (AFM)	In AFM, a sharp tip integrated with a soft spring (cantilever) deflects as a result of the local interaction forces present between the apex of the tip and the sample. The deflection of this cantilever can be monitored at its rear by a distance sensor. The forces existing between tip and sample, when they are close, can be van der Waals, electrostatic or magnetic force. Atomic-scale friction, elasticity and surface forces can also be measured. AFM can be employed for both conductive and non-conductive specimens, without having to apply a high vacuum, presenting a major advantage over STM.

Table 2.4 (Contd.)

Technique	Atomic process and type of information
<i>Spectroscopy</i> Auger electron spectroscopy (AES)	The sample surface is bombarded with an incident high energy electron beam, and the action of this beam produces electron changes in the target atoms; the net result is the ejection of Auger electrons, which are the characteristics of the element. Because of the small depth and small spot size of analysis, this process is most often used for chemical analysis of microscopic surface features.
X-ray photoelectron spectroscopy (XPS)	When a sample maintained in a high vacuum is irradiated with soft X-rays, photoionization occurs, and the kinetic energy of the ejected photoelectrons is measured. Output data and information related to the number of electrons that are detected as a function of energy are generated. Interaction of the soft X-ray photon with sample surface results in ionization from the core and valence electron energy levels of the surface elements.
Secondary ion mass spectroscopy (SIMS)	The sample surface is bombarded with a beam of around 1 keV ions of some gas such as argon and neon. The action of the beam sputters atoms from the surface in the form of secondary ions, which are detected and analyzed to produce a characterization of the elemental nature of the surface. The depth of the analysis is usually less than a nanometer, making this process the most suitable for analyzing extremely thin films.
Ion scattering spectroscopy (ISS)	In ISS, like in SIMS, gas ions such as helium or neon are bombarded on the sample surface at a fixed angle of incident. The ISS spectrum normally consists of a single peak of backscattered inelastic ion intensity at an energy loss that is characteristic of the mass of surface atom. From the pattern of scattered ion yield versus the primary ion energy, information about elements present on the sample surface can be obtained at ppm level.
Infrared (IR) and Fourier transform infrared (FTIR) spectroscopy	The absorption versus frequency characteristics are obtained when a beam of IR radiation is transmitted through a specimen. The absorption or emission of radiation is related to changes in the energy states of the material interacting with the radiation. In the IR region (between 800 nm and 250 μm in wavelength), absorption causes changes in rotational or vibrational energy states. The components or groups of atoms that absorb in the IR at specific frequencies are determined, providing information about the molecular structure. The FTIR technique employs a moving mirror to produce an optical transformation of the IR signal, with the beam intensity after the interferometer becoming sinusoidal. FTIR has been extensively used for the study of adsorption on polymer surfaces, chemical modification and irradiation of polymers on the fibersurfaces.
Raman spectroscopy (RS)	The collision between a photon of energy and a molecule results in two different types of light scattering: the first is Rayleigh scattering and the second is Raman scattering. The Raman effect is an inelastic collision where the photon gains energy from or loses energy to the molecule that corresponds to the vibrational energy of the molecule. Surface-enhanced Raman spectroscopy has been successfully used to obtain information about adsorption of polymers onto metal surfaces, polymer-polymer interaction and interdiffusion, surface segregation, stress transfer at the fiber-matrix interface, and surface structure of materials.

Table 2.4 (Contd.)

Technique	Atomic process and type of information
Nuclear magnetic resonance (NMR) spectroscopy	In NMR technique, a sample is placed in a magnetic field which forces the nuclei into alignment. When the sample is bombarded with radiowaves, they are absorbed by the nuclei. The nuclei topple out of alignment with the magnetic field. By measuring the specific radiofrequencies that are emitted by the nuclei and the rate at which the realignment occurs, the spectroscopist can obtain the information on molecular structure.

^aAfter Adamson (1982), Lee (1989) and Ishida (1994)

of adsorption on surfaces of polymers (Lee, 1991) and of chemical modification and irradiation of polymers on the fiber surfaces, including silane treated glass fibers (Ishida and Koenig, 1980; Garton and Daly, 1985; Grap et al., 1985; Miller and Ishida, 1986; Liao, 1989; DeLong et al., 1990). Fig. 2.7 shows typical IR spectra of glass fiber-epoxy matrix composites with and without an amino silane coating on the fiber.

2.3.3. Laser Raman spectroscopy

Laser Raman spectroscopy uses a light scattering process where a specimen is irradiated monochromatically with a laser. The visible light that has passed into the specimen causes the photons of the same wavelength to be scattered elastically, while

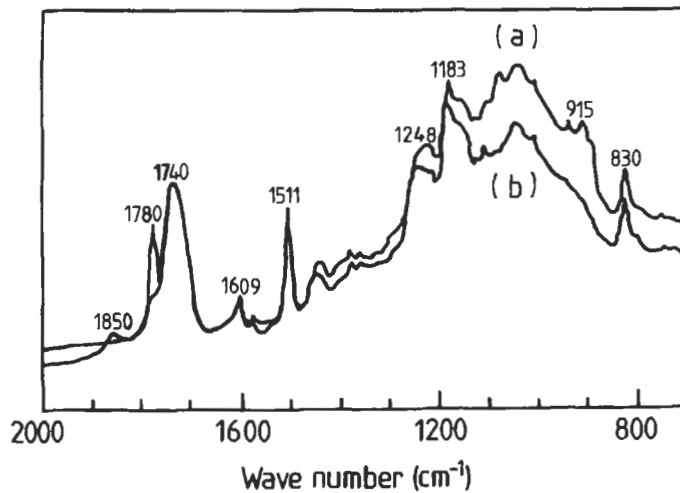


Fig. 2.7. Spectra of a glass fiber-epoxy matrix composite (a) before and (b) after hydrolysis. After Liao (1989).

it causes the light of slightly longer or shorter wavelengths to be scattered inelastically. The inelastic proportion of the photons imparts energy to the molecules, which are collected for analysis. An interesting feature of the Raman spectroscopy is that certain functional groups or elements scatter incident radiation at characteristic frequency shifts. The vibrational frequency of the group or element is the amount of shift from the exciting radiation. Functional groups with high polarizability on vibration can be best analyzed with Raman spectroscopy.

Raman and IR spectroscopies are complementary to each other because of their different selection rules. Raman scattering occurs when the electric field of light induces a dipole moment by changing the polarizability of the molecules. In Raman spectroscopy the intensity of a band is linearly related to the concentration of the species. IR spectroscopy, on the other hand, requires an intrinsic dipole moment to exist for charge with molecular vibration. The concentration of the absorbing species is proportional to the logarithm of the ratio of the incident and transmitted intensities in the latter technique.

As the laser beam can be focused to a small diameter, the Raman technique can be used to analyze materials as small as one micron in diameter. This technique has been often used with high performance fibers for composite applications in recent years. This technique is proven to be a powerful tool to probe the deformation behavior of high molecular polymer fibers (e.g. aramid and polyphenylene benzobisthiazole (PBT) fibers) at the molecular level (Robinson et al., 1986; Day et al., 1987). This work stems from the principle established earlier by Tuinstra and Koenig (1970) that the peak frequencies of the Raman-active bands of certain fibers are sensitive to the level of applied stress or strain. The rate of frequency shift is found to be proportional to the fiber modulus, which is a direct reflection of the high degree of stress experienced by the longitudinally oriented polymer chains in the stiff fibers.

In the case of carbon fibers, two bands are obtained: a strong band at about 1580 cm^{-1} and a weak band at about 1360 cm^{-1} , which correspond to the E_{2g} and A_{1g} modes of graphite (Tuinstra and Koenig, 1970). The intensity of the Raman-active band, A_{1g} mode, increases with decreasing crystalline size (Robinson et al., 1987), indicating that the strain-induced shifts are due to the deformation of crystallites close to the surfaces of the fibers. The ratio of the intensities of the two modes, $I(A_{1g})/I(E_{2g})$, has been used to give an indirect measure of the crystalline size in carbon fibers (Tuinstra and Koenig, 1970). Table 2.5 gives these ratios and the corresponding average crystal diameter, L_a , in the graphite plane, as determined by X-ray techniques. Typical examples of strain dependence of the Raman frequencies is shown in Fig. 2.8 for two different carbon fibers, and the corresponding plots of the shifted Raman frequency are plotted as a function of the applied strain in Fig. 2.9.

Enabled by the high resolution of spectra, which is enhanced by the use of spatial filter assembly having a small ($200\text{ }\mu\text{m}$) pin hole, the principle of the strain-induced band shift in Raman spectra has been further extended to the measurement of residual thermal shrinkage stresses in model composites (Young et al., 1989; Filiou et al., 1992). The strain mapping technique within the fibers is employed to study the

Table 2.5

Intensity ratio of Raman bands $I(A_{1g})/I(E_{2g})$ and the corresponding apparent crystal diameter, L_a , for various carbon fibers^a

Carbon fibers	$I(A_{1g})/I(E_{2g})$	L_a (Å)
Thornel 10 Union Carbide	0.85	50
Thornel 25	0.40	120
Thornel 50	0.29	155
Thornel 75	0.25	170
Thornel 40	0.30	150
Morganite I	0.22	200
Morganite II	0.83	50
H.M.G. 50 Hitco	0.56	80
Fortafil 5-Y Great Lakes	0.25	180

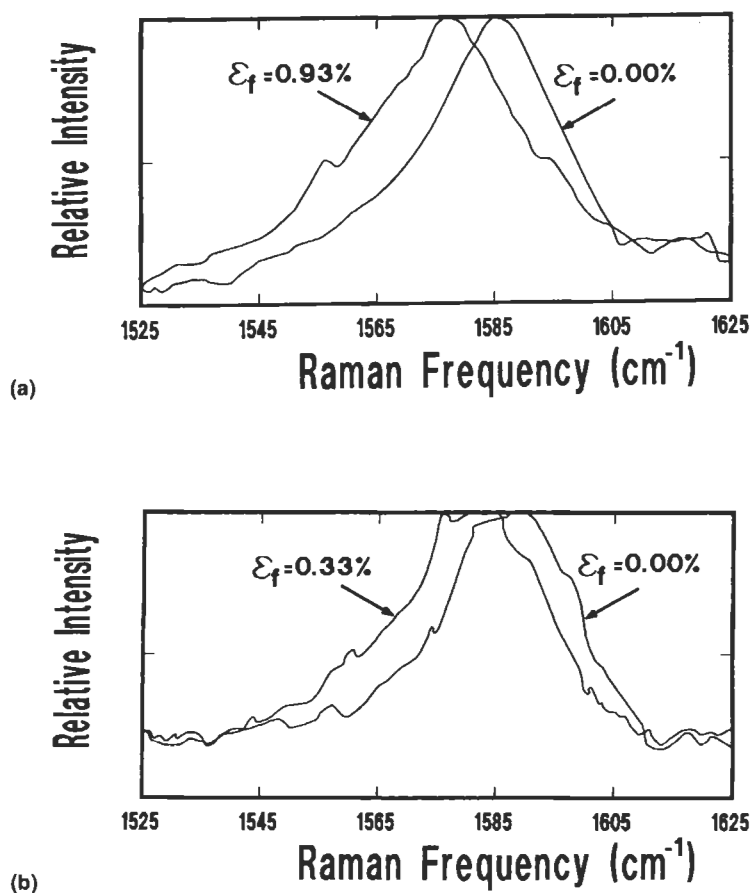


Fig. 2.8. Laser Raman spectra obtained (a) for a polyacrylonitrile (PAN)-based HMS4 carbon fiber, and (b) for a pitch-based P75S carbon fiber. After Robinson et al. (1987).

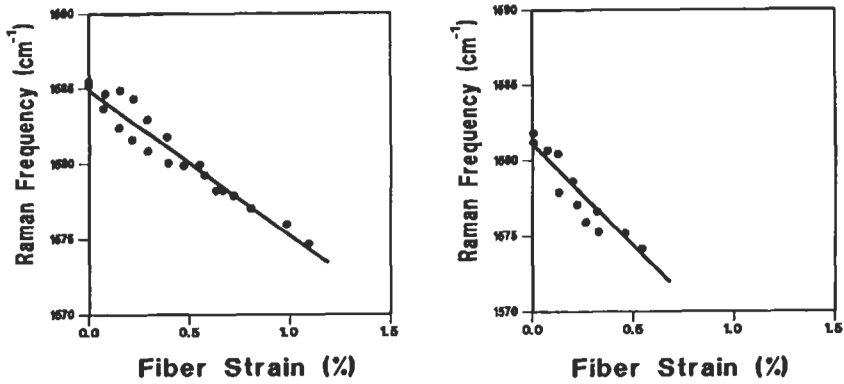


Fig. 2.9. Variation of the position of the 1580 cm^{-1} peak with fiber strain (a) for a polyacrylonitrile (PAN)-based HMS4 carbon fiber, and (b) for Thornel 50 carbon fiber. After Robinson et al. (1987).

stress transfer mechanisms across the fiber–matrix interface in the fiber fragmentation test geometry (Galiotis, 1993a). The variation of fiber axial strain and interface shear stress (IFSS) measured along the length of Kevlar 49 fiber embedded in an epoxy matrix is shown in Fig. 2.10 for different levels of applied strain. The IFSS is calculated based on the force balance between fiber axial direction and interface shear.

2.3.4. X-ray photoelectron spectroscopy

XPS, also known as electron spectroscopy for chemical analysis (ESCA), is a unique, non-destructive analytical technique that provides information regarding the chemical nature of the top 2–10 nm of the solid surface with outstanding sensitivity and resolution. In XPS, the solid surfaces are subjected to a beam of almost monochromatic X-ray radiation of known energy in a high vacuum environment (4×10^{-9} – 1×10^{-8} Torr). Electrons are emitted from the inner orbital with kinetic energies characteristic of the parent atoms. The intensities of the kinetic energy are analyzed and the characteristic binding energies are used to determine the chemical composition. The total absorbed X-ray photon energy, $h\nu$, is given by the sum of the kinetic energy, E_K , and the electron binding energy, E_B

$$h\nu = E_K + E_B \quad (2.12)$$

Once the kinetic energy is measured with an electron spectrometer for a given X-ray photon energy, the binding energy characteristic of the parent atoms can be directly determined. The electron binding energy represents the work expended to remove an electron from a core level of the inner orbital to the Fermi level in its removal from the atom. Peaks in the plots of electron intensity versus binding energy correspond to the core energy levels that are characteristic of a given element.

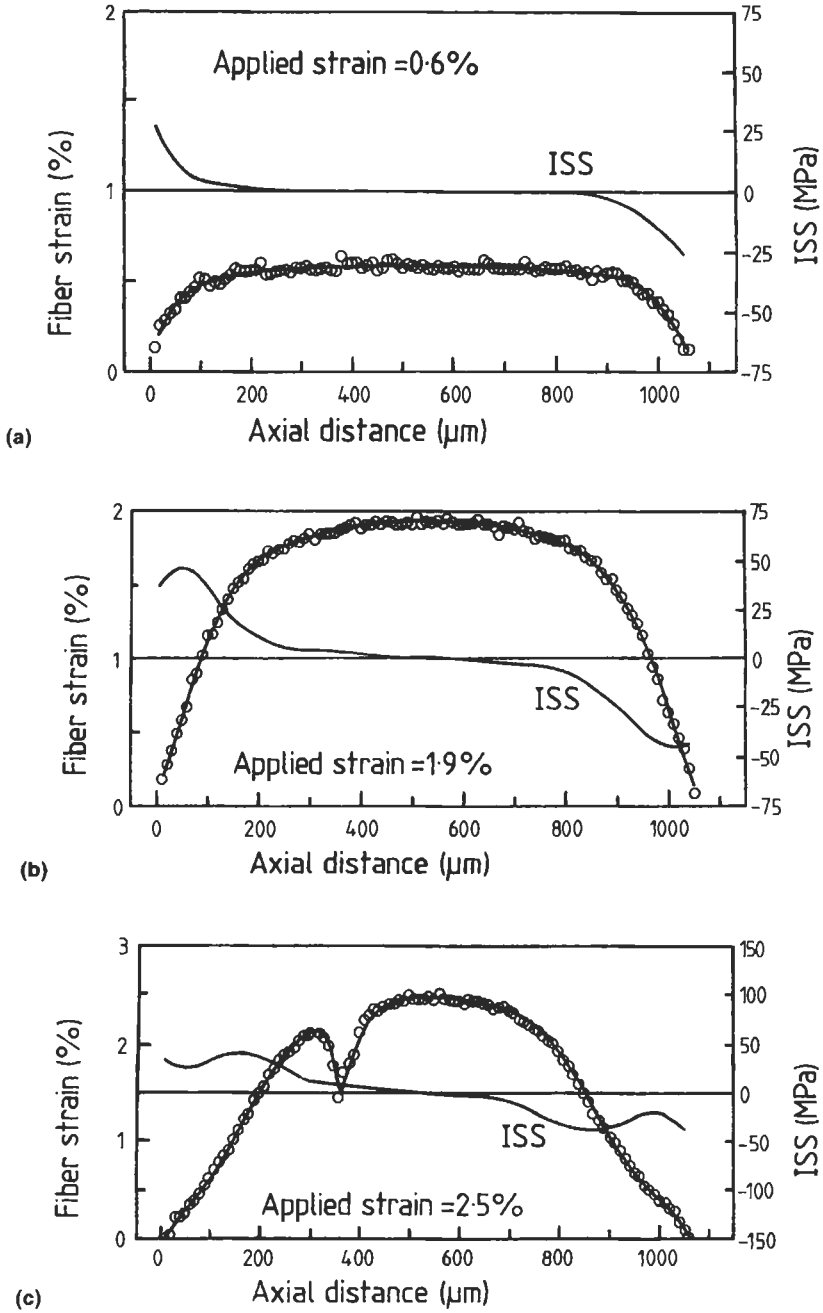


Fig. 2.10. Fiber strain and interfacial shear stress (IFSS) profiles along the fiber length for a heat-treated Kevlar 49 fiber-epoxy resin composite. At applied strains of (a) 0.60% (b) 1.90% and (c) 2.5%. After Galotis (1993a,b).

Table 2.6
XPS analysis, elemental composition of carbon fibers^a

Carbon fibers T300	C(%)	O(%)	N(%)	S(%)	Si(%)	Na(%)
Unsize	81.5	12.7	5.3	–	–	0.8
Sized	79.2	20.0	0.8	–	–	–

^aAfter Cazeneuve et al. (1990)

In XPS, only large areas can be analyzed because X-rays are difficult to focus with sufficient intensities on a small target area. Signals from small regions of a heterogeneous solid surface are usually weak and difficult to isolate. For these reasons, XPS is not well suited to depth profiling. One significant recent advance is the development of the X-ray monochromator, which collects some of the X-rays from a conventional source and refocuses them on the sample. This allows a small sample area to be illuminated and analyzed with X-rays, resulting in an increased ability to distinguish different chemical states. Another innovation is the addition of a parallel detection system, which has the ability to collect simultaneously all the points of a special range, substantially increasing the speed and sensitivity of the instrument. The conventional unit, which contains a single exit slit, is able to collect only a single point.

Applications of XPS for composite interface studies include the quantitative assessment of the local concentration of chemical elements and functional groups that are required to evaluate the contributions of chemical bonding at the fiber–matrix interface region in polymer matrix composites (Yip and Liu, 1990; Baillie et al., 1991; Nakahara et al., 1991; Shimizu et al., 1992; Kim et al., 1992; Wang and Jones, 1994). Fig. 2.11 shows examples of XPS spectra obtained for carbon fibers with and without surface sizing. The corresponding elemental compositions of these fibers are given in Table 2.6. The main difference between the sized and unsized carbon fibers is the quantity of nitrogen (i.e. 5.3% and 0.8% in unsized and sized fibers, respectively), which is considered to originate from the residue of a polyacrylonitrile (PAN) precursor or from the surface treatment at the end of the manufacturing process (Cazeneuve et al., 1990). To identify functional groups present on the fiber surface, the small chemical shifts are analyzed to obtain information of oxidation states and the overlapping peaks are deconvoluted (Kim et al., 1992). This means that the larger the chemical shifts the easier the identification of functional groups. However, certain functional groups can be difficult to distinguish, e.g. carboxylic acids, esters, alcohols, and aldehydes, which all contain a carbonyl oxygen and as a result have overlapping C_{1s} spectra.

2.3.5. Auger electron spectroscopy

AES is similar to XPS in its function, but it has unparalleled high sensitivity and spatial resolution (of approximately 30–50 nm). Both AES and XPS involve the identification of elements by measurement of ejected electron energies. Fig. 2.12

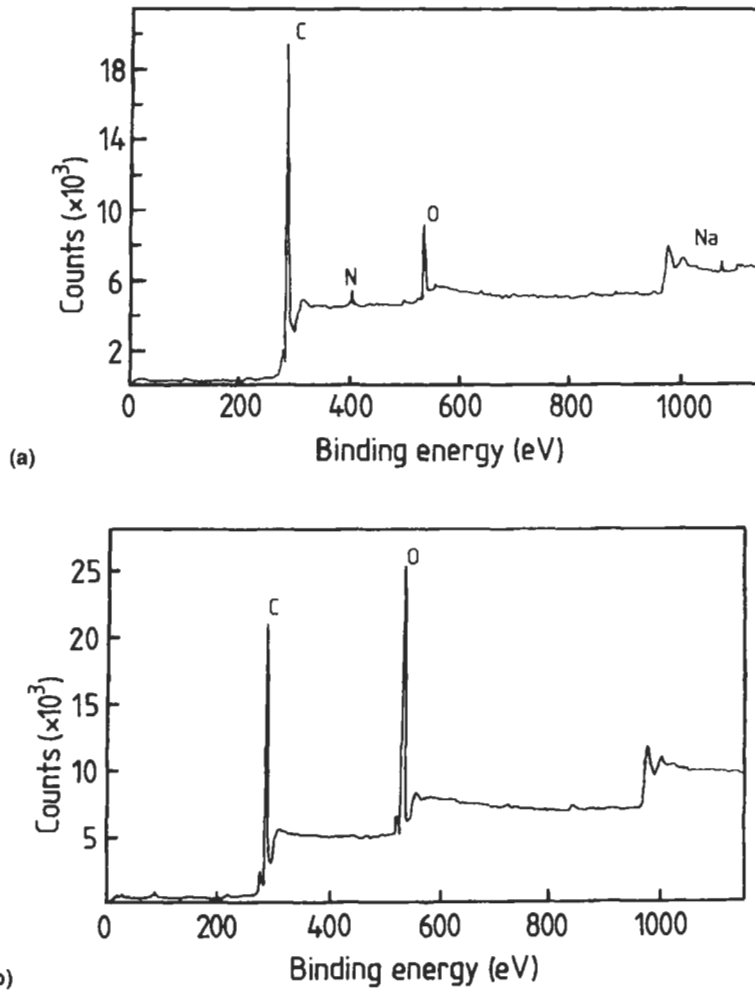


Fig. 2.11. Spectra of (a) unsized and (b) sized T300 carbon fibers which are obtained from XPS. After Cazeneuve et al. (1990).

compares the reactions in XPS, AES, SIMS and ISS, and the latter two techniques will be discussed in the following sections. In AES, it is possible to focus an electron beam laterally to identify features less than $0.5\mu\text{m}$ in diameter and into a monolayer in thickness. In addition, by simultaneous use of analytical and sputter etching, it may provide composition profiles. However, the AES electron beam is highly concentrated with high flux density and beam energy, which can damage the polymer surface causing pyrolysis during measurement. This makes it difficult to employ AES technique on a thin film. In this regard, XPS is a more delicate technique as the power required is an order of magnitude lower than in AES.

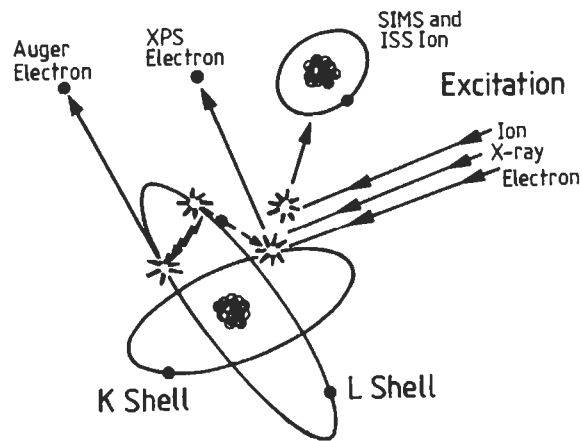


Fig. 2.12. A comparison of XPS, AES, SIMS and ISS reactions. After Lee (1989).

In AES, an energetic beam of electrons strikes the atoms of the sample in a vacuum and electrons with binding energies less than the incident beam energy may be ejected from the inner atomic level, creating a single ionized excited atom. This irradiation causes ejection of orbital electrons from the sample and the resulting excited atom either emits an X-ray (fluorescence) or an electron is ejected from the atom (Auger process). This vacancy is filled by de-excitation of electrons from other electron energy states. The energy released can be transferred to an electron in any atom. If this latter electron has a lower binding energy than the energy from the de-excitation, then it will be ejected with its energy related to the energy level of the separation in the atoms. Auger electrons are the result of de-excitation processes of these vacancies and electrons from other shells and re-emission of an electron to carry away excess energy. The electrons emitted have a short mean free path, and thus all Auger electrons are from the first few atomic surface layers. The kinetic energies of the free electrons are detected and they reflect the variations in binding energies of the levels involved in the process.

The Auger electron spectra shown in Fig. 2.13 contain peaks corresponding to the intensity of Auger electrons as a function of kinetic energy. These electrons are emitted following the creation of a core hole in the electron shells by radiation of an incident electron beam. The kinetic energy is independent of the energy of the incident beam, and the intensity of an Auger peak relates to the concentration of atoms or ions in the volume being analyzed. As in XPS, changes in chemical and oxidation states are reflected by the shifts in the peak position. Whether or not the chemical state can be recognized depends on the width of the Auger peak. A very wide peak cannot be used to provide information on the chemical state. The intensity of a peak or the peak area is a complex function of the angle of incidence and the current of the primary beam, the inelastic mean free path of the escaping electron, the local angle of the detected electrons, etc. It is essential to understand these factors to conduct proper composition analysis.

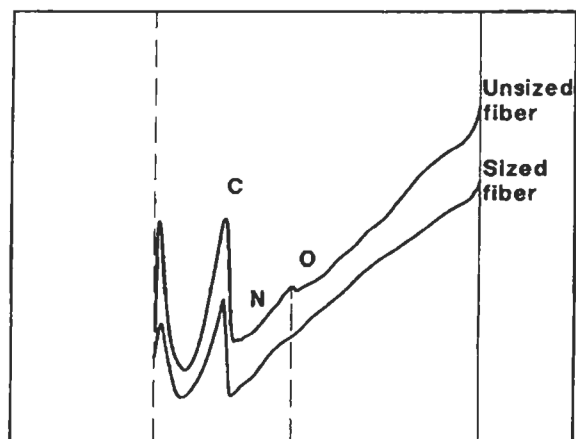


Fig. 2.13. Spectra of unsized and sized carbon fibers obtained from AES. After Cazeneuve et al. (1990).

Although this technique is not normally used for thin polymer films for the reasons described before, it can be used for analyzing the surface of polymer composites containing conductive fillers, e.g. carbon fibers. In addition, because of the surface specificity, the sampled area can be maintained almost identically to the beam cross-section so that the scanning Auger microscope (SAM) can have a spatial resolution that is much better than that of microprobe analysis.

2.3.6. Secondary ion mass spectroscopy

SIMS is a technique of direct mass analysis where the ion sputter is removed from the surface and, as a result of the ion bombardment, it is analyzed. By measuring both positive and negative ions, two different types of mass spectra are obtained. Positive SIMS is especially sensitive to low Z elements, which have low electronegativity and ionization potential, while the negative SIMS is most sensitive to low Z elements with high electronegativity. The SIMS spectrum shown in Fig. 2.14 (Denison et al., 1988a, b) as a function of mass number is typical of that obtained from a carbon fiber surface.

SIMS has the ability to detect an extremely small weight range (approximately 10^{-15} g), and can provide chemical information on polymers and composites by detection of ion fragments such as CH^+ , C_2H_2^+ , CN^+ , MOH^+ and MN , where M is another atom such as P , S , or metal atom. SIMS can analyze rapidly all elements and their isotopes without a problem of charge build-up due to its moderate energy beam of ions (about 1–20 keV). Spatial resolution (about 5 nm) of microfocused ion beams on an organic sample is comparable to those of XPS or AES without the need of an extremely high vacuum (7.5×10^{-6} Torr). SIMS also has a greater depth of resolution than that of the methods based on electron spectroscopy (e.g. AES and XPS), but in terms of quantitative use, SIMS still lags behind the other two

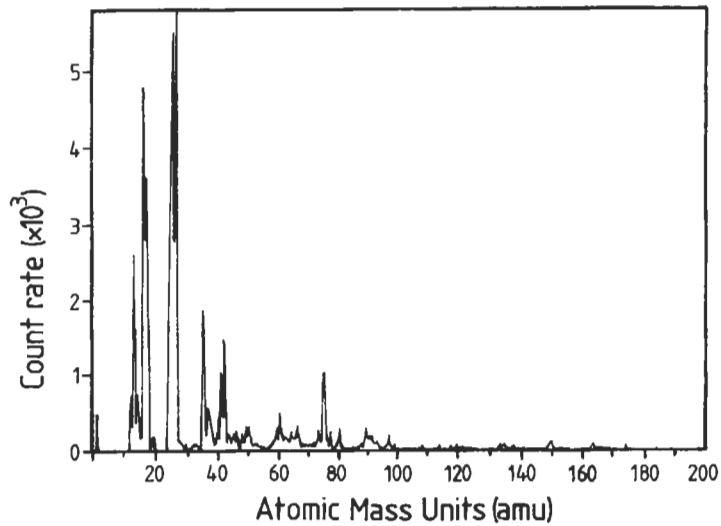


Fig. 2.14. A typical spectrum of a carbon fiber obtained from SIMS. After Denison et al. (1988a, b).

techniques by several years. There are two important features that make SIMS of particular value (Castle and Watts, 1988):

- (i) Hydrogen can be detected in the spectrum, a capability which is not possible in the other methods.
- (ii) Isotopes can be distinguished and thus the source of the material on the fiber surface can be discovered by using tracers. Therefore, it is possible to distinguish the oxygen derived from the atmosphere or matrix material from the oxygen incorporated during an oxidative treatment of carbon fibers.

2.3.7. Ion scattering spectroscopy

In ISS, a sample is bombarded with gas ions such as helium or neon at a fixed incident angle, as shown in Fig. 2.15, to obtain information about the atoms present in the top layer of the surface. The high sensitivity of ISS permits detection of elements at the ppm level. The ISS spectrum normally consists of a single peak of scattered ion intensity at an energy loss that is characteristic of the mass of the surface atom. Information regarding chemical bonding at the interface region can be generated from the yield pattern of scattered ions as a function of the primary ion energy.

The combined ISS/SIMS is an extremely useful surface analytical technique that can provide several types of data from the same surface. Both ISS and SIMS employ ion beams, and thereby both methods can utilize the same ion source for the surface probe, as schematically shown in Fig. 2.16. Addition of a specially designed ion lens and quadrupole mass spectrometer can make the whole system much more efficient. The value of information obtained from the combination of these two systems is

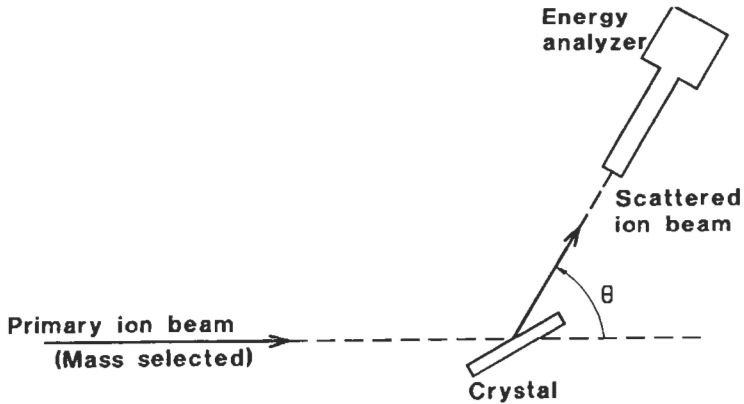


Fig. 2.15. Schematic diagram of ion scattering experiment.

further increased by yielding positive and negative ion mass spectra from elements as well as from molecular fragments. This combination uses energy analysis of backscattered beam ions, hydrogen detection and molecular ion identification by mass analysis of both negative and positive secondary sputtered ions. The ISS/SIMS technique is particularly useful for polymer matrix composites to determine the elemental distributions and the presence of F or Si originating from mold release agents.

2.3.8. Solid state nuclear magnetic resonance spectroscopy

Solid state NMR spectroscopy is used to determine molecular structures by analyzing the static and dynamic features of the material. In NMR experiments, both a magnetic field and a radio frequency field are applied to a solid sample or a solution resulting in an absorption of energy, which is detected as an NMR. Spectrometers are also available for high resolution solid state NMR. Nuclei in

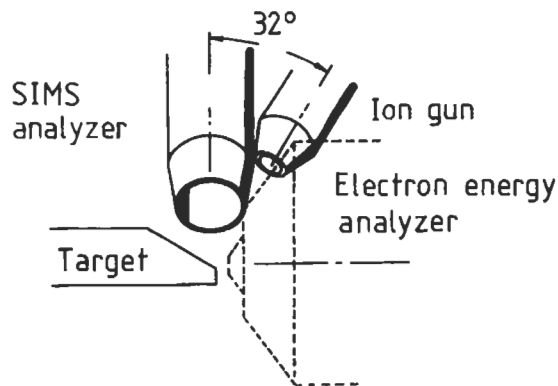


Fig. 2.16. A combination of SIMS and ISS. After Lee (1989).

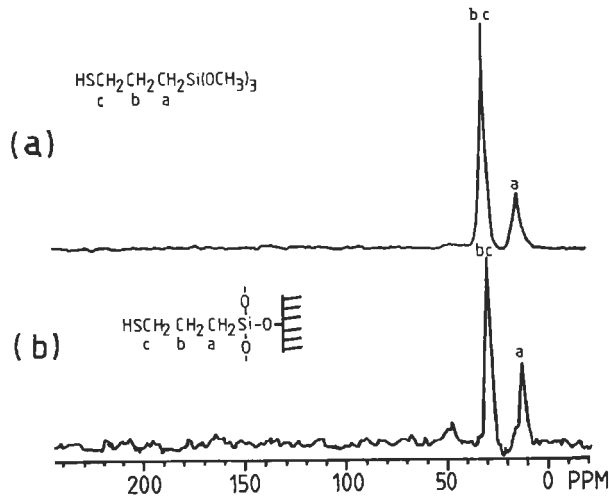


Fig. 2.17. NMR Spectra of (a) a polymerized coupling agent and (b) a coupling agent on a glass surface. After Zaper and Koenig (1985).

different chemical environments resonate at different frequencies and thus differ in their chemical shifts. Chemical shifts are used to assign these resonances to the specific structure of the sample. The nuclear environment of a nucleus results in multiple resonances that are also used to determine structural information. Recent development of high power proton decoupling cross-polarization and magic angle sample spinning (MAS) techniques have made it possible to study composite interfaces, in particular silane treated glass fiber interfaces (Zaper and Koenig, 1985; Drumm and Ulicny, 1989; Hoh et al., 1990), by using NMR spectroscopy. Fig. 2.17 shows a typical example of a NMR spectrum of a composite interface.

2.3.9. Wide-angle X-ray scattering

A technique for the characterization of polymer crystallinity as a bulk material or around the stiff fibers/particulates in composites is based on WAXS. The WAXS method is actually more of a bulk analytical tool than a surface technique, but it has been developed mainly for monitoring crystallinity in thermoplastics and fiber composites made therefrom.

Fig. 2.18 illustrates the nature of the intensity profiles in pure polyetheretherketone (PEEK) and carbon fiber reinforced PEEK composites in the transmission and reflection modes, respectively. The quenched amorphous and slowly cooled crystalline components from PEEK can be separated. The three prominent diffraction peaks from the crystalline components in Fig. 2.18(a) correspond to the three uniform rings which can be detected in X-ray photographs. In contrast, no clearly measurable signal is identified from the PEEK amorphous phase independent of the carbon fiber content.

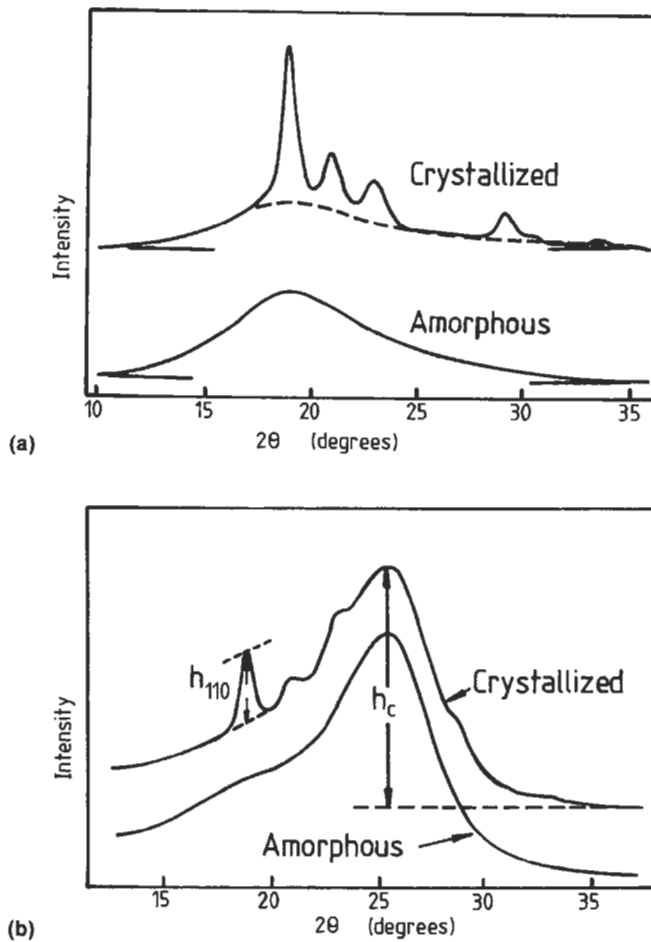


Fig. 2.18. (a) Transmission WAXS scans of pure PEEK sheets of thickness 1 mm; (b) reflection WAXS scans of carbon fiber-PEEK matrix composites. After Lee (1989).

2.3.10. Small-angle light scattering and small-angle X-ray scattering

Small-angle light scattering (SALS) is a technique developed to determine the morphological structures on a scale larger than the wave length 1–100 μm of the radiation used. Spherulites are structures of semicrystalline polymers that are in this size range. In SALS, a monochromatic, collimated and plane polarized laser beam is used to excite a thin polymer film. The scattered radiation is analyzed with a second polarizer, aligned with the first polarizer, and the scattering pattern is recorded on photographic film or by electron detectors. As light interacts with the polymer, there is polarization of the electronic charge distribution. The scattering of visible light is associated with variations in the anisotropy and reflective index or polarizability of

the specimen, which is influenced by the molecular structure. Therefore, the light scattering technique provides information about molecular structure and orientation. Typically, spherulite structures in crystalline polymers are characterized by complementary SALS and polarized light microscopy, where the scattering angle in the SALS pattern is used to determine the size of the spherulite. In a similar approach, SAXS can be used to characterize the structure and dimensions of rigid fillers or fibers in a thin polymer (Young et al., 1985).

2.3.11. Measurement of contact angle

2.3.11.1. Contact angle on a flat surface

Measurements of the contact angle are extremely useful for determining the wettability of a solid surface by a liquid. Various techniques for measuring the contact angle have been reviewed by Neumann and Good (1979) and Adamson (1982). The most commonly used method is to measure it directly from a drop of liquid resting on a flat surface of the solid, that is the 'sessile drop method', as shown in Fig. 2.19. Various techniques given in what follows can be employed in conjunction with this method to measure accurately the contact angle of a liquid droplet on a flat solid surface:

- (i) Through a comparator microscope filled with a goniometer scale.
- (ii) From photographs taken at an angle so that a portion of the liquid drop is reflected from the surface, the angle meeting the direct and reflected images then being twice the contact angle.
- (iii) A captive bubble method can be used wherein a bubble formed by manipulation of a micrometer syringe is made to contact the solid surface.
- (iv) From photographs of the bubble profile directly by means of a goniometer tele-microscope (Adamson et al., 1970). This technique has the advantages that it is easy to swell or shrink the bubble to obtain receding or advancing angles and adventitious contamination can be minimized.

In addition to the sessile drop method which measures the contact angle directly, Neumann and Renzow (1969) have developed the Wilhelmy slide technique to measure it to 0.1° precision. As shown in Fig. 2.20, the meniscus at a partially immersed plate rises to a finite length, h , if the contact angle, θ , is finite. θ is calculated from

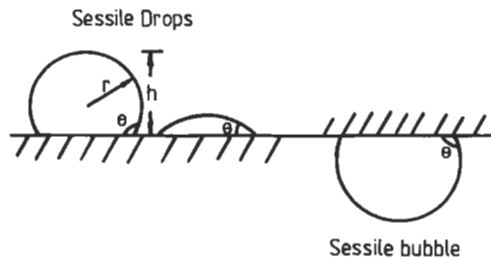


Fig. 2.19. Use of sessile drops or bubbles for the determination of contact angles. After Adamson (1982).

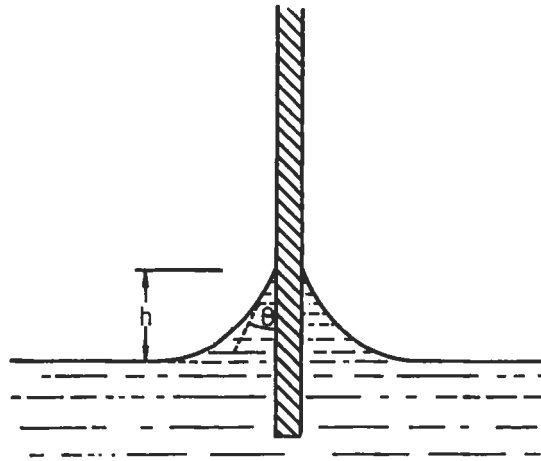


Fig. 2.20. Wilhelmy slide technique for contact angle measurement. After Adamson (1982).

$$\sin \theta = 1 - \frac{\rho g h^2}{2\gamma} = 1 - \left(\frac{h}{a}\right)^2, \quad (2.13)$$

where a is the capillarity constant. The termination of the meniscus is quite sharp under proper illumination (unless θ is small), and h can be measured by means of a traveling microscope.

2.3.11.2. Contact angle on a rough surface

The foregoing discussion considers the wetting of a smooth planar surface. The derivation for the contact angle equation given by Eq. (2.11) can be adapted in an empirical manner to the case of a non-uniform solid surface, whether the surface is rough (with a roughness index) or is a composite consisting of small patches of various kinds. Details of this subject have been reviewed by Adamson (1982) and a summary is given here.

Good (1952) showed that the surface roughness alone may change the advancing contact angle, θ_r , on a rough surface, compared with the contact angle, θ , on a smooth surface of identical surface chemistry. This change in the contact angle can be expressed by

$$\cos \theta_r = r_f \cos \theta \quad (2.14)$$

where r_f is the roughness factor, which is the ratio of actual to nominal surface areas of the solid. If θ is less than 90° , then roughening will result in a smaller θ_r on the chemically equivalent but rough surface. This will increase the apparent surface tension of the solid surface, γ_{SV} . In contrast, however, if for a smooth surface θ is greater than 90° , roughening the surface will increase θ_r still further, leading to a decrease in γ_{SV} .

2.3.11.3. Contact angle on a cylindrical surface

The techniques for measuring the contact angle of droplets on planar surfaces have been discussed above. The measurement of the contact angle for wettability of a cylindrical surface of the order of 10 μm in diameter as for advanced fibers requires a more sophisticated approach than is needed for a simple planar surface. A widely used method is based on the Wilhelmy balance method by use of gravimetry (Kaelble et al., 1974; Hammer and Drzal, 1980). The contact angle may be determined by measuring the force required to immerse or remove a single fiber from a liquid of known surface tension at constant velocity. Hammer and Drzal (1980) determined the polar and dispersive components of a small diameter graphite fiber by measuring the contact angle. A single fiber was immersed in a liquid and the force, F , exerted by the liquid on the fiber was measured with microbalance due to the wetting of the fiber. The force, F , is related to the surface tension of the liquid, γ_{LV} , by the equation

$$F = \gamma_{LV} \pi d \cos \theta \quad , \quad (2.15)$$

where d is the fiber diameter. The polar and dispersive components of the fiber surface tension, (γ_S^p and γ_S^d), are determined based on the following equation:

$$\frac{\gamma_{LV}(1 + \cos \theta)}{2(\gamma_L^d)^{1/2}} = (\gamma_S^d)^{1/2} + (\gamma_S^p)^{1/2} \left[\frac{\gamma_L^p}{\gamma_L^d} \right]^{1/2} \quad . \quad (2.16)$$

A plot of $\gamma_L (1 + \cos \theta)/2(\gamma_L^d)^{1/2}$ versus $(\gamma_L^p/\gamma_L^d)^{1/2}$ will yield a straight line with the slope and intercept providing a solution for the components γ_S^p and γ_S^d , respectively, for the fiber.

A simple and direct method of contact angle measurement has also been proposed (Yamaki and Katayama, 1975; Carroll, 1976) by observing the shape of the liquid droplet attached to a single fiber, the so-called 'droplet aspect ratio method'. The liquid is assumed to form a symmetrical droplet about the fiber axis as shown schematically in Fig. 2.21. Neglecting the effect of gravity, the droplet shape can be defined by the following expression:

$$L = 2[a F(\phi, \kappa) + n E(\phi, \kappa)] \quad , \quad (2.17)$$

where the parameters are:

$$L = \frac{\ell}{x_1} \quad , \quad (2.18)$$

$$n = \frac{x_2}{x_1} \quad , \quad (2.19)$$

$$a = \frac{x_2 \cos \theta - x_1}{x_2 - x_1 \cos \theta} \quad , \quad (2.20)$$

$$\kappa = \sqrt{1 - \left(\frac{a}{n}\right)^2}, \quad (2.21)$$

$$\Phi = \sin^{-1} \sqrt{\frac{n^2 - 1}{n^2 - a^2}}. \quad (2.22)$$

$F(\phi, \kappa)$ and $E(\phi, \kappa)$ are elliptical integrals of the first and second kind, respectively. n can be plotted versus L for a range of small values of contact angle, θ . By measuring the relative dimensions of the droplet, x_1 and x_2 , as illustrated in Fig. 2.21, θ can then be evaluated (Carroll, 1976).

Nardin and Ward (1987) successfully used this method to evaluate surface treatment for polyethylene fibers. A linear correlation was observed between the fiber γ_s measured by this method using a glycerol contact angle and the interfacial shear strength measured from fiber pull-out tests for chemically treated fibers. Wagner and coworkers (Wagner, 1990; Wagner et al., 1990) extended the droplet aspect-ratio method by introducing a computer program based on an initial estimate of θ , which allows the above equations to be solved iteratively, giving a more accurate value of θ .

Experimental evidence on composite materials has shown that the methods of contact angle measurement are useful in detecting changes in carbon fiber surface energy due to oxidative treatments, which can enhance the composite interlaminar shear strength (ILSS). The surface energy values increase with increasing surface concentrations of oxygen and nitrogen-containing groups, as determined from AES and corresponding ILSS of the composite laminates (Gilbert et al., 1990), as shown in Table 2.7. In a similar study, differences in wetting behavior of sized/unsized and surface treated/untreated carbon fiber immersed in a number of different thermoplastics (Weinberg, 1987) as well as in commercial silicon oil and epoxy resin (Lee et al., 1988) were observed by a wettability study. There is excellent correlation between the contact angle and composite transverse flexural strength for carbon fiber-PEEK matrix composites (Bucher and Hinkley, 1992).

In contrast to carbon fibers, no simple correlation has been reported between the work of adhesion to various polymer resins determined from the contact angle

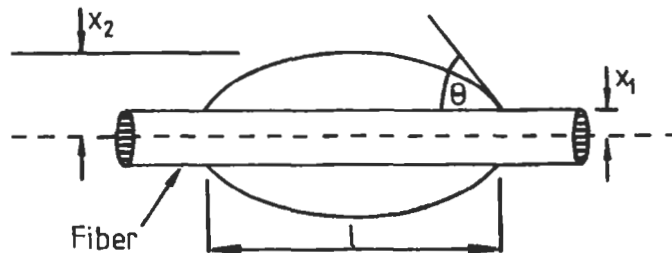


Fig. 2.21. A liquid droplet attached to a monofilament. Gilbert et al. (1990).

Table 2.7

Interlaminar shear strength (ILSS), AES atomic percent, contact angle, θ , and surface energy, γ_s , data for untreated and electrochemically oxidized pitch-based carbon fiber^a

Carbon fiber	ILSS ^b (MPa)	AES atomic % at the surface		θ ($^\circ$ /glycerol)	γ_{SV} (mJ/m ²)
		O	N		
LM untreated	58	2.4	0.5	57.8	40.6
PTC treated	72	5.7	3.2	42.3	49.4
IM untreated	39	1.5	0	57.2	41.1
PTC treated	56 ¹	6.9	3.4	35.4	53.0
HM untreated	36	2.9	0	62.4	38.3
PTC treated	52 ¹	9.3	2.4	43.0	48.9

^aAfter Gilbert et al. (1990).

^bCompression/tension failure in the short beam shear test.

measurement and the amount of silane coating applied to the glass fibers (Berger and Eckstein, 1984; Weinberg 1987). This is apparently because good wetting is not the primary mechanism for improved adhesion for these fibers. This also suggests that predictions about the work of adhesion should be limited to non-reactive systems, where no chemical bonds dominate the adhesion at the fiber–matrix interface.

References

- Adamson, A.W. (1982). In *Physical Chemistry of Surfaces*, 4th Edition, John Wiley and Sons, New York, pp. 294–318, 332–268.
- Adamson, A.W., Shirley, F.P. and Kunichika, K.T. (1970). Contact angle on molecular solids. *J. Colloid Interface Sci.* **34**, 461–468.
- Amateau, M.F. (1976). Progress in the development of graphite-Al composites using liquid infiltration technology. *J. Composite Mater.* **10**, 289–296.
- Baillie, C.A., Castle, J.E., Watts, J.F. and Bader, M.G. (1991). Chemical aspects of interface adhesion between electrolytically oxidised carbon fibers and epoxy resins. In *Proc. ICCM/8, Composites Design, Manufacture and Application*. (S.W. Tsai and G.S. Springer, eds.), SAMPE Pub. Paper 11E.
- Becher, P.F. and Tiegs, T.N. (1987). Toughening behavior involving multiple mechanisms: whisker reinforcement and zirconia toughening. *J. Am. Ceram. Soc.* **70**, 651–654.
- Berger, E.J. and Eckstein, Y. (1984). In *Adhesive Joints* (Mittal, K.L. ed.), Plenum Press, New York, p. 51.
- Blackburn, L.D., Herzog, J.A., Meyerer, W.J., Snide, J.A., Stuhrke, W.F. and Brisbane, A.W. (1966). MAMS internal study on metal matrix composites, MAM-TM-66-3.
- Bucher, R.A. and Hinkley, J.A. (1992). Fiber/matrix adhesion in graphite/peek composites. *J. Thermoplastic Composite Mater.* **5**, 2–13.
- Buxton, A and Baillie, C.A. (1995). Predicting the behavior of the carbon–fiber/epoxy interface under different service conditions. *Composite Interfaces* **3**, 411–423.
- Carroll, B.J. (1976). The accurate measurement of contact angle, phase contact areas, drop volume, and Laplace excess pressure in drop-on-fiber system. *J. Colloid. Interface Sci.* **57**, 488–495.
- Castle, J.E. and Watts, J.F. (1988). The study of interfaces in composite materials by surface analytical techniques. In *Interfaces in Polymer, Ceramic and Metal Matrix Composites (Proc. ICCI-II)* (H. Ishida ed.), Elsevier Science, New York, pp. 57–71.

- Cazeneuve, C., Castle, J.E. and Watts, J.F. (1990). The structure of the interface in carbon fiber composites by scanning Auger microscopy. *J. Mater. Sci.* **25**, 1902–1908.
- Cotterell, B. and Mai, Y.W. (1996). *Fracture Mechanics of Cementitious Materials*, Blackie Academic and Professional, London, UK.
- Day, R.J., Robinson, I.M., Zakikhani, M. and Young, R.J. (1987). Raman spectroscopy of stresses high modulus poly(*p*-phenylene benzobisthiazole) fibers. *Polymer* **28**, 1833–1840.
- DeLong, J.D., Hook, K.J., Rich, M.J., Kalnata, J. and Drzal, L.T. (1990). Spectroscopic characterization of fiber–polymer interphases. In *Controlled Interfaces in Composite Materials* (H. Ishida ed.), Elsevier, New York, pp. 87–95.
- Denison, P., Jones, F.R., Brown, A., Humphrey, P. and Harvey, J. (1988a). Scanning secondary ion mass spectroscopy studies of the micromechanics and chemical structure in the region of the interface in carbon fiber–epoxy composites. *J. Mater. Sci.* **23**, 2153–2156.
- Denison, P., Jones, F.R., Brown, A., Humphrey, P. and Paul, A.J. (1988b). Scanning SIMS fractography of CFRP. In *Interfaces in Polymer, Ceramic and Metal Matrix Composites* (H. Ishida ed.), Elsevier, New York, pp. 239–248.
- Drumm, C.A. and Ulicny, J.C. (1989). Analysis of coating on glass fiber reinforcements. *Polym. Composites* **10**, 44–51.
- Filiou, C., Galiotis, C. and Batchelder, D.N. (1992). Residual stress distribution in carbon fiber/thermoplastic matrix pre-impregnated composite tapes. *Composites*, **23**, 29–38.
- Galiotis, C. (1993a). A study of mechanisms of stress transfer in continuous and discontinuous fiber model composites by laser Raman spectroscopy. *Composites Sci. Technol.* **48**, 15–28.
- Galiotis, C. (1993b). Stress transfer characteristics in model composites. *Composite Interfaces* **1**, 321–336.
- Garton, A. and Daly, J.H. (1985). Characterization of the aramid–epoxy and carbon–epoxy interphases. *Polym. Composites* **6**, 195–200.
- Gilbert, A.H., Goldstein, B. and Marom, G. (1990). A liquid droplet measurement technique as a means of assessing the interlaminar shear strength of fiber reinforced composites. *Composites* **21**, 408–414.
- Good, R.J. (1952). A thermodynamic derivation of Wenzel's modification of Young's equation contact angles: Together with a theory of hysteresis. *J. Am. Chem. Soc.* **74**, 5041–5042.
- Grap, R.T., Koenig, J.L. and Ishida, H. (1985). Diffuse reflectance fourier transform infrared spectroscopic study of chemical bonding and hydrothermal stability of an aminosilane on metal oxide surfaces. *J. Adhesion* **18**, 93–110.
- Gutowski, W. (1988). A thermodynamic model of the matrix–reinforcement interface: Experimental verification. In *Interfaces in Polymer, Ceramic and Metal Matrix Composites (Proc. ICCI-II)* (H. Ishida ed.), Elsevier, New York, pp. 735–746.
- Gutowski, W. (1990). Effect of fiber–matrix adhesion on mechanical properties of composites. In *Controlled Interfaces in Composite Materials (Proc. ICCI-III)* (H. Ishida ed.), Elsevier, New York, pp. 505–520.
- Hammer, G.E. and Drzal, L.T. (1980). Graphite fiber surface analysis by X-ray photoelectron spectroscopy and polar/dispersive free energy analysis. *Application of Surf. Sci.*, **4**, 340–355.
- Hoh, K.P., Ishida, H. and Koenig, J.L. (1990). Silicon-29 solid state nuclear magnetic resonance spectroscopy of composite interfaces. *Polym. Composites* **11**, 121–125.
- Hull, D. (1981). *An Introduction to Composite Materials*, Cambridge University Press, Cambridge, pp. 36–58.
- Ishida, H. (1994). *Characterization of Composite Materials*, Butterworth-Heinemann, Boston.
- Ishida, H., Koenig, J.L. (1978). Fourier transformed infrared spectroscopic study of the silane coupling agent/porous silica interface. *J. Colloid. Interface Sci.* **64**, 555–564.
- Ishida, H. and Koenig, J.L. (1980). Effect of hydrolysis and drying on the siloxane bonds of a silane coupling agent deposited on E-glass fibers. *J. Polym. Sci.: Polym. Phys. Edition* **18**, 233–237.
- Kaelble, D.H., Dynes, P.J. and Mans, L. (1974). Surface energy analysis of treated graphite fibers. *J. Adhesion* **6**, 239–258.
- Kim, J.K. and Mai, Y.W. (1991). High strength high fracture toughness fiber composites with interface control—a review. *Composites Sci. Technol.* **41**, 333–378.

- Kim, J.K. and Mai, Y.W. (1993). Interfaces in composites. In *Structure and Properties of Fiber Composites*, Materials Science and Technology, Series Vol. 13 (T.W. Chou ed.) Ch. 6, VCH Publication, Weinheim, Germany, pp. 239–289.
- Kim, J.K., Mai, Y.W. and Kennedy, B.J. (1992). Surface analysis of carbon fibers modified with PVAL coating and the composite interfaces. *J. Mater. Sci.* **27**, 6811–6816.
- Kinloch, A.J. (1980). Review – The science of adhesion. part 1, surface and interfacial aspects. *J. Mater. Sci.* **15**, 2141–2166.
- Kinloch, A.J. (1982). Review – The science of adhesion. part 2, mechanics and mechanisms of failure. *J. Mater. Sci.* **17**, 617–651.
- Kinloch, A.J., Kodokian, G.K.A. and Watts, J.F. (1992). The adhesion of thermoplastic fiber composites. *Phil. Trans. Roy. Soc. Lond.* **A338**, 83–112.
- Lee, L.H. (1991). *Fundamentals of Adhesion* (Lee, L.H. ed.), Plenum Press, New York. pp. 1–30.
- Lee, S.M. (1989). Surface analysis of polymer composites. In *Reference Book for Composite Technology 2* (S.M. Lee ed.), Technomic, Lancaster, P.A. USA, pp. 81–103.
- Lee, W.J., Seferis, J.C. and Berg, J.C. (1988). Characterizing high performance composite processability with dynamic fiber wettability measurements. *Polym. Composites* **9**, 36–41.
- Liao, Y.T. (1989). A study of glass fiber–epoxy composite interfaces. *Polym. Composites* **16**, 424–428.
- Maso, J.C. (1993). *Interfaces in Cementitious Composites*, E & FN Spon, London & New York.
- Metcalfe, A.G. (1974). *Interfaces in metal matrix composites*. Composite Materials Series Volume 1. (A.G. Metcalfe ed.), Academic Press, New York, pp. 65–123.
- Miller, J.D. and Ishida, H. (1986). In *Chemically Modified Surfaces, Vol. 1. Silane, Surfaces and Interfaces*. (K. Leyden ed.), Gordon and Breach, New York. p. 525.
- Nakahara, M., Nakayama, Y. Katagiri, G. and Shimizu, K. (1991). Anodic oxidation effects on pyrolytic graphite surfaces in acid. *J. Mater. Sci.* **26**, 861–864.
- Nardin M. and Ward, I.M. (1987). Influence of surface treatment on adhesion of polyethylene fibers. *Mater. Sci. Technol.* **3**, 814–826.
- Naslain, R. (1993). Fiber–matrix interphase and interfaces in ceramic matrix composites processes by CVI. *Composite Interfaces* **1**, 253–286.
- Neumann, A.W., Absolom, D.R., Francis, D.W. and van Oss C.J. (1980). Conversion tables of contact angles to surface tension: For use in determining the contribution of the van der Waals attraction or repulsion to various separation processes. *Separ. Purif. Mech.* **9**, 69–163.
- Neumann, A.W. and Good, R.J. (1979). In *Surface and Colloid Science*, Vol. 2, (R.J. Good and R.R. Stromberg eds.), Plenum Press, New York.
- Neumann, A.W. and Good, R.J., Hope, C.J. and Sejpal, M. (1974). An equation of state approach to determine surface tension of low energy solids from contact angles. *J. Colloid. Interface Sci.* **49**, 291–303.
- Neumann, A.W. and Renzow, D. (1969). *Z. Phys. Chemi Neue Folge* **68**, 11.
- Owen, D.K. and Wendt, R.C. (1969). Estimation of the surface free energy of polymers. *J. Appl. Polym. Sci.* **13**, 1741–1747.
- Plueddemann, E.P. (1974). In *Interfaces in Polymer Matrix Composites*, Composite Materials Vol. 6. (E.P. Plueddemann ed.), Academic Press, New York.
- Plueddemann, E.P. (1988). Present status and research needs in silane coupling. In *Proc. ICCI-II, Interfaces in Polymer, Ceramic and Metal Matrix Composites*. (H. Ishida ed.), Elsevier Sci. Pub. New York. pp. 17–33.
- Plueddemann, E.P., Stark, G.L. (1980). In *Proc. 35th Annual Tech. Conf. Reinf. Plast./Composite*. SPI. Section 20-B.
- Robinson, I.M., Yeung, P.H.J., Galiotis, C. and Young, R.J., Batchelder, D.N. (1986). Stress induced twinning of polydiacetylene single crystal fibers in composites. *J. Mater. Sci.* **21**, 3440–3444.
- Robinson, I.M., Zakikhani, M. Day, R.J., Young, R.J. and Galiotis, C. (1987). Strain dependence of the Raman frequencies for different types of carbon fibers. *J. Mater. Sci. Lett.* **6**, 1212–1214.
- Rudy, E. (1969). A compendium of phase diagram, AFML-TR-65-2, Part V.
- Scolar, D.A. (1974). In *Interfaces in Polymer Matrix Composites*, Composite Materials, Vol. 6 (E.P. Plueddemann ed.), Academic Press, New York, pp. 217–284.

- Shimizu, K., Nakahara, M. and Noguchi, K. (1992). Interfacial debonding strength between the edge surfaces of pyrolytic graphite and epoxy resins. *J. Mater. Sci.* **27**, 6134–6140.
- Thomason, J.L. (1990). Investigation of composite interphase using dynamic mechanical analysis: artifacts and reality. *Polym. Composites* **11**, 105–113.
- Tsai, H.C., Arocho, A.M. and Gause, L.W. (1990). Prediction of fiber–matrix interphase properties and their influence on interface stress, displacement and fracture toughness of composite materials. *Mater. Sci. Eng.* **A126**, 295–304.
- Tuinstra, T. and Koening, J.L. (1970). Characterization of graphite fiber surfaces with Raman spectroscopy. *J. Composite Mater.* **4**, 492–499.
- Wagner, H.D. (1990). Spreading of liquid droplets on cylindrical surfaces: Accurate determination of contact angle. *J. Appl. Phys.* **67**, 1352–1355.
- Wagner, H.D., Wiesel, E. and Gallis, H.E. (1990). Spreading of liquid droplets on cylindrical surfaces: accurate determination of contact angle. In *Interfaces in Composites, Mat. Res. Soc. Symp. Proc.* Vol. 170 (C.G. Pantano and E.J.H. Chen, eds.), MRS, Pittsburgh, PA, pp. 141–145.
- Wake, W.C. (1978). Theories of adhesion and uses of adhesives: A review. *Polymer* **19**, 291–308.
- Wang, D. and Jones, F.R. (1994). TOM SIMS and XPS study of the interaction of aminosilanised E-glass fibers with epoxy resins. Part I. Diglycidyl ether of bisphenol S. *Composites Sci. Technol.* **50**, 215–228.
- Weinberg, M. (1987). In *Toughened Composites*, ASTM STP 937, (N.J. Johnston ed.), ASTM, Philadelphia, PA, p. 51.
- Williams, J.G., Donnellan, M.E., James, M.R. and Morris, W.L. (1990). Properties of the interphase in organic matrix composites. *Mater. Sci. Eng.* **A126**, 305–312.
- Yamaki, J. and Katayama, Y. (1975). New method of determining contact angle between monofilament and liquid. *J. Appl. Polym. Sci.* **19**, 2897–2909.
- Yip, P.W. and Liu, S.S. (1990). Effect of surface oxygen on adhesion of carbon fiber reinforced composites. In *Interfaces in Composites, Mat. Res. Soc. Symp. Proc.* Vol. 170, (C.G. Pantano and E.J.H. Chen, eds.), MRS, Pittsburgh, PA, pp. 339–344.
- Young, R.J., Al-khudhary, D. and Thomas, A.G. (1985). Analysis of filled rubbers using SAXS. In *Integration of Fundamental Polymer Science and Technology*. (L.A. Kleintjens and P.J. Lemstra eds.). Elsevier Appl. Sci., New York. p. 581.
- Young, R.J., Day, R.J., Zakikhani, M. and Robinson, I.M. (1989). Fiber deformation and residual thermal stresses in carbon fiber reinforced PEEK. *Composites Sci. Technol.* **34**, 243–258.
- Zaper, A.M. and Koenig, J.L. (1985). Application of solid state carbon-13 NMR spectroscopy to chemically modified surfaces. *Polym. Composites* **6**, 156–161.

Chapter 3

MEASUREMENTS OF INTERFACE/INTERLAMINAR PROPERTIES

3.1. Introduction

A number of experimental techniques have been devised to measure the mechanical properties of the fiber–matrix and laminar interfaces in composites. These techniques in general can be classified into two different methods depending on the nature of specimens employed and the scale of testing (Kim et al., 1994): one involves the testing of single fiber (or multiple fibers in some cases) microcomposites in which individual fibers are embedded in specially constructed matrix blocks of various shapes and sizes; and the other uses bulk laminate composites to measure the interlaminar/intralaminar properties. Much of the discussion presented in this chapter follows that given in our recent publications (Kim and Mai, 1991, 1993; Kim et al., 1994). The relative advantages and limitations of these testing techniques are critically assessed with respect to specimen preparation, and interpretation of data.

Given a combination of fiber and matrix, it is desirable that the testing method will provide a reproducible and reliable means of not only measuring the interface adhesion but also allowing the failure mode at the interface region to be studied. One important requirement of these tests, whether the microcomposite tests or the bulk composite tests, is that the mechanics model developed for data reduction must be consistent with the actual failure mechanisms. But more often than not, particular failure is assumed to have taken place without confirmation in experiments. This practice not only makes the interface properties obtained doubtful, but it also degrades the whole value of the test method. As will be shown later in the chapter, this may also explain why there is an extremely large data scatter in the test results for apparently the same materials tested in different laboratories. Efforts are being continued to improve the quality and accuracy of experimental data and to develop better mechanics models underpinning these testing methods.

3.2. The mechanical properties of fiber–matrix interfaces

3.2.1. Introduction

Test methods using microcomposites include the single fiber compression test, the fiber fragmentation test, the fiber pull-out test, the fiber push-out (or indentation) test and the slice compression test. These tests have a variety of specimen geometries and scales involved. In these tests, the bond quality at the fiber–matrix interface is measured in terms of the interface fracture toughness, G_{ic} , or the interface shear (bond) strength (IFSS), τ_b , for the bonded interface; and the interface frictional strength (IFS), τ_{fr} , which is a function of the coefficient of friction, μ , and residual fiber clamping stress, q_0 , for the debonded interface. Therefore, these tests are considered to provide direct measurements of interface properties relative to the test methods based on bulk composite specimens.

Microcomposite tests have been used successfully to compare composites containing fibers with different prior surface treatment and to distinguish the interface-related failure mechanisms. However, all of these tests can hardly be regarded as providing absolute values for these interface properties even after more than 30 years of development of these testing techniques. This is in part supported by the incredibly large data scatter that is discussed in Section 3.2.6.

3.2.2. Single fiber compression test

The single fiber compression test is one of the earliest test methods developed based on microcomposites to measure the bond strength of glass fibers with transparent polymer matrices (Mooney and McGarry, 1965). Two different types of specimen geometry are used depending on the modes of failure that occur at the fiber–matrix interface: one has a long hexahedral shape with a uniform cross-section (Fig 3.1(a)); the other has a curved neck in the middle (Fig 3.1(b)). When the parallel-sided specimen is loaded in longitudinal compression, shear stresses are generated near the fiber ends as a result of the difference in elastic properties between the fiber and the matrix, in a manner similar to the stress state occurring in uniaxial tension. Further loading eventually causes the debond crack to initiate from these regions due to the interface shear stress concentration (i.e., shear debonding). The curved-neck specimen under longitudinal compression causes interface debonding to take place in the transverse direction (i.e. tensile debonding) due to the transverse expansion of the matrix when its Poisson ratio is greater than that of the fiber. The equations used to calculate the interface bond strengths in shear, τ_b , and under tension, σ_b , are (Broutman, 1969):

$$\tau_b \approx 2.5 \sigma_N \quad (3.1)$$

$$\sigma_b = \frac{\sigma_N (v_m - v_f)}{(1 - v_m) + \alpha(1 - v_f - 2v_f^2)} \quad (3.2)$$

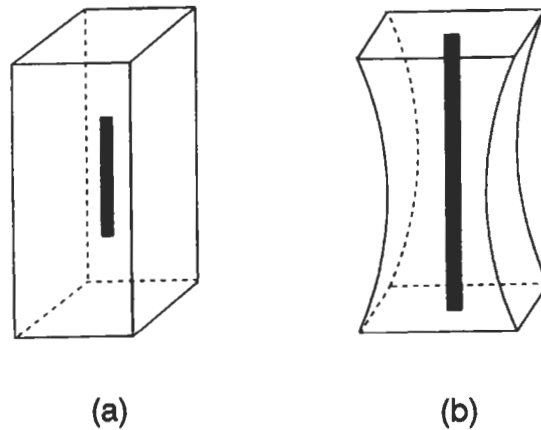


Fig. 3.1. Single fiber compressive tests with (a) parallel-sided and (b) curved-neck specimen.

for shear debonding in the parallel-sided specimen and for tensile debonding in the curved-neck specimen, respectively. σ_N is the net compressive stress at the smallest cross-section obtained upon interface debonding. $\alpha = E_m/E_f$ is Young's moduli ratio of the matrix to the fiber, and ν_f and ν_m are Poisson ratios of the fiber and matrix, respectively. The constant 2.5 in Eq. (3.1) is taken from the empirically measured shear stress concentration factor.

The single fiber compression test has not been as popular as other microcomposite tests because of the problems associated with specimen preparation and visual detection of the onset of interfacial debonding. To be able to obtain accurate reproducible results, the fibers have to be accurately aligned. With time, this test method became obsolete, but it has provided a sound basis for further development of other testing techniques using similar single fiber microcomposite geometry.

3.2.3. Fiber fragmentation test

The fiber fragmentation test is at present one of the most popular methods to evaluate the interface properties of fiber-matrix composites. Although the loading geometry employed in the test method closely resembles composite components that have been subjected to uniaxial tension, the mechanics required to determine the interface properties are the least understood.

This test is developed from the early work of Kelly and Tyson (1965) who investigated brittle tungsten fibers that broke into multiple segments in a copper matrix composite. Here a dog-bone shaped specimen is prepared such that a single fiber of finite length is embedded entirely in the middle of a matrix (Fig 3.2(a)). The failure strain of the matrix material must be significantly (i.e., ideally at least three times) greater than that of the fiber to avoid premature failure of the specimen due to fiber breakage. When the specimen is subjected to axial tension (or occasionally in compression (Boll et al., 1990)), the embedded fiber breaks into increasingly smaller

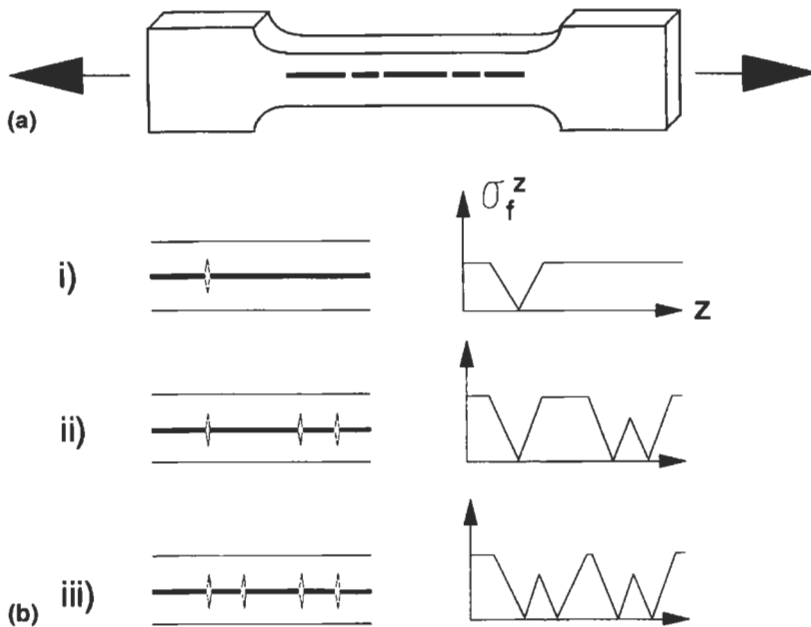


Fig. 3.2. (a) Dog-bone shape fiber fragmentation test specimen; (b) fiber fragmentation under progressively increasing load from (i) to (iii) with corresponding fiber axial stress σ_f^z profile.

segments at locations where the fiber axial stress reaches its tensile strength. Further stressing of the specimen results in the repetition of this fragmentation process until all fiber lengths are too short to allow its tensile stress to cause more fiber breakage. Fig 3.2 (b) illustrates the fiber fragmentation process under progressively increasing stress and the corresponding fiber axial stress profile, σ_f^z , along the axial direction. The shear stress at the fiber–matrix interface is assumed here to be constant along the short fiber length.

The fiber fragment length can be measured using a conventional optical microscope for transparent matrix composites, notably those containing thermoset polymer matrices. The photoelastic technique along with polarized optical microscopy allows the spatial distribution of stresses to be evaluated in the matrix around the fiber and near its broken ends.

Acoustic emission (Netravali et al., 1989a,b,c 1991; Vautey and Favre, 1990; Manor and Clough, 1992; Roman and Aharonov, 1992) is another useful technique to monitor the number of fiber breaks during the test, particularly for non-transparent matrix materials. Fig 3.3 shows a typical load–displacement curve of a carbon fiber–polyetheretherketone (PEEK) matrix composite sample with the corresponding acoustic emissions. Other techniques have also been used to obtain the fiber fragments after loading to a sufficient strain: the matrix material can be dissolved chemically or burned off, or the specimen can be polished to expose the broken fragments (Yang et al. 1991).

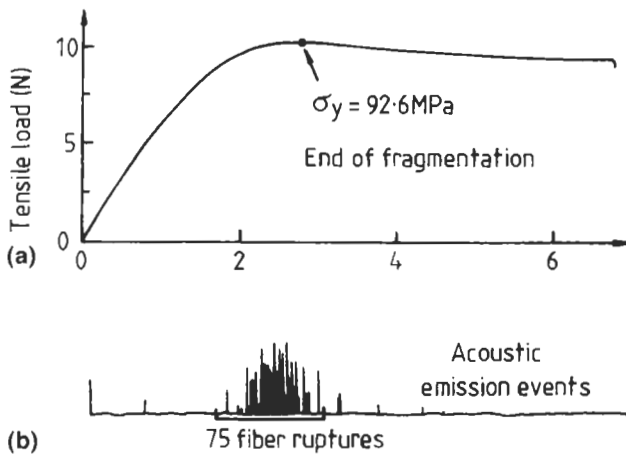


Fig. 3.3. (a) Typical load–displacement curve and (b) acoustic emission events for a fiber fragmentation test on an AS4 carbon fiber-PEEK matrix composite. After Vautey and Favre (1990).

The average value of fiber fragment lengths obtained at the end of the test when the application of stress does not cause any further fiber fragmentation is referred to as the ‘critical transfer length’, $(2L)_c$. The critical transfer length represents the complex tensile fracture characteristics of brittle fibers and the statistical distribution of fiber fragment lengths. Typical plots of the mean fragment length versus fiber stress are shown in Fig 3.4 for carbon fiber–epoxy and Kevlar 49–epoxy systems. It is interesting to note that the idea of the critical transfer length was originally derived from the concept of maximum embedded fiber length, L_{\max} , above which the fiber breaks without being completely pulled out in the fiber pull-out test, rather than in the fiber fragmentation test. In an earlier paper by Kelly and Tyson (1965), $(2L)_c$ for the composite with a frictionally bonded interface is defined as twice the longest embedded fiber length that can be pulled out without fracture, i.e. $(2L)_c = 2L_{\max}$. The solution of L_{\max} as a function of the characteristic fiber stresses and the properties of composite constituents and its practical implications are discussed in Chapter 4.

For analytical purposes, the critical transfer length is also defined as the fiber length necessary to build up a maximum stress (or strain) equivalent to 97% of that for an infinitely long fiber (Whitney and Drzal 1987). In this case, the knowledge of the critical transfer length is related principally to the efficient reinforcement effect by the fiber. (Compare this value with 90% of that for an infinitely long fiber for the definition of “ineffective length” (Rosen, 1964; Zweben, 1968; Leng and Courtney, 1990; Beltzer et al., 1992).)

The average shear strength at the interface, τ_a , whether bonded, debonded or if the surrounding matrix material is yielded, whichever occurs first, can be approximately estimated from a simple force balance equation for a constant interface shear stress (Kelly and Tyson, 1965):

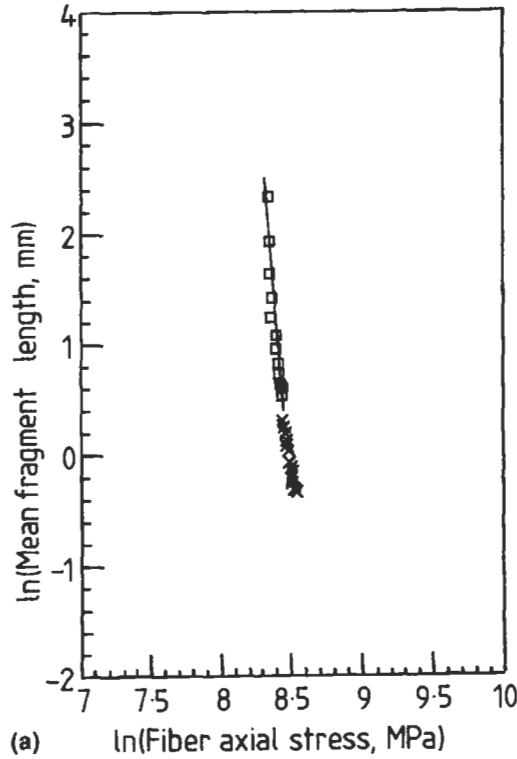


Fig. 3.4. Ln-Ln plot of fiber fragment length as a function of fiber stress (a) for Kevlar 29 fiber-epoxy matrix composite and (b) for a carbon fiber-epoxy matrix composite. Yabin et al. (1991).

$$\tau_a = \frac{a\sigma_f^*}{(2L)_c} \quad (3.3)$$

where σ_f^* is the average fiber tensile strength and a , the fiber radius. A non-dimensional correction factor χ has been introduced later to take into account the statistical distribution of tensile strength and fragment length of the fiber

$$\tau_a = \chi \frac{a\sigma_{TS}}{(2L)_c}, \quad (3.4)$$

where σ_{TS} is fiber tensile strength at the critical transfer length. It is noted that $\chi = 0.75$ (Ohsawa et al., 1978, Wimolkiatisak and Bell, 1989) is taken as a mean value if the fiber fragment lengths are assumed to vary uniformly between $(L)_c$ and $(2L)_c$. In a statistical evaluation of fiber fragment lengths and fiber strength, Drzal et al. (1980) expressed the coefficient in terms of the gamma function, Γ , and Weibull modulus, m , of the strength distribution of a fiber of length, l , as

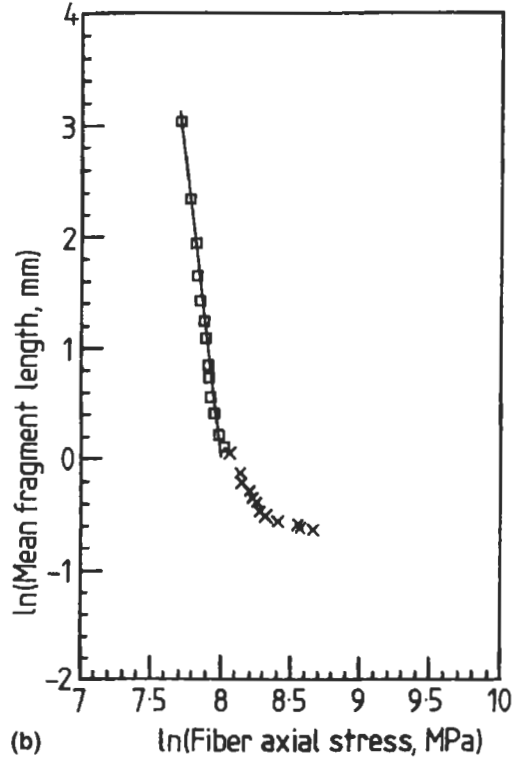


Fig. 3.4.(b)

$$\chi = \Gamma \left[1 - \frac{1}{m} \right]. \quad (3.5)$$

In a more vigorous analysis based on the Monte Carlo simulation approach, χ is obtained in a more complicated way (Henstenburg and Phoenix, 1989; Netravali et al., 1989a,b)

$$\chi = \left[\frac{1}{2} \left(\frac{\ell}{\ell_0} \right) \right]^{1+1/m} / \Gamma(1 + 1/m), \quad (3.6)$$

where ℓ/ℓ_0 refers to the non-dimensional mean fiber length, ranging between 1.337 and 1.764, and ℓ_0 is the characteristic length. Therefore, χ varies between 0.669 and 0.937 for m values between infinity and 3. $m = 3$ represents typically the smallest value (i.e. largest data scatter) for brittle fibers that can be obtained in experiments. In addition, some recent studies have progressed towards further advancement of sophisticated statistical techniques to characterize the fiber fragment length distribution through computer simulations of fiber fragmentation behavior

(Favre et al., 1991; Curtin, 1991; Yabin et al., 1991; Merle and Xie, 1991; Gulino and Phoenix, 1991; Ling and Wagner, 1993; Jung et al., 1993; Baxevanakis et al., 1993; Andersons and Tamuzs, 1993; Liu et al. 1994).

However, the basic form of the relationship between the critical transfer length and the IFSS remains virtually unchanged from the solution given by Kelly and Tyson (1965) three decades ago. A clearly emerging view in recent years, contrary to the conventional view of either perfect bonding or complete debonding, is that there are both bonded and debonded regions simultaneously present at the fiber–matrix interface during the fiber fragmentation process (Favre et al., 1991; Gulino et al., 1991; Lacroix et al., 1992). For composites containing ductile matrices, the fiber–matrix interface region tends to be yielded in preference to clear-cut debonding. A proper micromechanics model should accommodate these phenomena. Therefore, the limitation of this test associated with Eq. (3.3) has been addressed and improved analytical models have been presented (Kim et al., 1993; Kim, 1997), deriving the solutions required to satisfy the interface conditions, namely full bonding, partial debonding/yielding and full debonding/yielding. Recently, Zhou et al. (1995) have presented a fracture mechanics analysis of the fragmentation test including the Weibull distribution of fiber strength. Transverse matrix cracking at the sites of fiber breaks has also been considered by Liu et al. (1995). Further details of these various analyses will be discussed in Chapter 4.

Moreover, the validity of τ_a being determined based on the measurement of fragment length depends not only on the interface properties but strongly on the properties of the constituents, e.g. matrix shear yield strength, τ_m , and the difference in Poisson ratios between the fiber and matrix. The relative magnitude of these properties influences the actual failure mechanisms occurring at the interface region (i.e., interface debonding versus matrix yielding), which in turn determines the fiber fragmentation behavior. Bascom and Jensen (1986) argued that the shear stress transfer across the interface is often limited by the matrix τ_m rather than the interface τ_a .

Adding to the above problem, the critical transfer length, $(2L)_c$, has also been shown to be strongly dependent on Young's modulus ratio of fiber to matrix, E_f/E_m . Interestingly enough, some researchers (Galiotis et al., 1984; Asloun et al., 1989; Ogata et al., 1992) identified through experimental evidence that $(2L)_c$ varies with $(E_f/E_m)^{1/2}$, as the early shear-lag model by Cox (1952) suggests. (See Chapter 4 for solutions of fiber axial stress and interface shear stress). Finite element analyses on single fiber composites with bonded fiber ends, however, show that there is an almost linear dependence of $(2L)_c$ with E_f/E_m , if the modulus ratio is relatively small (i.e. $E_f/E_m < 20$). Experimental evidence of the dependence of the critical transfer length on Young's modulus ratio is shown in Fig 3.5, and is compared with theoretical predictions (Termonia, 1987, 1993). Additionally, Nardin and Schultz (1993) also proposed a strong correlation of the critical transfer length with the interface bond strength, which is represented by the thermodynamic work of adhesion, W_a , at the fiber–matrix interface.

Apart from the mechanical properties of the composite constituents that dominate the fiber fragment length, peculiar structural properties of the fiber may

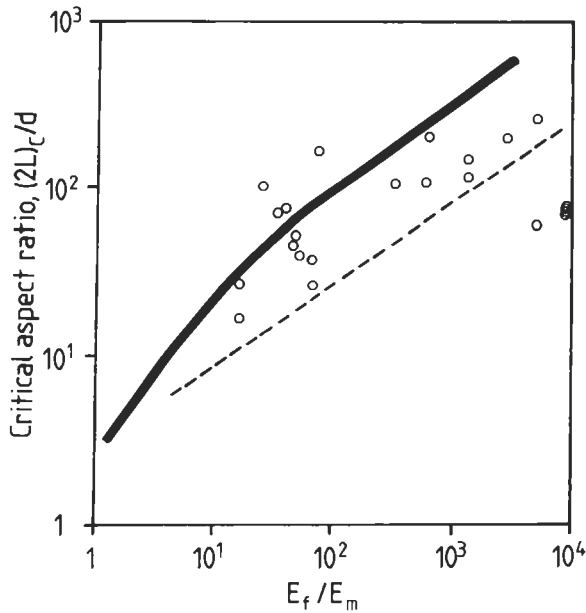


Fig. 3.5. Dependence of fiber critical aspect ratio, $(2L)_c/d$, on the Young's modulus ratio of fiber to matrix material, E_f/E_m . (○) Experimental data from Asloun et al. (1989); (—) Termonia (1993); (---) Cox (1952).

also complicate the interpretation of test results. For example, extensive splitting of highly oriented organic fibers, such as Kevlar and PBT (Morgan and Allred, 1993), into small fibrils on the fiber surface makes the test results doubtful (Kalanta and Drzal, 1990; Scherf et al., 1992). The fiber straightening pretension applied during specimen preparation is also found to influence the fragmentation behavior, causing significant data scatter unless carefully controlled (Ikuta et al., 1991; Scherf and Wagner, 1992). Another important drawback of this test is that the matrix must possess sufficient tensile strain and fracture toughness to avoid premature failure of the specimen, which is induced by fiber breaks, as mentioned earlier. A technique has been devised to circumvent this problem in that a thick layer of the brittle matrix material is coated onto the fiber, which is subsequently embedded in a ductile resin (Favre and Jacques, 1990).

3.2.4. Fiber pull-out test

In the fiber pull-out test, a fiber(s) is partially embedded in a matrix block or thin disc of various shapes and sizes as shown in Fig 3.6. When the fiber is loaded under tension while the matrix block is gripped, the external force applied to the fiber is recorded as a function of time or fiber end displacement during the whole debond and pull-out process. There are characteristic fiber stresses that can be obtained from the typical force (or fiber stress). The displacement curve of the fiber pull-out

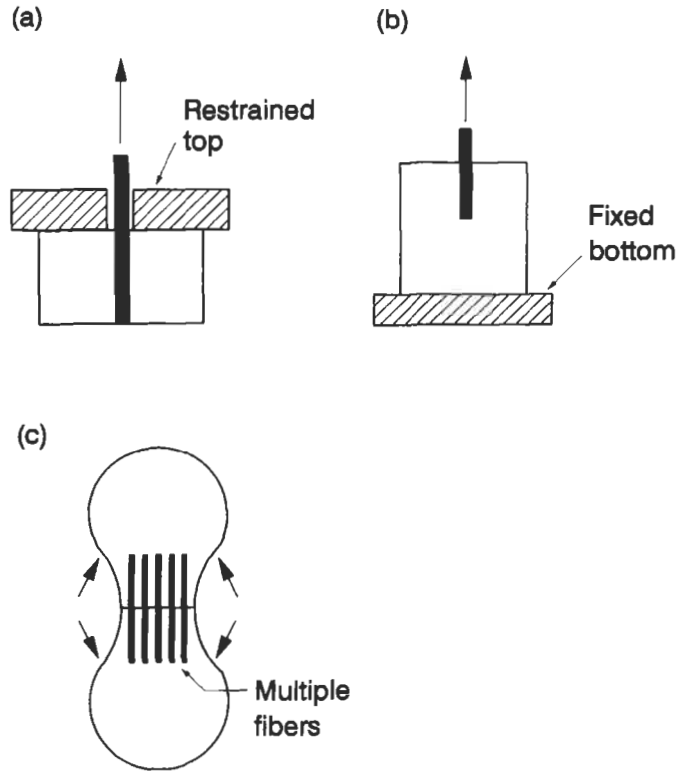


Fig. 3.6. Schematic illustrations of various specimen geometry of the fiber pull-out test: (a) disc-shaped specimen with restrained-top loading (b) long matrix block specimen with fixed bottom loading, (c) double pull-out with multiple embedded fibers.

test is shown in Fig 3.7, indicating the initial debond stress for interfacial debonding, σ_0 , the maximum debond stress at instability, σ_d^* , and the initial frictional pull-out stress against frictional resistance after complete debonding, σ_{fr} . A conventional way of determining the interface bond strength, τ_b , is by using an equation similar to Eq. (3.3), which is

$$\tau_b = \frac{d\sigma_d^*}{4L} \quad (3.7)$$

Fig 3.8 shows the interface shear bond strength, τ_b , determined from Eq. (3.7), which is not a material constant but varies substantially with embedded fiber length, L . However, to evaluate all the relevant interface properties properly, which include the interface fracture toughness, G_{ic} , the coefficient of friction, μ , and the residual clamping stress, q_0 , it is necessary to obtain experimental results for a full range of L and plot these characteristic fiber stresses as a function of L . More details of the

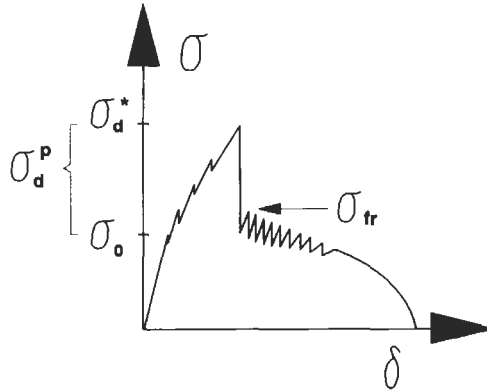


Fig. 3.7. Schematic presentation of the applied fiber stress versus displacement ($\sigma - \delta$) curve in a fiber pull-out test. After Kim et al. (1992).

characterization of these properties from experimental data will be discussed in Chapter 5.

The fiber pull-out test has been widely used not only for polymer matrix composites but also for some ceramic matrix (Griffin et al., 1988; Goettler and Faber, 1989; Butler et al., 1990; Barsoum and Tung, 1991) and cement matrix composites (see Bartos, 1981 for a useful review) as well as steel wire reinforced rubber matrix composites (Ellul and Emerson, 1988a, b; Gent and Kaang, 1989). However, this test method has some limitations associated with the scale of the test. There is a maximum embedded length of fiber, L_{\max} , permitted for pull-out without being broken. L_{\max} is usually very short, which causes experimental difficulties and

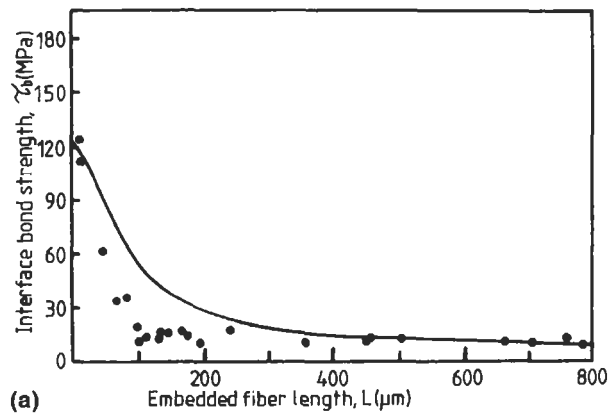


Fig. 3.8. Plots of interface bond strength, τ_i , versus embedded fiber length, L , (a) for a carbon fiber-epoxy matrix system and (b) for a Hercules IM6 carbon fiber-acrylic matrix system. After Pitkethly and Doble (1990) and Desarmont and Favre (1991).

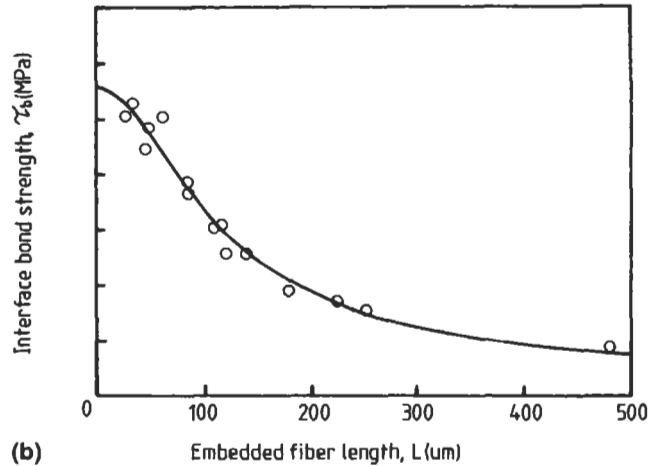


Fig. 3.8.(b).

large data scatter especially for composite systems with strong interface bonding and small fiber diameters. For example, for the carbon fiber–epoxy matrix system L_{max} is less than 1.0 mm (Pitkethly and Doble, 1990; Marshall and Price, 1991; Kim et al., 1992) (see Fig 3.8). Theoretical prediction of L_{max} for given interface properties will be discussed in Chapter 4. It is also necessary to design a special jig/fixture to fabricate and hold the thin matrix block needed for very short embedded fiber length (see for example Baillie, 1991). Moreover, an elevated meniscus, which forms around the fiber during curing of the matrix material, causes large stress concentrations and makes the test results often inaccurate.

A variation of this technique has recently been developed in the so-called ‘microdebond test’ (Miller et al., 1987, 1991; Penn et al., 1988; McAlea and Besio, 1988; Gaur and Miller, 1989, 1990; Chuang and Chu, 1990; Biro et al., 1991; Moon et al., 1992) to alleviate some of the experimental difficulties associated with conventional fiber pull-out tests. In this test, a small amount of liquid resin is applied onto the single fiber to form a concentric microdroplet in the shape of an ellipsoid after curing, as schematically illustrated in Fig 3.9 (Gaur and Miller, 1989). The smooth curvature at the boundary between the fiber and the microdroplet reduces the stress concentration at the fiber entry to a certain extent and, hence, the large variation in the experimental data is also reduced. The microdebond technique can be used for almost any combination of fiber and polymer matrices. However, as found in finite element and photoelastic analyses, this technique also has serious limitations associated with the nature of the specimen and loading condition (Herrera-Franco and Drzal, 1992). The stress state in the droplet varies significantly with the location and shape of the loading jigs, and the size of small microdroplet makes the in-situ observation of the failure process difficult. More importantly, the meniscus formed around the fiber makes the measurement of the embedded fiber length highly inaccurate, which has a more significant effect on the calculated bond

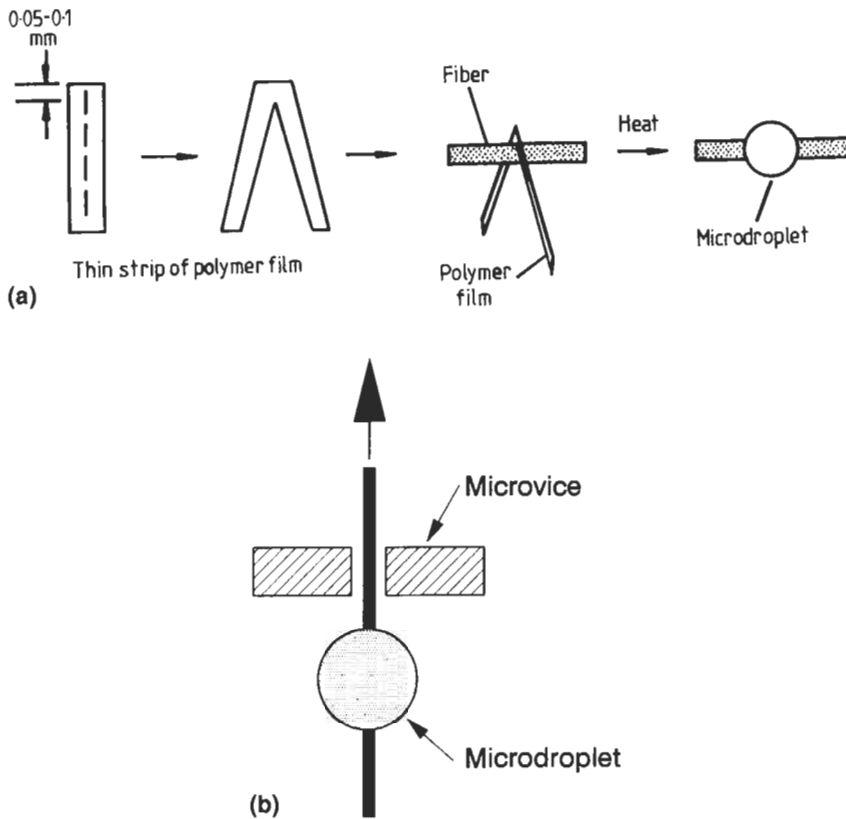


Fig. 3.9. Schematic presentation of (a) the procedure for forming thermoplastic resin microdrops and (b) the microdebond test. After Gaur and Miller (1989).

strength values than in the fiber pull-out test. Mechanical properties of the matrix microdroplet may also vary with size partly because of the variations of concentration of the curing agent as determined by differential scanning calorimetry (DSC), see Fig 3.10 (Rao et al., 1991). When compared with specimen geometry of other single fiber composite tests, the microdebond test shows the least resemblance to actual loading configuration of practical composite components.

In view of the fact that the above techniques examine single fibers embedded in a matrix block, application of the experimental measurements to practical fiber composites may be limited to those with small fiber volume fractions where any effects of interactions between neighboring fibers can be completely neglected. To relate the interface properties with the gross performance of real composites, the effects of the fiber volume fraction have to be taken into account. To accommodate this important issue, a modified version of the fiber pull-out test, the so-called microbundle pull-out test, has been developed recently by Schwartz and coworkers (Qui and Schwartz, 1991, 1993; Stumpf and Schwartz, 1993; Sastry et al., 1993). In

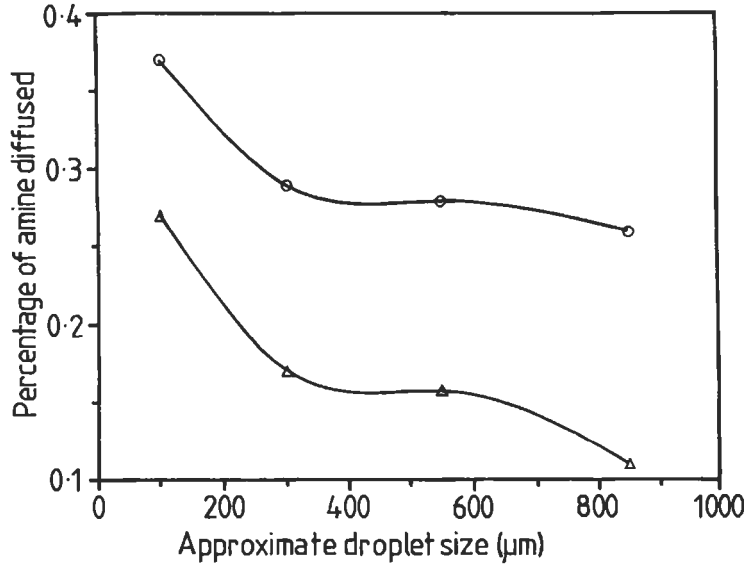


Fig. 3.10. Effect of curing cycle on the fraction of amine curing agent estimated to have diffused out of droplets as a function of their size. After Rao et al. (1991).

this test, a central fiber is pulled out of a seven-fiber microcomposite as shown in Fig 3.11. Great difficulties are encountered in constructing the specimens since accurate control of the geometry determines the embedded fiber length. No clear correlations exist between the IFSS and the fiber volume fraction. This indicates that the actual failure mechanisms during fiber pull-out are matrix dominated (Qiu and Schwartz, 1993).

3.2.5. Microindentation (or fiber push-out) test

The microindentation technique (or 'push-out' test as opposed to the 'pull-out' test) is a single fiber test capable of examining fibers embedded in the actual composite. The

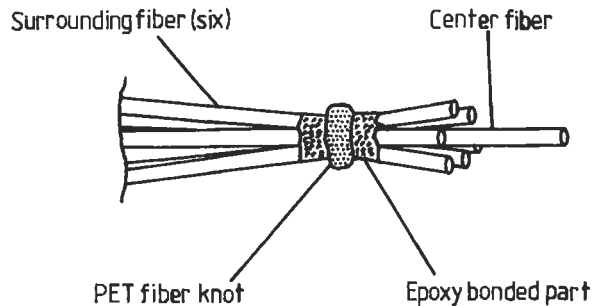


Fig. 3.11. Schematic presentation of a multi-fiber pull-out specimen.

slice compression test to be discussed in Section 3.2.6 serves the same purpose. The microindentation test utilizes a microhardness indenter with various tip shapes and sizes to apply a compressive force to push against a fiber end into the metallographically polished surface of a matrix block. In the original version of the test (Fig 3.12(a)), a selected fiber is loaded using spherical indenters in steps of increasing force, and the interface bonding is monitored microscopically between steps, until debonding is observed (Mandell et al., 1980). The IFSS, τ_b , is calculated from

$$\tau_b = \sigma_d \left(\frac{\tau_{\max}}{\sigma_f} \right)_{\text{FEM}}, \quad (3.8)$$

where σ_d is the average compressive stress applied to the fiber end at debonding. τ_{\max}/σ_f is the ratio of the maximum interface shear stress to the applied stress determined in the finite element method (FEM).

In the second approach shown in Fig 3.12(b), a force is applied continuously using a Vickers microhardness indenter to compress the fiber into the specimen surface (Marshall, 1984). For ceramic matrix composites where the bonding at the interface is typically mechanical in nature, the interface shear stress, τ_{fr} , against the constant frictional sliding is calculated based on simple force balance (Marshall, 1984):

$$\tau_{fr} = \frac{d \sigma_f}{4\ell}, \quad (3.9)$$

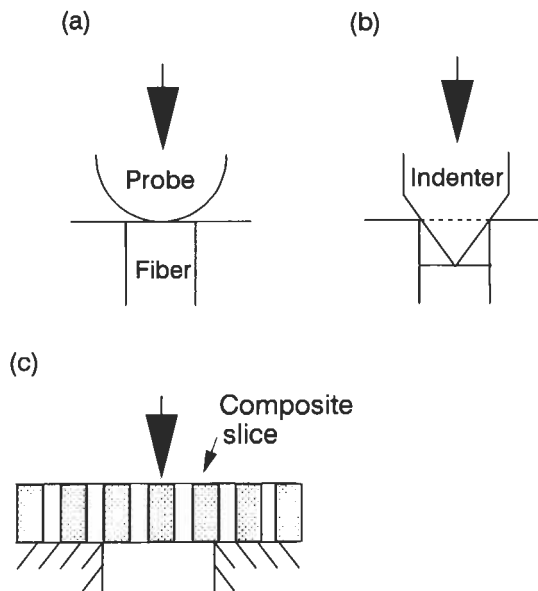


Fig. 3.12. Schematic drawings of indentation (or fiber push-out) techniques: using (a) a spherical indenter; (b) a Vickers microhardness indenter; (c) on a thin slice. After Grande et al. (1988).

where $\ell = 2E_f\delta/\sigma_f$ is the debonded length estimated from the displacement of the fiber end, δ , at an average external stress, σ_f , applied to the fiber.

In contrast to the thick specimens used in the above studies, very thin slice specimens of known embedded fiber lengths (Fig 3.12(c)) are also employed (Bright et al., 1989) to distinguish debonding and post-debond frictional push-out in a continuous loading test. The latter fiber push-out technique has become most popular in recent years among the variations of specimen geometry and loading methods. Rigorous micromechanics analyses dealing with interface debonding and fiber push-out responses are detailed in Chapter 4.

The above test techniques have been developed initially and used extensively for polymer matrix composites (Grande et al., 1988; Herrera-Franco and Drzal, 1992; Desaeger and Verpoest, 1993; Chen and Croman, 1993). Its usefulness has been extended to ceramic matrix composites (Grande et al., 1988; Brun and Singh, 1988; Netravali et al., 1989a, b; Morscher et al., 1990; Weihs and Nix, 1991; Wang et al., 1992; Watson and Clyne, 1992a, b; Ferber et al., 1993) where difficulties of specimen preparation and testing associated with fiber misalignment, breakage of high modulus fibers in grips, etc. are frequently experienced in fiber pull-out tests. Other major advantages include the ability to test real composites and the speed and simplicity of the test, once automated instruments are equipped with the testing machine. The main questions associated with this test method are concerned with its physical significance and the interpretation of experimental data. Other drawbacks are the inability to monitor the failure process during the test of opaque composites; problems associated with crushing and splitting of fibers by the sharp indenter under compression (Desaeger and Verpoest, 1993); and radial cracks within the matrix near the fiber-matrix interface (Kallas et al., 1992).

3.2.6. Slice compression test

The slice compression test is a modified version of the indentation test and was developed specifically for ceramic matrix composites utilizing the difference in elastic modulus between the fiber and the matrix material. This test involves compression of a polished slice of a unidirectional fiber composite cut perpendicularly to the fiber axis between two plates (Fig 3.13). The applied load is increased to a desired peak stress and then unloaded. At the critical load, interfacial debonding and sliding occur near the top surface of the specimen where the elastic mismatch is at its maximum and the fibers protrude against the soft top plate (e.g. pure aluminum) with known work-hardening characteristics. At the same time, the hard bottom plate (e.g. Si_3N_4) ensures a constant strain in the specimen bottom. Upon removing the load, the fibers partially relax back into the matrix, retaining a residual protrusion. Fig 3.14 schematically shows the sequence of the slice compression test based on a single fiber model composite (Hsueh, 1993). Therefore, the interface properties can be estimated from the fiber protrusion, δ , under a peak load and the residual fiber protrusion after unloading, δ_r . Shafry et al., (1989) derived approximate solutions for the relationship between the fiber protrusion length and the applied stress for a constant interface friction along the embedded fiber

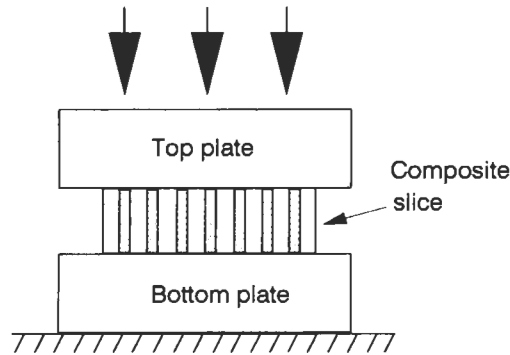


Fig. 3.13. Schematic drawing of slice compression test on a composite slice containing multiple fibers. After Shafry et al. (1989).

length based on the solutions previously obtained in fiber pull-out tests (Gao et al., 1988) and fiber stress relaxation after unloading (Marshall and Oliver, 1987). More rigorous analyses are still evolving (e.g., Hsueh, 1993; Lu and Mai, 1994), and further details are discussed in Chapter 4.

3.2.7. Comparison of microcomposite tests and experimental data

It has been noted in a round robin test of microcomposites that there are large variations in test results for an apparently identical fiber and matrix system between 13 different laboratories and testing methods (Pitkethly et al., 1993). Table 3.1 and Fig 3.15 summarize the IFSS values of Courtaulds XA (untreated and standard surface treated) carbon fibers embedded in an MY 750 epoxy resin. It is noted that the difference in the average ISS values between testing methods, inclusive of the fiber fragmentation test, fiber pull-out test, microdebond test and microindentation test, are as high as a factor of 2.7. The most significant variation in ISS is obtained in the fiber pull-out /microdebond tests for the fibers with prior surface treatments, and the microindentation test shows the least variation.

There are a number of factors contributing to this discrepancy, such as a lack of standardization in specimen preparation, the loading method, the measurement and data reduction methods. Details of major contributors to the large data scatter are summarized for each testing method in the following:

(i) *Fiber pull-out test*: measurement of embedded length, loading rate, alignment of fiber with loading axis, accuracy of measurements of fiber diameter.

(ii) *Microdebond test*: size and shape (e.g. symmetry) of the droplet, shape of the meniscus produced with the fiber, variations in the concentration of hardener within the droplet, shape and size of the specimen holder (i.e. microvice).

(iii) *Fragmentation test*: level of preload applied to the fiber during the curing process, loading method (e.g. continuous loading by electronic device versus

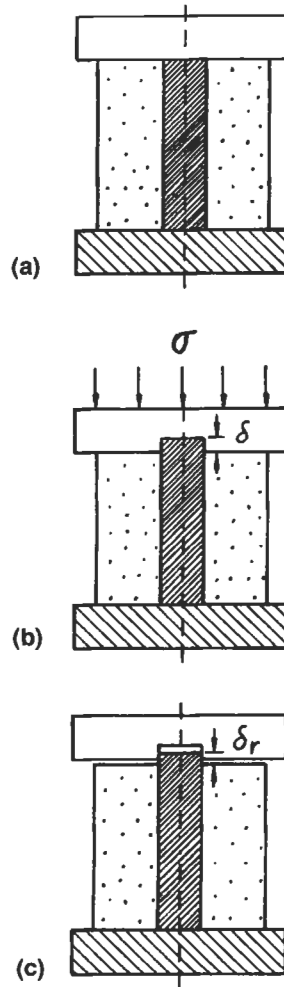


Fig. 3.14. Schematic drawings of slice compression test on a single fiber composite: (a) before loading; (b) peak loading with a maximum fiber protrusion length, δ ; (c) after unloading with a residual fiber protrusion length, δ_r . After Hsueh (1993).

intermittent manual loading), loading rate, methods of detection of fiber breakage (e.g. optical microscopy and acoustic emission).

(iv) *Micro-indentation test*: specimen preparation, size and shape of indenter, methods of detecting debonding (e.g. using microscope and from the load drop in the load–displacement curve), fiber splitting caused by indentation, methods for data reduction (e.g. finite element model and shear-lag type analysis).

3.3. Interlaminar/intralaminar properties

3.3.1. Introduction

In addition to the direct measurements of fiber–matrix interface properties discussed in Section 3.2, a number of testing techniques have been devised to assess the fiber–matrix interface bond quality by inference from the gross mechanical properties such as interlaminar shear strength (ILSS), translaminar or in-plane shear strength, and transverse tensile strength. These testing techniques invariably employ

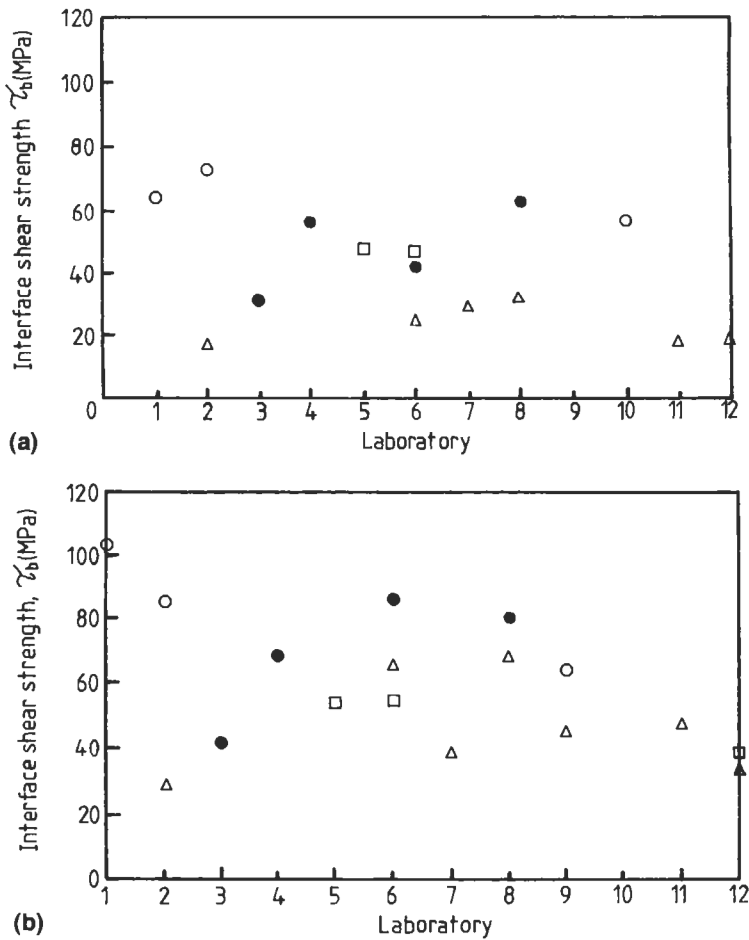


Fig. 3.15. Interface shear strength, τ_b , of (a) untreated and (b) treated LXA500 carbon fiber-epoxy matrix system measured at 10 different laboratories and using different testing methods. (○) fiber pull-out test; (●) microdebond test; (□) fiber push-out test; (△) fiber fragmentation test. After Pitkethly et al. (1993).

Table 3.1
Collated data obtained from all laboratories in a round robin test programme^a

Testing method	Pull-out		Microdebond		Fragmentation		Push-out	
	None	Std.	None	Std.	None	Std.	None	Std.
Fiber treatment	None	Std.	None	Std.	None	Std.	None	Std.
No. of laboratories	3	3	4	4	6	7	2	3
ISS, τ_a (MPa)	64.6	84.1	48.3	69.7	23.8	47.3	47.8	49.5
SD	8.2	19.4	14.1	19.7	6.6	15.4	0.5	9.1
CV (%)	13	23	29	28	28	33	1	18.9

Std., standard surface treatment; ISS, interfacial shear strength; SD, one standard deviation; CV, coefficient of variation.

^aAfter Pitkethly et al. (1993).

laminated composites reinforced with continuous and long fibers, whether unidirectional or cross-plyed.

Apart from the short beam shear test, which measures the interlaminar shear properties, many different specimen geometry and loading configurations are available in the literature for the translaminar or in-plane strength measurements. These include the Iosipescu shear test, the $[\pm 45^\circ]_S$ tensile test, the $[10^\circ]$ off-axis tensile test, the rail-shear tests, the cross-beam sandwich test and the thin-walled tube torsion test. Since the state of shear stress in the test areas of the specimens is seldom pure or uniform in most of these techniques, the results obtained are likely to be inconsistent. In addition to the above shear tests, the transverse tension test is another simple popular method to assess the bond quality of bulk composites. Some of these methods are more widely used than others due to their simplicity in specimen preparation and data reduction methodology.

Testing on bulk composite materials has a more serious limitation than in microcomposite tests in that the actual locus and modes of failure have to be consistent with what are originally designed for the composite in order for a specific test to be valid. Judgment of validity of the test by examining the onset of failure during the experiment is a tedious task, which cannot be assumed to have taken place for a given loading condition. Even in an apparent interlaminar shear failure, the failure may occur at the fiber–matrix interface, in the matrix or in a combination of these, depending on the loading direction relative to the interface concerned and, more importantly, on the relative magnitudes of the fiber–matrix interface bond strength and the shear strength of the matrix material. This makes the interpretation of experimental data more complicated since this requires proper micromechanics analysis to be developed together with prior knowledge of the matrix properties (Lee and Munro, 1986; Pindera et al., 1987).

3.3.2. Short beam shear test

The short beam shear test designated in ASTM D 2344 (1989) involves loading a beam fabricated from unidirectional laminate composites in three-point bending as

illustrated in Fig 3.16. In interpreting the short beam shear test, the maximum value τ_{\max} (i.e. the ILSS of the shear stress distribution along the thickness direction, is related to the maximum applied load P_{\max} , and specimen width b and thickness t , according to the classic short beam shear relationship

$$\tau_{\max} = \frac{3P_{\max}}{4bt} \quad (3.10)$$

It is easily seen that even in the absence of any substantial bonding at the fiber–matrix interface, ILSS of the composite laminate still has a lower-bound value which is contributed solely by the shear strength of the matrix τ_m . For a brittle matrix beam with cylindrical pores (in place of the fibers of volume fraction V_f in square array), the lower bound ILSS can be estimated from $\tau_m[1 - (4V_f/\pi)^{1/2}]$, which depends strongly on the fiber V_f . This implies that the ILSS cannot be regarded as giving the genuine values of the bond strength. Nevertheless, because of the simplicity of the test method and minimum complication in specimen preparation, the short beam shear test has become one of the most popular methods to determine the interlaminar bond quality of composites containing both polymer and metal matrices. It has been most widely used to assess the effects of fiber finish and surface treatments, fiber–matrix compatibility for the development of new fiber or matrix systems, etc.

This test has an inherent problem associated with the stress concentration and the non-linear plastic deformation induced by the loading nose of small diameter. This is schematically illustrated in Fig 3.17, where the effects of stress concentration in a thin specimen are compared with those in a thick specimen. Both specimens have the same span-to-depth ratio (SDR). The stress state is much more complex than the pure shear stress state predicted by the simple beam theory (Berg et al., 1972;

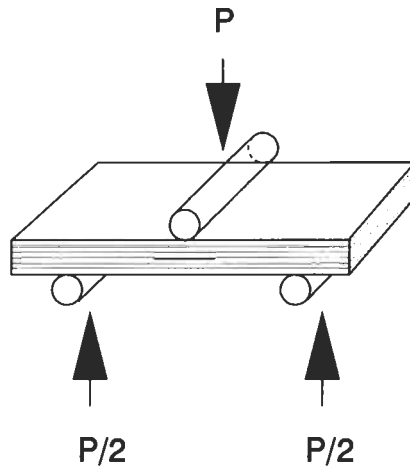


Fig. 3.16. Schematic of loading configuration of short beam shear test.

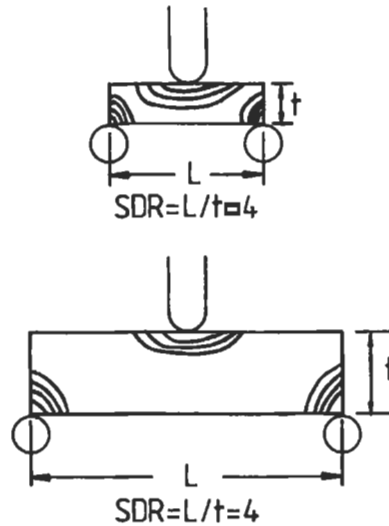


Fig. 3.17. Effect of stress concentrations on short beam shear specimens: (a) thin specimen; (b) thick specimen. After Browning et al. (1983).

Sandorf, 1980; Whitney, 1985; Whitney and Browning, 1985). According to the classical beam theory, the shear stress distribution along the thickness of the specimen is a parabolic function that is symmetrical about the neutral axis where it is at its maximum and decreases toward zero at the compressive and tensile faces. In reality, however, the stress field is dominated by the stress concentration near the loading nose, which completely destroys the parabolic shear distribution used to calculate the apparent ILSS, as illustrated in Fig 3.18. The stress concentration is even more pronounced with a smaller radius of the loading nose (Cui and Wisnom, 1992) and for non-linear materials displaying substantial plastic deformation, such as Kevlar fiber-epoxy matrix composites (Davidovitz et al., 1984; Fisher et al., 1986), which require an elasto-plastic analysis (Fisher and Marom, 1984) to interpret the experimental results properly.

The high stress concentration and damage by crushing in severe cases at the loading nose with a very small SDR may induce premature failure in the compressive face before interlaminar failure (Fig 3.19) (Berg et al., 1972; Whitney and Browning, 1985). This problem causes a significant limitation in relation to the failure mode transition depending on the SDR. It is well known that flexure specimens, which normally fail in the shear mode, may fail under compression with the increase in the SDR above a critical value (Sattar and Kellogg, 1969; Fisher et al., 1986). The critical SDR in general increases with large fiber volume fraction, V_f , and weakened interface bonding for a given fiber-matrix composite (Shih and Ebert, 1986; Birger et al., 1989). This failure mode transition behavior is very sensitive to the loading rate (Boukhili et al., 1991). Non-shear or mixed mode failure can result in invalid data with the calculated ILSS being too high with respect to the flexural

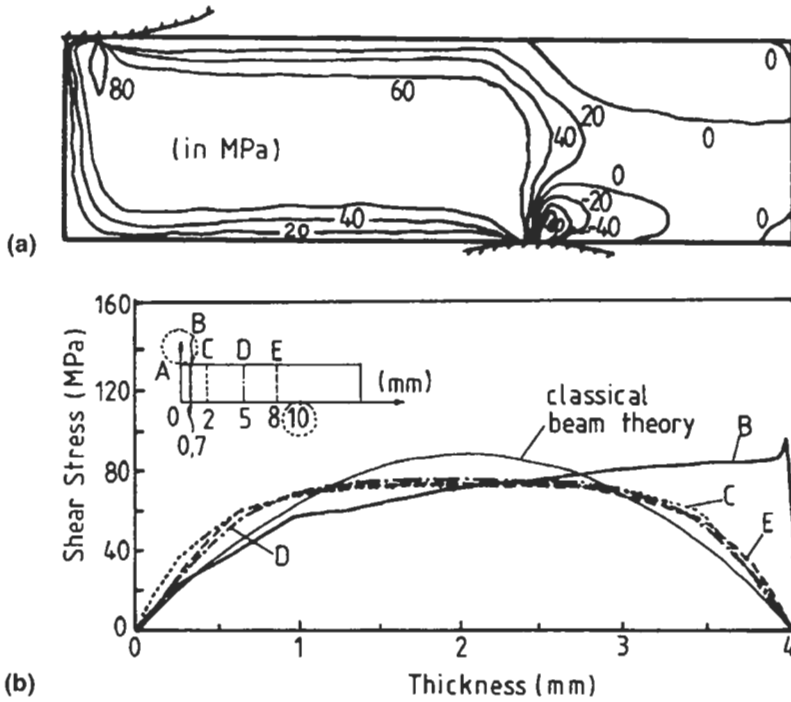


Fig. 3.18. (a) Shear stress contours and (b) shear stress distributions across the thickness of a three-point bending specimen in a short beam shear test. After Cui and Wisnom (1992). Reproduced by permission of Elsevier Science Ltd.

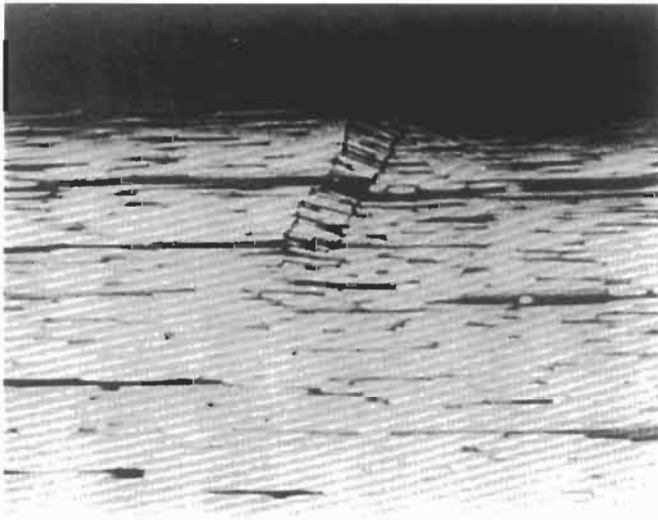


Fig. 3.19. Scanning electron microphotograph of buckling failure near the loading nose of a carbon fiber-epoxy matrix short beam shear specimen. After Whitney and Browning (1985).

strength. Therefore, in-situ microscopic examination is often necessary to ensure that interlaminar shear failure occurs at the maximum bending load.

Since the range of SDR that consistently produces interlaminar shear failure is very small (i.e. four or five when the Young's moduli for the composites are greater or less than 100 GPa, respectively, in accordance with the specification (ASTM D 2344, 1989)), the specimen has to be very thick, which is both expensive and more difficult to fabricate. As an alternative, four-point bending of a long thin specimen is suggested (Browning et al., 1983), whereby the sharing of the total load between two loading noses can reduce the local stress concentration compared to three-point bending (Cui and Wisnom, 1992).

3.3.3. Iosipescu shear test

The Iosipescu shear test (Iosipescu, 1967) is an ideal method that is relatively simple to conduct with small and easily fabricated specimens, and it is capable of measuring reliable shear strength and the modulus simultaneously (Lee and Munro, 1990). This test employs a double-edge notched specimen that is subjected to two counteracting moments produced by force couples as shown in Fig 3.20(a). In a qualitative photoelastic study, Iosipescu (1967) showed that when the depth of each 90° vee-notch is between 20% and 25% (typically 22%) of specimen depth and the notch tip radius is zero (i.e., a sharp notch), the stress state across the notched section is under pure and uniform shear for an isotropic material. This is a direct result from the coincidence between the directions of the principle stresses at $\pm 45^\circ$ to the specimen axis and the 90° notch angle in the region of the zero bending moment. In this case, there is no stress singularity at the notch tip because of the absence of normal stresses at the point. The average shear stress in the middle section of the specimen with width b is simply given by the applied load P , divided by the net cross-sectional area

$$\tau = \frac{P}{bt} \quad (3.11)$$

To calculate the shear modulus, strain gauges are used to obtain the shear stress–shear strain curve. Attracted by the almost pure shear state generated at the test section, a number of researchers have studied the applicability of this test technique to advanced composite materials, using FEMs as well as other experimental means. Adams and Walrath (1982, 1987a, b) in particular have evaluated the shear stress distribution as a function of notch depth, angle, notch tip radius, etc., which resulted in redesigning the specimen geometry and test fixture. It is clearly shown that there is a substantial stress concentration near the notch tip and the shear stress distribution in the middle section of orthotropic specimen is not uniform as opposed to isotropic materials. The stress concentration is found to be a function of the orthotropic ratio (i.e., Young's moduli ratio between two principal in-plane directions, E_{11}/E_{22} , which is governed by the fiber orientation and the fiber volume fraction) and notch geometry, and can be reduced by incorporating a large notch tip radius with a large

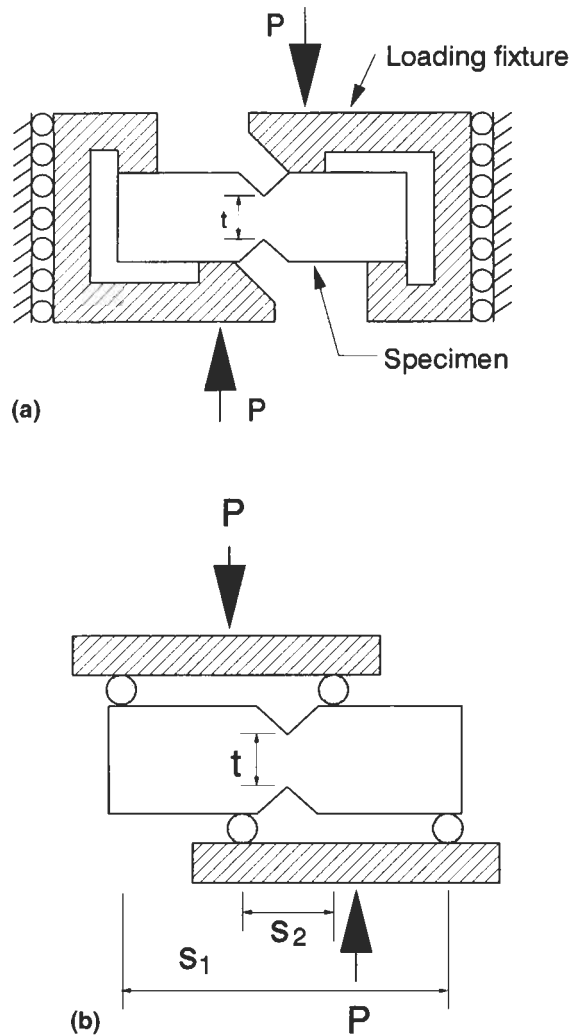


Fig. 3.20. Schematic drawings of loading configurations of (a) Iosipescu shear test and (b) asymmetric four-point bending (AFPB) test. After Iosipescu (1967) and Slepetz et al. (1978).

notch angle depending on the type of composites (Fig 3.21). In addition to the depth and tip radius of the specimen notch, there are other factors to consider in practice. Because the stress concentrations are highly localized, cracks easily form at the notch roots at a stress lower than the ultimate value for unidirectional fiber composites containing brittle matrix materials that are capable of little plastic deformation. These cracks subsequently relieve the stress concentration, facilitating more uniform shear loading of the material in the notched section (Adams and Walrath, 1987a, b; Adams 1990).

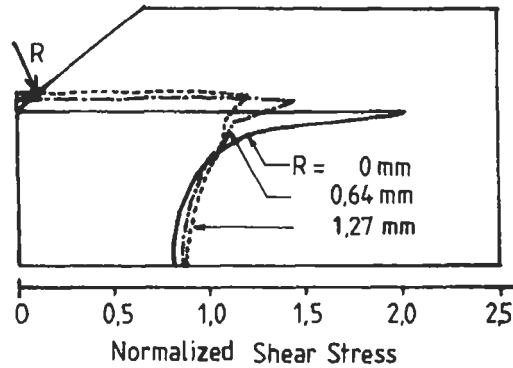


Fig. 3.21. Shear stress distributions across the notches in the Iosipescu shear test. After Adams and Walrath (1987a, b).

Slight modification was also made to the loading fixture (Slepetz et al., 1978), leading to the so-called asymmetrical four-point bending (AFPB) test as illustrated in Fig 3.20(b), which requires the use of fixture dimensions in calculating the shear stress

$$\tau = \frac{P(s_1 - s_2)}{bt(s_1 + s_2)} \quad (3.12)$$

Several investigators (Sullivan et al., 1984; Spigel et al., 1985; Abdallah and Gascoigne, 1989) have compared the AFPB and the Iosipescu test fixtures (Adams and Walrath, 1982, 1987a; Walrath and Adams 1983), using various techniques including FEMs, photoelastic and Moire interferometry. Although the information reported was rather inconsistent, the difference was only marginal in terms of both the stress concentration and the shear stress distribution. However, there is a disadvantage of the AFPB fixture in that the cylindrical loading noses may cause local stress concentration and crushing on the edges of the composite specimen, as in the short beam shear test, requiring the use of reinforcing tabs.

The major advantage of this test is that there is a large region of uniform shear in idealized conditions compared to the other shear tests, e.g. the short beam shear test, as already mentioned. It can measure both the in-plane shear strength and shear modulus in the direction parallel to the fiber with high accuracy and reproducibility. It can also be used to determine the interlaminar shear properties of laminate composite when the specimen is prepared in such a way that the axial direction is normal to the fiber direction for unidirectional composites. However, the pure shear is very easily distorted by various factors, such as loading nose, twist and the bending moment arising from misalignment. Loading noses and twist may cause stress concentration in the loading area and in the test section as in other testing techniques.

3.3.4. $[\pm 45]_s$ tensile test

In the $[\pm 45]_s$ tensile test (ASTM D 3518, 1991) shown in Fig 3.22, a uniaxial tension is applied to a $(\pm 45^\circ)$ laminate symmetric about the mid-plane to measure the strains in the longitudinal and transverse directions, ϵ_x and ϵ_y . This can be accomplished by instrumenting the specimen with longitudinal and transverse element strain gauges. Therefore, the shear stress–strain relationships can be calculated from the tabulated values of ϵ_x and ϵ_y , corresponding to particular values of longitudinal load, P_x (or stress σ_x over the width, b , and thickness, t , of the specimen), based on the relations derived from laminated plate theory (Petit, 1969; Rosen, 1972):

$$\tau_{12} = \frac{P_x}{2bt} = \frac{\sigma_x}{2} \quad , \quad (3.13)$$

$$\gamma_{12} = \epsilon_x - \epsilon_y \quad . \quad (3.14)$$

Therefore, the unidirectional translaminar (i.e. through-thickness) shear strength can be obtained for the maximum load and the in-plane shear modulus of elasticity, G_{LT} , taken from the initial linear portion of the unidirectional shear stress–shear strain ($\tau_{12} - \gamma_{12}$) curve:

$$G_{LT} = \frac{\Delta\tau_{12}}{\Delta\gamma_{12}} \quad . \quad (3.15)$$

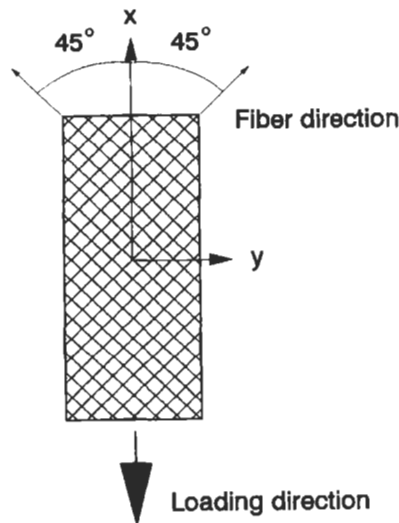


Fig. 3.22. Schematic drawing of specimen for $[\pm 45]_s$ tensile test. After ASTM D 3518. (1991).

The technique underlying this test has the advantage of utilizing the relatively inexpensive, straight-sided tensile specimens and conventional uniaxial tensile test equipment. Caution should be exercised, however, in interpretation of the ultimate shear strength values obtained from this test because the laminate is under combined normal and shear stresses. Nevertheless, there is generally a good agreement between the stress-strain response obtained in this test and other in-plane shear test geometry including the three-rail shear (Sims, 1973) and the torsion shear tests (Chiao et al., 1977).

3.3.5. $[10^\circ]$ off-axis tensile test

The $[10^\circ]$ off axis tension specimen shown in Fig 3.23 is another simple specimen similar in geometry to that of the $[\pm 45^\circ]_S$ tensile test. This test uses a unidirectional laminate with fibers oriented at 10° to the loading direction and the biaxial stress state (i.e. longitudinal, transverse and in-plane shear stresses on the 10° plane) occurs when it is subjected to a uniaxial tension. When this specimen fails under tension, the in-plane shear stress, which is almost uniform through the thickness, is near its critical value and gives the shear strength of the unidirectional fiber composites based on a procedure (Chamis and Sinclair, 1977) similar to the $[\pm 45^\circ]_S$ tensile test.

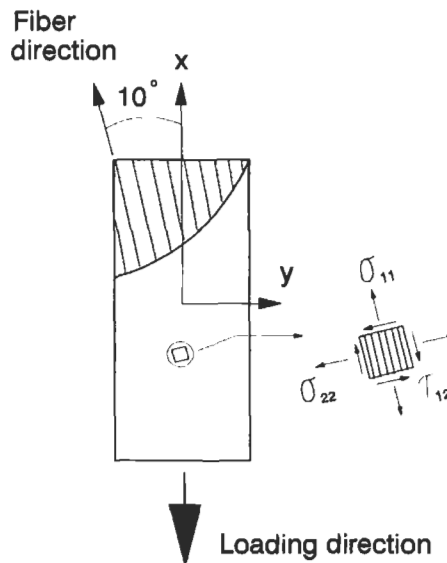


Fig. 3.23. Schematic drawing of specimen for $[10^\circ]$ off-axis tensile test. After Chamis and Sinclair (1976).

3.3.6. Rail shear test

In the rail shear test, which is specified in ASTM D 4255 (1983), a load, P , is applied either under tension or compression to the edges of the rails to displace one rail parallel to the other, as illustrated in Fig 3.24. Element strain gauges should be used to measure the longitudinal and transverse strains properly as in the $[\pm 45^\circ]_S$ tensile test. Therefore, the apparent shear strength, τ_{12} , and shear modulus, G_{12} , can be calculated over the cross-section of the specimen in the longitudinal direction using Eqs. (3.13) and (3.15), for the two-rail shear (Fig 3.24(a)), where b is now the total length of the specimen. In the case of three-rail shear (Fig 3.24(b)), a factor of 0.5 has to be multiplied to Eq. (3.13) for calculation of the shear strength. A theoretical stress analysis (Whitney et al., 1971) has shown that the two-rail shear test is capable of accurately measuring the shear strength/modulus when the length to width ratio, i.e., the aspect ratio, is at least 10. A laminate with a low effective Poisson ratio gives a higher accuracy because the shear stress distribution becomes irregular and leads to an underestimate of the shear strength if the Poisson ratio is very high as in the $[\pm 45^\circ]$ angle ply laminates. The influence of the aspect ratio of the rail-shear test specimen on the stress distribution has been confirmed by finite element analysis (Garcia et al., 1980).

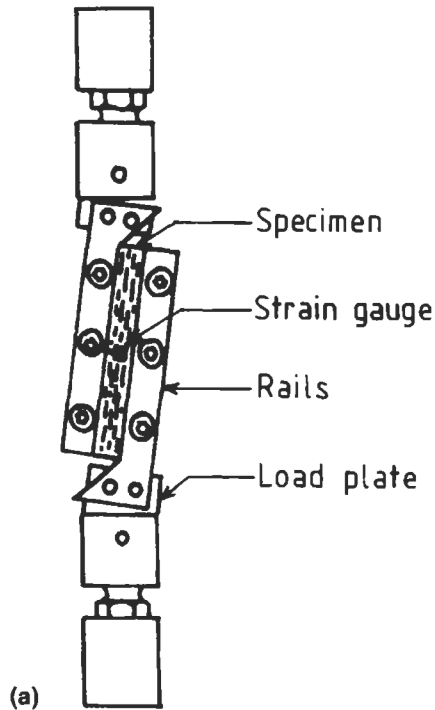


Fig. 3.24. Schematic drawings of loading fixtures in (a) two rail shear and (b) three rail shear test. After ASTM D 4255 (1983).

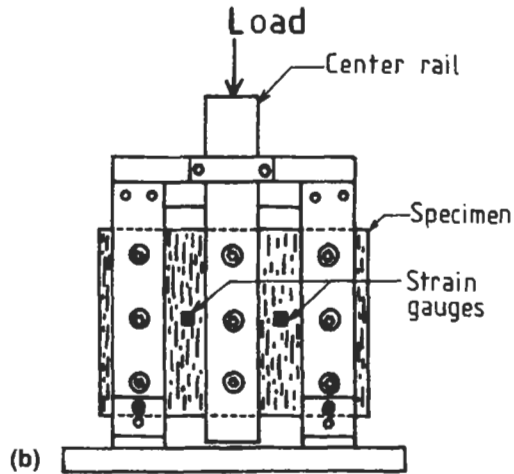


Fig. 3.24. (b).

3.3.7. In-plane lap-shear test

The in-plane lap-shear test specified in ASTM D 3846 (1985) employs a notched rectangular specimen of uniform width that is mounted in a supporting jig, as schematically illustrated in Fig 3.25. A compressive load is applied to the specimen edge, as opposed to the conventional tensile loading of lap-shear adhesive joints. Failure of the specimen occurs in the shear between two centrally located notches machined half-way through its thickness and spaced a fixed distance (i.e., 6.4 mm for specimen thickness of 2.54–6.60 mm) apart on opposite faces. The in-plane shear strength is subsequently calculated by dividing the maximum shear load by the product of the width of the specimen and the length of the failed area. While the lap-shear test lends itself to laminates containing continuous and uniformly distributed fibers, it is also useful to measure shear strength of laminates having randomly dispersed short fibers, which cannot be tested satisfactorily by other in-plane shear tests.

3.3.8. Transverse tensile test

The transverse tensile test (ASTM D 3039, 1982) assesses the quality of composites by measuring the tensile strength of unidirectional fiber composites in the direction transverse to the fiber direction (Fig 3.26). Early work by Chamis (1974) on finite element analysis of this test indicates that interfacial debonding is the most probable cause of transverse crack initiation. The most obvious feature of this test is that its strength is usually less than the shear yield strength of the matrix, τ_m , so that in contrast to the effect of fibers on the transverse modulus (which is higher than that of pure matrix material without fibers) the fibers have a negative reinforcing effect. In the case of a weak interfacial bond, the lower-bound

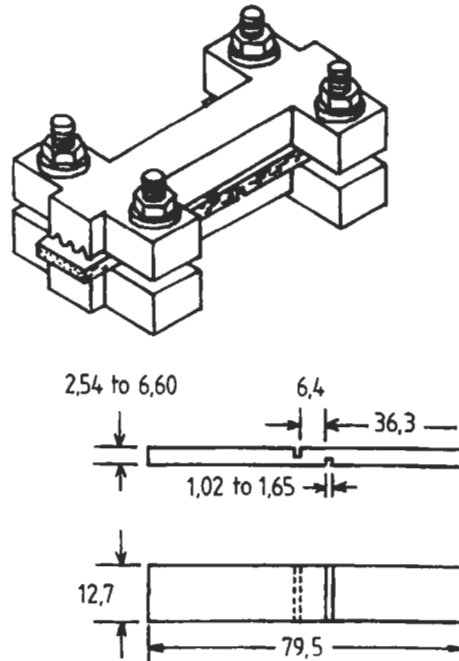


Fig. 3.25. Schematic drawings of specimen and loading jig for in-plane shear test. After ASTM D 3846 (1985).

transverse strength, σ_{\perp} , can also be estimated in the same way as for the ILSS by considering a brittle matrix with cylindrical pores, i.e. $\sigma_{\perp} = \sigma_m [1 - (4V_f/\pi)^{1/2}]$ (Greszczuk, 1967). For a good interface bond, the transverse strength will increase accordingly due to the constraints of the matrix material between the reinforcing fibers.

There is renewed evidence that shows the sensitivity of this test to interface properties. For example, recent transverse tensile and flexural tests on carbon fiber–epoxy matrix composites with several different levels of fiber surface treatments (Madhukar and Drzal, 1991; Drzal and Madhukar 1993) show that while there is little effect of the IFSS on the transverse tensile modulus, the transverse tensile strength and the maximum strain increase approximately in the same ratio as the increase in the IFSS (Fig 3.27). However, since the transverse tensile strength is governed not only by the interface bond strength, but also by the mechanical properties of the fiber and matrix and by the presence and distribution of voids and foreign objects, etc. (Chamis, 1974), the test results may sometimes be misleading unless care is taken in interpretation. In particular, the mode of failure in this test may relate only indirectly to the interfacial bond. Therefore, it can be rationalized that the significance of this test method is to provide some measure of the relative bond strength of different fiber–matrix composite systems.

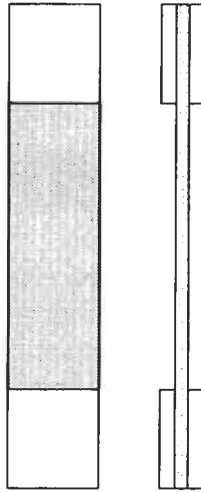


Fig. 3.26. Schematic drawing of transverse tensile test specimen.

3.4. Interlaminar fracture toughness

3.4.1. Delamination

Delamination represents the weakest failure mode in laminated composites, and is considered to be the most prevalent life-limiting crack growth mode in most composite structures. As such, ever-increasing attention has been directed toward the understanding and characterization of delaminations of various natures, and at

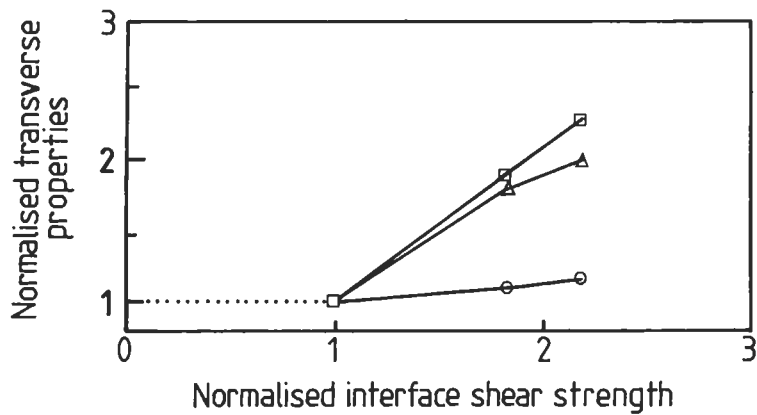


Fig. 3.27. Effect of the interface shear strength on mechanical properties of carbon fiber-epoxy matrix composites: (□) transverse tensile strength; (△) maximum transverse tensile strain; (○) transverse tensile modulus. After Madhukar and Drzal (1991).

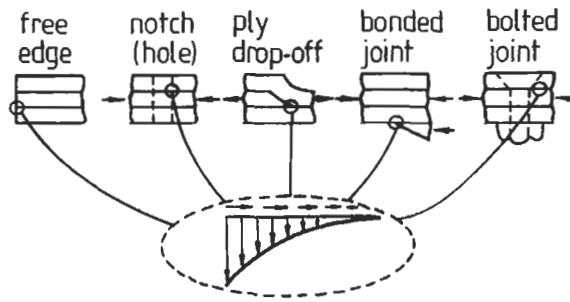


Fig. 3.28. Sources of delamination due to out-of-plane load from discontinuities in structure. After Wilkins et al. (1982).

the same time toward improving the durability of composites against interlaminar fracture. Delamination may be introduced during processing or subsequent service conditions. It may result from low-velocity impact, from eccentricities in the structural load path, or from discontinuities in structures, which induce a significant out-of-plane stress, as shown in Fig 3.28 (Wilkins, et al., 1982). These are (i) straight or (ii) curved (near holes) free edges, (iii) ply terminations or ply drop for tapering the thickness, (iv) bonded or co-cured joints, (v) a bolted joint and (vi) a cracked lap shear specimen. All these cases, the local stress near the discontinuities may be out-of-plane even if the loading at remote end is in-plane. Even in the absence of such discontinuities delamination can result from in-plane compressive loading, causing local or global buckling to occur.

In addition to mechanical loads, the moisture and temperature may also induce interlaminar stresses in a laminate. These may be the results from (i) the residual thermal stresses caused by cooling from the processing temperatures; and (ii) residual stresses created by the moisture absorption in the laminate; and (iii) moisture through the thickness of the laminate. Delamination growth in the composite structure can cause severe reductions in strength properties, though it seldom leads to immediate catastrophic failure. Instead, delamination occurring under in-plane loading normally induces local damages resulting in the loss of stiffness, local stress concentration and local instability. This delamination often leads to a redistribution of stresses, which would eventually promote gross failure. In this context, delamination is indirectly responsible for the final failure of a composite. This is one important reason why past applications of composite materials in the aerospace industries have been largely limited to secondary structural components, such as wings and stabilizers where load paths are well defined and load-induced failure is not life threatening.

Composite structures in service are often subjected to complex 3-D load paths. In general, a delamination will be subjected to a crack driving force with a mode I opening, a mode II forward shear and a mode III anti-plane shear, as illustrated in Fig 3.29. Because delamination is constrained to grow between individual plies, both interlaminar tension and shear stresses are commonly present at the

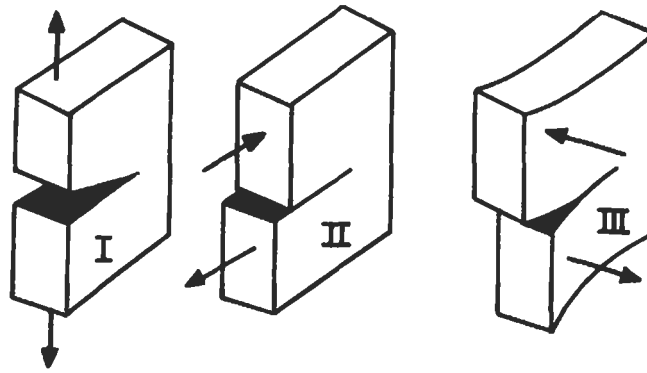


Fig. 3.29. Modes of interlaminar crack propagation: (a) Mode I opening mode; (b) Mode II sliding shear mode; (c) Mode III tearing mode.

delamination front. Therefore, delamination in practical composites is almost always a mixed-mode fracture process. It is generally accepted that the interlaminar fracture toughness of a composite is determined principally by the inherent properties of the matrix material including the failure strain, the ability of plastic deformation and fracture toughness, and further that the fiber–matrix interface properties are not the decisive factor in determining the interlaminar fracture toughness.

Test methods based on fundamental mechanics concepts have been developed to evaluate the interlaminar fracture resistance of laminate composites. Extensive research efforts have been devoted towards the standardization of interlaminar fracture tests (IFT). In particular, the American Society for Testing and Materials (ASTM) task group (D30.02.02) and the European Structural Integrity Group (ESIS), formerly the European Group on Fracture (EGF), have been studying the IFT for over a decade. A series of round robin tests have been performed by the ESIS and the ASTM task groups on glass fiber and carbon fiber thermoset and thermoplastic matrices composites. These exercises are aimed at establishing standardized methods in specimen preparation (e.g., thickness of specimen and type and thickness of starter crack), testing (e.g., loading rate and distance between supports in Mode II test) and data analysis (e.g., correction factors, compliance methods versus area method, which are discussed later) to improve reproducibility of the fracture toughness values. Results from the past exercises have been reported (Davies and Roulin, 1989; Davies and Moore, 1990; Davies et al., 1990, 1992; O'Brien and Martin, 1992, 1993).

3.4.2. Mode I Interlaminar Fracture Test

Historically, most attention has been devoted to mode I delamination growth to assess defects critically, as the first-generation composite systems exhibited low mode I fracture toughness when subjected to interlaminar normal stresses. The

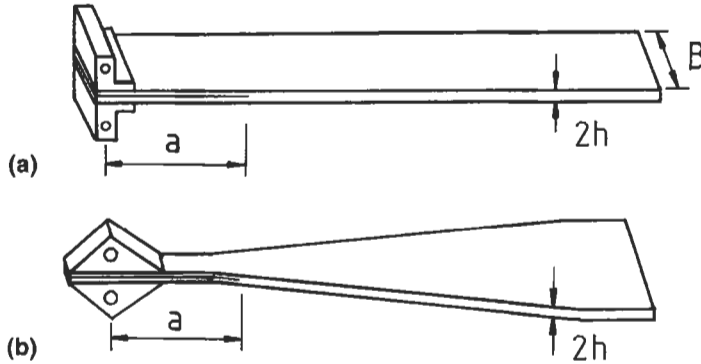


Fig. 3.30. Schematic illustrations of Mode I interlaminar fracture test specimens: (a) DCB specimen; (b) WTDCB specimen.

double-cantilever-beam (DCB) specimens shown in Fig 3.30 have been extensively used to measure the resistance of composites to mode I interlaminar crack growth. This specimen geometry has also been applied for testing adhesives where the specimen consists of a bond line between two metal adherends to measure the strain energy release rate, G_{Ic} , of the adhesive (Ripling et al., 1964). There are two basic configurations for the DCB geometry: the constant width and width tapered DCB (WTDCB) specimens. The latter geometry first employed by Wang (1984) is designed to allow the strain energy release rate to be constant and independent of the instantaneous crack length when the crack propagates under a constant load. Therefore, the crack length does not need to be monitored throughout the test. Its disadvantages are the cost for specimen preparation and the need for separate measurement of flexural modulus of the specimen.

A number of methods have been applied to evaluate the experimental data recorded during the tests, and they may be classified into two types: compliance method and direct fracture energy method.

3.4.2.1. Compliance methods

The compliance methods are all based on the equation for the critical strain energy release rate, G_{Ic} , based on Gurney and Hunt (1967)

$$G_{Ic} = \frac{P^2}{2b} \frac{dC}{da} \quad , \quad (3.16)$$

where P is the load taken when the delamination crack propagates, b the specimen width, and a the crack length. C is the compliance of the specimen given by

$$C = \frac{\delta}{P} \quad , \quad (3.17)$$

where δ is the displacement of the loading point measured at the load, P . To evaluate G_{Ic} via the compliance method, plots of C against crack length, a , need to

be constructed from which the differential compliance can be determined. Knowing the load, P , and the differential, dC/da , the G_{Ic} values at any crack length can be evaluated using Eq. (3.16).

A classic expression for the compliance, C , can be obtained by taking into account the strain energy due to the bending moment for a perfectly elastic and isotropic material

$$C = \frac{2a^3}{3EI} . \quad (3.18)$$

Because $I = bh_3/12$,

$$C = \frac{8a^3}{Ebh^3} , \quad (3.19)$$

where I is the second moment of area, and h , the half specimen thickness of the DCB specimen. Combining Eqs. (3.16)–(3.19) yields the strain energy release rate:

$$G_{Ic} = \frac{P^2 a^2}{bEI} , \quad (3.20)$$

$$G_{Ic} = \frac{3P\delta}{2ba} . \quad (3.21)$$

Eqs. (3.20) and (3.21) are called the ‘load method’ and ‘displacement method’ (Hashemi et al., 1989), respectively, since only load and displacement records corresponding to crack lengths are required to evaluate the G_{Ic} values, once the flexural modulus E of the beam is known. These equations also apply to the WTDCB specimens where the ratio of the crack length to width, a/b , is constant.

As opposed to the simplifying assumption of isotropic materials for Eqs. (3.20) and (3.21), practical composite components are mostly anisotropic and consist of orthotropic laminates. Further, there are a number of factors that cannot be properly accounted for in the elastic beam theory as a consequence of the various aspects of the practical DCB test. These include end rotation and deflection of the crack tip, effective shortening of the beam from a large deflection of the arms, and a stiffening effect of the beam due to the presence of the end tabs or hinges bonded to the specimens. All these factors cause the values of the apparent elastic modulus, E , calculated from Eq. (3.20) to vary with displacement or crack length. Therefore, a number of different analytical equations have been proposed in various forms to ascertain the correction factors in interpreting the experimental data. Among these, Williams and coworkers (Hashimi et al., 1990a, b; Wang and Williams, 1992) have presented one of the most rigorous analyses

$$G_{Ic} = \frac{F}{N} \frac{3P\delta}{2b(a + \chi h)} , \quad (3.22)$$

where χ is the correction factor required to account for the end rotation and deflection of the crack tip, giving the corrected compliance value

$$C = N \frac{8(a + \chi h)^3}{E b h^3} . \quad (3.23)$$

F and N are the correction factors for the stiffening of the specimen due to large displacements (i.e. shortening of the beam) and the metal blocks bonded to the specimen ends, respectively. These correction factors are a complex function of the measured displacement, length of specimen arms, distance of the load-point above the beam axis and other geometric factors, and are given in Hashemi et al., (1990b). It is increasingly realized that crack bridging by misaligned fibers across the crack faces gives rise to a crack-resistance or R-curve (Hu and Mai, 1993; Williams et al., 1995) and that such an R-curve will be useful for material comparison. Indeed, much earlier, Huang and Hull (1989) pointed out the importance of crack bridging and Hu and Mai (1993) indicated that this will affect the different compliance-based equations to evaluate the delamination resistance.

Assuming the coefficient F/N in Eq. (3.22) is close to unity, Eq. (3.22) is then simplified in the specification (ASTM D5528, 1994) to:

$$G_{Ic} = \frac{3P\delta}{2b(a + |\Delta|)} , \quad (3.24)$$

where Δ is the additional crack length arising from the end rotation and crack tip deflection. Δ can be determined experimentally from a least squares plot of the cube root of compliance, $C^{1/3}$, as a function of crack length, a . Eq. (3.24) is called the 'modified beam theory' (MBT) method. This approach also allows the modulus, E , to be determined as follows

$$E = \frac{64(a + |\Delta|)^3 P}{\delta b h^3} , \quad (3.25)$$

which should be independent of delamination length.

Another approach developed on the basis of an empirical compliance calibration, which was designed originally for isotropic brittle materials (Berry 1963), appears to avoid certain problems associated with correction factors. The compliance is given in the form of empirical equation

$$C = k a^n . \quad (3.26)$$

The compliance values for a given crack length, a , are obtained from the slope of the loading path in the loading-unloading experiments. A least squares line of a plot of C versus a in a log-log plot allows the parameter k and exponent n to be determined. The effect of crack bridging will also influence the exponent n as discussed by Hu and Mai (1993). Combining Eqs. (3.16) and (3.26), G_{Ic} is given

$$G_{Ic} = \frac{P^2}{2b} k n a^{n-1} . \quad (3.27)$$

Further combining Eqs. (3.17) and (3.26), Eq. (3.27) can be rewritten in terms of displacement, δ

$$G_{Ic} = \frac{n P \delta}{2 b a} , \quad (3.28)$$

which is the expression for the ‘compliance calibration’ (CC) method suggested by the specification (ASTM D5528, 1994) and the European Structural Integrity Society, TC4 Group as a Protocol (1990). A further modification is made to the “compliance method” given by Eq. (3.28), i.e., ‘modified compliance calibration’ (MCC) method (ASTM D5528, 1994):

$$G_{Ic} = \frac{3P^2 C^{2/3}}{2\alpha_1 b h} , \quad (3.29)$$

where the coefficient α_1 is obtained from the slope of the least squares line fit of the plot of a/h versus $C^{1/3}$. It is noted in the specification (ASTM D 5528, 1994) (O’Brien and Martin, 1993) that G_{Ic} values determined by the three methods of data reduction, i.e. MBT, CC and MCC methods, differ by no more than 3.1% , while the MBT data reduction method yields the most conservative value of G_{Ic} for 80% of the specimens tested.

3.4.2.2. Area method

An alternative to the compliance methods is a direct fracture energy measurement. In this method, the crack extension is related directly to the area, ΔU ,

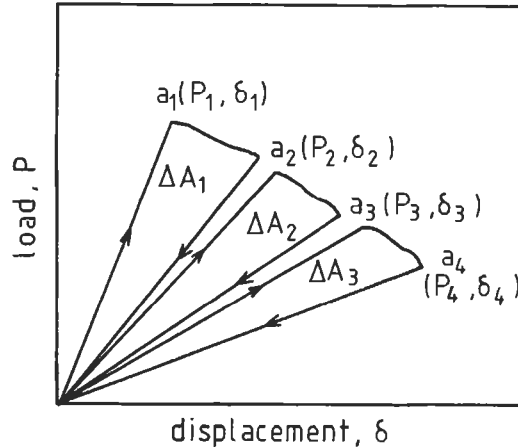


Fig. 3.31. Loading and unloading experiments used to determine the interlaminar fracture toughness, G_{Ic} , based on the area method.

enclosed between the loading and unloading paths for extension of a known crack length, Δa , as shown in Fig 3.31. The mode I strain energy release rate is defined by

$$G_{Ic} = \frac{\Delta U}{b \Delta a} = \frac{1}{2b} \frac{P_1 \delta_2 - P_2 \delta_1}{a_2 - a_1} \quad (3.30)$$

Therefore, an average value of G_{Ic} for an extension of crack length, $a_2 - a_1$, is determined by measuring the force, P , and the corresponding displacement, δ . However, the crack propagation must be stable for reliable application of Eq. (3.30). If large, unstable crack jumps with precipitous load drops are prevalent, the above expression becomes invalid due to the kinetic energy lost in the fracture process. For these reasons, interpretation of DCB test data should always be carried out in conjunction with an examination of the fracture surface. Further complication is encountered by the presence of long debonded fibers bridging the cracked surfaces as mentioned earlier.

3.4.3. Mode II interlaminar fracture tests

The pure mode II interlaminar fracture testing can be performed using both the end notched flexure (ENF) specimen (Russell and Street, 1984, 1985) and the end loaded split (ELS) specimen (Corleto and Bradley, 1987; Prel et al., 1989) (Fig 3.32).

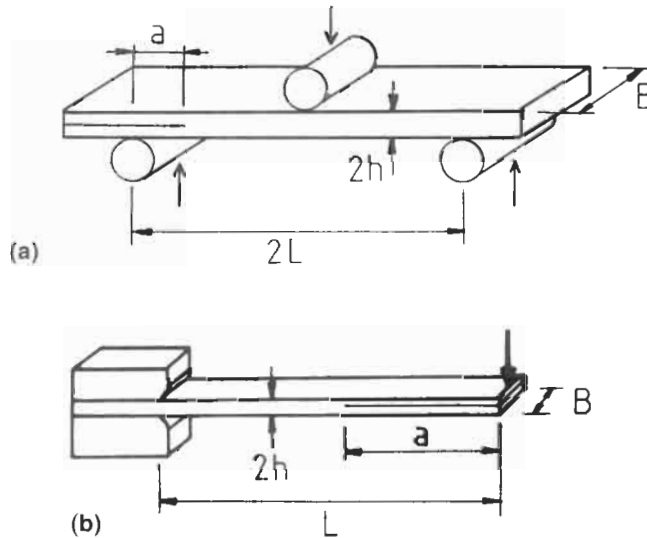


Fig. 3.32. Schematic illustrations of mode II interlaminar fracture test specimens: (a) ENF specimen; (b) ELS specimen.

The ENF specimen is essentially a three-point flexure specimen with an embedded delamination located at the mid-plane of the laminate where the interlaminar shear stress is at its maximum when loaded. An almost pure shear prevails at the tip of the mid-plane delamination (Gillespie et al., 1986). The major difficulty in designing a pure mode II specimen is in preventing any crack opening without introducing excessive friction between the crack faces. The compliance method given by Eq. (3.10) can also be used here to determine the mode II strain energy release rate, G_{IIc} . The relationship between C and a is much more complicated for the ENF test than for the DCB test. Although many equations have been proposed, the one based on the classic beam theory (Carlsson et al., 1986) has been most widely used

$$E' = \frac{2L^3 + 3a^3}{8Cbh^3} , \quad (3.31)$$

where E' is the effective Young's modulus and L , the half-span length. Therefore, the expression for G_{IIc} is obtained for small values of $(E'E/G_s)(h/a)^2$, where G_s is the interlaminar shear modulus (Carlsson and Gillespie, 1989)

$$G_{IIc} = \frac{9a^2P\delta}{2b(2L^3 + 3a^3)} . \quad (3.32)$$

One of the disadvantages of this geometry is that unstable crack propagation occurs, producing only one value, or only part of the propagation values, for tough materials. For this reason, ELS specimen has been favored as it promotes more stable crack propagation. For the ELS test, the compliance equation is given by

$$E' = \frac{L^3 + 3a^3}{8CBh^3} \quad (3.33)$$

and the corresponding expression for G_{IIc} is given

$$G_{IIc} = \frac{9a^2P\delta}{2b(L^3 + 3a^3)} . \quad (3.34)$$

In Eqs. (3.33) and (3.34) for the ELS specimen, L is the total length of the span. In general, interlaminar fracture toughness in mode II may also be derived from a mixed mode test, among which are the cracked lap shear (CLS) test, shown in Fig 3.33, which was originally developed for testing adhesively bonded metallic joints, the end notched cantilever beam (ENCB) test (O'Brien, 1985), and the cantilever beam enclosed notch (CBEN) test (Benzeggagh et al., 1985). Using the CLS specimen, the force-displacement ($P - \delta$) curves may be obtained for various crack lengths and dC/da be determined. The substitutions of P and dC/da in Eq. (3.16) directly give the interlaminar fracture toughness, G_{I-IIc} . Alternatively, G_{I-IIc} may also be calculated from the expression (Russell and Street, 1985)

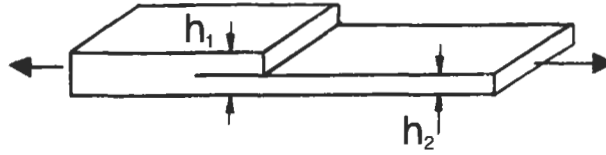


Fig. 3.33. CLS specimen for mixed mode interlaminar fracture tests.

$$G_{I-IIc} = \frac{P^2}{2b^2} \left[\frac{1}{(Eh)_2} - \frac{1}{(Eh)_1} \right], \quad (3.35)$$

where the subscripts 1 and 2 refer to the sections indicated in Fig 3.33. Because CLS gives total energy consisting of mode I and mode II, the individual components may be determined from beam theory using finite element analysis. For unidirectional specimens with the delamination placed at the mid-plane, beam theory gives a value $G_I/G_{I-II} = 0.205$ (Brussat et al., 1977). Details of the expressions for the strain energy release rate of other mixed-mode tests are not treated here as the stress states are much more complicated than in the pure mode II ENF test (Whitney, 1989).

It should be noted that a mode II crack-resistance R-curve may also be obtained for some fiber-matrix systems (Vu-Khanh, 1987). In conjunction with the mode I R-curve the additional information of a mode II R-curve will be of great use to the composite design engineers. This is increasingly the view of the ESIS task group on delamination crack growth resistance.

3.4.4. Mode I edge delamination tests

The problem of delamination along the straight free edge of laminates, which takes place under an in-plane uniaxial load, has attracted significant investigation because the presence and growth of edge delamination may cause progressive reduction in the laminate's stiffness and residual strength. In severe cases, this fracture phenomenon acts as a precursor to final failure of the laminates. The free edge delamination is attributed to the existence of interlaminar stresses, which are highly localized in the neighborhood of a free edge. The magnitude and distribution of these interlaminar stress components vary widely and depend on the laminate layup, stacking sequence, properties of the composite constituents and the nature of loading. Comprehensive reviews of the experimental observations have been presented (Kim, 1989) and a micromechanics analysis of the edge delamination test (EDT) has been performed (Whitney, 1989).

Due to the complex mixed-mode nature of composite delamination, no closed form solutions have been developed yet to express the influence of governing parameters that control the edge delamination behavior. Under tensile loading, delamination is normally preceded by a number of transverse cracks, particularly in the 90° plies. Because of the presence of these cracks, the location of delamination is not unique as in the case of compressive loading, which invariably results in gross buckling of the laminate. The path of delamination along the axial direction varies

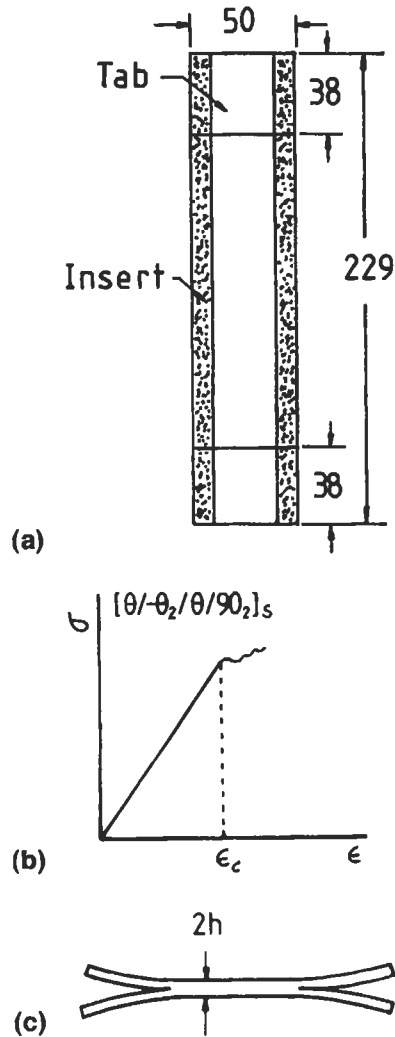


Fig. 3.34. Edge delamination test (EDT): (a) specimen configuration; (b) typical stress-strain curve; (c) outward curvature along specimen edges. After Whitney and Knight (1985).

widely and depends upon the size and location of transverse cracks, the types of laminate, and the fiber and matrix materials. The delamination threshold stress under which no delamination occurs also appears to vary according to the length or density of the transverse crack. Further details are presented in Section 8.3.1.

The EDT specimen shown in Fig 3.34(a) has been used to characterize the interlaminar failure of the composite in opening mode I (Whitney and Knight, 1985). The straight-sided tensile specimen has starter cracks placed along the free edges at the laminate mid-plane (Fig 3.34(a)). Due to the low interlaminar shear

stresses in the mid-plane, the crack propagation will be driven by the normal tensile stress to the laminar interface. At the onset of crack propagation, there may be an abrupt change in the stress-strain curve (Fig 3.34(b)). The strain energy release rate, G_c , associated with edge delamination growth has been analyzed based on the rule of mixtures and laminated plate theory, assuming the absence of the residual thermal stresses. The constant G_c is derived as a function of the critical applied tensile strain, ϵ_c , and the laminate thickness $2h$:

$$G_c = \epsilon_c^2 h (E - E') \quad , \quad (3.36)$$

where E' is the effective Young's modulus of the laminate in the longitudinal direction during edge delamination. By testing specimens made from laminates of different stacking sequences, different percentages of mode I and mode II can also be obtained (O'Brien, 1984). Although the EDT specimen with starter cracks produces a mode I response, the data reduction scheme is complicated due to the presence of lamination residual stresses (see Section 7.5.1). These residual stresses induce an initial outward curvature along the specimen edges, as schematically depicted in Fig 3.34(c), due to asymmetric nature of the specimen above and below the centerline. Such residual stresses can be very significant and the equation must be modified accordingly when residual stresses are included (Whitney, 1989).

References

- Abdallah, M.G. and Gascoigne, H.E. (1989). The influence of test fixture design on the Iosipescu shear test for fiber composite materials. In *Test Methods for Design Allowable for Fibrous Composites: 2nd Vol.* ASTM STP 1003, (C.C. Chamis ed.), ASTM, Philadelphia, PA, pp. 231-260.
- Adams, D.F. (1990). The Iosipescu shear test method as used for testing polymers and composite materials. *Polym. Composites* **11**, 286-290.
- Adams, D.F. and Walrath, D.E. (1982). Iosipescu shear properties of SMC composite materials. In *Composite Materials: Testing and Design (Sixth Conf.)*, ASTM STP 787 (I.M. Daniel ed.), ASTM, Philadelphia, PA, pp. 19-33.
- Adams, D.F. and Walrath, D.E. (1987a). Current status of the Iosipescu shear test method. *J. Composite Mater.* **21**, 494-507.
- Adams, D.F. and Walrath, D.E. (1987b). Further development of the Iosipescu shear test method. *Exper. Mech.* **27**, 113-119.
- Andersons, J. and Tamuzs, V. (1993). Fiber and interface strength distribution studies with the single fiber composite test. *Composites Sci. Technol.* **48**, 57-63.
- Asloun, El. M., Nardin, M. and Schultz, J. (1989). Stress transfer in single-fiber composites: Effect of adhesion, elastic modulus of fiber and matrix and polymer chain mobility. *J. Mater. Sci.* **24**, 1835-1844.
- ASTM D 2344 (1989). Test method for apparent interlaminar shear strength of parallel fiber composites by short-beam method.
- ASTM D 3039 (1982). Test method for tensile properties of fiber-resin composites.
- ASTM D 3518 (1991). Practice for in-plane shear stress-strain response of unidirectional reinforced plastics.
- ASTM D 3846 (1985). Test method for in-plane shear strength of reinforced plastics.
- ASTM D 4255 (1983). Guide for testing in plane shear properties of composite laminates.
- ASTM D 5528 (1994). Mode I interlaminar fracture toughness of unidirectional fiber-reinforced polymer matrix composites.
- Baillie, C.A. (1991). Ph.D. Thesis, University of Surrey, Surrey, United Kingdom.

- Barsoum, M. and Tung, I.C. (1991). Effect of oxidation on single fiber interfacial shear stresses in a SiC–borosilicate glass system. *J. Am. Ceram. Soc.* **74**, 2693–2696.
- Bartos, P. (1981). Review paper: Bond in fiber reinforced cements and concrete. *Intern. J. Cement Composites* **3**, 159–177.
- Bascom, W.D. and Jensen, M. (1986). Stress transfer in single fiber resin tensile tests. *J. Adhesion* **19**, 219–239.
- Baxevanakis, C. Jeulin, D., Valentin, D. (1993). Fracture statistics of single fiber composite specimen. *Composites Sci. Technol.* **48**, 47–56.
- Beltzer, A.I., Piau, M. and Weitsman, Y. (1992). Note on the ineffective length of a fiber. *Mech. Mater.* **13**, 285–294.
- Benzeggagh, M.L., Prel, Y.J. and de Charentenay, F.X. (1985). Instrumentation of mode I and mode II tests for crack tip strain profile study under static and cyclic loading. In *Proc. ECCM-I*, p. 291.
- Berg, C.A., Tirosh, J. and Israeli, M. (1972). Analysis of short beam bending of fiber reinforced composites. In *Composite Materials: Testing and Design (2nd Conf.)*, ASTM STP 497 (C.E. Browning ed.), ASTM, Philadelphia, PA, pp. 206–218.
- Berry, J.P. (1963). Determination of fracture surface energies by the cleavage technique. *J. Appl. Phys.* **34**, 62.
- Birger, S., Moshonov, A. and Kenig, S. (1989). Failure mechanisms of graphite fabric epoxy composites subjected to flexural loading. *Composites* **20**, 136–144.
- Biro, D.A., McAlea, P.K. and Deslandes, Y. (1991). Application of the microbond technique: characterization of carbon fiber-epoxy interfaces. *Polym. Eng. Sci.* **37**, 1250–1256.
- Boll, D.J., Jensen, R.M., Corder, L. and Bascom, W.D. (1990). Compression behaviour of single carbon filaments embedded in an epoxy polymer. *J. Composite Mater.* **24**, 208–219.
- Boukhili, B., Hubert, P. and Gauvin, R. (1991). Loading rate effect as a function of the span-to-depth ratio in three-point bend testing of unidirectional pultruded composites. *Composites* **22**, 39–45.
- Bright, J.D., Shetty, D.K., Griffin, C.W. and Limaye, S.Y. (1989). Interfacial bonding and friction in SiC filament-reinforced ceramic and glass matrix composites. *J. Am. Ceram. Soc.* **72**, 1891–1898.
- Brounman L.J. (1969). Measurement of the fiber-polymer matrix interfacial strength. In *Interfaces in Composites*, ASTM STP 452, ASTM, Philadelphia, PA, pp. 27–41.
- Browning, C.E., Abrahams, F.L. and Whitney, J.M. (1983). A four-point shear test for graphite/epoxy composites. In *Composite Materials: Quality Assurance and Processing*, ASTM STP 797, ASTM, Philadelphia, PA, pp. 54–74.
- Brun, M.K. and Singh, R.N. (1988). Effect of thermal expansion mismatch and fiber coating on the fiber/matrix interfacial shear stress in ceramic matrix composites. *Adv. Ceram. Mater.* **3**, 506–509.
- Brussat, T.R., Chiu, S.T. and Mostovoy, S. (1977). Fracture mechanics for structural adhesive bonds. AFML-TR-77-163, Air Force Materials Laboratory, Wright-Patterson Air Force base, Dayton, OH.
- Butler, E.P., Fuller, E.R. and Chan, H.M. (1990). Interface properties for ceramic composites from a single-fiber pull-out test. In *Interfaces in Composites, Mat. Res. Soc. Symp. Proc.*, Vol. 170 (C.G. Pantano and E.J.H. Chen eds.), MRS, Pittsburgh, PA, pp. 17–24.
- Carlsson, L.A., Gillespie, J.W. and Pipes, R.B. (1986). On the analysis and design of the end notched flexure (ENF) specimen for mode II testing. *J. Composite Mater.* **20**, 594.
- Carlsson, L.A. and Gillespie Jr., J.W. (1989). Mode II interlaminar fracture of composites. In *Application of fracture mechanics to composite materials*. (K. Friedrich ed.), Elsevier Sci. Pub. New York, pp. 113–157.
- Chamis, C.C. (1974). Mechanics of load transfer at the interface. In *Interfaces of Polymer Matrix Composites*, Composite Materials, Vol. 6, Ch. 2, (E.P. Plueddemann ed.), Academic Press, New York.
- Chamis, C.C. and Sinclair, J.H. (1976). 10° off-axis test for intralaminar shear characterization of fiber composites. NASA TN D-8215.
- Chamis, C.C. and Sinclair, J.H. (1977). 10° off-axis test for shear properties in fiber composites. *Exper. Mech.* **17**, 339–346.
- Chen, E.J.H. and Croman R.B. (1993). Microbonding investigation on the effects of thermal residual stress on the bond strength of a graphite/polyimide composites. *Composites Sci. Technol.* **48**, 173–179.

- Chiao, C.C., Moore, R.L. and Chiao, T.T. (1977). Measurement of shear properties of fiber composites. *Composites* **8**, 161–169.
- Chuang, S.L. and Chu, N.J. (1990). Effect of polyamic acids on interfacial shear strength in carbon fiber/aromatic thermoplastics. *J. Appl. Polym. Sci.* **41**, 373–382.
- Corleto, C.R. and Bradley, W.L. (1987). In *ASTM Second Symposium on Composite Materials: Fatigue and Fracture*, Cincinnati, OH.
- Cox, H.L. (1952). The elasticity and strength of paper and other fibrous materials. *Brit. J. Appl. Phys.* **3**, 72–79.
- Cui, W.C. and Wisnom, M.R. (1992). Contact finite element analysis of three- and four-point short beam bending of unidirectional composites. *Composites Sci. Technol.* **45**, 323–334.
- Curtin, W.A. (1991). Exact theory of fiber fragmentation in a single filament composite. *J. Mater. Sci.* **26**, 5239–5253.
- Davidovitz, M., Mittelman, A., Roman, I. and Marom, G. (1984). Failure modes and fracture mechanisms in flexure of Kevlar–epoxy composites. *J. Mater. Sci.* **19**, 377–384.
- Davies, P. and Moore, D.R. (1990). Glass/nylon-6.6 composites: Delamination resistance testing. *Composites Sci. Technol.* **38**, 211–227.
- Davies, P. and Roulin, A. (1989). A standard for interlaminar fracture testing of composites. In *Proc. ECCM 3, Developments in the Science and Technology of Composite Materials*. (A.R. Bunsell, P. Lamicq and A. Massiah eds.), Elsevier Appl. Sci., London, pp. 419–424.
- Davies, P., Moulin, C. and Kausch, H.H. (1990). Measurement of G_{Ic} and G_{IIc} in carbon/epoxy composites. *Composites Sci. Technol.* **39**, 193–205.
- Davies, P., Kausch, H.H., Williams, J.G. and 29 other researchers (1992). Round-robin interlaminar fracture testing of carbon fiber reinforced epoxy and PEEK composites. *Composites Sci. Technol.* **43**, 129–136.
- Desaeger, M. and Verpoest, I. (1993). On the use of the microindentation test technique to measure the interfacial shear strength of fiber reinforced polymer composites. *Composites Sci. Technol.* **48**, 215–226.
- Desarmot, G. and Favre, J.P. (1991). Advanced in pull-out testing and data analysis. *Composites Sci. Technol.* **42**, 151–187.
- Drzal, L.T., Rich, M.J., Camping, J.D. and Park, W.J. (1980). Interfacial shear strength and failure mechanisms in graphite fiber composites. In *35th Annual Tech. Conf., Reinforced Plast. Composites Inst.*, SPI, Paper 20C.
- Drzal, L.T. and Madhukar, M. (1993). Fiber-matrix adhesion and its relationship to composite mechanical properties. *J. Mater. Sci.* **28**, 569–610.
- Ellul, M.D. and Emerson, R.J. (1988a). A new pull-out test for tire cord adhesion-Part I. Hot bonding. *Rubber Chem. Technol.* **61**, 293–308.
- Ellul, M.D. and Emerson, R.J. (1988b). A new pull-out test for tire cord adhesion-Part II. Cold bonding. *Rubber Chem. Technol.* **61**, 309–323.
- Favre, J.P. and Jacques, D. (1990). Stress transfer by shear in carbon fiber model composites: Part I Results of single fiber fragmentation tests with thermosetting resins. *J. Mater. Sci.* **25**, 1373–1380.
- Favre, J.P., Sigety, P. and Jacques, D. (1991). Stress transfer by shear in carbon fiber model composites, Part 2. Computer simulation of the fragmentation test. *J. Mater. Sci.* **26**, 189–195.
- Ferber, M.K., Wereszczak, A.A., Hansen, D.H. and Homeay, J. (1993). Evaluation of interfacial mechanical properties in SiC fiber-reinforced macro-defect-free cement composites. *Composites Sci. Technol.* **49**, 23–33.
- Fisher, S., Rosensaft, M. and Marom, G. (1986). Dependence of the interlaminar shear strength on the loading span-to-depth ratio in aramid fiber-reinforced beams. *Composites Sci. Technol.* **25**, 69–73.
- Fisher, S. and Marom, G. (1984). A complete elastic-plastic analysis of Aramid fiber composites. *Composites Sci. Technol.* **20**, 91–98.
- Galiotis C., Young, R.J., Ycung, P.H.J. Melanitis, N. and Batchelder, D.N. (1984). The study of model polydiacetylene/epoxy composites. part 1. The axial strain in the fiber. *J. Mater. Sci.* **19**, 3640–3648.
- Gao, Y.C., Mai, Y.W. and Cotterell, B. (1988). Fracture of fiber-reinforced materials. *J. Appl. Math. Phys. (ZAMP)* **39**, 550–572.

- Garcia, R., Weisshaar, T.A. and McWithey, R.R. (1980). An experimental and analytical investigation of the rail shear test method as applied to composite materials. *Exper. Mech.* **20**, 273–279.
- Gaur, U. and Miller, B. (1989). Effects of Environmental exposure on fiber/epoxy interfacial shear strength. *Polym. Composites* **11**, 217–222.
- Gaur, U. and Miller, B. (1990). Microbond method for determination of the shear strength of a fiber/resin interface: evaluation of experimental parameters. *Composites Sci. Technol.* **34**, 35–51.
- Gent, A.N. and Kaang, S.Y. (1989). Pull-out and push-out tests for rubber-to-metal adhesion. *Rubber Chem. Technol.* **62**, 757–766.
- Gillespie Jr., J.W., Carlsson, L.A. and Pipes, R.B. (1986). Finite element analysis of the end notched flexure (ENF) specimen measuring mode II fracture toughness. *Composites Sci. Technol.* **26**, 177.
- Goettler, R.W. and Faber, K.T. (1989). Interfacial shear stress in fiber-reinforced glasses. *Composites Sci. Technol.* **37**, 129–147.
- Grande, D.H., Mandell, J.F. and Hong, K.C.C. (1988). Fiber-matrix bond strength studies of glass and metal matrix composites. *J. Mater. Sci.* **23**, 311–328.
- Greszczuk, L.B. (1967). in *Proc. 2nd Reinforced Plastics Meeting*, Washington DC. SPI, New York, Paper 20A.
- Griffin, C.W., Limayc, S.Y. and Richerson, D.W. (1988). Evaluation of interfacial properties in borosilicate SiC composites using pull-out tests. *Ceram. Eng. Sci. Proc.* **9**, 671–678.
- Gulino, R. and Phoenix, L. (1991). Weibull strength statistics for graphite fibers measured from the break progression in a model graphite/glass/epoxy microcomposites. *J. Mater. Sci.* **26**, 3107–3118.
- Gulino, R., Schwartz, P. and Phoenix, L. (1991). Experiments on shear deformation, debonding and local load transfer in a model graphite/ glass/epoxy microcomposites. *J. Mater. Sci.* **26**, 6655–6672.
- Gurney, C. and Hunt, J. (1967). Quasi-static crack propagation. *Proc. Roy. Soc. Lond.* **A299**, 508–524.
- Hashemi, S., Kinloch, A.J. and Williams, J.G. (1989). Corrections needed in double-cantilever beam tests for assessing the interlaminar failure of fiber-composites. *J. Mater. Sci. Lett.* **8**, 125–129.
- Hashemi, S., Kinloch, A.J. and Williams, J.G. (1990a). Mechanics and mechanisms of delamination in a PES-fiber composites. *Composites Sci. Technol.* **37**, 429–462.
- Hashemi, S., Kinloch, A.J. and Williams, J.G. (1990b). The analysis of interlaminar fracture in uniaxial fiber polymer composites. *Proc. Roy. Soc. Lond.* **A427**, 173–199.
- Heustenbug, R.B. and Phoenix, S.L. (1989). Interfacial shear strength studies using the single-filament-composite test, part II. A probability model and Monte Carlo simulation. *Polym. Composites* **10**, 389–408.
- Herrera-Franco, P.J. and Drzal, L.T. (1992). Comparison of methods for the measurement of fiber/matrix adhesion in composites. *Composites*, **23**, 2–27.
- Hsueh, C.H. (1993). Analysis of slice compression tests for aligned ceramic matrix composites. *Acta Metall. Mater.* **41**, 3585–3593.
- Hu, X.Z. and Mai, Y.W. (1993). Mode I delamination and fiber bridging in carbon fiber epoxy composites with and without PVAL coating. *Composites Sci. Technol.* **46**, 147–156.
- Huang, X.N. and Hull, D. (1989). Effects of fiber bridging on G_{Ic} of a unidirectional glass/epoxy composites. *Composites Sci. Technol.* **35**, 283–299.
- Ikuta, N., Mackawa, Z., Hamada, H., Ichihashi, M. and Nishio, E. (1991). Evaluation of interfacial properties in glass fiber-epoxy resin composites-reconsideration of an embedded single filament shear-strength test. *J. Mater. Sci.* **26**, 4663–4666.
- Iosipescu, N. (1967). New accurate procedure for single shear testing of metals. *J. Metal* **2**, 537–566.
- Jung, T., Subramanian, R.V. and Manoranjan, V.S. (1993). Prediction of fiber strength at the critical length: A simulation theory and experimental verification for bimodally distributed carbon fiber strength. *J. Mater. Sci.* **28**, 4489–4496.
- Kalanta, J. and Drzal, L.T. (1990). The debonding mechanism of aramid fibers to epoxy matrices, part II. An experimental investigation. *J. Mater. Sci.* **25**, 4194–4202.
- Kallas, M.N., Koss, D.A., Hahn, H.T. and Hellmann, J.R. (1992). Interfacial stress state present in a thin slice fiber push-out test. *J. Mater. Sci.* **27**, 3821–3826.
- Kelly, A. and Tyson, W.R. (1965). Tensile properties of fiber-reinforced metals: copper/tungsten and copper/molybdenum. *J. Mech. Phys. Solids* **13**, 329–350.

- Kim, J.K. (1997). Stress transfer in the fiber fragmentation test. part III. Effects of interface debonding and matrix yielding. *J. Mater. Sci.* **32**, 701–711.
- Kim, J.K. and Mai, Y.W. (1991). High strength, high fracture toughness fiber composites with interface control—a review. *Composites Sci. Technol.* **41**, 333–378.
- Kim, J.K., Baillic, C. and Mai, Y.W. (1992). Interfacial debonding and fiber pull-out stresses, part I. A critical comparison of existing theories with experiments. *J. Mater. Sci.* **27**, 3143–3154.
- Kim, J.K. and Mai, Y.W. (1993). Interfaces in composites. In *Structure and Properties of Fiber Composites*, Materials Science and Technology, Series Vol. 13, (T.W. Chou ed.), VCH Publishers, Weinheim, Germany, Ch. 6, pp. 239–289.
- Kim, J.K., Zhou, L.M. and Mai, Y.W. (1993). Stress transfer in the fiber fragmentation test. Part I. An improved model based on the shear strength criterion. *J. Mater. Sci.* **28**, 6233–6245.
- Kim, J.K., Zhou, L.M. and Mai, Y.W. (1994). Techniques for Studying Composite Interfaces. in *Handbook of Advanced Materials Testing* (N.P. Cheremisinoff ed.), Marcel Dekker, New York. Chapter 22, pp. 327–366.
- Kim, R.Y. (1989). Experimental observation of free-edge delamination. In *Interlaminar Response of Composite Materials*. (N.J. Pagano ed.), Elsevier Sci. Pub. Amsterdam, Ch. 3, pp. 111–160.
- Lacroix, Th., Tilmans, B., Keunings, R., Desaeger, M. and Verpoest, I. (1992). Modelling of critical fiber length and interfacial debonding in the fragmentation testing of polymer composites. *Composites Sci. Technol.* **43**, 379–387.
- Lee, S. and Munro, M. (1986). Evaluation of in-plane shear test methods for advanced composites materials by the decision analysis technique. *Composites* **17**, 13–22.
- Lee, S. and Munro, M. (1990). Evaluation of testing techniques for the Iosipescu shear test for advanced composite materials. *J. Composite Mater.* **21**, 419–440.
- Leng, Y. and Courtney, T.H. (1990). Ineffective length in metal matrix composites. *Mater. Sci. Eng.* **A124**, 141–149.
- Ling, S. and Wagner, H.D. (1993). Relationship between fiber flaw spectra and the fragmentation processes: a computer simulation investigation. *Composites Sci. Technol.* **48**, 35–46.
- Liu, H.Y., Mai, Y.W., Zhou, L.M. and Ye, L. (1994). Simulation of the fiber fragmentation process by a fracture mechanics analysis. *Composites Sci. Technol.* **52**, 253–260.
- Liu, H.Y., Mai, Y.W., Zhou, L.M. and Ye, L. (1995). On the effects of interface debonding and transverse matrix cracking in fiber fragmentation test. In Proc. *4th International SAMPE Symposium*, Tokyo, Japan. (Z. Maekawa et al. eds.) Vol. I, pp. 1–6
- Lu, G.Y. and Mai, Y.W. (1994). A theoretical model for evaluation of interfacial properties of fiber reinforced ceramics with the slice compression test. *Composites Sci. Technol.* **51**, 565–574.
- Madhukar, M.S. and Drzal, L.T. (1991). Fiber–matrix adhesion and its effects on composite mechanical properties: II. Longitudinal (0°) and transverse (90°) tensile and flexural behaviour of graphite/epoxy composites. *J. Composite Mater.* **25**, 958–991.
- Mandell, J.F., Chen, J.H. and McGarry, F.J. (1980). A microdebonding test for in situ assessment of fiber/matrix bond strength in composite materials. *Int. J. Adhesion Adhesives* **1**, 40–44.
- Marshall, D.B. (1984). An indentation method for measuring matrix–fiber frictional stresses in ceramic composites. *J. Am. Ceram. Soc.* **67**, C259–260.
- Marshall, D.B. and Oliver, W.C. (1987). Measurement of interfacial mechanical properties in fiber-reinforced ceramic composites. *J. Am. Ceram. Soc.* **70**, 542–548.
- Marshall, P. and Price, J. (1991). Fiber/matrix interface failure controlled by a critical energy criterion. *Composites*. **22**, 445–447.
- Manor, A. and Clough, R.B. (1992). In-situ determination of fiber strength and segment length in composites by means of acoustic emission. *Composites Sci. Technol.* **45**, 73–81.
- McAlea, K.P. and Besio, G.J. (1988). Adhesion between polybutylene terephthalate and E-glass measured with a microbond technique. *Polym. Composites*, **9**, 285–290.
- Merle, G. and Xie, M. (1991). Measurement of the adhesion of poly(ether block amide) to E-glass by single filament fragmentation. *Composites Sci. Technol.* **40**, 19–30.
- Miller, B., Muri, P. and Rebenfeld, L. (1987). A microbond method for determination of the shear strength of a fiber/resin interface. *Composites Sci. Technol.* **28**, 17–32.

- Miller, B., Gaur, U. and Hirt, D.E. (1991). Measurement of mechanical aspects of the microdebond pull-out technique for obtaining fiber/resin interfacial shear strength. *Composites Sci. Technol.* **42**, 207–219.
- Moon, C.K., Cho, H.H., Lee, J.O. and Park, T.W. (1992). A solution microbond method for determination of the shear strength of a fiber/thermoplastic resin interface. *J. Appl. Polym. Sci.* **44**, 561–563.
- Mooney, R.D. and McGarry, F.J. (1965). Resin-glass bond study. In *14th Annual Tech. Conf. Reinforced Plast. Composites Inst.* SPI, Paper 12E.
- Morgan, R.J. and Allred, R.E. (1993). Aramid fiber composites. In *Handbook of Composite Reinforcements*. (S.M. Lee ed.), VCH Publishers, New York. pp. 5–24.
- Morscher, G, Pirouz, P. and Hener, A.H. (1990). Temperature dependence of interfacial shear strength in SiC-fiber-reinforced RBSN. *J. Am. Ceram. Soc.* **73**, 713–720.
- Nardin, M. and Schultz, J. (1993). Effect of elastic moduli and interfacial adhesion energy on the critical fiber aspect ratio in single fiber composites. *J. Mater. Sci. Lett.* **12**, 1245–1247.
- Netravali, A.N., Henstenburg, R.B., Phoenix, S.L. and Schwartz, P. (1989a). Interfacial shear strength studies using the single filament composite test, part I Experiments on graphite fibers in epoxy. *Polym. Composites* **10**, 226–241.
- Netravali, A.N., Stone, D., Ruoff, S. and Topoleski, L.T.T. (1989b). Continuous micro-indenter push-through technique for measuring interfacial shear strength of fiber composites. *Composites Sci. Technol.* **34**, 289–303.
- Netravali, A.N., Topoleski, L.T.T., Sachse, W.H. and Phoenix, S.L. (1989c). An acoustic emission technique for measuring fiber fragment length distributions in single fiber composite test. *Composites Sci. Technol.* **35**, 13–29.
- Netravali, A.N., Li, Z.F., Sachse, W.H. and Wu, H.F. (1991). Determination of fiber/matrix interfacial shear strength by an acoustic emission technique. *J. Mater. Sci.* **26**, 6631–6638.
- O'Brien, T.K. (1984). Mixed-mode strain energy release rate effects on edge delamination of composites. In *Effects of Defects in Composite Materials*, ASTM STP 836, ASTM, Philadelphia, PA. pp. 125–142.
- O'Brien, T.K. (1985). Analysis of local deaminations and their influence on composite laminate behavior. In *Delamination and Debonding of Materials*, ASTM STP 876 (W.S. Johnson, ed.) ASTM, Philadelphia, PA. p 282.
- O'Brien, T.K. and Martin, R.H. (1992). Results of ASTM round robin testing for mode I interlaminar fracture toughness of composite materials, NASA TM 104222.
- O'Brien, T.K. and Martin, R.H. (1993). Round robin testing for mode I interlaminar fracture toughness of composite materials. *J. Composites Technol. Res.* **15**, 269–281.
- Ogata, N., Yasumoto, H., Yamasaki, K., Yu. H., Ogihara, T., Yanagawa, T., Yoshida, K. and Yamada, Y. (1992). Evaluation of interfacial properties between carbon fibers and semi-crystalline thermoplastic matrices in single fiber composites. *J. Mater. Sci.* **27**, 5108–5112.
- Ohsawa, T., Nakayama, A., Miwa, M. and Hasegawa, A. (1978). Temperature dependence of critical fiber length for glass fiber-reinforced thermosetting resins. *J. Appl. Polym. Sci.* **22**, 3203–3212.
- Penn, L.S., Tesoro, G.C. and Zhou, H.X. (1988). Some effects of surface-controlled reaction of Kevlar 29 on the interface in epoxy composites. *Polym. Composites* **9**, 184–191.
- Petit, P.H. (1969). A simplified method of determining the in-plane shear stress-strain response of unidirectional composites. In *Composite Materials: Testing and Design*, ASTM STP 460, ASTM, Philadelphia, PA, pp. 83–93.
- Pindera, M.J., Choksi, G., Hidde, J.S. and Herakovich, C.T. (1987). A methodology for accurate shear characterization of unidirectional composites. *J. Composites Mater.* **21**, 1164–1184.
- Pitkethly, M.J., Favre, J.P., Gaur, U., Jakubowski, J., Mudrich, S.F. Caldwell, D.L., Drzal, L.T., Nardin, M., Wagner, H.D., Di Landro, L., Hampe, A., Armistead, J.P., Desaegeer, M. and Verpoest, I. (1993). A round robin programme on interfacial test methods. *Composites Sci. Technol.* **48**, 205–214.
- Pitkethly, M.J. and Doble, J.B. (1990). Characterizing the fiber/matrix interface of carbon fiber-reinforced composites using a single fiber pullout test. *Composites* **21**, 389–395.
- Prel, Y.J., Davies, P., Benzeggagh, M.L. and de Charentenay, F.X. (1989). Model I and II delamination of thermosetting and thermoplastic composites. In *Composite Materials: Fatigue and Fracture, 2nd Volume*, ASTM STP 1012. ASTM, Philadelphia, PA, pp. 251–269.

- Qiu, Y. and Schwartz, P. (1991). A new method for study of the fiber-matrix interface in composites: Single fiber pull-out from a microcomposite. *J. Adhesion Sci. Technol.* **5**, 741-756.
- Qiu, Y. and Schwartz, P. (1993). Single fiber pull-out from a microcomposite test. *Composites Sci. Technol.* **48**, 5-10.
- Rao, V., Herrera-Franco, P., Ozzello, A.D. and Drzal, L.T. (1991). A direct comparison of the fragmentation test and the microbond pull-out test for determining the interfacial shear strength. *J. Adhesion*, **34**, 65-77.
- Ripling, E.J., Mostovoy, S. and Patrick, R.L. (1964). Measuring fracture toughness of adhesive joints. *Mater. Research and Standards*, p. 129.
- Roman, I. and Aharonov, R. (1992). Mechanical interrogation of interfaces in monofilament model composites of continuous SiC fiber-aluminium matrix. *Acta Metall. Mater.* **40**, 477-485.
- Rosen, B.W. (1964). Tensile failure of fibrous composites. *AIAA J.* **2**, 1985-1991.
- Rosen, B.W. (1972). A simple procedure for experimental determination of the longitudinal shear modulus of unidirectional composites. *J. Composites Mater.* **6**, 552-554.
- Russell, A.J. and Street, K.N. (1984). Factors affecting the interlaminar fracture energy of graphite/epoxy laminates. In *Proc. 4th Intern. Conf. on Composite Materials*. (T. Hayashi, K. Kawata and S. Umekawa eds.), Japan Society of Composites Materials, Tokyo, p. 129.
- Russell, A.J. and Street, K.N. (1985). Moisture and temperature effects on the mixed-mode delamination fracture of unidirectional graphite/epoxy. In *Delamination and Debonding of Materials*, ASTM STP 876 (W.S. Johnson ed.), ASTM, Philadelphia, PA, pp. 349-372.
- Sandorf, P.E. (1980). Saint-Venant effects in an orthotropic beam. *J. Composite Mater.* **14**, 199-212.
- Sastry, A.M., Phoenix S.L. and Schwartz, P. (1993). Analysis of interfacial failure in a composite microbundle pull-out experiment. *Composites Sci. Technol.* **48**, 237-251.
- Sattar, S.A. and Kellogg, D.H. (1969). The effect of geometry on the mode of failure of composites in short beam shear test. In *Composite Materials: Testing and Design*, ASTM STP 460, ASTM, Philadelphia, PA, pp. 62-71.
- Scherf, J., Cohen, Y. and Wagner, H.D. (1992). Interfacial strength measurements in poly (p-phenylene benzobisthiazole)/epoxy composites. *Intern. J. Adhesion Adhesive*, **12**, 251-256.
- Scherf, J. and Wagner, H.D. (1992). Interpretation of fiber fragmentation in carbon/epoxy single fiber composites: Possible fiber pre-tension effects. *Polym. Eng. Sci.* **32**, 298-304.
- Shafry, N., Brandon, D.G. and Terasaki, M. (1989). Interfacial friction and debond strength of aligned ceramic matrix composites, *Euro-Ceramics, Vol. 3, Engineering Ceramics* (G. de With, R.A. Terpstra and R. Metselaar eds.), Elsevier, London, pp. 453-457.
- Shih, G.C. and Ebert, L.J. (1986). Interface strength effects on the compressive-flexure/shear failure mode transition of composites subjected to four-point bending. *J. Mater. Sci.* **21**, 3957-3965.
- Sims, D.F. (1973). In-plane shear stress-strain response of unidirectional composite materials. *J. Composite Mater.* **7**, 124-128.
- Slepetz, J.M., Zegas, T.F. and Rovello, R. (1978). In-plane shear test for composite materials, Report No. AMMRC TR78-30, Army Materials and Mechanics Research Center, Watertown, MA (quoted in Lee and Munro (1990)).
- Spigel, B.S., Sawyer, J.W. and Prabhakaran, P. (1985). An investigation of the Iosipescu and asymmetric four-point bend tests for composite materials. In *Proc. 1985 SEM Spring Conf. Experimental Mechanics*, Society of Experimental Mechanics, pp. 833-843.
- Stumpf, H. and Schwartz, P. (1993). A Monte Carlo simulation of the stress rupture of seven fiber microcomposites. *Composites Sci. Technol.* **49**, 251-263.
- Sullivan, J.L., Kao, B.G. and van Oene, H. (1984). Shear properties and a stress analysis obtained from vinyl-ester Iosipescu specimens. *Exper. Mech.* **24**, 223-232.
- Termonia, Y. (1987). Theoretical study of the stress transfer in single fiber composites. *J. Mater. Sci.* **22**, 504-508.
- Termonia, Y. (1993). Dependence of fiber critical length on modulus in single fiber composites. *J. Mater. Sci. Lett.* **12**, 732-733.
- Vautey, P. and Favre, J.P. (1990). Fiber/matrix load transfer in thermoset and thermoplastic composites-single fiber models and hole sensitivity of laminates. *Composites Sci. Technol.* **38**, 271-288.

- Vu-khanh, T. (1987). Crack arrest study in mode II delamination in composites. *Polym. Composites* **8**, 331.
- Walrath, D.E. and Adams, D.F. (1983). The Iosipescu shear test as applied to composite materials. *Exper. Mech.* **23**, 105–110.
- Wang, S.S. (1984). Edge delamination in angle ply composite laminates. *AIAA J.* **2**, 256–264.
- Wang, S.W., Kahn, A., Sands, R. and Vasudevan, A.K. (1992). A novel nanoindenter technique for measuring fiber–matrix interfacial strength in composites. *J. Mater. Sci. Lett.* **11**, 739–741.
- Wang, Y. and Williams, J.G. (1992). Corrections for mode II fracture toughness specimens of composite materials. *Composites Sci. Technol.* **43**, 251–256.
- Watson, M.C. and Clyne, T.W. (1992a). The use of single fiber pushout testing to explore interface mechanisms in SiC monofilament-reinforced Ti. I. A photoelastic study of the test. *Acta Metall. Mater.* **40**, 131–139.
- Watson, M.C. and Clyne, T.W. (1992b). The use of single fiber pushout testing to explore interface mechanisms in SiC monofilament-reinforced Ti. II. Application of the test to composite material. *Acta Metall. Mater.* **40**, 140–148.
- Weih, T.P. and Nix, W. (1991). Experimental examination of the push-down technique for measuring the sliding resistance of SiC fibers in a ceramic matrix. *J. Am. Ceram. Soc.* **74**, 524–534.
- Whitney, J.M. (1989). Experimental Characterization of delamination fracture. In *Interlaminar Response of Composite Materials* (N.J. Pagano ed.), Elsevier Science Publishers, Amsterdam, pp. 161–250.
- Whitney, J.M., Stansbarger, D.L. and Howell, H.B. (1971). Analysis of the rail shear test-applications and limitations. *J. Composite Mater.* **5**, 24–34.
- Whitney, J.M. (1985). Elasticity analysis of orthotropic beams under concentrated loads, *Composites Sci. Technol.* **22**, 167–184.
- Whitney, J.M. and Browning, C.E. (1985). On short-beam shear tests for composite materials, *Exper. Mech.* **42**, 294–300.
- Whitney, J.M. and Knight, M. (1985). A modified free-edge delamination specimens. In *Delamination and Debonding of Materials*, ASTM STP 876 (W.S. Johnson, ed.), ASTM, Philadelphia, PA, pp. 298–314.
- Whitney, J.M. and Drzal, L.T. (1987). Axisymmetric stress distribution around an isolated fiber fragment. In *Toughened Composites*, ASTM STP 937, (N.J. Johnston ed.), ASTM, PA, pp. 179–196.
- Wilkins, D.J., Eisenmann, J.R., Chamin, R.A., Margolis, W.S. and Benson, R.A. (1982). Characterizing delamination growth in graphite-epoxy. In *Damage in Composite Materials: Basic Mechanisms, Accumulation, Tolerance and Characterization*. ASTM STP 775 (K.L. Reifsnider ed.), ASTM, Philadelphia, PA., p. 168.
- Williams, J.G., Davies, P. and Brunner, A.J. (1995). Standard tests for the toughness of composite laminates—some bones of contention. In *Proceedings of Intern. Conf. on Composite Materials (ICCM-10)*, Whistler, Canada. Vol. I, pp. 71–75.
- Wimolkiatisak, A.S. and Bell, J.P. (1989). Interfacial shear strength and failure modes of interphase modified graphite-epoxy composites. *Polym. Composites* **10**, 162–172.
- Yabin, B., Gallis, H.E., Scherf, H., Eitan, A. and Wagner, H.D. (1991). Continuous monitoring of the fragmentation phenomenon in single fiber composite materials. *Polym. Composites* **12**, 329–350.
- Yang, J.M., Jeng, S.M. and Yang, C.J. (1991). Fracture mechanisms of fiber reinforced titanium alloy matrix composites. Part I. interfacial behaviour. *Mater. Sci. Eng.* **A138**, 155–167.
- Zhou, L.M., Kim, J.K., Baillie, C.A. and Mai, Y.W. (1995). Fracture mechanics analysis of the fiber fragmentation test. *J Composite Mater.* **29**, 881–902.
- Zweben, C. (1968). Tensile failure of fiber composites. *AIAA J.* **6**, 2325–2331.

Chapter 4

MICROMECHANICS OF STRESS TRANSFER ACROSS THE INTERFACE

4.1. Introduction

One of the most important phenomena in fiber composite technology for applications to load bearing primary structures is the stress transfer between the fiber and matrix across the interface when the composites are subjected to various loading conditions (Kim and Mai, 1991a, b, 1993, Kim et al., 1994c, Zhou et al., 1995b). In the past several decades, a significant effort has been put into understanding the stress transfer in various forms of microcomposite tests as a means of evaluating the bond quality at the fiber–matrix interface region. This endeavor has been prompted by the rapid development of technologically important fibers and matrix materials and the corresponding new fiber surface treatment techniques of various natures which must not only be compatible with the composite fabrication processes, but also function properly in adverse service environments.

From the stress-transfer mechanics viewpoint, theoretical analyses dealing with the stress state at the interface region are vital to understanding how and to what extent the interface properties influence the mechanical performance and fracture behavior of the composites. Since the early pioneering work by Cox (1952) and Rosen (1964), a number of models have been developed to predict the response of composite materials in terms of thermo-mechanical properties and microfailure mechanisms under various loading conditions and different environmental situations. These range from simplified physical models such as the Kelly–Tyson model (1965) to numerical solutions of stress and strain fields in the composite constituents based on rigorous finite element (FE) analyses. The fiber fragmentation test has a significant analogy with practical composites containing aligned short fibers when subjected to uniaxial tension along the fiber direction as it exhibits the fundamental damage modes that are present in the multiple fiber composites in service.

Apart from the elastic stress transfer at the perfectly bonded interface, another important phenomenon that must be taken into account is the stress transfer by friction, which is governed by the Coulomb friction law after the interface bond fails. Furthermore, matrix yielding often takes place at the interface region in preference to interfacial debonding if the matrix shear yield strength, τ_m is significantly smaller than the apparent interface bond strength, τ_b . It follows thus

that the load-bearing capability of a composite depends on the efficiency of stress transfer, which is largely controlled by the nature of bonding at the interface region, in addition to the mechanical properties of the fiber and matrix.

Theoretical analysis of interfacial debonding has received significant attention especially for the fiber pull-out test. The condition of interface debonding has been defined by two distinct approaches: the shear strength criterion and the fracture mechanics approach. In the shear strength criterion, when the interface shear stress (IFSS) reaches the interface shear bond strength, τ_b , debonding occurs. In the fracture mechanics approach, extension of a debond crack requires the potential energy release rate of the composite constituents to reach a critical value, the interface fracture toughness, G_{ic} . In these two debond criteria, both τ_b and G_{ic} are assumed to be material constants, the characteristic interface properties to be determined in experiments.

Recognizing the significance of stress concentration at the fiber broken ends, many researchers have inclined to employ numerical methods, particularly FE analysis where the effects of specific end geometry as well as different matrix behavior at the interface region can be properly evaluated. The use of FE method allows a more accurate description of the interactions between neighboring fibers and the IFSS fields near the singularity as demonstrated in the fiber fragmentation test (MacLaughlin and Barker, 1972; Termonia, 1987, 1992; Fan and Hsu, 1992a, b; Daabin et al., 1992; Daoust et al., 1993; Ho and Drzal, 1995a, b), the fiber pull-out test (Atkinson et al., 1982; Wu and Claypool, 1991; Marotzke, 1993, 1994; Povirk and Needleman, 1993; Kim et al., 1994a, b) and microindentation test (Grande et al., 1988; Tsai, 1990; Kallas et al., 1992; Mital et al., 1993; Meda et al., 1993; Ho and Drzal, 1996). The stress recovery around the fiber ends after fiber breaks is also taken into account (Curtin, 1991) to describe the fragmentation distribution as a function of the fiber's underlying statistical strength and the interface bond strength.

In this chapter, the roles of the interface are discussed with regard to the efficiency of stress transfer in various loading geometry of the three most popular single fiber microcomposite tests, namely the fiber fragmentation test, the fiber pull-out test and the fiber push-out test. Among many different failure mechanisms that may be operative at the interface region, universally considered in this chapter as a predominant failure mode is the debonding along the fiber–matrix interface. Except for the fiber fragmentation test, only the fracture mechanics approach is employed to define the debond process. Much of the discussion here is based on the theoretical consideration of the micromechanics analysis using a shear lag model of the single fiber composite and other models extended therefrom.

4.2. Fiber fragmentation test

4.2.1. Introduction

Cox (1952) first considered a shear-lag model where an elastic fiber is embedded in an elastic matrix which is subjected to uniaxial tension. Perfect bonding is assumed

at the interface between the fiber and matrix, and the Poisson contraction in the lateral direction is the same in the fiber and matrix, to be detailed in Section 4.2.2. Later, Dow (1963) modified Cox's model, assuming that the matrix axial displacement is not constant as opposed to the original assumption of Cox, and there is no matrix present at the end of the fiber. Rosen (1964, 1965) further refined the models by Cox and Dow by considering that the matrix encapsulating the fiber is in turn surrounded by a material having the average properties of the composite. It was assumed, however, that the fiber and the average composite material carried only a tensile stress while the matrix carried only shear stresses. Rosen (1964) quantitatively defined the 'ineffective fiber length' by specifying a fraction (say, 90%) of the undisturbed stress field value below which the fiber will be considered 'ineffective'. Although the shear-lag analysis of this type is not accurate nor completely adequate to predict the gross mechanical performance of composites, it has provided a firm basis to help understand the fundamental micromechanics of load transfer at the interface region and to assist further development of more rigorous, reliable micromechanics models in various specimen geometry.

Besides the foregoing early shear-lag models, there have been a number of micromechanics analyses developed to quantify the stress transfer between the composite constituents, aiming specifically at describing the mechanical properties of the composites on the one hand, and estimating the interface bond quality using the fiber fragmentation experiments on the other. These studies on the single fiber (or simulated multiple fiber) composites include: Muki and Sternberg (1969, 1971), Sternberg and Muki (1970), Russel (1973), Berthelot et al. (1978, 1993), Piggott (1980), Eshelby (1982), Aboudi (1983), Whitney and Drzal (1987), Lhotellier and Brinson (1988), Hsueh (1989), Chiang (1991), Lacroix et al. (1992), Lee and Daniel (1992), Nairn (1992), Kim et al. (1993b), Zhou et al. (1995a). Feillard et al. (1994) has recently presented an in-depth review of the theoretical aspects of the fiber fragmentation test, with particular emphasis on practical applications of the models to predict interface bond quality.

Notably, Russel (1973) developed a slender body theory where the idealized composite consists of an elastic matrix containing elastic fibers aligned unidirectionally at concentrations dilute enough to neglect the interactions between the neighboring fibers. Russel derived a solution for the critical transfer length as a function of the inverse of Young's modulus ratio, E_f/E_m , and found it sensitive to the Poisson ratio of the matrix, ν_m . Using the composite model similar to that employed by Rosen (1964), Whitney and Drzal (1987) also proposed a two-dimensional thermo-mechanics model of stress transfer based on the superposition of solutions for two axi-symmetric problems of the exact far field solution and the approximate local transient solution. They obtained a solution for the critical transfer length as a function of the elastic properties of the composite constituents. The critical transfer length was defined as the fiber length required for the fiber axial stress (FAS) to reach 95% of that for infinitely long fiber (of its far field value).

In an approach similar to that adopted in the work of Greszczuk (1969) on the fiber pull-out test, Piggott (1980) has obtained solutions for the stress fields in the fiber for several different cases of fiber-matrix interface, including the perfectly

bonded (elastic) interface, the partially yielding interface and the partially slipped (or debonded) interface. These interface conditions are controlled by the failure mechanisms operating at the interface region, depending on the nature of interface bonding and ductility of matrix material. Hsueh (1988) also presented an analytical shear-lag model of stress transfer for both the bonded and debonded fiber ends. However, solutions for the fiber fragment length or the critical transfer length have not been generated in either of the above two studies.

More recently, Lacroix et al. (1992) obtained solutions for the critical transfer length using the stress equations previously derived by Cox (1952) for the bonded region and assuming either constant or varying frictional shear stress at the debonded region. They proposed three different interface conditions depending on the state of bonding at the interface, namely the full elastic bonding, the partially elastic bonding and the fully unbonded models. From the plots of the mean fragment length as a function of applied stress, the critical transfer length is found not to be a material constant but to vary with the applied stress, which rather contradicts with the findings of other investigators.

Apart from the shear-lag model without a distinct region in-between the fiber and matrix, composite models with interlayers have also been proposed for the fiber fragmentation loading condition, particularly based on FE analyses (Lhotellier and Brinson, 1988; Daabin et al., 1992; DiAnselmo et al., 1992; Daoust et al., 1993; Ho and Drzal, 1995a, b). In these studies, a cylindrical region of thin layer is included around the fiber having mechanical properties different from those of the bulk matrix material. Theoretical analyses for debond stresses in fiber pull-out models have also been developed (Lu and Mai, 1995; Hsueh, 1991) for the microcomposites containing plastic and visco-elastic coating layers. The effects of such an interlayer or fiber coating on the mechanical performance and fracture behavior of the bulk composites will be detailed in Chapter 7 from both the experimental and theoretical viewpoints.

As mentioned in Chapter 3, a recent development in understanding the interface states for the fiber fragmentation test geometry is that there are both bonded and debonded interfaces present simultaneously during the fiber fragmentation process of some polymer matrix composites (Favre and Jacques, 1990; Favre et al., 1991; Gulino et al., 1991; Lacroix et al., 1992). In this context, a comprehensive treatment is presented in the following sections of micromechanics analyses of the fiber fragmentation test. Three distinct conditions for the fiber-matrix interface are identified, i.e. full bonding, partial debonding and full frictional bonding, depending on the interface properties and the fiber tensile strength for given elastic constants of the composite constituents. It is assumed here that fiber breaks when the maximum FAS obtained at the fiber center reaches the average tensile strength, and debond crack propagates at the fiber ends when the debond criterion is satisfied whether a fracture mechanics approach or shear strength criterion is employed. The corresponding micromechanics analysis developed on the basis of the shear strength criterion for interfacial debond (Kim et al., 1993b) is given in Section 4.2.4. Considering the partial debonded interface as the most general case, a parametric study is performed for a model composite of carbon fiber-epoxy matrix.

4.2.2. Early shear-lag models

The shear-lag model, first described by Cox (1952), is the most widely used among various methods to study the micromechanics of stress transfer across the fiber–matrix interface, particularly the stress distribution near the ends of a broken fiber. In this model, the composite is regarded as a series of units containing a single fiber surrounded by a cylinder of matrix, the so-called ‘single fiber microcomposite’. It is assumed that the unit microcomposites are arranged in a hexagonal packing at random positions in its longitudinal direction in an aligned fiber composite. The fiber and matrix are assumed to be elastic and isotropic, and perfectly bonded across the infinitely thin interface. The lateral stiffness of the fiber and matrix are also assumed to be the same, causing the matrix axial stress (MAS) to be uniform along the whole length of the specimen. Fig. 4.1 shows a fiber of finite length, $2L$, embedded in a matrix that is subjected to a longitudinal tensile stress, σ_a , at its remote ends. From the differential displacement between the fiber and matrix in the axial direction, which is directly proportional to the shear stress at the interface, the FAS, $\sigma_f^z(z)$, and the IFSS, $\tau_i(a, z)$, are obtained as:

$$\frac{\sigma_f^z(z)}{\sigma_a} = \frac{1}{\alpha} \left\{ 1 - \frac{\cosh(\beta_1 z)}{\cosh(\beta_1 L)} \right\}, \quad (4.1)$$

$$\frac{\tau_i(a, z)}{\sigma_a} = \frac{a\beta_1 \sinh(\beta_1 z)}{2\alpha \cosh(\beta_1 L)}, \quad (4.2)$$

where

$$\beta_1 = \left[\frac{\alpha}{a^2(1 + \nu_m) \ln\left(\frac{b}{a}\right)} \right]^{1/2}, \quad (4.3)$$

and a and b are equivalent radii of the fiber and matrix, respectively. Young’s modulus ratio of the matrix to the fiber is $\alpha = E_m/E_f$, and ν is the Poisson ratio, with subscripts f and m referring respectively to the fiber and matrix. The stress distributions are illustrated in Fig. 4.2 for a carbon fiber–epoxy matrix composite

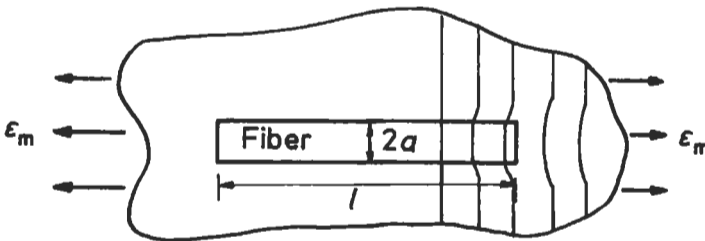


Fig. 4.1. Schematic representation of deformation around a short fiber embedded in a matrix subjected to an axial tension. After Hull (1981).

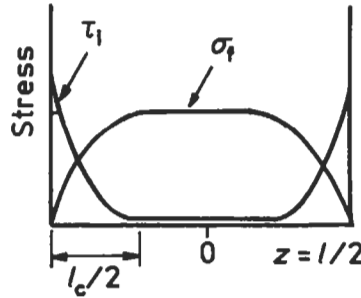


Fig. 4.2. Variations of fiber axial stress, σ_f^z , and interface shear stress, τ_i , according to Eqs. (4.1) and (4.2), respectively.

whose properties are given in Table 4.1. The FAS is a maximum in the fiber center diminishing toward zero at its ends, whereas the IFSS is a maximum (in the negative sense) at the fiber ends and falls to zero in the center. It is noted (Feillard et al., 1994) that one of the difficulties encountered in using the above shear lag model is associated with the determination of the effective matrix radius, b .

The implication of this early study is that there are regions near the fiber ends that do not carry the full load and that the average stress in the fiber of finite length, $2L$, is always less than that for a continuous fiber subjected to the same external loading. As a measure of the reinforcing efficiency in aligned short fiber composites, the average FAS, $\bar{\sigma}_f$, is given by

$$\frac{\bar{\sigma}_f}{\sigma_a} = \frac{1}{L\sigma_a} \int_0^L \sigma_f^z(z) dz = \frac{1}{\alpha} \left\{ 1 - \frac{\tanh(\beta_1 L)}{\beta_1 L} \right\}, \tag{4.4}$$

where Eq. (4.4) is plotted in Fig. 4.3 which indicates clearly that the average FAS decreases with decreasing fiber length because a greater proportion of the fiber length is not fully loaded. To achieve the maximum stress in the fiber center, the

Table 4.1
Elastic properties and radii of composite constituents^a.

Composite systems	Young's modulus (GPa)		Poisson ratio		Radius (mm)	
	E_f	E_m	ν_f	ν_m	a	b
Carbon fiber-epoxy matrix	230	3.0	0.2	0.4	0.003	1.0
Steel fiber-epoxy matrix	179	2.98	0.3	0.35	0.275	6.5
SiC fiber-glass matrix	400	70	0.17	0.2	0.071	2.8

^aKim et al. (1992).

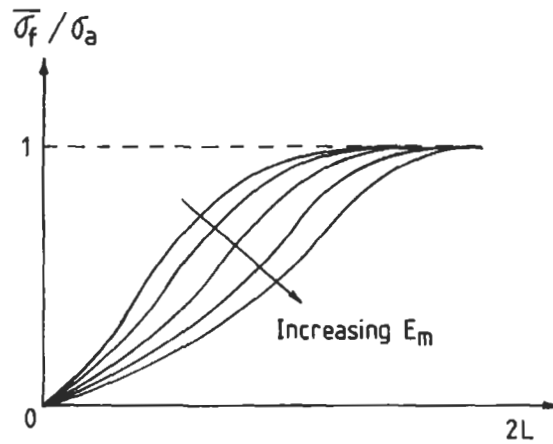


Fig. 4.3. Normalized average fiber axial stress, σ_f , as a function of fiber length, according to Eq. (4.4).

fiber length should at least not be shorter than the critical transfer length, $(2L)_c$, the idea of which was proposed by Kelly and Tyson (1965). The implication of the critical transfer length in evaluating the interface properties has been discussed in Section 3.2.3.

A modified shear-lag model has been proposed by Rosen (1964, 1965) based on a multiple fiber composite. Fig. 4.4 shows the composite model Rosen considered wherein a fiber is embedded in a matrix which in turn is surrounded by an average composite material. The FAS and IFSS are given in the same form as those of Eqs. (4.1) and (4.2) given earlier by Cox (1952):

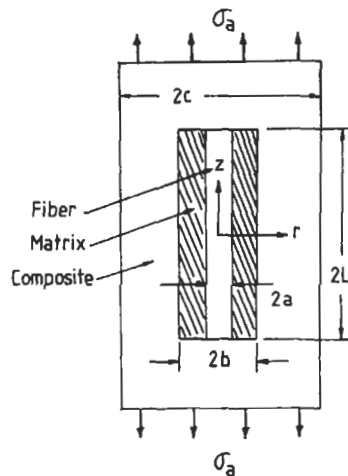


Fig. 4.4. Axi-symmetric single fiber composite model employed by Rosen (1964).

$$\frac{\sigma_f^z(z)}{\sigma_a} = \frac{1}{\alpha_2} \left\{ 1 - \frac{\cosh(\beta_1 z)}{\cosh(\beta_1 L)} \right\}, \quad (4.5)$$

$$\frac{\tau_i(a, z)}{\sigma_a} = \frac{\alpha \beta_1 \sinh(\beta_1 z)}{2\alpha_2 \cosh(\beta_1 L)}, \quad (4.6)$$

where β_1 is given in Eq. (4.3) and the Young's modulus ratio of the composite to the fiber, $\alpha_2 = E_c/E_f$. When Young's modulus of the composite, E_c , is calculated based on the simple rule of mixtures (i.e. $E_c = V_f E_f + (1 - V_f) E_m$), the stress distributions in Rosen's model are essentially identical to Cox's model, regardless of the fiber volume fraction, V_f . This is because a variation in V_f influence to the same extent both E_c and the applied stress, σ_a , in Eqs (4.5) and (4.6) due to the assumption of perfectly elastic and isotropic fiber and matrix.

The significance of Rosen's work lies in the attempt of quantifying the efficiency of stress transfer across the interface with respect to the fiber length, by introducing the concept of 'ineffective length'. The ineffective fiber length, $(2L)_e$, was defined by specifying some fraction, ϕ , of the undisturbed stress value below which the fiber shall be considered ineffective. $(2L)_e$ normalized with fiber diameter, $2a$, is derived as

$$\frac{(2L)_e}{2a} = \frac{1}{\sqrt{2\alpha}\beta_1} \cosh^{-1} \left\{ \frac{1 + (1 - \phi)^2}{2(1 - \phi)} \right\}, \quad (4.7)$$

where ϕ is the portion of the fiber in which the average FAS is greater than 90% of the stress that would exist for an infinite fiber. A plot of normalized ineffective lengths is shown in Fig. 4.5 as a function of Young's modulus ratio of the fiber to the

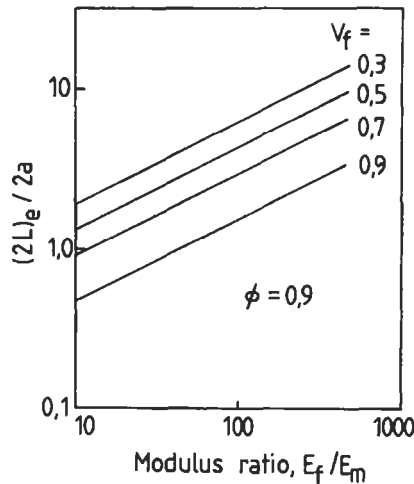


Fig. 4.5. Normalized ineffective fiber length, $(2L)_e/2a$, as a function of modulus ratio, E_f/E_m , for varying fiber volume fraction, V_f . After Rosen (1964).

matrix, $1/\alpha$. Clearly, the ineffective length varies inversely proportionally to $\alpha^{1/2}$ in this early model. A detailed discussion regarding the influence of the properties of composite constituents on the critical transfer length is given in Section 3.2.3.

4.2.3. An improved model based on a fracture mechanics approach

4.2.3.1. Solutions for stress distributions

In single fiber fragmentation experiments, an external stress, σ_a , is applied to the remote ends of the cylindrical matrix (of outer radius b) containing a fiber with finite length and radius a . The fiber breaks into increasingly smaller segments as the applied stress increases. For simplicity of mechanics analysis, a segment is taken in the present model as shown in Fig. 4.6. There are debonded regions of length ℓ present at the ends of the fiber of total length $2L$. A tensile stress, σ , is operative in the matrix at the fiber ends $z = \pm L$ caused by the applied stress, σ_a , at remote ends. It is also assumed that the fiber ends at $z = \pm L$ are debonded from the matrix so that there is no stress transfer taking place through the ends. A set of cylindrical coordinates (r, θ, z) is chosen wherein the z -axis corresponds to the coaxis of the fiber and the matrix cylinder. In the axi-symmetric deformation, the stress components $(\sigma^r, \sigma^\theta, \sigma^z, \tau^{rz})$ and the displacement components (u^r, u^z) vary independently of θ , and the remaining stress and displacement components are all zero. For perfectly elastic and isotropic fibers and matrix, the general relation between strains and stresses is given by:

$$\epsilon_f^z(r, z) = \frac{1}{E_f} \{ \sigma_f^z(r, z) - \nu_f [\sigma_f^r(r, z) + \sigma_f^\theta(r, z)] \} , \quad (4.8)$$

$$\epsilon_m^z(r, z) = \frac{1}{E_m} \{ \sigma_m^z(r, z) - \nu_m [\sigma_m^r(r, z) + \sigma_m^\theta(r, z)] \} , \quad (4.9)$$

$$\epsilon_m^{rz}(r, z) = \frac{2(1 + \nu_m)}{E_m} \tau_m^{rz}(r, z) , \quad (4.10)$$

where the subscripts f and m refer to fiber and matrix, and the superscripts are coordinate directions. Further, the mechanical equilibrium conditions between the composite constituents are:

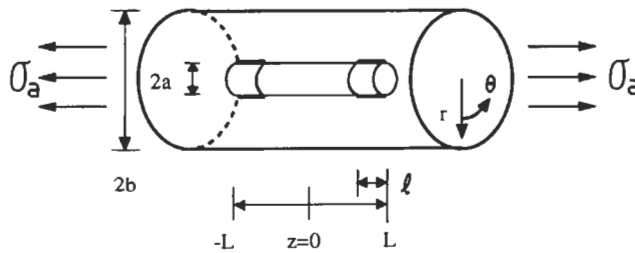


Fig. 4.6. Schematic drawing of a partially debonded single fiber composite model subject to external stress, σ_a , in the fiber fragmentation test.

$$\sigma = \gamma\sigma_f^z(z) + \sigma_m^z(z) , \quad (4.11)$$

$$\frac{d\sigma_f^z(z)}{dz} = -\frac{2}{a}\tau_i(a, z) , \quad (4.12)$$

$$\frac{\partial\sigma_m^z(z)}{\partial z} + \frac{\partial\tau_m^rz(r, z)}{\partial r} + \frac{\tau_m^rz(r, z)}{r} = 0 , \quad (4.13)$$

where $\gamma = a^2/(b^2 - a^2)$ is the volume ratio of the fiber to the matrix. It is assumed here that the plane normal to the z -direction remains plane in plane strain deformation of the matrix. The average MAS is thus defined by

$$\sigma_m^z(z) = \frac{2}{b^2 - a^2} \int_a^b \sigma_m^z(r, z)r dr . \quad (4.14)$$

In the bonded region $(-L - \ell) \leq z \leq (L - \ell)$, the applied stress is transferred from the matrix to the fiber through the IFSS, $\tau_i(a, z)$, such that the equilibrium condition can be obtained by combining Eqs. (4.11) and (4.12) as

$$\frac{d\sigma_m^z(z)}{dz} = \frac{2\gamma}{a}\tau_i(z) . \quad (4.15)$$

Since the matrix shear stress, $\tau_m^rz(r, z)$, has to be compatible with IFSS, $\tau_i(a, z)$, and the matrix cylindrical surface is stress free (Zhou et al. 1993)

$$\tau_m^rz(r, z) = \frac{\gamma(b^2 - r^2)}{ar}\tau_i^rz(z) . \quad (4.16)$$

Also, the axial displacement is continuous at the bonded interface (i.e. $u_m^z(a, z) = u_f^z(a, z)$). Combining Eqs. (4.8)–(4.10) and (4.16), and differentiating with respect to z gives

$$\frac{d\tau_i(a, z)}{dz} = \frac{aE_m[\epsilon_m^z(b, z) - \epsilon_f^z(a, z)]}{(1 + \nu_m)[2\gamma b^2 \ln(b/a) - a^2]} . \quad (4.17)$$

An additional radial stress, $q_1(a, z)$, acts at the interface that arises from the differential Poisson contraction between the fiber and the matrix when the matrix is subjected to an axial tension at remote ends. $q_1(a, z)$ is obtained from the continuity of tangential strain at the interface (i.e. $\epsilon_f^{\theta}(a, z) = \epsilon_m^{\theta}(a, z)$) (Gao et al., 1988)

$$q_1(a, z) = \frac{\alpha\nu_f\sigma_f^z(z) - \nu_m\sigma_m^z(z)}{\alpha(1 - \nu_f) + 1 + \nu_m + 2\gamma} . \quad (4.18)$$

Therefore, combining Eqs. (4.10), (4.11), (4.17) and (4.18) yields a second-order differential equation for the FAS

$$\frac{d^2 \sigma_f^z(z)}{dz^2} - A_1 \sigma_f^z(z) = A_2 \sigma, \quad (4.19)$$

where the coefficients A_1 and A_2 are complex functions of the elastic properties and geometric factors of the constituents, and are given by:

$$A_1 = \frac{2[\alpha(1 - 2k\nu_f) + \gamma(1 - 2k\nu_m)]}{(1 + \nu_m)[2\gamma b^2 \ln(b/a) - a^2]}, \quad (4.20)$$

$$\frac{A_2}{A_1} = -\frac{(1 - 2k\nu_m)}{\alpha(1 - 2k\nu_f) + \gamma(1 - 2k\nu_m)}, \quad (4.21)$$

$k = (\alpha\nu_f + \gamma\nu_m)/[\alpha(1 - \nu_f) + 1 + \nu_m + 2\gamma]$. The solution of FAS is subjected to the following boundary conditions

$$\sigma_f^z(L - \ell) = \sigma_f^z(-(L - \ell)) = \sigma_\ell = \omega_1(\bar{\sigma} + \sigma)[1 - \exp(-\lambda\ell)], \quad (4.22)$$

where $\omega_1 = \nu_m/(\alpha\nu_f + \gamma\nu_m)$. λ is the reciprocal length giving the effective frictional shear stress transfer and $\bar{\sigma}$ is the asymptotic debond stress for long embedded length. These parameters are related to the interfacial properties in the debonded region, namely the coefficient of friction, μ , and the residual fiber clamping stress, q_0 , as:

$$\lambda = \frac{2\mu k}{a}, \quad (4.23)$$

$$\bar{\sigma} = -\frac{q_0}{\omega_0 k}, \quad (4.24)$$

where $\omega_0 = \alpha\nu_f/(\alpha\nu_f + \gamma\nu_m)$. In Eq. (4.22) σ_ℓ is defined as the crack tip debond stress at the boundary between the bonded and debonded regions at $z = \pm(L - \ell)$ where the FAS given in Eq. (4.25) must be continuous. Therefore, from the consideration of cylindrical, elastic fiber and matrix, the solution of FAS and the corresponding MAS and IFSS are obtained for the bonded region $(-(L - \ell) \leq z \leq (L - \ell))$:

$$\sigma_f^z(z) = \frac{A_2}{A_1} \sigma - \left(\frac{A_2}{A_1} \sigma - \sigma_\ell \right) \frac{\cosh \sqrt{A_1} z}{\cosh \sqrt{A_1} (L - \ell)}, \quad (4.25)$$

$$\sigma_m^z(z) = \left(1 - \gamma \frac{A_2}{A_1} \right) \sigma + \gamma \left(\frac{A_2}{A_1} \sigma - \sigma_\ell \right) \frac{\cosh \sqrt{A_1} z}{\cosh \sqrt{A_1} (L - \ell)}, \quad (4.26)$$

$$\tau_m^rz(r, z) = \frac{\gamma \sqrt{A_1} (b^2 - r^2)}{2r} \left(\frac{A_2}{A_1} \sigma - \sigma_\ell \right) \frac{\sinh \sqrt{A_1} z}{\cosh \sqrt{A_1} (L - \ell)}, \quad (4.27)$$

$$\tau_i(a, z) = \frac{a \sqrt{A_1}}{2} \left(\frac{A_2}{A_1} \sigma - \sigma_\ell \right) \frac{\sinh \sqrt{A_1} z}{\cosh \sqrt{A_1} (L - \ell)}. \quad (4.28)$$

In the debonded regions $(-L \leq z \leq -(L - \ell))$ and $(L - \ell) \leq z \leq L$, frictional slip occurs between the fiber and matrix and the stress transfer is governed by the Coulomb friction law for a constant coefficient of friction, μ

$$\tau_i(a, z) = -\mu[q_0 + q_1(a, z)] \quad (4.29)$$

The radial (compressive) stress, q_0 , is caused by the matrix shrinkage and differential thermal contraction of the constituents upon cooling from the processing temperature. It should be noted that $q_1(a, z)$ is compressive (i.e. negative) when the fiber has a lower Poisson ratio than the matrix ($\nu_f < \nu_m$) as is the normal case for most fiber composites. It follows that $q_1(a, z)$ acts in synergy with the compressive radial stress, q_0 , as opposed to the case of the fiber pull-out test where the two radial stresses counterbalance, to be demonstrated in Section 4.3. Combining Eqs. (4.11), (4.12), (4.18) and (4.29), and for the boundary conditions at the debonded region

$$\sigma_f^z(L) = 0, \sigma_m^z(L) = \sigma \quad (4.30)$$

Solutions for the stress components are obtained as:

$$\sigma_f^z(z) = \omega_1(\bar{\sigma} + \sigma)\{1 - \exp[-\lambda(L - z)]\} \quad (4.31)$$

$$\sigma_m^z(z) = \sigma - \gamma\omega_1(\bar{\sigma} + \sigma)\{1 - \exp[-\lambda(L - z)]\} \quad (4.32)$$

$$\tau_m(r, z) = \frac{\gamma\lambda(b^2 - r^2)}{2r}\omega_1(\bar{\sigma} + \sigma)\exp[-\lambda(L - z)] \quad (4.33)$$

$$\tau_i(a, z) = \frac{\lambda a}{2}\omega_1(\bar{\sigma} + \sigma)\exp[-\lambda(L - z)] \quad (4.34)$$

Fig. 4.7 shows the approximate stress distributions in the constituents along the axial direction of the left half of the fiber for the carbon fiber–epoxy matrix composite with the relevant interface properties for the XA100 fibers given in Table 4.2. The FAS increases from the end towards the center while the MAS decreases in the same direction, both of which are opposite to the axial stress distributions in fiber pull-out and fiber push-out, to be shown in Sections 4.3 and 4.4. The IFSS increases from the debond crack tip towards the fiber ends in the debonded region. This response makes the debond propagation very difficult and is attributed to the radial compressive stress, q_1 , arising from the differential Poisson contraction between the fiber and matrix, which should be added to the residual compressive stress, q_0 . If the Poisson effects are completely neglected in the fiber fragmentation analysis, the frictional shear stress would become constant over the whole debonded region.

4.2.3.2. Interface debond criterion

The interface debond criterion used in this analysis is based on the concept of fracture mechanics where the strain energy release rate against the incremental debond length is equated to the interface fracture toughness, G_{ic} , which is considered to be a material constant

$$G_{ic} = \frac{1}{2\pi a} \frac{\partial U_t}{\partial \ell} \quad (4.35)$$

where U_t is the sum of the strain energy stored in the bonded region (U_b , for $\ell \leq z \leq L$) and debonded region (U_d , for $0 \leq z \leq \ell$), which can be obtained by

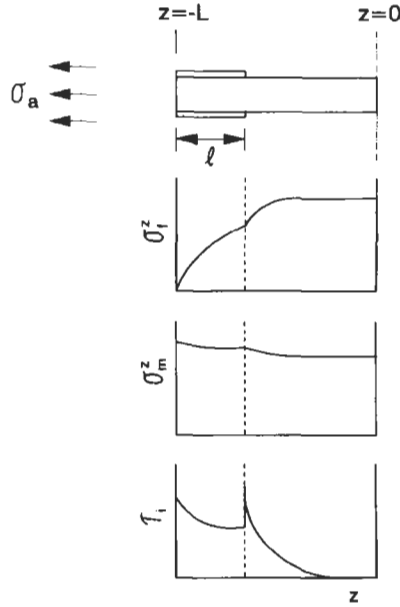


Fig. 4.7. Distributions of (a) fiber axial stress, σ_f^z , (b) matrix axial stress, σ_m^z , and (c) interface shear stress, τ_i , along half the embedded fiber length, L , in the fiber fragmentation test.

Table 4.2

Interface properties of carbon fiber–epoxy matrix composites and Weibull parameters of carbon fibers^a.

Interface properties	XA1	$G_{ic} = 13 \text{ J/m}^2$	$q_0 = 8.4 \text{ MPa}$	$\mu = 0.8$
	XA100	$G_{ic} = 37 \text{ J/m}^2$	$q_0 = 8.4 \text{ MPa}$	$\mu = 1.25$
Weibull parameters	XA1	$\sigma_{TS}(2L_0) = 2.45 \text{ GPa}$	$2L_0 = 12 \text{ mm}$	$m = 3.6$
	XA100	$\sigma_{TS}(2L_0) = 2.64 \text{ GPa}$	$2L_0 = 12 \text{ mm}$	$m = 4.6$

^aZhou et al. (1994).

integrating the stress components acting in the constituents over the volume of respective regions:

$$\begin{aligned}
 U_t &= U_d + U_b, \\
 &= \int_{\ell}^L \int_0^b \left[\frac{\sigma_f^z(z)^2}{E_f} + \frac{\sigma_m^z(z)^2}{E_m} + \frac{2(1 + \nu_m)\tau_m^z(r, z)^2}{E_m} \right] \pi r \, dr \, dz \\
 &\quad + \int_0^{\ell} \int_0^b \left[\frac{\sigma_f^z(z)^2}{E_f} + \frac{\sigma_m^z(z)^2}{E_m} + \frac{2(1 + \nu_m)\tau_m^z(r, z)^2}{E_m} \right] \pi r \, dr \, dz. \quad (4.36)
 \end{aligned}$$

Substituting the solutions for the three major stress components determined in the bonded and debonded regions, a fiber–matrix interface debond criterion is derived as

$$2\pi a G_{ic} = B_3 \sigma^2 + C_3 (\bar{\sigma} + \sigma) \sigma + D_3 (\bar{\sigma} + \sigma)^2 , \quad (4.37)$$

where the coefficients B_3 , C_3 and D_3 are the complex functions of material properties of the constituents and geometric factors, and are given in Appendix B. Therefore, the stress applied to the matrix at the remote ends, $\sigma_a = \sigma_{od} (= \sigma(b^2 - a^2)/b^2)$, for debond crack propagation is obtained

$$\sigma_{od} = \frac{a^2}{\gamma b^2} \left\{ \left[\frac{2\pi a G_{ic}}{(B_3 + C_3 + D_3)^2} + \frac{C_3^2 - 4B_3 D_3}{4(B_3 + C_3 + D_3)^2} \bar{\sigma}^2 \right]^{1/2} - \frac{C_3 + 2D_3}{2(B_3 + C_3 + D_3)} \bar{\sigma} \right\} . \quad (4.38)$$

4.2.3.3. Fiber fragmentation

When the external stress is sufficiently high to cause the maximum FAS to reach the local fiber tensile strength at the fiber center, the fiber fractures. A fiber tensile strength model is used in this analysis to predict the average strength of the fiber corresponding to a given gauge length based on the Weibull probability of failure (Weibull, 1951). According to the cumulative failure probability function proposed by van der Zwaag (1989), the average fracture stress of length ($2L_0$) is given by

$$\sigma_{TS}(2L_0) = (2L_0)^{-1/m} \Gamma \left(1 + \frac{1}{m} \right) \sigma_u , \quad (4.39)$$

where m and σ_u are the Weibull modulus and scale factor, and Γ is the gamma function. Therefore, the average tensile strength of the fiber segment of length ($2L$) is given by

$$\sigma_{TS}(2L) = \left(\frac{L_0}{L} \right)^{1/m} \sigma_{TS}(2L_0) . \quad (4.40)$$

Since the loading is assumed to be perfectly symmetrical about the fiber center, fiber breakage is always expected to occur at the center ($z = 0$)

$$\sigma_f^z(0) = \sigma_{TS}(2L) . \quad (4.41)$$

The maximum FAS at $z = 0$ can be determined from Eqs. (4.25) and (4.31)

$$\sigma_f^z(0) = \frac{A_2}{A_1} \sigma - \left(\frac{A_2}{A_1} \sigma - \sigma_\ell \right) \operatorname{sech} \sqrt{A_1} (L - \ell) \quad (4.42)$$

for the partially debonded interface, and

$$\sigma_f^z(0) = \omega_1(\bar{\sigma} + \sigma)[1 - \exp(-\lambda L)] \quad (4.43)$$

for the fully debonded interfaces. For the fully bonded interface, the corresponding maximum FAS can be obtained by substituting the debond length $\ell = 0$ and $\sigma_\ell = 0$ into Eq. (4.42)

$$\sigma_f^z(0) = \frac{A_2}{A_1} \sigma [1 - \operatorname{sech}(\sqrt{A_1} L)] . \quad (4.44)$$

Therefore, combining Eqs. (4.41)–(4.44), the fiber fragmentation criterion is derived in terms of the applied stress, $\sigma_a = \sigma_{of}$, at the remote ends of the matrix

$$\sigma_{of} = \frac{\left(\frac{a}{b}\right)^2 A_1 \sigma_{TS}(2L) \cosh(\sqrt{A_1} L)}{\gamma A_2 [\cosh(\sqrt{A_1} L) - 1]} \quad (4.45)$$

for the fully bonded interface, and

$$\sigma_{of} = \frac{\left(\frac{a}{b}\right)^2 \sigma_{TS}(2L) \cosh[\sqrt{A_1}(L - \ell)] - \omega_1 \bar{\sigma} [1 - \exp(-\lambda \ell)]}{\gamma \frac{A_2}{A_1} \{ \cosh[\sqrt{A_1}(L - \ell)] - 1 \} + \omega_1 [1 - \exp(-\lambda \ell)]} \quad (4.46)$$

for the partially debonded interface. The corresponding equation for the fully bonded interface is given by

$$\sigma_{of} = \frac{\left(\frac{a}{b}\right)^2 \left\{ \frac{\sigma_{TS}(2L)}{\omega_1 [1 - \exp(-\lambda L)]} - \bar{\sigma} \right\}}{\gamma} . \quad (4.47)$$

4.2.3.4. Debond length and mean fiber fragment length

The effect of interface properties on the debond process is shown in Fig. 4.8 where the debond length, ℓ , is plotted as a function of the applied stress, σ_a . Three different coefficients of friction, μ , are used at a given fiber length $(2L) = 2.0$ mm for this plot. In general, ℓ decreases exponentially with increasing σ_a towards a plateau value. A lower coefficient of friction, μ , results in a longer ℓ at a given σ_a . It should be emphasized that there is a critical value of applied stress below which no debonding takes place at the interface. This value corresponds to the initial debond stress where a sharp transition occurs from the fully bonded interface to the partially debonded interface, and is found to increase slightly with increasing μ as a result of the enhanced frictional resistance discouraging debond propagation.

From Eqs. (4.45) and (4.46), the solutions for the mean fiber fragment length are derived

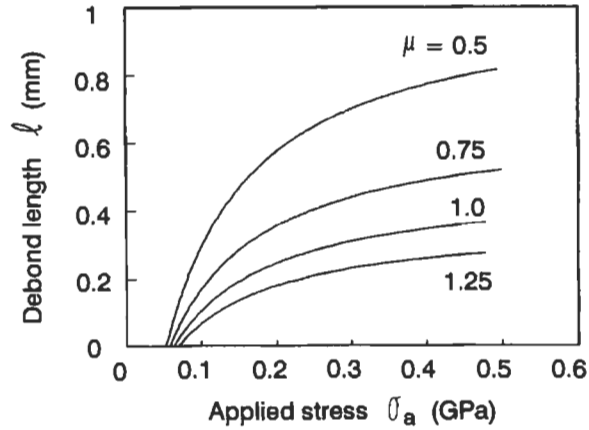


Fig. 4.8. Variations of debond length, ℓ , as a function of applied stress, σ_a , for different coefficients of friction, μ , for a XA100 carbon fiber–epoxy matrix composite. After Zhou et al. (1995a, b).

$$2L = \frac{2}{\sqrt{A_1}} \cosh^{-1} \left[\frac{1}{1 - \left(\frac{a}{b}\right)^2 \left(\frac{1}{\gamma}\right) \left(\frac{A_1}{A_2}\right) \frac{\sigma_{TS}(2L)}{\sigma_{of}}} \right] \quad (4.48)$$

for the fully bonded interface, and

$$2L = 2\ell + \frac{2}{\sqrt{A_1}} \cosh^{-1} \left[\frac{\gamma \left(\frac{A_2}{A_1}\right) \sigma_{of} + \omega_1 (\sigma_{of} + \bar{\sigma}) [1 - \exp(-\lambda\ell)]}{\left(\frac{a}{b}\right)^2 \sigma_{TS}(2L) - \gamma \left(\frac{A_2}{A_1}\right) \sigma_{of}} \right] \quad (4.49)$$

for the partially debonded interface. The mean fiber fragment lengths, ($2L$), are compared between the theoretical predictions and experimental results for the carbon fiber–epoxy matrix composites with two different levels of fiber surface treatments as shown in Fig. 4.9. It is noted that when the applied stress, σ_a , is greater than a critical value that corresponds to the initial debonding, the mean fiber fragment length ($2L$) consists of two components: namely the bond length and the debond length. As σ_a is increased, the debond length gradually increases towards an asymptotic value, whereas the bond length drops dramatically to a plateau value within a narrow range of applied stress. Therefore, the contribution of the debond length to the mean fiber fragment length becomes increasingly more important with increasing σ_a .

For both composites good agreement is obtained between theory and experiment over the whole range of σ_a . Two major differences can be identified between the composites of two different fiber surface treatments: shorter mean fiber fragment length and shorter debond length at a given σ_a for the XA 100 fibers (Fig. 4.9(b)) than for the XA 1 fibers (Fig. 4.9(a)). This implies that a higher level of surface

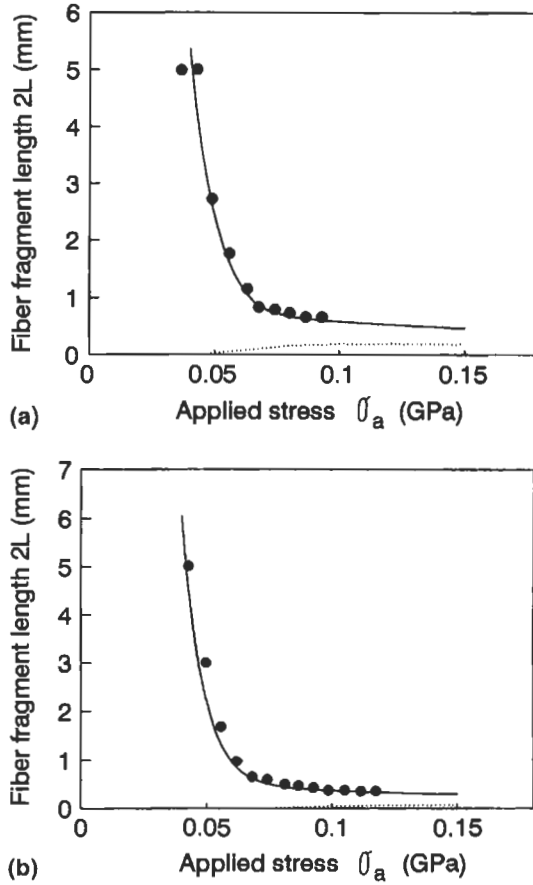


Fig. 4.9. Comparisons of mean fiber fragment length, $2L$, as a function of applied stress, σ_a , between experiments and theory for carbon fiber-epoxy matrix composites with (a) XA1 fiber and (b) XA100 fiber: (●) experiment; (—) prediction (-----) debond length. After Zhou et al. (1995a, b).

treatment (on the XA 100 fibers) gives a stronger interface bond with shorter debond length. The strong interface bond in turn permits efficient stress transfer, causing the FAS to reach more easily the tensile strength of the fiber (and eventual fiber fracture). The average length of fractured fiber segments at a given applied stress is a measure of efficiency of stress transfer across the fiber-matrix interface in the fiber fragmentation test. The above observations regarding the different fiber fragmentation response for the composites with different fiber surface treatments confirm that the interface properties influence significantly the fiber fragment behavior, as opposed to the suggestion of the dominant role of the Young's modulus ratio in determining the critical transfer length (see Section 3.2.3). Another important implication is that, since there are debonded regions of substantial lengths at both ends of the fiber, the efficiency of stress transfer at the interface cannot be

related to a single parameter such as the interface bond strength, τ_b , as in conventional analyses of the test given by Eq. (3.3).

4.2.4. An improved model based on a shear strength criterion

Although a fracture mechanics approach presented in Section 4.2.3 in general deals with a more fundamental aspect of the interface debond problem for a given loading configuration, a shear strength criterion has an important advantage in that the interfacial shear strength, whether for the bonded or debonded regions, can be directly determined from the experimental results of the fiber fragmentation test. Therefore, in this section, a micromechanics analysis is presented based on the shear strength criterion for interfacial debonding. A particular emphasis is placed on the identification of the specific criteria required to satisfy each interface condition, i.e. full bonding, partial debonding and full frictional bonding. The approximate analysis given in this model leads to relatively simple, closed-form equations for all basic solutions for the stress distributions in the constituents, the external stress required for debonding or fiber fragmentation, and the mean fiber fragmentation length for the three different interface conditions.

4.2.4.1. Solutions for stress distributions

For the cylindrical coordinates of the shear-lag model shown in Fig. 4.6, the governing conditions adopted in this analysis are essentially the same as those described in Section 4.2.3. There is one exception in that the mechanical equilibrium condition between the external stress, σ , and the internal stress components given by Eq. (4.11) is replaced by

$$b^2\sigma = a^2\sigma_f^z(z) + 2 \int_a^b r\sigma_m^z(r,z)dr dz . \quad (4.50)$$

It is assumed here that the axial displacements are independent of the radial position, and the stress components in the radial and circumferential directions are neglected for Eqs. (4.8) and (4.9). Also, the radial displacement gradient with respect to the axial direction is neglected compared to the axial displacement gradient with respect to the radial direction in Eq. (4.10). Combination of Eqs. (4.10) and (4.16) for the boundary condition of the axial displacement continuity at the bonded interface (i.e. $u_m^z(a,z) = u_f^z(z)$) and integration gives:

$$\tau_m^z(r,z) = \frac{\gamma(b^2 - r^2)}{ar} \frac{E_m[u_m^z(b,z) - u_f^z(z)]}{2a(1 + \nu_m)[(1 + \gamma) \ln(\frac{b}{a}) - \frac{1}{2}]} , \quad (4.51)$$

$$\tau_i(a,z) = \frac{E_m[u_m^z(b,z) - u_f^z(z)]}{2a(1 + \nu_m)[(1 + \gamma) \ln(\frac{b}{a}) - \frac{1}{2}]} . \quad (4.52)$$

Therefore, from Eqs (4.8) (4.10) and (4.49), the MAS is obtained

$$\sigma_m^z(r, z) = \sigma_m^z(a, z) + \frac{\left[\frac{b^2 \ln(r/a) - \frac{r^2 - a^2}{2}}{2} \right] [\sigma_m^z(b, z) - \sigma_m^z(a, z)]}{(b^2 - a^2)[(1 + \gamma) \ln(b/a) - 1/2]}, \quad (4.53)$$

where $\sigma_m^z(a, z) (= \alpha \sigma_f^z(z))$ and $\sigma_m^z(b, z)$ are the MASs at the fiber–matrix interface ($r = a$) and the cylindrical surface (at $r = b$), respectively. Further, combining Eqs. (4.50) and (4.52) yields the MAS at the cylindrical surface

$$\sigma_m^z(b, z) = \sigma_f^z(z) \left[\alpha - \frac{1}{\beta_3^2 \gamma} - \frac{\alpha}{\beta_3^2 \gamma^2} \right] + \sigma \frac{1 + \gamma}{\beta_3^2 \gamma^2}, \quad (4.54)$$

where the coefficient β_3 is a function of the elastic properties and geometric factors of the constituents, and is given by

$$\beta_3^2 = \frac{\left(\frac{b}{a} \right)^4 \ln\left(\frac{b}{a}\right) - \frac{1}{2\gamma^2} - \frac{1}{4\gamma} \left[\left(\frac{b}{a} \right)^2 + 1 \right]}{(1 + \gamma) \ln\left(\frac{b}{a}\right) - \frac{1}{2}}. \quad (4.55)$$

Therefore, combining Eqs. (4.12) and (4.50)–(4.54) gives a differential equation for the FAS as

$$\frac{d^2 \sigma_f^z(z)}{dz^2} = \beta_2^2 \left[\sigma_f^z(z) - \frac{1 + \gamma}{\alpha + \gamma} \sigma \right], \quad (4.56)$$

where

$$\beta_2^2 = \frac{a^2 \left[\left(\frac{b}{a} \right)^2 - 1 \right] \left(1 + \frac{\alpha}{\gamma} \right)}{(1 + \gamma) \left\{ \left(\frac{b}{a} \right)^4 \ln\left(\frac{b}{a}\right) - \frac{1}{2\gamma^2} - \frac{1}{4\gamma} \left[\left(\frac{b}{a} \right)^2 + 1 \right] \right\}}. \quad (4.57)$$

The solution of Eq. (4.56) and the corresponding solutions for the IFSS are obtained for the boundary conditions

$$\sigma_f^z(\pm(L - \ell)) = \sigma_\ell \quad (4.58)$$

for the partially debonded interface as a general case. Thus:

$$\sigma_f^z(z) = \frac{1 + \gamma}{\alpha + \gamma} \left\{ 1 - \frac{\cosh(\beta_2 z)}{\cosh[\beta_2(L - \ell)]} \right\} \sigma + \frac{\cosh(\beta_2 z)}{\cosh[\beta_2(L - \ell)]} \sigma_\ell, \quad (4.59)$$

$$\tau_1(a, z) = \frac{a\beta_2}{2} \left[\frac{1 + \gamma}{\alpha + \gamma} \sigma - \sigma_\ell \right] \frac{\sinh(\beta_2 z)}{\cosh[\beta_2(L - \ell)]}. \quad (4.60)$$

The corresponding solutions for the fully bonded interface can be obtained by substituting $\sigma_\ell = 0$ when $\ell = 0$ in Eqs. (4.59) and (4.60).

Based on the Coulomb friction law, which governs the frictional stress transfer in the debonded interface, and combining Eqs. (4.12) and (4.18) yield the MAS at the interface ($r = a$)

$$\sigma_m^z(a, z) = -\frac{1}{\omega_1} \frac{d\sigma_f^z(z)}{\lambda dz} + \frac{\omega_0}{\omega_1} \{\sigma_f^z(z) - \bar{\sigma}\} . \quad (4.61)$$

Therefore, combination of Eqs. (4.50), (4.52), (4.53) and (4.60) yields a differential equation for the FAS at the debonded interface

$$\frac{d^2\sigma_f^z(z)}{dz^2} + P_1 \frac{d\sigma_f^z(z)}{dz} - P_2\sigma_f^z(z) = P_3 , \quad (4.62)$$

where the coefficients P_1 , P_2 and P_3 are given in Appendix C. The general solution of Eq. (4.62) is obtained for the partially debonded interface in the region $((L - \ell) \leq z \leq L)$, which is subjected to the boundary conditions:

$$\sigma_f^z(L) = 0, \quad \sigma_f^z(L - \ell) = \sigma_\ell . \quad (4.63)$$

Thus,

$$\begin{aligned} \sigma_f^z(z) = & \frac{P_3}{P_2} [Q_1 \exp(m_2 z) + Q_2 \exp(m_1 z)] \\ & + \sigma_\ell [Q_3 \exp(m_2 z) + Q_4 \exp(m_1 z)] , \end{aligned} \quad (4.64)$$

$$\begin{aligned} \tau_i(a, z) = & -\frac{a}{2} \left\{ \frac{P_3}{P_2} [m_2 Q_1 \exp(m_2 z) + m_1 Q_2 \exp(m_1 z)] \right. \\ & \left. + \sigma_\ell [m_2 Q_3 \exp(m_2 z) + m_1 Q_4 \exp(m_1 z)] \right\} , \end{aligned} \quad (4.65)$$

where the coefficients Q_1 , Q_2 , Q_3 , Q_4 , m_1 and m_2 are given in Appendix C. Eqs. (4.63) and (4.65) hold for the positive axial direction (i.e. the right-hand part of the fiber in Fig. 4.6). The corresponding solutions valid for the negative axial direction are obtained by symmetry of the FAS and anti-symmetry of the IFSS with respect to the fiber center at $z = 0$.

Determination of the crack tip debond stress, σ_ℓ , at a debond length, ℓ , is contingent to the condition that the fiber axial strain is equivalent to the matrix axial strain at the boundary between the bonded and debonded regions (i.e. $\partial u_f^z(z)/\partial z = \partial u_m^z(a, z)/\partial z$ at $z = \pm(L - \ell)$). Within the debonded region, the matrix axial strain at the interface is greater than the fiber axial strain due to the relative slip between fiber and matrix. Therefore, combining Eqs. (4.8), (4.9) and (4.61) at the boundary, σ_ℓ is obtained from

$$\sigma_\ell = \frac{\sigma(1 + \gamma)v_m R_1 + \bar{\sigma}\alpha v_f(R_1 + \lambda)}{\alpha\lambda(v_m - v_f) + (\alpha v_f + \gamma v_m)R_2} , \quad (4.66)$$

where R_1 and R_2 are given in Appendix C.

4.2.4.2. Interface debond and fiber fragmentation criteria

In the shear strength criterion, the debond crack propagates when the maximum IFSS at the debond crack tip $z = \pm(L - \ell)$ reaches the shear bond strength, τ_b , i.e.

$$\tau_i(a, (L - \ell)) = \tau_b . \quad (4.67)$$

By substituting Eq. (4.67) into Eq. (4.60), the debond crack tip stress, σ_ℓ , is expressed as a function of the material properties and σ . Thus,

$$\sigma_\ell = \frac{1 + \gamma}{\alpha + \gamma} \sigma - \frac{2\tau_b}{a\beta_2} \coth[\beta_2(L - \ell)] . \quad (4.68)$$

Therefore, by combining Eqs. (4.66) and (4.68), one can derive the stress applied to the matrix at the remote ends, $\sigma_a (= (b^2 - a^2)/a^2) = \sigma_{od}$, for debond crack propagation

$$\sigma_{od} = \frac{\frac{2R_3}{a\beta_2} \tau_b \coth[\beta_2(L - \ell)] - \frac{a^2}{\gamma b^2} \alpha v_f (R_1 + \lambda) \sigma}{(1 + \gamma) \left[\frac{R_3}{\alpha + \gamma} + v_m R_1 \right]} , \quad (4.69)$$

where R_3 is given in Appendix C.

Based on the same average fiber tensile strength model as that employed in Section 4.2.3, the fiber fragmentation criterion is derived in terms of the external stress, $\sigma_a (= (b^2 - a^2)/a^2) = \sigma_{of}$, for the partially debonded interface:

$$\sigma_{of} = \frac{\left(\frac{a}{b}\right)^2 (\alpha + \gamma)}{\gamma(1 + \gamma)} \left\{ \sigma_{TS}(2L) + \frac{2\tau_b}{a\beta_2} \operatorname{cosech}[\beta_2(L - \ell)] \right\} . \quad (4.70)$$

4.2.4.3. Three different interface conditions

Depending on the applied stress relative to the fiber tensile strength and the interfacial properties for given elastic properties of the constituents and the geometric factors of the composite model, three distinctive cases are considered with regard to the fiber–matrix interface condition: namely full bonding, partial debonding and complete debonding or full frictional bonding. The conditions required to satisfy each interface state are systematically identified in the following in terms of the relationship between the applied stress and the properties of the constituents and the interface. The stress distributions in the constituents are also characterized for each interface state, and the important factors governing the stress fields are identified. Therefore, the fiber fragmentation criterion is applied to each interface condition to derive the mean fiber fragment length, $2L$, as a function of the applied stress.

(i) Full bonding: Let us first consider the perfectly bonded interface over the whole fiber length where the stress transfer is purely elastic. The FAS and IFSS normalized with σ are plotted along the axial direction, z/a , for the half the fiber

length as shown in Fig. 4.10. The carbon fiber–epoxy matrix composite (Tables 4.1 and 4.2) is also employed for calculation throughout this section. It is noted that varying the fiber length only changes the effective length of the central part of the curve whose stress values are almost constant. Both the maximum FAS and IFSS, which are obtained in the center and at the ends of the fiber respectively, increase with decreasing modulus ratio, E_m/E_f , at a given applied stress. This implies that the efficiency of stress transfer across the interface is significantly dependent on the elastic properties of the composite constituents, E_m/E_f . A lower external stress is required to cause fiber fragmentation or debond initiation for a composite with a smaller value of E_m/E_f if other parameters remain the same.

Based on the shear strength criterion for the interface debonding, the condition for the fully bonded interface requires that the maximum IFSS be obtained at the

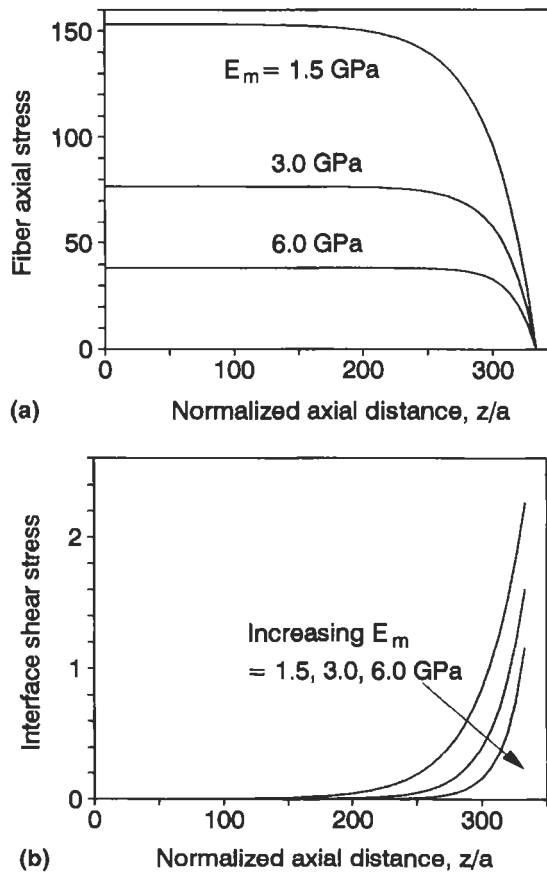


Fig. 4.10. Distribution of (a) normalized fiber axial stress, σ_f^z/σ , and (b) normalized interface shear stress, τ_{fz}^z/σ , along the fiber axis, z/a , for elastic moduli $E_m = 1.5, 3.0$ and 6.0 GPa with a constant $E_f = 230$ GPa. After Kim et al. (1993b).

fiber ends are smaller than the interface shear bond strength, τ_b , (i.e. $\tau_i(a, z) < \tau_b$). Substituting this requirement (along with $\sigma_\ell = 0$ and $\ell = 0$) into Eq. (4.60) gives

$$\sigma_a < \frac{2a}{b^2 \beta_2} \frac{\alpha + \gamma}{\gamma(1 + \gamma)} \tau_b \coth(\beta_2 L) \quad (4.71)$$

Under this circumstance, the external stress corresponding to the fiber fragmentation, $\sigma_a = \sigma_{of}$, is obtained from Eq. (4.59)

$$\sigma_{of} = \frac{a^2}{\gamma b^2} \frac{\alpha + \gamma}{1 + \gamma} \sigma_{TS}(2L) \frac{\cosh(\beta_2 L)}{\cosh(\beta_2 L) - 1} \quad (4.72)$$

Because Eq. (4.72) also has to satisfy the condition for full bonding at the interface governed by Eq. (4.71), the condition for fiber fragmentation while the interface is fully bonded requires

$$\tau_b > \frac{a \beta_2}{2} \sigma_{TS}(2L) \frac{\sinh(\beta_2 L)}{\cosh(\beta_2 L) - 1} \quad (4.73)$$

The critical combination of the interface bond strength, τ_b , and the fiber length, $2L$, required for the initial interface debonding is plotted according to Eq. (4.73) in Fig. 4.11. The regions above and below the curve represent full bonding and partial debonding at the interface, respectively, with the average fiber tensile strength estimated from Eq. (4.40). Therefore, for a given value of τ_b , one can evaluate the minimum fiber length $(2L)_d$ for interfacial debonding during the fiber fragmentation process by taking the value of the curve. For example, $(2L)_d \approx 2.71$ mm for $\tau_b = 72.7$ MPa.

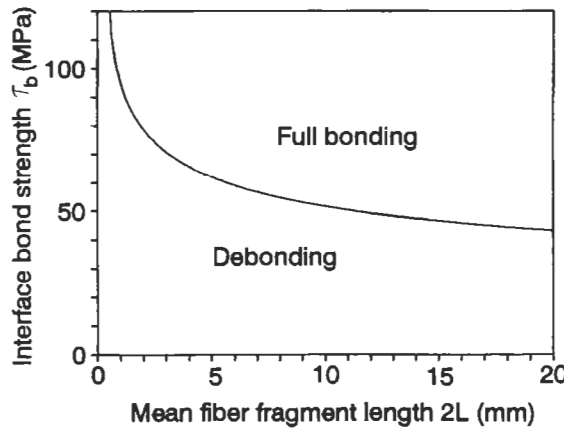


Fig. 4.11. Plot of interface shear bond strength, τ_b , as a function of fiber length, $2L$, showing the interface debond criteria, according to Eq. (4.71). After Kim et al. (1993b).

Having satisfied the requirements for full bonding, the mean fiber fragmentation length, $2L$, is determined from Eq. (4.72)

$$2L = \frac{2}{\beta_2} \cosh^{-1} \left\{ \frac{\gamma \left(\frac{b}{a}\right)^2 \sigma_{of}}{\gamma \left(\frac{b}{a}\right)^2 \sigma_{of} - \frac{\alpha+\gamma}{1+\gamma} \sigma_{TS}(2L)} \right\}. \quad (4.74)$$

The mean fiber fragment length, $2L$, is plotted as a function of applied strain, $\epsilon (= \sigma_a/E_m)$, in Fig. 4.12. Also superimposed are the results obtained when the fiber tensile strengths are assumed to be constant. The fully bonded model predicts that $2L$ decreases drastically within a narrow range of ϵ . The decrease is even more instantaneous if a constant σ_{TS} is used, which is followed immediately by an almost constant value as ϵ is further increased. The threshold value of the applied strain for the precipitous drop in fiber fragment length increases with increasing σ_{TS} . In contrast, there is no such threshold observed when σ_{TS} is given by the Weibull equation. It is also worth noting that the mean fiber fragment length becomes almost identical, regardless of whether the fiber tensile strength is Weibull-controlled or constant, when the applied strain is sufficiently large. This result suggests that for the fully bonded interface, the critical transfer length obtained at a large value of ϵ at the end of the fragmentation test would be almost independent of the fiber tensile strength model employed.

However, it should be emphasized here that only the initial decending part of the curves at low applied strains would satisfy the requirements of full bonding according to Eq. (4.73) and Fig. 4.11. The characteristic length, $(2L)_d$, which is the maximum fiber length obtainable before debond initiation, is controlled by the interface bond strength, τ_b , of the composite. In other words, unless τ_b is sufficiently large to prevent the interface from debonding (or, alternatively the matrix can

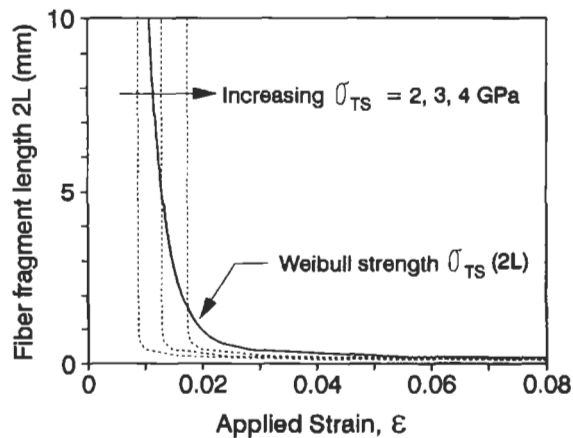


Fig. 4.12. Variation of mean fiber fragment length, $2L$, versus applied strain, ϵ , in the full bonded interface model: (-----) varying $\sigma_{TS}(2L)$; (——) constant fiber tensile strength σ_{TS} . After Kim et al. (1993b).

withstand an extremely large strain), it is most unlikely that the fully bonded model can fully describe the relationship between $(2L)$ and ε during the whole fiber fragmentation process for practical fiber composites.

(ii) Partial debonding: Once the maximum IFSS determined from the fiber ends reaches the shear bond strength, τ_b , debonding occurs. Fig. 4.13 shows typical plots of the FAS and IFSS for different values of τ_b ($= 50, 72.7$ and 100 MPa) when a constant external stress ($\sigma = 117.4$ MPa corresponding to initial debonding for $\tau_b = 72.7$ MPa) is applied to the composite of a given total fiber length $2L = 2$ mm. The FASs are almost identical for these τ_b values, except near the boundary between the bonded and debonded regions where the stresses are only moderately high for a low τ_b . There is discontinuity of the IFSS at the interface boundary where the stress drop is large with a high τ_b (which is equivalent to the maximum stress just before

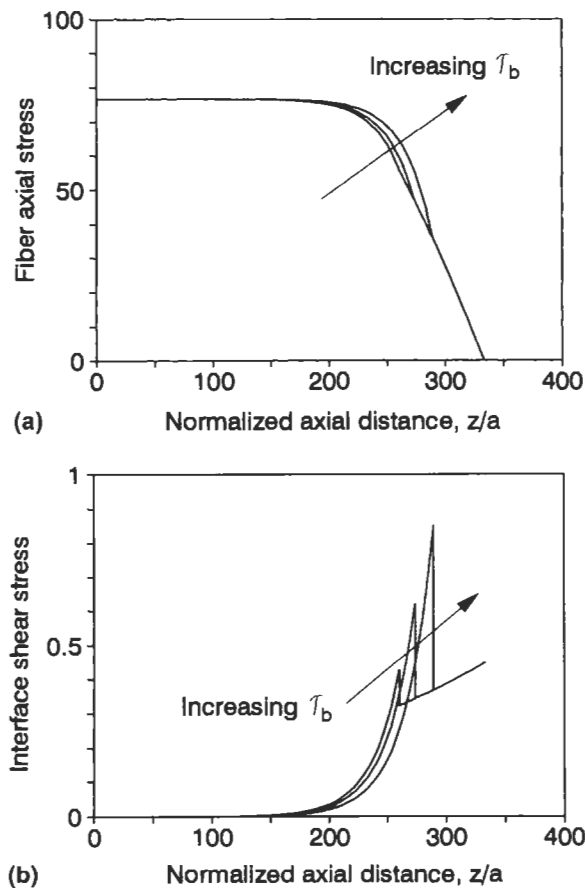


Fig. 4.13. Distributions of (a) normalized fiber axial stress, σ_z^f/σ , and (b) normalized interface shear stress, τ_z^f/σ , along the fiber axis, z/a , at a given applied stress $\sigma = 117$ MPa for $\tau_b = 50, 72.7$ and 100 MPa. After Kim et al. (1993b).

the stress drop). Near the fiber ends of the debonded interface, the IFSS increases non-linearly towards the fiber ends as a result of the smaller Poisson contraction of the fiber than the matrix.

The basic requirement necessary to satisfy the partially debonded interface is that the crack tip debond stress, σ_ℓ , (and the debond length, ℓ) must be greater than zero. From the debond criterion given by Eq. (4.68)

$$\sigma_a > \frac{2a}{b^2 \beta_2} \frac{\alpha + \gamma}{\gamma(1 + \gamma)} \tau_b \coth[\beta_2(L - \ell)] \quad (4.75)$$

In the partially debonded model, whether debonding continues or not depends strictly on the relative magnitude of the stresses required for debond propagation, σ_{od} , and for fiber fragmentation, σ_{of} , at a given debond length ℓ . If σ_{od} of Eq. (4.69) is smaller than σ_{of} of Eq. (4.70) interfacial debonding continues in preference to fiber fragmentation, and vice versa if σ_{od} is greater than σ_{of} . These requirements can be expressed as

$$\tau_b < \frac{a\beta_2}{2} \frac{[n_3 + v_m n_1(\alpha + \gamma)]\sigma_{TS}(2L) + \alpha v_f(n_1 + \lambda)\bar{\sigma}}{n_3 \coth[\beta_2(L - \ell)] - [n_3 + v_m n_1(\alpha + \gamma)] \operatorname{cosech}[\beta_2(L - \ell)]} \quad (4.76)$$

for debond crack propagation and,

$$\begin{aligned} & \frac{a\beta_2}{2} \frac{[n_3 + v_m n_1(\alpha + \gamma)]\sigma_{TS}(2L) + \alpha v_f(n_1 + \lambda)\bar{\sigma}}{n_3 \coth[\beta_2(L - \ell)] - [n_3 + v_m n_1(\alpha + \gamma)] \operatorname{cosech}[\beta_2(L - \ell)]} \\ & < \tau_b < \frac{a\beta_2}{2} \sigma_{TS}(2L) \frac{\sinh[\beta_2(L - \ell)]}{\cosh[\beta_2(L - \ell)] - 1} \end{aligned} \quad (4.77)$$

for fiber fragmentation.

The relationship between the applied stresses σ_{od} and σ_{of} is plotted as a function of normalized debond length, ℓ/a , in Fig. 4.14. It is interesting to note that σ_{od} is almost independent of the mean fiber fragment length, $2L$, with respect to ℓ/a , and hence only one curve for σ_d is shown. The implication of this figure is that when the fiber is sufficiently long (e.g. $2L = 4$ mm), it fractures without debonding (because $\sigma_{od} > \sigma_{of}$) until its length reaches a characteristic value $(2L)_d$. $(2L)_d = 2.71$ mm is obtained for $\tau_b = 72.7$ MPa by equating $\sigma_{od} = \sigma_{of}$ (i.e. $\ell = 0$, in Fig. 4.14(a)), which is exactly identical to the value obtained for the full bonded interface (Fig. 4.11).

The relationship between the applied stresses σ_{od} and σ_{of} is further evaluated in Fig. 4.15 in which τ_b is plotted as a function of the debond length, ℓ/a , for different fiber lengths based on Eqs. (4.76) and (4.77). The solid lines represent the upper bounds for interface debond (or, the lower bounds for fiber fragmentation), and the dotted lines represent the upper bounds for fiber fragmentation. There are three different regions identified: region A for debonding only; region B for fiber fragmentation without further debonding; region C for neither debonding nor fiber fragmentation. It is found that if τ_b is greater than a certain value (i.e. $\tau_b = 94.7$ MPa for $2L = 2$ mm and $\tau_b = 78.8$ MPa for $2L = 1$ mm), further fiber

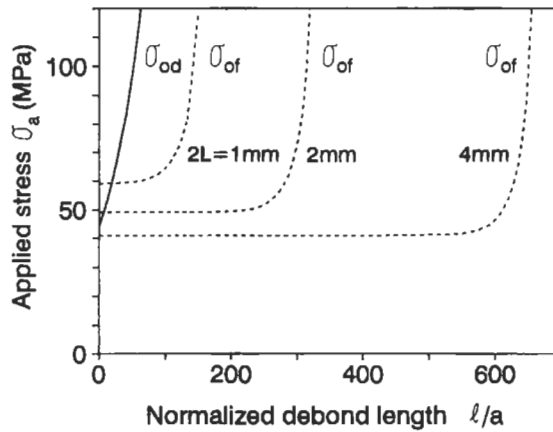


Fig. 4.14. Plots of applied stresses required for interface debonding, σ_{od} (solid lines), and for fiber fragmentation, σ_{of} (dotted lines), as a function of normalized debond length, ℓ/a , for different fiber length $2L = 1, 2$ and 4 mm. After Kim et al. (1993b).

fragmentation is not possible, although debonding can occur for a very short length. As the fiber length decreases the upper bounds for both debond and fragmentation increase as a result of corresponding increase in the debond length for a given τ_b . There is a maximum debond length corresponding to the external stress that causes the fiber of a given length to fracture. Summarizing the phenomena occurring in the partially debonded interface, interface debond and fiber fragmentation alternate

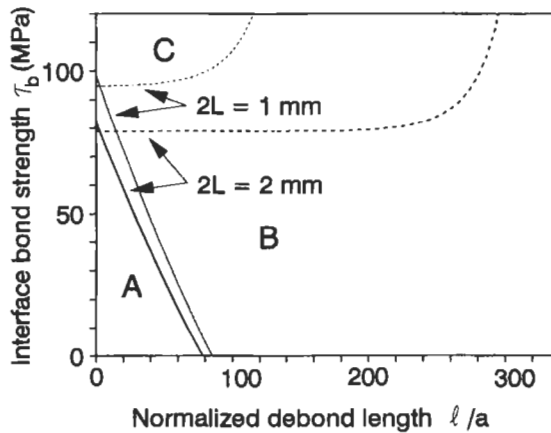


Fig. 4.15. Plots of interface shear bond strength, τ_b , as a function of normalized debond length, ℓ/a , illustrating the areas corresponding to debonding only (region A), fiber fragmentation without further debonding (region B) and neither debonding nor fiber fragmentation (region C): (—) upper bounds for interface debond; (---) upper bounds for fiber fragmentation. After Kim et al. (1993b).

depending on the relative values of the interface bond strength and the external stress.

Finally, the solution for the mean fiber fragmentation length, $2L$, which is the sum of the debonded and bonded lengths in the partial debond model, is derived from the fiber fragmentation criterion given by Eq. (4.70)

$$2L = 2\ell + \frac{2}{\beta_2} \sinh^{-1} \left\{ \frac{\frac{2\tau_b}{a\beta_2}}{\left(\frac{b}{a}\right)^{2\gamma(1+\gamma)} \sigma_{of} - \sigma_{TS}(2L)} \right\}. \quad (4.78)$$

Eq. (4.78) is plotted in Fig. 4.16 where the bond length ($2L - 2\ell$) and the debond length 2ℓ balance each other to determine the instantaneous mean fiber fragmentation length, $2L$, at a given applied strain. At low strains the bond length component dominates, but at high strains the debond length component becomes increasingly more important, and eventually the debond length outpaces the bond length under certain favorable circumstances. When the mean fiber fragment length is sufficiently short at a high applied strain, an infinitesimal increase in debond length or additional fiber fragmentation requires the applied strain to increase dramatically toward an infinite value. A severalfold increase in the applied strain at this stage would not cause any further fiber fragmentation. In practical fiber fragmentation tests, the mean fiber fragment length obtained after substantial increase in load application without further fiber fragmentation is called the 'critical transfer length'. In the present analysis, the shortest mean fiber fragment length determined at the end of the curve shown in Fig. 4.16 can be regarded as the critical transfer length, $(2L)_c$, theoretically predicted for the carbon fiber-epoxy matrix composite.

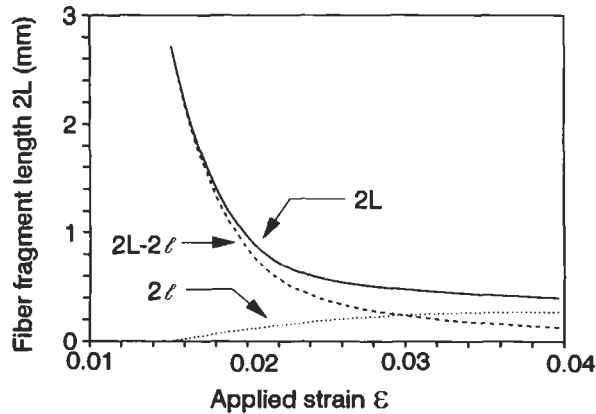


Fig. 4.16. Variation of mean fiber fragmentation length, $2L$, versus applied strain, ϵ , in the partially debonded interface model for $\tau_b = 50$ MPa. After Kim et al. (1993b).

(iii) Complete debonding: Complete interfacial debonding means that the fiber length and the debond length are identical, and the IFSS is maximum at the debond crack tip, which now coincides with the fiber center ($z = 0$). These requirements cannot be satisfied in practice because the FAS always has to be at a maximum in the center regardless of debond length. However, if the interfacial bonding consists solely of friction where the IFSS is governed wholly by the Coulomb friction law, then the above requirements can be satisfied. In this case, which is most likely in some ceramic matrix composites, the IFSS is minimal in the center where no radial contraction takes place due to the difference in Poisson ratio between the fiber and matrix. For the frictionally bonded interface, the solutions for the FAS and IFSS given by Eqs. (4.64) and (4.63) are valid with σ_r being substituted by the FAS in the center, $\sigma_r^z(0)$, and $\ell = L$ for the non-dimensional coefficients Q_j (where $j = 1, 2, 3, 4$) given in the Appendix C:

$$\sigma_r^z(z) = \frac{P_3}{P_2} [Q'_1 \exp(m_2 z) + Q'_2 \exp(m_1 z)] + \sigma_r^z(0) [Q'_3 \exp(m_2 z) + Q'_4 \exp(m_1 z)] , \quad (4.79)$$

$$\tau_i(a, z) = -\frac{a}{2} \left\{ \frac{P_3}{P_2} [m_2 Q'_1 \exp(m_2 z) + m_1 Q'_2 \exp(m_1 z)] + \sigma_r^z(0) [m_2 Q'_3 \exp(m_2 z) + m_1 Q'_4 \exp(m_1 z)] \right\} , \quad (4.80)$$

where

$$Q'_j = Q_j|_{\ell=L} . \quad (4.81)$$

In Eqs. (4.79) and (4.80) $\sigma_r^z(0)$ can be determined for the boundary condition that the IFSS is minimal in the center, i.e. $\tau_i(a, 0) = -\mu q_0$ from Eq. (4.29)

$$\sigma_r^z(0) = -\frac{\omega_1(1 + \gamma)(m_2 Q'_1 + m_1 Q'_2)\sigma + \omega(\lambda + m_2 Q'_1 + m_1 Q'_2)\bar{\sigma}}{m_2 Q'_3 + m_1 Q'_4} . \quad (4.82)$$

The normalized FAS and IFSS are shown in Fig. 4.17. Both the FAS and IFSS distributions are higher for larger values of residual clamping stress, q_0 , (in absolute terms) for a given fiber length. Varying the coefficient of friction, μ , would have similar effects on the stress distributions. The predominant effect of differential Poisson contraction between the fiber and matrix is obvious, particularly in Fig. 4.17(b), where the IFSS values at the fiber ends are several-fold the values obtained in the center.

For the fully frictional interface model, the external stress corresponding to fiber fragmentation is determined from Eq. (4.82) and $\sigma_{TS}(2L)$

$$\sigma_{of} = -\left(\frac{a}{b}\right)^2 \frac{1}{\gamma\omega_1(1 + \gamma)} \frac{(m_2 Q'_3 + m_1 Q'_4)\sigma_{TS}(2L) + \omega(\lambda + m_2 Q'_1 + m_1 Q'_2)\bar{\sigma}}{m_2 Q'_1 + m_1 Q'_2} . \quad (4.83)$$

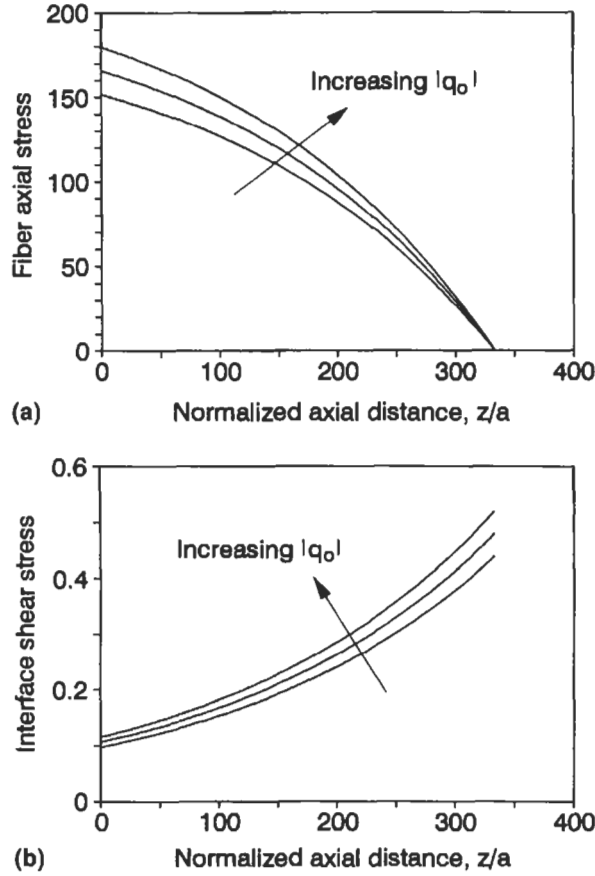


Fig. 4.17. Distribution of (a) normalized fiber axial stress, σ_f^z/σ , and (b) normalized interface shear stress, τ_f^z/σ , along the fiber axis, z/a , at a given applied stress for different residual clamping stresses $q_0 = -7, -10$ and -13 MPa. After Kim et al. (1993b).

Taking the approximate values for the non-dimensional coefficients given in Eq. (4.80), the solution for the mean fiber fragment length, $2L$, is given in a closed form equation

$$2L = \frac{-2}{m_2} \ln \left\{ \frac{\frac{m_1 v_m}{\omega_1} \sigma_{TS}(2L) + \alpha v_f (\lambda - m_1) \bar{\sigma} - \left(\frac{a}{b}\right)^2 m_1 v_m \gamma (1 + \gamma) \sigma_{of}}{(m_2 - m_1) \left[\alpha v_f \bar{\sigma} - \left(\frac{b}{a}\right)^2 v_m \gamma (1 + \gamma) \sigma_{of} \right]} \right\}. \quad (4.84)$$

The mean fiber fragment length, $2L$, is plotted as a function of the applied strain, ϵ , in Fig. 4.18. Similar to the results for the fully bonded interface model shown in Fig. 4.12, the full frictional interface model predicts that $(2L)$ decreases sharply with increasing applied strain within a short range of ϵ . A high fiber tensile strength

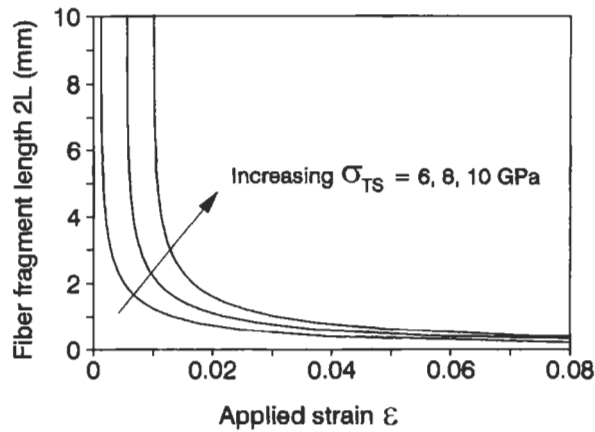


Fig. 4.18. Variation of mean fiber fragment length, $2L$, as a function of applied strain, ϵ , predicted in the fully debonded interface model for constant fiber tensile strengths $\sigma_{TS} = 6.0, 8$ and 10 GPa. After Kim et al. (1993b).

results in a high applied strain required to initiate the fiber fragmentation. However, varying the constant fiber tensile strength does not much influence ($2L$) at a high applied strain.

4.2.4.4. Comparisons with earlier shear-lag models

A major improvement of the models presented in this section compared to the earlier models given in Section 4.2.2 is that the conditions required to satisfy the three different interfaces, i.e. full bonding, partial debonding and full frictional bonding, are systematically identified. This gives an idea how the interface condition changes with increasing load during the whole course of the fiber fragmentation test. It is also shown that depending on the relative properties at the bonded and debonded interfaces, the IFSS at the debonded region increases from the boundary of the two regions toward the fiber ends as a consequence of the differential contraction between the fiber and matrix. This effectively discourages debond propagation during the fiber fragmentation process. This response makes it most unlikely that the interface becomes debonded along the whole fiber length even at a very high applied strain in most practical polymer matrix composites.

Nevertheless, there are also important issues which remain unresolved in this model. Apart from the three different interface states discussed above, there are other states of the interface due to yielding of matrix material immediately surrounding the cylindrical fiber, and the combination of partial debonding and partial yielding. Plastic yielding occurs in the matrix instead of interface debonding if the interface shear bond strength, τ_b , is sufficiently higher than the matrix yield strength in shear, τ_{my} , as in some composites containing ductile thermosets/thermoplastics and metal matrices. To be able to model this behavior analytically the exact knowledge regarding the effective thickness of the interphase region being

involved in plastic yielding and the elasto-plastic stress–strain response of the matrix material need to be established. The stress transfer phenomena affected by matrix yielding has been analyzed recently, along with its effect on fiber fragment length and effective fiber length (Kim, 1997).

There are other limitations of the model, besides the assumption of perfectly elastic stress–strain behavior for both the fiber and matrix: neglect of the anisotropy of fiber elastic properties (e.g. carbon and aramid fibers) and residual stresses in the axial direction (in addition to those in the radial direction) generated from the differential thermal contraction between fiber and matrix and a simplified fiber fracture criterion. In particular, with regard to the fiber strength model, the fiber is considered to have a strength varying only with its length, and thus it fractures always in the center due to the axi-symmetric stress field. In other words, the mean number of fiber segments always has to be a multiple of two independent of the initial fiber length. In practice, however, the fiber can break at any weak spot when the local stress exceeds the load-bearing capacity. The local stress is strongly influenced by the spatial distribution of the flaws of random sizes inherent in the brittle fiber surface, which cannot be adequately accounted for in the average tensile strength model. Liu et al.(1994a, b) have recently developed a fracture mechanics based computer simulation model by including both the spatial and size distributions of flaws along the fiber length to predict the evolution of the fiber fragmentation process. There is good agreement between simulation and experiment.

Within the foregoing limitations of the micromechanics analysis, it is clearly demonstrated for a carbon fiber–epoxy matrix composite that one interface condition cannot represent the interface debond/fiber fragmentation behavior during the whole fiber fragmentation process. While the fully bonded interface model can describe the early stage of the fiber fragmentation process (until the fiber length reaches a characteristic value $(2L)_d$ corresponding to initial debonding) at low applied strains, the interface soon becomes partially debonded as the applied strain increases. In the partially debonded interface model, the mean fiber fragment length is the sum of the bonded and debonded lengths, the former diminishes while the latter grows with the applied strain. Therefore, a non-zero critical value is always reached for the mean fiber fragment length when the applied strain required for further fiber fragmentation or interfacial debonding approaches infinity. In experiment, the critical transfer length, $(2L)_c$, is defined as the mean fiber fragment length determined after a further substantial increment in the applied strain leading to no additional fiber fragmentation, which is exactly the same as what is predicted in the analysis. It follows then that the critical transfer length can be considered as a material constant for given properties of the composite constituents and the interface. In view of the coexistence of bonded and debonded regions in the critical transfer length, accurate measurements of their lengths in experiments are absolutely necessary to properly characterize the relevant interfacial properties.

There is increasing evidence in recent years in the fragmentation test of some brittle fiber–brittle matrix composites that a matrix crack is developed at the position of the fiber break. The presence of the matrix crack and its physical size are shown to alter the stress distributions at the fiber–matrix interface. As the applied strain

(stress) is increased, there is a competition between interface debonding and matrix crack propagation. This phenomenon of fiber fragmentation has been recently analyzed by Liu et al.(1997) using fracture mechanics and a constant average fiber strength model.

4.3. Fiber pull-out test

4.3.1. Introduction

Theoretical analyses of interfacial debonding and frictional pull-out in the fiber pull-out test were initially modeled for ductile matrices (e.g. tungsten wire-copper matrix (Kelly and Tyson, 1965, Kelly, 1966)) assuming a uniform IFSS. Based on the matrix yielding over the entire embedded fiber length, L , as a predominant failure mechanism at the interface region, a simple force balance shown in Fig. 4.19 gives the fiber pull-out stress, which varies directly proportionally to the cylindrical surface area of the fiber

$$\sigma_{po} = 2\tau_m \left(\frac{L}{2a} \right) + \sigma_e, \quad (4.85)$$

where τ_m is the matrix shear yield strength, and σ_e the fiber stress at its embedded end (with $\sigma_e = 0$ for specimens without such bonding). However, in most practical composites containing brittle matrix materials, the distribution of IFSS is neither uniform nor continuous due to the coexistence of the bonded and debonded regions along the interface. Moreover, the functional dependence of the external stress for

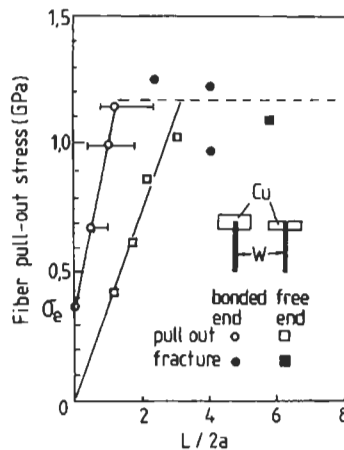


Fig. 4.19. Fiber pull-out stress as a function of embedded fiber length, $L/2a$, for a tungsten wire embedded copper matrix composite system. Open symbols for pulled-out specimens; solid symbols for fractured specimens. After Kelly and Tyson (1965).

interfacial debonding is non-linear due to the effect of the Poisson contraction of the fiber, which is subjected to uniaxial tension.

In Section 4.2.1, it was mentioned that the condition for debonding along the interface has been defined by two approaches: i.e., the shear strength criterion and the fracture mechanics approach. The first approach is typified by the work of Greszczuk (1969) who modified Cox's shear-lag model to fit into the fiber pull-out loading geometry, assuming that the tensile stress in the matrix is negligible relative to the fiber while the shear stress in the fiber is small compared to the matrix. Lawrence (1972) and Laws et al. (1973) (and later Laws, 1982) further modified Greszczuk's model, taking into account the influence of frictional resistance of fiber pull-out in the debonded region. They identified that the maximum debond stress for complete debonding is dependent on the embedded fiber length, L , and the ratio of the shear bond strength to the frictional shear strength, τ_b/τ_{fr} . The non-linear variation of debond stress with the embedded fiber length is attributed to the reduction in the frictional stress as a result of Poisson contraction of the fiber when subjected to tension (Takaku and Arridge, 1973). Also identified is the initial pull-out stress against the frictional resistance from the experiments on model composites of steel wire-epoxy matrices (Takaku and Arridge, 1973). Since Gray (1984) gave a comprehensive review of the shear strength approach to this problem, there have been significant recent advances. In particular, Hsueh (1988, 1990a, 1992) postulated a progressive stable debond including the effect of shear deformation in the matrix, which is further improved by taking into account the radial dimension of the matrix cylinder.

Recently, other investigators (Banbaji, 1988; Leung and Li, 1991; Yue and Cheung, 1992; Fu et al., 1993; Hsueh, 1993) proposed the so-called 'two-way debonding' model where IFSS concentration occurs both at the loaded and embedded ends of the fiber, suggesting the possibility of debond propagation from both ends in the context of a shear strength criterion. This phenomenon is different from the conventional assumption of debond crack propagation inward only from the loaded fiber end. Details of the two-way debonding phenomenon are presented in Section 4.3.7 in conjunction with the three-cylinder model based on the micromechanical and the FE analyses.

The fracture mechanics approach includes the early work of Gurney and Hunt (1967) and Outwater and Murphy (1969). In this approach the rate of strain energy released from the fiber for complete debonding of embedded fiber length, L , is equated to the incremental interfacial fracture energy (which is the product of interface fracture toughness, G_{ic} , and cylindrical debond area, $2\pi aL$), deriving the solution for the constant fiber debond stress

$$\sigma_d^* = 2\sqrt{\frac{E_f G_{ic}}{a}} \quad (4.86)$$

More recently, Stang and Shah (1986) derived a debond criterion based on a compliance analysis, and Wells and Beaumont (1985) took into account the effect of the Poisson contraction of the fiber and non-linear friction in the debonded region.

Piggott (1987, 1990) have equated the increase in debond length with the energy changes arising from the fiber axial tension and matrix shear. Gao et al. (1988) also presented a debond criterion using the assumptions similar to those made previously (Wells and Beaumont, 1985). Based on the relationship between the debond and post-debond frictional pull-out stresses versus embedded fiber length established in the work of Gao et al. (1988), it has been demonstrated (Kim et al., 1992) that the model is able to determine the inherent interfacial properties including interfacial fracture toughness G_{ic} , coefficient of friction, μ , and the residual fiber clamping stress, q_0 . Hutchinson and Jensen (1990) and Keran and Parthasarathy (1991) considered the effect of residual stresses in the fiber axial direction in a thermo-mechanical analysis, giving a solution for the pull-out stresses similar to that obtained earlier by Gao et al. (1988). Other recent studies using the fracture mechanics approach include those of Pally and Stevens (1989), Sigl and Evans (1989), Marshall et al. (1992) and Jiang and Penn (1992), the latter based on the stress solutions derived earlier by Piggott (1987). Zhou and Mai (1993) also took into account the anisotropy of the embedded fiber for the fiber pull-out problem.

As opposed to the common perception of perfectly cylindrical surface of the fiber, several investigators, including Jero and Keran (1990), Jero et al. (1991), Carter et al. (1991), Waren et al. (1992), Mackin et al. (1992a, b), have noted substantial surface roughness of some ceramic fibers, notably the SCS-6 SiC fibers and sapphire fibers. They found that surface roughness contributes significantly to the frictional resistance of fiber pull-out (and fiber push-out). It is assumed that the fiber and matrix geometry, once removed from their original position, would create a uniform asperity pressure, as schematically illustrated in Fig. 4.20, that simply adds to the existing radial clamping stress. Assuming the separation of fiber and matrix during frictional sliding is equivalent to the roughness amplitude, Keran and Parthasarathy

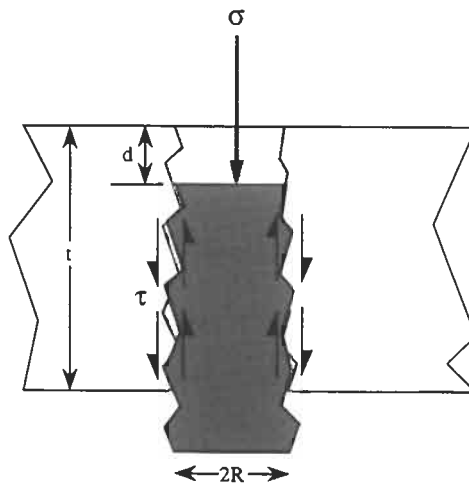


Fig. 4.20. Schematic presentation of rough fiber surface in a fiber push-out test. After Mackin et al. (1992a, b).

(1991) analyzed the effect of asperity pressure in the fiber pull-out and push-out tests. The asperity interactions have also been modeled based on the classical Hertzian contact law, leading to a sinusoidal modulation of the sliding stress (Carter et al., 1991). Mackin et al. (1992a) also proposed a fractal model to incorporate the asperity effects in the push-out loading geometry. In addition, rigorous fracture mechanics analyses are presented by Liu et al. (1994a, b, 1995) for fiber pull-out and push-out using a Fourier series representation of the fiber roughness effect. It has been emphasized (Keran and Parthasarathy, 1991; Mackin et al., 1992a) that a proper asperity wear mechanism must be introduced to explain the variation of the fiber reseating behavior with sliding distance. This is viewed as gradual degradation of the interface (frictional) properties due to the cyclic sliding in fatigue.

4.3.2. Solutions for stress distributions

Much of the analysis to be presented in the following sections will encompass what has been reported in recent publications (Kim et al., 1991, 1992, 1993a, b, 1994b; Zhou et al., 1992a, b, c, 1993, 1994). A shear-lag model of the fiber pull-out test shown in Fig. 4.21 is essentially similar to the composite model employed in the fiber fragmentation test, except for the fiber end, which is exposed and is subjected to external tensile stress in the fiber pull-out test. L is the total embedded fiber length with a partial debond region of length ℓ from the free fiber end. In the present analysis, the matrix is fixed at the embedded (bottom) end ($z = L$) and a tensile stress σ is applied to the free fiber end (at $z = 0$). Other models with identical specimen geometry but different loading condition in the fiber pull-out test, e.g. restrained top and fixed fiber/matrix bottom ends, have been presented elsewhere (Zhou et al.,

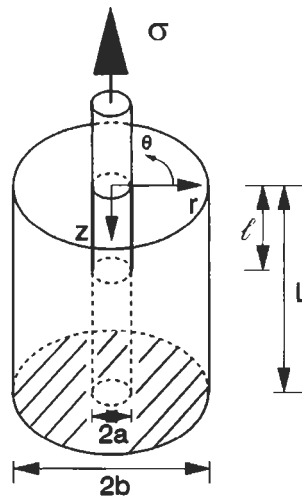


Fig. 4.21. Schematic drawing of the partially debonded fiber in fiber pull-out test.

1992b). The external stress, σ , is represented by σ_0 , σ_d^p , σ_d^* and σ_{fr} for (frictionless) initial debond stress, partial debond stress, maximum debond stress and initial frictional pull-out stress after complete debonding, respectively, at different stages of the fiber pull-out process. A typical fiber pull-out stress–displacement (σ – δ) diagram along with these characteristic external stresses is schematically shown in Fig. 3.7.

For the cylindrical coordinates (r, θ, z) in the fiber pull-out test, the basic governing equations and the mechanical equilibrium conditions between the composite constituents are essentially the same as those given in Section 4.2.3, i.e. Eqs. (4.8)–(4.18). The only exception is the equilibrium condition between the external stress and the axial stresses in the fiber and the matrix given by Eq. (4.11), which has to be modified to

$$\sigma = \sigma_f^z(z) + \frac{1}{\gamma} \sigma_m^z(z) . \quad (4.87)$$

Therefore, in a procedure similar to that used in the fiber fragmentation test, combining Eqs. (4.10), (4.17), (4.18), and (4.87) yields a second-order differential equation for the FAS

$$\frac{d^2 \sigma_f^z(z)}{dz^2} - A_1 \sigma_f^z(z) = \gamma A_2 \sigma , \quad (4.88)$$

where the coefficients A_1 and A_2 are given in Eqs. (4.20) and (4.21). The solution of the FAS is subjected to the following boundary conditions:

$$\sigma_f^z(\ell) = \sigma_\ell = \sigma - \omega(\bar{\sigma} - \sigma)[\exp(\lambda\ell) - 1], \quad \sigma_f^z(z) = 0 . \quad (4.89)$$

σ_ℓ is the crack tip debond stress at the boundary between the bonded and debonded regions at $z = \ell$, as defined in Section 4.2.3. It should be noted, however, that the actual values of σ_ℓ are different for different specimen geometry even for an identical debond length, ℓ . Therefore, the solutions of FAS, and the corresponding MAS, MSS and IFSS are obtained for the bonded region ($\ell \leq z \leq L$):

$$\sigma_f^z(z) = \frac{\left[\gamma \frac{A_2}{A_1} \sigma + \sigma_\ell \right] \sinh[\sqrt{A_1}(L-z)] - \gamma \frac{A_2}{A_1} \sigma \sinh[\sqrt{A_1}(\ell-z)]}{\sinh[\sqrt{A_1}(L-\ell)]} - \gamma \frac{A_2}{A_1} \sigma . \quad (4.90)$$

$$\begin{aligned} \sigma_m^z(z) = & -\gamma \frac{\left[\gamma \frac{A_2}{A_1} \sigma + \sigma_\ell \right] \sinh[\sqrt{A_1}(L-z)] - \gamma \frac{A_2}{A_1} \sigma \sinh[\sqrt{A_1}(\ell-z)]}{\sinh[\sqrt{A_1}(L-\ell)]} \\ & + \gamma^2 \frac{A_2}{A_1} \sigma , \end{aligned} \quad (4.91)$$

$$\begin{aligned} \tau_m(r, z) = & \gamma \frac{\left[\gamma \frac{A_2}{A_1} \sigma + \sigma_\ell \right] \cosh[\sqrt{A_1}(L-z)] - \gamma \frac{A_2}{A_1} \sigma \cosh[\sqrt{A_1}(\ell-z)]}{\sinh[\sqrt{A_1}(L-\ell)]} \\ & \times \sqrt{A_1} \frac{b^2 - r^2}{2r} , \end{aligned} \quad (4.92)$$

$$\tau_i(a, z) = \frac{a\sqrt{A_1}}{2} \frac{[\gamma \frac{A_2}{A_1} \sigma + \sigma_\ell] \cosh[\sqrt{A_1}(L-z)] - \gamma \frac{A_2}{A_1} \sigma \cosh[\sqrt{A_1}(\ell-z)]}{\sinh[\sqrt{A_1}(L-\ell)]} . \quad (4.93)$$

The solutions in the debonded region ($0 \leq z \leq \ell$) are obtained previously (Gao et al., 1988) for the boundary condition that the FAS at the loaded end ($z = 0$) is the same as the applied stress, σ

$$\sigma_f^z(0) = \sigma . \quad (4.94)$$

Thus,

$$\sigma_f^z(z) = \sigma - \omega(\bar{\sigma} - \sigma)[\exp(\lambda z) - 1] , \quad (4.95)$$

$$\sigma_m^z(z) = \gamma\omega(\bar{\sigma} - \sigma)[\exp(\lambda z) - 1] , \quad (4.96)$$

$$\tau_m(r, z) = \frac{\gamma\lambda\omega(b^2 - r^2)}{2r} (\bar{\sigma} - \sigma) \exp(\lambda z) , \quad (4.97)$$

$$\tau_i(a, z) = \frac{a\lambda\omega}{2} (\bar{\sigma} - \sigma) \exp(\lambda z) , \quad (4.98)$$

where the coefficients A_1 and A_2 are given in Eqs. (4.20) and (4.21). The stress distributions in the constituents along the axial direction are schematically illustrated in Fig. 4.22 for a partially debonded interface during the debond process for the carbon fiber–epoxy matrix composite whose properties are given in Tables 4.2 and 4.3. Similar plots for the interface before debond initiation or after complete debonding can be taken simply from the respective regions of the stress distribution. The stress gradients for FAS and IFSS increase (or that for MAS decreases) rapidly from the fiber end ($z = L$) toward the debond crack tip at the bonded region, while the gradients of all these stresses become almost constant at the debonded region. The high level of stresses concentration near the debond crack tip for the IFSS is a direct reflection of the imminent debond crack propagation.

Unlike the axial stress in the fiber or matrix, the IFSS is discontinuous at the boundary between the bonded and debonded regions. The non-linear variations of the stresses in the debonded region, and particularly the decrease of IFSS towards the loaded fiber end, reflect the prominent Poisson effect of radial contraction of the fiber under axial tension. If the embedded fiber length is sufficiently long, the maximum debond stresses, σ_d^* , to be shown in Figs. 4.26(a), 4.27(a) and 4.28(a) would become a plateau value, $\bar{\sigma}$, such that the induced residual stress, $q_1(a, z)$, in the radial direction compensates completely for the residual clamping (compressive) stress, q_0 . Under this circumstance, the IFSS at the debonded region given by Eq. (4.29) will be equivalent to zero. Complete separation ensues between the fiber and matrix at the loaded end ($z = 0$), which will further extend along the debonded interface upon continuing loading. This can be proven in Eq. (4.29) by substituting q_0 and $q_1(a, z)$ with Eqs. (4.24) and (4.18) for $\sigma_f^z(0) = \sigma$ and $\sigma_m^z(0) = 0$.

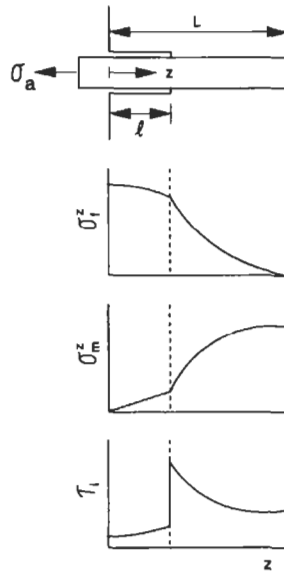


Fig. 4.22. Distributions of (a) fiber axial stress, σ_f^z , (b) matrix axial stress, σ_m^z , and (c) interface shear stress, τ_i , along the embedded fiber length in fiber pull-out. After Zhou et al. (1992a, b, c).

4.3.3. Interface debond criterion and partial debond stress

The interface debond criterion used in this analysis is based on the concept of fracture mechanics. Substituting the solutions for the three major stress components determined in the bonded and debonded regions, a fiber–matrix interface debond criterion is derived for the pull-out test as

$$2\pi a G_{ic} = B_1 \sigma^2 + C_1 (\bar{\sigma} - \sigma) \sigma + D_1 (\bar{\sigma} - \sigma)^2, \quad (4.99)$$

where the coefficients B_1 , C_1 and D_1 are complex functions of material properties of the constituents and geometric factors, and are given in Appendix A.

Partial debond stress, σ_d^p , is the applied fiber stress during the progressive debonding process that may be written as a function of the debond length, ℓ , and the crack tip debond stress, σ_ℓ , from Eq. (4.89)

$$\begin{aligned} \sigma_d^p &= \sigma_\ell + (\bar{\sigma} - \sigma_\ell) \frac{\omega[\exp(\lambda\ell) - 1]}{1 + \omega[\exp(\lambda\ell) - 1]} \\ &\approx \sigma_\ell + (\bar{\sigma} - \sigma_\ell)[1 - \exp(-\lambda\ell)]. \end{aligned} \quad (4.100)$$

It follows that σ_d^p consists of two stress components: a crack tip debond stress, σ_ℓ , and a friction stress component. σ_ℓ is not only a function of the interfacial fracture toughness, G_{ic} , but is also dependent on the debond length, ℓ , relative to the total

Table 4.3
Fiber pull-out parameters and interfacial properties for several different fiber composites^a.

Composite system	Fiber surface condition	Fiber pull-out parameters					Interfacial properties		
		σ_0^* (GPa)	λ (mm ⁻¹)	σ (GPa)	z_{\max} (mm)	L_{\max} (mm)	G_{ic} (J/m ²)	μ	q_0 (MPa)
Carbon fiber-epoxy matrix	Untreated	3.4	1.5	5.4	0.152	0.955	37.7	1.25	- 9.97
Steel wire-epoxy matrix	Uncoated	1.95	0.0142	2.41	7.8	10.9	1316	0.48	- 8.85
	Release agent coated	0.316	0.0065	2.18	6.5	342	34.7	0.22	- 8.01
SiC fiber-glass matrix	Untreated	0.149	0.0304	2.92	0.5	49.3	0.964	0.048	-64.5
	Acid treated	0.235	0.049	3.27	0.6	23.4	2.40	0.078	-72.3

^aAfter Kim et al. (1992) and Zhou et al. (1993).

embedded fiber length, L . The friction stress component is directly proportional to $(\bar{\sigma} - \sigma_\ell)$, and is also controlled by λ (or, in turn by the coefficient of friction, μ).

The partial debond stress, σ_d^p , calculated based on Eq. (4.100) using the properties given in Table 4.1 and the interface properties in Table 4.3 are plotted as a function of debond length, ℓ , in Figs. 4.23 and 4.24, respectively, for carbon fiber–epoxy matrix and untreated SiC fiber–glass matrix composites. These two composite systems are considered to be typical of those with adhesion mechanisms at the fiber–matrix interface which are chemical and frictional in nature, respectively. It is clearly shown that the crack tip debond stress, σ_ℓ , decreases toward zero depending on the fiber embedded length L . For short L , it decreases from the beginning whereas for long L it is initially constant and decreases toward zero as ℓ increases. In contrast, the friction stress component always increases with increasing ℓ for a given L , the increase being non-linear due to Poisson contraction of the fiber in the debonded region. These two stress components balance each other to determine the instantaneous values of σ_d^p . It can thus be summarized that the variation of the partial debond stress with respect to the debond length during the fiber debond process is largely controlled by the embedded fiber length given the properties of the composite constituents. Figs. 4.23 and 4.24 also indicate that when the embedded fiber is sufficiently long, the frictional properties at the debonded interface relative to the interface fracture toughness, G_{ic} , (or interface shear bond strength, τ_b) in the bonded region are a key factor that determines the stability of the debond process. The interfacial property-dependent debonding process is reflected by the amount of stress drop (i.e. from the maximum debond stress, σ_d^* , to a lower value σ_{fr} , corresponding to the initial frictional pull-out at $\ell = L$, which is commensurate with the load drop frequently observed in pull-out stress versus displacement curves in experiments (Fig. 3.7).

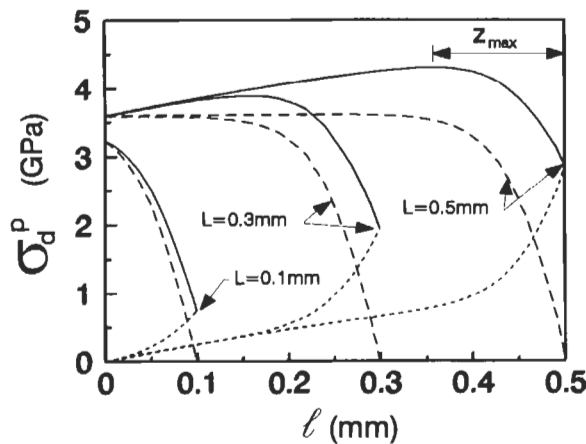


Fig. 4.23. Plot of partial debond stress, σ_d^p , as a function of debond length, ℓ , for a carbon fiber–epoxy matrix composite. After Kim et al. (1992).

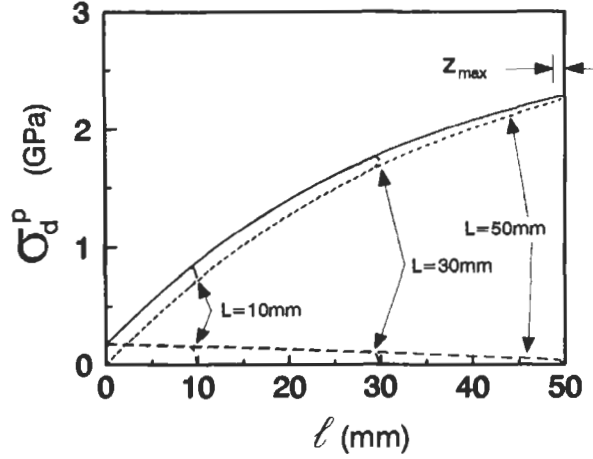


Fig. 4.24. Plot of partial debond stress, σ_d^p , as a function of debond length, ℓ , for untreated SiC fiber-glass matrix composite. After Kim et al. (1991).

In light of the foregoing discussion concerning the functional partitioning of the partial debond stress, the characteristic debond stresses can be evaluated. The initial debond stress, σ_0 , is obtained for an infinitesimal debond length where the frictional stress component is zero, i.e.,

$$\sigma_0 = \sigma_\ell|_{\ell \rightarrow 0} . \quad (4.101)$$

The maximal debond stress, σ_d^* , is determined immediately before the load instability (Karbhari and Wilkins, 1990; Kim et al., 1991) of the partial debond stress, σ_d^p , when the debond length becomes $\ell = L - z_{\max}$:

$$\begin{aligned} \sigma_d^* &= \sigma_\ell + (\bar{\sigma} - \sigma_\ell) \frac{\omega \{ \exp[\lambda(L - z_{\max})] - 1 \}}{1 + \omega \{ \exp[\lambda(L - z_{\max})] - 1 \}} \\ &\approx \sigma_\ell + (\bar{\sigma} - \sigma_\ell) \{ 1 - \exp[-\lambda(L - z_{\max})] \} . \end{aligned} \quad (4.102)$$

Details of the instability conditions of the debond process and z_{\max} are discussed in Section 4.3.4. Further, the solution for the initial frictional pull-out stress, σ_{fr} , upon complete debonding is determined when the debond length, ℓ , reaches the embedded length, L , and the crack tip debond stress, σ_ℓ , is zero:

$$\sigma_{fr} = \bar{\sigma} \frac{\omega \{ \exp(\lambda L) - 1 \}}{1 + \omega \{ \exp(\lambda L) - 1 \}} \approx \bar{\sigma} [1 - \exp(-\lambda L)] . \quad (4.103)$$

In Eq. (4.103), it is assumed that the influence of the instantaneous fiber displacement relative to the matrix due to the sudden load drop after instability is negligible.

4.3.4. Instability of debond process

The instability condition requires that the derivative of the partial debond stress with respect to the remaining bond length ($z = L - \ell$) is equal to or less than zero, i.e., $d\sigma_d^p/dz \leq 0$ (Kim et al., 1991). Therefore, the fiber debond process becomes unstable if $(L - \ell)$ is smaller than a critical bond length, z_{\max} , where the slopes of the curves become zero in Figs. 4.23 and 4.24. At these bond lengths, the partial debond stress, σ_d^p , corresponds to the maximum debond stress, σ_d^* . The z_{\max} value is determined from Eq. (4.102) as

$$z_{\max} = L + \frac{1}{\lambda} \ln \left[\frac{\omega(\bar{\sigma} - \sigma_d^*)}{(\sigma_d^* - \sigma_\ell) + (\bar{\sigma} - \sigma_d^*)} \right] . \quad (4.104)$$

Numerical treatment of Eq. (4.104) gives z_{\max} values for the different composite systems as shown in Table 4.3. It is worth emphasizing that for the SiC fiber–glass matrix composites, z_{\max} values are very small relative to L_{\max} values, irrespective of the fiber surface treatments and when compared to other epoxy matrix based composites.

To show clearly how and to what extent the parameter, z_{\max} , varies with the properties of the interface and the composite constituents, a simple fiber pull-out model by Karbhari and Wilkins (1990) is chosen here. This model is developed based on the assumption of a constant friction shear stress, τ_{fr} , in the context of the shear strength criterion for interface debonding. In this model, the partial debond stress may be written as

$$\sigma_d^p = \sigma_0 + 2\tau_{fr} \left[\frac{L - z}{a} \right] , \quad (4.105)$$

where the frictionless debond stress, σ_0 , is given by

$$\sigma_0 = \frac{2(\alpha + \gamma)\tau_b}{a\alpha\beta_4} \tanh(\beta_4 z) . \quad (4.106)$$

Eq. (4.106) is essentially similar to the solution of the debond stress derived earlier by Takaku and Arridge (1973). The above instability condition for the partial debond stress of Eq. (4.105) gives a rather simple equation for z_{\max} as

$$z_{\max} = \frac{1}{\beta_4} \cosh^{-1} \sqrt{\frac{\tau_b}{\tau_{fr}} \left(1 + \frac{\gamma}{\alpha} \right)} \quad (4.107)$$

where β_4 is a complex function of α and γ , and is given by

$$\beta_4^2 = \frac{1 + \frac{\alpha}{\gamma}}{a^2(1 + \nu_m) \left[\left(\frac{b}{a} \right)^2 \ln \left(\frac{b}{a} \right) - \frac{1}{2\gamma} \right]} , \quad (4.108)$$

whose approximate solution for $b \gg a$ is identical to β_1 given in Eq. (4.3). Eq. (4.107) suggests that the ratio of the bond strength at the bonded region to that at the debonded region, τ_b/τ_r , and the Young's modulus ratio, $\alpha = E_m/E_f$, are key material properties that determine z_{\max} and thus control the stability of the debond process. It should be noted here that in the early work of Lawrence (1972), Laws et al. (1973) and later Gopalaratnam and Shah (1987) the maximum debond stress is found to be dependent on these properties. Eq. (4.107) has a limiting value $z_{\max} = 0$ when $\tau_b \approx \tau_r$ and $\gamma \approx 0$ in which the debond process becomes totally stable as in some ceramic matrix composites (e.g. SiC fiber-glass matrix composites (Butler et al., 1990)).

From the discussion presented above, it is clear that the stability of the debond process can be evaluated by a single parameter, z_{\max} , which is the shortest (remaining) bond length needed to maintain the debond process stable, and is a constant for a given composite system. Therefore, three different interface debond processes are identified in the following: totally unstable, partially stable and totally stable debond processes. The schematic plots of the applied stress versus displacement curves are illustrated in Fig. 4.25 for these debond processes.

(i) If $L \leq z_{\max}$, the debond process is totally unstable and the initial debond leads immediately to complete debonding (i.e. $\sigma_0 = \sigma_d^*$). Therefore, the corresponding stress-displacement curve shows a monotonic increase in stress until debonding is initiated, followed by an instantaneous load drop (Fig. 4.25(a)). Totally unstable debonding may also occur when the frictional resistance in the debonded region is negligible (i.e. either zero residual clamping stress, q_0 , or negligible coefficient of friction μ) such that z_{\max} approaches an infinite value as can be envisaged from Eq. (4.107). However, this situation seems most unlikely to occur in practical composites.

(ii) If $L > z_{\max}$, which is the most common case where practical fiber pull-out tests are performed, the stress increases linearly until debond initiates. Then, the debond crack propagates in a macroscopically stable manner, leading to a non-linear increase in the debond stress, though 'stick-slips' are normally observed in the rising stress-displacement curve (Fig. 4.25(b)). Stable debonding proceeds until the

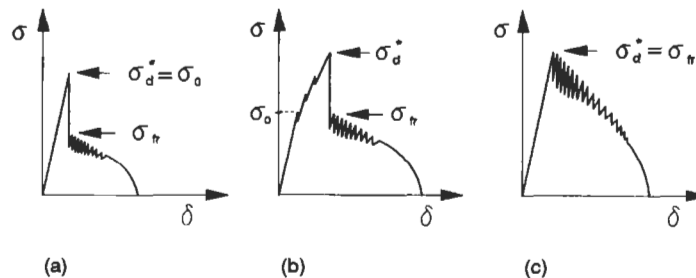


Fig. 4.25. Schematic presentations of applied stress versus displacement (σ - δ) relationship in fiber pull-out test: (a) totally unstable, (b) partially stable and (c) totally stable debond processes. After Kim et al. (1992).

debond length reaches $\ell = L - z_{\max}$, followed by unstable debonding leading to complete debonding. Therefore, this debond process is partially stable.

(iii) In the extreme case of z_{\max} value approaching zero, as in some ceramic matrix composites, the debond process is always stable until complete debonding independent of embedded fiber length, L . The rising portion of the debond stress versus displacement curve (Fig. 4.25(c)) is typically linear without apparent 'stick-slips' and there is no appreciable load drop after complete debonding (Bright et al., 1991). This is because the interface is in principle frictionally bonded and there is little chemical bonding. That is G_{ic} , or τ_b is very small. Therefore, the linear increase in stress represents primarily the frictional shear stress transfer across the interface without virtual debonding until the frictional resistance over the entire embedded fiber length is overcome. The maximum debond stress, σ_d^* , is then approximately equal to the initial frictional pull-out stress, σ_{fr} , because the frictionless debond stress, σ_f , is negligible (due to small G_{ic} or τ_b).

The concept of z_{\max} with regard to the issue of the stability of the debond process has practical implications for real composites reinforced with short fibers. There is a minimum fiber length required to maintain stable debonding and thus to achieve maximum benefits of crack-tip bridging between fracture surfaces without the danger of catastrophic failure. It should also be mentioned that in practical fiber pull-out experiments the stability for interface debonding deviates significantly from what has been discussed above, and is most often impaired by adverse testing conditions (e.g. soft testing machine, long free fiber length, etc.). Therefore, debonding could become unstable even for $L > z_{\max}$ and in composites with $z_{\max} \approx 0$. Moreover, when L is very short, as is the normal case in the microdebond test, the precipitous load drop after complete debonding may be aggravated by the release of the strain energy stored in the stretched fiber. The load drops to zero if the fiber is completely pulled out from the matrix. Alternatively, if the fiber is regripped by the clamping pressure exerted by the surrounding matrix material frictional pull-out of the fiber is possible to resume.

Another important parameter related to the fiber length in the fiber pull-out test is the maximum embedded fiber length, L_{\max} , above which the fiber breaks instead of being completely debonded or pulled out. L_{\max} value for a given composite system can be evaluated by equating σ_d^* of Eq. (4.102) to the fiber tensile strength, σ_{TS} , (which is measured on a gauge length identical to the embedded fiber length used in fiber pull-out test), i.e.,

$$L_{\max} = \frac{1}{\lambda} \ln \left[\frac{(\bar{\sigma} - \sigma_f) + \frac{1-\omega}{\omega} (\sigma_{TS} - \sigma_f)}{\bar{\sigma} - \sigma_{TS}} \right] + z_{\max} \quad , \quad (4.109)$$

where σ_f is the crack tip debond stress determined for bond length $z_{\max} = (L - \ell)$. L_{\max} values calculated for a constant fiber tensile strength $\sigma_{TS} = 4.8, 1.97$ and 2.3 GPa for carbon fiber, steel fiber and SiC fiber, respectively, are included in Table 4.3. These predictions are approximately the same as the experimental L_{\max} values, e.g., the predictions for $L_{\max} = 49.3$ and 23.4 mm compare with experimental values $L_{\max} = 51.0$ and 21.7 mm, respectively, for the untreated and acid treated SiC fibers

(Fig. 4.28). It is worth noting that the L_{\max} value decreases significantly when the fiber surface is treated to improve the interfacial bonding (and thus the interface fracture toughness, G_{ic}), e.g. acid treated SiC fibers versus untreated fibers. This observation is analogous to what is expected from the fiber fragmentation test of single fiber composites: the stronger the interface bond the shorter is the fiber fragment length at the critical stage (see Section 4.2).

4.3.5. Characterization of interface properties

Microcomposite tests including fiber pull-out tests are aimed at generating useful information regarding the interface quality in absolute terms, or at least in comparative terms between different composite systems. In this regard, theoretical models should provide a systematic means for data reduction to determine the relevant properties with reasonable accuracy from the experimental results. The data reduction scheme must not rely on the trial and error method. Although there are several methods of micromechanical analysis available, little attempt in the past has been put into providing such a means in a unified format. A systematic procedure is presented here to generate the fiber pull-out parameters and ultimately the relevant fiber–matrix interface properties.

In single fiber pull-out experiments, the most useful data that are readily obtained from the load–deflection records are the maximum debond stress, σ_d^* , and the initial frictional pull-out stress, σ_{fr} , as a function of L . If the debond process is carefully monitored for a large embedded fiber length, L , the initial debond stress, σ_0 , can also be determined directly in the average sense, depending on the composite system. Most important properties to be calculated are the fracture toughness, G_{ic} , at the bonded region, and the coefficient of friction, μ , and the residual clamping stress, q_0 , at the debonded region, by evaluating the pull-out parameters σ_ℓ , λ and σ . There are several steps to be followed for this purpose.

(i) Firstly, σ_{fr} versus L data allow the initial slope at $L = 0$ to be determined based on Eq. (4.103),

$$\left. \frac{d\sigma_{fr}}{dL} \right|_{(L=0)} = \lambda \bar{\sigma} = \frac{2\mu k}{a} \bar{\sigma} . \quad (4.110)$$

(ii) Secondly, the gradient can be taken from the linear region of the stress drop $\Delta\sigma (= \sigma_d^* - \sigma_{fr})$ versus L plots for large L where the crack tip debond stress is almost constant and independent of L , i.e.,

$$\frac{d \ln(\Delta\sigma)}{dL} \approx -\lambda , \quad (4.111)$$

where the difference between the stresses obtained immediately before and after the load instability is given by

$$\Delta\sigma = \sigma_d^* - \sigma_{fr} = \{ \sigma_\ell + \bar{\sigma} [\exp(-\lambda z_{\max}) - 1] \} \exp[-\lambda(L - z_{\max})] . \quad (4.112)$$

(iii) Thirdly, combining Eqs. (4.110) and (4.111) allows λ and $\bar{\sigma}$ (and thus μ and q_0 from Eqs. (4.23) and (4.24)) to be determined. Alternatively, the asymptotic debond stress, $\bar{\sigma}$, can be directly estimated at a long embedded length through linear regression analysis of the maximum debond stress, σ_d^* . Once λ and $\bar{\sigma}$ are known, Eq. (4.102) may be used to evaluate the optimum value of G_{ic} (and also for z_{max}) that would give the best fit to the σ_d^* versus L experimental results. In this procedure theoretical values for the maximum debond stress, σ_d^* , have to be obtained at instability. Alternatively, data for the initial debond stress, σ_0 , versus L , if available from experiments, can be directly evaluated to determine G_{ic} based on the debond criterion of Eq. (4.99) for infinitesimal debond length. Application of this procedure to obtain G_{ic} , μ and q_0 have been demonstrated in fiber pull-out for several fiber composites materials (Kim et al., 1992, Zhou et al., 1993).

Having determined the relevant interface properties (Table 4.3), the maximal debond stress, σ_d^* , and the initial frictional pull-out stress, σ_{fr} , are compared with experimental data in Figs. 4.26–4.28 for three different composite systems of carbon fiber–epoxy matrix, steel fiber–epoxy matrix and SiC fiber–glass matrix. In general, there is very good agreement between theories and experiments over the whole range of the embedded fiber length, L , for all the composite systems considered. A new methodology has also been proposed recently by Zhou et al. (1994) to determine systematically the longest embedded fiber length for instability, z_{max} , without iteration and curve fitting of Eq. (4.102).

4.3.6. *Multiple fiber composite model*

From the review of the theoretical studies of the fiber pull-out test as discussed in Section 4.3.1, it is identified that most micromechanics theories are developed based on a shear-lag model of single fiber composites where the cylindrical surface of the matrix is invariably assumed to be stress free. Although this assumption is required to obtain the final solutions in closed form for the stress distributions it often leads to an unacceptably high applied stress required to initiate/propagate interface debonding when the radial dimension of the matrix is similar to that of the fiber (i.e. for a high fiber volume fraction, V_f). This in turn implies that the application of the conventional models to practical composites is limited to those with a very small V_f where any effects of interactions between neighboring fibers are completely neglected. Therefore, a three-cylinder composite model is developed (Kim et al., 1994b) to simulate the response of practical composites of large V_f and thus to accommodate the limitation of the shear-lag model of single fiber microcomposite test properly. Both the micromechanics analysis and the FE method are employed in parallel for fully bonded interface to validate the results obtained from each model.

To analyze the stress transfer in the fiber pull-out test of a multiple fiber composite, the specimen is treated as a three-cylinder composite (Zhou and Mai, 1992) where a fiber is located at the center of a coaxial shell of the matrix, which, in turn, is surrounded by a trans-isotropic composite medium with an outer radius B ,

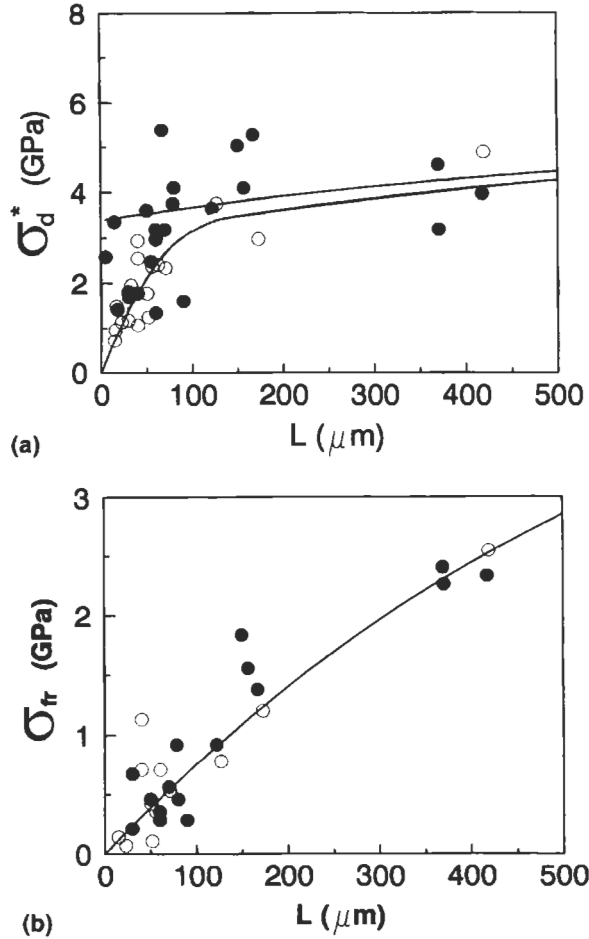


Fig. 4.26. Comparisons between experiments and theory of (a) maximum debond stress, σ_d^* , and (b) initial frictional pull-out stress for carbon fiber-epoxy matrix composites. After Kim et al. (1992).

as schematically illustrated in Fig. 4.29. The radii of the fiber and matrix, a and b , are related to the fiber volume fraction $V_f = a^2/b^2$, which is the same as that of the composite medium. When the fiber is subjected to an external stress, σ , at the loaded end ($z = 0$) while the matrix and composite medium are fixed at the embedded end ($z = L$), stress transfers from the fiber to the matrix and in turn from the matrix to the composite medium via the IFSSs, $\tau_i(a, z)$ and $\tau_i(b, z)$, respectively. For the cylindrical coordinates of the three-cylinder composite, the basic governing equations are essentially the same as those for the single fiber composite. However, the equilibrium equations between the external and the internal stresses have to be modified to take into account the presence of the composite medium. Eq. (4.87) is now replaced by:

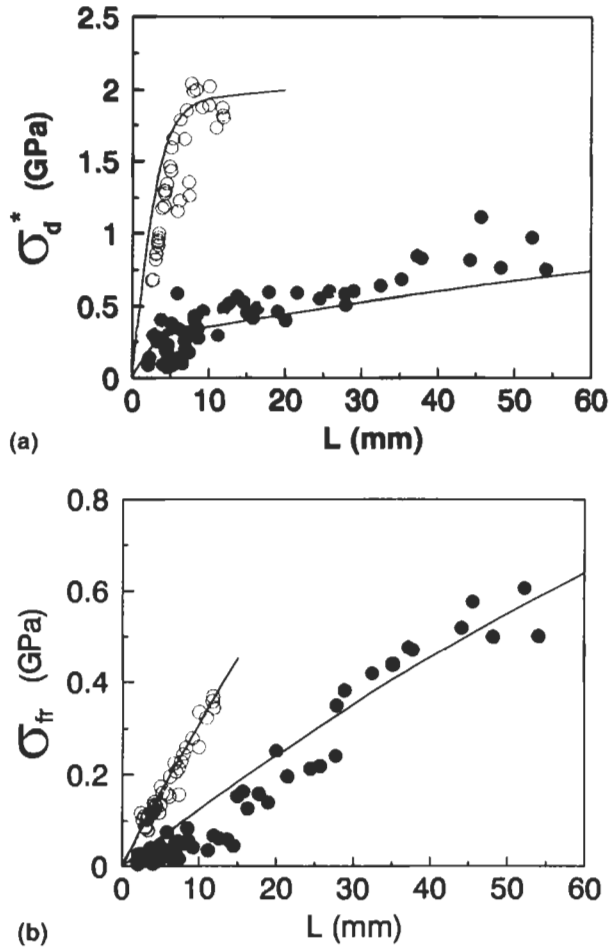


Fig. 4.27. Comparisons between experiments and theory of (a) maximum debond stress, σ_d^* , and (b) initial frictional pull-out stress for steel fiber-epoxy matrix composites: (O) uncoated fibers; (●) release agent coated fibers. After Kim et al. (1992).

$$\sigma = \sigma_f^z(z) + \frac{1}{\gamma} \sigma_m^z(z) + \frac{1}{V_f \gamma_1} \sigma_c^z(z) , \quad (4.113)$$

$$\sigma - \frac{2b}{a^2} \int_0^z \tau_b(z) dz = \sigma_f^z(z) + \frac{1}{\gamma} \sigma_m^z(z) , \quad (4.114)$$

where $\gamma_1 = b^2/(B^2 - b^2)$, and B is the outer radius of the composite medium. The subscript c refers to the composite medium. In addition to Eq. (4.12) for the relationship between FAS and IFSS, equilibrium between IFSSs and MAS requires

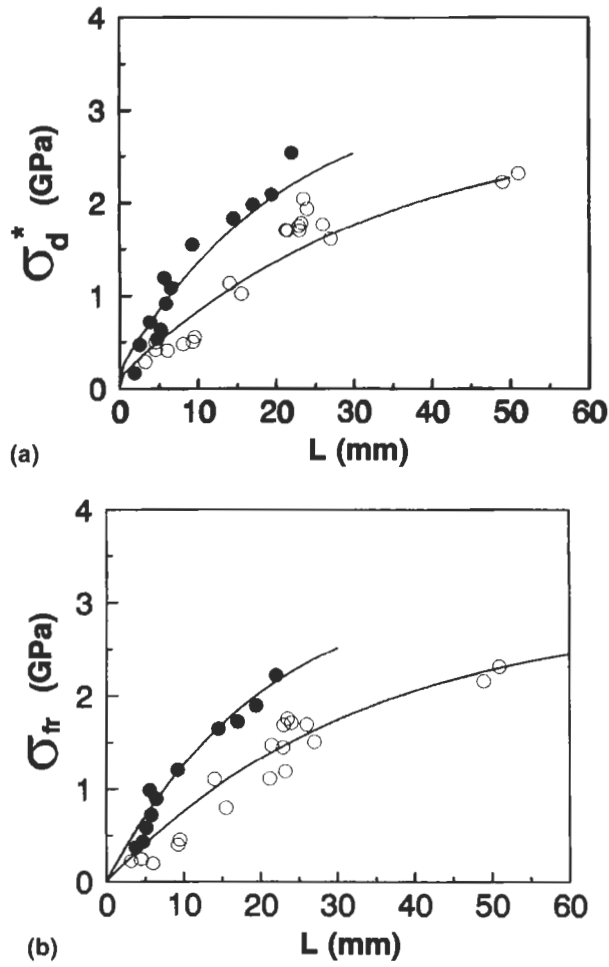


Fig. 4.28. Comparisons between experiments and theory of (a) maximum debond stress, σ_d^* , and (b) initial frictional pull-out stress for SiC fiber-glass matrix composites: (○) untreated fibers; (●) acid treated fibers. After Kim et al. (1992).

$$\frac{d\sigma_m^z(z)}{dz} = \frac{2}{a^2\gamma} [a\tau_i(a, z) - b\tau_i(b, z)] \quad (4.115)$$

Based on Lamé's solution, the relationship between the IFSSs is taken as

$$\tau_i(b, z) = \frac{b\gamma_2}{a\gamma_1} \tau_i(a, z) \quad (4.116)$$

where $\gamma_2 = a^2/(B^2 - a^2)$. The additional radial stress, $q_2(a, z)$, acting at the fiber-matrix interface, which is caused by Poisson contraction of the fiber when subjected

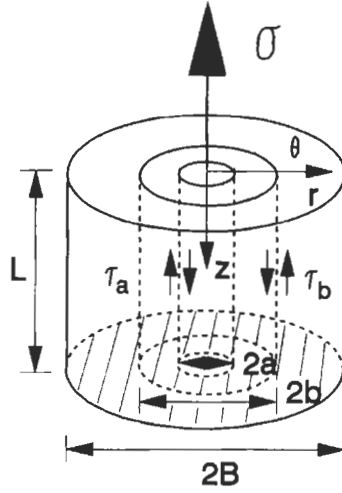


Fig. 4.29. Schematic illustration of fiber pull-out test on a three cylinder composite. After Kim et al. (1994b).

to an axial tension, is obtained from the continuity of tangential strain at the interface

$$q_2(a, z) = \frac{-\alpha v_f V_f k_1 \sigma_f^z(z) + [v_m V_f k_1 - 2\gamma(v_m - \alpha v_c)] \sigma_m^z(z)}{V_f k_1 [\alpha(1 - v_f) + 1 + v_m + 2\gamma] - 4\gamma^2} , \quad (4.117)$$

where $\alpha_1 = E_m/E_c$ and $k_1 = 1 + 2\gamma - v_m + \alpha_1(1 + 2\gamma_1 + v_c)$. Eq. (4.117) replaces $q_1(a, z)$ given by Eq. (4.18) applied for the single fiber composite model. Combining Eqs. (4.12) and (4.113) to (4.117) yields a differential equation for the FAS

$$\frac{d^2 \sigma_f^z(z)}{dz^2} - A_3 \sigma_f^z(z) = A_4 \sigma . \quad (4.118)$$

The coefficients A_3 and A_4 are complex functions of the elastic properties and geometric factors of the constituents and are given in Appendix D. The solution for Eq. (4.118) is subjected to the following boundary conditions assuming an unbonded cross-section of the embedded fiber end

$$\sigma_f^z(0) = \sigma, \quad \sigma_f^z(L) = 0 . \quad (4.119)$$

Therefore, the solutions for the FAS, MAS, MSS and IFSSs normalized with the applied stress σ , are obtained:

$$\frac{\sigma_f^z(z)}{\sigma} = \frac{\left(\frac{A_4}{A_3} + 1\right) \sinh[\sqrt{A_3}(L - z)] + \frac{A_4}{A_3} \sinh(\sqrt{A_3}z)}{\sinh(\sqrt{A_3}L)} - \frac{A_4}{A_3} , \quad (120)$$

$$\frac{\sigma_m^z(z)}{\sigma} = \gamma_2 \left(1 + \frac{A_4}{A_3} \right) - \gamma_2 \frac{\left(\frac{A_4}{A_3} + 1 \right) \sinh[\sqrt{A_3}(L-z)] + \frac{A_4}{A_3} \sinh(\sqrt{A_3}z)}{\sinh(\sqrt{A_3}L)}, \quad (121)$$

$$\frac{\tau_1(a,z)}{\sigma} = \frac{a\sqrt{A_3} \left(\frac{A_4}{A_3} + 1 \right) \cosh[\sqrt{A_3}(L-z)] - \frac{A_4}{A_3} \cosh(\sqrt{A_3}z)}{2 \sinh(\sqrt{A_3}L)}, \quad (122)$$

$$\frac{\tau_1(b,z)}{\sigma} = \frac{b\gamma_2\sqrt{A_3} \left(\frac{A_4}{A_3} + 1 \right) \cosh[\sqrt{A_3}(L-z)] - \frac{A_4}{A_3} \cosh(\sqrt{A_3}z)}{2\gamma_1 \sinh(\sqrt{A_3}L)}. \quad (123)$$

Finite element analysis (FEA) is also developed in parallel to validate the results generated from the micromechanical model. Both the composites containing single and multiple fibers are considered for the present FEA. The geometry, the loading method and the boundary conditions are selected to represent those of the actual experimental technique for both the single and multiple fiber composites, as illustrated in Fig. 4.30, which are analogous to those used in the corresponding micromechanics analyses. For the axi-symmetric loading geometry of a two dimensional model, a uniformly distributed constant stress, $\sigma = 100$ MPa, is applied to the partially embedded fiber at the surface ($z = 0$). The boundary conditions are imposed such that the bottom surfaces of the matrix and composite medium are fixed at $z = 2L$, and the axis of symmetry ($r = 0$) is fixed where there is no displacement taking place.

Specific results are calculated for SiC fiber–glass matrix composites with the elastic constants given in Table 4.1. A constant embedded fiber length $L = 2.0$ mm, and constant radii $a = 0.2$ mm and $B = 2.0$ mm are considered with varying matrix radius b . The stress distributions along the axial direction shown in Fig. 4.31 are predicted based on micromechanics analysis, which are essentially similar to those obtained by FE analysis for the two extremes of fiber volume fraction, V_f , shown in Fig. 4.32. The corresponding FAS distribution calculated based on Eqs. (4.90) and (4.120), and IFSS at the fiber–matrix interface of Eqs. (4.93) and (4.132) are plotted along the axial direction in Fig. 4.32.

The three-cylinder composite model predicts that both the FAS and IFSS decrease from a maximum near the loaded fiber end towards zero at the embedded fiber end. Increase in V_f (and the equivalent improvement of stiffness in the composite medium) increases slightly both the maximum IFSS and the stress gradient, without changing the general trend of the stress fields. For small V_f , stress distributions in the single fiber composite model are equivalent to those of the three-cylinder model. In sharp contrast, the stress fields change drastically in the single fiber composite model when V_f is large. The FAS values in the central portion of the fiber are approximately constant and do not diminish to zero at the embedded fiber end. More importantly, the IFSS displays two peaks at the ends of the fiber, the one at the embedded end being increasingly greater than the other at the loaded end with

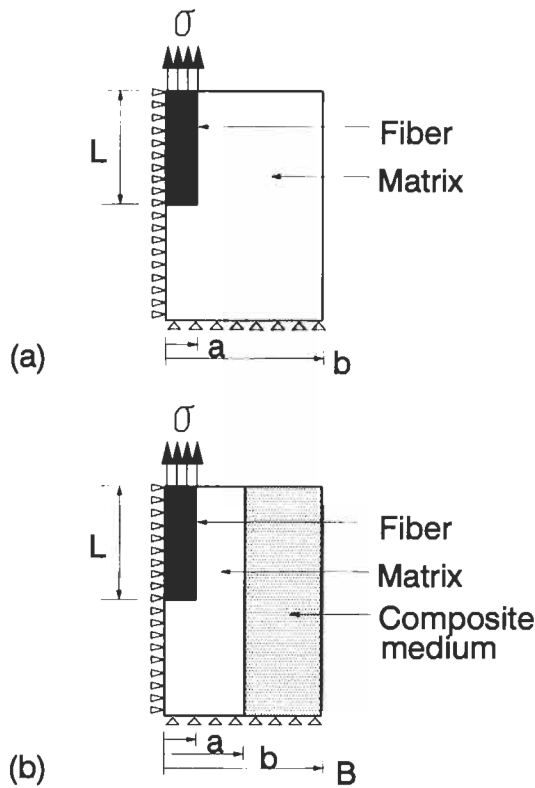


Fig. 4.30. Schematic illustrations of the finite element models of (a) single fiber pull-out specimen and (b) a three cylinder composite. After Kim et al. (1994b).

increasing V_f . It is also interesting to note that the single fiber composite model predicts that the IFSS obtained at the loaded end remains almost constant regardless of V_f .

The pronounced effect of fiber V_f is further manifested in Figs. 4.33 and 4.34, where the characteristic IFSS values obtained at the ends of the fiber are plotted as a function of V_f for the micromechanics and FE analyses, respectively. It is clearly demonstrated for the three-cylinder model that these stresses vary only marginally with V_f , and the magnitude of IFSS at the loaded end is always greater than that at the embedded fiber end. This ensures that when the fiber is loaded continuously, debonding is always expected to initiate at the loaded fiber end for all V_f , if the shear strength criterion is employed for the interface debonding. However, for the single fiber composite model, IFSS at the embedded fiber end increases rapidly whereas that obtained at the loaded fiber end either remains almost constant (Fig. 4.33) or decreases with increasing V_f (Fig. 4.34). Therefore, there is a critical fiber volume fraction above which the maximum IFSS at the embedded end exceeds that of the loaded end, allowing debond initiation from the embedded fiber end in preference to

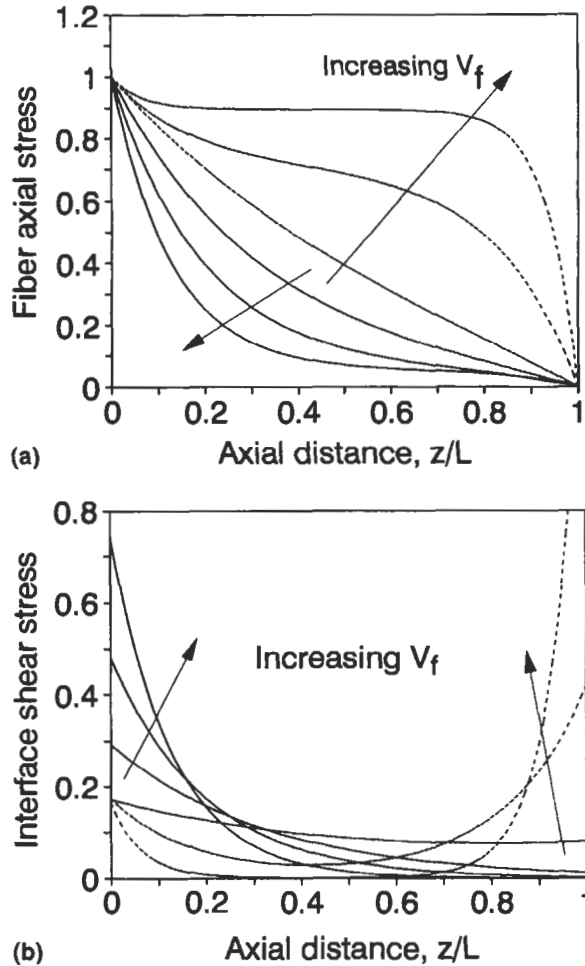


Fig. 4.31. Distributions of (a) fiber axial stress and (b) interface shear stress along the axial direction obtained from micromechanics analysis for different fiber volume fractions, $V_f = 0.03, 0.3$ and 0.6 : (---) single fiber composite; (—) three cylinder composite model. After Kim et al. (1994b).

the loaded fiber end. The critical fiber volume fractions $V_f \approx 0.15$ and 0.26 are estimated from the superimposed curves of the data points in Figs. 4.33 and 4.34, respectively.

One of the major differences between the results obtained from the micromechanics and FE analyses is the relative magnitude of the stress concentrations. In particular, the maximum IFSS values at the loaded and embedded fiber ends tend to be higher for the micromechanics analysis than for the FEA for a large V_f . This gives a slightly lower critical V_f required for the transition of debond initiation in the micromechanics model than in the FE model of single fiber composites. All these

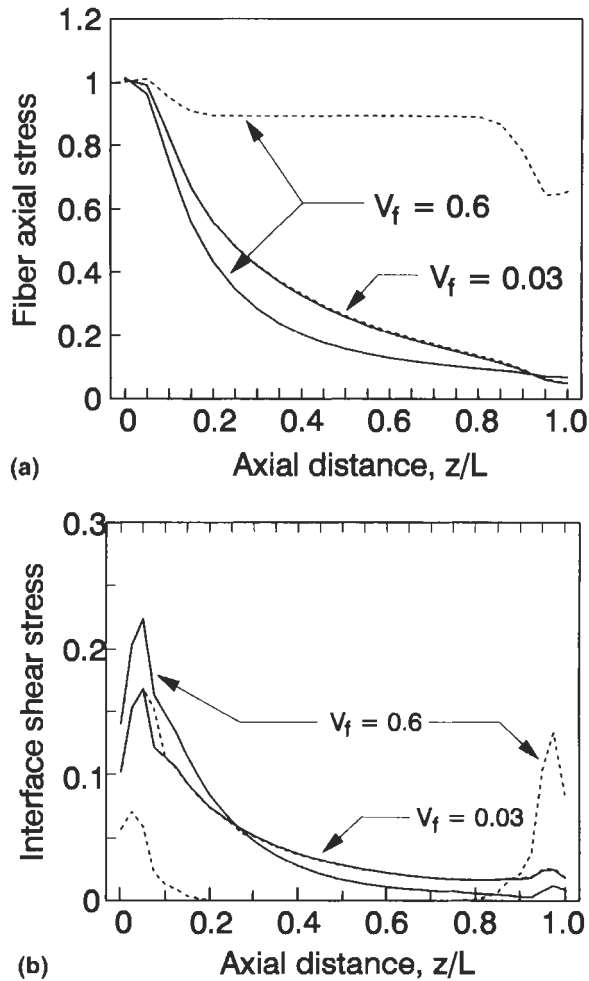


Fig. 4.32. Distributions of (a) fiber axial stress and (b) interface shear stress along the axial direction obtained from FEM calculations for two fiber volume fraction, $V_f = 0.03$ and 0.6. Symbols as in Fig. 4.31. After Kim et al. (1994b).

observations appear to be associated with the slightly different boundary conditions used in these models.

4.3.7. Two-way debonding phenomenon

In the light of the discussion presented in Section 4.3.6, it is seen that the surrounding composite medium in the three-cylinder composite model acts as a stiff annulus to suppress the development of IFSS at the embedded fiber end by constraining the radial boundary of the matrix cylinder. This ensures that regardless

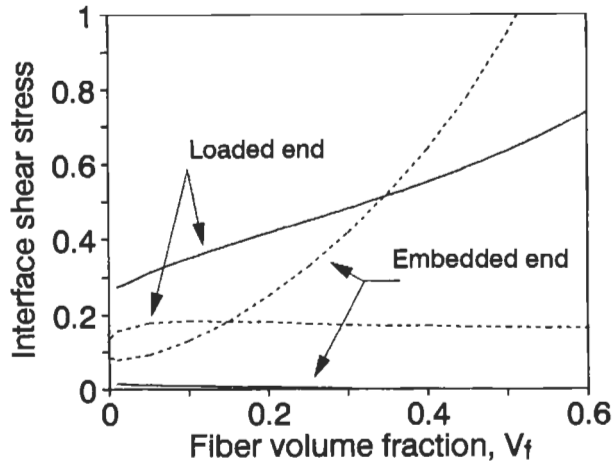


Fig. 4.33. Interface shear stresses as a function of fiber volume fraction, V_f , obtained from micromechanics analysis. Symbols as in Fig. 4.31. After Kim et al. (1994b).

of V_f the maximal IFSS always occurs at the loaded fiber end where the interface debond initiates and grows inward. The maximum IFSS tends to increase slightly with increasing V_f , allowing debond initiation at a low external stress.

In contrast, the single fiber composite model predicts that the IFSS concentration becomes higher at the embedded end than at the loaded end if fiber V_f is greater than a critical value, suggesting the possibility of debond initiation at the embedded fiber

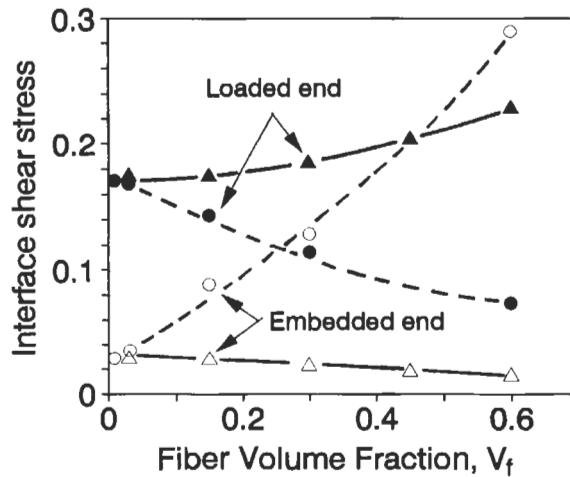


Fig. 4.34. Maximum interface shear stresses obtained at loaded and embedded fiber ends from FEM calculations which are plotted as a function of fiber volume fraction, V_f . (---) single fiber composite; (—) three cylinder composite model. After Kim et al. (1994b).

end in a so-called 'two-way debonding' phenomenon. This phenomenon, peculiar to the single fiber composite model as introduced in Section 4.3.1, has been studied theoretically (Banbaji, 1988; Leung and Li, 1991, Hsueh, 1993; Hsueh and Becher, 1993) as well as experimentally for a relatively stiff fiber embedded in a soft matrix (e.g. polyurethane matrix (Betz, 1982) and silicone resin (Gent and Liu, 1991) reinforced with glass rods), which can satisfy the criterion given by Eq. (4.124).

The criterion for debond initiation at the embedded end in preference to the loaded end is derived based on the shear strength criterion (i.e. $\tau_i(a, 0) < \tau_i(a, L)$ in Eq. (4.93))

$$\gamma > \alpha \frac{1 - 2k\nu_f}{1 - 2k\nu_m} \quad (4.124)$$

Eq. (4.124) is essentially the same as those previously developed based on the shear strength criterion (Leung and Li, 1991; Hsueh, 1993), and is found independent of embedded fiber length, L , and insensitive to both ν_f and ν_m . This means that the relative magnitudes of fiber volume ratio, $\gamma (= a^2/(b^2 - a^2))$, and Young's modulus ratio, $\alpha (= E_m/E_f)$, control the two-way debonding phenomenon in a single fiber pull-out test. A plot of γ as a function of α based on Eq. (4.124) is shown in Fig. 4.35 where a comparison is made with the predictions by Leung and Li (1991) and Hsueh (1993).

The results presented in Section 4.3.6 suggest that the shear lag models based on a single fiber composite is inadequate for modelling a composite with a high fiber V_f . From the experimental viewpoint, to measure the relevant fiber-matrix interface properties, the fiber volume fraction in single fiber pull-out tests is always very low (i.e. $V_f < 0.01$). This effectively means that testing with these specimens has the

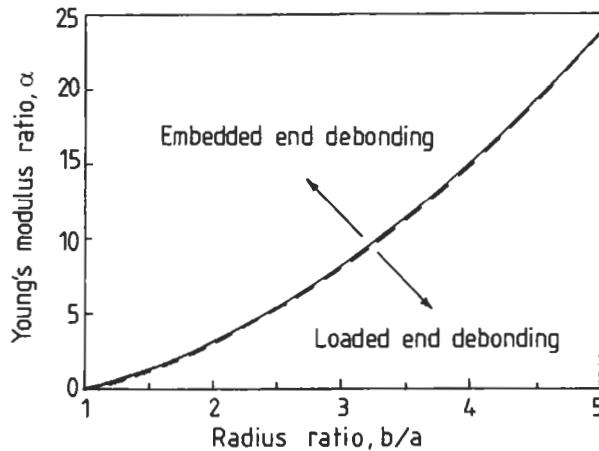


Fig. 4.35. The relationship between Young's modulus ratio, E_f/E_m , and radius ratio, b/a , showing the criterion for debonding initiation at embedded fiber end or loaded fiber end.

fundamental limitation of generating interface properties only valid in the comparative sense for given conditions that seldom represent those of practical composites of large fiber V_f . In this regard, the use of multiple fiber composite specimens (made from real composites or from model composites with a regular fiber arrangement for the surrounding composite medium) can eliminate such a limitation of the single fiber pull-out test. Details of the experimental technique have yet to be developed although significant difficulties are envisaged in specimen preparation with the current technology. In fact, the micro-bundle pull-out test has recently been devised (Qiu and Schwartz, 1991), although still in its early stage of development, to account for the high fiber volume fraction of real composites.

4.4. Fiber push-out

4.4.1. Solutions for stress distributions

Many investigators have studied the micromechanics analyses of fiber push-out, notably Bright et al. (1989, 1991), Hsueh (1990b, c), Keran and Parthasarathy (1991), Lau and Mai (1990, 1991), Marshall (1992), Marshall and Oliver (1987, 1990), Shetty (1988), Singh and Sutcu (1991), Liang and Hutchinson (1993), and more recently Zhou and Mai (1995). Among these, Keran and Parthasarathy (1991), Marshall (1992) and Liang and Hutchinson (1993) took into account the effects of the axial residual stresses in the fiber in addition to the residual radial stresses across the interface, both of which are caused by the matrix shrinkage during the processing of the composite. The influence of redistribution of residual stress due to slicing the composite in preparation of the specimen (Liang and Hutchinson, 1993) is also specifically addressed. The effects of fiber surface roughness on push-out have also been analysed by Liu et al. (1995). Numerical analysis based on the finite element method (Grande et al., 1988; Tsai et al., 1990; Chen and Young, 1991; Kallas, 1992; Meda et al., 1993; Mital et al., 1993; Ananth and Chandra, 1995; Chandra and Ananth, 1995; Majumda and Miracle, 1996; Ho and Drzal, 1996) is also becoming increasingly popular with this loading geometry. Similar to the microbundle pull-out test a fiber bundle push-out test has also been proposed for CMCs and a theoretical analysis has been given recently by Zhou and Mai (1994).

However, some theoretical treatment considers only the special case of friction sliding of a single fiber along a mechanically bonded interface, particularly for some ceramic matrix composites, where the Coulomb friction law applies. See for example Zhou and Mai (1995) and Shetty (1988). Assuming a constant friction at the fiber–matrix interface and neglecting the Poisson effects, Shetty (1988) reported a simple force balance equation for the frictional shear strength, τ_{fr}

$$\tau_{fr} = -\mu q_0 \quad (4.125)$$

q_0 is determined from the data for the maximal frictional push-out stress, σ_{fr} , when the sliding length reaches the entire embedded fiber length (i.e. $\ell = L$). σ_{fr} is given by

$$\sigma_{fr} = \frac{q_0}{k_5} \left[\exp\left(\frac{2\mu k_5 L}{a}\right) - 1 \right], \quad (4.126)$$

where $k_5 = \alpha_f \nu_f / (1 + \nu_m)$, which is an approximate form of the coefficient k given in Section 4.2.3.

There are many features in the analysis of the fiber push-out test which are similar to fiber pull-out. Typically, the conditions for interfacial debonding are formulated based on the two distinct approaches, i.e., the shear strength criterion and the fracture mechanics approach. The fiber push-out test can be analyzed in exactly the same way as the fiber pull-out test using the shear lag model with some modifications. These include the change in the sign of the IFSS and the increase in the interfacial radial stress, $q_1(a, z)$, which is positive in fiber push-out due to expansion of the fiber. These modifications are required as a result of the change in the direction of the external stress from tension in fiber pull-out to compression in fiber push-out.

For the cylindrical coordinates of the fiber push-out model shown in Fig. 4.36 where the external (compressive) stress is conveniently regarded as positive, the basic governing equations and the equilibrium equations are essentially the same as the fiber pull-out test. The only exceptions are the equilibrium condition of Eq. (4.15) and the relation between the IFSS and the resultant interfacial radial stress given by Eq. (4.29), which are now replaced by:

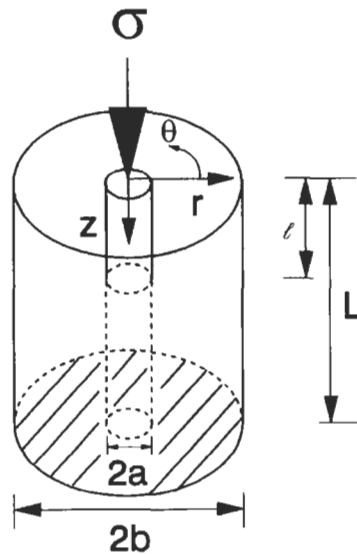


Fig. 4.36. Schematic drawing of the partially debonded fiber in fiber push-out test.

$$\frac{d\sigma_f^z(z)}{dz} = -\frac{2}{a}\tau_i(a, z) , \quad (4.127)$$

$$\tau_i(a, z) = -\mu[q_0 - q_1(a, z)] . \quad (4.128)$$

In the same procedure as that employed for the fiber pull-out test, the solutions for stress distributions are obtained in the bonded region, which are exactly the same as those given in Eqs. (4.90)–(4.92). The solutions for the stress distributions in the debonded regions are:

$$\sigma_f^z(z) = \sigma - \omega(\bar{\sigma} + \sigma)[1 - \exp(-\lambda z)] , \quad (4.129)$$

$$\sigma_m^z(z) = \gamma\omega(\bar{\sigma} + \sigma)[1 - \exp(-\lambda z)] , \quad (4.130)$$

$$\tau_m(r, z) = \frac{\gamma\lambda\omega(b^2 - r^2)}{2r}(\bar{\sigma} + \sigma)\exp(-\lambda z) , \quad (4.131)$$

$$\tau_i(a, z) = \frac{a\lambda\omega}{2}(\bar{\sigma} + \sigma)\exp(-\lambda z) . \quad (4.132)$$

In these equations, the crack tip debond stress, σ_ℓ , at the boundary between the bonded and debonded regions is given by

$$\sigma_\ell = \sigma - \omega(\bar{\sigma} + \sigma)[1 - \exp(-\lambda\ell)] . \quad (4.133)$$

Fig. 4.37 illustrates the approximate stress fields in the composite constituents along the axial direction which are generally very much similar to those of the fiber pull-out test (Fig. 4.22), except for the IFSS in the debonded region. The rising portion of the IFSS towards the free fiber end reflects the radial expansion of the fiber under compression due to the Poisson effect. The increase in the radial compressive stress discourages debond propagation in fiber push-out. This response is in sharp contrast to the radial contraction of the fiber which effectively encourages further debonding in fiber pull-out test. More details of the differences in the stress distributions and the debond processes between the two loading geometries are discussed in Section 4.5.3.

4.4.2. Debond criterion and debond stresses

Based on the same energy balance theory as employed for the fiber pull-out, a fiber–matrix interface debond criterion is derived for fiber push-out in a form similar to that for fiber pull-out

$$2\pi a G_{ic} = B_2\sigma^2 - C_2(\bar{\sigma} + \sigma)\sigma + D_2(\bar{\sigma} + \sigma)^2 , \quad (4.134)$$

where the coefficients B_2 , C_2 and D_2 are related to B_1 , C_1 and D_1 (see Appendix A) by changing the sign for μ (or λ) due to the change in the direction of loading:

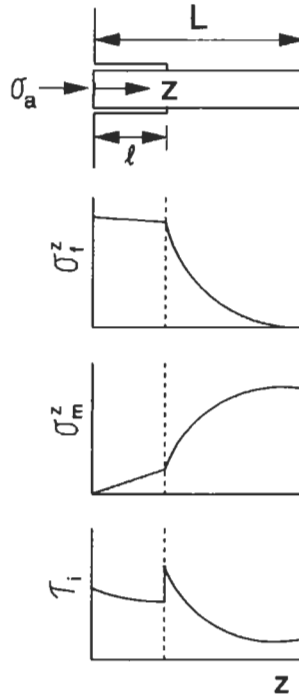


Fig. 4.37. Distributions of (a) fiber axial stress, σ_f^z , (b) matrix axial stress, σ_m^z , and (c) interface shear stress, τ_i , along the embedded fiber length in fiber push-out. After Kim et al. (1994c).

$$B_2 = B_1]_{\mu=-\mu}, \quad C_2 = C_1]_{\mu=-\mu}, \quad D_2 = D_1]_{\mu=-\mu}. \quad (4.135)$$

Therefore, once the external stress for debond propagation is obtained, the partial debond stress, σ_d^p , can be determined as

$$\begin{aligned} \sigma_d^p &= \sigma_\ell + (\bar{\sigma} + \sigma_\ell) \frac{\omega[1 - \exp(-\lambda\ell)]}{1 - \omega[1 - \exp(-\lambda\ell)]} \\ &\approx \sigma_\ell + (\bar{\sigma} + \sigma_\ell)[\exp(\lambda\ell) - 1]. \end{aligned} \quad (4.136)$$

Similarly, the initial debond stress, σ_0 , is obtained for the infinitesimal debond length, the maximum debond stress, σ_d^* , at the instability where the debond length becomes $\ell = L - z_{\max}$ and the post-debond initial friction pull-out stress, σ_{fr} , at $\ell = L$:

$$\begin{aligned} \sigma_d^* &= \sigma_\ell + (\bar{\sigma} + \sigma_\ell) \frac{\omega\{1 - \exp[-\lambda(L - z_{\max})]\}}{1 - \omega\{1 - \exp[-\lambda(L - z_{\max})]\}} \\ &\approx \sigma_\ell + (\bar{\sigma} + \sigma_\ell)\{\exp[\lambda(L - z_{\max})] - 1\}, \end{aligned} \quad (4.137)$$

$$\begin{aligned}\sigma_{fr} &= \bar{\sigma} \frac{\omega[1 - \exp(-\lambda L)]}{1 - \omega[1 - \exp(-\lambda L)]} \\ &\approx \bar{\sigma}[\exp(\lambda L) - 1] .\end{aligned}\quad (4.138)$$

One can easily note that Eq. (4.138) is similar to the solution given by Eq. (4.126), which is derived from the assumption of a constant friction and complete neglect of the Poisson expansion. The solution for z_{\max} , which is the shortest bond length required to maintain a stable debonding process, is obtained from Eq. (4.137)

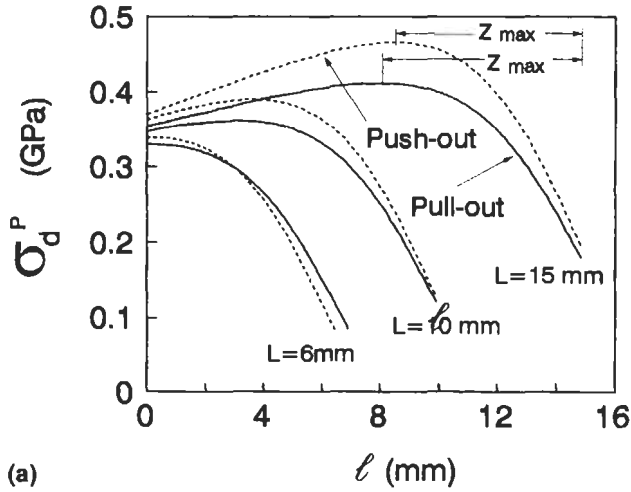
$$z_{\max} = L + \frac{1}{\lambda} \ln \left[\frac{\omega(\bar{\sigma} + \sigma_d^*) - (\sigma_d^* - \sigma_\ell)}{\omega(\bar{\sigma} + \sigma_d^*)} \right] . \quad (4.139)$$

4.4.3. Comparisons between fiber pull-out and fiber push-out

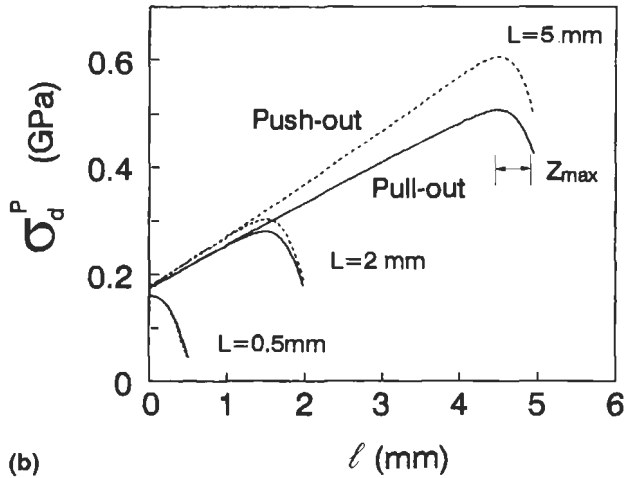
When comparing with the solution given in Eq. (4.100) for partial debond stress in fiber pull-out, it is noted that Eq. (4.133) is similar in that it is composed of two stress components: a crack tip debond stress, σ_ℓ , which is a function of the interfacial fracture toughness, G_{ic} , and the debond length, ℓ , relative to L ; a friction stress component which is proportional to $(\bar{\sigma} + \sigma_\ell)$ and is controlled by λ . There are also differences between fiber pull-out and fiber push-out particularly in the magnitude of debond stresses. To illustrate these functional similarities and differences in the failure processes between the two loading geometry, specific results are calculated (Zhou et al., 1992b) for the composite systems studied in the previous sections. From the plots of partial debond stress, σ_d^p , as a function of debond length, ℓ , as shown in Fig. 4.38, the rate of stress increase (or decrease) is found to be slightly larger in fiber push-out than in fiber pull-out, although the functional relationship between σ_d^p and ℓ is basically similar for a given embedded fiber length, L . Therefore, for a given L , larger stresses σ_0 and σ_d^* are required for debond crack initiation and propagation in fiber push-out than in fiber pull-out as shown in Fig. 4.39.

All these results are apparently associated with the difference in the friction stress component in the debonded region. In fiber push-out, the Poisson expansion of the fiber under axial compression generates radial compressive stresses across the interface, while the fiber is contracted radially in fiber pull-out. These stresses balance the existing residual clamping stress, q_0 , controlling further debond propagation. This conclusion is further manifested in Fig. 4.40 where the difference in IFSS distribution is clearly illustrated, in the debonded region in particular, between the two loading geometry.

To evaluate the stability of the debond process, the instability parameter, z_{\max} , is compared. z_{\max} values calculated based on Eqs. (4.104) and (4.139) respectively for fiber pull-out and fiber push-out give $z_{\max} = 6.5, 6.2$ mm for coated steel wire-epoxy matrix and $z_{\max} = 0.5, 0.49$ mm for the untreated SiC-fiber-glass matrix composite



(a)



(b)

Fig. 4.38. Comparisons of partial debond stress, σ_d^p , between fiber pull-out and fiber push-out as a function of debond length, ℓ , for (a) release agent coated steel fiber-epoxy matrix composites and (b) untreated SiC fiber-glass matrix composites. After Kim et al. (1994c).

systems. z_{\max} is only marginally greater for fiber pull-out than fiber push-out, the difference being almost negligible for the latter composite, which is typical of frictional bonding at the interface. Considering the observation that z_{\max} is determined mainly by the material properties such as τ_b/τ_{fr} and E_m/E_f , this result confirms that the differences in the debond stresses between the two loading geometry arise mainly from the Poisson effects at the debonded interface, which are distinct in each loading.

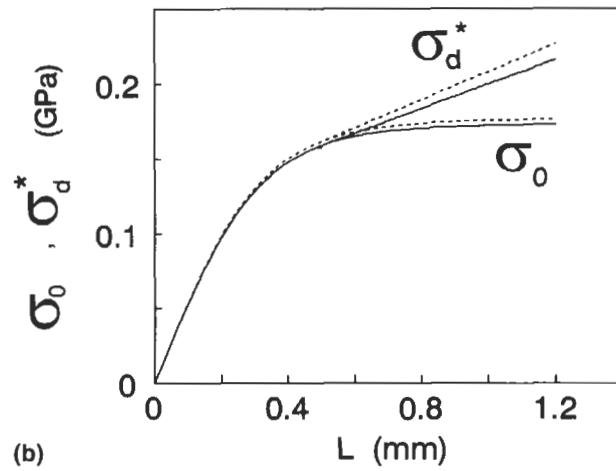
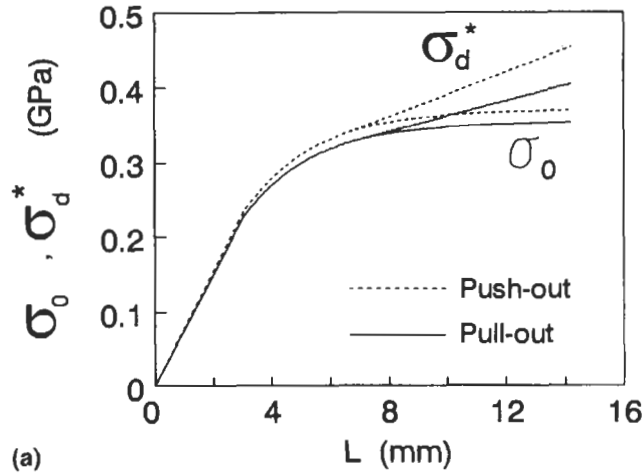


Fig. 4.39. Comparisons of initial debond stress, σ_0 , and maximum debond stress, σ_d^* , between fiber pull-out and fiber push-out as a function of embedded fiber length, L , for (a) release agent coated steel fiber-epoxy matrix composites and (b) untreated SiC fiber-glass matrix composites. After Kim et al. (1994c).

4.5. Cyclic loading in fiber pull-out and fiber push-out

4.5.1. Introduction

The analytical solutions derived in Sections 4.3 and 4.4 for the stress distributions in the monotonic fiber pull-out and fiber push-out loadings are further extended to cyclic loading (Zhou et al., 1993) and the progressive damage processes of the interface are characterized. It is assumed that the cyclic fatigue of uniform stress amplitude causes the frictional properties at the debonded interface to degrade

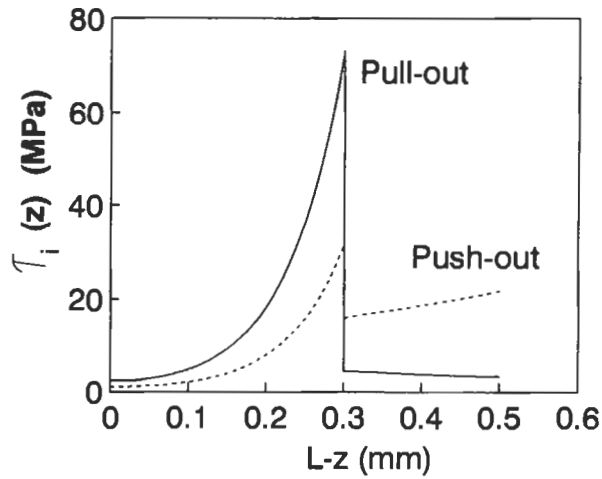


Fig. 4.40. Distributions of interface shear stress, τ_i , along the fiber length at a constant applied stress $\sigma = 4.0$ GPa for carbon fiber–epoxy matrix composites in fiber pull-out and fiber push-out. After Kim et al. (1994c).

gradually through wearing out or smoothing of the fiber surface roughness due to abrasions under repeated loading and unloading. Experimental evidence on some ceramic matrix composites containing SCS-6 SiC fibers (Jero and Keran, 1990; Jero et al., 1991; Carter et al., 1991; Waren et al., 1992; Mackin et al., 1992a) and sapphire fibers (Mackin et al., 1992b) has shown that the roughness interaction contributes significantly to the interfacial clamping stress, as mentioned in Section 4.3.1. Frictional resistance is reduced when a fiber predisplaced in pull-out (or in push-out), is then forced back to its original position, due probably to the fiber re-seating in the matrix socket where the fiber surface roughness matches that of the matrix. Mode I fatigue tests on a meta-stable β -titanium alloy reinforced with unidirectional SCS-6 SiC fibers also strongly indicate that degradation of the interface properties allows large debonding and sliding.

Fatigue tests can be conducted on the same single fiber–matrix cylinder model as used for monotonic pull-out and push-out tests. A simple alternating tensile (or compressive) stress of magnitude $\Delta\sigma$ ($= \sigma_{\max} - \sigma_{\min}$ where $\sigma_{\min} = 0$) is applied repeatedly to the fiber for each loading geometry, as schematically shown in Fig. 4.41. It is assumed here that the smoothed fiber surface due to repeated abrasion eventually leads to a reduction in the frictional shear stress at the interface, which is equivalent to a decrease in the coefficient of friction μ . Based on the theoretical results, a simple experimental method is proposed to evaluate the frictional degradation of the interface.

4.5.2. Relative displacements and degradation function

Degradation of frictional resistance at the debonded interface will cause the relative axial displacement between fiber and matrix to increase gradually. There are

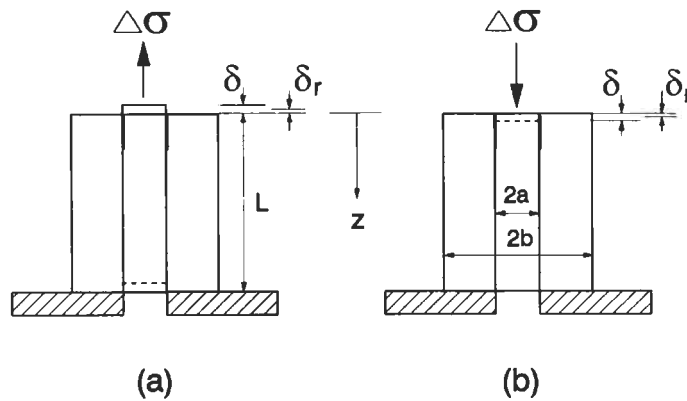


Fig. 4.41. Schematic drawings of loading and unloading processes measuring the relative displacements δ and δ_r in (a) fiber pull-out and (b) fiber push-out models under cyclic loading. After Zhou et al. (1993).

two types of relative displacements of particular interest in this analysis: one occurring under load, δ , and the other after unloading, with the latter being the residual relative displacement, δ_r (Fig. 4.42). For the perfectly elastic fiber and matrix materials, the relative displacement measured at the loaded fiber end is equal to the sum of the relative strain over the debonded interface since the displacements in the fiber and matrix are identical in the bonded region. Thus,

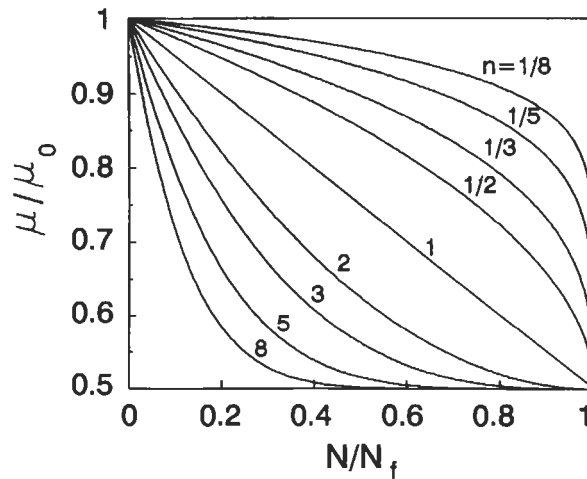


Fig. 4.42. Plots of normalized coefficient of friction, μ/μ_0 , versus normalized elapsed cycles, N/N_f , for different exponent n . After Zhou et al. (1993).

$$\delta = \int_0^{\ell} [\epsilon_f^z(a, z) - \epsilon_m^z(a, z)] dz = \frac{1}{E_f} (1 - 2\nu_f k) \ell \sigma - \frac{1}{\alpha E_f} [\alpha + \gamma - 2k(\alpha\nu_f + \gamma\nu_m)] \left[\frac{\exp(\lambda\ell) - 1}{\lambda} - \ell \right] \omega(\bar{\sigma} - \sigma) \quad (4.140)$$

in fiber pull-out. The residual relative displacement, δ_r , is the sum of the residual strains in the fiber, $\epsilon_{f-\text{res}}^z(a, z)$, and matrix, $\epsilon_{m-\text{res}}^z(a, z)$, after complete unloading over the debonded region

$$\delta_r = \int_0^{\ell} [\epsilon_{f-\text{res}}^z(a, z) - \epsilon_{m-\text{res}}^z(a, z)] dz . \quad (4.141)$$

The solution for Eq. (4.141) requires a knowledge of the stress (and strain) distributions after unloading, which can be obtained in a procedure similar to that for loading with minor modifications. The sign of the IFSS during unloading has to be altered while other conditions of equilibrium remain the same for both fiber pull-out and fiber push-out. In particular, the equilibrium condition between the external and internal stresses given by Eq. (4.87) is still valid during unloading. Accordingly, the condition for the stress transfer from the fiber to the matrix during unloading is governed by Eq. (4.128) for fiber pull-out. Therefore, solving these equations with other equilibria and boundary conditions given in Sections 4.3 and 4.4 yields the following solutions for the FAS and MAS during unloading in fiber pull-out:

$$\sigma_f^z(z) = \sigma + \omega(\bar{\sigma} - \sigma)[1 - \exp(-\lambda z)] , \quad (4.142)$$

$$\sigma_m^z(z) = -\gamma\omega(\bar{\sigma} - \sigma)[1 - \exp(-\lambda z)] . \quad (4.143)$$

Also, from the general relations between strains and stresses given by Eqs. (4.8) and (4.9), and the additional radial stress $q_1(a, z)$ of Eq. (4.18), the strains in the fiber and matrix at the interface for fiber pull-out are obtained as:

$$\epsilon_f^z(a, z) = \frac{1}{E_f} [\sigma_f^z(z) - 2\nu_f q^*(z)] , \quad (4.144)$$

$$\epsilon_m^z(a, z) = \frac{1}{E_m} [\sigma_m^z(z) + 2\gamma\nu_m q^*(z)] . \quad (4.145)$$

Therefore, from Eqs. (4.142)–(4.145):

$$\epsilon_f^z(a, z) = \frac{1}{E_f} \{ \omega(1 - 2k\nu_f)[1 - \exp(-\lambda z)](\bar{\sigma} - \sigma) + (1 - 2k\nu_f + \omega k)\sigma \} , \quad (4.146)$$

$$\epsilon_m^z(a, z) = \frac{1}{E_m} \{2\alpha\omega k v_f \sigma - \gamma\omega(1 - 2k v_m)[1 - \exp(-\lambda z)](\bar{\sigma} - \sigma)\} . \quad (4.147)$$

Hence, for the fiber pull-out, the residual strains after complete unloading when the external stress is zero now become:

$$\epsilon_{f-res}^z(a, z) = \frac{1}{E_f} \omega(1 - 2k v_f)[1 - \exp(-\lambda z)]\bar{\sigma} , \quad (4.148)$$

$$\epsilon_{m-res}^z(a, z) = -\frac{1}{E_m} \gamma\omega(1 - 2k v_m)[1 - \exp(-\lambda z)]\bar{\sigma} . \quad (4.149)$$

Consequently, the residual relative displacement in fiber pull-out is obtained by combining Eqs. (4.141), (4.148) and (4.149):

$$\delta_r = \frac{1}{\alpha E_f} [\alpha + \gamma - 2k(\alpha v_f + \gamma v_m)] \left[\ell - \frac{1 - \exp(-\lambda \ell)}{\lambda} \right] \omega \bar{\sigma} . \quad (4.150)$$

Similarly, the expressions for δ and δ_r for the fiber push-out are derived as:

$$\begin{aligned} \delta &= \int_0^{\ell} [\epsilon_f^z(a, z) - \epsilon_m^z(a, z)] dz = \frac{1}{E_f} (1 - 2v_f k) \ell \sigma \\ &\quad - \frac{1}{\alpha E_f} [\alpha + \gamma - 2k(\alpha v_f + \gamma v_m)] \left[\ell - \frac{1 - \exp(-\lambda \ell)}{\lambda} \right] \omega (\bar{\sigma} + \sigma) , \\ \delta_r &= \frac{1}{\alpha E_f} [\alpha + \gamma - 2k(\alpha v_f + \gamma v_m)] \left[\frac{\exp(-\lambda \ell) - 1}{\lambda} - \ell \right] \omega \bar{\sigma} . \end{aligned}$$

Eqs. (4.140) and (4.150)–(4.152) are used to evaluate the response of the model composites in cyclic loading and the displacements δ and δ_r can be expressed as a function of the alternating stress, $\Delta\sigma$, and the number of cycles, N . In experiments, degradation of the interface properties, e.g., the coefficient of friction, μ or $\lambda (= 2\mu k/a)$, can also be expressed in terms of the cyclic loading parameters, $\Delta\sigma$ and N . In practice δ and δ_r can be measured using optical methods (with a microscope) or by means of more complicated instruments (see for example Naaman et al. (1992)) in fiber pull-out. Alternatively, they can be directly determined from the load and load–point displacement records in the case of fiber push-out.

It is envisaged that the degradation of the frictional interface properties and the corresponding increase in the relative displacements eventually lead to debond crack growth once the debond criterion is satisfied. The debond criterion based on the energy balance theory given by Eq. (4.35) under monotonic loading can be rewritten as

$$G = G(\mu_0, \sigma_d^p, \ell) \geq G_{ic} , \quad (4.153)$$

where μ_0 is the original value of the coefficient of friction before degradation and σ_d^p represents the applied fiber stress corresponding to debond length, ℓ . Under cyclic loading the debond criterion becomes

$$G = G(\mu(N), \sigma_{\max}, \ell) \geq G_{ic} \quad (4.154)$$

where $\mu(N) (< \mu_0)$, which is smaller than the original value, is now a function of the elapsed cycles, and σ_{\max} is smaller than the instantaneous debond stress, σ_d^p , in both fiber pull-out and push-out. G_{ic} is a material constant that is identical to that defined for monotonic loading. For the convenience of analysis, the following degradation function for $\mu(N)$ is employed for the two loading geometry

$$\frac{\mu(N)}{\mu_0} = \frac{\mu_1}{\mu_0} + \left(1 - \frac{\mu_1}{\mu_0}\right) \left(\frac{1 - N}{N_1}\right)^n \quad (4.155)$$

μ_1 is the steady state or final value of the coefficient of friction, and N_1 is the corresponding maximum number of cycles after which there is no further degradation in μ . n is a power law exponent and is positive. Other functions such as an exponential function or a reciprocal function can be used in place of the power law as far as they eliminate the boundary condition of $\mu(N) = \mu_1$ for the number of cycles greater than N_1 . However, any realistic friction degradation function should always be consistent with independent experimental measurements.

4.5.3. Degradation of interface frictional properties

Fig. 4.42 illustrates the general trend of the normalized coefficient of friction $\mu(N)/\mu_0$ plotted as a function of normalized elapsed cycles, N/N_1 , for $\mu_1 = \mu_0/2$. The dependence of μ on $\Delta\sigma$ is not explicitly shown in this simple relationship but is reflected by the different values of n , or alternatively the steady state N_1 value for a given μ_1 . In the absence of relevant experimental data, which would allow comparison against the analytical model, specific results are calculated using material properties for the coated steel wire-epoxy matrix composite system (Tables 4.1 and 4.3). An alternating stress, $\Delta\sigma$, is applied, which corresponds to 90% of the instantaneous debond stress, σ_d^p , in both fiber pull-out and fiber push-out for an identical initial debond length $\ell_0 = 10$ mm. This enables a direct comparison of the friction degradation behavior of the two loading processes.

Debond length, ℓ , and the relative displacement, δ , are simultaneously solved by evaluating μ for a given N using the debond criterion. Therefore, Fig. 4.43 plots the predictions calculated for the steady state values $\mu_1 = 0.07$ and $N_1 = 10^6$ cycles, and the total embedded fiber length $L = 80$ mm. It is noted that n plays an important role in controlling the trend of ℓ (and thus δ) versus N in both loading geometry. For $n > 1$, ℓ increases rapidly with increasing N at the initial stage of loading, which is followed by an almost saturated value when n approaches the steady state value, N_1 . In contrast, if $n \leq 1$ the debond crack grows relatively slowly at the initial stage until N is close to N_1 where it grows instantaneously to a saturated value. These two types of crack growth behavior reflect the manner in which μ decreases with increasing N as illustrated in Fig. 4.42. A similar functional dependence of δ on N is also noted, which suggests that either of these two parameters ℓ and δ can be used to represent

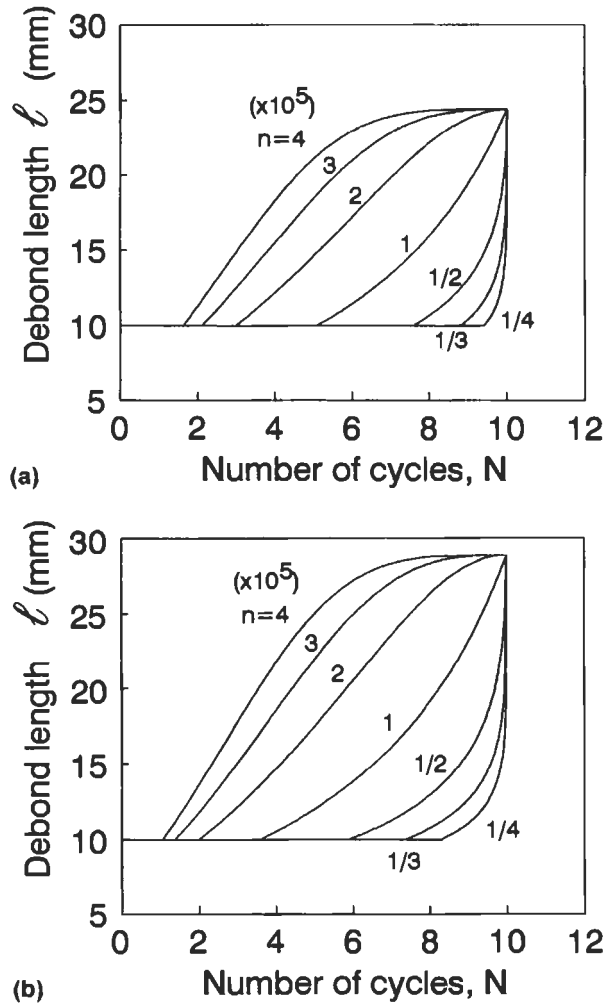


Fig. 4.43. Growth of debond length, ℓ , with increasing number of cycles, N , for (a) fiber pull-out and (b) fiber push-out. Initial debond length $\ell = 10$ mm. After Zhou et al. (1993).

the degradation of frictional properties at the interface. This justifies in part the adoption of the degradation function given by Eq. (4.155), which can be substantiated in experiments by measuring the protrusion (or intrusion) length, δ , under cyclic loading.

Figs. 4.44 and 4.45 show the increase in the debond length, ℓ , and displacement, δ , as a result of the reduction of μ (from $\mu_0 = 0.22$ to $\mu_1 = 0.07$) under cyclic loading. It is interesting to note that both ℓ and δ remain constant until the coefficient of friction, μ , is reduced to a critical value μ_c ($= 0.144$ and 0.166 , respectively for fiber pull-out and fiber push-out). The implication is that the debond crack does not grow

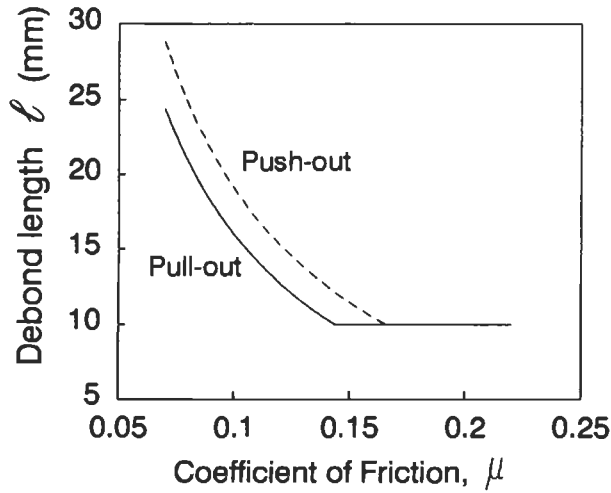


Fig. 4.44. Variation of debond length, ℓ , as a function of coefficient of friction, μ . After Zhou et al. (1993).

until the debond criterion given in Eq. (4.154) is strictly satisfied, which requires a substantial reduction in μ under a given $\Delta\sigma$. It appears that the critical value μ_c is dependent mainly on the stress amplitude, $\Delta\sigma$, which in turn determines the elapsed cycles for debond crack growth.

From comparison of the plots between the two loading geometry in Figs. 4.44 and 4.45, it is generally noted that a substantially larger N is required for debond crack

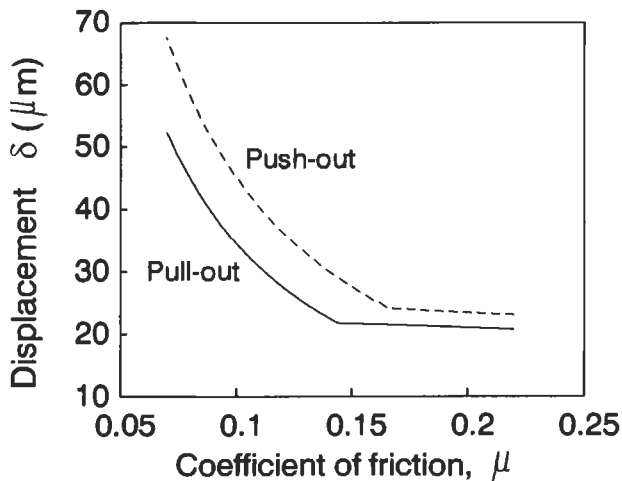


Fig. 4.45 Variation of relative displacement, δ , as a function of the coefficient of friction, μ . After Zhou et al. (1993).

growth for fiber pull-out than for fiber push-out. Also, the final crack length at steady state is significantly shorter for fiber pull-out than fiber push-out. In the same context, the increase in the relative displacements is more difficult for fiber pull-out than for fiber push-out under an identical stress amplitude. These results are more clearly demonstrated by the critical value μ_c , which is smaller for fiber pull-out than for fiber push-out. All these results of the parametric study based on the power law function imply that the degradation of interface frictional properties is more severe in fiber push-out than in fiber pull-out under cyclic loading of given values of μ_0 , μ_1 , N_1 and $\Delta\sigma$.

References

- Aboudi, J. (1983). The effective moduli of short fiber composites. *Int. J. Solids Struct.* **19**, 693–707.
- Ananth, C.R. and Chandra, N. (1995). Numerical modelling of fiber push-out test in metallic and intermetallic matrix composites mechanics of failure process. *J. Composite Mater.* **29**, 1488–1514.
- Atkinson, C., Avila, J., Betz, E. and Smelser, R.E. (1982). The rod pull-out problem, theory and experiment. *J. Mech. Phys. Solids* **30**, 97–120.
- Banbaji, J. (1988). On a more generalised theory of the pull-out test from an elastic matrix. Part I-theoretical considerations. *Composites Sci. Technol.* **32**, 183–193.
- Berthelot, J.M., Cupcic, A. and Maufrais, J.M. (1978). Experimental flexural strength-deflection curves of oriented discontinuous fiber composites. *Fiber Sci. Technol.* **11**, 367–398.
- Berthelot, J.M., Cupcic, A. and Brou, K.A. (1993). Stress distribution and effective longitudinal Young's modulus of unidirectional discontinuous fiber composites. *J. Composite Mater.* **27**, 1391–1425.
- Betz, E. (1982). Experimental studies of the fiber pull-out problem. *J. Mater. Sci.* **17**, 691–700.
- Bright, J.D., Danchaiwijit, S. and Shetty, D.K. (1991). Interfacial sliding friction in silicon carbide-borosilicate glass composites: a comparison of pullout and pushout tests. *J. Am. Ceram. Soc.* **74**, 115–122.
- Bright, J.D., Shetty, D.K., Griffin, C.W. and Limaye, S.Y. (1989). Interfacial debonding and friction in SiC filament-reinforced ceramic and glass matrix composites. *J. Am. Ceram. Soc.* **72**, 1891–1898.
- Butler, E.P., Fuller, E.R. and Chan, H.M. (1990). Interface properties for ceramic composites from a single-fiber pull-out test. In *Tailored Interfaces in Composite Materials*, Mat. Res. Soc. Symp. Proc. Vol. 170, Materials Research Society, Pittsburgh, PA, pp. 17–24.
- Carter, W.C., Butler, E.P. and Fuller, Jr. E.R. (1991). Micromechanical aspects of asperity-controlled friction in fiber-toughened ceramic composites. *Scripta Metall. Mater.* **25**, 579–584.
- Chandra, N. and Ananth, C.R. (1995). Analysis of interfacial behaviour in MMCs and IMCs by the use of thin-slice push-out test. *Composites Sci. Technol.* **54**, 87–110.
- Chen, E.J.H. and Young, J.C. (1991). The microdebonding testing system: A method for quantifying adhesion in real composites. *Composites Sci. Technol.* **42**, 189–206.
- Chiang, C.R. (1991). On the stress transfer in fiber reinforced composites with bonded fiber ends. *J. Mater. Sci. Lett.* **10**, 159–160.
- Cox, H.L. (1952). The elasticity and strength of paper and other fibrous materials. *Brit. J. Appl. Phys.* **3**, 72–79.
- Curtin, W.A. (1991). Exact theory of fiber fragmentation in a single filament composite. *J. Mater. Sci.* **26**, 5239–5253.
- Daabin, A., Gamble, A.J. and Sumner, N.D. (1992). The effect of the interphase and material properties on load transfer in fiber composites. *Composites* **23**, 210–214.
- Daoust, J., Vu-Khanh, T., Ahlstrom, C. and Gerard, J.F. (1993). A finite element model of the fragmentation test for the case of a coated fiber. *Composites Sci. Technol.* **48**, 143–149.
- DiAnselmo, A., Accorsi, M.L. and DiBenedetto, A.T. (1992). The effect of an interphase on the stress and energy distribution in the embedded single fiber test. *Composites Sci. Technol.* **44**, 215–225.

- Dow, N.F. (1963). Study of stresses near a discontinuity in a filament-reinforced composite metal. In *Space Sci. Lab. Missile and Space Div., General Electric Co. Tech. Report*, No. R63SD61.
- Eshelby, J.D. (1982). The stress on and in a thin inextensible fiber in a stretched elastic medium. *Eng. Frac. Mech.* **16**, 453–455.
- Fan, C.F. and Hsu, S.L. (1992a) A study of stress distribution in model composites by using finite-element analysis. I. End effects. *J. Polym. Sci.: Part B. Polym. Phys.* **30**, 603–618.
- Fan, C.F. and Hsu, S.L. (1992b) A study of stress distribution in model composites by using finite-element analysis. II. Fiber/matrix interfacial effects. *J. Polym. Sci.: Part B. Polym. Phys.* **30**, 619–635.
- Favre, J.P. and Jacques, D. (1990). Stress transfer by shear in carbon fiber model composites: Part I Results of single fiber fragmentation tests with thermosetting resins. *J. Mater. Sci.* **25**, 1373–1380.
- Favre, J.P., Sigety, P. and Jacques, D. (1991). Stress transfer by shear in carbon fiber model composites, Part 2. Computer simulation of the fragmentation test. *J. Mater. Sci.* **26**, 189–195.
- Feillard, P., Desarmot, G. and Favre, J.P. (1994). Theoretical aspects of the fragmentation test. *Composites Sci. Technol.* **50**, 265–279.
- Fu, S.Y., Zhou, B.L., Chen, X., Xu, C.F., He, G.H. and Lung, C.W. (1993). Some further considerations of the theory of fiber debonding and pull-out from an elastic matrix. *Composites* **24**, 5–11.
- Gao, Y.C., Mai, Y.W. and Cotterell, B. (1988). Fracture of fiber-reinforced materials. *J. Appl. Math. Phys. (ZAMP)* **39**, 550–572.
- Gent, A.N. and Liu, G.L. (1991). Pull-out and fragmentation on model fiber composites. *J. Mater. Sci.* **26**, 2467–2476.
- Gopalaratnam, V.S. and Shah, S.P. (1987). Tensile failure of steel fiber-reinforced mortar. *ASCE J. Eng. Mech.* **113**, 635–652.
- Grande, D.H., Mandell, J.F. and Hong, K.C.C. (1988). Fiber-matrix bond strength studies of glass, ceramic and metal matrix composites. *J. Mater. Sci.* **23**, 311–328.
- Gray, R.J. (1984). Analysis of the effect of embedded fiber length on the fiber debonding and pull-out from an elastic matrix. *J. Mater. Sci.* **19**, 861–870.
- Greszczuk, L.B. (1969). Theoretical studies of the mechanics of the fiber-matrix interface in composites. In *Interfaces in Composites*, ASTM STP 452, ASTM, Philadelphia, PA, pp. 42–58.
- Gulino, R., Schwartz, P. and Phoenix, L. (1991). Experiments on shear deformation, debonding and local load transfer in a model graphite/ glass/epoxy microcomposites. *J. Mater. Sci.* **26**, 6655–6672.
- Gurney, C. and Hunt, J. (1967). Quasi-static crack propagation. *Proc. R. Soc. Lond. A* **299**, 508–524.
- Ho, H. and Drzal, L.T. (1995a). Non-linear numerical study of the single fiber fragmentation test, part I. Test mechanics. *Composites Eng.* **5**, 1231–1244.
- Ho, H. and Drzal, L.T. (1995b). Non-linear numerical study of the single fiber fragmentation test, part II. Parametric study. *Composites Eng.* **5**, 1245–1259.
- Ho, H. and Drzal, L.T. (1996). Evaluation of interfacial mechanical properties of fiber reinforced composites using the microindentation method. *Composites Part A* **27A**, 961–971.
- Hsueh, C.H. (1988). Elastic load transfer from partially embedded axially loaded fiber to matrix. *J. Mater. Sci. Lett.* **7**, 497–500.
- Hsueh, C.H. (1989). Analytical analyses of stress transfer in fiber-reinforced composites with bonded and debonded ends. *J. Mater. Sci.* **24**, 4475–4482.
- Hsueh, C.H. (1990a). Interfacial debonding and fiber pull-out stresses of fiber-reinforced composites. *Mater. Sci. Eng. A* **123**, 1–11 & 67–73.
- Hsueh, C.H. (1990b). Interfacial friction analysis for fiber-reinforced composites during fiber push-down (indentation). *J. Mater. Sci.* **25**, 818–828.
- Hsueh, C.H. (1990c). Effect of interfacial bonding on sliding phenomena during compressive loading of an embedded fiber. *J. Mater. Sci.* **25**, 4080–4086.
- Hsueh, C.H. (1991). Interfacial debonding and fiber pull-out stresses of fiber reinforced composites, part V, with a viscous interface. *Mater. Sci. Eng. A* **149**, 1–9.
- Hsueh, C.H. (1992). Interfacial debonding and fiber pull-out stresses of fiber-reinforced composites. VII: Improved analyses for bonded interfaces. *Mater. Sci. Eng. A* **154**, 125–132.
- Hsueh, C.H. (1993). Embedded-end debond theory during fiber pull-out. *Mater. Sci. Eng. A* **163**, L1–L4.

- Hsueh C.H. and Becher, P.F. (1993). Some consideration of two-way debonding during fiber pull-out. *J. Mater. Sci. Lett.* **12**, 1933–1936.
- Hull, D. (1981). *An Introduction to Composite Materials*, Cambridge University Press, Cambridge, pp. 81–101.
- Hutchinson, J.W. and Jensen, H.M. (1990). Models for fiber debonding and pullout in brittle composites with friction. *Mech. Mater.* **9**, 139–163.
- Jero, P.D. and Keran, R.J. (1990). The contribution of interfacial roughness to sliding friction of ceramic fibers in a glass matrix. *Scripta Metall. Mater.* **24**, 2315–2318.
- Jero, P.D., Keran, R.J. and Parthasarathy, T.A. (1991). Effect of interfacial roughness on the frictional stress measured using pushout tests. *J. Am. Ceram. Soc.* **74**, 2793–2801.
- Jiang, K.R. and Penn, L.S. (1992). Improved analysis and experimental evaluation of the single filament pull-out test. *Composites Sci. Technol.* **45**, 89–103.
- Kallas, M.N., Koss, D.A., Hahn, H.T. and Hellmann, J.R. (1992). Interfacial stress state present in a thin slice fiber pull-out test. *J. Mater. Sci.* **27**, 3821–3826.
- Karbhari, V.M. and Wilkins, D.J. (1990). A theoretical model for fiber debonding incorporating both interfacial shear and frictional stresses. *Scripta Metall. Mater.* **24**, 1197–1202.
- Kelly, A. (1966). *Strong Solids*. Clarendon Press, Oxford, Chapter 5.
- Kelly, A. and Tyson, W.R. (1965). Tensile properties of fiber-reinforced metals: copper-tungsten and copper-molybdenum. *J. Mech. Phys. Solids.* **13**, 329–350.
- Keran, R.J. and Parthasarathy, T.A. (1991). Theoretical analysis of the fiber pullout and pushout tests. *J. Am. Ceram. Soc.* **74**, 1585–1596.
- Kim, J.K. (1997). Stress transfer in the fiber fragmentation test, part III. effects of interface debonding and matrix yielding. *J. Mater. Sci.* **32**, 701–711.
- Kim, J.K., Baillie, C. and Mai, Y.W. (1991). Instability of interfacial debonding during fiber pull-out. *Scripta Metall. Mater.* **25**, 315–320.
- Kim, J.K. and Mai, Y.W. (1991a). High strength, high fracture toughness fiber composites with interface control—a review. *Composites. Sci. Technol.* **41**, 333–378.
- Kim, J.K. and Mai, Y.W. (1991b). The effect of interfacial coating and temperature on the fracture behaviors of unidirectional KFRP and CFRP. *J. Mater. Sci.* **26**, 4701–4720.
- Kim, J.K., Baillie, C. and Mai, Y.W. (1992). Interfacial debonding and fiber pull-out stresses, part I. a critical comparison of existing theories with experiments. *J. Mater. Sci.* **27**, 3143–3154.
- Kim, J.K. and Mai, Y.W. (1993). Interfaces in composites in *Structure and Properties of Fiber Composites*, Materials Science and Technology, Series Vol. 13, (T.W. Chou, ed.), VCH Publishers, Weinheim, Germany, Ch. 6, pp. 229–289.
- Kim, J.K., Zhou, L.M. and Mai, Y.W. (1993a). Interfacial debonding and pull-out stresses: part III. Interfacial properties of cement matrix composites. *J. Mater. Sci.* **28**, 3923–3930.
- Kim, J.K., Zhou, L.M. and Mai, Y.W. (1993b). Stress transfer in the fiber fragmentation test. part I. An improved analysis based on a shear strength criterion. *J. Mater. Sci.* **28**, 6233–6245.
- Kim, J.K., Lu, S.V. and Mai, Y.W. (1994a). Interfacial debonding and fiber pull-out stresses: part IV. Influence of interface layer on the stress transfer. *J. Mater. Sci.* **29**, 554–561.
- Kim, J.K., Zhou, L.M. Bryan, S.J. and Mai, Y.W. (1994b). Effect of fiber volume fraction on interfacial debonding and fiber pull-out. *Composites* **25**, 470–475.
- Kim, J.K., Zhou, L.M. and Mai, Y.W. (1994c). Techniques for studying composite interfaces. In *Handbook of Advanced Materials Testing* (N.P. Cheremisinoff, ed.), Marcel Dekker, New York, Ch. 22, pp. 327–366.
- Lacroix, Th., Tilmans, B., Keunings, R., Desaeger, M. and Verpoest, I. (1992). Modelling of critical fiber length and interfacial debonding in the fragmentation testing of polymer composites. *Composites Sci. Technol.* **43**, 379–387.
- Lau, M.G., Mai, Y.W. (1990). The fiber pushout problem in ceramic composites. In *Proc. Symp. Composites-Proc., Microstructures and Prop.*, (M.D. Sacks, ed.), Orlando, pp. 583–591.
- Lau, M.G. and Mai, Y.W. (1991). A comparison of fiber pullout and pushout in ceramic fiber composites. *Key Eng. Mater.* **53-55**, 144–152.

- Lawrence, S. (1972). Some theoretical considerations of fiber pull-out from an elastic matrix. *J. Mater. Sci.* **7**, 1–6.
- Laws, L., Lawrence, P. and Nurse, R.W. (1973). Reinforcement of brittle matrices by glass fibers. *J. Phys. D. Appl. Phys.* **6**, 523–537.
- Laws, V. (1982). Micromechanical aspects of the fiber-cement bond. *Composites* **13**, 145–151.
- Lec, J.W. and Daniel, I.M. (1992). Deformation and failure of longitudinally loaded brittle matrix composites. In *Composite materials: Testing and Design (Tenth Vol.)*, ASTM STP 1120, (G.C. Grimes, ed.), ASTM, Philadelphia, P.A., pp. 204–221.
- Leung, C.K.Y and Li, V.C. (1991). A new strength-based model for the debonding of discontinuous fibers in an elastic matrix. *J. Mater. Sci.* **26**, 5996–6100.
- Lhotellier, F.C. and Brinson, H.F. (1988). Matrix fiber stress transfer in composite materials: Elastoplastic model with an interphase layer. *Composite Structures* **10**, 281–301.
- Liang, C. and Hutchinson, J.W. (1993). Mechanics of the fiber pushout test. *Mech. Mater.* **14**, 207–221.
- Liu, H.Y., Zhou, L.M. and Mai, Y.W. (1994a). On fiber pull-out with a rough interface. *Phil. Mag. A*, **70**, 359–372.
- Liu, H.Y., Zhou, L.M. and Mai, Y.W. (1995). Effect of interface roughness on fiber push-out stress. *J. Am. Ceram. Soc.*, **78**, 560–566.
- Liu, H.Y., Mai, Y.W., Zhou, L.M. and Ye, L. (1994b). Simulation of the fiber fragmentation process by a fracture mechanics analysis. *Composites Sci. Technol.* **52**, 253–260.
- Liu, H.Y., Mai, Y.W., Ye, L. and Zhou, L.M. (1997). Stress transfer in the fiber fragmentation test. 3. Effect of matrix cracking and interface debonding. *J. Mater. Sci.* **32**, 633–641.
- Lu, G.Y. and Mai, Y.W. (1995). Effect of plastic coating on fiber-matrix interface debonding. *J. Mater. Sci.* **30**, 5872–5878.
- Mackin, T.J., Warren, P.D. and Evans, A.G. (1992a). Effects of fiber roughness on interface sliding in composites. *Acta Metall. Mater.* **40**, 1251–1257.
- Mackin, T.J., Yang, J. and Warren, P.D. (1992b). Influence of fiber roughness on the sliding behavior of sapphire fibers in TiAl and glass matrices. *J. Am. Ceram. Soc.* **75**, 3358–3362.
- MacLaughlin, T.F. and Barker, R.M. (1972). Effect of modulus ratio on stress near a discontinuous fiber. *Exp. Mech.* **12**, 178–183.
- Majumda, B.S. and Miracle, D.B. (1996). Interface measurement and applications in fiber reinforced MMCs. *Key Eng. Mater.* **116-117**, 153–172.
- Marotzke, Ch. (1993). Influence of the fiber length on the stress transfer from glass and carbon fibers into a thermoplastic matrix in the pull-out test. *Composite Interfaces* **1**, 153–166.
- Marotzke, Ch. (1994). The elastic stress field arising in the single fiber pull-out test. *Composites Sci. Technol.* **50**, 393–405.
- Marshall, D.B. (1992). Analysis of fiber debonding and sliding experiments in brittle matrix composites. *Acta Metall. Mater.* **40**, 427–442.
- Marshall, D.B. and Oliver, W.C. (1987). Measurement of interfacial mechanical properties in fiber-reinforced ceramic composites. *J. Am. Ceram. Soc.* **70**, 542–548.
- Marshall, D.B. and Oliver, W.C. (1990). An indentation method for measuring residual stresses in fiber reinforced ceramics. *Mater. Sci., Eng. A* **126**, 95–103.
- Marshall, D.B., Shaw, M.C. and Morris, W.L. (1992). measurement of interfacial debonding and sliding resistance in fiber reinforced intermetallics. *Acta Metall. Mater.* **40**, 443–454.
- Meda, G., Hoysan, S.F. and Steif, P.S. (1993). The effect of fiber Poisson expansion in micro-indentation tests. *Trans. ASME J. Appl. Mech.* **60**, 986–991.
- Mital, S.K., Murthy, P.L.N. and Chamis, C.C. (1993). Interfacial microfracture in high temperature metal matrix composite. *J. Composite Mater.* **27**, 1678–1694.
- Muki, R. and Sternberg, E. (1969). On the diffusion of an axial load from an infinite cylindrical bar embedded in an elastic medium. *Int. J. Solids Structures* **5**, 587–605.
- Muki, R. and Sternberg, E. (1971). Load-absorption by a discontinuous filament in a fiber-reinforced composite. *J. Appl. Math. Phys. (ZAMP)* **22**, 809–824.
- Naaman, A.E., Namur, G.G., Alwan, J.M. and Najm, H.S. (1992). Fiber pullout and bond slip. II: Experimental validation. *ASCE J. Struc. Eng.* **117**, 2791–2800.

- Nairn, J.A. (1992). Variational mechanics analysis of the stresses around breaks in embedded fibers. *Mech. Mater.* **13**, 131–157.
- Outwater, J.D. and Murphy, M.C. (1969). On the fracture energy of unidirectional laminates. In *24th Annual Tech. Conf. Reinforced Plast. Composites Inst.* SPI, New York, Paper 11C.
- Pally, I. and Stevens, D. (1989). A fracture mechanics approach to the single fiber pull-out problem as applied to the evaluation of the adhesion strength between the fiber and the matrix. *Adhesion Sci. Technol.* **3**, 141–153.
- Piggott, M.R. (1980). *Load Bearing Fiber Composites*, Pergamon Press, Oxford, Ch. 5.
- Piggott, M.R. (1987). Debonding and friction at fiber–polymer interface. I: Criteria for failure and sliding. *Composites Sci. Technol.* **30**, 295–306.
- Piggott, M.R. (1990). Tailored interphases in fiber reinforced polymers. in *Interfaces in Composites, Mat. Res. Soc. Symp. Proc.*, Vol. 170 (C.G. Pantano and E.J.H. Chen, eds.), MRS, Pittsburgh, PA, pp. 265–274.
- Povirk, G.C. and Needleman, A. (1993). Finite element simulations of fiber pull-out. *J. Eng. Mater. Technol.* **115**, 286–291.
- Qiu, Y. and Schwartz, P. (1991). A new method for study of the fiber-matrix interface in composites: single fiber pull-out from a microcomposite. *J. Adhesion Sci. Technol.* **5**, 741–756.
- Rosen, B.W. (1964). Tensile failure of fibrous composites. *AIAA J.* **2**, 1985–1991.
- Rosen, B.W. (1965). Mechanics of composite strengthening. In *Fiber Composite Materials*, American Society for Metals, Metal Park, OH, pp. 37–75.
- Russel, W.B. (1973). On the effective moduli of composite materials: effect of fiber length and geometry at dilute concentrations. *J. Appl. Math. Phys. (ZAMP)* **24**, 581–599.
- Shetty, D.K. (1988). Shear-lag analysis of fiber push-out (indentation) tests for estimating interfacial friction stress in ceramic-matrix composites. *J. Am. Ceram. Soc.* **71**, C.107–109.
- Sigl, L.S. and Evans, A.G. (1989). Effects of residual stress and frictional sliding on cracking and pull-out in brittle matrix composites. *Mech. Mater.* **8**, 1–12.
- Singh, R.N. and Suteu, M. (1991). Determination of fiber-matrix interfacial properties in ceramic-matrix composites by a fiber push-out technique. *J. Mater. Sci.* **26**, 2547–2556.
- Stang, H. and Shah, S.P. (1986). Failure of fiber-reinforced composites by pull-out fracture. *J. Mater. Sci.* **21**, 953–957.
- Stenberg, E. and Muki, R. (1970). Load-absorption by a filament in a fiber-reinforced material. *J. Appl. Math. Phys. (ZAMP)* **21**, 552–569.
- Takaku, A. and Arridge, R.G.C. (1973). The effect of interfacial radial and shear stress on fiber pull-out in composite materials. *J. Phys. D: Appl. Phys.* **6**, 2038–2047.
- Termonia, Y. (1987). Theoretical study of the stress transfer in single fiber composites. *J. Mater. Sci.* **22**, 210–214.
- Termonia, Y. (1992). Effect of strain rate on the mechanical properties of composites with a weak fiber/matrix interface. *J. Mater. Sci.* **27**, 4878–4882.
- Tsai, H.C., Arocho, A.M. and Gause, L.W. (1990). Prediction of fiber–matrix interphase properties and their influence on interface stress, displacement and fracture toughness of composite materials. *Mater. Sci. Eng. A* **126**, 295–304.
- van der Zwaag, S. (1989). The concept of filament strength and the Weibull modulus. *J. Test. Eval. (JTEVA)* **17**, 292–298.
- Waren, P.P., Mackin, T.J. and Evans, A.G. (1992). Design, analysis and application of an improved push-through test for the measurement of interfacial properties on composites. *Acta. Metall. Mater.* **40**, 1243–1249.
- Weibull, W. (1951). A statistical distribution function of wide applicability. *J. Appl. Mech.* **18**, 293–297.
- Wells, J.K. and Beaumont, P.W.R. (1985). Debonding and pull-out processes in fibrous composites. *J. Mater. Sci.* **20**, 1275–1284.
- Whitney, J.M. and Drzal, L.T. (1987). Axisymmetric stress distribution around an isolated fiber fragment. In *Toughened Composites*, ASTM STP 937, (N.J. Johnston ed.) ASTM, Philadelphia, PA, pp. 179–196.
- Wu, H.F. and Claypool, C.M. (1991). An analytical approach of the microbond test method used in characterizing the fiber-matrix interface. *J. Mater. Sci. Lett.* **10**, 260–262.

- Yue, C.Y. and Cheung, W.L. (1992). Interfacial properties of fibrous composites. *J. Mater. Sci.* **27**, 3173–3180.
- Zhou, L.M. and Mai, Y.W. (1992). A three-cylinder model for evaluation of sliding resistance in fiber push-out test. in *Ceramics Adding the Value* (M.J. Bannister, ed.), CSIRO Pub, Melbourne. pp. 1113–1118.
- Zhou, L.M., Kim, J.K. and Mai, Y.W. (1992a). Interfacial debonding and fiber pull-out stresses: Part II. A new model based on the fracture mechanics approach. *J. Mater. Sci.* **27**, 3155–3166.
- Zhou, L.M., Kim, J.K. and Mai, Y.W. (1992b). A comparison of instability during interfacial debonding in fiber pull-out and fiber push-out. In *Proc. Second Intern. Symp. on Composite Materials and Structures (ISCMS-2)* (C.T. Sun and T.T. Loo, eds.), Peking University press, Beijing, pp. 284–289.
- Zhou, L.M., Kim, J.K. and Mai, Y.W. (1992c). On the single fiber pull-out problem: Effect of loading methods. *Composites Sci. Technol.* **45**, 153–160.
- Zhou, L.M., Kim, J.K. and Mai, Y.W. (1993). Micromechanical characterization of fiber–matrix interface. *Composites Sci. Technol.* **48**, 227–236.
- Zhou, L.M., Mai, Y.W. and Baillie, C. (1994). Interfacial debonding and fiber pull-out stresses. part V. A methodology for evaluation of interfacial properties. *J. Mater. Sci.* **29**, 5541–5550.
- Zhou, L.M., Kim, J.K., Baillie, C. and Mai, Y.W. (1995a). Fracture mechanics analysis of the fiber fragmentation test. *J. Composite Mater.* **29**, 881–902.
- Zhou, L.M., Mai, Y.W., Ye, L. and Kim, J.K. (1995b). Techniques for evaluating interfacial properties of fiber–matrix composites. *Key Eng. Mater.* **104–107**, 549–600.
- Zhou, L.M. and Mai, Y.W. (1993). On the single fiber pullout and pushout problem: effect of fiber anisotropy. *J. Appl. Math. Phys. (ZAMP)* **44**, 769–775.
- Zhou, L.M. and Mai, Y.W. (1994). Analysis of fiber frictional sliding in fiber bundle pushout test. *J. Am. Ceram. Soc.* **77**, 2076–2080.
- Zhou, L.M. and Mai, Y.W. (1995). Analyses of fiber push-out test based on fracture mechanics approach. *Composites Eng.* **5**, 1199–1219.

Chapter 5

SURFACE TREATMENTS OF FIBERS AND EFFECTS ON COMPOSITE PROPERTIES

5.1. Introduction

The interaction of a fiber with a matrix material depends strongly on the chemical/molecular features and atomic composition of the fiber surface layers as well as its topographical nature. The chemical composition of the fiber surface consists of weakly adsorbed materials that are removable by heat treatments as well as strongly adsorbed materials that are chemically attached with strong covalent bonds. Both types of adsorbed material influence significantly the interaction at the fiber–matrix interface. In addition, the fiber surface topography or morphology is vital not only to constituting the mechanical bonding with matrix resins or molten metals, but also to adsorption behavior of the fiber (Kim and Mai, 1993). It is well known that surfaces of many fibers, e.g. carbon, silicon carbide and boron fibers in particular, are neither smooth nor regular.

Although the techniques of bonding organic polymers to inorganic surfaces have long been applied to protective coatings on metal surfaces, the majority of new bonding techniques developed in recent years is a result of the use of fibers as reinforcement of polymer resins, metals and ceramic matrices materials. Since the advent of organofunctional silane as a coupling agent for glass fibers, there have been a number of attempts to promote the bond quality at the interface between the fiber (or rigid filler, broadly speaking) and organic resins. For polymer matrix composites (PMCs), fiber surfaces are treated to enhance the interface bonding and preserve it in a service environment, particularly in the presence of moisture and at moderate temperatures. For many metal and ceramic matrix composite systems, chemical incompatibility is a severe problem due to inadequate or excessive reactivity at the interphase region at very high temperatures required during the fabrication processes. Therefore, fibers are usually treated with a diffusion barrier coating to protect them from damages by excessive reaction. Further, stability of the interface is an important requirement that is made critical by the high temperature service desired for these composites.

This chapter is concerned primarily with the surface treatments of high performance fibers, including glass, carbon (or graphite), aramid, polyethylene

and some ceramic fibers, such as boron (B/W), SiC and Al_2O_3 fibers. The methods of surface treatment, the choice of reaction barrier coatings and the resulting mechanisms for improving the mechanical performance of a given fiber are different for different types of matrix material as for the thermodynamic and chemical compatibilities required. To fully understand the mechanisms of bonding or failure at the interface region and thus to apply the many different surface treatment techniques, it is also necessary to have an adequate understanding of the microstructure/properties of the fibers concerned. Proper characterization of the interfaces modified by surface treatments or fiber coatings, and evaluation of the mechanical performance of the composites made therefrom are as important as the development of novel techniques of surface modification. Extensive and in-depth discussions on surface analytical techniques and mechanical testing methods are already given in Chapters 2 and 3, respectively.

5.2. Glass fibers and silane coupling agents

5.2.1. Structure and properties of glass fibers

A variety of chemical compositions of mineral glasses have been used to produce fibers. The most commonly used are based on silica (SiO_2) with additions of oxides of calcium, aluminum, iron, sodium, and magnesium. The polyhedron network structure of sodium silicate glass is schematically illustrated in Fig. 5.1, where each polyhedron is a combination of oxygen atoms around a silicon atom bonded together by covalent bonds. The sodium ions are not linked to the network, but only form ionic bonds with oxygen atoms. As a result of the three-dimensional network structure of glass, the properties of glass fibers are isotropic, as opposed to most

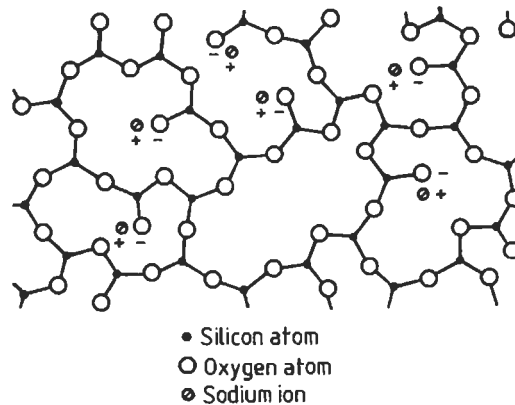


Fig. 5.1. Two dimensional illustration of the polyhedron network structure of sodium silicate glass. After Hull (1981).

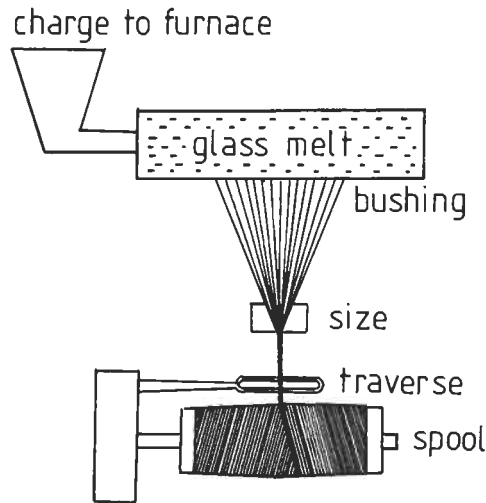


Fig. 5.2. Schematic diagram of glass fiber manufacturing.

ceramic and organic fibers discussed in the following sections. Glass fibers can be produced in either continuous filament or staple form. The continuous glass fibers are generated from molten glass by being drawn through small orifices, as schematically shown in Fig. 5.2. The fiber diameter is controlled by adjusting the orifice size, the winding speed and the viscosity of molten glass.

Typical combinations of three most popular glass fibers are given in Table 5.1, and their representative properties are shown in Table 5.2. The designations E, C and S stand for electrical, chemical/corrosion and structural grades, respectively. E-glass fibers are a good electrical insulator, possessing good strength and a moderate Young's modulus. They are most widely used for printed circuit boards in microelectronic applications and boat hull constructions. C-glass fibers have a better resistance to chemical corrosion than E-glass fibers, and are suitable for applications in chemical plants. S-glass fibers have a high strength and high modulus designed for

Table 5.1
Composition (wt%) of glass used for fiber manufacture^a

Elements	E-glass	C-glass	S-glass
SiO ₂	52.4	64.4	64.4
Al ₂ O ₃ , Fe ₂ O ₃	14.4	4.1	25.0
CaO	17.2	13.4	—
MgO	4.6	3.3	10.3
Na ₂ O, K ₂ O	0.8	9.6	0.3
Ba ₂ O ₃	10.6	4.7	—
BaO	—	0.9	—

^aAfter Hull (1981).

Table 5.2
Properties of glass fibers

Property	E-glass	S-glass
Diameter (μm)	5–25	5–15
Density (g/cm^3)	2.54	2.49
Tensile strength (GPa)	2.4	4.5
Elongation at break (%)	3–4	5.4
Young's modulus (GPa)	72.4	85
Coefficient of thermal expansion ($10^{-6}/\text{K}$)	5.0	5.6

military applications. Their moduli are about 20% greater and the creep resistance is significantly better than E-glass fibers.

5.2.2. Silane treatments of glass fibers

5.2.2.1. Chemical bonding theory

Glass fiber-PMCs have been used extensively for over three decades, partly indebted to the development of silane coupling agents. Silane agents are intended to act as a protective coating for glass fiber surfaces and as a coupling agent to promote the adhesion with the polymer matrix. The silane agents are applied to glass fiber surface as a size along with other components. The composition of a size is complicated with the silane agent comprising a relatively small portion of the material. Table 5.3 lists the general proportion of components in a commercial size used for epoxy systems, the balance being the solvent or carrier.

The subject of silane chemistry and its interaction with both glass surface and polymer resins have been studied extensively. Since the silane coupling agent for improving the bond quality has first appeared in the literature (Rochow, 1951), a wide variety of organofunctional silanes has been developed, prominently by Plueddemann and coworkers. An early compilation of this subject for epoxy and polyester matrix composites (Plueddemann et al., 1962, Clark and Plueddemann, 1963; Plueddemann, 1974), and more recent reviews on the use of silane agents and

Table 5.3
Typical components of a glass fiber size^a

Component	Per cent
Film-forming resin	1–5
Antistatic agent	0.1–0.2
Lubricant	0.1–0.2
Coupling agent	0.1–0.5

^aAfter Dow Corning Corporation (1985).

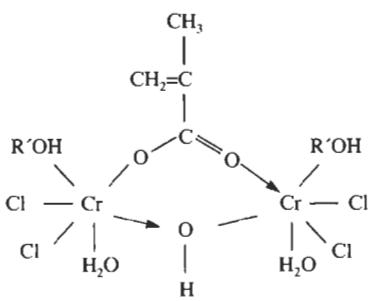
their effects on composite mechanical properties (Plueddemann 1981, 1982, 1988; Ishida, 1984) are useful references on this subject.

Several theories have been proposed to explain the interfacial bonding mechanisms of silane coupling agents which are responsible for the improvement of mechanical performance and hygrothermal stability of composites. Among these, the most widely accepted is chemical bonding (Schrader et al., 1967; Schrader and Block, 1971; Koenig and Shih, 1971; Ishida and Koenig, 1980). Other theories include those associated with preferential absorption (Erickson, 1970), restrained layer (Hooper, 1956), coefficient of friction (Outwater, 1956), and wettability and surface energy effect (McGarry, 1958; Bascom, 1965). Although all of these theories have some merits, the chemical bonding theory has been well established and confirmed many times. Therefore, development of silane coupling agents have been based on the concept of chemical reactivity between the inorganic substrate and the organic resin. A large variety of silanes containing different organofunctional groups have been developed for different resin chemistry (e.g. epoxy, vinyl and amino). Representative commercial coupling agents are listed in Table 5.4, according to Plueddemann (1982). Among the various silane agents with vinyl, hydroxy, thio, carboxy, amine, alkyl and ester substitutions, γ -methacryloxypropyl trimethoxysilane (γ -MPS) in particular has established wide commercial applications for polyester resin composites today.

In the chemical bonding theory, the bifunctional silane molecules act as a link between the resin and the glass by forming a chemical bond with the surface of the glass through a siloxane bridge, while its organofunctional group bonds to the polymer resin. This co-reactivity with both the glass and the polymer via covalent primary bonds gives molecular continuity across the interface region of the composite (Koenig and Emadipour, 1985). A simple model for the function of silane coupling agents is schematically illustrated in Fig. 5.3, according to Hull (1981). The general chemical formula is shown as X_3Si-R , multi-functional molecules that react at one end with the glass fiber surface and the other end with the polymer phase. R is a group which can react with the resin, and X is a group which can hydrolyze to form a silanol group in aqueous solution (Fig. 5.3(a)) and thus react with a hydroxyl group of the glass surface. The R-group may be vinyl, γ -aminopropyl, γ -methacryloxypropyl, etc.; the X-group may be chloro, methoxy, ethoxy, etc. The trihydroxy silanols, $Si(OH)_3$, are able to compete with water at the glass surface by hydrogen bonding with the hydroxyl groups at the surface (Fig. 5.3(b)), where M stands for Si, Fe, and/or Al (see Table 5.1). The type of organofunctional group and the pH of the solution dictates the composition of silane in the dilute aqueous solution. When the treated fibers are dried, a reversible condensation takes place between the silanol and M-OH groups on the glass fiber surface, forming a polysiloxane layer which is bonded to the glass surface (Plueddemann, 1974) (Fig. 5.3(c)).

Therefore, once the silane coated glass fibers are in contact with uncured resins, the R-groups on the fiber surface react with the functional groups present in the polymer resin, such as methacrylate, amine, epoxy and styrene groups, forming a stable covalent bond with the polymer (Fig. 5.3(d)). It is essential that the R-group

Table 5.4
Representative commercial coupling agents^a

Trade name	Organofunctional group	Chemical structure
Q9-6300	Vinyl	$(\text{CH}_3\text{O})_3\text{SiCH}=\text{CH}_2$
Z-6067	Chloropropyl	$(\text{CH}_3\text{O})_3\text{SiCH}_2\text{CH}_2\text{CH}_2\text{Cl}$
Z-6040	Epoxy	$(\text{CH}_3\text{O})_3\text{SiCH}_2\text{CH}_2\text{CH}_2\text{OCH}_2\text{CH}(\text{O})\text{CH}_2$
Z-6030	Methacrylate	$(\text{CH}_3\text{O})_3\text{SiCH}_2\text{CH}_2\text{CH}_2\text{OOC}(\text{CH}_3)=\text{CH}_2$
A-1100 (UCC)	Primary amine	$(\text{C}_2\text{H}_5\text{O})_3\text{SiCH}_2\text{CH}_2\text{CH}_2\text{NH}_2$
Z-6020	Diamine	$(\text{CH}_3\text{O})_3\text{SiCH}_2\text{CH}_2\text{CH}_2\text{NHCH}_2\text{CH}_2\text{NH}_2$
Z-6062	Mercapto	$(\text{CH}_3\text{O})_3\text{SiCH}_2\text{CH}_2\text{CH}_2\text{SH}$
Z-6032	Cationic styryl	$(\text{CH}_3\text{O})_3\text{SiCH}_2\text{CH}_2\text{CH}_2\text{NHCH}_2\text{CH}_2\text{H}^+\text{Cl}^-$
S-3076S (Hercules)	Azide	$(\text{CH}_3\text{O})_3\text{Si}-\text{R}-\text{SO}_2\text{N}_3$
Volan-A (DuPont)	Methacrylatochrome	
TTN-33 (Kenrich)	Methacrylate-titanate	$(\text{CH}_2=\text{C}(\text{CH}_3)\text{COO})_3\text{TiOCH}(\text{CH}_3)_2$
Caveco-Mod	Methacrylate-Al-zirconate	Undisclosed
XI-6100	90/10 mix PhSi(OCH ₃) ₃ /Z-6020	
XI-6106	Z-6040-modified Cymel-303 melamine resin	
XI-6121	Product of Z-6020 with isocyanatoethylmethacrylate (IEMA)	

^aAfter Plueddemann (1982).

and the functional group be chosen so that they can react with the functional groups in the resin under given curing conditions. Furthermore, the X-groups must be chosen, that can hydrolyze to allow reactions between the silane and the M-OH group to take place on the glass surface. Once all these occur, the silane coupling agents may function as a bridge to bond the glass fibers to the resin with a chain of primary strong bond.

A number of factors affect the microstructure of the coupling agent which, in turn, controls the mechanical and physical properties of the composites made therewith. They are the silane structure in the treating solution and its organofunctionality, acidity, drying conditions and homogeneity, the topology and the chemical

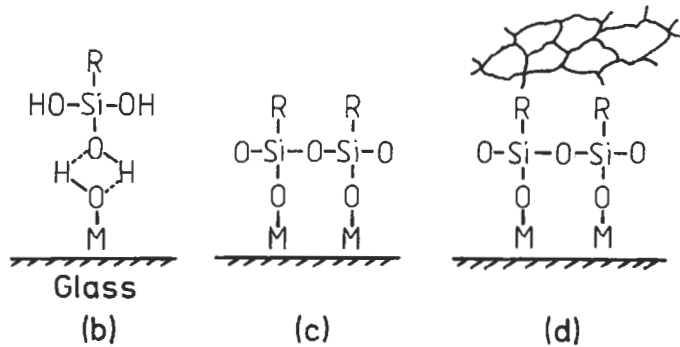


Fig. 5.3. Functions of a coupling agent: (a) hydrolysis of organosilane to corresponding silanol; (b) hydrogen bonding between hydroxyl groups of silanol and glass surface; (c) polysiloxane bonded to glass surface; (d) organofunctional R-group reacted with polymer. After Hull (1981).

composition of the fiber surface. Much of previous work has been concentrated on the examination of the interaction of thermosetting resins, most notably epoxy and polyester resins, and silane coupling agents with the glass surface. FTIR spectroscopy (Ishida and Koenig, 1978, 1979, 1980; Chiang et al., 1980; Antoon and Koenig, 1981; Ishida et al., 1982; Chiang and Koenig, 1981; Culler et al., 1986; Liao, 1989) and NMR (Culler et al., 1986; Hoh et al., 1988; Albert et al., 1991) have been the principal techniques used for this purpose. In particular, with the development of FTIR spectroscopy, it is possible to observe the chemical reaction in the silane interface region during cure. In recent years, a surface-sensitive technique of time-of-flight secondary ion mass spectroscopy (TOF SIMS) in combination with XPS has been extensively used by Jones and coworkers (Jones and Pawson, 1989; Cheng et al., 1992; Wang D. et al., 1992a, b, c; Wang and Jones, 1993a, b).

5.2.2.2. Interpenetrating polymer network

The chemical bonding theory explains successfully many phenomena observed for composites made with silane treated glass fibers. However, a layer of silane agent usually does not produce an optimum mechanical strength and there must be other important mechanisms taking place at the interface region. An established view is that bonding through silane by other than simple chemical reactivity are best explained by interdiffusion and interpenetrating network (IPN) formation at the interphase region (Plueddemann and Stark, 1980; Ishida and Koenig, 1980). A schematic representation of the IPN is shown in Fig. 2.4. In a study of γ -methylamino-propyltrimethoxysilane (γ -MPS) with a styrene matrix using FTIR, Ishida and Koenig (1979) showed that the frequency of the carbonyl group of γ -MPS shifted upon polymerization of the matrix. The frequency of the polymerized γ -MPS was different from the homopolymerized γ -MPS without the matrix. This suggests that copolymerization has taken place through interdiffusion. A similar

indication of interpenetration was also observed at the γ -aminopropyl-triethoxysilane (APS)/polyethylene interface (Sung et al., 1981). The coupling agent–resin matrix interface is a diffusion boundary where intermixing takes place, due to penetration of the resin into the chemisorbed silane layers and the migration of the physisorbed silane molecules into the matrix phase (Schrader, 1970).

The synergism of these two major bonding mechanisms with a silane coupling agent, i.e., the chemical reaction and the IPN theories, is of particular importance in composites containing thermoset matrices. It is yet to be shown, however, to what extent chemical bonding contributes to the total interface bond strength in thermoplastic matrices, although there are appreciable improvements in flexural strength of composites containing silane treated fibers, particularly those fabricated by compression molding, see Table 5.5. The compatibility between the silane and the matrix resin appears to be more important than chemical bonding in thermoplastic matrix composites, although chemical reaction can add additional strength. The reactivity may be improved by tailoring the unreactive molecules in the thermoplastic so that it consists of special functional groups capable of bonding with the coupling agent. Another approach is to include chemicals in the size that may cause local chain scission of the molecules near the fiber, allowing chemical reaction to take place so that coupling occurs directly with the molecules.

The mechanical properties of the blend of silane/size and bulk epoxy matrix (at concentrations representing likely compositions found at the fiber–matrix interface region) also suggest that the interaction of size with epoxy produces an interphase which is completely different to the bulk matrix material (Al-Moussawi et al., 1993). The interphase material tends to have a lower glass transition temperature, T_g , higher modulus and tensile strength and lower fracture toughness than the bulk matrix. Fig. 5.4 (Drown et al., 1991) presents a plot of T_g versus the amount of

Table 5.5
Improvement in flexural strength due to silane treatments in glass fiber thermoplastic matrix composites^a

Polymer–silane system	Percentage strength improvement			
	Compression molded		Injection molded	
	Dry	Wet	Dry	Wet
Nylon–aminosilane F	55	115	40	36
Nylon–cationic silane H	85	133	40	45
PBT–aminosilane F	21	–	23	24
PBT–cationic silane H	60	47	28	11
Polypropylene–silane F	8	18	7	10
Polypropylene–silane H	86	89	16	16

^aAfter Plueddemann (1988).

Wet, after 2 h in boiling water; PBT, polybutylene terephthalate.

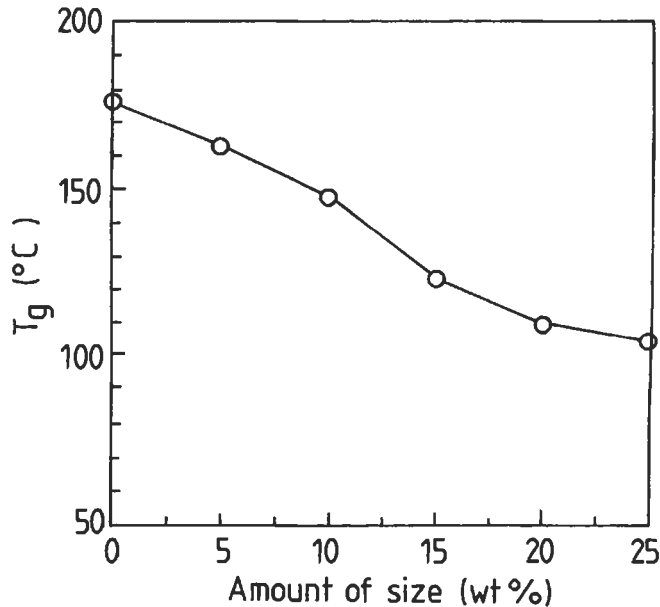


Fig. 5.4. Glass transition temperature, T_g , measured by dynamic mechanical analysis as a function of wt% epoxy-compatible PPG size. After Drown et al. (1991).

epoxy-compatible size added to the stoichiometric mixture. It is clearly seen that the polymer created by the addition of the commercial size exhibits a monotonic decrease in T_g , suggesting that the silanes and other ingredients present in the size act to reduce the crosslink density of mixtures. When the fiber was treated with epoxy-compatible sizing containing silane agents, the composite shows a higher interlaminar shear strength (ILSS), and flexural strengths in both the longitudinal and transverse directions than the composite without silane sizing, as shown in Fig. 5.5 (Drown et al., 1991). This finding is attributed to the improved interface bond quality due to the silane size. However, the brittle interphase material promoted matrix cracks near the broken fiber ends as observed in fiber fragmentation tests.

On the contrary, a completely opposite result was reported by Chua and Piggott (1992). The presence of large amounts of siloxane γ -MPS in a polyester resin was found to reduce the modulus and compressive strength, while increasing the fracture toughness of the interphase material. This anomaly appears to be associated with plasticization of the inherently brittle resin by the silane size, making the interphase material softer and more ductile than the bulk matrix. As a result, the debonding and the fiber pull-out forces were reduced substantially, suggesting that the chemisorbed layer on the fiber surface constituted the debonding and sliding surface (Chua et al., 1992a). Whether the interphase material created by interdiffusion of silane sizing is more ductile or brittle than the bulk matrix material is an issue of great importance because the interphase properties often dictate the gross

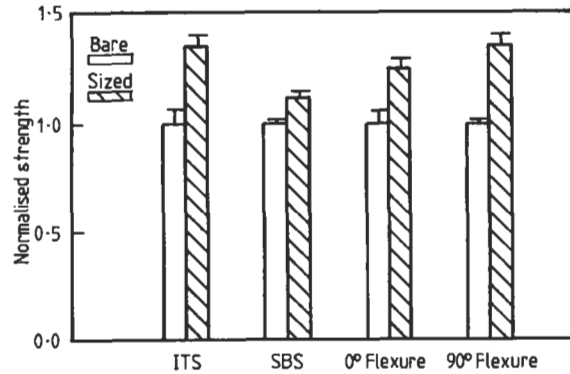


Fig. 5.5. Normalized interfacial shear strength of unsized (bare) and sized E-glass fiber-epoxy matrix composites measured from the interfacial testing system (ITS, equivalent to fiber push-out test), short beam shear (SBS) test, 0° flexural test and 90° flexural test. After Drown et al. (1991).

mechanical performance and structural integrity of the composite as a whole. Since the details of the interface reaction is specific to each combination of fiber and matrix materials with totally different chemical and atomic compositions and morphological nature, no general conclusions can be drawn regarding the ductility and fracture toughness of the interphase relative to the surrounding matrix.

5.2.2.3. Effects of water

Apart from the chemical reaction and the IPN discussed in the foregoing, another important characteristic of silane treatment is its ability to provide the glass fibers with a water resistant bond. The effect of water degradation on untreated glass fiber-resin matrix interface is found to be much pronounced. Small molecules of water penetrate into the interface of untreated fibers by diffusion and filtering through voids and cracks of the resin or by capillary migration along the fibers, that are eventually absorbed by the glass fiber. The randomly distributed groups of oxides on the surface of glass, such as SiO_2 , Fe_2O_3 and Al_2O_3 , absorb water as a hydroxyl group. The water then forms a weak hydrogen bond with these oxides. Other oxides also absorb water and become hydrated. Water hydrolyzes the existing physical bonds at the interface and destroys the adhesion, which ultimately results in mechanical failure of the composite system (Ishida and Koenig, 1978, 1980). Immersion of untreated fiber composites in hot water for a long period causes the polymer resin to swell, followed by shrinkage due to leaching out of low molecular weight materials from the resin, in addition to the above water absorption processes.

When glass fibers are treated with hydrolyzed silane solution, multi-layers of the silane coupling agent are deposited on the fiber surface. The thickness and orientation of the layers are determined by a number of factors, such as conditions of deposition, topology of the glass surface, concentration of the solution and the length of the treatment time (Ishida and Koenig, 1979, 1980). Schrader (1970) has proposed that there are three different structural regions in the deposited layer: (i)

physisorbed region; (ii) chemisorbed region; and (iii) chemically reacted region. The physisorbed region is the outermost layer, and consists mainly of the bulk of the deposited silane. The layer of weak oligomeric siloxanols hydrolyzes easily and is extracted with water even at room temperature. The chemisorbed region is the next layer which can only be extracted by boiling water after prolonged immersion. It consists mainly of higher oligomeric siloxanols that possess better resistance to hydrolysis than the lower siloxanols.

The innermost region next to the glass surface is stable and resistant to extraction by hot water and may be regarded as the chemically reacted region. The interconnecting cross-linking exists in this region in the form of a three-dimensional network of siloxane. The extent of cross-linking is found to increase from the outer layers to the glass surface with corresponding increase in the mechanical and hydrothermal stability (Ishida and Koenig, 1980). Fig. 5.6 shows the schematic structure of the silane remaining on the glass surface after extractive hydrolysis with hot water, according to Cheng et al., (1993). The individual characteristics of each of these silane regions play a major role in controlling the interface stability and the mechanical properties of the composites under both dry and hot/wet conditions. The chemically reacted region is most likely responsible for the high resistance of the interfacial bond of silane treated composites to hygrothermal attack. Fig. 5.7 exemplifies the shear strength measured as a function of immersion time in water. It is also suggested that the silane agent, when present as a chemisorbed layer, not only provides protection against attack by water, but also restores, to some extent, the damage produced along the fiber–matrix interface once dried at a high temperature (Chua et al., 1992b).

Schrader (1974) reported that the interface shear strength in a hygrothermal environment is at its maximum when the multi-layer silanes on the glass fibers remain after being washed in boiling water. On the other hand, the pull-out strength

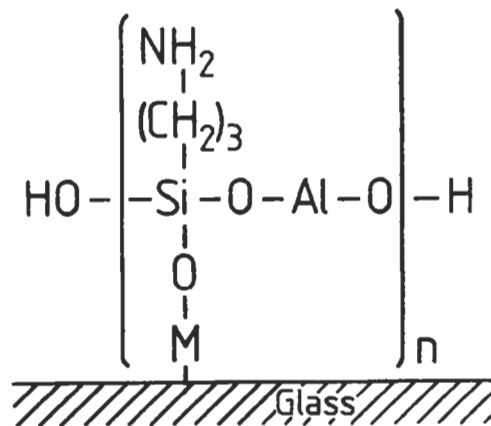


Fig. 5.6. Schematic structure of the silane remnant remaining on the glass fiber surface after extractive hydrolysis with hot water. After Cheng et al. (1993).

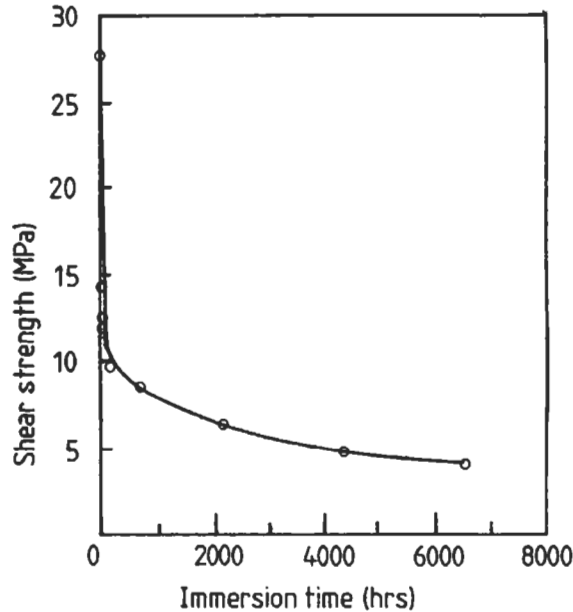


Fig. 5.7. Effect of immersion in hot water on interfacial bond strength of silane treated glass fiber-epoxy matrix composite. After Koenig and Emadipour (1985).

under dry condition is found to be highest when the multilayer silanes on the glass fibers are washed with boiling water (Emadipour et al., 1982). It appears that the amount of silanes needed for protection against hygrothermal condition is different from that for dry condition (Liao, 1989). It is repeatedly confirmed that a thicker silane layer does not necessarily result in improvement in hydrothermal stability of the interface bond; but on the contrary, it may have an adverse effect on the bond strength of the interface. An excessive amount of coupling agent is not effective, rather impairing the properties of the interphase (Chua et al., 1992b). Koenig and Emadipour (1985) also suggested that there is an optimum concentration of silane which would produce the most favorable result on interfacial shear strength, for example approximately 0.5% concentration of *N*-2-aminoethylene-3-aminopropyl trimethoxysilane (AAPS) for glass fiber-epoxy matrix composites. For this purpose, partial removal of the thick silane layer is suggested prior to fabrication of the composite to enhance the mechanical performance, as demonstrated in Fig. 5.8. The interlaminar fracture toughness of glass fiber-polyester matrix composites is also influenced by the type of silane and solution concentration used (Suzuki et al., 1993). There is an optimum amount of silane required to achieve the maximum fracture toughness as measured in double-cantilever-beam tests. An excessive amount of silane decreases the fracture toughness with unstable crack propagation, as evidenced in force-displacement curves as shown in Fig. 5.9.

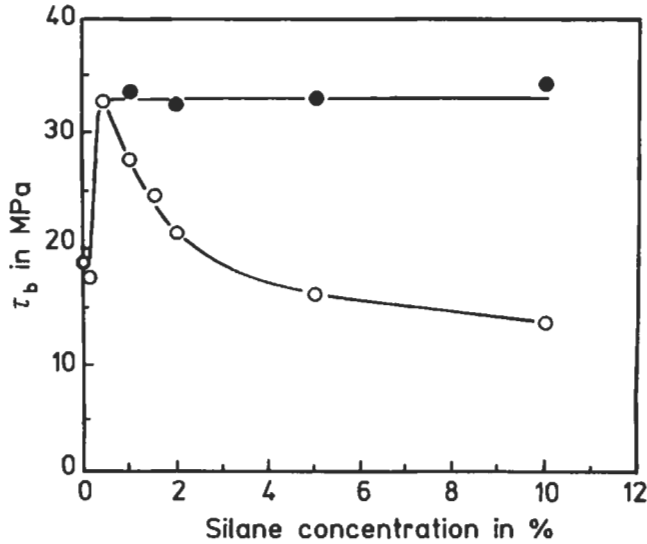


Fig. 5.8. Effect of diamino-silane solution concentration and modification on interfacial bond strength τ_b of GFRP: (○) silane treated; (●) silane treated and partially removed. After Koenig and Emadipour (1985).

5.3. Carbon fibers

5.3.1. Structure and properties of carbon fibers

The surface properties of carbon fibers are intimately related to the internal structure of the fiber itself, which needs to be understood if the surface properties are to be modified for specific end applications. Carbon fibers have been made from a number of different precursors, including polyacrylonitrile (PAN), rayon (cellulose) and mesophase pitch. The majority of commercial carbon fibers currently produced are based on PAN, while those based on rayon and pitch are produced in very limited quantities for special applications. Therefore, the discussion of fiber surface treatments in this section is mostly related to PAN-based carbon fibers, unless otherwise specified.

The properties of a carbon fiber are a direct reflection of the structure of graphite which is highly anisotropic on a nanoscopic scale. The basic structure of the carbon fibers is the graphite crystallites which, in turn, are composed of turbostratically layered basal planes, as schematically shown in Fig. 5.10. The high bond strength between the carbon atoms in the basal plane gives an extremely high modulus along the fiber axis, while the weak van der Waals type of bonding between the neighboring layers produces a low modulus along the edge plane. The edges and corners of these crystallites intersect the fiber surface. A schematic three-dimensional representation of the structure of a PAN-based carbon fiber is shown in Fig. 5.11, where irregular space filling and the distortion of the graphite basal planes are seen.

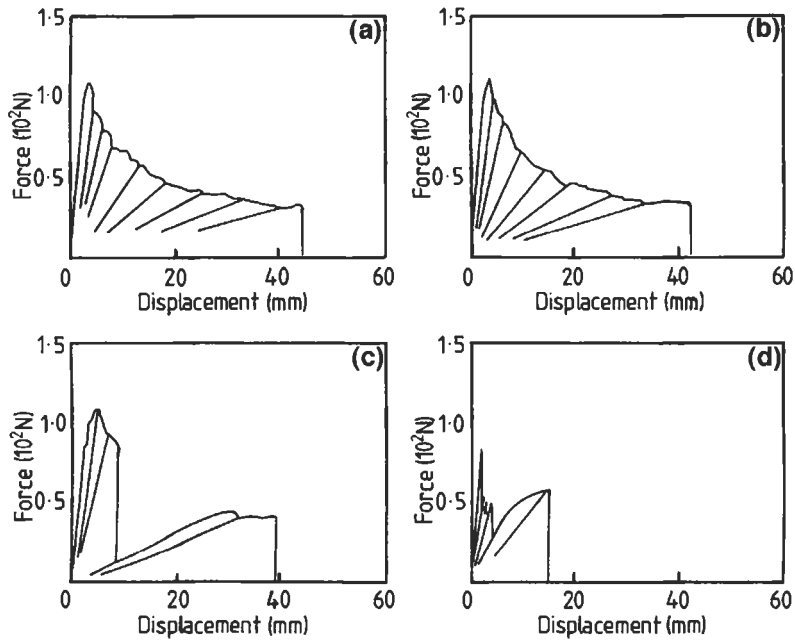


Fig. 5.9. Load–displacement records of double-cantilever-beam tests on E-glass fiber–vinyl ester matrix composites. (a) 0.4 wt% epoxy silane; (b) 0.01 wt% methacrylate silane; (c) 0.4 wt% methacrylate silane; (d) 1.0 wt% methacrylate silane. After Suzuki et al. (1993).

This means that it is necessary to have a high degree of preferred orientation of hexagonal planes along the fiber axis if a high modulus is desired. To improve the orientation of graphite crystals, various kinds of thermal and stretching treatments,

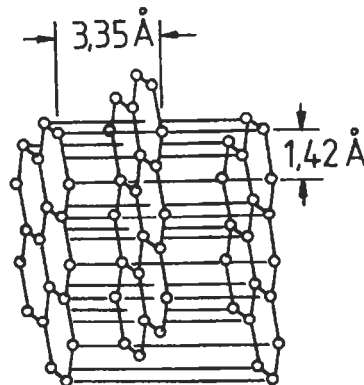


Fig. 5.10. Schematic drawing of graphite lattice structure. After Singer (1989).

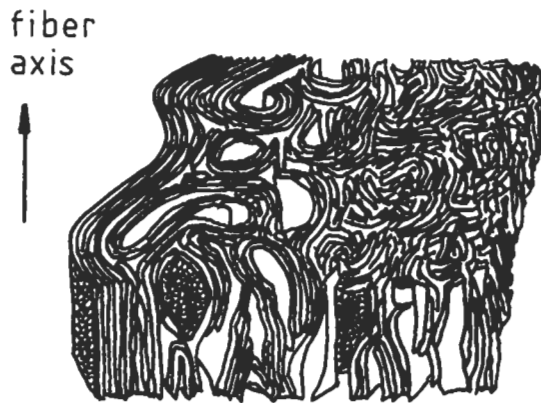


Fig. 5.11. Schematic drawing of a three-dimensional model of a carbon fiber. After Bennett and Johnson (1978).

i.e., stabilization and carbonization followed by graphitization, are carried out with accurate control of temperature and time.

Carbon fibers can be grouped into high strength (Type I), high modulus (Type II) and ultra-high modulus (Type III) types, and their representative properties are given in Table 5.6. Mechanical properties of these fibers are determined by the composition of the precursor and the temperature–time profile of the manufacturing processes. Generally speaking, the higher the maximum processing temperature, the greater is the degree of crystalline orientation in the fiber axis, and hence the higher is the fiber modulus. An increase in modulus is normally achieved at the expense of a reduction in strength and ductility because of increasing sensitivity to flaws.

Table 5.6
Properties of carbon fibers

Property	High strength (HS, Type I)	Intermediate modulus (IM, Type II)	High modulus (HM, Type III)
Diameter (μm)	6–8	6–9	7–9
Density (g/cm^3)	1.7–1.8	1.74	1.85–1.96
Tensile strength (MPa)	3000–5600	4800	2400–3000
Elongation at break (%)	1.0–1.8	2.0	0.38–0.5
Young's modulus (GPa)	235–295	296	345–520
Specific strength (10^6 cm)	17.5–32.7	28.2	15.7
Specific modulus (10^6 cm)	1370–1720	1740	1850–2790
Coefficient of thermal expansion ($10^{-6}/\text{K}$)			
Axial	–0.5	–	–1.2
Radial	7	–	12

At the end of the fiber manufacturing processes, a size is normally applied to the carbon fibers for use as reinforcement of PMCs. Sizing of carbon fiber involves application of an organic film to protect the fiber during fabrication into structural parts and components. The amount of sizing varies between 0.5–1.5 wt% of the fiber depending on the type and application of fibers. Sizes are intended:

- (1) to protect the fiber surface from damage,
- (2) to bind fibers together for ease of processing,
- (3) to lubricate the fibers so that they can withstand abrasive tension during subsequent processing operations,
- (4) to impart anti-electrostatic properties, and
- (5) to provide a chemical link between the fiber surface and the matrix and thus to improve the bonding at the interface.

Sizing for different fabrication processes serves different purposes. Specifically, the sizing for filament winding is designed to hold the tow of fibres as a relatively cohesive bundle so that it can pass through the eyelets and guide without spreading. At the same time, the size must also be sufficiently flexible to allow the tow to be opened up and readily impregnated by the liquid resin. Similar requirements are necessary for weaving. In contrast, the primary role of sizing in prepregging is to hold down loose fiber ends and gather them into small bundles to avoid severe misalignment in the final prepreg sheet. Apart from these purposes of sizing, there are no appreciable effects on the mechanical properties of composites when compared with those containing unsized fibers (Bascom and Drzal, 1987).

5.3.2. Surface treatments of carbon fibers

5.3.2.1. Types of surface treatment

The poor shear strength of carbon fiber reinforced polymers, those reinforced with high modulus fibers in particular, is generally attributed to a lack of bonding at the fiber–matrix interface. Extensive research has been directed toward the development of surface treatment techniques for carbon fibers to improve the fiber–matrix interface bonding. The mechanisms of bonding between carbon fibers and polymer matrices are as complex as that of glass fibers, and there are more complications associated with the carbon fiber surface because it is highly active and readily absorbs gases. A range of active functional groups can be produced by surface treatment. Reviews on this subject, such as important parameters controlling the effectiveness of various surface treatment methods, can be found in numerous references including Scolar (1974), Delmonte (1981), Riggs et al. (1982), Donnet and Bansal (1984), Ehrburger and Donnet (1985), Wright (1990) and Hughes (1991).

Surface treatments of carbon fibers can in general be classified into oxidative and non-oxidative treatments. Oxidative treatments are further divided into dry oxidation in the presence of gases, plasma etching and wet oxidation; the last of which is carried out chemically or electrolytically. Deposition of more active forms of carbon, such as the highly effective whiskerization, plasma polymerization and grafting of polymers are among the non-oxidative treatments of carbon fiber surfaces.

Dry oxidation: Dry oxidative treatments are normally carried out with air, oxygen or oxygen containing gases such as ozone and CO₂ at low or elevated temperatures. The dry oxidative treatment at a high temperature results in drastic changes in surface properties, and often causes excessive pitting of the fiber surface, impairing the fiber tensile strength (Novak, 1969). In this process, the surface layers simply burn away unevenly to create pits in lines that coalesce into channels, resulting in a high surface rugosity. These active sites could be related to the edge plane of the fiber surface. Metallic impurities such as oxides of Cu, Pb, V and transition metals are found to enhance the degradation rate even at a low temperature (McKee, 1970).

Plasma etching: Plasma treatment or electric discharge has become one of the most popular methods for improving the fiber–matrix adhesion in recent years. Brief reviews of this topic for surface treatments of carbon, aramid and polyethylene fibers are given by Donnet et al. (1988), Yuan et al. (1991), Bascom and Chen (1991) and Garbassi and Occhiello (1993), and a summary is presented below. Plasma is a region of space in which high energy species, like electrons, ions, radicals, ionized atoms and molecules, are present. Immersion of an object of any shape in a plasma induces strong interactions of its surface with the energetic species present therein. The fundamental principle of a plasma treatment technique is to induce the formation of active species in a gas by a suitable energy transfer. Different types of plasma can be generated depending on the experimental conditions. Among the most frequently used are thermal (i.e. hot) plasma, glow discharge (i.e. cold plasma), and corona discharge.

Thermal plasma of very high temperature is generated by coupling the energy into a high pressure gas under equilibrium conditions. There are many different sources of energy that include dc, ac, radio frequency and microwave. The result of treatment is that many chemical bonds on the surfaces are broken, forming very reactive species. Non-equilibrium corona discharges are generated at a high pressure gas, such as air, by using highly charged wires or points. Cold plasma operates at a low pressure under non-equilibrium conditions, and has been used extensively for neon light tubes. The process is relatively easy to control and flexible compared to other methods generating plasma, because any gas can be used. Schematic presentation of a continuous cold plasma treatment system is shown in Fig. 5.12. One of the major advantages of cold plasma treatment is that both etching and deposition can be performed on the substrate surface. When a low pressure gas, such as oxygen, chloride and fluoride, is introduced, active species are formed that can hit and interact/functionalize the surface. This leads to abstraction of materials from the surface (i.e. etching). On the other hand, if hydrogen or fluorocarbon is excited, radicals can be formed (i.e. deposition or grafting). One of the characteristic differences between these processes is the treatment time: surface etching is very fast, requiring only seconds, whereas the deposition of sizeable coating needs minutes. Further details of deposition techniques are included in the discussion of the non-oxidative treatment methods.

Wet oxidation: Several types of liquid-phase oxidizing agents, such as nitric acid, acidic potassium permanganate, acidic potassium dichromate, dichromate permanganate, hydrogen peroxide, ammonium bicarbonate and potassium persulfate, have

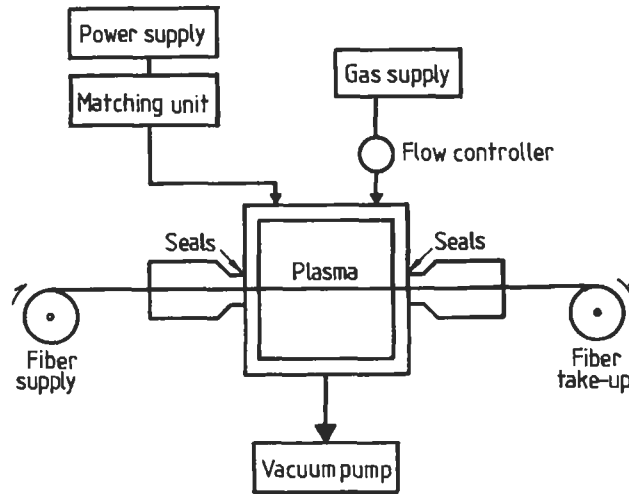


Fig. 5.12. Schematic representation of a continuous cold plasma treatment. After Garbassi and Occhiello (1993).

been used with varying degrees of success. These liquid-phase treatments are generally milder than the ones with a gaseous-phase, and do not cause excessive pitting and hence degradation of the fiber strength. Several factors, such as acid concentration, exposure time and temperature and mode of treatment, influence the effectiveness of these oxidative processes. Depending on the type of carbon fibers, nitric acid treatment in general increases the surface area, surface functionality and surface oxide contents with increasing treatment time and temperature and acid concentration (Scolar, 1974). This treatment generally causes an appreciable weight loss and smoothing of the fiber surface by removing the surface irregularities (Donnet and Ehrburger, 1977).

Electrolytic or anodic oxidation is fast, uniform and best suited to mass production. This process is most widely used for treatment of commercial carbon fibers. The oxidation mechanism of most carbon fibers is characterized by simultaneous formation of CO_2 and degradation products that are dissolved in the electrolyte of alkaline solution or adhere onto the carbon fiber surface in nitric acid. Only minor changes in the surface topography and the surface area of the fiber are obtained with a small weight loss, say, normally less than 2%.

Non-oxidative treatments: Several non-oxidative treatment techniques have been developed for carbon fibers, which include whiskerization and plasma deposition of organic and polymer coatings. Whiskerization involves a nucleation process and the growth of very thin and high strength single crystals of the chemical compounds, such as silicon carbide (SiC), titanium dioxide (TiO_2) and silicon nitride (Si_3N_4), on the fiber surface perpendicular to the fiber axis (Goan and Prosen, 1969). The whiskers grow from individual fibers, which usually initiate at the points of defects, compositional heterogeneities, metallic inclusions or structural irregularities and

imperfections. The plasma polymerization process employs polymerizable organic vapors, such as polyamide (Goan and Prosen, 1969), polyimide (Marks et al., 1975), organosilanes (Goan and Prosen, 1969), other alternating and block polymers like styrene and maleic anhydride (Riess et al., 1974), propylene (Jang et al., 1988), and acrylonitrile and styrene monomers (Sung et al., 1982; Dagli and Sung, 1989). Plasma polymerization is shown to increase the polar component of surface free energy of the carbon fiber (Dagli and Sung, 1989; Donnet and Guilpain, 1991). The polymers used for plasma treatment should possess not only the capability of being fixed on the fiber surface by covalent or ionic bonds, but also on the compatibility with the resin matrix. Further details of fiber coating techniques with appropriate polymeric materials, including plasma polymerization to improve the transverse composite fracture toughness, are presented in Section 7.2.

5.3.2.2. Effects of surface treatment on fiber properties

Improvements in ILSS, flexural, tensile, compressive and off-axis strengths of the composite which arise from various surface treatments are attributed to the changes in surface area, rugosity and surface functional groups and the removal of weak outer layers. Nevertheless, there is no simple, direct relationship of the interfacial bond strength with these factors. The increase in fiber surface area by the formation of pits or enhancement of longitudinal striations certainly improves mechanical anchoring of the matrix and interpenetration between fiber and matrix. However, because the rugosity develops mainly in the fiber axial direction, the improvement of interfacial bonding is realized only in the same direction. This is evidenced by the preferential increase in the adhesion when a force is applied parallel to the fiber axis (Donnet et al., 1974). Moreover, the rugosity becomes an ameliorating factor only when the fiber is perfectly wetted by the liquid resin. This means that unless the resin penetrates into all the asperities present on the fiber surface, cure or polymerization of the resin always results in the formation of interfacial cavities, causing premature failure of the interfacial bond. Another important characteristic of chemically treated carbon fibers is that an outer weak layer containing various types of defects is removed by oxidation, which, in turn, results in a surface capable of supporting a high shear load (Drzal et al., 1983a). An incidental improvement of fiber strength is also reported with light anodic treatment (Bader et al., 1991). However, plasma etching in nitrogen or oxygen causes excessive removal of the fiber surface layer, reducing the fiber diameter by up to 22% (Jang et al., 1988).

Significant attention has been devoted to characterize the nature of the chemical groups produced by surface treatments as discussed above. However, there is still much controversy as to whether chemical bonding actually takes place at the interface region, and if so, to what extent it contributes to the fiber–matrix interface bonding of carbon fiber composites. A schematic model for chemical reaction between oxidized fibers and an epoxy resin is presented in Fig. 5.13, according to Horie et al. (1977). The strong covalent bonds could be either ether (–COH) or ester (–COOH) bonds which are produced by the reactions between the hydroxyl and carboxyl groups present at the fiber surface and the epoxy group of the resin. Oxidative treatments increase the oxygen (often more than double) and nitrogen

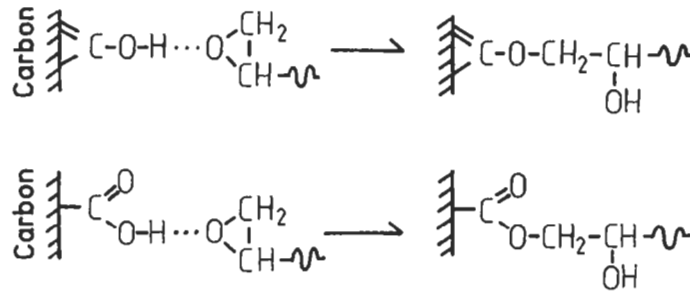


Fig. 5.13. Schematic models for chemical reaction between oxidized carbon fiber surface and epoxy matrix. After Horie et al. (1977).

contents (if nitric acid or ammonia is used as an oxidative medium) on the fiber surface, in the form of carboxyl, hydroxyl, carbonyl and phenolic groups, as illustrated by Fig. 5.14 (Scolar, 1974; Hopfgarten, 1978). In support of the chemical bonding theory, Scolar (1974) has previously attributed the large increase in ILSS to the surface reactivity of the treated fiber. Ko et al. (1982) also showed better retention of the composite strength with oxidized fibers when subjected to hydrothermal ageing. In addition, the oxidized carbon fibers may possess polar surface species, such as carboxylic group, which offers good wetting by the resin, as evidenced by a decrease in the contact angle after fiber surface treatment (Yamamoto et al., 1971). Other minor effects of surface groups are to promote

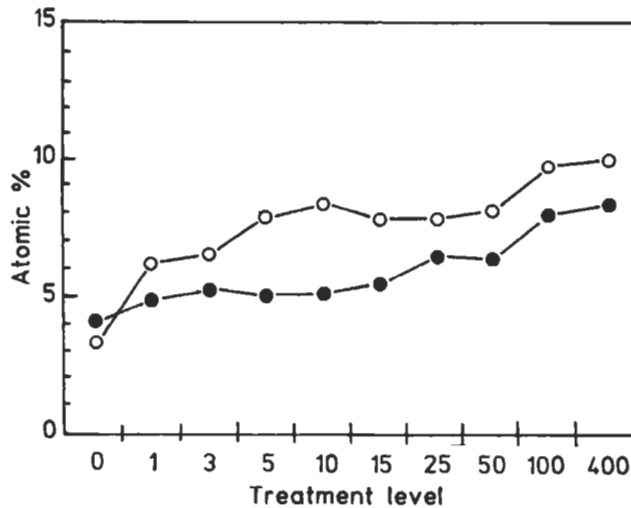


Fig. 5.14. Atomic percentage of oxygen (○) and nitrogen (●) contents for different levels of electrolytic oxidative surface treatment of XA carbon fibers. Commercial treatment level regarded as 100. After Baillie and Bader (1991).

additional bonding by developing weak adhesion mechanisms at the interface, such as dispersion force, dipolar interaction and hydrogen bonds.

In the light of the foregoing experimental evidence, the following can be summarized regarding the effects of carbon fiber surface treatments, depending on the methods and media employed:

- (1) There are substantial changes in fiber surface area with associated variations in rugosity depending on the oxidative treatment medium.
- (2) A weak surface layer may be removed, the removal being more serious in plasma etching than in wet oxidation.
- (3) There is an increase in the polar surface energy.
- (4) Chemical modification takes place and carboxyl, hydroxyl and carbonyl groups are produced on the fiber surface.

The mechanisms of chemical bonding due to the presence of functional groups have yet to be more thoroughly clarified, which change the energetics of the carbon fiber surface considerably. Better mechanical anchoring arising from the surface rugosity and the increased physical surface area involved in adhesion as well as the beneficial effect of removing the surface weak layers all contribute to an improved interfacial bond. However, there must be a limit to the improvement in bond strength by fiber surface treatment only. A decrease in bond strength and other deteriorating effects are expected to occur if the surface treatment is excessive, leading to severe damage of the fiber.

5.3.2.3. Effects of surface treatment on composite properties

The interlaminar shear, flexural and tensile strengths are increased as the principal effects of carbon fiber surface treatment on composite properties. The enhancement of these strength properties depend on the fiber elastic modulus, the degree of surface treatment and the type of resin and curing agent used. The largest improvement in ILSS is obtained for high modulus fibers. The compressive strength is also increased slightly (Norita et al., 1986), and the mode I interlaminar fracture toughness G_{Ic} for crack initiation is almost doubled (Ivens et al., 1991) with increasing degree of treatment. In general, an increase in the interfacial bond strength, τ_b , enhances the composite compressive strength by augmenting the load required to cause the interface to fail in transverse tension due to the fiber Poisson effect. Delamination is reduced in favor of microbuckling of surface treated fibers (Drzal and Madhukar, 1993). The improvement in interface bond strength, τ_b , or fracture toughness, G_{Ic} , due to fiber surface treatments has been confirmed using microcomposite tests, e.g. the fragmentation tests (Drzal et al., 1983a, b) and the fiber pull-out tests (Baillie and Bader, 1991). However, all these beneficial effects of improved strength properties are inevitably accompanied by a loss in the impact fracture toughness of unidirectional laminates or notched tensile strength of angle-ply laminates, as shown in Fig. 5.15 (Goan et al., 1973; Dauksys, 1973). Therefore, a careful balance has to be sought to ensure both adequate strength and toughness properties.

More recently Drzal and coworkers (Madhukar and Drzal, 1991a, b, 1992a, b; Drzal and Madhukar, 1993) have spent significant research efforts to establish the

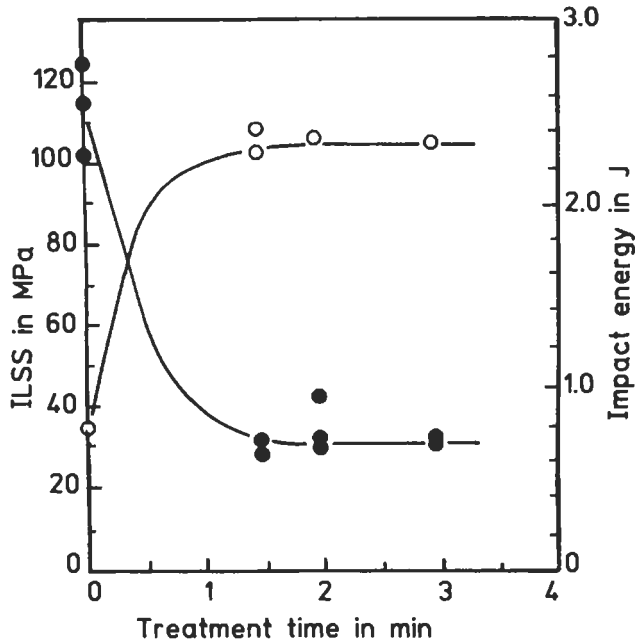


Fig. 5.15. Effect of carbon fiber surface treatment level on ILSS (○) and impact energy (●) for a carbon fiber-epoxy matrix composite. After Goan et al. (1973).

relationship between the interface bond strength and various mechanical properties of carbon fiber-epoxy matrix composites. A summary is given in the following for the composite containing AS4 PAN-based carbon fibers (Hercules, Inc.) with three different surface conditions. These are designated as AU4, AS4 and AS4C, that stand for 'as received' without any surface treatment, 'surface-treated' with an optimal electrochemical oxidation procedure, and 'surface treated and coated' with a 100–200 μm thick layer of epoxy. Fig. 5.16 shows a series of photoelastic stress patterns with increasing strain obtained in fiber fragmentation tests of AU and AS fibers embedded in an epoxy matrix. Examination of the different stress patterns has revealed that the AU fiber interacts with the matrix only through weak frictional force, whereas a relatively high stress is built up along the whole AS fiber. The interfacial bond strengths, τ_b , calculated based on the critical transfer lengths are 37.2, 68.3 and 81.4 MPa for the composites with AU4, AS4 and AS4C fibers, respectively.

The longitudinal tensile strength of the composite is found to increase with interfacial bond shear strength, Fig. 5.17(a), in particular when the failure process is dominated by the interface. When the interface bond strength is very high, the failure location changes from the interface to the surrounding matrix and the composite becomes brittle. With increasing interface bond strength, the compressive strength is also shown to be enhanced to a greater extent than the tensile strength.

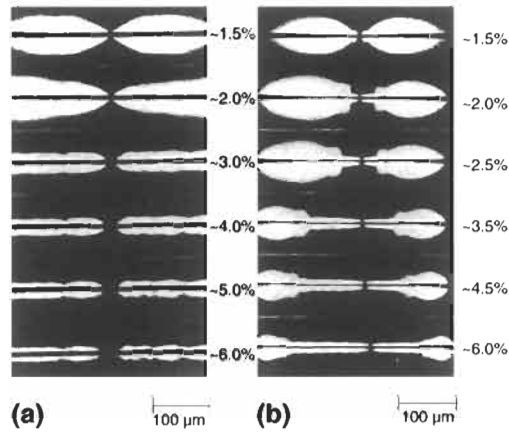


Fig. 5.16. Photoelastic patterns of carbon fibers in an epoxy matrix (a) without and (b) with surface treatment, at varying applied strains. After Drzal et al. (1983a). Reproduced by permission of Gordon and Breach Science Publishers.

This is attributed to the load increase required to cause the interface failure in transverse tension due to the Poisson effect under compression. In contrast, the tensile and compressive moduli are relatively insensitive to changes in the interface bond strength (Fig. 5.17(b)). However, for very high bond strength, the compressive modulus shows a marginal increase, due presumably to the presence of a brittle interphase surrounding the carbon fibers. There is little difference, within experimental scatter, between the flexural strength and bending moduli of the composites with low and intermediate interface bonding. But for the composites with the strongest interface bond strength, there is a significant increase in the flexural strength due to a change in the failure mode. That is, from an interface-initiated mode to a predominantly tensile (or compressive) mode.

The average values of the off-axis properties for three different composites are summarized in Table 5.7. It is noted that all strength values measured are sensitive to the level of interface bonding, while the modulus values are relatively insensitive to the interface adhesion. In particular, the transverse tensile and flexural strengths are a good indication of the interfacial adhesion. In case of ILSS, the results obtained from the Iosipescu shear test method show the least scatter amongst the three types of mechanical tests carried out. SEM study shows that the failure in both Iosipescu and short beam shear test specimens are matrix-dominated, while the ± 45 tension specimen is relatively insensitive to the variation of failure modes. Although the transverse tensile and transverse flexural modulus values are similar in terms of absolute magnitude and insensitivity to the interface adhesion level, there are significant differences between the transverse tensile and transverse flexural strengths. The transverse flexural strength is more sensitive to interface bonding, and is much higher than the transverse tensile strength. This observation may be explained in terms of the non-uniform stress distribution across the thickness of the specimen in three-point bending. In contrast, in transverse tension, the whole

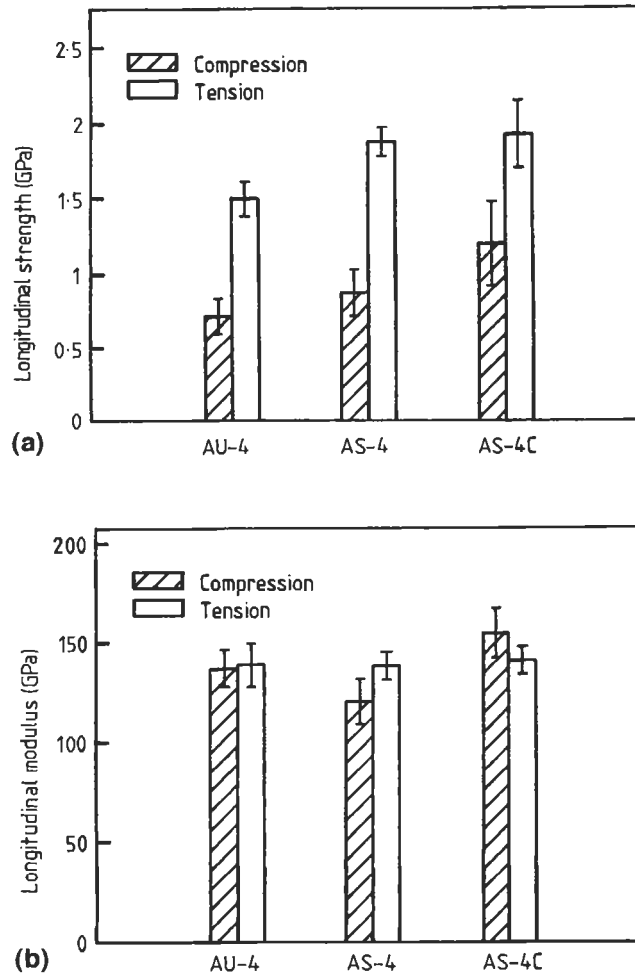


Fig. 5.17. Comparison between the compressive and tensile (a) strengths and (b) moduli of carbon fiber-epoxy matrix composites with three types of fiber surface condition. AU-4 without surface treatment; AS-4 with surface treatment; AS-4C with coating of pure epoxy after surface treatment. After Drzal and Madhukar (1993).

cross-sectional area of the specimen is under relatively uniform tension. The interlaminar/in-plane shear strength values obtained from these shear tests are consistent with each other, within experimental scatter, as shown in Fig. 5.18.

A good correlation of mode I interlaminar fracture toughness with interface bond quality is shown in Table 5.8. An increase in interfacial bond strength causes a slight improvement in mode I interlaminar fracture toughness. Its sensitivity is quite similar to that of transverse tensile strength, which is expected as one can envisage from the similar transverse tensile stress dominating the failure process in both the test methods. One of the most dominant failure mechanisms responsible for the

Table 5.7

Summary of off-axis properties of carbon fiber–828 mPDA epoxy matrix composites with different fiber surface treatments^a

Off-axis properties	AU-4 fiber	AS-4 fiber	AS-4C fiber
Transverse tensile strength (MPa)	18.0 ± 3.9	34.2 ± 6.2	41.2 ± 4.7
Transverse tensile modulus (GPa)	8.9 ± 0.6	9.8 ± 0.6	10.3 ± 0.6
Transverse flexural strength (MPa)	21.4 ± 5.8	50.2 ± 3.4	75.6 ± 14.0
Transverse flexural modulus (GPa)	10.2 ± 1.5	9.9 ± 0.5	10.7 ± 0.6
[±45] _{3s} in-plane shear strength (MPa)	37.2 ± 1.8	72.2 ± 12.4	97.5 ± 7.4
[±45] _{3s} in-plane shear modulus (GPa)	9.1 ± 1.5	6.2 ± 0.5	6.0 ± 0.2
Iosipescu in-plane shear strength (MPa)	55.0 ± 3.0	95.6 ± 5.1	93.8 ± 3.3
Iosipescu in-plane shear modulus (GPa)	7.2 ± 0.5	6.4 ± 1.0	7.9 ± 0.4
Short beam interlaminar shear strength (MPa)	47.5 ± 5.4	84.0 ± 7.0	93.2 ± 3.8

^aAfter Drzal and Madhukar (1993).

improved interlaminar fracture toughness is the matrix deformation enhanced by the strong interface bond. The improvement in fracture toughness from this source seems to be larger than the loss arising from the brittle interphase material surrounding the AS fiber. This observation has a practical implication in that for a composite containing a very brittle resin, such as a highly cross-linked epoxy, the interlaminar fracture toughness can be maximized by improving the interfacial bond to a sufficiently high level.

The increase in mode II interlaminar fracture toughness is even more significant than the mode I interlaminar fracture toughness. The similarity in the changes of magnitude of the mode II fracture toughness and the ILSS with regard to the level of

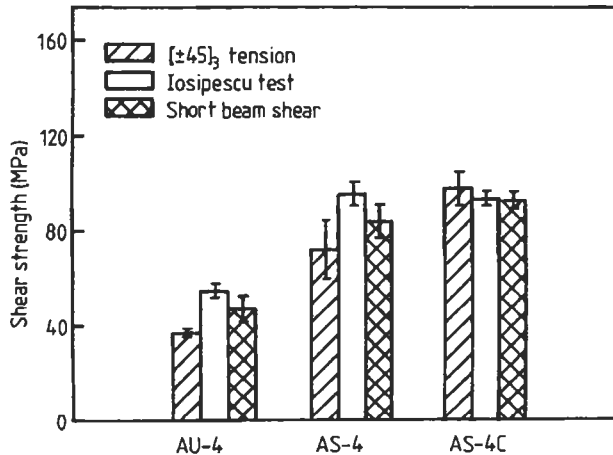


Fig. 5.18. Comparison of shear strengths of carbon fiber–epoxy matrix composites determined from three different test methods. Fiber surface conditions as in Fig. 5.17. After Drzal and Madhukar (1993).

Table 5.8

Summary of Mode I and Mode II interlaminar fracture toughness values for unidirectional carbon fiber-828 mPDA epoxy matrix composites with different fiber surface treatments^a

Interlaminar properties	AU-4 fiber	AS-4 fiber	AS-4C fiber	mPDA epoxy
Mode I interlaminar fracture toughness, G_{Ic} (kJ/m ²)	Unable to determine	0.33 ± 0.02	0.39 ± 0.03	0.13
Mode II interlaminar fracture toughness, G_{IIc} (kJ/m ²)	0.40 ± 0.08	1.04 ± 0.17	1.15 ± 0.13	-

^aAfter Drzal and Madhukar (1993).

interfacial adhesion is expected in view of the analogy in loading geometry of the two test methods. Enhancement of the interfacial bond strength changes the failure mode from “interface-dominated” to “matrix-dominated”, which is mainly responsible for the increase in mode II interlaminar fracture toughness. The above finding suggests that when the interface bond strength approaches the matrix shear strength, further increase in interface bonding may not impart additional improvement in mode II interlaminar fracture toughness.

5.4. Polymeric fibers

5.4.1. Aramid fibers

5.4.1.1. Structure and properties of aramid fibers

The commercial aramid fibers are currently produced by several companies, including du Pont (Kevlar), AKZO (Twaron) and Tenjin (Technora). Table 5.9 (Morgan and Allred, 1993) presents the chemical structures of aromatic polyamides that are developed for commercial fiber production. Among these, Kevlar fibers were the first developed and are now most popular. Thus, discussion in the following will be mainly concerned with this fiber type, unless otherwise specified. The Kevlar fibers are produced from liquid crystal dopes through a dry-jet wet-spinning process. It is a polycondensation product of terephthaoyl chloride and p-phenylene diamine. The molecules form a planar array with interchain hydrogen bonding as shown in Fig. 5.19(a). The stacking sheets form a crystalline array whose bonding is rather weak. Electron microscopy and diffraction studies show (Dobb et al., 1977) that Kevlar fibers consist of radially arranged and axially pleated crystalline supramolecular sheets, as schematically presented in Fig. 5.19(b).

Kevlar fibers are available in four forms: Kevlar, Kevlar 29, Kevlar 49 and the recently developed Kevlar 149. Kevlar is designed specifically for reinforcements of elastomers (e.g. tires and belts), while Kevlar 29 is used primarily for tensile members such as ropes, cables, webbings and ballistic cloth. Kevlar 49 and 149 are designed for reinforcement of high performance PMCs. Kevlar 149 offers a 40%

Table 5.9
Aromatic polyamides developed for commercial fiber production^a

Chemical name	Trade name	Chemical structure
Poly(<i>m</i> -phenylene isophthalamide) (PmPI)	Nomex (du Pont); Conex (Teijin)	$(OC-\text{C}_6\text{H}_4-\text{OC}-\text{HN}-\text{C}_6\text{H}_4-\text{NH})$
Polybenzamine (PBA)	PRD 49-1 ₁ (du Pont)	$(\text{HN}-\text{C}_6\text{H}_4-\text{CO})$
Poly(<i>p</i> -phenylene terephthalamide) (PPTA)	Kevlar (du Pont); Twaron (Akzo N.V.)	$(OC-\text{C}_6\text{H}_4-\text{OC}-\text{HN}-\text{C}_6\text{H}_4-\text{NH})$
Polyterephthaloyl- <i>p</i> -aminobenzhydrazide (PABH-T)	X-500 ^b (Monsanto)	$(\text{HN}-\text{C}_6\text{H}_4-\text{CO}-\text{NH}-\text{NH}-\text{OC}-\text{C}_6\text{H}_4-\text{CO})$
Copolyterephthalamide of <i>p</i> -phenylenediamine and 3,4'-diaminodiphenyl ether (CPTA)	HM-50, Technora ^b (Teijin)	$\left[\begin{array}{c} \text{HN}-\text{C}_6\text{H}_4-\text{NH} \\ \text{HN}-\text{C}_6\text{H}_4-\text{O}-\text{C}_6\text{H}_4-\text{NH}-\text{O} \end{array} \right]_{(50)}-\text{CO}-\text{C}_6\text{H}_4-\text{CO}$
Polyamidobenzimidazole (PABI)	FVM (Russia)	$\left(\begin{array}{c} \text{H} \\ \\ \text{N} \\ \\ \text{N} \\ \\ \text{H} \end{array} \text{C}_6\text{H}_4 \begin{array}{c} \text{N} \\ // \\ \text{C} \\ // \\ \text{N} \\ \\ \text{H} \end{array} \text{C}_6\text{H}_4 \begin{array}{c} \text{H} \\ \\ \text{N} \\ \\ \text{O} \\ \\ \text{C} \\ // \\ \text{O} \end{array} \text{C}_6\text{H}_4 \begin{array}{c} \text{O} \\ \\ \text{C} \end{array} \right)$

^aAfter Morgan and Allred (1993).

^bNo longer commercially produced

higher modulus and significantly lower moisture absorption than Kevlar 49. Table 5.10 gives representative properties of these fibers. All these fibers normally fracture by splitting into small fibrils in the axial direction instead of being broken transversely, as evidenced by the SEM microphotograph shown in Fig. 5.20 (Kim and Mai, 1991a, b). This fracture behavior directly mirrors the microstructure and ductile nature of the fiber.

5.4.1.2. Surface treatments of aramid fibers

There are three major approaches to the surface treatment of aramid fibers: chemical etching/grafting, plasma treatment and application of coupling agents. All these techniques are basically aimed at enhancing the chemical interaction between the fiber and organic resins by introducing reactive functional groups on the fiber surface. The first two methods have the additional advantage of intensifying the roughness and rugosity of the fiber surface for improved mechanical anchoring.

Chemical treatments: Keller et al. (1981) hydrolyzed Kevlar 49 fibers with acid (HCl, H₂SO₄) or base (NaOH) to produce reactive amino groups, to which a small

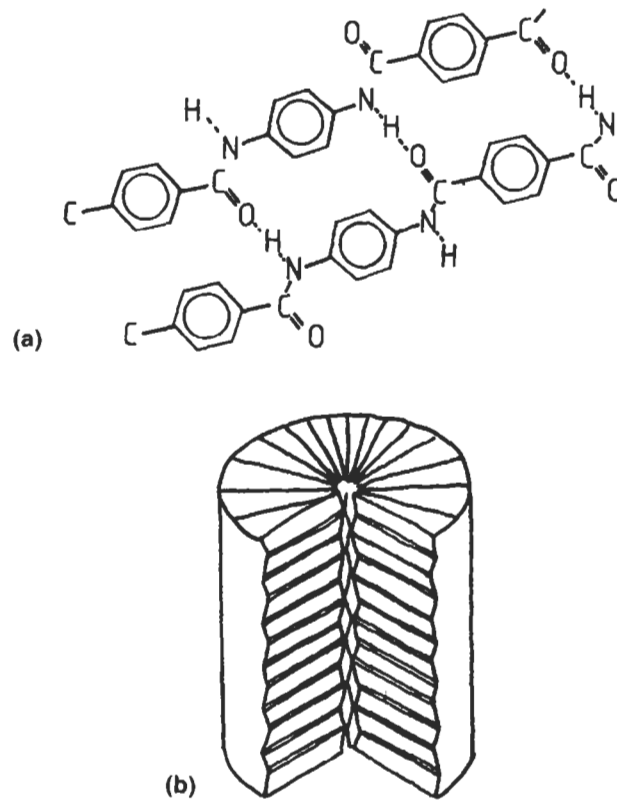


Fig. 5.19. Schematic presentations of (a) hydrogen bonding and (b) supramolecular structure of Kevlar 49 aramid fiber. After Dobb et al. (1977).

Table 5.10
Properties of aramid fibers^a

Property	Kevlar 29	Kevlar 49	Kevlar 149
Diameter (μm)		11.7	
Density (g/cm^3)	1.44	1.45	1.47
Tensile strength (GPa)	3620	3620	3440
Elongation at break (%)	4.0	2.8	2.0
Young's modulus (GPa)	83	135	186
Specific strength (10^6 cm)	25.5	25.5	23.9
Specific modulus (10^6 cm)	580	950	1290
Coefficient of thermal expansion ($10^{-6}/\text{K}$)			
Axial	-2.26	-2.0	-1.49
Radial	-	59 ^a	-

^aFrom Morgan and Allred (1993).



Fig. 5.20. Scanning electron microphotograph of a fibrillated Kevlar 49 fiber. After Kim and Mai (1991b).

diepoxide molecule may be attached. A long exposure time causes direct mechanical damage to the fiber which may outweigh any advantages gained by improved interface bonding. In a similar study, Andreopoulos (1989) has also treated Kevlar 49 fibers with reactive chemicals, such as acetic acid anhydride, methacryloyl chloride, sulfuric acid and acrylamide, to ensure grafting in the aramid chain while avoiding excessive loss in fiber weight. Tensile strengths of both fiber and polyester matrix composite decrease as a result of fiber etching by most of the above chemical agents used. Only methacryloyl chloride is effective in producing an intermediate surface roughness and chemical grafting that are favorable for a strong interface bond.

Chemical surface treatment influences the properties of semicrystalline thermoplastic matrix composites in a different manner. Yu et al. (1991a, b) reported that a treatment with suberoyl chloride promotes the growth of a trans-crystalline zone around the Kevlar fibers which is considered favorable for good fiber–matrix interface bonding. A wide-angle X-ray diffraction study has indicated that chemical treatment modifies the nucleating ability of the fiber. Takayanagi et al. (1982) also modified Kevlar 29 by polymer reaction via the metalation reaction in dimethyl sulfoxide to provide the fiber surface with several functional groups such as n-octadecyl, carboxymethyl and acrylonitrile. They have shown that the treatment increases the roughness of the fiber surface, hence improving the mechanical properties of the composites made with ionomer matrices. Bromine water attack on the fiber surfaces has produced similar roughening effects on the composite ILSS, but with a slight loss in fiber tensile strength due to splitting of the fiber skin layer from the core (Lee-Sullivan et al., 1994).

Plasma treatment: More promising results have been obtained by modifying the aramid fiber surface with cold plasma in the presence of vacuum, ammonia or argon. The improvement in bond strength varies between 50% to a remarkable 400%, depending on the exposure time and atmosphere (Wertheimer and Schreiber, 1981). Plasma treatment in ammonia increases the amine concentration on fiber surfaces which is thought to be responsible for strong covalent bonding at the

interface with epoxy resins (Allred et al., 1985). The high nitrogen content in the form of an amine group is usually accompanied by a decrease in oxygen content with increase in treatment time. The treatment also increases the ILSS of epoxy matrix composites by 30% to 50% with associated dominant failure mechanisms of fiber splitting and matrix cracking, in contrast to the apparent interface debonding in untreated counterparts (Brown et al., 1991). Fig. 5.21 shows the increase in the amine group and the corresponding ILSS with treatment time.

In addition, the increase in flexural strength of treated fiber composites can be attributed to a lower extent of fiber buckling in the compressive face as a result of improved interfacial bonding (Brown et al., 1992a). A similar improvement in mechanical properties is also reported for vinylester matrix composites (Brown et al., 1992b), which is associated with enhanced fiber wettability rather than chemical functionality. Improvements in retainability of composite flexural strength and ILSS have also been shown under water aging condition for plasma treated Twaron aramid fibers (Verpoest and Springer, 1988; Janssens et al., 1989).

Coupling agents: The application of coupling agents to aramid fibers has not been particularly successful. Vaughan (1978) applied onto Kevlar fibers several silane coupling agents that were developed originally for glass fibers with limited improvement in the composite strength under both dry and water aging conditions. Application of organotitanate and organozirconate coupling agents (Sugerman et al., 1989) also shows only a slight improvement in flexural strength of epoxy matrix composites. The addition of coupling agents after oxygen plasma treatment appears to be a good combination to maximize the benefits of improvement in interface bonding, as evidenced by the 250% increase in the fiber pull-out force for Kevlar 49 fiber reinforced silicon rubber matrix composites, Table 5.11 (Inagaki

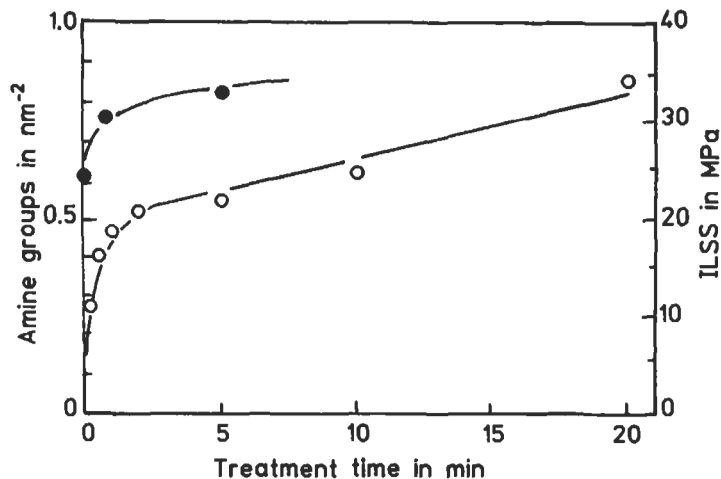


Fig. 5.21. Surface amine concentration (○) of aramid fiber and ILSS (●) of epoxy matrix composites as a function of ammonia plasma treatment time. After Brown et al. (1991).

Table 5.11
Effect of surface modification on pull-out force of PPTA silicone rubber composite^a

Surface modification		Pull-out force (g/cm)
Plasma treatment ^b	Coupling agent treatment ^c	
No	No	458 ± 5.8
No	Yes	1240 ± 63
Yes	No	1250 ± 50
Yes	Yes	3120 ± 34

^aAfter Inagaki et al. (1992).

^bPlasma treatment: exposed to oxygen plasma at 150 mA, 26.6 Pa for 2 min.

^cCoupling agent treatment: coupled with silicone adhesive TSE322 at 150°C for 1 h.

et al., 1992). It is suggested that oxygen plasma treatment removes some carbon-rich surface layers of the Kevlar fiber, hence exposing the nitrogen-rich layer. The high carbon content on the fiber surface is considered to be detrimental to chemical bonding with the liquid resin.

In summary, novel techniques have yet to be evolved to further improve the interfacial bonding with aramid fibers. Modification of aramid fibers to produce chemical functionality or improved wettability based on chemical agents or plasma treatment warrants much further research before applications to commercial production can be realized. In particular, the importance of wettability is evidenced by the fact that higher interface bond strengths are obtained with epoxy resins in the order of uncoated (i.e. chemically reactive and wettable), gold-coated (chemically inert but thermodynamically wettable) and silicone coated (inert and non-wettable) Kevlar fibers (Kalanta and Drzal, 1990b). An optimum surface condition should always be chosen after a compromise with the mechanical properties of fiber, as the fibers are sensitive to severe damage by the attack received during the surface modification process. This is particularly true with aramid fibers which are characterized by the skin-to-core inhomogeneity coupled with extremely low transverse and compressive strengths. This has a practical implication in that a strong interface bond does not always guarantee the best mechanical performance, unless the inherent microstructure is properly modified to produce a more homogeneous and isotropic material (Kalanta and Drzal, 1990a).

5.4.2. Ultrahigh modulus polyethylene fibers

Several high modulus, high strength polyethylene fibers are commercially available, including Spectra (Allied Signals), Dyneema (DSM/Toyobo), Tekmilon (Mitsui Petrochemical), Snia (Snia Fibers) and Celanese (Celanese Research). They are produced via a gel-spinning process where the low concentration solution of ultrahigh molecular weight polyethylene (UHMWPE) ($M > 2 \times 10^6$) is extended to form gel precursor fibers. The precursor fibers are then hot drawn to produce very highly oriented fibers with an extended chain fibrillar microstructure, as schemat-

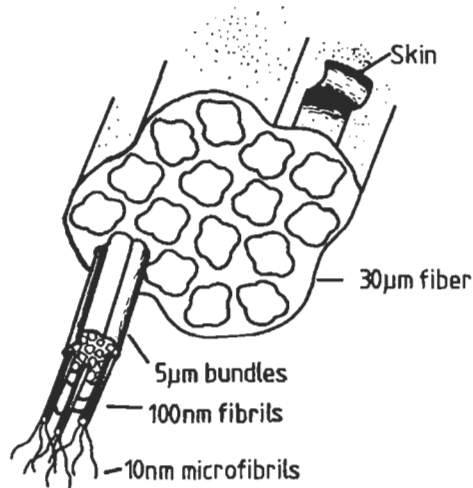


Fig. 5.22. Schematic illustration of UHMWPE fiber's structural hierarchy. After Ward (1985).

ically shown in Fig. 5.22 (Ward, 1985). The polyethylene fibers have modulus and strength values close to those of aramid and Type I carbon fibers. Representative properties of typical UHMWPE fibers (Spectra 900 and 1000) are given in Table 5.12. Because of the extremely low density ($\approx 0.97 \text{ g/cm}^3$), their specific tensile properties are the highest ever achieved with any organic materials. They also have a high failure strain. In contrast to the high strength properties in tension, they have a very low compressive strength which could severely limit the application of these fibers.

Polyethylene fibers are chemically inert, which is considered to be a positive factor, allowing excellent sunlight resistance and little degradation in aqueous environment, as compared to other organic and inorganic fibers. However, their chemical inertness does not allow sufficient interactions to occur to form a high interfacial bond with most polymer resins. Significant efforts have been put forward to improving the fiber-resin adhesion by introducing the functionalities at the fiber surface that could interact with organic resins. As for the aramid fibers discussed in the preceding section, three methods have been explored for polyethylene fibers, namely chemical etching, plasma treatment and coupling agents.

Many different etchants have been studied, including potassium permanganate (KMnO_2), hydrogen peroxide (H_2O_2) and chromic acid ($\text{K}_2\text{Cr}_2\text{O}_7$). Among these, chromic acid shows the most promising result of a six-fold increase in interfacial bonding of Spectra 1000 fibers with an epoxy resin in the microbond test, Table 5.13 (Silverstein and Breuer, 1993b). This remarkable gain is attributed to the removal of oxygen-rich weak boundary layers which are present on the non-polar fiber surfaces, and subsequently exposing the fibrillar structure of the fiber core by the strong acid. The severe surface rugosity created by the acid also has contributed, to a lesser

Table 5.12
Properties of UHMWPE fibers^a

Property	Spectra 900	Spectra 1000
Diameter (μm)	38	38
Density (g/cm^3)	0.97	0.97
Tensile strength (GPa)	2584	1964
Elongation at break (%)	3.5	2.7
Young's modulus (GPa)	117	172
Specific strength (10^6 cm)	16.8	20.6
Specific modulus (10^6 cm)	1220	1810
Coefficient of thermal expansion ($10^{-6}/\text{K}$)		
Axial	-10.8	-
Radial	-	-

^aAfter Adams and Zimmerman (1986).

degree, to improved bonding (Silverstein and Breuer, 1993a, 1993c). Hot fuming with nitric acid on Spectra 900 fibers has also shown to be useful. The FTIR diffusive transmittance analysis on treated fibers has identified that the mechanism responsible for the improved composite ILSS is due mainly to better wettability of the fiber by the resin. Grafting polymerization of monomers, such as allylamine (Rostami et al., 1992) and ethylene (Wang Q. et al., 1992a, b), on the plasma treated fiber surface further improves the interface bonding.

Ladizesky and Ward (1983, 1989), Ward and Ladizesky (1986) and Ward (1993) reported that plasma treatment of polyethylene fibers in an atmosphere of oxygen is the most effective among the many techniques studied. There are four major mechanisms responsible for improved fiber-matrix interface adhesion:

- (1) oxidation of the fiber surface,
- (2) removal of weak boundary layer by the formation of a cross-linked skin,
- (3) enhanced surface roughness and rugosity,
- (4) improved wettability due to the increase in surface free energy.

Table 5.13
Interface shear bond strength of epoxy droplets on a UHMWPE fiber^a

Etchant	Exposure time (h)	Interface bond strength (MPa)
None	-	1.7 ± 0.9
$\text{K}_2\text{Cr}_2\text{O}_7$	4	11.3 ± 2.0
	24	6.1 ± 1.2
KMnO_4	4	3.2 ± 1.0
	24	2.4 ± 1.0
H_2O_2	4	1.3 ± 0.8

^aAfter Silverstein and Breuer (1993b).

The first mechanism is thought to be particularly important for the ultrahigh modulus polyethylene (UHMPE) fibers as the poor adhesive properties of polyolefine are commonly associated with the presence of weak boundary layers (Tissington et al., 1991). Fig. 5.23 compares the SEM microphotographs of untreated and plasma treated (for 120 s) Tekmilon fiber surfaces, which display dramatic changes in the surface morphology after treatment. The surface cross-linking of polyethylene fibers appears to start as soon as the fiber is exposed to plasma, and its growth rate being a function of the discharge power and exposure time. The increase in surface free energy is due to the introduction of polar groups on the fiber surface during the treatment (Gao and Zeng, 1993a, b).

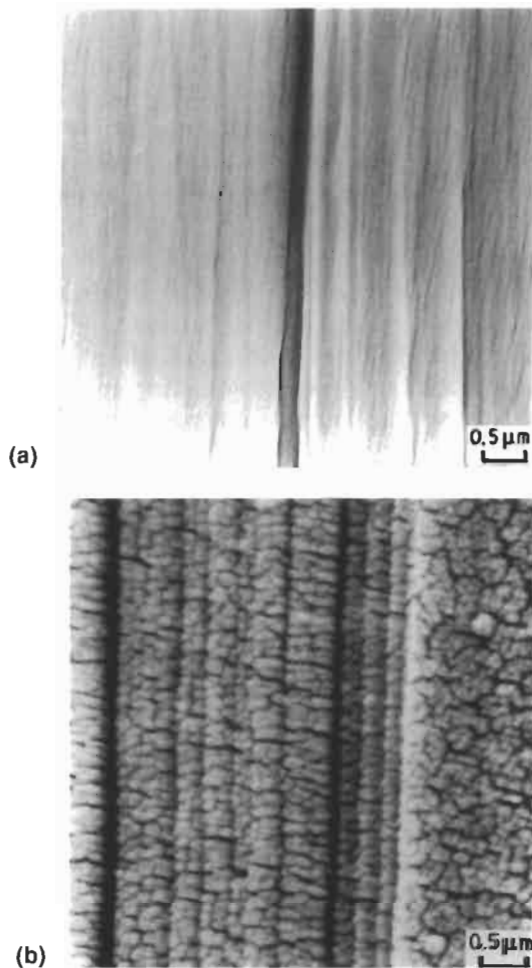


Fig. 5.23. Scanning electron microphotographs of (a) untreated and (b) plasma treated (120 s) Tekmilon UHMWPE fibers. After Tissington et al. (1991). Reproduced by permission of Chapman & Hall.

Encouraged by the remarkable improvements in interface adhesion, many researchers have employed plasma treatment techniques, notably Netravali and coworkers (Li et al., 1992; Li and Netravali, 1992; Hild and Schwartz, 1992a, b). An optimum treatment time has been established, which would impart the highest interface shear strength given the treatment conditions. Fig. 5.24 presents an example for a constant plasma power of 30 W and a chamber pressure of 0.5 Torr in an atmosphere of ammonia for Spectra 900 fibers. Grafting of functional groups onto the fiber surface is achieved using ammonia plasma (Holms and Schwartz, 1990) and allylamine plasma (Li and Netravali, 1992). The allylamine thin coating, however, does not change the surface topography, while decreasing the contact angle, an indication of a large improvement in wettability. A similar increase in the wettability of fibers treated in gas plasma using nitrogen, argon and carbon dioxide, and in radio-frequency (RF) plasma is attributed to the addition of polar groups to the fiber surface as characterized by XPS (Li and Netravali, 1992; Biro et al., 1993a, b). It is also worth highlighting that the application of a silane agent after plasma treatment further improves the interface adhesion for an optimum plasma treatment time (Cho and Jang, 1990).

5.5. Inorganic fibers

5.5.1. Introduction

In the previous sections, techniques developed for improving the interface bond quality are discussed mainly for glass, carbon, aramid and UHMWPE fibers with

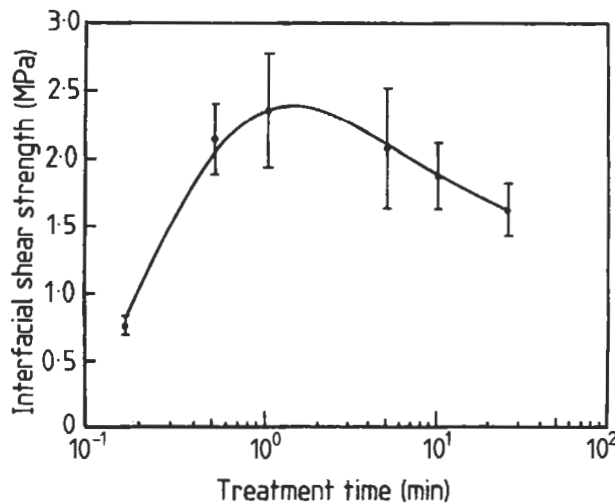


Fig. 5.24. Effect of ammonia plasma treatment time on interface shear strength. After Li et al. (1992).

polymeric matrices. For polymer matrix composites (PMCs), although the chemistry and thermodynamic compatibilities required are as complicated as in other composites, the prime objectives of the interface characteristics are mostly a strong bond for efficient stress transfer and a good resistance to prolonged environmental attack in service conditions. Similarly, a strong interface bond with high strength properties are often desirable in metal matrix composites (MMCs). The reaction products formed at the interface region at high processing temperatures generally increase the chemical bonding, but degrades the gross mechanical properties of the composite. Therefore, a compromise is necessary between the desired properties, and proper control of chemical reaction is a primary concern in the design and manufacture of MMCs. Because the service temperatures for most MMCs are significantly lower than those for ceramic matrix composites (CMCs), the avoidance of environmental attack is of secondary importance, as is the issue of fracture toughness due to their inherently high ductility and inelastic fracture behavior.

The high Young's modulus and good thermal stability of CMCs coupled with their low density and corrosion resistance, compared with MMCs, make them very attractive for high temperature applications. In particular, those reinforced with SiC and Al₂O₃ fibers are increasingly applied to manufacture engineering components requiring high performance. As for other composite materials, the structure and mechanical characteristics of the fiber-matrix interface provide a key to effective control of damage in designing CMCs. The aim is usually to make the interface rather weak in order to improve the fracture toughness through interface-related failure mechanisms, because the weakest aspect of most CMCs is their inherent brittleness and extremely low damage tolerance. On the other hand, an adequate interfacial strength is sometimes required to provide good strength properties, in particular in the transverse direction. Indeed, proper control of the interface properties is essential to achieving often conflicting requirements of high strength and high fracture toughness.

In this section, surface treatments and coatings of fibers now popularly used for MMCs and CMCs, particularly carbon, boron (B/W), silicon carbide (SiC) and alumina (Al₂O₃) fibers are discussed. Several approaches have been used to achieve the desired compatibility between fiber and matrix, that include the applications of diffusion barrier coating and fiber size, and the control of matrix composition (i.e. alloying elements), impurity content and composite fabrication procedure. Among these techniques, fiber coating and alloying element control methods are used extensively, that are the subject of the present section. Recent advances on the development, availability and applications of a wide range of new and existing inorganic fibers have been reviewed in a special volume of the journal, *Composites Science and Technology* (Mai, 1994).

5.5.2. Selection of coating materials and coating techniques

5.5.2.1. Coating materials

The interfacial characteristics can be optimized by the application of appropriate coatings to the fiber, allowing desired mechanical properties of the composites to be

preserved at service temperatures. The effects of interface reaction depend on the nature and reactivity of fiber and matrix combinations; and the morphology and mechanical properties of the reaction products are expected to be responsible for the diverse fracture behavior at the interface region. Both in CMCs and MMCs, a suitable coating should be chosen such that the bonding mechanism at the interphase region becomes primarily mechanical in nature. In MMCs, the coating should also allow the fibers to be properly wetted by the molten matrix material because the wettability plays an important role in improving the interface bonding. For example, metal oxide fibers, such as Al_2O_3 , are not readily wetted by many metals unless they are very reactive or the fibers are coated with appropriate materials (Ward-Close and Partridge 1990).

On the other hand, because of the accelerated reactivity of the surfaces of many fibers when in contact with metal and ceramic matrices at elevated temperatures, considerable precautions need to be exercised to ensure the fiber–matrix compatibility and avoid fiber degradation. The composite constituents and the reaction barrier coatings must also be chemically stable at the processing and service temperatures. Any chemical interactions occurring between the fibers, coating and matrix during the manufacturing processes would influence the interface bond strength. Once fabricated, the service temperature must not exceed some maximum level, otherwise an interdiffusion-controlled reaction may occur between the elements of fiber, coating and matrix to form compound layers of substantial thicknesses which are often detrimental to the mechanical performance of the composites. A balance is thus always required between the reaction necessary for efficient interfacial bonding and fiber degradation caused by excessive reaction. A coating is also required to protect the fiber from mechanical degradation during handling.

The choice of a coating for a given combination of fiber and matrix materials depends on the processing and service requirements. The criteria for thermodynamic stability in the temperature range encountered during the fabrication process and in service are clearly of most importance. In this regard, highly stable oxides such as, Y_2O_3 , MgO , ZrO_3 , HfO_2 , SiO_2 , Al_2O_3 , SnO_2 and other non-reactive refractory species such as C, W, Mo, BN, SiC, are considered to be strong candidates among many coating materials hitherto developed. Any coating material certainly has an inherent upper temperature limit, although this limit can be enhanced by modifying the elements of the coating material or by introducing multi-layer coatings. For example, a BN coating tends to oxidize in air at about 600°C , the behavior of which is considered to be slightly better than that with a carbon coating. A SiC coating tends to form a reaction product SiO_2 at temperatures above 1200°C . Some porous oxide coatings that eliminate the problem of an upper temperature limit appear to provide an opportunity, but further research is needed regarding their influence on fiber strength and degradation along with their macro structural stability, before they can be accepted for wider applications.

Another important mechanical property of a coating layer is the coefficient of thermal expansion (CTE). Residual stresses generated due to the differential thermal contraction between the composite constituents are extremely detrimental to the

mechanical performance of the coated fibers and the composites fabricated therefrom. In particular, large tensile circumferential and axial stresses may be generated in the coating layer during cooling if the fiber has a very low CTE compared to the coating material, such as in yttria coated-SiC monofilament (see Section 5.5.5). The coating layer undergoes severe cracking or spallation due to the large difference in the residual stresses, as shown in the SEM photo micrograph in Fig. 5.25.

The thickness of coating applied onto the fiber is a predominant parameter which limits the performance of the coating. The coating thickness should be chosen to protect the fiber from environmental attack, minimize the residual thermal stresses, and induce a non-brittle failure mode. Coating thicknesses in the range of 0.1 - 1.0 μm are commonly applied for MMCs and CMCs. Furthermore, a uniform, reliable and reproducible application of a coating material without generating pores is a very difficult task. Numerous areas of poor bonding and porosity can lead to a general failure of the coating itself.

5.5.2.2. *Coating techniques*

The first major obstacle encountered in developing a successful coating seems to be the method of application. The coating must wet the fiber properly, be uniform in thickness and, most preferably, be free of porosity extending to the surface of the substrate. The conventional methods of applying coatings to bulk substrates are not suitable nor adequate for fibers of small diameter. It is important to note that the selection criteria for one coating technique over another are most often different.



Fig. 5.25. A scanning electron microphotograph of fractured yttria coating on a SiC monofilament after cooling through 500°K. After Kiescheke et al. (1991a). Reproduced by permission of Elsevier Science Ltd.

However, there are several common requirements that a coating technique should satisfy. They are:

- (1) the coating should not impair the properties of the substrate fiber,
- (2) the deposition process must be compatible with the fiber,
- (3) the coating deposition should be a continuous process, and
- (4) the coating technique must be capable of coating the fiber with a uniform thickness.

Several processing techniques are available for deposition of thin coatings on continuous and short fibers, which can be grouped into chemical vapor deposition (CVD), physical vapor deposition (PVD, inclusive of sputtering and ion-plating), plating and spraying techniques and sol-gel method. In the CVD process, a vaporized species decomposes thermally or reacts with another vapor to form a deposit on a hot substrate fiber, as schematically shown in Fig. 5.26. This technique has been used to manufacture boron and SiC monofilaments. Selection of a suitable carrier gas and control of deposition procedure for particular coating materials are critical to the properties of the final products. A review given by Alam and Jain (1990) describes important factors involved in the use of the CVD technique for fiber coating.

The PVD process constitutes a similar procedure to the CVD technique. The main difference is that the vapor is formed by evaporation or sputtering without a chemical reaction being involved. It is also possible to generate a discharge, causing the deposit to be bombarded as it is formed (i.e. ion plating). These processes can also be performed in a reactive atmosphere. The plating and spraying techniques are

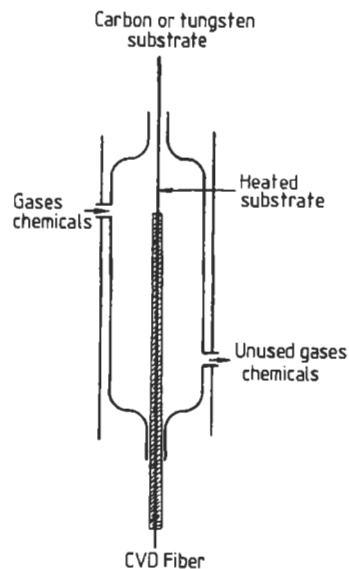


Fig. 5.26. Schematic presentation of boron filament production.

used mainly to promote the wetting of fibers by molten metals, without due consideration of the structure and integrity of the coating layer formed. The efficiency of the plating process can be enhanced by producing an ion in a suitable electrolyte. Thermal spraying is a process in that a coating precursor is heated rapidly in a hot gaseous medium and simultaneously projected at a high velocity onto the substrate fiber surface. The sol-gel method involves dipping or spinning of fibers in a colloidal dispersion of particles in a carrier liquid, which is followed by aggregation, gelation and final drying to form a thin layer of coating in the form of very fine particles.

5.5.3. Carbon fibers

Various fabrication processes and the properties of carbon fibers are discussed in Section 5.3.1. In general, carbon fibers are unique in that they do not react with corrosive environment, except oxygen, at moderately high temperatures. They exhibit even a slight increase in strength at temperatures up to 2200–2775°C, depending on the precursor material and the heat treatment temperature used during manufacture. Once processed, the carbon fibers display no changes in grain size until they exceed their initial processing temperature. Therefore, many CMCs containing carbon fibers can be used at very high operating temperatures without much property degradation.

Carbon fiber reinforced aluminum matrix composites are very attractive for structural applications due to their high specific strength, high modulus and near zero CTE. However, there are major problems associated with the fabrication processes of these composites; namely chemical reactivity of aluminum and poor wetting of fiber by the matrix at its melting point. The interface shear strength of the composite normally increases with increasing amount of reaction product, which in turn leads to a decrease in the composite longitudinal strength (Yoon and Okura, 1990). High resolution electron microscopy and XPS reveal that the carbide, e.g., Al_4C_3 , form and grow by nucleation preferentially at the edge planes of the carbon fiber surface (Diwanji and Hall, 1992). The amount of the interfacial reaction product, Al_4C_3 , in carbon fiber–aluminum matrix composites depends on the surface structure and treatment of carbon fibers. The interfacial shear strength is enhanced significantly after oxidative treatment of the fiber surface, which is attributed to the increased number of exposed crystalline edges where the carbides are preferentially nucleated.

One common remedy to the problem of excessive interfacial reaction is the application of an appropriate fiber coating. The structure and morphology of nickel coated carbon fibers for aluminum matrix have been studied by Abraham et al. (1989, 1990). NiAl_3 intermetallics are found near the coated carbon fiber surface without evidence of interaction at the coated fiber–matrix interface region. It is believed that the interaction between the nickel coating and the carbon fiber took place during the coating process, and the intermetallics acted as a nucleating site for NiAl_3 precipitate during the composite synthesis. A Cu coating on carbon fiber is also shown to be effective to reduce the chemical reaction (Abraham et al., 1992).

Two coating techniques have been employed successfully, namely the cementation and electroless plating processes. The cementation process produces relatively thick coating, reducing significantly the tensile strength of the coated fiber, compared to the electroless process, as shown in Fig. 5.27. A small amount of precipitate of the CuAl_2 phase is observed at the interface region of the Cu coated carbon fiber–aluminum matrix composite.

Another effective method of reducing the chemical reaction is the use of alloying elements in the matrix. Additions of small amounts of titanium and zirconia resulted in an increase in strength after thermal exposure (Li et al., 1989; Zhuang and Zhang, 1991). For a composite containing 0.5 wt% Zr, the strength is over 80% of the rule of mixtures (RoM) strength after exposure for one hour at 600°C , which is well above 55% of the RoM strength for the as-received composite without the Zr alloying element in the matrix. This is attributed to the reduction of growth rate of the reaction product, Al_4C_3 , at the interface region. The reaction product in general increases the chemical bonding, but impairs other mechanical properties of the composite. An addition of Ti also reduces the interfacial reactions and improves the wettability (Wu et al., 1993a, b). In sharp contrast, the inherent alloying phase, i.e. CuAl_2 , present in Al–Cu and Al–Cu–Mg alloys is detrimental to the strength of the composites because the elements tend to precipitate at the fiber–matrix interface region during the solidification process and thermal exposure (Li et al., 1989; Li, 1990).

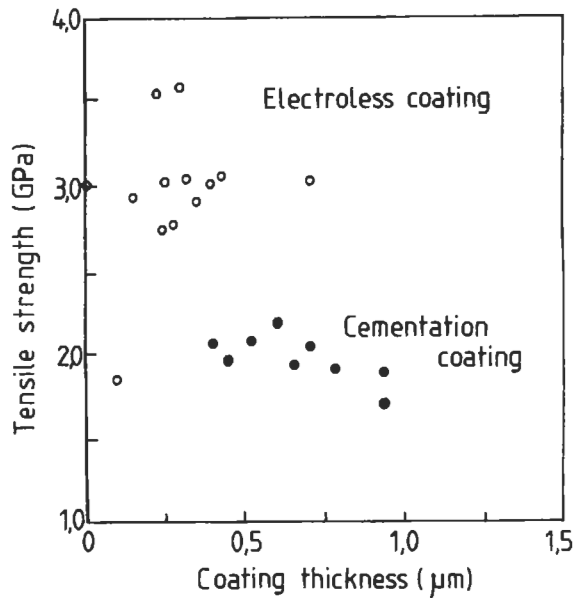


Fig. 5.27. Variation of tensile strength of copper coated carbon fibers as a function of coating thickness determined by single fiber pull-out test. After Abraham et al. (1992).

It is also interesting to note that electroless plating of silver on carbon fiber surface improves the wettability between molten aluminum and PAN based carbon fibers using the liquid infiltration technique in vacuum (Warrier et al., 1993). This is attributed to the formation of an eutectic phase between silver and aluminum, and the silver coating of the fibers during processing.

Alloying addition techniques have also been used to improve the wetting of carbon fibers by liquid copper (DeVincent, 1991; DeVincent and Michal, 1993a, b). Among the alloying elements studied, Fe, La, Mn, Nb, Si, Ta and Ti do not wet the H-490 carbon fibers for the alloying levels examined. On the contrary, additions of Cr and V at 1 at. wt% are able to enhance the wetting behavior so that a contact angle of 45° or less is produced. However, because of the difficulties associated with dissolving V in molten Cu, a temperature of 1530°C is needed to achieve the same degree of wetting. This makes the Cu-V alloy systems rather impractical for fabrication. Energy dispersive spectroscopy (EDS), Auger electron spectroscopy (AES) and X-ray diffraction analyzes show that a reaction layer, Cr_3C_2 , is formed by bulk diffusion of carbon and the alloying atoms through the reaction layer, which is followed by surface diffusion of the alloying atoms along the reaction layer. Fig. 5.28 illustrates an AES survey scan of the Cu-Cr (1.22 at. wt%) reaction layer. Due to the high mobility of the alloying atoms along the reaction layer, it extends outward much faster than it grows via bulk diffusion. When the Cr content is varied from 0.6 to 1.22, the corresponding contact angle and the interfacial energy at the C/Cu interface drops drastically. An increase in Cr_3O_2 improves the interface bonding and the longitudinal tensile strength, as does the amount of Cr_3C_2 with increasing Cr content in the Cu matrix. A thermodynamic analysis of the formation of Cr_3C_2 phase from Cr dissolved in liquid Cu and C on carbon fiber shows that Cr_3O_2 is the most stable phase. It is also found that the formation of a Cr_3O_2 reaction layer in the solid state places the carbon fibers and the reaction layer under residual tension and the Cu-Cr alloy matrix in pure shear.

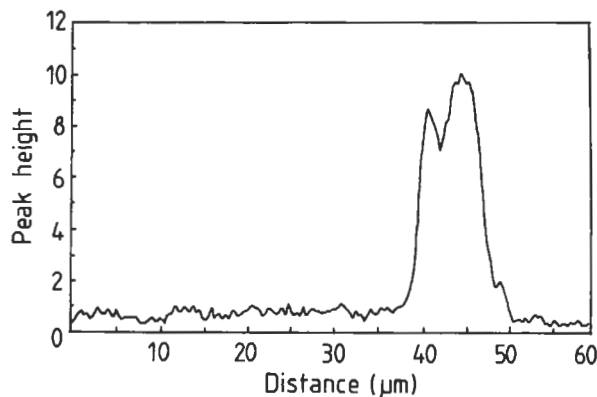


Fig. 5.28. AES line scan of Cr over the interfacial region of a Cu-1.22 at.% Cr sessile drop specimen after sputtering for 6 s. After DeVincent and Michal (1993).

Similar to aluminum matrix composites, a major problem encountered with carbon fiber–Mg matrix composites is the lack of wetting. Deposition of a thin protective TiB coating on carbon fibers by a CVD process improves the wettability of magnesium (Katzmann, 1987). However, the TiB coating oxidizes rapidly when exposed to air, which limits the applications of the coated fibers. Alternatively, a SiO₂ coating which is stable in air has been applied successfully to improve wetting (Katzmann, 1987; Chen and Li, 1993). Reaction products, such as Mg₂Si and MgO, are normally precipitated at the interface region of the uncoated fiber. In contrast, when there is a SiO₂ coating present at the interface, the magnesium matrix reacts with the coating to form a microprecipitate MgO layer. This reaction is found to facilitate the infiltration process. Surface treatment of carbon fibers also results in a marked increase in the interfacial shear strength causing a corresponding decrease in the longitudinal tensile strength of the magnesium matrix composites, as shown in Table 5.14 (Hall, 1991).

In addition to the MMCs containing aluminum and magnesium matrices as discussed above, SiC matrix composites reinforced with carbon fibers have been developed successfully by the CVD process. This CMC is designed for potential applications for fusion reactor components, heat exchangers, turbine engines, etc. TEM and X-ray diffraction studies identify that a graphite layer formed on the carbon fiber through the thermal decomposition reaction of the silane gas before SiC infiltration. This graphite layer is seen to assist the crystal growth of SiC for structural stability of this composite. A CVD coating of the carbon fiber by refractories, such as TiC, TiN, SiC and pyrolytic carbon, is also able to protect the carbon fibers from reaction bonding by liquid SiC impregnation (Fitzer et al., 1984). The tensile strength of the CVD coated high modulus carbon fibers strongly depends

Table 5.14

Effect of size and surface treatment of carbon fibers on mechanical properties of magnesium matrix composites^a

Fiber/matrix	Sized/surface treated	Tensile strength (MPa)	Interfacial shear strength (MPa)
X550 ^b /AS41 ^c	Yes/yes	360	–
X550/c.p. Mg	Yes/yes	680	–
X550/AS41	No/yes	298	–
T300-90 ^d /c.p. Mg	No/yes	325	133 ± 5
T300-99 ^e /c.p. Mg	No/no	522	40 ± 4
T300-90/Mg-4Al	No/yes	328	140 ± 4
T300-99/Mg-4Al	No/no	645	20 ± 5

^aAfter Hall (1991).

^bX550 fibers: epoxy-based sizing and anodic oxidized.

^cAS41 = Mg-4Al-1Si-0.3Mn.

^dT300-90: unsized and surface treated.

^eT300-99: unsized and untreated.

on the decomposition parameters, which are responsible for the crystal structure, the layer thickness and the chemical attack of hydrogen on the carbon fiber.

5.5.4. Boron fibers

5.5.4.1. Introduction

Boron fibers are normally made by CVD of boron on a substrate, such as a fine tungsten wire or carbon core. Fig. 5.26 shows a schematic drawing of boron fiber production. A fine tungsten wire of 10–12 μm in diameter is pulled into a reaction chamber at one end through a mercury seal and out at the other end through another mercury seal. There is a critical temperature (above about 1150°C) to obtain a boron fiber with optimum properties and structure, depending on the substrate wire speed (Krukonis, 1977). The structure and morphology of boron fibers are controlled by the conditions of deposition, temperature, composition of glasses, gas dynamics, etc. In general, boron fibers have a corn-cob structure, as shown in Fig. 5.29, which consists of nodules separated by boundaries originating from the nature of CVD process. However, the surface of boron fibers based on a carbon substrate is relatively smooth, a reflection of the smooth surface of the carbon core.

Boron fibers produced on a tungsten substrate contain a series of compounds, such as W_2B , WB , W_2B_5 and WB_5 , which are formed at the interface region by diffusion of B into W. On the contrary, boron fibers with a carbon core do not produce boron carbides as the interface reaction compound. Due to the composite nature of boron fibers, complex internal stresses and defects such as voids and structural discontinuities result from the presence of a core and the deposition process. The strength of a boron fiber is equivalent to the intrinsic strength of boron, with an average tensile strength of about 3.8 GPa and a Young's modulus between 380 and 400 GPa. Representative properties of boron fibers and other non-oxide inorganic fibers are given in Table 5.15. Fibers are often post-treated chemically or thermally to make them more compatible with metal and ceramic matrices for composites fabrication. Chemical treatment also serves to remove the surface defects, whereas thermal treatment is intended to remove the residual stresses.

5.5.4.2. Reaction barrier coatings on boron fibers

Coatings on boron fibers have been applied to prevent the formation of reaction products at the interface region with common matrices, such as Al and Ti, and other ferrous metals including Fe, Co and Ni. The oxide films preexisting on the fiber surface and the Al matrix may act to delay the reaction if the composite is made in the solid state. However, the oxides are not useful in the presence of molten Al. Coating materials developed specifically for aluminum matrices include SiC, BC and BN (Carlsson, 1986). A SiC coating of thickness in the range 1.5–2.0 μm is applied by a CVD process at 1200–1300°C using a mixture of hydrogen and chlorosilane, while a BC coating of 2–8 μm in thickness is obtained by a similar CVD process at 1150–1300°C using a mixture of hydrogen, boron trichloride and methane. A BN coating is also applied through oxidation of the fiber surface in air at 1000°C, followed by heating in the presence of ammonia at 1100°C. It is also found that SiC

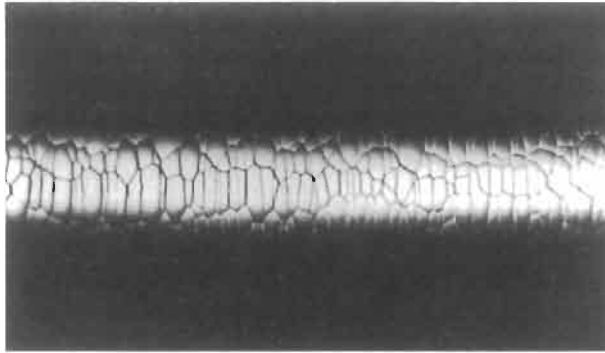


Fig. 5.29. Surface of boron fiber on tungsten substrate showing a "corn-cob" structure with nodules.

coatings on boron fibers, so-called Borsic fiber, provide some protection so that direct contact with molten aluminum for a prolonged time does not degrade the fiber strength (Basche, 1969; Prewo and McCarthy, 1972). BN coatings of thickness in the range 0.3 to 0.4 μm are very stable in the presence of molten aluminum at temperatures as high as 800°C if the coating remains intact. This coating improves slightly the average fiber strength (Vidoz et al., 1969; Ryder et al., 1970).

Early work on Ti matrix composites (Metcalf, 1974) shows limited success for diffusion barrier coatings on boron fiber reinforcements. Coatings of BN, B_4C and SiC causes a reaction rate similar to the uncoated fibers. The basic difference between these coatings is the reaction products formed at the interface region: TiB_2 is primarily formed with boron-containing coatings, while titanium silicides and carbides are formed with SiC coatings (Wawner, 1988). The B_4C coating of thickness approximately 7 μm obtained by a CVD process from boron trichloride in methane gas improves substantially the composite tensile strength (Morin, 1976).

Table 5.15
Representative properties of SiC and boron fibers

Properties	SiC (SCS-6) monofilament	SiC (Nicalon) fiber	Boron (B W) fiber
Diameter (μm)	140	10 20	142 400
Density (g/cm^3)	3	2.32 2.55	2.34 2.6
Tensile strength (GPa)	3500	2960	3800
Elongation at break (%)	0.56	1.5	—
Young's modulus (GPa)	430	192	380 400
Specific strength (10^6 cm)	11.9	12.6	16.1
Specific modulus (10^6 cm)	1460	820	1700
Linear coefficient of thermal expansion ($10^{-6}/\text{K}$)	—	4	0.05
Melting temperature ($^{\circ}\text{C}$)	2700	2700	2040

5.5.5. Silicon carbide fibers

5.5.5.1. Introduction

One of the most important fibers for high temperature applications is the SiC fiber. There are two major processes developed to produce continuous SiC fibers. The first is achieved by coating SiC on either a tungsten or a carbon filament by a CVD process. The SiC fiber obtained from a CVD process is very thick (say, 100–150 μm in diameter) and is rigid. The surface of SiC fibers, i.e. SiC/W fiber, produced on a tungsten fiber is bumpy and nodular. Although the nodules are smaller than those seen in boron fibers, they are very sensitive to self-abrasion which may reduce significantly the fiber tensile strength. More importantly, prolonged exposure to elevated temperature causes significant degradation of the fiber strength, due probably to the deleterious tungsten core reaction. Later, the tungsten core is replaced with a carbon monofilament substrate to produce SiC/C fibers. The carbon core is routinely coated with a thin (about 1 μm) layer of pyrolytic graphite before deposition of SiC to minimize the reaction between the carbon core and SiC. To reduce the extreme surface sensitivity of SiC/C fibers, a thin layer of carbon is deposited onto the surface. The carbon coating may also lower the stress concentrating ability of grain boundaries at the fiber surface. However, the amorphous carbon-rich surface also has a serious disadvantage: a low wettability with metal matrices particularly cast aluminum, which causes poor adhesion and forms reaction products, such as aluminum carbide with an aluminum matrix. To reduce this detrimental problem, the fiber surface is further modified by covering the carbon layer with an additional SiC coating. This is designated the SCS fiber (Textron Specialty Materials Co).

The other process is the transformation of an organic precursor into a continuous thin ceramic fiber. In the spinning process, polycarbosilane, a high molecular weight polymer containing Si and C, is obtained by thermal decomposition and polymerization of polydimethylsilane. The fiber thus produced consists of a mixture of β -SiC, carbon crystallite and SiO_2 . The presence of carbon crystallite suppresses the growth of SiC crystals. Yajima and coworkers (Yajima et al., 1976, 1978, 1979) were the first to produce fine (10–30 μm in diameter), continuous and flexible fibers, which are commercialized with the trade name of Nicalon (Nippon Carbon Co.).

SiC monofilaments produced by the CVD process is generally superior to Nicalon SiC fibers in mechanical properties because of its almost 100% β -SiC purity while Nicalon is a mixture of SiC, SiO_2 and free carbon. Representative properties of SiC monofilaments and Nicalon fibers are given in Table 5.15.

5.5.5.2. Reaction barrier coatings on SiC monofilaments

There are four types of SCS fibers depending on the thickness of the final SiC coating designed for different metal matrices. They are the standard SCS, SCS-2, SCS-6 and SCS-8. Fig. 5.30 illustrates schematically the cross sections of two commercially produced SiC fibers, the standard SCS and SCS-6 fibers, according to DiCarlo (1988). Both types of fibers consist of a carbon core of 37 μm in diameter, a SiC sheath of varying thickness and a carbon-rich surface coating of 0–4 μm in

thickness. SCS-2 and SCS-8 fibers are designed for and functional in Al matrices, whereas SCS-6 fibers with a thicker stoichiometric β -SiC coating are designed specifically for Ti matrices which require more protection from the high temperature fabrication process.

The original coatings present on SCS-2 fibers are found to be effective for retaining the fiber strength after exposure in molten aluminum for up to 1.5 h. However, the strength decreases systematically with continuing exposure due to fragmentation of the coating and formation of reaction products such as aluminum carbides. The fracture behavior of Ti alloy matrix composites containing SCS-6 fibers and their reaction barrier coatings have received much attention in recent years. SCS-6 fibers show little sign of degradation after 5 h exposure at 900°C when incorporated in a Ti-6Al-4V matrix (Strife and Prewo, 1982; Martineau et al., 1984). On the contrary, when the same SCS-6 fibers are incorporated in a Ti-24Al-11Nb intermetallic alloy at the solidification temperature of 1040°C, a reaction layer is created at the interface region. Its thickness depends on the time exposed: 1.1 and 1.7 μm for 0.5 and 4 h exposure, respectively (Cantonwine and Wadley, 1994). Fiber push-out tests identify an increase in the interface bond strength with increasing reaction layer thickness, and associated characteristic debond behavior. In the composite with a thin reaction layer, debonding occurs predominantly at the outer SCS coating-reaction layer interface, whereas the composite with a thick reaction product displays multiple debond paths branching between the fiber-SCS coating-reaction product interfaces. The interfacial reaction between the SCS-6 fiber and Ti matrix is identified as a result of interdiffusion between Ti, Si and C atoms, and the major reaction products are TiC, Ti_5Si_3 and Ti_3Si_2 (Lancin et al., 1988).

Additional surface modifications on vapor deposited SiC fibers, including WC, TaC, TiN, B_4C , Al, Ni and Fe, have been applied with varying degree of success (Wawner and Nutt, 1980; DeBolt, 1982; Wawner, 1988). After exhaustive trial and error, TiB is selected as an additional coating material to further prevent the diffusion-induced reactions between the SCS-6 fibers and matrix materials, including Ti alloys and Ti-Al intermetallic alloys (e.g. Ti_3Al , TiAl and TiAl_3) (Donnellan and Frazier, 1991; James et al., 1991). When the coated fiber is subjected to tensile

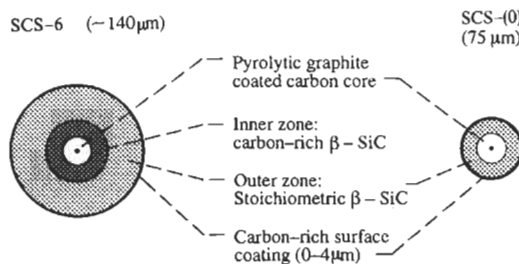


Fig. 5.30. Schematic illustrations of two SCS-type SiC fibers. After Chawla (1993), Fig. 3.35, p. 95. Reproduced by permission of Chapman & Hall.

loading, the brittle TiB_2 layer cracks easily, promoting interfacial failure, which in turn allows the inherent fiber strength to be preserved (Jeng et al., 1991).

Later, aiming to improve the stability of SCS-6 monofilaments at high temperatures, a TiB/C duplicate coating has been developed. However, its application in Ti-6Al-4V matrix composites is marred by the formation of TiB needles at the interface region (Jones et al., 1989; Guo and Derby, 1994). Fig. 5.31 compares the interfacial morphologies between the uncoated and TiB/C coated SCS-6 fibers after exposure at 970°C for 2 h. The needles are thought to increase the stress concentration and the tendency of cracking at the interface region, even in the absence of external loading, which are highly undesirable. In contrast, the TiB_2/C duplicate coating performs very effectively in protecting the SCS-6 fibers from chemical reactions in a Ti_3Al matrix (Guo et al., 1993; Guo and Derby, 1994). Only limited reaction is observed without the harmful TiB needles at the interface region, and the reaction mechanism arises due to the diffusion of boron through the reaction layer toward the matrix. Thermo-mechanical and high temperature isothermal fatigue loading of SCS-6 fibers embedded in a Ti-6Al-4V matrix show that the matrix cracking with unbroken fiber bridging is a major failure mechanism (Jeng et al., 1992). Damage initiation appears to be controlled by the rate of oxidation layer formation on the specimen surface. Oxygen diffuses through the matrix internal cracks into the interface layer, resulting in severe fiber-matrix separation and the formation of oxidation pits on the SCS-6 fiber surface.

Further studies on duplex barrier coatings consisting of a metallic layer with an overlayer of metal oxide have been performed on SCS-6 monofilaments for reinforcement of Ti matrices (Kiescheke et al., 1991a, b; Warwick et al., 1991). After depositing an initial layer of yttria by a sputtering process, a covering oxide layer of Y_2O_3 is applied in the second sputtering process. Fig. 5.32 shows a duplex coated SCS-6 monofilament. The duplex layer offers some advantages over a single layer

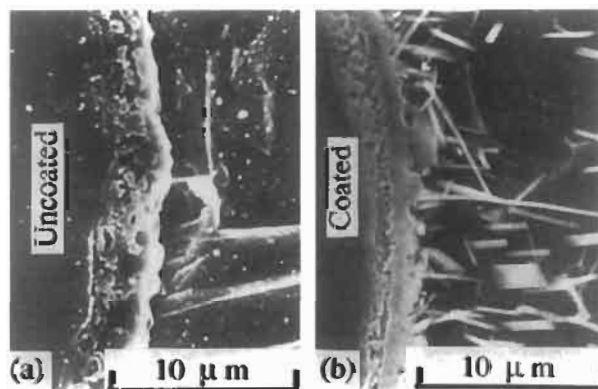


Fig. 5.31. Scanning electron microphotographs of the interface morphology for (a) uncoated SiC monofilament and (b) Ti-6Al-4V coated SiC monofilament after exposure at 1070°C for 2 h. After Guo et al. (1993). Reproduced by permission of Blackwell Science Ltd.

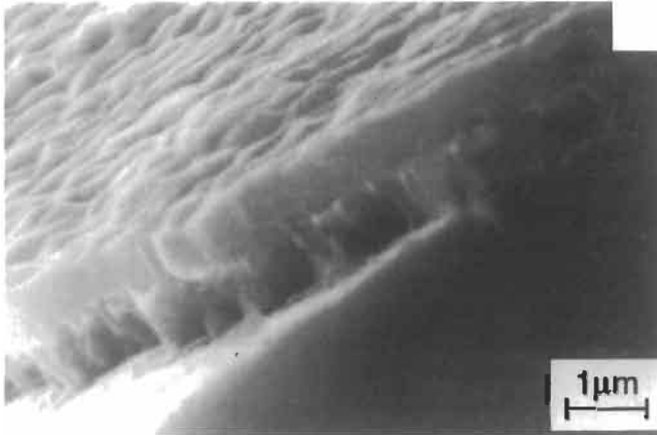


Fig. 5.32. Scanning electron microphotograph of a duplex Y/Y₂O₃ coating on a SiC monofilament. After Clyne and Withers (1993). Reproduced by permission of Cambridge University Press.

coating of oxide: reduced danger of crack propagation from the oxide layer to the fiber, and ability to self-cure the damage to the oxide layer as a result of the gettering action of dissolved oxygen from the matrix by the exposed yttria (Kiescheke et al., 1991a). The thin coating on SiC fibers is also found to provide considerable protection for Mg–Li matrix composites at temperatures up to 400°C, while the uncoated fibers suffer catastrophic embrittlement by penetration of Li into the grain boundaries (Kiescheke et al., 1991b).

A study of mechanical properties of uniaxial SCS-6 fiber reinforced zircon matrix composites (Singh, 1988; Singh and Gaddipati, 1991; Singh, 1993) shows significant strengthening and improvement of fracture toughness compared to those without fiber reinforcement. A BN coating on the fiber further improves the stability of the interface and the toughness values in particular, at both ambient and elevated temperatures. This is evidenced by the force–displacement curves given in Fig. 5.33, where the differences in strength and ductility between the unreinforced zircon and the reinforced composites with and without the BN coating are quite remarkable.

5.5.5.3. Reaction barrier coatings on Nicalon SiC fibers

The properties of Nicalon SiC fibers start to degrade above about 600°C because of the thermodynamic instability of composition and microstructure, leading to the evolution of SiO and CO (Johnson et al., 1988). Nicalon fibers are coated with pyrolytic graphite, normally in an argon atmosphere, to protect the fibers from chemical damage during composite processing and thus to improve the strength and modulus of the CMCs made therefrom (Hwang and Jang, 1991). The coating, shown in Fig. 5.34, reduces the interface bond strength due to the reduced chemical reaction taking place at the interface region.

Lowden and More (1989) and Lowden (1991) studied extensively the effects of graphite coating thickness on the mechanical properties of Nicalon fiber–SiC matrix

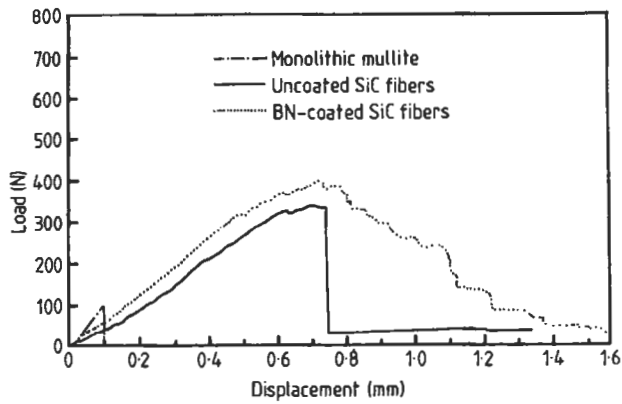


Fig. 5.33. Load-displacement records of monolithic mullite, and SiC fiber reinforced mullite composites with and without BN coating. After Singh (1988).

composites. The coatings are deposited isothermally onto the fiber preform of plain weave fabric from an argon/polypropylene mixture at 1100°C. By varying the deposition time, coating thickness in the range 0.1–1.0 μm are obtained. Fig. 5.35 shows the load–displacement curves obtained in flexure tests of the composites with and without coating layers of varying thickness. The uncoated fiber composite exhibits poor strength response and brittle fracture without any fiber pull-out, as do the specimens with prior oxidation treatments. Incorporation of a graphite coating promotes fiber pull-out, whose length increases with coating thickness. The linear inverse relationship between interfacial shear strength and coating thickness has also been identified, Fig. 5.36. The uncoated fiber composite with a strong chemical bonding possesses the highest interfacial shear stress, while the specimen with an oxidized interlayer shows no interfacial bonding because the oxidation of carbon produces a gap between the fiber and matrix.

Apart from functioning as a reaction barrier, another important role of the low modulus interlayer by the pyrolytic graphite, is the reduction of the radial compressive stress arising from differential thermal contraction between fiber and matrix. Thicker carbon coatings give more reduction in thermal stresses than thinner coatings, which is partly responsible for the inverse relationship between interfacial shear strength and coating thickness (Fig. 5.36). A compliant coating is most useful when the CTE for the fiber is smaller than the matrix material (Arnold et al., 1990), as in most practical CMCs.

BN is also proven to be an efficient reaction barrier coating for Nicalon fiber–SiC matrix systems (Naslain et al., 1991a, b). The coating promotes a non-linear and non-catastrophic fracture behavior under tensile and impact loading. A coating of 0.5 μm in thickness exhibits the best mechanical properties (Prouhet et al., 1994). The use of C, BN, BN/SiC coatings on Nicalon SiC fibers is also suggested for Zr-based matrix materials. Bender et al. (1986) have shown that the BN-coated Nicalon fibers in a zirconia-based matrix ($\text{ZrO}_2 + 50 \text{ mol}\% \text{ SiO}_2$ and $\text{ZrO}_2 + 50 \text{ mol}\%$



Fig. 5.34. Scanning electron microphotograph of a pyrocarbon coated Nicalon SiC fiber. After Chawla (1993), Fig. 9.15, p. 320. Reproduced by permission of Chapman & Hall.

TiO₂) result in substantial improvement in strength and toughness of the composites. The BN coating reduces the interface bond strength between the SiC reaction layer and the matrix. A duplex coating of SiC/BN applied to the Nicalon

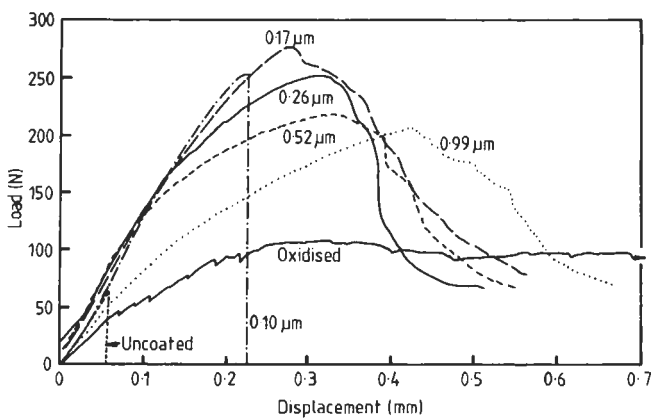


Fig. 5.35. Load displacement records of Nicalon SiC fiber SiC matrix composites with varying thicknesses of carbon coating. After Lowden (1991).

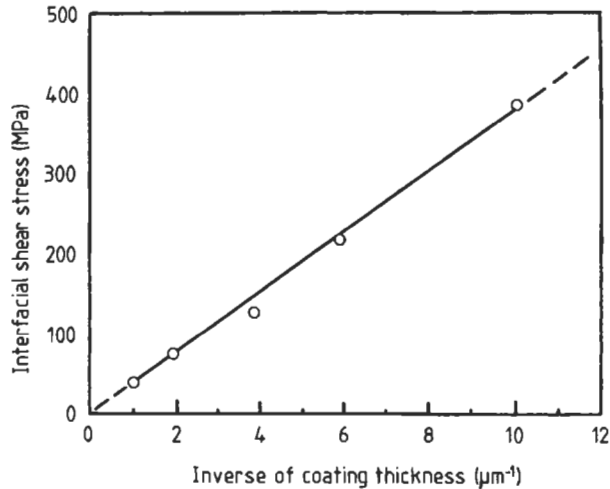


Fig. 5.36. Interface shear strength as a function of coating thickness for Nicalon SiC fiber-SiC matrix composites. After Lowden (1991).

fibers by a CVD process is also shown to be quite promising for improved high-temperature mechanical properties of barium magnesium aluminosilicate (BMAS) matrix composites (Sun et al., 1994). The duplex coating produces a stable interface structure which is resistant to gross reaction at 1100°C for extended periods of time. The turbostratic BN layer offers a relatively weak interfacial zone, allowing crack deflection with associated high fracture toughness.

Some interesting results have been reported based on the studies using Nicalon SiC fibers-glass matrix composites containing lithium aluminosilicate (LAS). X-ray diffraction study shows two distinct carbon-rich reaction layers (Bender et al., 1986). The first layer is essentially amorphous carbon of thickness about 100 nm, which is adjacent to the SiC fiber. The carbon layer originates from excess carbon in the SiC fiber which migrates to the fiber surface (Chaim and Heuer, 1987). Another source of carbon is the residue left after heat cleansing of the organic size from the SiC and of the organic binder from the prepreg. The second reaction layer is located between the first layer and the LAS matrix, consisting predominantly of microcrystals of NbC. The niobium originates from the additive to the LAS glass as a crystallization aid. The thickness of the second layer varies from 20 to 100 nm. Trace amounts of impurities like Zr, Mg, Ti, K, Ba, Fe and As are also detected in the second layer, that migrate to the interface region during processing. In this SiC-LAS system, the interface is relatively weak compared to the bulk fiber and matrix. It follows then that debonding occurs inevitably between the two reaction layers where the NbC microcrystals are well developed (see Fig. 5.37).

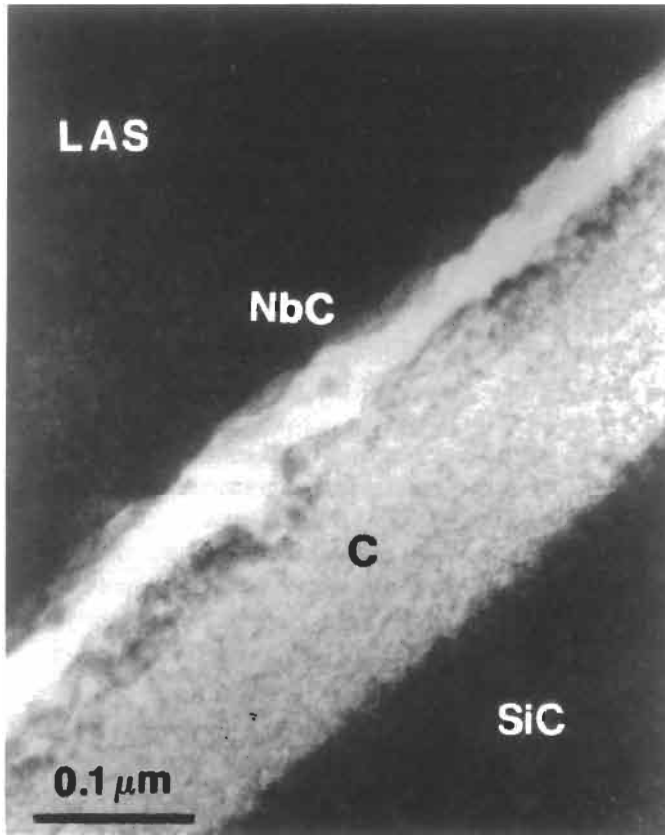


Fig. 5.37. Debonding in a carbon coating between a SiC (Nicalon) fiber and a LAS matrix. After Evans and Marshall (1989).

5.5.6. Alumina fibers

5.5.6.1. Introduction

Alumina fibers are available commercially in many different forms, that include continuous polycrystalline alpha-alumina yarn (FP, Du-Pont; Almax, Mitsui Mining Co.), alpha-alumina + 15–20% ZrO_2 yarn (PDR-166, Du Pont), alpha-alumina (Nextel 610, 3M Co), 70–100% Al_2O_3 + 30–0% SiO_2 (Sumitomo Chemical Co.) and short and very fine (about 3 μm in diameter) staple 96% delta-alumina fiber (Saffil, ICI). The addition of oxide of silicon, phosphorous or zirconium to pure alumina is aimed to inhibit the grain growth at service temperatures. FP, PRD-166 and Almax fibers are produced by dry spinning of a viscous slurry solution, while Nextel 610 fibers are produced via a sol-gel route. Silica-stabilized alumina fibers, e.g. Saffil, are also produced via the sol-gel method. Single crystal continuous aluminum oxide or sapphire fibers, e.g. Saphikon, are produced by drawing from

molten alumina. The low viscosity of molten alumina and its high melting temperature ($\sim 2070^\circ\text{C}$) preclude the melt spinning process so that slurry and sol-gel spinning processes have been developed to avoid the melting step. A particular advantage of the sol-gel spinning process is the ability to control the fiber diameter in the range of 1–7 μm .

Scanning electron microphotographs and surface roughness profiles of three alumina fibers, PRD-166, Nextel 610 and Saphikon fibers, are shown in Fig. 5.38. It is noted that the surface of the PRD-166 fiber is significantly rougher than the other two fibers, which is attributed to its relatively large grain size ($\approx 0.5 \mu\text{m}$). The Nextel 610 fiber, although polycrystalline, is very smooth because of its extremely fine grain size. It contains 0.4–0.7 wt% Fe_2O_3 and about 0.5 wt% SiO_2 , the latter is to reduce the final grain size. The roughness of the fiber and the relative magnitude of the thermal expansion coefficient between fiber and matrix are the predominant factors determining the fracture behavior of the composite involving interface debonding and subsequent fiber pull-out. Representative properties of some alumina fibers are given in Table 5.16.

5.5.6.2. Reaction barrier coatings on Al_2O_3 fibers

Most α -alumina fibers are not readily wetted by most metals, due to their low surface energy, particularly if the fibers are in the form of short whiskers. The wettability of these fibers and whiskers can be improved by a CVD process of a thin metallic coating, such as Ni (Sutton, 1966) or Ni alloys containing active metals like Ti (Noone et al., 1969) for a molten silver matrix. A duplex Ti–Ni coating further promotes the wetting and improves significantly the bonding, as revealed by the improvement in composite tensile strength. The fracture mode changes from interfacial failure to matrix shear failure with the coated fibers. The Ti–Ni coatings are also found to be effective for other matrices like Al and Ni–Cr alloy (Nicholas, 1968).

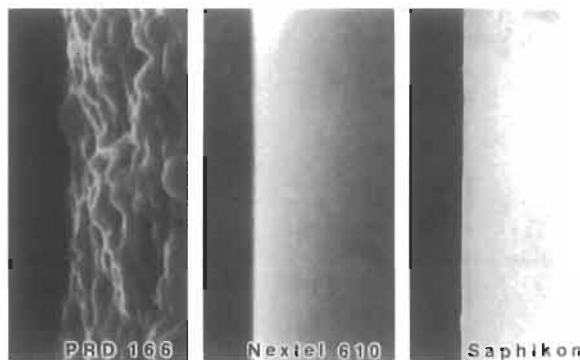


Fig. 5.38. Scanning electron microphotographs of (a) PRD-166, (b) Nextel 610 and (c) Saphikon Al_2O_3 fibers, showing different surface roughness profiles. After Chawla (1993), Fig. 9.25, p. 330. Reproduced by permission of Chapman & Hall.

Table 5.16
Mechanical properties of major oxide fibers^a

Properties	Fiber FP	PRD-166	Saffil RF	Saffil HA	Safimax	Fiberfrax	Nextel 312	Nextel 440
Diameter (μm)	20	20	1–5	1–5	3.0	1–7	11	11
Density (g/cm^3)	3.9	4.2	3.3	3.4	3.3	2.73	2.7	3.1
Tensile strength (MPa)	> 1400	2070	2000	1500	2000	1000	1720	1720
Young's modulus (GPa)	380	380	300	> 300	300	105	152	220
Specific strength (10^6 cm)	> 3.7	5.0	6.2	4.5	6.2	3.8	6.5	5.7
Specific modulus (10^6 cm)	> 970	920	930	> 900	930	390	570	720

^aAfter Birchall (1986).

Fiber FP: α - Al_2O_3 yarn (Du Pont).

PRD-166: Al_2O_3 - ZrO_2 yarn (Du Pont).

Saffil RF: 5% $\text{SiO}_2/\text{Al}_2\text{O}_3$ staple (ICI).

Saffil HA: 5% $\text{SiO}_2/\text{Al}_2\text{O}_3$ staple (ICI).

Safimax: 4% $\text{SiO}_2/\text{Al}_2\text{O}_3$ semi-continuous, standard density (ICI).

Fiberfrax: 50% $\text{SiO}_2/\text{Al}_2\text{O}_3$ staple (Carborundum).

Nextel 312: 24% $\text{SiO}_2/14\%$ $\text{B}_2\text{O}_3/\text{Al}_2\text{O}_3$ (3M).

Nextel 440: 28% $\text{SiO}_2/2\%$ $\text{B}_2\text{O}_3/\text{Al}_2\text{O}_3$ (3M).

Another good example of interfacial modification can be found in alumina fiber-glass matrix composites that are essentially an oxide-oxide system. A series of intermediate compounds has been identified by Aksay and Pask (1975). The reaction product gives rise to a strong chemical bonding at the interface region and thus a brittle fracture behavior of the composite (Michasle and Hellman, 1988; Maheshwari et al., 1989). Tin dioxide, SnO_2 , is known to have no mutual solubility with aluminum up to 1600°C (Barczak and Insley, 1962), and has a low solubility in silica (Manfredo and McNally, 1984). This knowledge has been applied by Chawla et al., (1993) to PRD-166 and Saphikon-single crystal alumina fibers. The SnO_2 coating prevents chemical reactions that otherwise occur with the glass matrix. The bonding

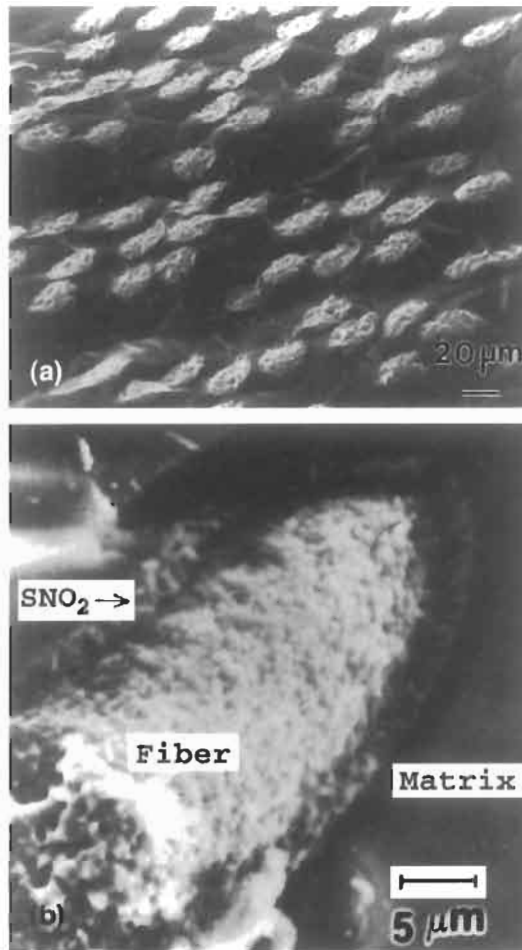


Fig. 5.39. Scanning electron microphotographs of fracture surfaces of (a) uncoated and (b) SnO_2 coated PRD-166 Al_2O_3 fiber reinforced glass matrix composites. After Chawla (1993), Fig. 9.26 and Fig. 9.27, p. 333. Reproduced by permission of Chapman & Hall.

at the fiber–SnO₂ interface is purely mechanical, whereas that between SnO₂ and glass is a combination of chemical and mechanical bonds. Fig. 5.39 shows a characteristic planar brittle fracture and pull-out fibers in uncoated and SnO₂ coated PRD-166 fiber–glass matrix composites, respectively. The major toughening mechanisms in the coated fiber composite are mainly crack bridging and crack deflection (Chawla, 1993). The beneficial effects of SnO₂ coating on Al₂O₃ fiber has also been demonstrated in flexure and compression tests (Siadati et al., 1991).

A micromechanics analysis of the residual thermal stresses present in glass matrix composites with and without SnO₂ coating has been studied by Chawla (1993), and a summary is given in Fig. 5.40. Both the radial and axial stresses in the fiber are greater for the coated fibers than the uncoated fibers, whereas these stresses remain almost constant in the matrix. From the composite toughness viewpoint, the presence of the high tensile radial stress at the fiber–coating and coating–matrix interfaces is deemed particularly desirable. It is also interesting to note that there is a large axial stress discontinuity at the interface region when the coating layer is present.

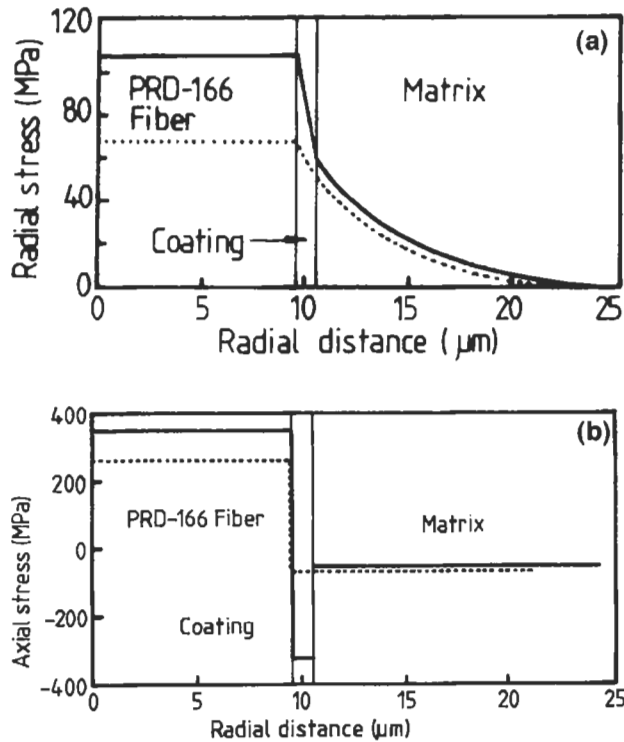


Fig. 5.40. Distributions of thermal residual stresses in the (a) radial and (b) axial directions of SnO₂ coated PRD-166 Al₂O₃ fiber reinforced glass matrix composites: (....) uncoated fiber; (—) coated fiber. After Chawla (1993), Fig. 9.29, p. 335. Reproduced by permission of Chapman & Hall.

The improvement in fracture toughness of a Nextel 480 mullite ($3\text{Al}_2\text{O}_3\text{-}2\text{SiO}_2$) fiber in a glass matrix has also been achieved by incorporating a BN coating on the fiber surface (Vaidya et al. 1992). The uncoated fiber composite shows a brittle and planar fracture, while those containing BN coated fibers exhibit extensive fiber pull-out, in a similar manner shown for SnO_2 coated PRD-166 fibers (Fig. 5.39(b)). However, when a very thin, say about $0.3\ \mu\text{m}$, coating is applied, no BN layer is observed after the process, because the thin coating becomes easily oxidized, followed by vaporization of the oxidation product. Otherwise, the BN coating tends to decompose during the hot pressing of the matrix material. This indicates that the choice of coating thickness is an important factor which controls the effectiveness of the coating material. Ha and Chawla (1993) and Ha et al. (1993) used a similar BN coating successfully to obtain tough mullite fiber–mullite matrix composites. A duplex SiC/BN coating is also recommended for use to reduce the interface bond strength.

A diffusion barrier coating has also been successfully applied to aluminide-based intermetallic matrix composites (Misra, 1994). For example, Ti coating on Al_2O_3 fiber for reinforcements of NiAl or FeAl matrices produces a rather strong bonding at the interface which is desirable to eliminate the longitudinal matrix cracks arising from thermally induced residual stresses. However, a weak interface is needed for easy debonding and fiber pull-out which are required for improvement of fracture toughness.

Alloying elements can also have a significant effect on reaction processes at the interface region. For example, the addition of a small amount of magnesium, say less than 0.4 wt% (Chapman et al., 1991), or about 3 wt% lithium (Birchall et al., 1985; Birchall, 1986) in Al_2O_3 fiber–aluminum matrix composite is found to be beneficial for metal infiltration and fracture resistance without causing a harmful reaction at the interface. Increasing the magnesium content, however, deteriorates the flexural strength due to a corresponding increase in thickness of the reaction product, MgAl_2O_4 , at the interface region (Johnston and Greenfield, 1991).

References

- Abraham, S., Pai, B.C., Satyanarayana, K.G. and Vaidyan, V.K. (1989). In *Proc. Interfacial Phenomenon in Composite Materials* (F.R. Jones ed.), Butterworth, London, pp. 276–281.
- Abraham, S., Pai, B.C., Satyanarayana, K.G. and Vaidyan, V.K. (1990). Studies on nickel coated carbon fibers and their composites. *J. Mater. Sci.* **25**, 2839–2845.
- Abraham, S., Pai, B.C., Satyanarayana, K.G. and Vaidyan, V.K. (1992). Copper coating on carbon fibers and their composites with aluminum matrix. *J. Mater. Sci.* **27**, 3479–3486.
- Adams, D.F. and Zimmerman, R.S. (1986). Static and impact performance of polyethylene fiber/graphite fiber hybrid composites. Allied Fibers, Petersburg, VA.
- Aksay, I.A. and Pask, J.A. (1975). *J. Am. Ceram. Soc.* **58**, 507.
- Alam, M.K. and Jain, S.C. (1990). The CVD coating of fibers for composite materials. *J. Metals* **42**, 56–58.
- Albert, K., Pfeleiderer, B., Bayer, E. and Schnabel, R. (1991). Characterization of chemically modified glass surfaces by ^{13}C and ^{29}Si CP/MAS NMR spectroscopy. *J. Colloid. Interface Sci.* **142**, 35–40.
- Allred, R.E., Merrill, E.W. and Roylance, D.K. (1985). Surface chemical modification of polyaramid filaments with amine plasma. In *Molecular characterization of composite interfaces* (H. Ishida and G. Kumar, eds.), Plenum Press, New York, pp. 333–375.

- Al-Moussawi, H., Drown, E.K., and Drzal, L.T. (1993). The silane/sizing composite interphase. *Polym. Composites* **14**, 195–200.
- Andreopoulos, A.G. (1989). A new coupling agent for aramid fibers. *J. Appl. Polym. Sci.* **38**, 1053–1064.
- Antoon, M.K., Koenig, J.L. (1981). Irreversible effects of moisture on the epoxy matrix in glass-reinforced composites. *J. Polym. Sci.: Polym. Phys. Edition* **19**, 197–212.
- Arnold, S.M., Arya, V.K. and Melis, M.E. (1990). Elastic/plastic analysis of advanced composite investigating the use of the compliant layer concept in reducing residual stresses resulting from processing, NASA TM-103204.
- Bader, M.G., Charalambides, B., Ling, J. (1991). The influence of fiber-matrix interface strength on the tensile strength and failure mode in uniaxial CFRP. In *Proc. ICCM-VIII, Composites: Design, Manufacture and Application* (S.W. Tsai and G.S. Springer, eds.), SAMPE Pub. Paper 111.
- Baillie, C., Bader, M.G. (1991). Chemical aspects of interfacial adhesion between electrochemically oxidized carbon fibers and epoxy resins. In *Proc. ICCM-VIII, Composites: Design, Manufacture and Application* (S.W. Tsai and G.S. Springer, eds.), SAMPE Pub. Paper 11B.
- Barczak, V.J. and Insley, R.H. (1962). *J. Am. Ceram. Soc.* **45**, 144.
- Bascom, W.D. (1965). in *Proc. SPI 20th Annual Tech. Conf.*, Reinf. Plast. 15-B.
- Basche, M. (1969). In *Interfaces in Composites*. ASTM STP 452, ASTM, Philadelphia, PA, pp. 130–136.
- Bascom, W.D., Chen, W.J. (1991). Effect of plasma treatment on the adhesion of carbon fibers to thermoplastic polymers. *J. Adhesion* **34**, 99–119.
- Bascom, W.D. and Drzal, L.T. (1987). The surface properties of carbon fibers and their adhesion to organic polymers. NASA contract Report 4084.
- Bender, B., Shadwell, D., Bulik, C., Inorvat, L. and Lewis III, D. (1986). Effect of fiber coating and composite processing on properties of zirconia-based matrix SiC fiber composites. *Am. Ceram. Soc. Bull.* **65**, 363–369.
- Bennett, S.C. and Johnson, D.J. (1978). In *Proc. 5th London Carbon and Graphite Conference*, Vol. 1, Society for Chemical Industry, London, p. 377
- Birchall, J.D., Bradbury, J.A.A. and Dinwoodie, J. (1985). Alumina fibers. In *Handbook of Composites* (W. Watt and B.V. Perov, eds.), Vol. 1, Strong Fibers, North Holland, Amsterdam, pp. 115–155.
- Birchall, J.D. (1986). Inorganic fibers. In *Encyclopedia of Material Science and Engineering* (M.B. Bever, ed.), Pergamon Press, Oxford, pp. 2333–2335.
- Biro, D.A., Pleizeier, G. and Deslandes, Y. (1993a). Application of the microbond technique. III. Effects of plasma treatment on the ultra-high modulus polyethylene fiber–epoxy interface, *J. Mater. Sci. Lett.* **11**, 698–710.
- Biro, D.A., Pleizeier, G. and Deslandes, Y. (1993b). Application of the microbond technique. IV. Improved fiber–matrix adhesion by RF plasma treatment of organic fibers. *J. Appl. Polym. Sci.* **47**, 883–894.
- Brown, J.R., P.J.C. Chappell, Z. Mathys (1991). Plasma surface modification of advanced organic fibers: part I. Effects on the mechanical, fracture and ballistic properties of aramid/aramid composites. *J. Mater. Sci.* **26**, 4172–4178.
- Brown, J.R., P.J.C. Chappell, Z. Mathys (1992a). Plasma surface modification of advanced organic fibers: part II. Effects on the mechanical, fracture and ballistic properties extended chain polyethylene-epoxy composites. *J. Mater. Sci.* **27**, 3167–3172.
- Brown, J.R., P.J.C. Chappell, Z. Mathys (1992b). Plasma surface modification of advanced organic fibers: part III. Effects on the mechanical properties of aramid/vinylester and extended chain polyethylene/vinylester composites. *J. Mater. Sci.* **27**, 6475–6480.
- Cantonwine, P.E. and H.N.G. Wadley (1994). The effect of fiber matrix reactions on the interface properties in a SCS-6/Ti-24Al-11Nb composite. *Composite Eng.* **4**, 67–80.
- Carlsson, J.O. (1986). Boron fibers. In *Encyclopedia of Materials Science and Engineering* (M.B. Bever, ed.), Pergamon Press, Oxford, pp. 402–464.
- Chaim, R. and Heuer, A.H. (1987). The interface between (Nicalon) SiC fibers and a glass-ceramic matrix. *Advanced Ceram. Mater.* **2**, 154–158.
- Chapman, A.R., Scott, V.D., Yang, M. (1991). In *Proc. ICCM-VIII, Composites: Design, Manufacturing and Application* (S.W. Tsai and G.S. Springer, eds.), SAMPE Pub. Paper 19G.

- Chawla, K.K., Ferber, M.K., Venkatesh, R. and Xu, Z.R. (1993). Interface engineering in alumina/glass composites. *Mater. Sci. Eng. A* **162**, 35–44.
- Chawla, K.K. (1993). *Ceramic Matrix Composites*. Chapman & Hall, London. pp. 162–194.
- Chen, R. and Li, Z. (1993). A study of silica coatings on the surface of carbon or graphite fiber and the interface in a carbon/magnesium composite. *Composites Sci. Technol.* **49**, 357–362.
- Cheng, T.H., Jones, F.R. and Wang, D. (1992). Silane interactions with glass fibers and resins at the interface in composite materials. In *Proc. Fiber reinforced Composites, FRP'92*. The Plastics and Rubber Institutes, UK. Paper 19.
- Cheng, T.H., Jones, F.R. and Wang, D. (1993). Effect of fiber conditioning on the interfacial shear strength of glass–fiber composites. *Composites Sci. Technol.* **48**, 89–96.
- Chiang, C.H., Ishida, H. and Koenig, J.L. (1980). The structure of γ -aminopropyl-triethoxysilane on glass surfaces. *J. Colloid. Interface Sci.* **74**, 396–404.
- Chiang, C.H. and Koenig, J.L. (1981). Fourier transform infrared spectroscopic study of the absorption of multiple aminosilane coupling agents on glass surfaces. *J. Colloid. Interface Sci.* **83**, 361–370.
- Cho, C.R. and Jang, J. (1990). Adhesion of ultrasonic high modulus polyethylene fiber-epoxy composite interfaces. In *Controlled Interphases in Composite Materials, Prod. ICCI-III*. (H. Ishida ed.), Elsevier Sci. Pub., New York, pp. 97–107.
- Chua, P.S., Dai, S.R. and Piggott, M.R. (1992a). Mechanical properties of the glass fiber–polyester interphase. Part 1 – Effects due to silane. *J. Mater. Sci.* **27**, 913–918.
- Chua, P.S., Dai, S.R. and Piggott, M.R. (1992b). Mechanical properties of the glass fiber–polyester interphase. Part 2 – Effect of water on debonding. *J. Mater. Sci.* **27**, 919–924.
- Chua, P.S. and Piggott, M.R. (1992). Mechanical properties of the glass fiber–polyester interphase. Part 3 – Effect of water on interface pressure and friction. *J. Mater. Sci.* **27**, 925–929.
- Clark, H.A. and Plueddemann, E.P. (1963). Bonding of silane coupling agents in glass-reinforced plastics. *Modern Plastics* **40**, 133–138, 195–196.
- Clyne, T.W. and Withers, P.J. (1993). *An introduction to Metal Matrix Composites*. Cambridge University Press, Cambridge, UK. Ch. 6, pp. 166–217.
- Culler, S.R., Ishida, H. and Koenig, J.L. (1986). The silane interphase of composites: effects of process condition on γ -aminopropyl triethoxysilane. *Polym. Composites* **7**, 231–238.
- Dagli, G., Sung, N.H. (1989). Properties of carbon/graphite fibers modified by plasma polymerization. *Polym. Composites* **10**, 109–116.
- Dauksys, R.J. (1973). Graphite fiber treatments which affect fiber surface morphology and epoxy bonding characteristics. *J. Adhesion* **5**, 211–244.
- DeVincent, S.M. (1991). Development of graphite/copper composites utilizing engineered interfaces. NASA CR-187143.
- DeVincent, S.M. and Michal, G.M. (1993a). Reaction layer formation at the graphite/copper–chromium alloy interface. *Metal. Trans A* **24A**, 53–60.
- DeVincent, S.M. and Michal, G.M. (1993b). Improvement of thermal and mechanical properties of graphite/copper composite through interfacial modification. *J. Mater. Eng. Performance (JMEPEG)* **2**, 323–332.
- DeBolt, H.E. (1982). Boron and other high strength, high modulus, low density filamentary reinforcing agents. In *Handbook of Composites*, (G. Lubin ed.), Van Nostrand Reinhold, New York, pp. 171–195.
- Delmonte, J. (1981). Surface treatments of carbon/graphite fibers and their effect on composites. In *Technology of Carbon and Graphite Fiber Composites*. Van Nostrand Reinhold, New York, pp. 171–197.
- DiCarlo, J.A. (1988). Creep of chemically vapor deposited SiC fibers. *J. Mater. Sci.* **21**, 217–224.
- Diwanji, A.P. and Hall, I.M. (1992). Fiber and fiber-surface treatment effects in carbon-aluminum metal matrix composites. *J. Mater. Sci.* **27**, 2093–2100.
- Dobb, M.G., Johnson, D.J. and Saville, B.P. (1977). Supramolecular structure of a high modulus polyaromatic fiber (Kevlar 49). *J. Polym. Sci., Polym. Phys. Ed.* **15**, 2201–2211.
- Donnellan, M.E., Frazier, W.E. (1991). In *Proc. ICCM-8, Composites: Design, Manufacture and Applications*. (S.W. Tsai and G.S. Springer, eds.), SAMPE Pub. Paper 25B.

- Donnet, J.B., Bansal, R.C. (1984). Surface properties of carbon fibers. In *Carbon Fibers*. Marcel Dekker New York, pp. 109–161.
- Donnet, J.B., Dong, S., Guilman, G., Brendle, M. (1988). Carbon fibers electrochemical and plasma surface treatment. In *Proc. ICCI-II, Interfaces in Polymer, Ceramic and Metal Matrix Composites* (H. Ishida ed.). Elsevier Sci. Pub., New York, pp. 35–42.
- Donnet, J.B., Ehrburger, P. (1977). Carbon fiber in polymer reinforcement. *Carbon* **15**, 143–152.
- Donnet, J.B., Guilman, G. (1991). Surface characterization of carbon fibers. *Composites* **22**, 59–62.
- Donnet, J.B., Papirer, E., Dauksch, H. (1974). Carbon Fibers – Their Place in Modern Technology. Plast. Inst. London, p. 58.
- Dow Corning Corporation (1985). A guide to Dow Corning Silane Coupling Agent, p. 15.
- Drown, E.K., Al-Moussawi, H. and Drzal, L.T. (1991). Glass fiber sizings and their role in fiber-matrix adhesion. *J. Adhesion Sci. Technol.* **5**, 865–881.
- Drzal, L.T., Rich, M.J., Lloyd, P.F. (1983a). Adhesion of graphite fibers to epoxy matrices: I. the role of fiber surface treatment. *J. Adhesion* **16**, 1–30.
- Drzal, L.T., Rich, M.J., Koenig, M.F. and Lloyd, P.F. (1983b). Adhesion of graphite fibers to epoxy matrices: II. the effect of fiber finish. *J. Adhesion* **16**, 133–152.
- Drzal, L.T. and Madhukar, M.S. (1993). Fiber-matrix adhesion and its relationship to composite mechanical properties. *J. Mater. Sci.* **28**, 569–610.
- Ehrburger, P., Donnet, J.B. (1985). Surface treatment of carbon fiber for resin matrices. In *Strong Fibers, Handbook of Composites, Vol. 1* (W. Watt, and B.V. Perov, eds.), Elsevier Sci., Amsterdam, pp. 577–603.
- Emadipour, H., Chiang, C.H. and J.L. Koenig (1982). *Res Mechanica* **5**, 165.
- Erickson, P.W. (1970). In *Proc. 25th Ann. Int. Conf. Reinforced Plastic Div.* SPI, Sec. 13A.
- Evans, A.G. and Marshall, D.B. (1989). Overview No. 85, The mechanical behavior of ceramic matrix composites. *Acta Metall.* **37**, 2567–2583.
- Evans, A.G., Zok, F.W. and Davies, J. (1991). The role of interfaces in fiber-reinforced brittle matrix composites. *Composites Sci. Technol.* **42**, 3–24.
- Fitzer, E., Fritz, W. and Gadov, R. (1984). Carbon fiber reinforced silicon carbide. In *Proc. International Symp. on Ceramic Components for Engineering* (S. Somiya, E. Kanai and K. Ando, eds.), Elsevier, London, pp. 505–518.
- Garbassi, F. and Occhiello, E. (1993). Surface Plasma Treatment. In *Handbook of Composite Reinforcement* (S.M. Lee ed.), VCH Publications, New York, pp. 625–630.
- Gao, S. and Zeng, Y. (1993a). Surface modification of ultrahigh molecular weight polyethylene fibers by plasma treatment. I. Improving surface adhesion. *J. Appl. Polym. Sci.* **47**, 2065–2071.
- Gao, S. and Zeng, Y. (1993b). Surface modification of ultrahigh molecular weight polyethylene fibers by plasma treatment. II. Mechanism of surface modification. *J. Appl. Polym. Sci.* **47**, 2093–2101.
- Garbassi, F. and Occhiello, E. (1993). Surface plasma treatment. In *Handbook of Composites Reinforcements* (S.M. Lee ed.), VCH Publications, New York, pp. 625–630.
- Goan, J.C., Prosen, S.P. (1969). Interfacial bonding in graphite fiber-resin composites. In *Interfaces in Composites*. ASTM STP 452, ASTM, Philadelphia, PA, pp. 3–26.
- Goan, J.C., Martin, T.W., Prescott, R. (1973). The influence of interfacial bonding on the properties of carbon fiber composites. In *Proc. 28th Annual Tech. Conf. Reinf. Plast. Composites Inst.*, SPI, Paper 21B.
- Guo, Z.X., Derby, B. and Cantor, B. (1993). Comparison of interfaces in Ti composites reinforced with uncoated and TiB₂/C-coated SiC fibers. *J. Microscopy* **169**, 279–287.
- Guo, Z.X. and Derby, B. (1994). Interfaces in Ti₃Al composites reinforced with SIGMA SiC fibers. *Scripta Metall. Mater.* **30**, 89–94.
- Ha, J.S. and Chawla, K.K. (1993). Effect of SiC/BN double coating on fiber pullout on mullite fiber/mullite matrix composites. *J. Mater. Sci. Lett.* **12**, 84–86.
- Ha, J.S., Chawla, K.K. and Engdahl, R.E. (1993). Effect of processing and fiber coating on fiber-matrix interaction in mullite fiber-mullite matrix composites. *Mater. Sci. Eng. A* **161**, 303–308.
- Hall, I.M. (1991). The interface in carbon-magnesium composites: Fiber and matrix effects. *J. Mater. Sci.* **26**, 776–781.

- Hild, D.N. and Schwartz, P. (1992a). Plasma treated ultrahigh strength polyethylene fibers. part I. Characterization by electron spectroscopy for chemical analysis. *J. Adhesion Sci. Technol.* **6**, 879–896.
- Hild, D.N. and Schwartz, P. (1992b). Plasma treated ultrahigh strength polyethylene fibers. Part II. Increased adhesion to poly(methyl methacrylate). *J. Adhesion Sci Technol.* **6**, 897–917.
- Hoh, K.P., Ishida, H. and Koenig, J.L. (1988). Spectroscopic studies of the gradient in the silane coupling agent/matrix interface in fiber glass-reinforced epoxy. *Polym. Composites* **9**, 151–157.
- Holms, S. and Schwartz, P. (1990). Amination of ultra-high strength polyethylene using ammonia plasma. *Composites Sci. Technol.* **38**, 1–21.
- Hooper, R.C. (1956). In *Proc. 11th Annual Tech. Conf. Reinforced Plastics Div.*, SPI, Sec. 8-B.
- Hopfgarten, F. (1978). Surface study of carbon fibers with ESCA and Auger electron spectroscopy. *Fibre Sci. Technol.* **11**, 67–79.
- Horie, K., Murai, H., Mita, I. (1977). Bonding of epoxy resin to graphite fibers. *Fibre Sci. Technol.* **9**, 253–264.
- Hughes, J.D.H. (1991). The carbon fiber–epoxy interfaces – a review. *Composites Sci. Technol.* **41**, 13–45.
- Hull, D. (1981). *An Introduction to Composite Materials*. Cambridge University Press. Cambridge.
- Hwang, L.R., Jang, B.Z. (1991). In *Proc. ICCM-VIII: Composites: Design, Manufacture and Applications* (S.W. Tsai and G.S. Springer, eds.). SAMPE Pub, Paper 24G.
- Inagaki, N., Tasaka, S. and Kawai, H. (1992). Surface modification of Kevlar 49 fiber by a combination of plasma treatment and coupling agent treatment for silicon rubber composite. *J. Adhesion Sci. Technol.* **6**, 279–291.
- Ishida, H. (1984). A review of recent progress in the studies of molecular and micro structures of coupling agents and their functions in composites, coatings and adhesive joints. *Polym. Composites* **5**, 101–123.
- Ishida, H., Chiang, C.H. and Koenig, J.L. (1982). The structure of aminofunctional silane coupling agents. *Polymer* **23**, 251–262.
- Ishida, H., Koenig, J.L. (1978). Fourier transformed infrared spectroscopic study of the silane coupling agent/porous silica interface. *J. Colloid. Interface Sci.* **64**, 555–564.
- Ishida, H., Koenig, J.L. (1979). An investigation of the coupling agent/matrix interface of fiberglass reinforced plastic by fourier transform infrared spectroscopy. *J. Polym. Sci.: Part B. Polym. Phys. Edition* **17**, 615–626.
- Ishida, H., Koenig, J.L. (1980). Effect of hydrolysis and drying on the siloxane bonds of a silane coupling agent deposited on E-glass fibers. *J. Polym. Sci., Part B. Polym. Phys. Ed.* **18**, 233–237.
- Ivens, J., Wevers, M. and Verpoest, I. (1991). In *Proc. 8th Intern. Conf. Composite Mater. (ICCM-VIII), Composite Design, manufacture and Applications* (S.W. Tsai and G.S. Springer, eds.) SAMPE Publ., Corina, CA, Paper IIC.
- James, N.A., Lovett, D.J. and Warwick, C.M. (1991). Mechanical behavior of a continuous fiber reinforced titanium matrix composites. In *Proc. ICCM/8, Composites: Design, Manufacture and Application* (S.W. Tsai and G.S. Springer, eds.), SAMPE Pub., paper 19I.
- Jang, B.J., Das, H., Hwang, L.R., Chang, T.C. (1988). Plasma treatments of fiber surfaces for improved composite performance. In *Proc. ICCI-II, Interfaces in Polymer, Ceramic and Metal Matrix Composites* (H. Ishida ed.), Elsevier Sci. Pub. New York, pp. 319–333.
- Janssens, W., Doxsee Jr., L., Verpoest, I. and de Meester, P. (1989). Influence of the fiber-matrix interface on the transverse bending strength of dry and moist aramid-epoxy composites. In *Proc. Interfacial Phenomena in Composite Materials'89*, (F.R. Jones ed.), Butterworths, London, pp 147–154.
- Jeng, S.M., Yang, C.J., Alasoeur, P., Yang, J.M. (1991). In *Proc. ICCM-IIIIV, Composites: Design, Manufacture and Application* (S.W. Tsai and G.S. Springer, eds.), SAMPE Pub, Paper 25C.
- Jeng, S.M., Yang, J.M. and Aksoy, S. (1992). Damage mechanisms of SCS-6/Ti-6Al-4V composites under thermal-mechanical fatigue. *Mater. Sci. Eng. A* **156**, 117–124.
- Johnson, S.M., Brittain, R.D., Lamoreaux, R.H. and Rowcliff, D.J. (1988). Degradation mechanisms of silicon carbide fibers. *J. Am. Ceram. Soc.* **71**, C 132–135.
- Johnston, W.D. and Greenfield, I.G. (1991). Evaluation of techniques for interface modification in aluminum matrix composites. In *Proc. ICCM-VIII. Composites Design, Manufacture and Application* (S.W. Tsai and G.S. Springer, eds.), SAMPE Pub., Paper 19E.

- Jones, C., Keily, C.J. and Wang, S.S. (1989). The characterization of an SCS-6/Ti-6Al-4V MMC interface. *J. Mater. Res.* **4**, 327–335.
- Jones, F.R. and Pawson, D. (1989). The effect of surface treatment on the interfacial strength of corrosion resistant glass fibers in a vinylester resin. In *Proc. ECCM-3, Developments in the Science and Technology of Composite Materials* (A.R. Bunsell, P. Lamicq and A. Massiah, eds.), Elsevier Appl. Sci., London.
- Kalanta J. and Drzal L.T. (1990a). Structural properties of aramid fibers and their influence on fiber adhesion. In *Proc. ICCI-2, Controlled Interphases in Composite Materials* (H. Ishida ed.), Elsevier, New York, pp. 685–690.
- Kalanta J. and Drzal L.T. (1990b). The bonding mechanism of aramid fibers to epoxy matrices. Part II – an experimental investigation. *J. Mater. Sci.* **25**, 4194–4202.
- Katzmann, H.A. (1987). Fiber coatings for the fabrication of graphite reinforced magnesium composites. *J. Mater. Sci.* **22**, 144.
- Keller, T.S., Hoffmann, A.S., Ratner, B.D., McElroy, B.J. (1981). Chemical modification of Kevlar surfaces for improved adhesion to epoxy resin matrices: I. Surface characterization. In *Proc. Intern. Symp. Polymer Surfaces, Vol. 2* (K.L. Mittal ed.), Plenum Press, New York, pp. 861–879.
- Kiescheke, R.R., Somehk, R.E. and Clyne T.W. (1991a). Sputter deposited barrier coatings on SiC monofilaments for use in reactive metallic matrices – Part I. Optimisation of barrier structure. *Acta Metall. Mater.* **39**, 427–436.
- Kiescheke, R.R., Warwick, C.M. and Clyne T.W. (1991b). Sputter deposited barrier coatings on SiC monofilaments for use in reactive metallic matrices – part III. Microstructural stability in composites based on magnesium and titanium. *Acta Metall. Mater.* **39**, 445–452.
- Kim, J.K. and Mai, Y.W. (1991a). High strength, high fracture toughness fiber composites with interface control – a review. *Composites Sci. Technol.* **41**, 333–378.
- Kim, J.K. and Mai, Y.W. (1991b). The effect of interfacial coating and temperature on the fracture behaviors of unidirectional KFRP and CFRP. *J. Mater. Sci.* **26**, 4701–4720.
- Kim, J.K. and Mai, Y.W. (1993). Interfaces in composites. In *Structure and Properties of Fiber Composites*. Materials Science and Technology, Series Vol. 13, (T.W. Chou ed.), VCH Publishers, Weinheim, Germany, Ch. 6, pp. 239–289.
- Ko, Y.S., Forsman, W.C. and Dziemianowicz, T.S. (1982). Carbon fiber-reinforced composites: effect of fiber surface on polymer properties. *Polym. Eng. Sci.* **22**, 805–814.
- Koenig, J.L., Shih, P.T.K. (1971). Raman studies of the glass fiber–silane–resin interface. *J. Colloid. Interface Sci.* **36**, 247–253.
- Koenig, J.L., Emadipour, H. (1985). Mechanical characterization of the interfacial strength of glass reinforced composites. *Polym. Composites* **6**, 142–150.
- Krukonic, V. (1977). In *Boron and Refractory Borides*, Springer Verlag, Berlin, p 517.
- Ladizesky, N.H. and Ward, I.M. (1983). A study of the adhesion of drawn polyethylene fiber/polymer resin systems. *J. Mater. Sci.* **18**, 533–544.
- Ladizesky, N.H. and Ward, I.M. (1989). The adhesion behaviour of high modulus polyethylene fibers following plasma and chemical treatments. *J. Mater. Sci.* **24**, 3763–3773.
- Lancin, M., Bour, J.S. and Thibault-desseaux, J. (1988). HREM characterization of the interface in a SiC fiber/Ti matrix composite. In *High Temperature/High Performance Composites, Mat. Res. Soc. Symp. Proc.* Vol. 120 (F.D. Lemkey, S.G. Fishman, A.G. Evans and J.R. Strife eds.), MRS, Pittsburgh, PA, pp. 351–356.
- Lee-Sullivan, P. Chian, K.S., Yue, C.Y. and Looi, H.C. (1994). Effects of bromination and hydrolysis treatments on the morphology and tensile properties of Kevlar-29 fiber. *J. Mater. Sci. Lett.* **13**, 305–309.
- Li, P.X., Ma, Z.Y. and Liu, G.B. (1989). In *Interfaces in Metal Matrix Composites*. (R.Y. Liu ed.), The 3M Society, pp. 307–316.
- Li, Q. (1990). In *Proc. ICCI-III, Controlled Interface Structures* (H. Ishida ed.), Elsevier Sci. Pub., New York.
- Li, Z.F. and Nctravali, A.N. (1992). Surface modification of UHSPE fibers through allylamine plasma deposition. II. effect on fiber and fiber/epoxy interface. *J. Appl. Polym. Sci.* **44**, 319–332.

- Li, Z.F., Netravali, A.N. and Sachse, W. (1992). Ammonia plasma treatment of ultra-high strength polyethylene fibers for improved adhesion to epoxy resin. *J. Mater. Sci.* **27**, 4625–4632.
- Liao, Y.T. (1989). A study of glass fiber–epoxy composite interface. *Polym. Composites* **10**, 424–428.
- Lowden, R.A. (1991). In *Advanced Composite Materials*, Ceramic Trans., 19, American Ceramic Soc. Westerville, OH, p. 619.
- Lowden, R.A. and More, K.L. (1989). The effect of fiber coatings on interfacial shear strength and the mechanical behavior of ceramic composites, in *Interfaces in Composites*, *Mat. Res. Soc. Symp. Proc.* Vol. 170 (C.G. Pantano and E.J.H. Chen, eds.), MRS, Pittsburgh, PA.
- McGarry, F.J. (1958). In *Proc. 13th Annual Tech. Conf. Reinforced Plastics Div. SPI*, Sec. 11-A.
- McKee, D.W. (1970). The copper-catalyzed oxidation of graphite. *Carbon* **8**, 131–139.
- Madhukar, M.S. and Drzal, L.T. (1991a). Fiber–matrix adhesion and its effect on composite mechanical properties: I. In plane and interlaminar shear behavior of graphite/epoxy composites. *J. Composite Mater.* **25**, 932–957.
- Madhukar, M.S. and Drzal, L.T. (1991b). Fiber–matrix adhesion and its effect on composite mechanical properties: II. Longitudinal (0°) and transverse (90°) tensile and flexure behavior of graphite/epoxy composites. *J. Composite Mater.* **25**, 958–991.
- Madhukar, M.S. and Drzal, L.T. (1992a). Fiber–matrix adhesion and its effect on composite mechanical properties: III. Longitudinal (0°) and transverse (90°) tensile and flexure behavior of graphite/epoxy composites. *J. Composite Mater.* **25**, 958–991.
- Madhukar, M.S. and Drzal, L.T. (1992b). Fiber–matrix adhesion and its effect on composite mechanical properties: IV. Mode I and Mode II fracture toughness of graphite/epoxy composites. *J. Composite Mater.* **26**, 936–968.
- Maheshwari, A., Chawla, K.K. and Michalske, T.A. (1989). Behavior of interface in alumina/glass composite. *Mater. Sci. Eng.* **A107**, 269–276.
- Mai, Y.W. (1994). *Advances in Inorganic Fiber Technology*, Guest Editor, Special Issue, *Composites Sci. Technol.* **51**, 123–125.
- Marks, B.S., Mauri, R.E., Bradshaw, W.G. (1975). New graphite surface treatments. In *Proc. 12th Biennial Conference on Carbon*, Pittsburg, PA, p. 337.
- Manfredo, L.J. and McNally, R.N. (1984). *J. Am. Ceram. Soc.* **67**, C-155.
- Martineau P., Pailler, R., Lahaye, M. and Naslain, R. (1984). SiC filament/titanium matrix composites regarded as model composites. part II, *J. Mater. Sci.* **19**, 2749–2770.
- Metcalf, A.G. (1974). Physical chemical aspects of the interface. In *Interfaces in Metal Matrix Composites*, Composite Materials, Vol. 1. Academic Press, New York.
- Michalske, T.A. and Hellmann, J. (1988). Strength and toughness of continuous alumina fiber reinforced glass matrix composites. *J. Am. Ceram. Soc.* **71**, 725–731.
- Morin, D. (1976). Boron carbide-coated boron filament as reinforcement in aluminium alloy matrices. *J. Less Common Metals* **47**, 207–213.
- Misra, A.K. (1994). Modification of the fiber/matrix interface in aluminide-based intermetallic matrix composites. *Composites Sci. Technol.* **50**, 37–48.
- Morgan, R.J. and Allred, R.E. (1993). Aramid fiber composites. In *Handbook of Composite Reinforcement*, VCH Publication, New York, pp. 5–24.
- Naslain, R., Dugne, O., Guette, A., Sevely, J., Robin-Brosse, C.R., Rocher, J.P. and Cotteret, J. (1991a). Boron nitride interphase in ceramic-matrix composites, *J. Am. Ceram. Soc.* **74**, 205–214.
- Naslain, R., Dugne, O., Guette, A., Sevely, J., Brosse, C.R., Rocher, J.P. and Cotteret, J. (1991b). Boron nitride interphase in ceramic-matrix composites. *J. Am. Ceram. Soc.* **74**, 2482–2488.
- Nicholas, M. (1968). The strength of metal/alumina interfaces. *J. Mater. Sci.* **3**, 571–576.
- Noone, M.J., Feingold, E., Sutton, W.H. (1969). In *Interfaces in Composites*. ASTM STP 452, ASTM, Philadelphia, PA, pp. 59–89.
- Norita, T., Matsui, J., Matsuda, H.S. (1986). Effects of surface treatment of carbon fiber on mechanical properties of CFRP. In *Proc. ICCI-I, Composite Interfaces* (H. Ishida and J.L. Kocnig, eds.), Elsevier Sci. Pub. New York, pp. 123–132.
- Novak, R.C. (1969). Fracture in graphite filament reinforced epoxy. In *Composite Materials: Testing and Design*. ASTM STP 460. ASTM, Philadelphia, PA, pp. 540–549.

- Outwater, J.O. (1956). In *Proc. 11th Annual Tech. Conf. Reinforced Plastics Div. SPI Sec. 9-B*.
- Plueddemann, E.P. (1972). Cationic organofunctional silane coupling agents. In *Proc. 27th Annual Tech. Conf. Reinf. Plastic. SPI, Section 21-B*.
- Plueddemann, E.P. (1974). In *Interfaces in Polymer Matrix Composites*, Composite Materials, Vol. 6 (E.P. Plueddemann ed.), Academic Press, New York.
- Plueddemann, E.P., Clark, H.A., Nelson, L.E. and Hoffmann, K.R. (1962). *Modern Plastics* **39**, p. 135.
- Plueddemann, E.P. (1981). Principles of interfacial coupling in fiber-reinforced plastics, *Int. J. Adhesion Adhesive* **1**, pp. 305–310.
- Plueddemann, E.P. (1982). *Silane Coupling Agents*, Plenum Press, New York.
- Plueddemann, E.P. (1988). Present status and research needs in silane coupling. In *Proc. ICCI-II, Interfaces in Polymer, Ceramic and Metal Matrix Composites* (H. Ishida ed.), Elsevier Sci. Pub. New York, pp. 17–33.
- Plueddemann, E.P. and Stark, G.L. (1980). In *Proc. 35th Annual Tech. Conf. Reinf. Plast./Composite. SPI. Section 20-B*.
- Prewo, K.M. and McCarthy, G. (1972). Interfacial characterization of silicon carbide coated boron reinforced aluminum matrix composites. *J. Mater. Sci.* **7**, 919–928.
- Prouhet, S., Camus, G., Labrugere, C., Gette, A. and Martin, E. (1994). Mechanical characterization of SiC fiber/SiC (CVD) matrix composites with a BN-interphase. *J. Am. Ceram. Soc.* **77**, 649–659.
- Riess, G., Bourdeux, M., Brie, M., Jouquet, G. (1974). Carbon Fibers – Their Place in Modern Technology, *Plast. Inst.*, London, p. 52.
- Riggs, D.M., Shuford, R.J., Lewis, R.W. (1982). In *Handbook of Composites* (G. Lubin ed.), Van Nostrand Reinhold, New York, Ch. 2.
- Rochow, E.G. (1951). *An Introduction to the Chemistry of Silane*, 2nd ed., Chapman & Hall, London.
- Rostami, H., Iskandarni, B. and Kamel, I. (1992). Surface modification of Spectra 900 polyethylene fibers using RF-plasma. *Polym. Composites* **13**, 207–212.
- Ryder, C., Vidoz, A., Crossman, F., Camahort, J. (1970). Mechanical properties of nitrided boron-aluminium composites. *J. Composite Mater.* **4**, 264–272.
- Schrader, M.E., Lerner, I. and D'oria, F.J. (1967). *Modern Plastics* **45**, 195.
- Schrader, M.E. (1970). Radioisotopic studies of bonding at the interface. *J. Adhesion* **2**, 202–212.
- Schrader, M.E. and Block, A. (1971). Tracer study of kinetics and mechanism of hydrolytically induced interfacial failure. *J. Polym. Sci., Part C, Polym. Symposia.* **34**, 281–291.
- Schrader, M.E. (1974). In *Composite Materials* (L.J. Broutman and R.H. Krock, eds.), Vol. 6, Academic, New York, p. 109.
- Scolar, D.A. (1974). In *Interfaces in Polymer Matrix Composites*, Composite Materials, Vol. 6 (E.P. Plueddemann ed.), Academic Press, New York, pp. 217–284.
- Siadati, M.H., Chawla, K.K. and Ferber, M. (1991). The role of the SnO₂ interphase in an alumina/glass composite: a fractographic study. *J. Mater. Sci.* **26**, 2743–2749.
- Silverstein, M.S. and Breuer, O. (1993a). Mechanical properties and failure of etched UHMW-PE fibers. *J. Mater. Sci.* **28**, 4153–4158.
- Silverstein, M.S. and Breuer, O. (1993b). Adhesive properties and failure of etched UHMW-PE fibers. *J. Mater. Sci.* **28**, 4718–4724.
- Silverstein, M.S. and Breuer, O. (1993c). Relationship between surface properties and adhesion for etched UHMW-PE fibers. *Composites Sci. Technol.* **48**, 151–157.
- Singer, L.S. (1989). Carbon fiber reinforced plastics. In *Concise Encyclopedia of Composite Materials* (A. Kelly, ed.), Pergamon Press, Oxford, pp. 39–55.
- Singh, R.N. (1988). Role of fiber–matrix interfacial shear stress on the toughness of reinforced oxide matrix composites. In *High Temperature/High Performance Composites, Mat. Res. Soc. Symp. Proc.*, Vol. 120 (F.D. Lemkey, S.G. Fishman, A.G. Evans and J.R. Strife, eds.), MRS, Pittsburgh, PA, pp. 259–264.
- Singh, R.N. and Gaddipati, A.R. (1991). A uniaxially reinforced zirconia–silicon carbide composite. *J. Mater. Sci.* **26**, 957.
- Singh, R.N. (1993). Interfacial properties and high temperature mechanical behavior of fiber reinforced ceramic fiber reinforced ceramic composites. *Mater. Sci. Eng. A* **166**, 185–198.

- Strife, J., Prewo, K.M. (1982). Silicon carbide fiber-reinforced resin matrix composites. *J. Mater. Sci.* **17**, 65–72.
- Sugerman, G., Gabayson, S.M., Chitwood, W.E. and Monte, S.J. (1989). In *Proc. ECCM-3, Developments in Science and Technology of Composite Materials* (A.R. Bunsell, P. Lamicq and A. Massiah, eds.), Elsevier Appl. Sci. London, pp. 51–56.
- Sun, E.Y., Nutt, S.R. and Brennan, J.J. (1994). Interfacial microstructure and chemistry of SiC/BN dual-coated Nicalon-fiber reinforced glass-ceramic matrix composites. *J. Am. Ceram. Soc.* **77**, 1329–1239.
- Sung, N.H., Dagli, G. and Ying, L. (1982). In *Proc. 37th SPI Ann. Conf. Sect. 23-B*.
- Sung, N.H., Kahl, A., Ni, S., Sung, C.S.P., Chin, I.J. (1981). In *Proc. 36th Annual Tech. Conf. Reinf. Plast./Composite. SPI. Section 2B*.
- Sutton, W.H. (1966). In *Proc. 21st Annual Tech. Conf. Reinf. Plast./Composite. SPI. Section 18A*.
- Suzuki, Y., Maekawa, Z., Hamada, H., Yokoyama, A. and Sugihara, T. (1993). Influence of silane coupling agents on interlaminar fracture in glass fiber fabric reinforced unsaturated polyester laminates. *J. Mater. Sci.* **28**, 1725–1723.
- Takayanagi, M., Kajiyama, T., Katayose, T. (1982). *J. Appl. Polym. Sci.* **21**, 3903–3917.
- Tissington, B., Pollard, G. and Ward, I.M. (1991). A study of the influence of fiber/resin adhesion on the mechanical behavior of ultrahigh modulus polyethylene fiber composites. *J. Mater. Sci.* **26**, 82–92.
- Vaidya, R.U., Fernando, J., Chawla, K.K. and Ferber, M.K. (1992). Effect of fiber coating on the mechanical properties of a Nextel-480 fiber reinforced glass matrix composites. *Mater. Sci. Eng.* **A151**, 161–169.
- Vaughan, D.J. (1978). The use of coupling agents to enhance the performance of aramid reinforced composites. *Polym. Eng. Sci.* **18**, 167–169.
- Verpoest, I. and Springer, G.S. (1988). Moisture characteristics of aramid-epoxy composites. *J. Reinf. Plast. Composites* **7**, 2–22.
- Vidoz, A., Camahort, J., Crossman, F. (1969). Development of nitride boron reinforced metal matrix composites. *J. Composite Mater.* **3**, 254–261.
- Wang, D., Jones F.R. and Denison, P. (1992a). Surface analytical study of the interaction between τ -aminopropyltriethoxysilane (APS) and E-glass surface. Part 1-Time of flight secondary ion mass spectroscopy. *J. Mater. Sci.* **27**, 36–48.
- Wang, D., Jones F.R. and Denison, P. (1992b). TOF SIMS and XPS study of the interaction of hydrolysed τ -aminopropyltriethoxysilane (APS) and E-glass surface. *J. Adhesion Sci. Technol.* **6**, 79–98.
- Wang, D., Jones F.R. and Denison, P. (1992c). A TOF SIMS study of the incorporation of aluminum into the silane coating on E-glass fibers. *Catalysis Today* **12**, 375–383.
- Wang, D. and Jones F.R. (1993a). TOF SIMS and XPS study of the interaction of silanized E-glass with epoxy resin. *J. Mater. Sci.* **28**, 1396–1408.
- Wang, D. and Jones F.R. (1993b). TOF SIMS and XPS study of the interaction of silanized E-glass with epoxy resin. *J. Mater. Sci.* **28**, 2481–2488.
- Wang, Q., Ait-kadi, A. and Kaliaguine, S. (1992a). Catalytic grafting: a new technique for polymer/fiber composites. II. Plasma treated UHMPE fibers/polyethylene composites. *J. Appl. Polym. Sci.* **45**, 1023–1033.
- Wang, Q., Kaliaguine, S. and Ait-kadi, A. (1992b). Polyethylene-plasma treated Kevlar fiber composites: analysis of the fiber surface, *J. Appl. Polym. Sci.* **48**, 121–136.
- Ward, I.M. (1985). Preparation, properties and structure of high modulus polyolefines and polyoxymethylene. In *Handbook of Composites*, Vol. 1. Strong Fibers (W. Watt and B.V. Perov, eds.), Northholland, Amsterdam, pp. 705–741.
- Ward, I.M. (1993). A review of recent developments in the processing and properties of oriented polyethylene. *Plastics, Rubber and Composites Proc. Appl.* **19**, 7–13.
- Ward, I.M. and Ladizesky, N.H. (1986). High modulus polyethylene fibers and their composites. In *Proc. ICCI-1, Composite Interfaces* (H. Ishida and J.L. Koenig, eds.), Elsevier, New York, pp. 37–46.
- Ward-Close, C.M. and Partridge, P.G. (1990). A fiber coating process for advanced metal matrix composites, *J. Mater. Sci.* **25**, 4315–4323.
- Warrier, S.G., Blue, C.A. and Lin, R.Y. (1993). Control of interfaces in Al-C fiber composites. *J. Mater. Sci.* **28**, 760–768.

- Warwick, C.M., Kiescheke, R.R. and Clyne, T.W. (1991). Sputter deposited barrier coatings on SiC monofilaments for use in reactive metallic matrices – part II. System stress state. *Acta Metall. Mater.* **39**, 437–444.
- Wawner, F.E., Jr. (1988). Boron and silicon carbide/carbon fibers. In *Fiber Reinforcements for Composite Materials* (A.R. Bunsell ed.), Elsevier, Amsterdam, pp. 371–425.
- Wawner, F., Nutt, S. (1980). Investigation of diffusion barrier materials on SiC filaments. *Ceram. Eng. Sci. Proc.* **1**, 709–719.
- Wertheimer, M.R. and Schreiber, H.P. (1981). Surface property modification of aromatic polyamides by microwave plasmas. *J. Appl. Polym. Sci.* **26**, 2087–2096.
- Wright, W.W. (1990). The carbon fiber-epoxy resin interfaces-a review, part I. In *Composite Polymer* Vol. 3. (P. Dickin, ed.), pp. 231–401.
- Wu, J.X., Li, P.X., Gu, M.Y. and Wu, R.J. (1993a). Interface evolution and its relationship with fracture strength in C/Al, A/Al–Ti and C/Al–Cu composite materials. *Composite Interfaces* **1**, 75–86.
- Wu, J.X., Liu, W., Li, P.X. and Wu, R.J. (1993b). Effect of matrix alloying elements on the corrosion resistance of C/Al composites materials. *J. Mater. Sci. Lett.* **12**, 1500–1501.
- Yajima, S., Hayashi, J., Omori, M. and Okamura, K. (1976). Development of a silicon carbide fiber with high tensile strength. *Nature* **261**, 683–685.
- Yajima, S., Hasegawa, Y., Hayashi, J., Imura, M. (1978). Synthesis of continuous silicon carbide fiber with high tensile strength and high Young's modulus, part I, synthesis of polycarbosilane as precursor. *J. Mater. Sci.* **13**, 2569–2576.
- Yajima, S., Okamura, K., Matsuwa, T., Hasegawa, Y., Shishido, T. (1979). Anomalous characteristics of the microcrystalline state of SiC fibers. *Nature* **279**, 706–707.
- Yamamoto, M., Yamada, S., Sakatani, Y., Taguchi, M., Yamaguchi, Y. (1971). In *Proc. 1st Carbon Fibre Conf.* Plast. Inst., London, p. 179.
- Yao, Y., Liu, X. and Zhu, Y. (1993). Surface modification of high-density polyethylene by plasma treatment. *J. Adhesion Sci. Technol.* **7**, 63–75.
- Yoon, H.S. and Okura, A. (1990). The influence of interfacial reaction on the strength of C/Al composites. *SAMPE J.* **26**, 19–27.
- Yu, Z., Ait-kadi, A. and Brisson, J. (1991a). Nylon/Kevlar composites: I. Mechanical properties. *Polym. Eng. Sci.* **31**, 1222–1227.
- Yu, Z., Ait-kadi, A. and Brisson, J. (1991b). Investigation of interfaces. *Polym. Eng. Sci.* **31**, 1228–1232.
- Yuan, L.Y., Shyu, S.S., Lai, J.Y. (1991). Plasma surface treatments on carbon fibers. II. mechanical properties and interfacial shear strength. *J. Appl. Polym. Sci.* **42**, 2525–2534.
- Zhuang, W.D. and Zhang, G.D. (1991). Designing the matrix of Gr/Al Composites. In *Proc. ICCM/VIII, Composite Design, Manufacture and Application* (S.W. Tsai and G.S. Springer, eds.), SAMPE, Pub. Paper 19H.

Chapter 6

INTERFACE MECHANICS AND FRACTURE TOUGHNESS THEORIES

6.1. Interface-related fracture toughness theories

6.1.1. Introduction

Fundamental considerations of design efficiency for improved mechanical performance and structural reliability of composite materials require a basic understanding of how the fracture process initiates and progresses to final failure. There are ever-increasing concerns pertaining to the ability of a composite to sustain both static and dynamic loads without the danger of sudden catastrophic failure. The local response of the fiber–matrix interface within the composite during fracture is particularly important. If the interface in a composite is to be designed to resist fracture and thus to enhance the damage tolerance prior to failure, it is necessary to understand the basic failure mechanisms or origin of fracture toughness.

The term ‘fracture toughness’ or ‘toughness’ with a symbol, R or G_c , used throughout this chapter refers to the work dissipated in creating new fracture surfaces of a unit nominal cross-sectional area, or the critical potential energy release rate, of a composite specimen with a unit kJ/m^2 . Fracture toughness is also often measured in terms of the critical stress intensity factor, K_c , with a unit $\text{MPa}\sqrt{\text{m}}$, based on linear elastic fracture mechanics (LEFM) principle. The various micro-failure mechanisms that make up the total specific work of fracture or fracture toughness are discussed in this section.

Theories for both elastic modulus and strength of composites have been well developed, and the factors governing these fundamental mechanical properties are relatively well understood. The rule of mixtures (RoM) concept has been most widely used for strength and modulus predictions although it is not completely adequate for composites containing short, randomly oriented fibers. The fracture process in fiber composites is seldom straightforward because of their microstructural inhomogeneity and macroscopic anisotropy. Because the presence of interfaces that form the boundaries between dissimilar media makes the fracture behavior of composites even more complicated, the simple RoM cannot be employed to quantify their fracture resistance. It is well known that the fracture toughness of a

composite is not simply the sum of the weighted contributions by the constituents, but is governed more importantly by the extent of synergistic energy absorption processes through various toughening mechanisms, depending on the nature of physicochemical bonding and elemental constitutions at the fiber–matrix interface region.

There are many theoretical and experimental studies carried out on the fracture behavior and toughening mechanisms in fiber reinforced composites. When a composite having internal cracks is loaded, there is a highly strained region at the crack tip, the so-called fracture process zone (FPZ) or damage zone, where failure mechanisms of various kinds take place before the cracks propagate. Summaries of the failure mechanisms in polymer matrix composites can be found in many references including Kelly (1973), Marston et al. (1974), Atkins (1975) and Harris (1980), and these are reviewed recently by Kim and Mai (1991a, b, 1993). Reviews on failure mechanisms are also available for MMCs (Ochiai, 1989; Taya and Arsenault, 1989; Clyne and Withers, 1993), CMCs (Davidge, 1989; Warren and Sarin, 1989; Evans, 1989; Ruhle and Evans, 1989; Chawla, 1993), and cementitious fiber composites (Mai, 1985; Cotterell and Mai, 1996).

Many fracture toughness theories of composite materials have been developed mainly for those with unidirectional fibers. The various origins of fracture toughness in composites may be characterized by considering the sequence of microscopic fracture events that lead to crack propagation macroscopically under monotonic increasing loads. The cracks in composites can propagate preferentially along the fiber–matrix and laminar interfaces (i.e. longitudinal splitting) or transversely right through the fiber and matrix (i.e. transverse cracking), depending on the properties of the interface relative to the fiber and matrix. The criteria for these two opposing fracture phenomena are given in Section 6.4. Consideration of a microcomposite model shown in Fig. 6.1 (Harris, 1980) makes it most convenient to isolate the individual micromechanisms of toughening. When a crack present in the matrix approaches an isolated fiber, the following failure mechanisms may be expected to take place:

- (1) matrix fracture,
- (2) fiber–matrix interface debonding,
- (3) post-debonding friction,
- (4) fiber fracture,
- (5) stress redistribution,
- (6) fiber pullout.

The underlying physical bases of these toughening mechanisms are presented in the following sections, and the corresponding equations are summarized in Table 6.1. All these mechanisms, except fracture of fibers and matrix, are a direct consequence of shear failure at the imperfectly bonded fiber–matrix interface. In conjunction with these mechanisms, fiber bridging, crack deflection and bifurcation, and microcracking also take place depending on the strength of the constituents relative to that of the interface, microstructure of the composite constituents, and the loading configuration of the composite structure.

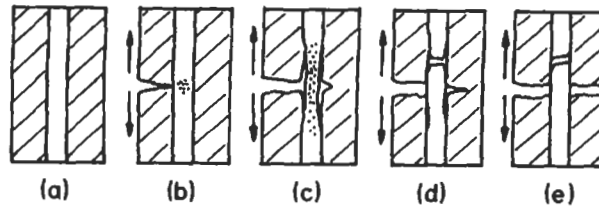


Fig. 6.1. Model of crack–fiber interaction in a simple composite. (a) In the uncracked composite, the fiber is gripped by the matrix. (b) A matrix crack is halted by the fiber. Increasing the load allows the crack to pass around the fiber without breaking the interfacial bond. (c) Interfacial shearing and lateral contraction of the fiber result in debonding and a further increment of crack extension. (d) After considerable debonding the fiber breaks at some weak spot within the matrix and further crack extension occurs. (e) The broken fiber end must be pulled out against the frictional grip of the matrix if total separation of the composite is to occur. After Harris (1980).

A weak interface bond is detrimental to some mechanical properties, particularly the longitudinal compressive strength and transverse tensile strength, as described in Chapter 5. However, it has an ameliorating effect of allowing the above failure mechanisms to take place more readily and extensively with enhanced stability in crack growth. The ability of a composite material to arrest cracks through longitudinal splitting contributes to the overall improvement in energy absorption capability and thus its fracture toughness. The crack arrest or blunting by longitudinal splitting or matrix plastic deformation along the fiber direction gives a substantial reduction in the stress concentration ahead of the crack, enabling the fibers to sustain higher levels of load prior to fracture. All these microfailure mechanisms apply, in principle, to most composites containing short and continuous fibers with polymer, ceramic, metal and cement matrices, although the extent to which and how they occur are the characteristics of individual fiber–matrix systems. It is also not necessary for these failure mechanisms to operate simultaneously for a given system, and in some cases one of these toughness contributions may dominate the total fracture toughness. This implies that no simple unified theory can be applied to predict the fracture toughness of all types of fiber composites.

Table 6.1
Summary of the failure mechanisms in fiber reinforced composites^a

Toughness sources		Equation
Interfacial debonding	$R_d = V_f(\sigma_f^*)^2 \ell_d / 2E_f$	(6.1)
Post-debonding friction	$R_{df} = 2V_f \tau_f \ell_c^2 \Delta \epsilon / d$	(6.4)
Stress redistribution	$R_r = V_f \sigma_f^* \ell_c / 3E_f$	(6.5)
Fiber pull-out	$R_{po} = (V_f \tau_f \ell_c^2 / 6d) \approx V_f \sigma_f^* \ell_c / 12$ for $\ell < \ell_c$	(6.8)
Surface energy	$R_s = V_f R_f + (1 - V_f) R_m + V_f \frac{\ell_c}{d} G_{ic} \approx V_f (\frac{\ell_c}{d} - 1) R_m$	(6.11)
Fiber plastic shear	$R_{fs} = 2V_f d \sigma_f^* \epsilon_f$	(6.12)
Matrix plastic shear	$R_{ms} = ((1 - V_f)^2 / V_f) d \sigma_m^* \epsilon_m$	(6.13)

^aAfter Kim and Mai (1991a).

6.1.2. Fiber–matrix interface debonding in mode II shear

For a composite containing fibers whose maximum strain is greater than that of matrix (i.e. $\epsilon_f > \epsilon_m$), the crack propagating in the matrix is halted by the stiff fiber if the current level of stress is not high enough as shown in Fig. 6.1(b). Alternatively, the crack may pass around the fiber with little damage to the interface bond. As the applied load is further increased, the fiber and matrix attempt to deform differentially, causing local Poisson contraction. Relatively large local stresses are built up in the fiber at the same time. This allows the level of shear force developed at the interface to exceed the apparent interfacial shear bond strength, τ_b , and results in interfacial debonding at the crack plane if the maximum shear strength criterion is employed as the failure criterion. The debond will extend some distance along the fiber with further increase in the external load (Fig. 6.1(c)). The debonding toughness, R_d , first proposed by Outwater and Murphy (1969) can be evaluated by the total elastic strain energy stored in the fiber over the debond length ℓ_d at its breaking stress σ_f^* divided by the cross-section area of the composite:

$$R_d = \frac{V_f(\sigma_f^*)^2 \ell_d}{2E_f} \quad (6.1)$$

It has been well established that the debonding process is often the major contributor to the total fracture toughness of glass fiber reinforced polymer matrix composites (GFRPs) (Murphy and Outwater, 1973), although there may be some confusion as to the exact nature of the energy absorption mechanism. Harris (1980) later pointed out that the debonding process implicit in the Outwater–Murphy analysis requires that the fibers separate from the matrix in shear, and the debond toughness, R_d , given by Eq. (6.1) appears to be a consequence of debonding rather than the debonding itself. If R_d were to arise from the latter case, it is necessary to consider the fiber debond stress, σ_d , which is a function of either the fiber–matrix interface fracture toughness, G_{ic} , or the interface bond strength, τ_b , depending on the debond criterion being used (see Chapter 4). The debond toughness of Eq. (6.1) may then be modified to

$$R_d = \frac{V_f \sigma_d^2 \ell_d}{2E_f} \quad (6.2)$$

An upper limit to the interface fracture toughness, G_{ic} , can thus be estimated from the work of debonding divided by the cylindrical debond area

$$G_{ic} = \frac{\sigma_d^2 d}{8E_f} \quad (6.3)$$

An implication of Eq. (6.3) is that debonding only occurs when $\sigma_d < \sigma_f^*$, or $G_{ic} < \sigma_f^{*2} d / 8E_f$, otherwise the fiber will break prior to debonding. Other criteria for fiber fracture in single fiber pull-out test, refer to Section 4.2.4.

6.1.3. Post-debond friction

After interface debonding has taken place the fiber and matrix move relative to each other as the loading continues. Kelly (1970) has proposed a toughness contribution due to post-debonding friction whose dissipated energy is equivalent to the frictional shear force times the differential displacement between fiber and matrix. The displacement is approximately equal to the product of the average ℓ_d and the differential strain, $\Delta\epsilon = \epsilon_f - \epsilon_m$, between the fiber and matrix. Therefore, the post-debonding friction toughness, R_{df} , is given by

$$R_{df} = \frac{2V_f\tau_f\ell_d^2\Delta\epsilon}{d} \quad (6.4)$$

$\Delta\epsilon$ can be approximated to ϵ_f if ϵ_m is neglected in brittle matrix composites (Harris, 1980). It is shown that R_{df} contributes substantially to the total fracture toughness of glass fiber-polymer matrix composites (Harris et al., 1975; Kirk et al., 1978; Beaumont and Anstice, 1980; Munro and Lai, 1988).

6.1.4. Stress redistribution

Once there is considerable debonding along the interface, the continuous fiber is effectively loaded in tension over the debonded length. The fiber may break at a weak point within this region near the main fracture plane. Upon fracture the fiber instantly relaxes back and its ends are gripped by the matrix as it regains its original diameter (Fig. 6.1(d)). There is another source of toughness of fiber composites, due to the redistribution of strain energy from the fiber to the matrix after fiber fracture (Piggott, 1970; Fitz-Randolph et al., 1972). Assuming the stress builds up linearly from the broken end over a distance equivalent to half the critical transfer length, $\ell_c/2$, for an elastic fiber, the strain energy lost from the fiber due to stress redistribution, R_r , is given by

$$R_r = \frac{V_f\sigma_f^{*2}\ell_c}{3E_f} \quad (6.5)$$

It is noted that R_r is $2\ell_c/3\ell_d$ times the Outwater-Murphy debonding toughness given in Eq. (6.1). The critical transfer length, ℓ_c , represents the shortest fiber length required to bring the maximum fiber axial stress up to its tensile strength, σ_f^* , as discussed in Chapter 4. It is shown that R_r contributes substantially to the total fracture toughness of boron fiber reinforced epoxy matrix composites (Fitz-Randolph et al., 1972; Marston et al., 1974).

6.1.5. Fiber pull-out

As the external loading continues and the crack propagates, the broken fibers are pulled out from the matrix (Fig. 6.1(e)), resulting in a continuation of the post-

debonding frictional work. The pull-out energy (Cottrell, 1964; Kelly, 1970) is the work done against sliding friction in extracting the broken fiber. Based on the work done by the frictional shear stress, τ_f which is assumed to be constant over a pull-out distance, ℓ_{po} , the fiber pull-out toughness, R_{po} , is given by

$$R_{po} = \frac{2V_f\tau_f\ell_{po}^2}{d} \quad (6.6)$$

Since fiber pull-out length, ℓ_{po} , is difficult to measure with any accuracy from the fracture surface of composite specimens containing high V_f , R_{po} is often expressed in terms of the inherent properties of the composite constituents. There are three cases considered here depending on the fiber length relative to the critical transfer length.

(i) If the fiber length is less than the critical transfer length, $\ell < \ell_c$, all the debonded fibers are pulled out. Assuming the pull-out length, ℓ_{po} , varies between 0 and $\ell/2$ with a mean value of $\ell/4$ (Kelly and Tyson, 1965; Cooper and Kelly, 1969), R_{po} becomes

$$R_{po} = \frac{V_f\tau_f\ell^2}{6d} \quad \text{for } \ell < \ell_c \quad (6.7)$$

(ii) R_{po} is maximum when $\ell = \ell_c$,

$$R_{po} = \frac{V_f\tau_f\ell_c^2}{6d} \approx \frac{V_f\sigma_f^*\ell_c}{12} \quad \text{for } \ell < \ell_c \quad (6.8)$$

In Eq. (6.8) an upper bound estimate of τ_f is made by the apparent bond strength τ_a for the critical transfer length, i.e., $\ell_c \approx \sigma_f^*d/2\tau_f$, based on the early work of Kelly and Tyson (1965). Therefore, R_{po} is shown directly proportional to the critical transfer length.

(iii) If the composite contains fibers of lengths greater than the critical transfer length, $\ell > \ell_c$, then the fraction of fibers that can be pulled out is ℓ_c/ℓ on the basis of normal probability, and ℓ_{po} ranges from 0 to $\ell_c/2$. Thus, R_{po} becomes

$$R_{po} = \frac{V_f\tau_f\ell_c^2}{6d} \frac{\ell_c}{\ell} \quad \text{for } \ell > \ell_c \quad (6.9)$$

Graphical presentation of Eqs. (6.7)–(6.9) are given in Fig. 6.2 where the fiber pull-out toughness, R_{po} , is plotted as a function of fiber length, ℓ . It is worth noting that for most polymer matrix composites reinforced with carbon, glass and aramid fibers, the estimated fiber pull-out toughness values are approximately the same as the measured composite fracture toughness (Harris et al., 1971, 1975; Atkins, 1975; Gershon and Marom, 1975; Kim and Mai, 1991a, b).

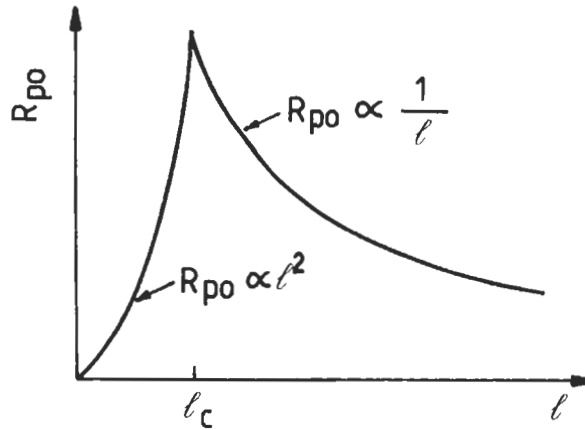


Fig. 6.2. Variation of fiber pull-out toughness, R_{po} , as a function of discontinuous fibers of length, l . After Kelly (1970).

6.1.6. Total fracture toughness theories

Marston et al. (1974) and Atkins (1975) have developed a theory based on the coexistence of the three major sources of fracture toughness, i.e., stress redistribution (R_r of Eq. (6.5)), fiber pull-out (R_{po} of Eq. (6.8)) and generation of new surfaces R_s . Therefore, the total fracture toughness, R_t , is given by

$$R_t = R_r + R_{po} + R_s$$

$$= \frac{V_f \sigma_f^*}{\tau_f} \left[\frac{\sigma_f^* d}{6} \left(\frac{1}{4} + \frac{\sigma_f^*}{E_f} \right) + \frac{R_m}{2} \right] + (1 - V_f) R_m . \quad (6.10)$$

Here, R_s is regarded as the sum of the specific energies absorbed in creating new surfaces in fiber R_f , matrix R_m and at the interface G_{ic} based on the nominal transverse area neglecting the cylindrical interface area

$$R_s = V_f R_f + (1 - V_f) R_m + V_f \frac{l_c}{d} G_{ic} = \left[V_f \left(\frac{l_c}{d} - 1 \right) + 1 \right] R_m . \quad (6.11)$$

The interface fracture toughness is implicit of the debond toughness R_d . In Eq. (6.11), R_f is neglected and R_{ic} is taken as approximately equal to R_m .

In using Eq. (6.10) to predict R_t of a given composite system it is important that the said failure mechanisms all exist. If any one mechanism is apparently absent the corresponding toughness term must be excluded from the R_t equation. It is also worth emphasizing that R_t varies linearly with reciprocal of the frictional shear strength of the interface, i.e. $1/\tau_f$, with the lower limit of $(1 - V_f)R_m$ when τ_f approaches infinity. This relationship has been shown to apply to many carbon fiber polymer matrix composites (CFRPs) (Harris et al., 1971; Beaumont and Phillips,

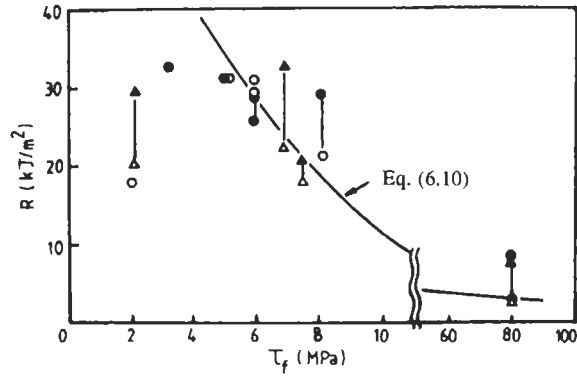


Fig. 6.3. A theoretical plot of fracture toughness, R , with variation of frictional shear stress, τ_f , compared with experimental fracture toughness values: (\blacktriangle) Charpy impact and (\triangle) slow bend tests for carbon-epoxy composites; (\bullet) Charpy impact and (\circ) slow bend tests for carbon-polyester composites. After Beaumont and Harris (1972).

1972; Beaumont and Harris, 1972), as shown in Fig. 6.3, where R_{p0} is the primary source of fracture toughness. It is suggested that the total toughness is, to a first approximation, inversely proportional to the interface shear bond strength, τ_b , because τ_b and τ_f are approximately proportional to each other. For example, τ_f is found to be approximately one-half of τ_b for aramid fiber-epoxy matrix composites in single fiber pull-out experiments (Penn et al., 1983). Fig. 6.4 plots the variation of tensile strength of composites σ_c against R_t or $1/\tau_f$ according to Marston et al.

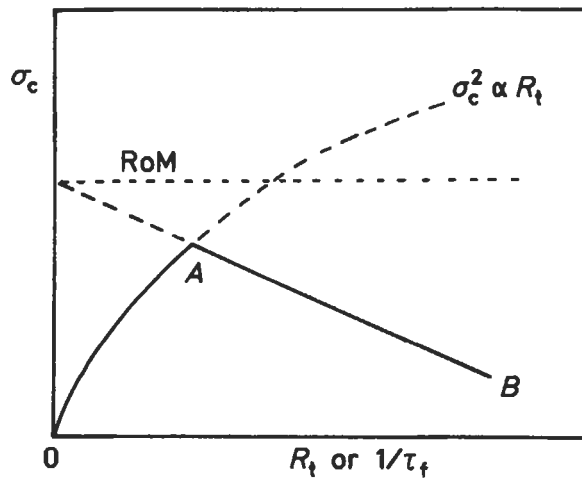


Fig. 6.4. Relationship between composite strength, σ_c , and total fracture toughness, R_t , or equivalently the inverse of frictional shear strength, τ_f . After Marston et al. (1974).

(1974). For high interface bond strength, σ_c is determined based on LEFM where the stress intensity factor, or the composite strength, σ_c , of a brittle material is proportional to the square root of the strain energy release rate, i.e., $\sigma_c^2 \propto R_f$. For low τ_f , σ_c decreases almost linearly with $1/\tau_f$. They proposed that both high strength and high toughness cannot be achieved simultaneously in (brittle fibre–brittle matrix) composites although these properties can be optimized as indicated by the peak point in Fig. 6.4.

6.1.7. Fracture of ductile fibers and ductile matrices

The descriptions presented in the foregoing sections are concerned mainly with composites containing brittle fibers and brittle matrices. If the composite contains ductile fibers or matrix material, the work of plastic deformation of the composite constituents must also be taken into account in the total fracture toughness equation. If a composite contains a brittle matrix reinforced with ductile fibers, such as steel wire–cement matrix systems, the fracture toughness of the composite is derived significantly from the work done in plastically shearing the fiber as it is extracted from the cracked matrix. The work done due to the plastic flow of fiber over a distance on either side of the matrix fracture plane, which is of the order of the fiber diameter d , is given by (Tetelman, 1969)

$$R_{fs} = 2V_f d \sigma_f^* \epsilon_f . \quad (6.12)$$

If a ductile matrix is reinforced with brittle fibers as in most thermoplastic and metal matrix composites, the matrix forms ‘bridges’ in the plane of the broken fibers and the work of matrix shearing R_{ms} is given by (Cooper and Kelly, 1967; Tetelman, 1969; Cooper, 1970)

$$R_{ms} = \frac{(1 - V_f)^2}{V_f} d \sigma_m^* \epsilon_m . \quad (6.13)$$

6.2. Toughness theories for short and randomly oriented fiber composites

6.2.1. Introduction

The foregoing discussion on the theories of fracture toughness is primarily concerned with unidirectional continuous fiber composites. While these theories can generally be employed for short fiber composites, particularly those due to debonding, post-debonding friction, fiber pull-out and matrix surface energy, some modifications are required. Although short fiber composites normally have poorer in-plane mechanical properties than continuous fiber composites, they have advantages of low production costs, and more variety in the selection of thermal, mechanical and chemical properties of the matrix material. The evolution of many engineering thermoplastics as high performance matrix materials has made it

possible to mold into very complex shapes using techniques, such as injection molding, sheet molding, dough molding, etc. at very high production rates. The large number of material and process variables coupled with complex geometry have made the analysis of fracture toughness of these composites rather difficult.

The presence of fiber ends within the body of a short fiber composite means that there are considerable stress concentrations taking place near the fiber ends where microcracks form and fibers debond from the matrix even in ductile matrices (Curtis et al., 1978). These microcracks coalesce under static load in a fiber-avoidance mode to form a main crack (Sato et al., 1983, 1985, 1986a, b, c, 1988, 1991; Lhymn and Schultz, 1983; Schultz and Friedrich, 1984; Karger-Kocsis and Friedrich, 1987; Takahashi and Choi, 1991), and a typical example is shown in Fig. 6.5. The interactions between neighboring fibers constrain the matrix flow significantly, resulting in a deteriorating effect of matrix embrittlement (Ramsteiner and Theysohn, 1979). It follows therefore that the failure process of short fiber composites is dependent primarily on the fracture mode of matrix material and V_f , length distribution and orientation of the fibers.

6.2.2. Fiber pull-out dominant fracture mechanisms

Helfet and Harris (1972) have shown that the fracture toughness of composites containing randomly oriented ductile fibers, such as nickel and steel wires, of length greater than the critical transfer length can be even greater than that of aligned short fiber composites, Fig. 6.6. This result is a direct reflection of the extra energy dissipation mechanisms, in addition to the fiber pull-out work, taking place during pull-out of the non-aligned fibers (Helfet and Harris, 1972; Harris et al., 1972; Hing and Groves, 1972; Morton and Groves, 1974):

- the fibers suffer plastic deformation;
- the frictional stress is enhanced near the exit point of the fiber from the matrix;
- the matrix is fragmented to allow pull-out of non-aligned fibers.

Fig. 6.7 schematically shows plastic bending of fiber and fragmentation of matrix material during pull-out of non-aligned fibers. Assuming that the mean fiber pull-out length is $\ell_c/4$ and the effective total number of fibers intersecting the main crack plane with inclined angle θ to the applied stress direction is equivalent to half of V_f , the work of fiber plastic shear, R_{ps} , is approximately given by (Helfet and Harris, 1972; Harris et al., 1972)

$$R_{ps} \approx \frac{V_f \tau_y \theta \ell_c}{8}, \quad (6.14)$$

where τ_y is the shear yield strength of the fiber. Assuming the shear yield strength is half the tensile strength, $\tau_y \approx \sigma_f^*/2$, and the mean dispersion of θ is approximately $\pi/6$ (Harris et al., 1972), R_{ps} of Eq. (6.14) gives approximately a third of the pull-out toughness of aligned fibers obtained from by Eq. (6.8). This value is slightly smaller than the upper-bound value estimated by Hing and Groves (1972): $R_{ps} \approx V_f \sigma_f \ell / 22$, which is slightly more than half the value given in Eq. (6.8). The extent to which the

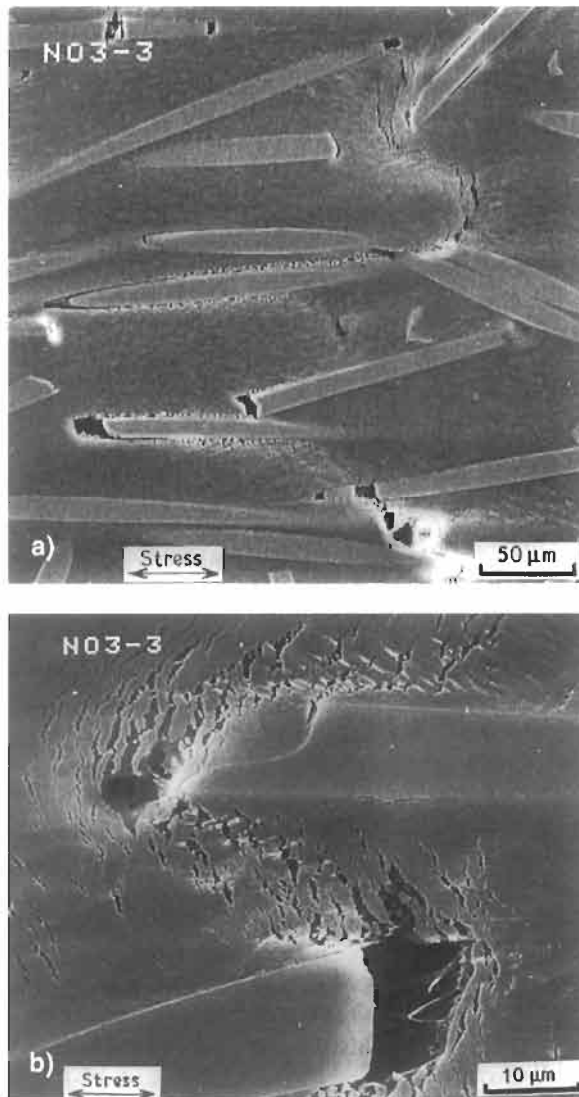


Fig. 6.5. (a) A zigzag band of matrix microcracks in randomly dispersed short fiber reinforced thermoplastic composites; (b) a magnified view of fiber ends. After Sato et al. (1991). Reproduced by permission of Chapman & Hall.

plastic shear occurs appears rather uncertain and depends on the relative properties of the fiber and matrix components and the bonding at the interface. Nevertheless, if large scale fragmentation of brittle matrix is accompanied by plastic bending of the fiber, substantial amounts of energy would be required under these circumstances (Williams et al., 1973).

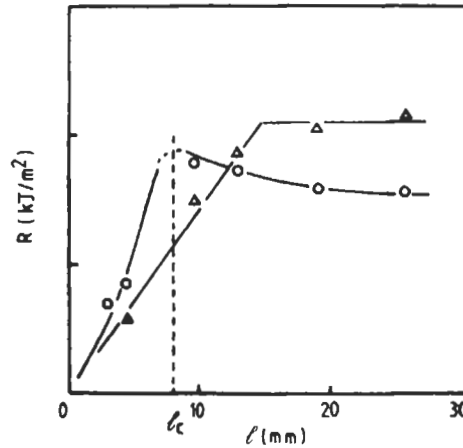


Fig. 6.6. Fracture toughness of steel wire-polyester resin composites ($V_f = 0.1$) as a function of fiber length, l : (○) aligned wires; (△) randomly oriented wires. After Helfet and Harris (1972).

6.2.3. Matrix dominant fracture mechanisms

It is generally accepted that for relatively brittle matrix materials, such as epoxy and polyester resins, ceramics and cements, the fracture toughness of short fiber composites increases systematically with V_f (Williams et al., 1973), and the contribution of matrix toughness to the total fracture toughness is insignificant. In contrast, if brittle fibers are added to an otherwise ductile thermoplastic matrix, e.g., polycarbonate (PC), polypropylene (PP), polyamide (PA), polyetheretherketone (PEEK), polytetrafluoroethylene (PTFE), etc., the work of fracture either increases only marginally or even decreases significantly with increasing V_f , although tensile strength always increases with V_f (Friedrich, 1985; Voss and Friedrich, 1986).

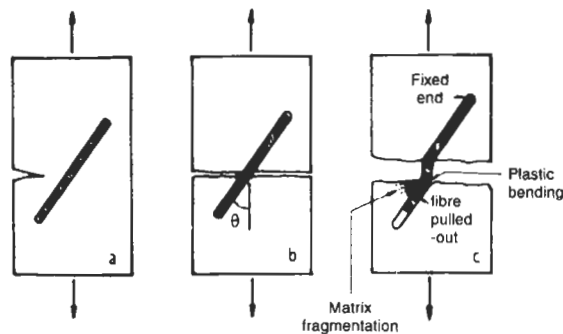


Fig. 6.7. A model for plastic bending of fiber and fragmentation of matrix during fracture of randomly oriented fiber composites. After Helfet and Harris (1972) and Hing and Groves (1972).

For example, see glass fiber-PC matrix composites in Fig. 6.8. This is partly associated with the matrix embrittlement by the constraint imposed by the stiff fibers and the interaction between neighboring short fibers; and partly due to the loss of volume of the tough matrix material taken up by the fibers. Matrix fracture is predominant over other failure mechanisms, such as interfacial debonding and fiber pull-out, because of the very short fiber length and relatively low V_f that can be accommodated by manufacturing processes like injection molding. Matrix-dominant fracture behavior is promoted by weak interfacial bonding, but is discouraged once the matrix ductility is suppressed such as at low temperatures. Experimental results on the critical stress intensity factor, K_c , of injection molded thermoplastic composites containing glass and carbon fibers (Friedrich, 1985; Voss and Friedrich, 1986; Karger-Kocsis and Friedrich, 1988; Friedrich and Karger-Kocsis, 1989; Karger-Kocsis, 1991) show that it is generally a function of the matrix toughness K_m and 'microstructural efficiency factor' (M)

$$K_c = MK_m = (A + B\Omega)K_m \quad (6.15)$$

where Ω is a 'reinforcing effectiveness parameter' which is related to V_f and the geometrical arrangement of the fibers across the thickness, i.e., fiber orientation

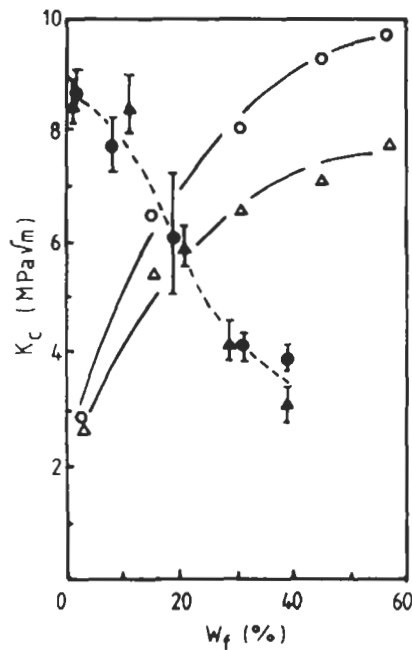


Fig. 6.8. Fracture toughness, K_c , of short glass fiber-thermoplastics injection molded composites as a function of weight fraction of fiber, W_f : (○) and (△) polyethylene terephthalate (PET) matrix; (●) and (▲) polycarbonate (PC) matrix. Notches made transverse (○, ●) and parallel (△, ▲) to the mold fill direction. After Friedrich (1985).

factor, of the composite. A is a 'matrix stress condition factor' which reflects changes in the fracture toughness of matrix material due to the presence of the fibers and specimen thickness; and B is related to the energy absorbing mechanisms of the fibers and can be determined from the empirical linear relationship between K_c and Ω . If $\Omega = 0$, A becomes very close to 1, and thus $K_c \approx K_m$. However, if the measured value of K_m is higher than the real value due to specimen thickness, then $0 < A < 1$. If the fibers have a ductility-enhancing effect on the surrounding matrix, A becomes greater than unity. B can be either positive or negative depending on the relative magnitude between the loss of effective matrix toughness due to the presence of fibers, i.e., $(1 - V_f)K_m$, and the increase in toughness due to other mechanisms, fiber pull-out in particular. For very ductile matrices, e.g., PC and PTFE, $B < 0$; and for moderately ductile thermoplastic matrices, e.g., PEEK, polyphenylene sulfide (PPS) and low ductility polyethylene terephthalate (PET), $B > 0$ since toughness increase due to the fiber pull-out mechanism is greater than the loss of matrix toughness as in thermoset matrix composites. Experimental fracture toughness data shown in Fig. 6.8 for glass fiber-PET composites and in Fig. 6.9 for glass fiber-PTFE and glass fiber-PEEK composites are all in good agreement with Eq. (6.15).

6.2.4. Total fracture toughness theory

The failure processes in thermoplastics composites with aligned glass fibers of sub-critical transfer length have been characterized (Lauke and Schultrich, 1983, 1986a, b; Lauke et al., 1985; Lauke and Pompe, 1988) in terms of matrix fracture mode which is determined mainly by the ductility of the matrix material, loading rate and temperature. The total specific work of fracture, R_t , is expressed as the sum

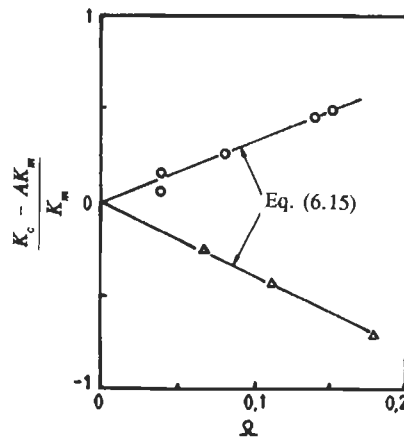


Fig. 6.9. Normalized fracture toughness, $(K_c - AK_m)/K_m$, of short glass fiber-thermoplastics injection molded composites as a function of reinforcing effectiveness parameter, Ω : (○) polyetheretherketone (PEEK) matrix ($K_m = 6.5 \text{ MPa}\sqrt{\text{m}}$); (△) polytetrafluoroethylene (PTFE) matrix ($K_m = 1.9 \text{ MPa}\sqrt{\text{m}}$). After Voss and Friedrich (1986).

of the contributions from fiber–matrix interfacial debonding, R_d of Eq. (6.1), post-debonding friction, R_{df} of Eq. (6.4), fiber pull-out, R_{po} of Eq. (6.8), and matrix fracture, R_m , (Lauke et al., 1985), in much the same manner as for continuous unidirectional fiber composites and is given by Eq. (6.10)

$$R_t = (R_d + R_{df}) \frac{c_0}{\ell} + R_{po} + (1 - V_f)R_m, \quad (6.16)$$

where c_0 is the size of the damage zone which corresponds to a critical distance from the tip of the main crack where the local stress is just sufficient to initiate an interface crack. A factor c_0/ℓ is applied to the R_d and R_{df} terms to account for the localized process of intensive energy dissipation by interface failure at the fiber ends. The contribution of fiber fracture has not been specifically considered here because of the assumption of subcritical fiber length, i.e., $\ell < \ell_c$.

The matrix material becomes brittle under dynamic loading or at low temperatures, in which case the fracture process is dominated by interface failures, such as debonding, post-debonding friction and fiber pull-out. The implication is that the fracture toughness value is at its maximum for a relatively small V_f when increasing number of effective fiber ends for interface failure prevails. On the contrary, with larger V_f , this trend is dominated by the decreasing length of interface debond and pull-out, resulting in a smaller toughness contribution. The fracture work of brittle matrix gives only an insignificant contribution to R_t . In contrast, with ductile matrix composites and under static loading conditions intensive plastic flow occurs locally and the matrix toughness term in Eq. (6.16) can be replaced by the matrix shear work, R_{ms} , in Eq. (6.13). In this case, R_t is dominated mainly by the work of matrix fracture decreasing monotonously with fiber volume fraction, V_f , and the contribution of fiber pull-out work is negligible because of the plastic flow and necking of the matrix material. Yielding occurs preferentially near the fiber ends with high stress concentrations. Fig. 6.10 shows schematically the dependence of fracture toughness contributions on V_f at different loading rates (Lauke et al., 1985).

Mai (1985) has also given a review of the fracture mechanisms in cementitious fiber composites. The total fracture toughness, R_t , is given by the sum of the work dissipation due to fiber pull-out, fiber and matrix fractures, fiber–matrix interfacial debonding and stress redistribution, i.e.,

$$R_t = \frac{V_f \ell_c^2 \tau_f}{6d} \left[(1 - V_f) + \frac{V_f \ell_c}{3E_f d^2} \right] R_m + \frac{4\chi V_f \ell_c^3 \tau_f^2}{d} + \chi V_f R_f, \quad (6.17)$$

where $\chi (\approx \ell_c/\ell)$ is the fraction of fibers that are broken when $\ell > \ell_c$ as in glass and polymeric fiber–cement composites. The third and fourth terms in Eq. (6.17), i.e. stress redistribution and fiber fracture, respectively, can be neglected for high strength fibers such as carbon. However, for ductile fibers such as glass, Kevlar and PP, fiber fracture work can be quite substantial. Since the fiber reinforcement in cementitious matrices is always randomly oriented, the orientation efficiency factor, i.e. either 0.41 or 0.637 for planar or three-dimensional randomness, respectively,

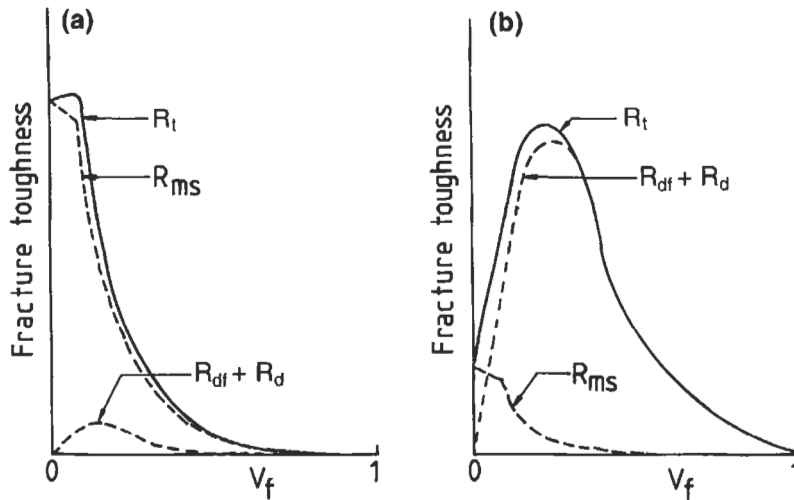


Fig. 6.10. Schematics of the dependence of total fracture toughness, R_t , on fiber volume fraction of short fiber reinforced thermoplastic composites at different loading rates: (a) static loading; (b) dynamic loading. After Lauke et al. (1985).

should be multiplied with the fiber pull-out term. This reduces effectively the fiber pull-out toughness and hence R_t . However, random orientation of ductile fibers, such as steel and nickel wires, in a brittle matrix (Helfet and Harris, 1972; Harris et al., 1972) may increase R_t due to the additional plastic shear work of fibers, as discussed in Section 6.2.2.

6.3. Fracture toughness maps

Wells and Beaumont (1982, 1985) have related the composite fracture toughness to the properties of the composite constituents using a 'toughness map' based on the study of the energy absorption processes that operate at the crack tip in unidirectional fiber composites. The microfailure mechanisms dominating the whole composite fracture processes would determine which of the parameters are to be used as variables. Having predicted the maximum energy dissipated for each failure mechanism, a map is then constructed based on the available material data, including fiber strength, modulus, fiber diameter, matrix modulus and toughness and interface bond strength, as well as the predicted values of the debond length and the average fiber length. By varying the two material properties while the remaining parameters are being held constant, the contours of constant total fracture toughness are superimposed on the map. These toughness maps can be used to characterize the roles of the constituent material properties in controlling fracture toughness, but they also describe the effects of testing conditions, such as loading rate, fatigue and adverse environment on mechanical performance of a given combination of composite constituents.

6.3.1. Continuous fiber composites

Once the characteristic ℓ_d , ℓ_{po} values and other important parameters, such as the fiber debond and pull-out stresses, are estimated from the known properties of composite constituents, the total fracture toughness for composites can be predicted based on the three principal failure mechanisms, i.e. interfacial debonding, stress redistribution and fiber pull-out (Beaumont and Anstice, 1980; Anstice and Beaumont, 1981; Wells and Beaumont, 1985). Matrix fracture energy and post-debonding friction are also considered in their earlier work (Wells and Beaumont, 1982). Fracture toughness equations have been modified taking into account the matrix shrinkage stress. Also considered are the non-linear fiber stress distributions between the debond crack front and matrix fracture plane before and after fiber fracture and Poisson contraction during fiber pull-out. The effect of two simultaneously varying parameters on fracture toughness can be clearly studied from the typical toughness maps shown in Fig. 6.11. The effect of hygrothermal aging on the variation of σ_f^* and τ_f and thus the toughness, and the change in dominant failure mechanisms from post-debonding friction to interfacial debonding are also superimposed. The gradient of the toughness contours and their spacing imply the sensitivity of the composite toughness to a particular material parameter. Based on the parametric study, one can identify the key material variables controlling the composite toughness, which in turn allows better optimization of material performance. It is concluded that fracture toughness can be enhanced by increasing σ_f^* , d , V_f and tow size (or fiber bundle diameter); or by reducing fiber and matrix stiffness, E_f and E_m , τ_b , τ_f and matrix shrinkage stress.

6.3.2. Short fiber composites

Toughness maps for short fiber composites can also be established in a similar manner, but no such maps have been reported. The difficulty stems from the large number of material and process variables that are used to fabricate these

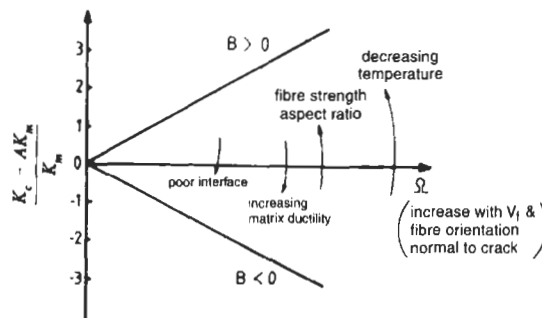


Fig. 6.11. Schematic representation of normalized fracture toughness, $(K_c - AK_m)/K_m$, versus reinforcing effectiveness parameter, Ω . After Friedrich (1985).

composites. Nonetheless, if one can identify a dominant failure mechanism for a given composite system, the fracture toughness may be directly related to the properties of the composite constituents and the interface as well as other variables. For example, in injection molded CFRPs and GFRPs containing thermoplastic matrices where matrix fracture dominates the total fracture toughness, K_C is shown to be a linear function of the parameters, K_m and Ω , according to Eq. (6.15) (Friedrich, 1985). This relationship is schematically plotted in Fig. 6.12 for a range of thermoplastic matrix materials with varying ductility. It is clearly seen that for a given K_m and Ω , higher values of fiber aspect ratio, σ_f , E_f and τ_b result in improved fracture toughness, since all these factors increase B in Eq. (6.15). A high V_f is

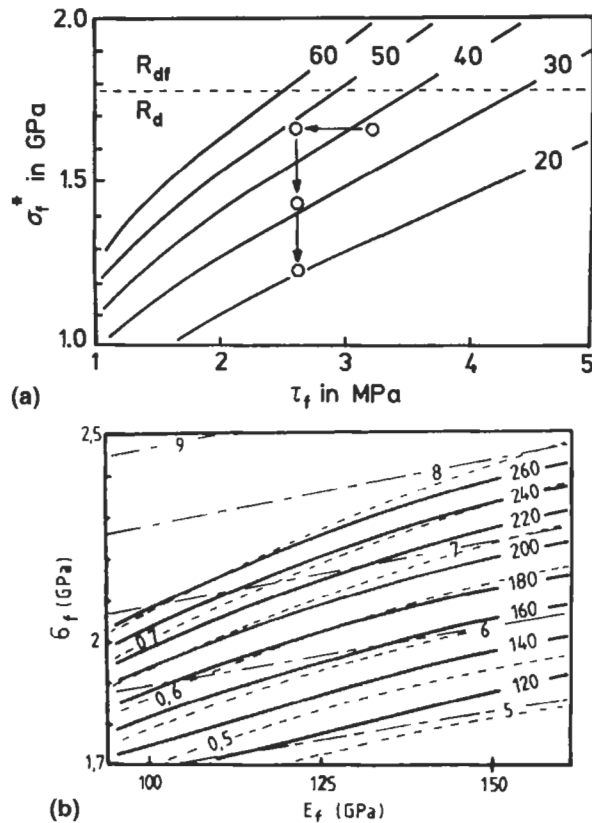


Fig. 6.12. Toughness maps depicting contours of predicted fracture toughness (solid lines in kJ/m^2) for (a) glass-epoxy composites as a function of fiber strength, σ_f , and frictional shear stress, τ_f ; and (b) Kevlar-epoxy composites as a function of σ_f and clastic modulus of fiber, E_f . The dashed line and arrows in (a) indicate a change in dominant failure mechanisms from post-debonding friction, R_{df} , to interfacial debonding, R_d , and the effect of moisture on the changes of σ_f and τ_f , respectively. Bundle debond length (--- in mm) and fiber pull-out length (- - - - in mm) are shown in (b). After Wells and Beaumont (1985, 1987).

favorable only when the thermoplastic matrix is brittle or at least moderately ductile and at low temperatures.

It is shown that the interface debonding and associated mechanisms are the principal mechanisms of toughening of composites containing glass and carbon fibers, regardless of the fiber lengths. It is clear from the maps shown in Fig. 6.12 that toughness increases rapidly with increasing fiber length, but decreasing rather slowly with increasing fiber Young's modulus. In a similar manner, toughness increases with increasing fiber diameter and decreasing fiber-matrix interface bond strength. Toughness is, to a lesser degree, sensitive to the matrix properties: it increases with decreasing matrix modulus and increasing matrix toughness.

6.4. Crack-interface interactions

It is clear from the foregoing section that composites made with brittle fibers and brittle matrices can exhibit high fracture toughness when failure occurs preferentially along the interface before fibers fracture. Most of the important toughening mechanisms are a direct result of the interface-related shear failure which gives rise to an improved energy absorption capability with a sustained crack growth stability through crack surface bridging and crack tip blunting. In contrast, a tensile or compressive failure mode induces unstable fracture with limited energy absorption capability, the sources of the composite toughness originating principally from surface energies of the fiber and matrix material, R_f and R_m . Therefore, the overall toughness of the composite may be controlled by optimizing the interface properties between the reinforcing fibers and the matrix phase, details of which are presented in Chapters 7 and 8. In this section, discussion is made of the interactions taking place between the cracks impinging the fiber-matrix or laminar interface. The criteria for crack deflection into or penetration transverse to the interface are of particular importance from both the micromechanics and practical design perspectives.

6.4.1. Tensile debonding phenomenon

In the discussion presented in Section 6.1.2, it is assumed that debonding occurs at the fiber-matrix interface along the fiber direction in mode II shear. If τ_b is sufficiently smaller than the matrix tensile strength σ_m , tensile debonding transversely to the fiber direction may occur at the interface ahead of crack tip, due to the transverse stress concentration, as shown in Fig. 6.13 (Cook and Gordon, 1964). The criterion for tensile debonding has been formulated based on stress calculations, proposing that the strength ratios of the interface to the matrix, τ_b/σ_m , are approximately 1/5 for isotropic materials (Cook and Gordon, 1964) and 1/50 for anisotropic materials (Cooper and Kelly, 1967). A substantially higher ratio of about 1/250 is suggested later (Tirosh, 1973) for orthotropic laminates of carbon fiber-epoxy matrix system with a sharp crack tip. Based on a J -integral approach, Tirosh (1973) derived a closed-form solution for the ratio of the transverse tensile stress to the shear yield stress of the matrix material, σ_T/τ_{my} , with reference to Fig. 6.14

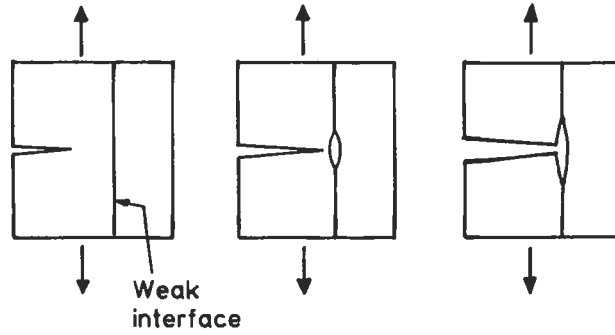


Fig. 6.13. The Cook-Gordon (1964) mechanisms: tensile debonding occurs at the weak interface ahead of crack tip as a result of lateral stress concentration and crack tip is effectively blunted.

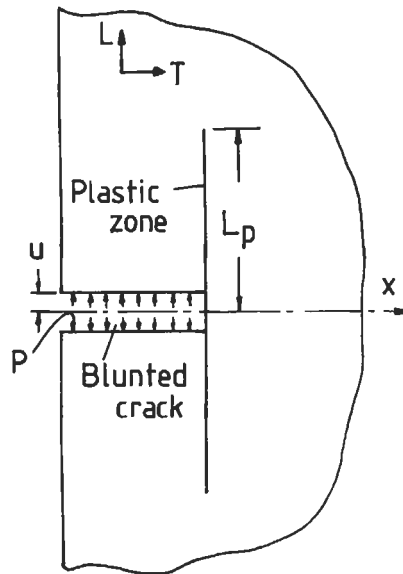


Fig. 6.14. Blunted crack tip and longitudinal splitting in unidirectional continuous fiber composites. After Tirosh (1973).

$$\frac{\sigma_T}{\tau_{my}} = \operatorname{Re} \left[\frac{1}{k_1 - k_2} \frac{1}{\pi i} \ln \left(\frac{L_p^2 - z_1^2}{u^2 - z_1^2} \right) + \ln \left(\frac{L_p^2 - z_2^2}{u^2 - z_2^2} \right) \right], \quad (6.18)$$

where z_1 and z_2 are complex variables that are functions of the coordinate directions x and y , and complex constants k_1 and k_2 :

$$z_1 = x + k_1 y, \quad z_2 = x + k_2 y. \quad (6.19)$$

The constants k_1 and k_2 are given by:

$$\begin{aligned} k_1 &= \frac{\sqrt{2}}{2} \left[i(\phi_1 + \phi_2)^{1/2} + (\phi_1 + \phi_2)^{1/2} \right], \\ k_2 &= \frac{\sqrt{2}}{2} \left[i(\phi_1 + \phi_2)^{1/2} - (\phi_1 - \phi_2)^{1/2} \right], \end{aligned} \quad (6.20)$$

where ϕ_1 and ϕ_2 are defined in Eq. (6.36). Graphical solutions of Eq. (6.18) are presented in Fig. 6.15 for carbon fiber–epoxy matrix orthotropic laminates for two levels of uniaxial tension. It is clearly shown that the transverse stress is at its maximum at some distance away from the crack tip, except for zero crack opening displacement, although its magnitude is relatively lower than that of the longitudinal tensile stress.

Many investigators (Tetelman, 1969; Kelly, 1970; Tirosh, 1973; Marston et al., 1974; Atkins, 1975) have recognized the occurrence of this failure mechanism in unidirectional fiber composites, and several researchers (Cooper and Kelly, 1967; Pan et al., 1988) presented physical evidence of tensile debonding ahead of crack tip. Nevertheless, it appears that the longitudinal splitting at the weak interface occurs due to the large shear stress component developed in the crack tip region as a result of the high anisotropy of a high V_f composite, rather than the tensile stress component (Harris, 1980). Although the occurrence of splitting can be promoted if there is a large tensile stress component under certain favorable conditions, its contribution to the total fracture toughness may be insignificant (Atkins, 1975). Therefore, it can be concluded that the tensile debonding model applies originally to laminate structures and the associated toughening mechanisms as a result of longitudinal splitting or delamination are crack tip blunting with reduced stress

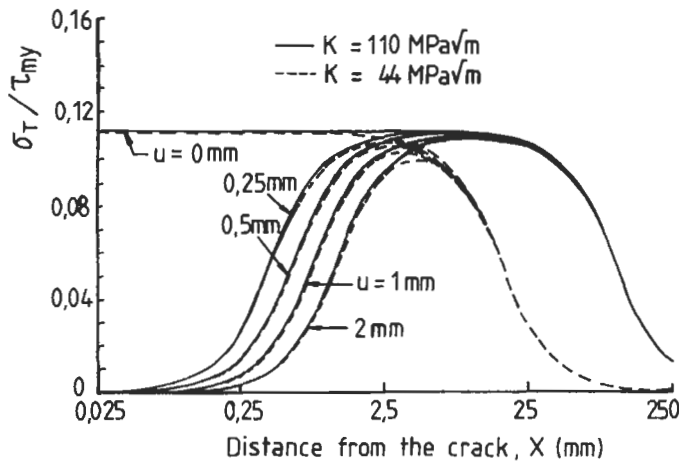


Fig. 6.15. Stress distributions ahead of crack tip in the transverse direction of orthotropic laminate in tensile loading. After Tirosh (1973).

concentration in the transverse direction and crack arrest with further increase in the amount of delamination (Sakai et al., 1986, 1988).

6.4.2. Transverse cracking versus longitudinal splitting

When a brittle crack momentarily impinges on an interface between a matrix and a reinforcing stiff fiber at right angles, there are basically two choices of crack propagation, and are schematically shown in Fig. 6.16. The crack can either propagate ahead into the fiber (i.e., penetration or transverse cracking), or be deflected (singly or doubly) and continues to propagate along the interface (i.e. deflection or longitudinal splitting). The requirements to achieve the latter failure mode rely on two complementary criteria based on either local crack-tip stresses or the strain energy stored in the composite constituents, similar to the fiber–matrix interface debond criteria as discussed in Chapter 4. The local stress criterion for crack deflection requires that the debond stress, in mode I tension, mode II shear or combination of these two modes, be reached before the cohesive strength is attained in the fiber or composite at the crack tip. The complementary fracture mechanics criterion requires that when the crack is about to grow the work of fracture along the interface, R_i , or the fracture toughness for longitudinal splitting, R_L , would be less than that ahead into the fiber, R_T , the fracture toughness for transverse cracking.

6.4.2.1. Fracture mechanics criterion

The transition between cohesive and adhesive failure in a simple bi-material joint has been studied by Kendall (1975). Based on Griffith's energy approach, a criterion is derived for deflection along the interface for a short crack for an isotropic material

$$\frac{R_L}{R_T} < \frac{1}{4\pi(1-\nu^2)} \quad (6.21)$$

The implication of Eq. (6.21) is that the criterion is dependent mainly on the ratio of the energies for longitudinal splitting and transverse cracking, and is relatively insensitive to crack length and the elastic modulus. It is also noted from experimental study that crack speed has a pronounced effect on the toughness ratio, R_L/R_T , and thus the crack deflection phenomenon.

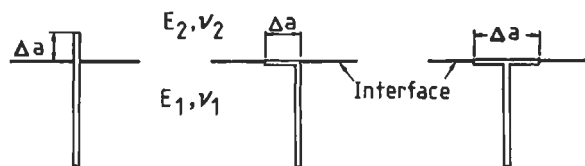


Fig. 6.16. Crack paths at the bi-material interface: (a) penetrating crack; (b) singly deflected crack; and (c) doubly deflected crack. After He and Hutchinson (1989).

Based on a shear-lag model, Nairn (1990) has also derived an expression for the energy release rates due to the two opposing fracture modes in unidirectional fiber composites. The material heterogeneity, material anisotropy and finite width effects have been considered. The fracture mechanics criterion requires that the strain energy release rate ratio, G_L/G_T , is equal to or greater than the toughness ratio for longitudinal splitting

$$\frac{R_L}{R_T} < \frac{G_L}{G_T} = \frac{1}{2} \sqrt{\frac{G_{LT}}{E_L}}, \quad (6.22)$$

where G_L is the strain energy release rate for longitudinal splitting parallel to the fiber, whether failure occurs due to debonding at the fiber–matrix interface, shear failure of matrix materials or combination of these two. G_T is the strain energy release rate for transverse fracture of the fiber or composite by a self-similar crack. G_{LT} and E_L are the effective in-plane shear modulus and Young's modulus of the unidirectional fiber composite, respectively. It follows that depending on the type of longitudinal splitting, the critical R_L should be related to the matrix shear fracture toughness in mode II, or to the fiber–matrix interface fracture toughness, R_i .

In real composites, transverse cracking or longitudinal splitting does not occur purely due to the mode I or mode II stress component, respectively. Two materials making contact at an interface are most likely to have different elastic constants. Upon loading, the modulus mismatch generates shear stresses, resulting invariably in a mix-mode stress state at the crack tip. This, in turn, allows mixed-mode debonding to take place not only at the crack tip, but also in the wake of the crack, as schematically shown in Fig. 6.17. This justifies the argument that the fracture

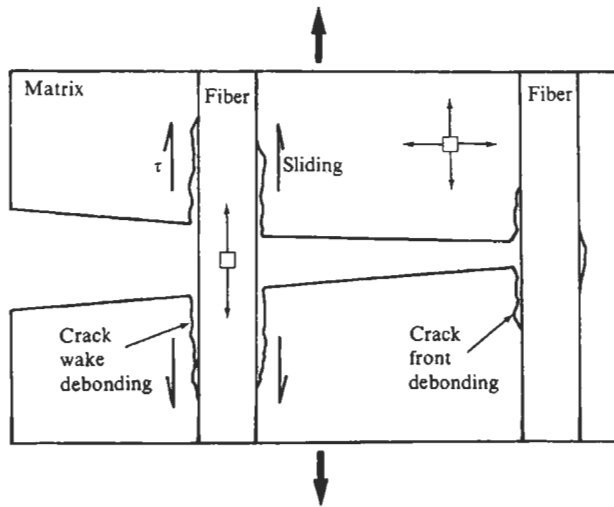


Fig. 6.17. Fracture process zone (FPZ) in transverse fracture of unidirectional fiber composite. After Chawla (1993).

behavior of the composite cannot be fully expressed by a single parameter, the critical stress intensity factor, K_{Ic} , or the critical strain energy release rate, G_{Ic} , used in elastic, homogeneous systems, but needs more complex functions of fracture mechanics to describe the phenomenon.

He and Hutchinson (1989) considered a crack approaching an interface as a continuous distribution of dislocations along a semi-infinite half space. The effect of mismatch in elastic properties on the ratio of the strain energy release rates, G_L/G_T , is related to two non-dimensional parameters, the elastic parameters of Dundurs, α and β (Dundurs, 1968):

$$\alpha = \frac{\mu_1(1 - \nu_1) - \mu_2(1 - \nu_2)}{\mu_1(1 - \nu_1) + \mu_2(1 - \nu_2)} = \frac{\bar{E}_2 - \bar{E}_1}{\bar{E}_2 + \bar{E}_1}, \quad (6.23)$$

$$\beta = \frac{\mu_1(1 - 2\nu_1) - \mu_2(1 - 2\nu_2)}{\mu_1(1 - \nu_1) + \mu_2(1 - \nu_2)}, \quad (6.24)$$

where μ is shear modulus, ν is Poisson ratio and $\bar{E} = E/(1 - \nu^2)$. The subscripts refer to the cracked material 1 and the uncracked material 2, shown in Fig. 6.16. Therefore, a criterion for a crack to deflect along the interface is given by (He and Hutchinson, 1989)

$$\frac{R_L}{R_T} < \frac{G_L(\Psi)}{G_T} = \frac{1 - \beta^2 |d^2| + |e^2| + 2 R_e(de)}{1 - \alpha c^2} \quad (6.25)$$

where $G_L(\Psi)$ is the fracture toughness for longitudinal splitting at a phase angle of loading Ψ . c , d and e are non-dimensional complex valued functions of α and β . The expression for the phase angle, Ψ , in terms of the elastic coefficient of the two media, radius r from the crack tip and the displacements u and v at the crack tip, Fig. 6.18, is (Evans, 1989):

$$\begin{aligned} \phi &= \tan^{-1} \left(\frac{v}{u} \right), \\ \Psi &= \phi - \frac{\ln r}{2\pi} \ln \frac{1 - \beta}{1 + \beta} - \tan^{-1} \frac{1}{\pi} \ln \frac{1 - \beta}{1 + \beta}. \end{aligned} \quad (6.26)$$

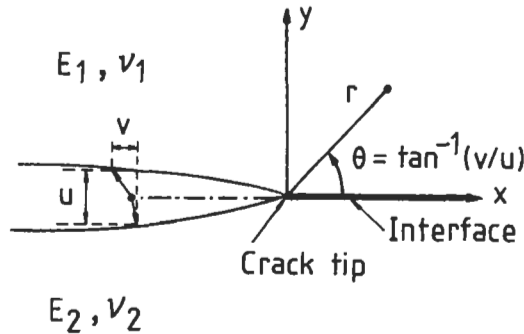


Fig. 6.18. A crack at the bi-material interface. After Evans (1989).

It follows then that for opening mode I, $\Psi = 0^\circ$, while for pure mode II shear, $\Psi = 90^\circ$. The predictions plotted in Fig. 6.19 (He and Hutchinson, 1989) clearly shows the fracture transition criterion under which the crack will deflect along the interface or propagate transversely, depending on the variations of phase angle, Ψ , and elastic anisotropic parameter, α . For all values of $G_L(\Psi)/G_T$ below the line, longitudinal splitting or crack deflection is expected to occur. It is noted that for the special case of zero elastic mismatch for $\alpha = 0$, longitudinal splitting into a single deflection will occur when $G_L(\Psi)/G_T \approx 0.25$. In general, for $\alpha > 0$, the minimum value of $G_L(\Psi)$ for longitudinal splitting increases with increasing α . This suggests that high modulus fibers tend to encourage interfacial debonding and shear failure.

Gupta et al. (1991, 1993) have further extended the above analysis taking into account the anisotropy of materials. Based on the method of singular integral equation employed earlier by Erdogan (1972), an energy criterion similar to Eq. (6.25) is established with material parameters given in Eqs. (6.28)–(6.33). A plot is shown in Fig. 6.20 for the energy release rate ratio, G_L/G_T , for doubly deflected cracks as a function of the parameters α and λ_1 . Other parameters including ρ_1 , λ_2 and ρ_2 are assumed to be unity with $\beta = 0$. It is noted that for $\alpha = -0.9$, the energy release rate ratio can differ by almost 100% over the range of $\lambda_1 = 0.2$ –5.0. Similar variations are also observed with respect to the orthotropic parameter ρ_1 . It is worth noting that the energy release rate ratio is insensitive to the variation of the parameter β in the range -0.2 to 2.0, provided that other parameters are assumed to be unity. As the issue of longitudinal splitting and transverse cracking is a topic of practical importance in composites technology, continuing research efforts have been directed to predict the two opposing fracture phenomena (Tohogo et al., 1993; Tullock et al., 1994).

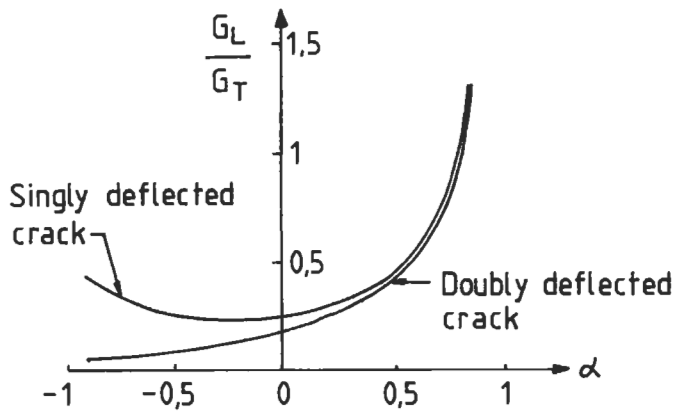


Fig. 6.19. Ratio of the strain energy release rates, G_L/G_T , plotted as a function of crack length. After He and Hutchinson (1989).

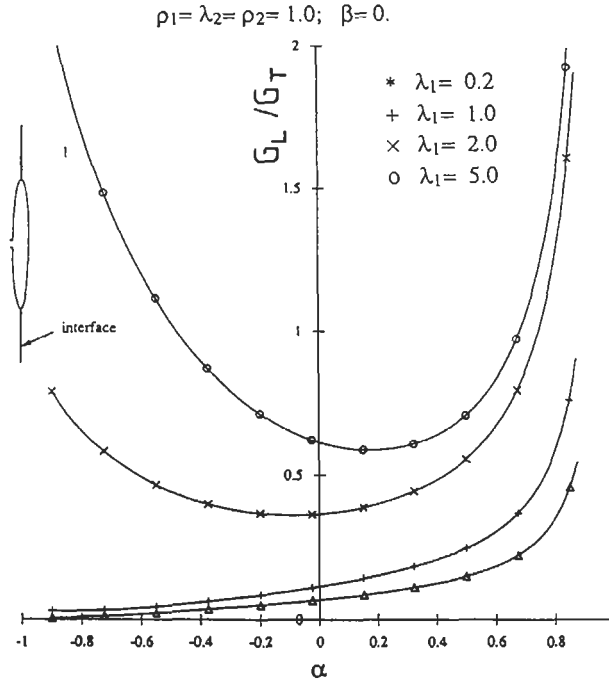


Fig. 6.20. Ratio of the strain energy release rates, G_L/G_T , plotted as a function of the material parameter, α , for a doubly deflected interface crack. After Gupta et al. (1993).

6.4.2.2. Maximum stress criterion

A criterion has been developed based on the tensile normal stress and the anisotropic tensile strength on arbitrary planes about the crack tip. It is assumed that the crack grows along the plane on which the stress ratio is maximum (Buczck and Herakovich, 1985). A maximum stress criterion is also proposed (Gupta et al., 1993) for a crack which deflects along the interface

$$\frac{\sigma_L^*}{\sigma_T^*} < \frac{\sigma_{yy}(0^\circ)}{\sigma_{xx}(90^\circ)}, \quad (6.27)$$

where σ_L^* and σ_T^* are the interface (longitudinal splitting) and fiber (transverse fracture) strengths, and $\sigma_{yy}(0^\circ)$ and $\sigma_{xx}(90^\circ)$ are the stresses at the interface and in the fiber, respectively, as determined by the method of singularity integral equations (Erdogan, 1972). Taking into account the elastic anisotropy, Gupta et al. (1993) introduced the anisotropy parameters λ and ρ which depend on the elastic compliances S_{ij} as follows:

$$\lambda = \frac{S_{11}}{S_{22}}, \quad (6.28)$$

$$\rho = \frac{2S_{12} + S_{66}}{2\sqrt{S_{22}S_{11}}}. \quad (6.29)$$

It is noted that these parameters become unity for an isotropic material. The two elastic parameters, α and β , are also modified accordingly, taking into account the anisotropy:

$$\alpha = \frac{\gamma_2 - \gamma_1}{\gamma_2 + \gamma_1}, \tag{6.30}$$

$$\beta = \frac{(\gamma + s_{12})_2 - (\gamma + s_{12})_1}{\left[(2g\lambda^{1/4}\gamma)_1 + (2g\lambda^{1/4}\gamma)_2 \right]^{1/2} \left[(2g\lambda^{-1/4}\gamma)_1 + (2g\lambda^{-1/4}\gamma)_2 \right]}. \tag{6.31}$$

where

$$\gamma = \sqrt{s_{22}s_{11}}, \tag{6.32}$$

$$g = \sqrt{\frac{(1 + \rho)}{2}}. \tag{6.33}$$

The subscripts 1 and 2 refer to materials 1 and 2, respectively (see Fig. 6.18). It is worth noting that the longitudinal splitting criterion given by Eq. (6.27) is insensitive to the variation of λ and ρ of the two materials if the isotropic values are used. Therefore, the longitudinal splitting criterion is plotted as a function of the bi-material parameters, α and β , in Fig. 6.21. The regions above and below the curves represent the failure loci due to longitudinal splitting and transverse cracking, respectively. The interface and transverse strengths, σ_I^* and σ_T^* , can be determined

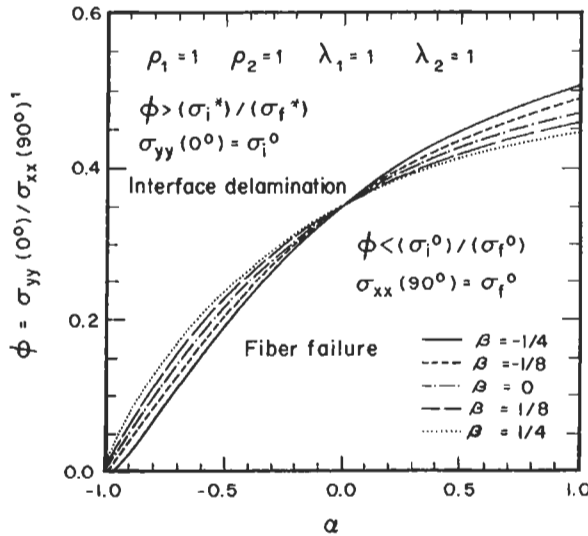


Fig. 6.21. The criterion for longitudinal splitting in terms of the stress ratio, $\sigma_{yy}(0^\circ) / \sigma_{xx}(90^\circ)$. After Gupta et al. (1991). Reprinted with permission of ASME International.

Table 6.2
Maximum allowable interface strength for interface delamination^a

Composite system (fiber/ matrix or coating)	α	Required interface strength, σ_L^* (MPa)	Calculated transverse strength, σ_T^* (MPa) ^b
P-55/Al	0.001	475	197
P-100/Al	0.153	726	300
P-55/SiC (HBE)	-0.605	209	86
P-55/SiC (LBE)	0.574	836	350
P-100/SiC (HBE)	-0.499	330	136
P-100/SiC (LBE)	0.668	946	390
Al ₂ O ₃ /SiC (LBE)	0.904	788	326
Nicalon SiC/Al	0.468	1148	470
Al ₂ O ₃ /TiC	-0.085	508	210

^aAfter Gupta et al. (1993).

^bBased on transverse stress concentration factor of 2.40.

HBE: high ion beam energy; LBE: low ion beam energy.

from Fig. 6.21 for the corresponding values of α and β . Table 6.2 presents such predictions for various combinations of fiber–ceramic matrix (or coating) systems. A practical implication of Fig. 6.21 is that the level of interface bond strength required to satisfy the longitudinal splitting can be enhanced by choosing appropriate combinations of fiber and matrix (or coating) materials, and thereby allowing the composite to sustain a higher external stress without causing catastrophic failure.

6.4.2.3. Length of longitudinal splitting

In the study of the effect of plasticity and crack blunting on longitudinal and transverse stress distributions in orthotropic composites materials, Tirosh (1973) analyzed the longitudinal splitting problem for uniaxially oriented, continuous fiber composites with a transverse single edge notch (SEN). For large scale plasticity where the length of splitting, L_p , is comparable to the characteristic dimension of the specimen which is loaded in axial tension, the J -integral is given by

$$J_c \approx 4 \frac{\tau_y^2}{G_{LT}} L_p, \quad (6.34)$$

where τ_y is the shear yield stress of the fiber–matrix interface, and G_{LT} is the in-plane shear modulus of the composite. The split length, L_p , is obtained by equating the J -integral to the solution for the crack extension force derived earlier by Sih and Liebowitz (1968). It is seen that the J -integral in Eq. (6.34) is analogous to the interface toughness given by Eq. (6.1) or Eq. (6.2) which is obtained from LEFM. The J -integral can be related to the uniform normal stress, σ_n , acting on the notch surface. Therefore, the splitting length, L_p , is

$$L_p = F \left(\frac{K_I}{\tau_{my}} \right)^2 = \frac{a\pi}{4} \left(\frac{\sigma_n}{\tau_{my}} \right)^2 \frac{G_{LT}}{E_t} \phi_1 \left(\frac{\phi_1 + \phi_2}{2} \right)^{1/2}. \quad (6.35)$$

$K_I = \sigma_n \sqrt{a}$ is the stress intensity factor, and F , the material constant, both of which depend on the degree of anisotropy of the composite controlled by the composite elastic moduli in the longitudinal and transverse directions, E_L and E_T , in-plane Poisson ratio, ν_{LT} , and G_{LT} . For a perfectly isotropic material, $F \approx \pi/8(1 + \nu_{LT}) \approx 0.3$. Also, the material parameters, ϕ_1 and ϕ_2 , are given by:

$$\begin{aligned} \phi_1 &= \left(\frac{E_L}{E_T} \right)^{1/2} \\ \phi_2 &= \frac{E_L}{2G_{LT}} - \nu_{LT} \end{aligned} \quad (6.36)$$

The predictions based on Eq. (6.35) are found to be consistent with the results from finite element analysis, Fig. 6.22, for a carbon fiber–epoxy matrix orthotropic laminate.

Based on the above analysis, Newaz (1985, 1986) measured the interfacial fracture toughness using SEN specimens: $J_c = 3.7$ and 6.6 kJ/m^2 for unidirectional glass–polyester and glass–epoxy composites, respectively. Clearly, these values are thought to be over one order of magnitude greater than those determined from single fiber pull-out tests for similar composite systems (Chua and Piggott, 1985), even though the shear yield stresses are similar in the two different experiments. It appears that the J_c values obtained using the SEN geometry represent the total fracture

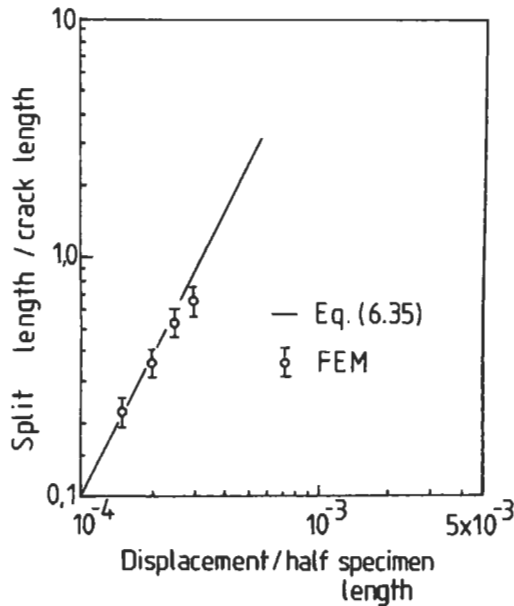


Fig. 6.22. Comparisons of the longitudinal splitting length, L_p , between analysis and finite element method for graphite fiber–epoxy matrix orthotropic laminates. After Tirosh (1973).

toughness in mode II delamination which comprises toughness contributions from matrix fracture, fiber–matrix interface debonding, frictional work due to sliding between the opposite fracture surfaces as well as any fiber fracture and fiber bridging. On the other hand, the failure mechanisms taking place in pull-out tests is much simpler and idealised, and the experiment gives only the interface debond toughness.

6.4.3. Crack growth resistance (*R*-curve) behavior in transverse fracture

6.4.3.1. *R*-curve behavior

LEFM of composites uses a simplified model of classical homogeneous isotropic materials on a macroscopic scale, and assumes that crack propagation occurs when the local stress exceeds the finite allowable critical strength which is measured on the materials with notches. Many researchers including Konish et al. (1972), Ellis and Harris (1973), Owen and Bishop (1973), Mandell et al. (1981, 1982) and Alexander et al. (1982), have demonstrated that LEFM principles can be employed to characterize the fracture toughness of short fiber composites by determining the critical stress intensity factor, K_c , with different specimen geometry. Fiber reinforced composites, however, generally show a substantial amount of stable crack growth before instability, even in composites with unidirectional continuous fibers, and the fracture toughness increases with crack extension before it reaches a plateau value. Therefore, a single parameter such as K_c is not totally appropriate to characterize the whole fracture behavior and the concept of crack resistance curve (i.e. *R*-curve) has to be adopted.

Usually, an *R*-curve is represented by one of the fracture parameters: stress intensity factor, K_R ; potential energy release rate, G_R ; contour integral, J ; and crack tip opening displacement, δ , as a function of crack growth, Δa , including the length of damage zone and any real crack extension. Comprehensive reviews on the crack resistance behavior and its analysis and measurement of various engineering materials, including fiber composites and cementitious composites, are given by Mai (1988) and Cotterell and Mai (1996). Our discussion on *R*-curve behavior of fiber composites presented below is focused mainly on transverse fracture.

Following the early report on *R*-curve determination for randomly oriented glass–epoxy and glass–polyester systems (Gaggar and Broutman, 1975), many workers (Agarwal and Giare, 1982; Morris and Hahn, 1977; Kim, 1979; Bathias et al., 1983; Ochiai and Peters, 1982; Wells and Beaumont, 1987; Solar and Belzunce, 1989) have studied the *R*-curve behavior for various types of composites. The effects of fiber concentration, specimen thickness and width, and test temperature and material have been specifically considered on the fracture toughness of short glass–epoxy composites using the *R*-curve approach. In particular, Wells and Beaumont (1987) developed a *R*-curve model based on the energy absorbed due to the microfailure mechanisms in polymer matrix composites, including off-angle fracture and delamination for cross-ply laminates in addition to those described in Section 6.1 for unidirectional fiber composites. Reasonable agreement is obtained between the predictions and the established data for the *R*-

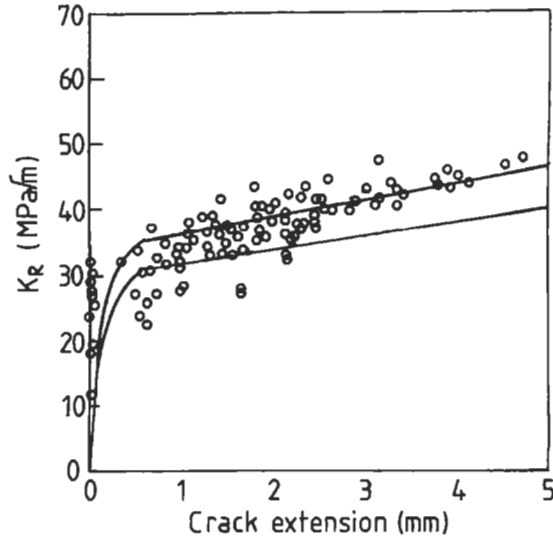


Fig. 6.23. R-curve prediction (—) and experimental data (○) for a carbon fiber-epoxy matrix quasi-isotropic $[0^\circ / \pm 45^\circ / 90^\circ]_s$ laminate. After Wells and Beaumont (1987).

curve (Fig. 6.23) and composite notch strength (Fig. 6.24). They noted that the crack resistance increases even at large crack extensions, particularly for laminates containing symmetric $[\pm 45^\circ]$ plies (Fig. 6.23). This is attributed to the large scale damage zone ahead of the fracture path where the energy is absorbed mainly by delamination. This observation rather contradicts the earlier finding by Ochiai and

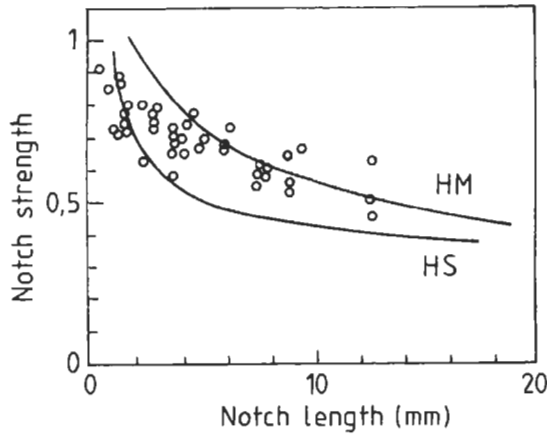


Fig. 6.24. Comparison of notched strength of carbon fiber-epoxy matrix quasi-isotropic $[0^\circ / \pm 45^\circ / 90^\circ]_s$ laminate between predictions (—) and experimental data (○): HM = high modulus carbon fiber; HS = high strength carbon fiber. After Wells and Beaumont (1987).

Peters (1982) in that the experimental R-curve is slightly higher for $[0^\circ/90^\circ]_{2s}$ glass-epoxy laminates than for $[0^\circ/\pm 45^\circ/0^\circ]_s$ laminates in center notched (CN) tension specimens, particularly for long crack lengths. The K_R values are compared in Fig. 6.25 between the two laminates with different layup sequence. The ever-increasing R-curve for Kevlar fiber composite laminates with all layup sequences is due to large fiber pull-out lengths and damage zone size. Thinner specimens normally give higher R-curves in SEN tension tests of laminates (Solar and Belzunce, 1989), and short fiber composites (Agarwal and Giare, 1982).

6.4.3.2. Fracture process zone or damage zone

The R-curve study normally involves the characterization of critical size of the FPZ or damage zone, c_0 , at the crack tip region, which is analogous to the approach used for predicting the plastic zone in metallic materials. The damage zone is directly responsible for the increasing crack growth resistance, R-curve, behavior observed in composites whether the direction of loading is along or transverse to the fiber direction (i.e. interlaminar/intralaminar or transverse fracture). The damage in transverse fracture of composites, as schematically shown in Fig. 6.17, can be divided into two regions:

- (1) the damage zone ahead of the advancing crack tip where matrix cracking, interfacial debonding, post-debonding friction occur;
- (2) the fiber bridging zone or tied zone at the wake of the crack tip where fibers bridge the opposite fracture surfaces and pull-out.

The size of damage depends on fiber V_f , fiber aspect ratio, types of fiber and matrix material, bonding at the fiber-matrix interface, layup sequence in multi-angle ply laminates, specimen geometry including laminate thickness, and loading

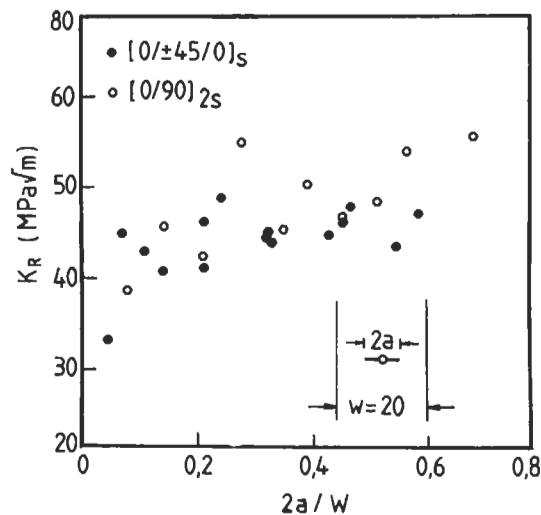


Fig. 6.25. Maximum fracture toughness, K_R , as a function of relative crack length, $2a/W$, for carbon fiber-epoxy matrix $[0^\circ/\pm 45^\circ/0^\circ]_s$ and $[0^\circ/90^\circ]_{2s}$ laminates. After Ochiai and Peters (1982).

configuration. In the case of interlaminar/intralaminar fracture where the crack propagates parallel to the fiber direction, the fibers are peeled off or fractured rather than being pulled out. The fiber bridging in interlaminar fracture arises mainly from the misalignment of fibers across the main crack plane, localized concentration of fibers and matrix material (i.e. fiber rich and resin rich regions) and the growth of the crack on more than one plane.

Based on the 'inherent flaw model' (IFM) proposed earlier by Waddoups et al. (1971), Caprino et al. (1979, 1980) predicted c_0 to be approximately 2 mm for double edge notch (DEN) and CN tension specimens of continuous epoxy matrix composites containing carbon, glass and boron fibers. The IFM was originally developed to predict the notch strength of laminates with finite width and an inherent flaw of length, $2c_0$. c_0 is found to be sensitive to the variations in ply layup sequence, fiber orientation and type of fibers used. Slightly higher values of c_0 have been obtained for CN and SEN tension specimens of carbon-epoxy system based on the 'damage zone model (DZM)': $c_0 = 2-4$ mm (Hillerborg et al., 1976; Aronsson and Bachlund, 1986). In the DZM, the closure stresses due to the bridging fibers act on the entire crack surfaces in accordance with a particular closure stress-crack face relationship which is consistent with the damage mechanisms taking place. The predictions of c_0 and the notched strength, σ_n , using the DZM are shown (Aronsson and Backlund, 1986) to agree better with experimental measurements than the IFM model. For example, the experimental value of c_0 for three-point bend specimens of short glass-polyester systems is about 6 mm which is almost the same as the DZM prediction of 6-7 mm, while the IFM model predicts a lower value of 4.1 mm. A summary of all these previous models including the well-known Mar-Lin model (Mar and Lin 1979) and a recent effective crack growth model to predict the residual strength of composite laminates with notches and other forms of discontinuities have been given by Afaghi-Khatibi et al. (1996a,b).

Because cracks in multi-angle ply laminates seek the easiest paths to propagate preferentially along the fiber-matrix and laminar interfaces, the shape and size of the damage zone in these composites depend strongly on the loading configuration relative to the fiber orientation within the individual plies. The damage zone sizes are compared between the laminates of different layup configurations for varying notch lengths in Fig. 6.26. It is noted that the $[90^\circ]$ sub-cracks in $[0^\circ/90^\circ]_s$ carbon-epoxy laminates are approximately 10 times longer than $[45^\circ]$ sub-cracks in $[0^\circ/\pm 45^\circ/0^\circ]_s$ laminates, while $[0^\circ]$ sub-cracks for the former laminates are about twice those for the latter laminates. The complex appearance of the damage zone together with the interactions between laminae make the quantitative characterization of the damage zone size in multi-angle laminates extremely difficult.

In short fiber composites, energy absorption mechanisms, such as interfacial debonding and matrix cracking, most often occur at the fiber ends (Curtis et al., 1978). The damage model proposed by Bader et al. (1979) assumes that short fiber composites fail over a critical cross-section which has been weakened by the accumulation of cracks, since the short fibers bridging this critical zone are unable to carry the load. In fatigue loading, sudden fracture takes place as a direct result from the far-field effect of the composite, rather than due to the near field of the crack tip

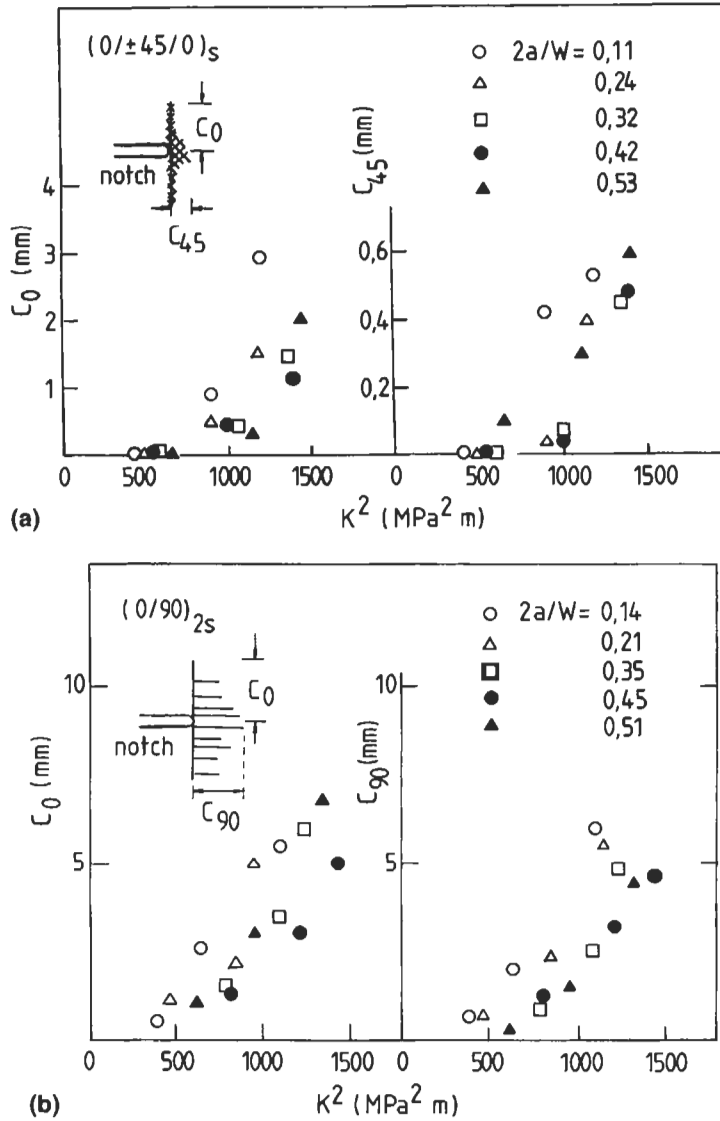


Fig. 6.26. Sub-crack lengths, l_0 and l_{90} , plotted as a function of K^2 for different relative crack length, $2a/W$: (a) $[0^\circ/\pm 45^\circ/0^\circ]_s$ laminates; (b) $[0^\circ/90^\circ]_{2s}$ laminates. After Ochiai and Peters (1982).

(Lhymn and Schultz, 1983). This observation is analogous to the fracture process in the outer process zone which is termed the 'dissipation zone' as distinct from the inner process zone ahead of crack tip (Lauke and Schultrich, 1986b; Lauke and Pompe, 1988). In the dissipation zone, intensive energy dissipation by fiber-matrix interfacial debonding and post-debonding friction is concentrated mainly at the fiber

ends in aligned short fiber–thermoplastic composites. Depending on the interfacial bond strength and matrix ductility, the main crack propagates in a fiber avoidance mode, as illustrated clearly in Fig. 6.5. The cracks bypass the regions of agglomeration of locally aligned fibers without breaking them (Mandell et al., 1981, 1982). It follows therefore that a critical distance from the main crack where the stress is just enough to initiate debonding (i.e. fiber debond stress, σ_d) can be regarded as the size of damage zone, c_0 , in these composites. It is proposed that in the absence of large scale yielding, the effective length of these long fibers that are exceeded by 5% of the total fibers in injection molded thermoplastic composites is approximately equal to c_0 (Mandell et al., 1981, 1982). Assuming that the stress field near the crack tip varies linearly with $1/\sqrt{r}$ as in isotropic materials, where r is the distance from the crack tip, the stress in the damage zone is given by

$$\sigma = \sigma_d \sqrt{\frac{c_0}{r}} . \quad (6.37)$$

It is assumed that the maximum stress in the next fiber located at a distance $d/\sqrt{V_f}$ away is approximately equivalent to the composite tensile strength, σ_c^* . It follows then that the damage zone size, c_0 , for aligned short fiber composites is given by (Lauke et al., 1985)

$$c_0 \approx \frac{d}{\sqrt{V_f}} \left(\frac{\sigma_c^*}{\sigma_d} \right)^2 . \quad (6.38)$$

References

- Afaghi-Khatibi, A., Ye, L. and Mai, Y.W. (1996a). An effective crack growth model for residual strength evaluation of composite laminates with circular holes. *J. Composite Mater.* **30**, 142–163.
- Afaghi-Khatibi, A., Ye, L. and Mai, Y.W. (1996b). Effective crack growth and residual strength of composite laminates with a sharp notch. *J. Composite Mater.* **30**, 333–357.
- Agarwal, B.D. and Giare, G.S. (1982). Influence of the properties of the matrix material on the fracture toughness of short fiber composites. *Mater. Sci. Eng.* **52**, 139–145.
- Alexander, R.M., Schapery, R.A., Jerina, K.L. and Sander, B.A. (1982). Fracture Characterization of a random fiber composite material. In *Short Fiber Reinforced Composite Materials*, ASTM STP 722 (B.A. Sanders ed.), ASTM, Philadelphia, PA, pp. 208–224.
- Anstice P.D. and Beaumont P.W.R. (1981). Hygrothermal aging effects on the micromechanisms of crack extension in glass fiber and carbon fiber composites. In *Proc. ICF 5* (Francois D. et al., eds.), Pergamon Press, Oxford, Vol. 1, pp. 473–483.
- Aronsson C.G. and Backlund, J. (1986). Tensile fracture of laminates with cracks. *J. Composite Mater.* **20**, 287–307.
- Atkins A.G. (1975). Intermittent bonding for high toughness/high strength composites. *J. Mater. Sci.* **10**, 819–832.
- Backlund, J. and Aronsson, C.G. (1986). Tensile fracture of laminates with holes. *J. Composite Mater.* **20**, 259–285.
- Bader M.G., T.W. Chou and J. Quigley (1979). In *New Developments and Application Composites*, (D. Wilsdorf ed.), The Metallurgical Society, AIME, New York.

- Bathias, C., Esnault, R. and Pellas, J. (1983). On the increasing fracture toughness at increasing notch length of 0/90 and 0/ \pm 45/0 graphite/epoxy laminates. *Composites* **14**, 365–369.
- Beaumont P.W.R. and Anstice P.D. (1980). A failure analysis of the micro-mechanisms of fracture of carbon fiber and glass fiber composites in monotonic loading. *J. Mater. Sci.* **15**, 2691–2635.
- Beaumont P.W.R. and Harris B. (1972). The energy of crack propagation in carbon fiber-reinforced resin systems. *J. Mater. Sci.* **7**, 1265–1279.
- Beaumont P.W.R. and Phillips D.C. (1972). The fracture energy of glass fiber composites. *J. Mater. Sci.* **7**, 682–686.
- Buczck, M.B. and Herakovich, C.T. (1985). A normal stress criterion for crack extension direction in orthotropic composite materials. *J. Composite Mater.* **19**, 544–553.
- Caprino, G. Halpin, J.C. and Nicolais, L. (1979). Fracture mechanics in composite materials. *Composites* **10**, 223–227
- Caprino, G. Halpin, J.C. and Nicolais, L. (1980). Fracture toughness of graphite/epoxy laminates. *Composites* **11**, 105–107.
- Chawla, K.K. (1993). *Ceramic Matrix Composites*. Chapman & Hall, London.
- Chua P.S. and Piggott M.R. (1985). The glass fiber–polymer interface: IV – Controlled shrinkage polymers. *Composites Sci. Technol.* **22**, 245–258.
- Clyne, T.W. and Withers, P.J. (1993). *An Introduction to Metal Composites*. Cambridge University Press, Cambridge, UK.
- Cook J. and Gordon J.E. (1964). A mechanism for the control of crack propagation in all-brittle systems. *Proc. Roy. Soc. Lond. A* **282**, 508–520.
- Cooper, G.A. (1970) The fracture toughness of composites reinforced with weakened fibers. *J. Mater. Sci.* **5**, 645–654.
- Cooper G.A. and Kelly A. (1967). Tensile properties of fiber-reinforced metals: Fracture mechanics. *J. Mech. Phys. Solids* **15**, 279–297.
- Cooper G.A. and Kelly A. (1969). Role of the interface in the fracture of fiber composite materials. In *Interfaces in Composites*, ASTM STP 452, ASTM, Philadelphia, PA, pp. 90–106.
- Cotterell, B. and Mai, Y.W. (1996). *Fracture Mechanics of Cementitious Materials*, Blackie Academic & Professional, London, UK.
- Cottrell A.H. (1964). Strong solids. *Proc. Roy. Soc. Lond. A* **282**, 2–9.
- Curtis P.T., Bader M.G. and Bailey J.E. (1978). The stiffness and strength of a polyamide thermoplastic reinforced with glass and carbon fibers. *J. Mater. Sci.* **13**, 377–390.
- Davidge, R.W. (1989). In *Application of Fracture Mechanics to Composite Materials*. Composite Materials Series, Vol. 6 (K. Friedrich ed.), Elsevier, Amsterdam, pp. 547–569.
- Dundurs, J. (1968). Elastic interaction of dislocation in homogeneities. In *Mathematical Theory of Dislocation*, ASME, New York, pp. 70–115.
- Ellis C.D. and Harris B. (1973). The effect of specimen and testing variables on the fracture of some fiber reinforced epoxy resins. *J. Composite Mater.* **7**, 76–88.
- Erdogan, F. (1972). Fracture problems in composite materials. *Eng. Fract. Mech.* **4**, 811–840.
- Evans, A.G. (1989). The mechanical performance of fiber-reinforced ceramic matrix composites. *Mater. Sci. Eng. A* **107**, 227–239.
- Fitz-Randolph J., Phillips D.C., Beaumont P.W.R. and Tetelman A.S. (1972). The fracture energy and acoustic emission of a boron–epoxy composite. *J. Mater. Sci.* **7**, 289–294.
- Friedrich K. (1985). Microstructural efficiency and fracture toughness of short fiber/thermoplastic matrix composites. *Composites Sci. Technol.* **22**, 43–74.
- Friedrich, K. and Karger-Kocsis, J. (1989). Unfilled and short fiber reinforced semi-crystalline thermoplastics. In *Fractography and Failure Mechanisms of Polymers and Composites*, (A.C. Roulin-Moloney ed.), Elsevier Appl. Science, London, pp. 437–494.
- Gaggar, S. and Broutman, L.J. (1975). Crack growth resistance of random fiber composites. *J. Composite Mater.* **9**, 216–227.
- Gershon B. and Marom G. (1975). Fracture toughness and mechanical properties of glass fiber–epoxy composites. *J. Mater. Sci.* **10**, 1549–1556.

- Gupta, V., Argon, A.S. and Suo, Z. (1991). Crack deflection at an interface between two orthotropic media. *Trans. ASME J. Appl. Mech.* **91-WA/APM-42**, 1–9.
- Gupta, V., Yuan, J. and Martinez, D. (1993). Calculation, measurement and control of interface strength in composite. *J. Am. Ceram. Soc.* **76**, 305–315.
- Harris B. (1980). Micromechanisms of crack extension in composites. *Metal Sci.* **14**, 351–362.
- Harris B., Beaumont P.W.R. and Moncunill de Ferran E. (1971). Strength and fracture toughness of carbon fiber polyester composites. *J. Mater. Sci.* **6**, 238–251.
- Harris B., Morley J. and Phillips D.C. (1975). Fracture mechanisms in glass-reinforced plastics. *J. Mater. Sci.* **10**, 2050–2061.
- Harris B., Varlow J. and Ellis C.D. (1972). The fracture behaviour of fiber reinforced concrete. *Cement Concrete Res.* **2**, 447–461.
- He, M.Y. and Hutchinson, J.W. (1989). Crack deflection at an interface between dissimilar elastic materials. *Int. J. Solids Structures* **25**, 1053–1067.
- Helfet J.L. and Harris B. (1972). Fracture toughness of composites reinforced with discontinuous fibers. *J. Mater. Sci.* **7**, 494–498.
- Hillerborg, A., Modeer, M. and Petersson, P.E. (1976). Analysis of crack formation and crack growth in concrete by means of fracture mechanics and finite elements. *Cement Concrete Res.* **6**, 773–782.
- Hing P. and Groves G.W. (1972). The strength and fracture toughness of poly-crystalline magnesium oxide containing metallic particles and fibers. *J. Mater. Sci.* **7**, 427–434.
- Karger-Kocsis J. (1991). Microstructural aspects of fracture and fatigue behavior in short fiber-reinforced, injection-molded PPS-, PEEK- and PEN-composites. *Polym. Bulletin* **27**, 109–116.
- Karger-Kocsis J. and Friedrich K. (1987). Microstructural details and the effect of testing conditions on the fracture toughness of injection molded poly(phenylene sulphide). *J. Mater. Sci.* **22**, 947–961.
- Karger-Kocsis J. and Friedrich K. (1988). Fracture behaviour of injection-molded short and long glass fiber-polyamide 6.6 composites. *Composites Sci. Technol.* **32**, 293–325.
- Kelly A. (1973). *Strong Solids*. Second Edition, Oxford University Press, Oxford.
- Kelly A. (1970). Interface effects and the work of fracture of a fibrous composites. *Proc. Roy. Soc. Lond. A* **319**, 95–116.
- Kelly A. and Tyson W.R. (1965). Tensile properties of fiber-reinforced metals: Copper/tungsten and copper/molybdenum. *J. Mech. Phys. Solids* **13**, 329–350.
- Kendall K. (1975). Transition between cohesive and interfacial failure in a laminate. *Proc. Roy. Soc. Lond. A* **344**, 287–302.
- Kim, R.Y. (1979). Fracture of composite laminates by three-point bend. *J. Composite Mater.* **19**, 50–55.
- Kim, J.K. and Mai, Y.W. (1991a). High strength, high fracture toughness fiber composites with interface control – a review. *Composites Sci. Technol.* **41**, 333–378.
- Kim, J.K. and Mai, Y.W. (1991b). The effect of interfacial coating and temperature on the fracture behaviours of unidirectional KFRP and CFRP. *J. Mater. Sci.* **26**, 4701–4720.
- Kim, J.K. and Mai, Y.W. (1993). Interfaces in Composites. In *Materials Science and Technology: Vol. 13 – Structure and Properties of Fibre Composites*. (T.W. Chou ed.), Ch. 6, VCH Publishers, Weinheim, Germany, pp. 239–289.
- Kirk J.N., Munro M. and Beaumont P.W.R. (1978). The fracture energy of hybrid carbon and glass fiber composites. *J. Mater. Sci.* **13**, 2197–2204.
- Konish, H.J., Swedlow, J.L. and Cruse, T.A. (1972). Experimental investigation of fracture in an advanced fiber composite. *J. Composite Mater.* **6**, 114–126.
- Lauke B. and Schultrich B. (1983). Deformation behaviour of short fiber reinforced materials with debonding interfaces. *Fiber Sci. Technol.* **19**, 111–126.
- Lauke B., Schultrich B. and Barthel R. (1985). Contribution to the micromechanical interpretation of fracture work of short-fiber reinforced thermoplastics. *Composites Sci. Technol.* **23**, 21–35.
- Lauke B. and Schultrich B. (1986a). Calculation of fracture work of short glass fiber reinforced polyethylene for static and dynamic loading rates. *Composites Sci. Technol.* **26**, 1–16.
- Lauke B. and Schultrich B. (1986b). Fracture toughness of short fiber reinforced thermoplastics. *Composites. Sci. Technol.* **26**, 37–57.

- Lauke B. and Pompe W. (1988). Relation between work of fracture and fracture toughness of short fiber reinforced polymers. *Composites Sci. Technol.* **31**, 25–33.
- Lhymn C. and Schultz J.M. (1983). Fracture behaviour collimated thermoplastic poly(ethylene terephthalate) reinforced with short E-glass fiber. *J. Mater. Sci.* **18**, 2029–2046.
- Mai Y.W. (1985). Fracture measurements of cementitious composites. In *Application of Fracture Mechanics to Cementitious Composites*, (S.P. Shah ed.), Martinus Nijhoff, Dordrecht, pp. 289–319.
- Mai Y.W. (1988). Fracture resistance and fracture mechanisms of engineering materials. *Mater. Forum* **11**, 232–267.
- Mandell J.F., Darwish, A.Y. and McGarry F.J. (1981). Fracture testing of injection-molded glass and carbon fiber-reinforced thermoplastics. In *Testing Methods and Design Allowable for Fibrous Composites*, ASTM STP 734 (C.C. Chamis ed.), ASTM, Philadelphia, PA, pp. 73–90.
- Mandell J.F., Huang, D.D. and McGarry F.J. (1982). Crack propagation modes in injection molded fiber reinforced thermoplastics. In *Short Fiber Reinforced Composite Materials*, ASTM STP 772 (B.A. Sanders ed.), ASTM, Philadelphia, PA, pp. 3–32.
- Mar, J.W. and Lin, K.Y. (1979). Characterization of slitting process in graphite/epoxy composites. *J. Composite Mater.* **13**, 278.
- Marston T.U., Atkins A.G. and Felbeck D.K. (1974). Interfacial fracture energy and the toughness of composite. *J. Mater. Sci.* **9**, 447–455.
- Morris, D.H. and Hahn, H.T. (1977). Fracture resistance characterisation of graphite/epoxy composites. In *Composite Materials: Testing and Design (Fourth Conf.)*, ASTM STP 617, ASTM, Philadelphia, PA, pp. 5–17.
- Morton J. and Groves G.W. (1974). The cracking of composites consisting of discontinuous ductile fibers in a brittle matrix-effect of fibre orientation. *J. Mater. Sci.* **9**, 1436–1445.
- Munro M. and Lai C.P.Z. (1988). The elevated-temperature dependence of fracture energy mechanisms by hybrid carbon-glass fiber reinforced composites. *J. Mater. Sci.* **23**, 3129–3136.
- Murphy M.C. and Outwater J.O. (1973). Toughness of reinforced plastics. In *Proc. 28th Annual Tech. Conf. Reinforced Plast. Composites*, SPI, Paper 17A.
- Nairn J.A. (1990). Fracture mechanics of unidirectional composites. *J. Reinf. Plast. Composites* **9**, 91–101.
- Newaz, G.M. (1985). On interfacial failure in notched unidirectional glass/epoxy composites. *J. Composite Mater.* **19**, 276–286.
- Newaz, G.M. (1986). Evaluation of fiber-matrix interphasial toughness in unidirectional composites. *Polym. Composites* **7**, 421–425.
- Ochiai, S. (1989). In *Application of Fracture Mechanics to Composite Materials*. Composite Materials Series Vol. 6 (K. Friedrich ed.), Elsevier, Amsterdam, pp. 491–545.
- Ochiai, S. and Peters, P.W.M. (1982). Tensile fracture of center-notched angle ply ($0^\circ / \pm 45^\circ / 0^\circ$), and ($0^\circ / 90^\circ$), graphite epoxy composites. *J. Mater. Sci.* **17**, 417–428.
- Outwater J.O. and Murphy M.C. (1969). On the fracture energy of unidirectional laminates. In *Proc. 24th Annual Tech. Conf. Reinforced Plast. Composites*, SPI Paper 11C.
- Owen M.J. and Bishop, P.T. (1973). Critical stress intensity factors applied to glass reinforced polyester resin. *J. Composite Mater.* **7**, 146–159.
- Pan, T.Y., Robertson, R.E. and Filisko, F.K. (1988). Fractographic study of transverse cracks in a fiber composite. *J. Mater. Sci.* **23**, 2553–2563.
- Penn L.S., Bystry F.A. and Marchionni H.J. (1983). Relation of interfacial adhesion in Kevlar/epoxy systems to surface characterisation and composite performance. *Polym. Composites* **4**, 26.
- Piggott M.R. (1970). Theoretical estimation of fracture toughness of fibrous composites. *J. Mater. Sci.* **5**, 669–675.
- Ramsteiner F. and Theysohn R. (1979). Tensile and impact strength of uni-directional short fiber reinforced thermoplastics. *Composites* **10**, 111–119.
- Ruhle, M. and Evans, A.G. (1989). High toughness ceramics and ceramic composites. *Progress in Mater. Sci.* **33**, 85–167.
- Sakai M., Bradt R.C. and Fischbach D.B. (1986). Fracture toughness anisotropy of a pyrolytic carbon. *J. Mater. Sci.* **21**, 1491–1501.

- Sakai M., Takeuchi S., Fischbach D.B. and Bradt R.C. (1988). Delamination toughening from interfacial cracking in ceramics and ceramic composites. In *Proc. Ceramic Microstructures '86* (J.A. Pask and A.G. Evans, ed.), Plenum Press, New York, pp. 869–876.
- Sato N., Kurauchi T., Sato S. and Kamigaito O. (1983). SEM observation of the initiation and propagation of cracks in a short fibre reinforced thermoplastic composite under stress. *J. Mater. Sci. Lett.* **2**, 188–190.
- Sato N., Kurauchi T., and Kamigaito O. (1985). In situ SEM observation of fracture in short glass fiber reinforced thermoplastic composites. In *Fracture Mechanics: Sixteenth Symposium*, ASTM STP 868 (M.F. Kanninen and A.T. Hopper, eds.), ASTM, Philadelphia, PA, pp. 493–503.
- Sato N., Kurauchi T., Sato, S. and Kamigaito O. (1986). Fracture mechanism of unidirectional carbon-fibre reinforced epoxy resin composites. *J. Mater. Sci.* **21**, 1005–1010.
- Sato N., Kurauchi T., Sato, S. and Kamigaito O. (1988). Reinforcing mechanism by small diameter fiber in short fiber composite. *J. Composites Mater.* **22**, 850–873.
- Sato N., Kurauchi T., Sato, S. and Kamigaito O. (1991). Microfailure behaviour of randomly dispersed short fiber reinforced thermoplastic composites obtained by direct SEM observation. *J. Mater. Sci.* **26**, 3891–3898.
- Schultz J.M. and Friedrich K. (1984). Effect of temperature and strain rate on the strength of a PBT/glass fiber composite. *J. Mater. Sci.* **19**, 2246–2258.
- Sih, G.C. and Liebowitz, H. (1968). In *Fracture* (H. Liebowitz ed.), Academic Press, New York, Vol. 2, pp. 68–190.
- Solar, M.A. and Belzunce, F.J. (1989). Fracture toughness and R-curves of glass fiber reinforced polyester. *Composites* **20**, 120–124.
- Takahashi, K. and Choi, N.S. (1991). Influence of fiber weight fraction on failure mechanisms of poly(ethylene terephthalate) reinforced by short-glass fibers. *J. Mater. Sci.* **26**, 4648–4656.
- Taya M. and Arsenault R.J. (1989). In *Metal Matrix Composites – Thermomechanical Behaviour*. Pergamon Press, Oxford, pp. 9–40.
- Tetelman A.S. (1969). Fracture process in fiber composite materials. In *Composite Materials: Testing and Design*, ASTM STP 460, ASTM, Philadelphia, PA, pp. 473–502.
- Tirosh J. (1973). The effect of plasticity and crack blunting on the stress distribution in orthotropic composite materials. *ASME Trans. J. Appl. Mech.* **40**, 785–790.
- Tohgo, K. Wang, A.S.D. and Chou, T.W. (1993). A criterion for splitting crack initiation in unidirectional fiber-reinforced composites. *J. Composite Mater.* **27**, 1054–1076.
- Tulloch, D.L., Reimanis, I.E., Graham, A.L. and Petrovic, J.J. (1994). Deflection and penetration of cracks at an interface between two dissimilar materials. *Acta Metall. Mater.* **42**, 3245–3252.
- Voss H. and Friedrich K. (1986). Fracture and fatigue of short glass fiber reinforced PTFE composites. *J. Mater. Sci. Lett.* **5**, 569–572.
- Warren, R. and Sarin, V.K. (1989). In *Application of Fracture Mechanics to Composite Materials*. Composite Materials Series, Vol. 6 (K. Friedrich ed.), Elsevier, Amsterdam, pp. 571–614.
- Waddoups, M.E., Eisenmann, J.R., Kaminski, B.E. (1971). Macroscopic fracture of advanced composite materials. *J. Composite Mater.* **5**, 446–457.
- Wells J.K. and Beaumont P.W.R. (1982). Construction and use of toughness maps in a fracture analysis of the micromechanisms of composite failure. In *Composite Materials: Testing and Design*, ASTM STP 787 (I.M. Daniel ed.), ASTM, Philadelphia, PA, pp. 147–162.
- Wells J.K. and Beaumont P.W.R. (1985). Crack tip energy absorption processes in fiber composites. *J. Mater. Sci.* **20**, 2735–2794.
- Wells J.K. and Beaumont P.W.R. (1987). The prediction of R-curves and notched tensile strength for composite laminates. *J. Mater. Sci.* **22**, 1457–1468.
- Williams, T., Allen, G. and Kaufman M.S. (1973). The impact strength of fibre composites. *J. Mater. Sci.* **8**, 1765–1787.

Chapter 7

IMPROVEMENT OF TRANSVERSE FRACTURE TOUGHNESS WITH INTERFACE CONTROL

7.1. Introduction

In view of the interface-related fracture toughness theories presented in Chapter 6, it is seen that the transverse fracture toughness of composites containing brittle fibers and brittle matrix, typically CFRPs and GFRPs, increases with increasing V_f and σ_f^* of the fiber, but decreases with increasing interfacial bond strength, τ_b . High τ_b discourages interfacial debonding and subsequent fiber pull-out. Along with the techniques specifically designed to improve the delamination resistance discussed in Chapter 8, significant research efforts have been directed towards the development of techniques to improve the fracture toughness of brittle fiber–brittle matrix composites in the transverse direction without impairing other important mechanical properties. These techniques can be classified into two major approaches: one relies on the improvement of the intrinsic properties of the composite constituents, whether the reinforcement or the matrix phase; and the other depends on the control of interface and/or interlaminar properties. Examples of the first approach include the use of fiber hybrids, tough matrices and large diameter or bundle fibers. The second approach includes fiber coatings with appropriate polymers, delamination promoters and reduction of shrinkage stresses in the matrix through the modification of interface properties. Comprehensive reviews have been given on these toughening methods by Kim and Mai (1991a, 1993a), and they are briefly described in the following.

(1) Different types of fibers can be incorporated into a matrix material to produce a hybrid fiber composite. Typical hybrid fiber composites are made from glass or aramid fibers that are added to otherwise brittle carbon fiber composites to enhance the fracture toughness resulting from the toughening mechanisms associated with the ductile fibers, while maintaining a high strength and high modulus gained from carbon fibers. The effect of toughening relies heavily on how the hybrid fibers are mixed and the ply layup is arranged. A review on this topic has been presented by Hancox (1981).

(2) Tough matrices, such as thermoplastics and rubber-modified epoxies, are particularly useful for high fracture toughness and damage tolerance against

interlaminar fractures and low energy impact where the fracture toughness and ductility of the matrix material play a dominant role. Comprehensive reviews of the failure mechanisms have been given for thermoplastics (Mascia, 1989) and toughened epoxies (Kinloch, 1993; Garg and Mai, 1988a, b). Tough adhesives and/or composite strips are often interleaved between plies as delamination resister or arrester to improve the interlaminar fracture toughness. Details of these techniques are given in Chapter 8.

(3) The use of large diameter fibers can also result in improved fracture toughness of brittle fiber–ductile metal matrix composites, such as tungsten wire–copper matrix systems (Cooper and Kelly, 1967; Tetelman, 1969). This can be explained in terms of increased volume of ductile matrix involved in shear flow at the interface region, which gives rise to the fiber pull-out force proportional to the fiber diameter. A large diameter fiber is also found to be beneficial for brittle fiber–brittle matrix composites (Piggott, 1970; Wells and Beaumont, 1985): it increases the debond and fiber pull-out lengths by increasing the critical transfer length, l_c , given the mechanical properties of the fiber and the fiber–matrix interface. However, care should be taken in using this technique because the tensile strength and modulus of many fibers show a systematic decrease with increasing fiber diameter (Metcalf and Schmitz, 1964; Kelly, 1970). This problem may be overcome by using bundle fibers that are impregnated with polymers prior to being incorporated in a resin matrix (Fila et al., 1972; Kim and Mai, 1993b).

(4) If the fiber is coated intermittently along its length with an appropriate coating material before being embedded in a matrix so that there are regions of both strong and weak interfacial bonds, high transverse fracture toughness can be achieved without deteriorating the composite strength and stiffness. The triaxial stress distribution at the advancing crack tip allows easy debonding and crack tip blunting at the weak interface due to the tensile debonding mechanism (Cook and Gordon, 1964). Simultaneously, a good composite strength is maintained through the interface with strong bonding. The intermittent bonding concept has been further extended to laminate composites where different kinds of thin films with perforated holes are inserted between plies as delamination promoters.

(5) The energy absorption capability of composites can be enhanced significantly by promoting interface debonding and fiber pull-out, while maintaining a ductile interphase. This method is most effective if fibers are coated with an appropriate material for both polymer, metal and ceramic matrices composites. A review has recently been given of fiber coating methods, coating materials and associated toughening mechanisms of the interlayer for polymer matrix composites (Labronici and Ishida, 1994).

(6) Reduction of residual stresses that arise from the differential thermal shrinkage between the fiber and matrix materials when cooling from the processing temperature has a beneficial effect of enhancing the fracture resistance of composites. This can be achieved by applying a soft, compliant coating onto the reinforcing fibers (Marom and Arridge, 1976) and/or by adding an expanding monomer into the matrix material (Piggott and Woo, 1986). Reduction of thermal residual stresses may also have the benefits of reducing the tendency of fiber

Table 7.1
Comparison of toughening methods for fiber composites^a.

Toughening method	Composite system (V_f)	Modifying material	% increase in toughness	% decrease in strength	Test method
Intermittent bonding	Boron-epoxy (0.25)	80% PUV coating	280	8	Compact tension
	Boron-epoxy (0.25)	100% PUV coating	500	25	Compact tension
	Kevlar-epoxy (0.06)	63% Estapol coating	40	nil	Three-point bending
	Kevlar-epoxy (0.06)	100% Estapol coating	340	10-15	Charpy impact
Energy absorption method	Carbon-epoxy (0.6)	Silicon rubber coating	140	nil-60	Izod impact
	Glass-polyester (0.06)	SVF coating	150	NA	Izod impact
	Glass-epoxy (0.3)	Latex PBA coating	600	5	Izod impact
	Kevlar-epoxy (0.5)	PVAL coating	100	nil	Charpy impact
Delamination promoters	Carbon-epoxy (NA)	Nylon films	270	25	Charpy impact
	Boron-epoxy (0.2)	Perforated Mylar films	170	40	Compact tension
Reduction of shrinkage stress	Carbon-epoxy (0.4)	Spiro monomer additive	50	15	Izod impact

^aAfter Kim and Mai (1991a).

Estapol, a blend of polyester/polyether resins; NA, not available; PBA, polybutyl acrylate; PUV, polyurethane varnish; PVAL, polyvinylalcohol; SVF, silicone vacuum fluid; V_f , fiber volume fraction.

buckling, unnecessary interfacial debonding, matrix microcracking and warping of asymmetric laminates consisting of cross-ply, all of which are detrimental to mechanical/structural performance of the composite.

Further details of the above techniques to improve the transverse fracture toughness of composites by controlled interfaces of various nature and modifying materials are discussed in the following sections. The effectiveness of these toughening methods on transverse fracture toughness and strength in relation to the controls are summarized in Table 7.1.

7.2. Fiber coating and intermittent bonding concept – experimental studies

Although the criteria and functional requirements for the use of fiber coating are different between PMCs, MMCs and CMCs, the major common aim of fiber coatings discussed in this section is to improve the energy absorption characteristics

of the composites. For polymer matrix composites (PMCs), the fiber coatings should be able to promote such toughening mechanisms as interfacial debonding, post-debonding friction, stress redistribution and fiber pull-out, while minimizing possible reduction of strength and modulus due to the presence of the compliant coating material. It should be recalled (see Section 5.5 for details) that for ceramic matrix composites (CMCs), as for some brittle PMCs, the main objective of fiber surface modification is to make the interface rather weak in order to improve the fracture toughness, which is the major drawback of CMCs. On the other hand, an adequate interfacial strength is often needed to offer good strength properties, in particular in the transverse direction (Chawla, 1993). Therefore, a proper control of the interface is essential to satisfy these conflicting requirements.

In contrast, for metal matrix composites (MMCs) a strong interfacial bond with high composite strength and a good resistance to prolonged environmental attack in service are often desirable because the inherently ductile nature of most metal matrix materials does not require the composite to be further toughened (Taya and Arsenault, 1989). The reaction products formed at the interphase region at high processing temperatures generally increase the chemical bonding, but degrades the gross mechanical properties. As such, a compromise is required between the desired mechanical properties. At the same time, for both PMCs, MMCs and CMCs, the coating materials should provide a means to protect the fibers from chemical reaction, oxidation, hygrothermal aging and other mechanical degradation (i.e. reaction barrier coating) during handling, fabrication and in service.

The fiber coating technique, either fully or intermittently along the fiber, has been proven to be the most effective method for achieving both high strength and high fracture toughness of fiber composites when appropriate coating materials are selected, although its application to practical PMCs is still in question. The principal effect of altering the interfacial properties by fiber coating, including the nature of interfacial bonding, molecular constituents, morphology and ductility of the interphase, is to modify the mode of failure and thus the potential energy absorption capacity which, in turn, determines the fracture toughness of composites. Because of the simplicity in the application to practical composites compared to other techniques and the feasibility of direct comparison of fracture behaviors between composites containing uncoated and coated fibers, the fiber coating technique has received considerable attention, making significant progress in our understanding of the underlying physics and failure mechanisms associated with the presence of the coating layer. The fiber coating techniques are reviewed in the following sections, which have been developed specifically for brittle PMCs.

7.2.1. Intermittent bonding concept

The intermittent fiber bonding method originates from the early work on failure processes in single fiber micro-composites (Mullin et al., 1968; Gatti et al., 1969; Mullin and Mazio, 1972). In these studies, coatings on boron fibers were found to be effective in isolating fiber fracture by encouraging interface debonding immediately next to the matrix cracks. The corn-cob shape surface of the boron fiber (see Fig.

5.29) allows non-uniform application of coatings on the fiber with a resulting pattern of intermittently coated and uncoated regions. This condition provides good bonding in the low spots, while high points are shielded from the matrix by the coating, allowing extensive interface crack propagation. Graphite and polytetrafluoroethylene (PTFE) coatings on boron fibers and a viscous polyurethane coating on carbon fibers were shown to be effective in avoiding fiber-initiated catastrophic failure of the composites.

The intermittent bonding concept was further developed by Marston et al. (1974) and Atkins (1975). The argument is that as far as there are enough regions of strong interface, ensuring that the rule of mixtures (RoM) composite strength is retained, the rest of the composite could have quite a weak interface which may serve to blunt the running crack by the tensile debonding mechanism (Cook and Gordon, 1964). It follows then that if a composite is laid up randomly with respect to weak and strong interface regions, as schematically shown in Fig. 7.1, both high strength and high toughness should be simultaneously obtained. A remarkable 400% improvement in fracture toughness was achieved with a 10% loss of tensile strength in the unidirectional boron fiber-epoxy resin (BFRP) system with an 80% coating of polyurethane varnish (PUV) (Atkins, 1974, 1975). In contrast, the improvement with silicone vacuum fluid (SVF) coating for the same composite system was only 10–15%, even though the interface shear bond strengths, τ_b , of the fibers coated with the two coating materials were similar. This indicates that similar τ_b does not necessarily mean similar fracture toughness. The explanation lies probably with the tensile debonding mechanism which might have taken place with the PUV coating

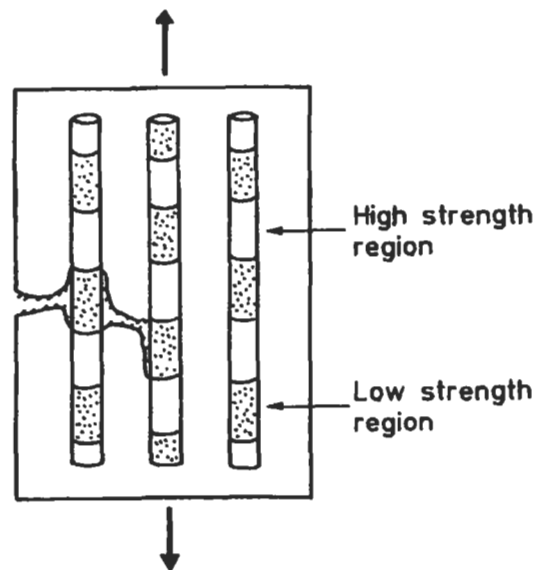


Fig. 7.1. Fibers containing deliberately produced regions of low interfacial strength are shown in the staggered manner. After Atkins (1975).

giving rise to long fiber pull-out lengths, whereas this mechanism was apparently absent with the SVF coating.

The effectiveness of the intermittent bonding concept has been confirmed under adverse environmental conditions, such as hygrothermal aging (Atkins and Mai, 1976). In follow-up studies with Kevlar fiber-epoxy matrix systems (Mai, 1983, 1988; Mai and Castino, 1984, 1985), the coatings based on SVF and a blend of polyester-polyether resins (Estapol) were explored. The effects of hygrothermal aging, percentage coating over a repeated fiber length, fatigue damage, strain rate and temperature on tensile strength, modulus, impact fracture toughness and pull-out toughness of the composite were investigated. The fracture toughness of composites with Estapol coated fibers was increased by some 200–300%, particularly at high temperatures and low strain rates, as shown in Fig. 7.2, without sacrificing other strength properties.

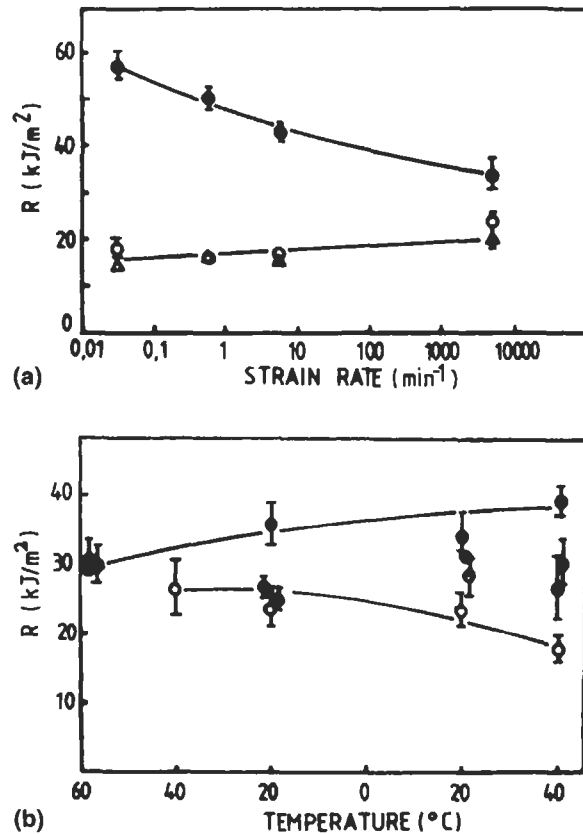


Fig. 7.2. Fracture toughness, R , of Kevlar 49-epoxy matrix composites (a) under varying strain rates in three-point bending and (b) at different temperatures under impact loading: (○) uncoated fibers; (◐) 41%, (◑) 63% and (●) 100% Estapol coated fibers; (△) silicone vacuum fluid (SVF) coated fibers. After Mai and Castino (1984).

The tensile debonding model associated with the intermittently bonded interface, schematically shown Fig. 7.1, appears to be rather unrealistic in unidirectional fiber composites as the stress state near the crack tip should be three-dimensional in nature (Kim and Mai, 1991a). The model certainly needs further verification as it requires complicated stress conditions to be satisfied. Nevertheless, there is no doubt that the longitudinal splitting promoted by the weakened interface increases the interfaced debonding and subsequent fiber pull-out with large contributions to the composite fracture toughness. The beneficial effect of the tensile debonding mechanisms with crack bifurcation may be more clearly realized in the delamination promoter concept which is discussed in Section 7.4.

7.2.2. Fiber coating for improved energy absorption capability

It has been confirmed in Chapter 6 that for brittle polymer matrix composites, typically CFRPs, a strong interface favors a brittle fracture mode with relatively low energy absorption, but a weak interface allows high energy absorption through multiple shear failure (Novak, 1969; Bader et al., 1973). Carbon fibers coated with a silicone fluid resulted in the fibers being surrounded by an inert film which reduced the interfacial bond strength with increased toughness (Harris et al., 1971; Beaumont and Phillips, 1972). The major source of fracture toughness for CFRP was found to be fiber pull-out following interface debonding (Harris, 1980). It follows then that a sufficiently high frictional shear stress, τ_f , is needed while maintaining the lowest possible shear bond strength, τ_b , so that the work required to pull-out the fibers against friction can be enhanced.

Several different viscous fluids have been investigated as interlayer for several different combinations of composite constituents. Sung et al. (1977) were the first to use the concept of strain rate sensitive coatings, e.g. SVF and silicone grease, to improve the impact toughness of glass fiber polyester matrix composites (GFRPs). Provided the silicone fluid is Newtonian and the shear stress is uniform, the pull-out toughness of a composite with short fibers of embedded length, ℓ_c and pull-out distance, ℓ_{po} is given by

$$R_{po} = \left(\frac{2V_f}{d} \right) \left(\frac{\eta v_0}{t} \right) \left[\ell_c \ell_{po} - \frac{\ell_{po}^2}{2} \right], \quad (7.1)$$

where η and t are the viscosity and thickness of the viscous fluid, and v_0 is the velocity of fiber pull-out. The fiber pull-out toughness is proportional to the viscous shear stress acting on the fibers during pull-out at a given strain rate, which could be maximized by selecting appropriate coatings of high fluid viscosity and small thickness. Fig. 7.3 shows the inverse relationship between fracture toughness and coating thickness, with a higher viscosity giving a higher fracture toughness for a given coating thickness.

Rubbers of various kinds have been among the major coating materials that received significant interest. The toughness of carbon fiber composites was improved

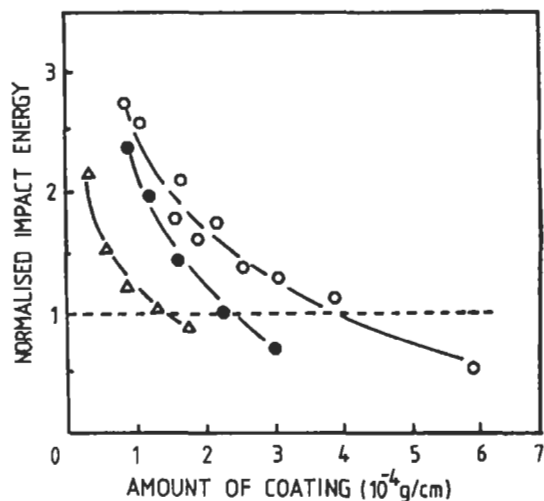


Fig. 7.3. Normalized impact toughness of glass fiber-polyester matrix composites with different fiber coatings: (O) silicone vacuum fluid (SVF); (●) Dow Corning 200 Fluid of viscosity 10^6 cP; (Δ) Dow Corning 200 Fluid of viscosity 10^5 cP. After Sung et al. (1977).

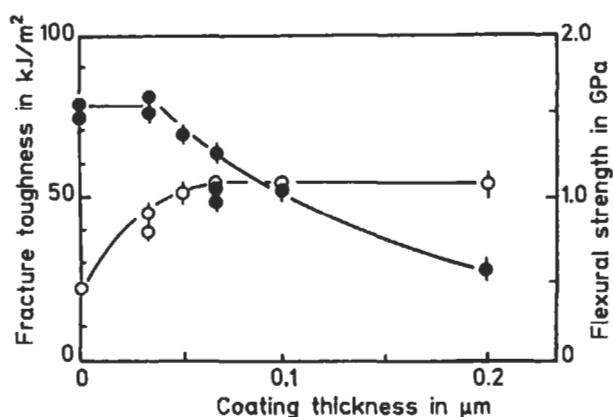


Fig. 7.4. Fracture toughness (O) and flexural strength (●) of silicone rubber coated carbon fiber-epoxy matrix composites as a function of coating thickness. After Hancox and Wells (1977).

by some 100% with a silicone rubber coating at the expense of approximately 60% loss of flexural strength depending on the coating thickness (Hancox and Wells, 1977), Fig. 7.4. It should be noted that there is an optimum coating thickness which imparts both high flexural strength and impact toughness. Other studies using rubber coatings include silicone rubber for carbon fiber-polyester matrix (Harris et al., 1971); carboxyl terminated butadiene acrylonitrile (CTBN) copolymer for carbon fiber-epoxy matrix system (Gerard, 1988); rubber coating for glass fiber-

nylon matrix system (Jao and McGarry, 1992a, b); ethylene-propylene elastomers for glass fiber-epoxy matrix composite (Mascia et al., 1993).

Many researchers have shown promising results with a range of different polymer coatings for many different types of composites: polysulfone, polybutadiene and silicone rubber on CFRP (Hancox and Wells, 1977; Williams and Kousiounelos, 1978); latex coatings, e.g. polybutyl acrylate, polyethyl acrylate, etc. on GFRPs (Peiffer, 1979; Peiffer and Nielson, 1979); polyvinyl alcohol (PVAL) on KFRPs and CFRPs (Kim and Mai, 1991b; Kim et al., 1993a); anhydride copolymers, e.g. polybutadiene-co-maleic anhydride and polymethylvinylether-co-maleic anhydride (Crasto et al., 1988) and acrylonitrile copolymers, e.g. acrylonitrile/methylacrylate and acrylonitrile/glycidylacrylate (Bell et al., 1987) on CFRPs; polyamide coating on CFRPs and carbon-Kevlar hybrid composites (Skourlis et al., 1993; Duvis et al., 1993). Particularly, Peiffer and Nielsen (1979) achieved a significant 600% increase in impact toughness of GFRPs with a negligible strength reduction using colloidal latex particles that were attracted to glass fibers by electrostatic forces to form a rubbery acrylic polymer layer of uniform thickness. The impact toughness was shown to be a function of both thickness and glass transition temperature, T_g , of the coating: the toughness was maximum when the coating had a low T_g and a thickness of about 0.2 μm .

Kim and Mai (1991b) have made an extensive study on CFRPs and KFRP with PVAL coated fibers. The coating increased the composite impact toughness by more than 100%, particularly at sub-zero temperatures, without causing any significant loss of flexural strength and interlaminar fracture toughness. These promising results are highlighted in Figs. 7.5 and 7.6, and Table 7.2. The thermoplastic coating reduced the bond strength at the fiber-matrix interface significantly as indicated by the average interlaminar shear strengths (ILSSs) obtained in short beam shear tests. High resolution scanning electron microscopy (SEM) of the fracture surface further supports the weak interfacial bonding due to the PVAL coating. For KFRP, the uncoated fibers most often split into small fibrils longitudinally due to the weak bond between the fibrils and the skin-core heterogeneity of the fiber (see Fig. 5.20). In contrast, the PVAL coated Kevlar fibers debonded clearly from the matrix with little fibrillation. Clear distinction was also evident between the interlaminar fracture surfaces of CFRPs, as shown in Fig. 7.7. The composite without coating consisted of substantial deformation of the matrix material which covered the majority of the surface and tiny matrix particles adhering to the debonded fiber surfaces. However, the coated fiber composite displayed a relatively clean fiber surface, with partial removal of the rugosity generated by the surface oxidative treatment, which effectively deteriorates the mechanical anchoring of the resin to the fiber. The above findings support the appreciable difference in surface chemical composition and functional groups of CFRPs that have been revealed by X-ray photoelectron spectroscopy (XPS) (Kim et al., 1992). The uncoated fiber composite showed a significant amount, say about 6 at. wt%, of silicon associated with the epoxy matrix, whereas the coated fiber composite had little trace of silicon with a larger amount of C-O group, which is a reflection of the PVAL coating. All these observations strongly suggest that the coating acts as a physical barrier to the

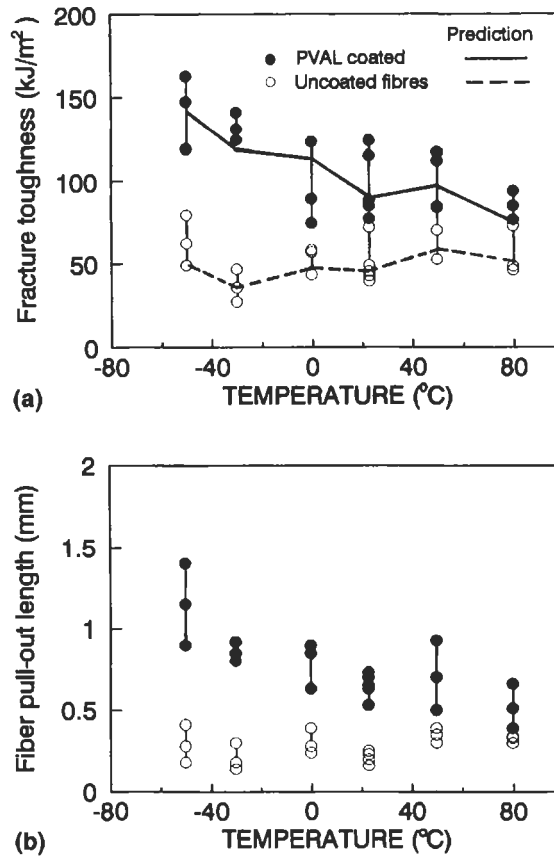


Fig. 7.5. (a) Transverse impact fracture toughness and (b) fiber pull-out length versus testing temperature for carbon fiber-epoxy matrix composites with and without PVAL coatings on fibers. After Kim and Mai et al. (1991b).

chemical bonding between the functional groups present in the fiber surface and epoxy matrix.

Several different thermoplastic materials including, polyamide (PA), polyether sulfone (PES), polycarbonate (PC), polysulfone (PS), polyetherimide (PEI) and polymethyl methacrylate (PMMA), were also found to have significant effects on the mechanical properties of carbon fiber-nylon matrix composites (Tomlinson and Barnes, 1992). Polyamide nylon 6.6 coating on carbon and Kevlar fibers for epoxy matrix composites by in-situ polymerization techniques were also shown to be effective for promoting localized plastic deformation around the crack tip and protecting the brittle fiber surface during processing (Skourlis et al., 1993; Duvis et al., 1993). The thermoplastic coatings have advantages over other coating materials in that they would form a microductile layer at the interface (Dauksys, 1973). The interlayer functions satisfactorily as a stress relief medium in reducing the

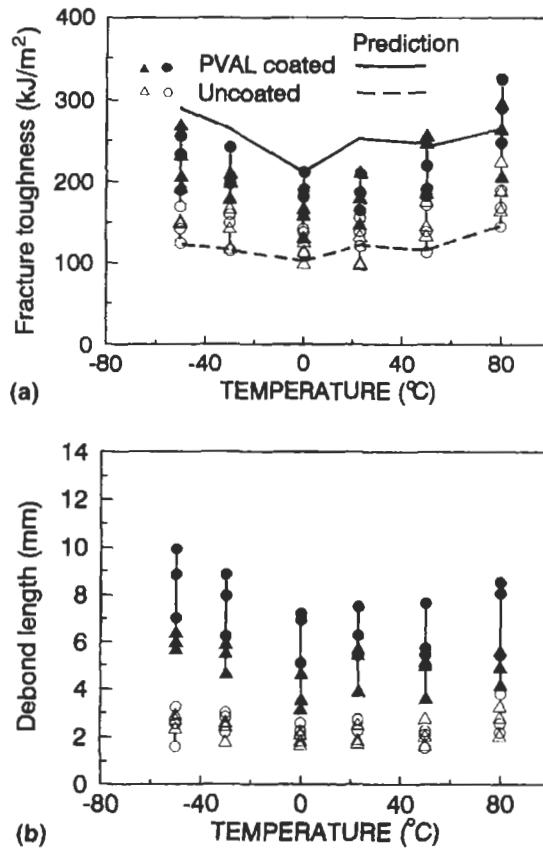


Fig. 7.6. (a) Transverse impact fracture toughness and (b) interface debond length versus testing temperature for carbon fiber-epoxy matrix composites with and without PVAL coatings on fibers. After Kim and Mai (1991b).

Table 7.2

Mechanical properties of carbon fiber-epoxy matrix and Kevlar fiber-epoxy matrix composites with and without PVAL coating at room temperature^a.

Fibers	Transverse fracture toughness (kJ/m ²)	Flexural strength (MPa)	Interlaminar shear strength (MPa)	Interlaminar fracture toughness (kJ/m ²)
Carbon fiber				
Uncoated	50.3	683	58.9	0.428
PVAL coated	98.7	758	50.5	0.431
Kevlar fiber				
Uncoated	139	518	42.6	—
PVAL coated	187	522	25.4	—

^aAfter Kim and Mai (1991b).

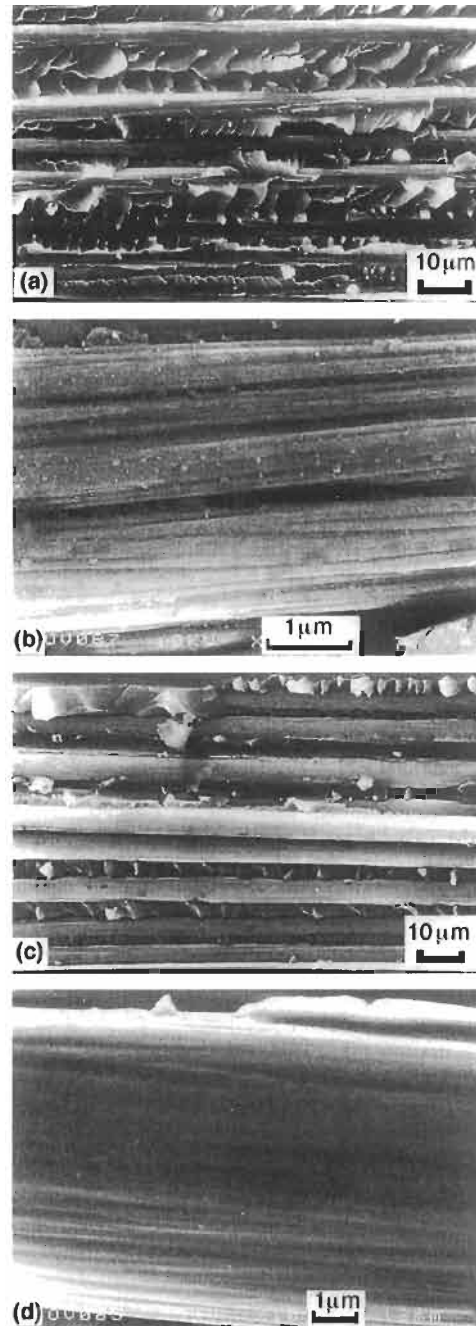


Fig. 7.7. Scanning electron microphotographs of fracture surfaces for carbon fiber epoxy matrix composites: (a) and (b) without PVAL coatings; (c) and (d) with PVAL coatings on fibers. After Kim et al. (1992).

residual thermal stresses caused by differential shrinkage between the fiber and matrix upon cooling from the processing temperature (Arridge, 1975; Marom and Arridge, 1976); and as a crack inhibitor or arrester, allowing large debonding and fiber pull-out to take place, thus making substantial contributions to the total toughness of the composites.

Apart from the discrete layers that form at the fiber–matrix interface, reactive functionality of the coating material has been studied for CFRP systems (Rhee and Bell, 1991). Two different coating materials were used, namely acrylonitrile/methyl acrylate (AN/MA) and glycidyl acrylate/methyl acrylate (GA/MA) copolymers which represent, respectively, non-reactive and reactive systems. These coatings were applied to fiber bundles by electrochemical copolymerization which allows accurate control of the coating thickness. The reactive coating system showed 10–30% simultaneous improvement in impact fracture toughness and ILSS when appropriate combinations were used, as illustrated in Fig. 7.8. In contrast, the non-reactive coating system improved the impact toughness with a concomitant loss in ILSS, due to the weak interface between the coating and the matrix material.

In view of the foregoing discussion, the effectiveness of coating materials can be summarized and some general conclusions can be drawn. The principal aim of the fiber coating is to optimize the interfacial characteristics, which, in turn, allows desired failure mechanisms to take place more extensively during the fracture process. Depending on the specific combination of fiber and matrix materials, the thermo-mechanical properties and the thickness of the coating material are the predominant parameters that limit the performance of the coating. Polyurethane coatings are found to be effective for improving the fracture toughness of BFRPs and KFRPs. Silicone rubbers on CFRPs and GFRPs, PVAL coatings on CFRPs and KFRPs, and liquid rubber coatings on CFRPs have also shown to be quite promising. However, the selection of an appropriate coating material for a given composite has relied entirely on the trial and error method, there are apparently no established principles to determine which coating materials are most suited for a specific combination of fiber and matrix materials. Even so, some points of generalization may still be made with respect to the criteria required for a potential coating material to improve the fracture toughness of brittle polymer matrix composites. According to Kim and Mai (1991a) these are:

- (1) If the coating remains fluidic or becomes rubbery at the fiber–matrix interface after cure, such as SVF and Estapol, a coating having a high viscosity is preferred because the frictional shear work during the fiber pull-out is proportional to the coating viscosity (Sung et al., 1977).
- (2) If the coating forms a discrete, rigid interlayer after cure, it should be more ductile and compliant than the matrix material, such as some thermoplastic coatings for thermoset-based matrices. At the same time, it should also provide a weak bonding at the interface while retaining sufficiently high frictional bonding.
- (3) Coating thickness should be chosen to optimize the benefit in toughness and minimize the loss in strength and some other properties. As a rule of thumb, the thickness of the coating should be kept minimum compared to the fiber diameter in order to eliminate any reductions of composite stiffness and strength in both

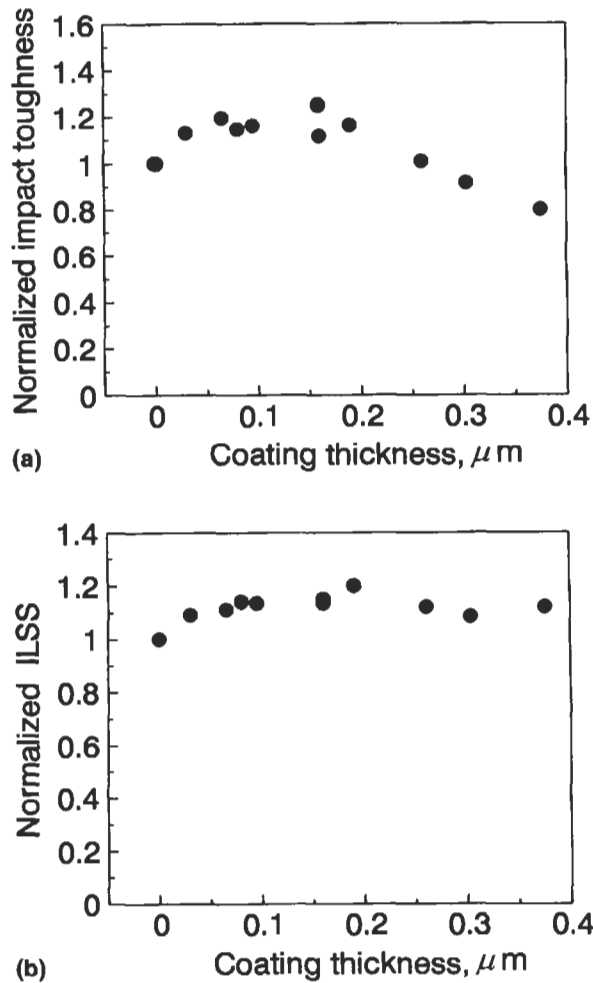


Fig. 7.8. (a) Normalized impact fracture toughness and (b) interlaminar shear strength (ILSS) of carbon fiber–epoxy matrix composites as a function of glycidyl acrylate/methyl acrylate (GA/MA) interlayer thickness. After Rhee and Bell (1991).

the longitudinal and transverse directions, in particular for those coatings providing a low bond strength with the fibers. Systematic reductions in flexural strength and ILSS with increasing coating thickness, e.g. silicon rubber coating (Hancox and Wells, 1977) and polyvinyl acetate (PVA) coating (Kim and Mai, 1991b), have been reported.

- (4) There are contradicting views with regard to the reactivity and miscibility of the coating material with the resin matrix during curing. Sung et al. (1977) suggested that the coating should form and remain in a discrete layer at the interface without reaction with the composite constituents. However, a certain degree of

chemical reaction between the coating and matrix could enhance the frictional shear stress (Mai and Castino, 1984; Rhee and Bell, 1991). Partial or complete mixing of the coating material during the curing process with the matrix, for example, CTBN rubber in an epoxy (Gerard, 1988; Kim and Mai, 1991b), produces composites with hardly modified interfaces that may not be desirable as it only changes the matrix properties.

7.2.3. Fiber coating techniques

Several processing methods have been developed to apply organic polymer coatings to both continuous and short fibers for applications in PMCs. They can be classified into three broad categories: solution dip coating and roll coating; electrodeposition techniques, including electrochemical deposition, electropolymerization and electrostatic deposition; and polymerization techniques. A summary of the reviews (Hughes, 1984; Wicks et al., 1992; Labronici and Ishida, 1994) on the application techniques of organic coatings is presented below.

7.2.3.1. Solution dip coating and roll coating

The solution dip coating technique has been most widely used for fiber coatings because of the ease of application and the simplicity of principle (Sung et al., 1977; Dauksys, 1973; Hancox and Wells, 1977; Mascia et al., 1993; Tomlinson and Barnes, 1992; Kim and Mai, 1991a, b; de Kok, 1995; Jao and McGarry, 1992a, b). Almost every type of polymer, ranging from thermoplastics, thermosets to elastomers, has been successfully applied with the aid of appropriate solvents. The continuous immersion coating process involves drawing of a fiber tow or yarn through the coating solution bath and complete evaporation of the solvent, before being embedded into a matrix material. The thickness of the coating layer may be controlled by varying the solution concentration and the drawing speed. Maintaining a uniform thickness in a batch of fiber is a critical aspect of this process. When bundle fibers or tows are immersed in a polymer solution, the individual filaments in a bundle tend to stick together, making it difficult to wet or coat them thoroughly. Good impregnation of the individual filaments can be achieved by using a low viscosity solution; and ultrasonic stirring of the solution bath was helpful in dispersing the filaments from the bundle (Gerard, 1988). It may also be necessary to separate the fiber bundles by using techniques such as gas jets, ultrasonic horns and mechanical combs (Sung et al., 1977), during the drying process after immersion. In this respect, care must be exercised in selecting volatile solvents for dip coating because of the changes in viscosity of the solution, resulting from evaporation of the solvent, in addition to flammability hazards. Viscosity can increase not only by loss of solvent, but also by chemical reactions of the coating components.

Roll coating is widely used for uniform, whether flat or cylindrical, surfaces including fiber bundles. In a roll coating process, fibers are coated between two rollers, an applicator roller and a backup roller: coating is fed continuously to the applicator roller by a feed roller which runs partially immersed in a coating bath; and the backup roller pulls the fibers by rotating in opposite directions. Slow

evaporating solvents must be used to avoid viscosity buildup on the rollers. The coating thickness on the fiber is controlled mainly by the clearance between the feed roll and applicator roll and by the viscosity of the coating solution. The roll coating process has a major advantage over other coating techniques in that the coating solution is uniformly applied to the individual filaments as they are forced to disperse between the two rollers when being pulled. This technique has been successfully used (Atkins, 1975; Mai and Castino, 1984, 1985) to apply polyurethane and silicon rubber coatings onto carbon and Kevlar fiber tow surfaces, with resulting intermittently coated and uncoated regions along the fiber.

7.2.3.2. Electrochemical processes

Most suitable for electrically conducting materials such as carbon fibers, the electrochemical processes involve deposition of polymer coatings on the fiber surface through electrodeposition or electropolymerization techniques. The major advantage of these processes is that a uniform layer of controlled thickness and variable polymer structure and properties can be obtained by controlling the current and the solution concentration.

The electrodeposition process utilizes the migration of polymer carrying ionized groups to the oppositely charged electrode under an applied voltage. In anionic systems, negatively charged particles of coating in an aqueous dispersion are electrochemically attracted to a substrate which is the anode of an electrochemical cell. In cationic systems, the substrate is made the cathode, and positively charged particles of coating are attracted to the cathode and precipitated on its surface by the hydroxide ions generated there. The system must be designed so that it allows all coating components to be attracted to the electrode at the same rate; otherwise the composition will change with time. In the process employed by Subramanian and Crasto (1986) and Crasto et al. (1988), carbon fibers acted as the anode of an electrolytic cell containing solutions of ionic polymers, such as butadiene-maleic anhydride and ethylene-acrylic acid copolymers. As the polymer is formed, the increased electrical resistance of the coating directs film formation to uncoated regions which are more conducting. This enables a film of uniform thickness to be deposited. Even so, the deposit growth process is not completely uniform, and it rather becomes faceted, resulting in surface discontinuities, because the process involves the condensation of polymer atoms at rough sites on the substrate surface. Organic additives are used to modify the nucleation process and thus to eliminate undesirable deposition modes. Another critical requirement for the electrodeposition process is that the coating solution be closely monitored to maintain a constant particle concentration. The dispersion must also have a high level of stability against coalescence by continuous stirring and recirculation.

The electrochemical polymerization process is achieved by polymerization of monomers in an electrolytic cell (Subramanian and Jakubowski, 1978). The electrode is the source of active species that initiates the polymerization. It is necessary to select a solvent electrolyte system which is capable of forming a solution with the monomer and having sufficient current-conducting properties. In the process employed by Bell and coworkers (Bell et al., 1987; Wimolkiatisak and

Bell, 1989; Rhee and Bell, 1991), random copolymers of methyl acrylate and acrylonitrile were directly polymerized onto the carbon fiber surface. Dimethyl formamide, dimethyl sulfoxide and distilled water proved to be useful as solvents for this process. Polymerization can take place on the carbon fiber electrode, with initial wetting of the fiber surface leading to better adhesion of the polymer formed. The structure and properties of the polymer can be varied by employing different vinyl and cyclic monomers in homopolymerization. Chemical bond can also be formed, such as polymer grafting to the carbon fiber surface.

7.2.3.3. Electrostatic deposition

Glass fibers are coated with a uniform layer of acrylic latex polymer by using electrostatic forces (Peiffer, 1979; Peiffer and Nielsen, 1979). This method is based on the earlier work of Iler (1966) where cathodically charged particles, such as ion, polar molecules, lattices, are attracted to the anionic surface of glass. Because further deposition is inhibited by electrostatic repulsion after a monolayer of charged particles are formed, the formation of multi-layers requires layers of oppositely charged particles between each layer of like charges. As such, alternate layers of negatively and positively charged colloidal particles can be deposited from dilute sol to form coating layers. Since the acrylic polymer particles are normally negatively charged, the neutral coupling agent must be removed before the deposition process to expose the glass surface, so that the particles can be attracted. In this process, pH control of the coating solution is of prime importance as it determines the ability of the particle attraction of the glass surface.

7.2.3.4. Plasma polymerization and condensation polymerization

The plasma polymerization technique (Benatar and Gutowski, 1986) utilizes polymerizable organic vapors, producing a highly cross-linked thin film on the fiber surface with good adhesion. This technique is very flexible for treating carbon fibers, but is limited to the use of monomers having a low surface energy to ensure thorough wetting of fiber surface. Many different polymer coatings have been successfully applied to carbon fibers using this technique (see Section 5.3).

The condensation polymerization process, employed recently by Skourlis et al. (1993) and Duvis et al. (1993), involves immersion of carbon fibers in a solution containing hexamethylenediamine and sodium carbonate. Dried carbon fibers are then immersed in a dipolychloride solution in carbon tetrachloride where the interfacial polycondensation reaction takes place. The result is that a thin layer of polyamide (nylon 6,6) coating is deposited on the continuous carbon fiber, whose thickness is controlled though by varying the diamine concentration.

7.3. Theoretical studies of interphase and three engineered interphase concepts

The term 'interphase' has been used to refer to the region which is formed as a result of the bonding and reaction between the fiber and matrix. The morphological or chemical composition and thermo-mechanical properties of the interphase are

distinct from those of the bulk fiber and matrix materials. In a broad sense, the interphase can also include interlayers of various nature and thickness that are formed between the fiber and matrix as a result of the application of coating materials on the fiber before being incorporated into the matrix. Apart from the polymeric coatings that are applied to improve the fracture toughness of brittle polymer matrix composites as discussed in the foregoing section, coatings of different materials are also used extensively in MMCs and CMCs for various other purposes. In particular, compatibility of the coating material with the composite constituents during the manufacturing processes and in service conditions is the most important for MMCs and CMCs. The coating should also prevent deterioration of fiber strength and stiffness and enhance the fiber–matrix wettability and adhesion. In this section, a review is given of theoretical advances on the roles of the interphase/interlayers and the effects of various parameters on the mechanical performance of fiber composites containing such an interphase/interlayer.

Previous studies of the interphase/interlayer have mainly focused on the coefficient of thermal expansion (CTE) and residual thermal stresses. The importance of residual thermal stresses cannot be overemphasized in composites technology because the combination of dissimilar materials in a composite creates inevitably an interphase across which residual stresses are generated during fabrication and in service due to the difference in thermo-mechanical characteristics. The importance of an interlayer is clearly realized through its effects in altering the residual stress fields within the composite constituents.

7.3.1. Theoretical studies of interphase

Many publications have appeared in the literature, which analyze the effects of interphase/interlayers on stress distribution, in particular those arising from differential shrinkage between fiber and matrix. Also specifically studied are the overall thermo-mechanical properties of the composites, including Young's modulus, CTE and strength under various loading conditions. The idea behind these interphase/interlayer models is ultimately to provide practical guidance for controlling the local failure mode, and thus for the optimum design of the interphase/interlayer. Jayaraman et al. (1993) and Jayaraman and Reifsnider (1993) have recently given a comprehensive review on theoretical analyses of composites containing an interphase/interlayer.

The thermo-mechanical properties of the interlayer can be assumed to be either uniform or non-uniform. The properties of the non-uniform interphase can vary continuously or in a step-wise manner across the thickness between the bulk fiber and the matrix material. For varying interphase/interlayer properties, several different models have been proposed. The longitudinal shear modulus of the interphase was expressed by an exponential law (Van Fo Fy, 1967) based on a hexagonal fiber arrangement. The representative longitudinal modulus of the interphase was also proposed following the relationship involving heat capacity jump and volume fraction of the fiber in a calorimetric analysis for unidirectional glass reinforced epoxy matrix composites (Theocaris, 1984). Reciprocal and cubic

variation functions were also considered to represent the Young's modulus and the CTE of the interphase (Jayaraman and Reifsnider, 1993).

For analytical purposes, the fiber composites are conveniently modeled using axisymmetric three-phase (i.e. fiber–interlayer–matrix), four-phase (i.e. fiber–interlayer–matrix–composite medium) cylindrical composites, or in rare cases multi-layer composites (Zhang, 1993). These models are schematically presented in Fig. 7.9. The three-phase uniform interphase model is typified by the work of Nairn (1985) and Beneveniste et al. (1989), while Mitaka and Taya (1985a, b, 1986) were the pioneers in developing four-phase models with interlayer/interphase of varying stiffness and CTE values to characterize the stress fields due to thermo-mechanical loading. The four phase composite models contain another cylinder at the outermost surface as an equivalent composite (Christensen, 1979; Theocaris and Demakos, 1992; Lhotellier and Brinson, 1988).

Thermal stresses in composites have been studied using numerous mathematical models of varying complexity (Mitaka and Taya, 1985a, b; Nairn, 1985; Pagano and Tandon, 1988, 1990; Jayaraman and Reifsnider, 1992, 1993). The thermal stress concentration in composites is in general very sensitive to the material properties of the composite constituents. An increase in the interphase CTE decreases the in-plane residual thermal stresses in the matrix, but increases the residual stresses in the interphase (Nairn, 1985). Gardener and coworkers (Gardener et al., 1993a, b; Low et al., 1994, 1995a, b) have studied specifically elastomeric interlayers for carbon fiber-epoxy matrix composites. They used column element unit cells of three phases, similar to the earlier work by Aboudi (1991), to represent unidirectional fiber composites with an interlayer of uniform or varying properties. It is confirmed that the interphase thickness and Young's modulus were the dominant parameters determining the stress distributions and the effective properties of the composite,

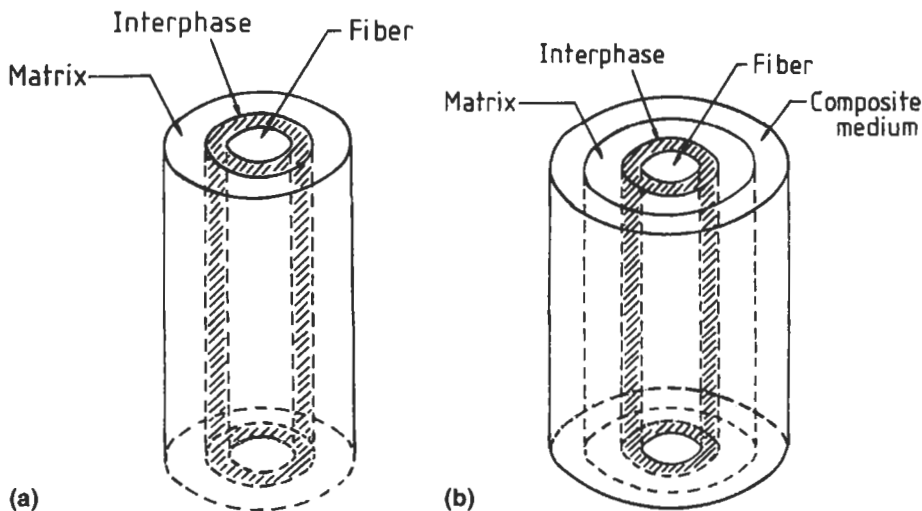


Fig. 7.9. Schematic illustrations of the interphase in (a) three cylinder model and (b) four cylinder model.

which in turn control the specific failure modes. Jao and McGarry (1992b) have also used an elastomer for injection molded glass fiber–nylon matrix composites, showing that a thin rubber coating mitigates significantly the stress concentration at the fiber ends. The CTEs of composites are calculated to determine the effect of the interphase which depends on the interfacial bond strength (Siderisodis, 1994). Using a three-cylinder model, Gao (1993) also studied the effect of interface bond strength on global failure of carbon fiber–epoxy matrix composite under multi-directional loading.

Stress distributions are estimated based on two typical three cylinder phase models with both uniform and varying interphase properties and with the interlayer thickness being 15% of the fiber diameter (Gardener et al., 1993a, b). The major results are compared in Fig. 7.10 for a carbon–epoxy system with a fiber volume fraction of 36%. The stresses are normalized with the matrix shrinkage stress ($\sigma = E_m \alpha_m \Delta T$, see Eq. (7.10)) which is the product of the matrix Young's modulus, matrix CTE and the temperature change. It is noted that both models predicted a constant axial stress within each phase, which is consistent with previous results (Pagano and Tandon, 1988; Benveniste et al., 1989).

Driven mainly by aerospace industries for applications to engine components and high temperature structures, many researchers studied interlayers that were designed to reduce the residual stresses in MMCs. The deformation behavior and the strength of unidirectional MMCs were modeled taking into account the yielding of the matrix material in an elasto-plastic analysis of the three-phase model (Craddock and Savides, 1994), and in compression (Waas, 1992). The effect of plastic deformation of the interlayer on matrix stress reduction was found to be equivalent to increasing the CTE of the layer by 1.5 times. The failure of composite materials containing interlayers was also predicted based on different failure criteria (Walpole, 1978; Aboudi, 1991; Mitaka and Taya, 1986). The elastic constant and CTE of the Ni and SiC interlayer in carbon fiber–aluminium matrix composites were assumed to be linear functions of the radial coordinate (Mitaka and Taya, 1985a). It was found that the variability of thermo-elastic constants of the interlayer had little direct influence on the stress distributions in the fiber and matrix. However, the maximum shear stress occurred at the interlayer when its modulus was comparable to the matrix. Ni coating was found to be advantageous over SiC coating from the fracture mechanics viewpoint (Mitaka and Taya, 1985a). The Young's modulus of the interphase was treated as a variable for a three-cylinder model of carbon fiber–aluminum matrix composites (Vedula et al., 1988; Jansson and Leckie, 1992; Doghri et al., 1990). It was proposed that the compliant layer in MMCs with a high CTE was much more efficient for reducing the residual thermal stresses than the compliant layer with a Young's modulus lower than the other composite constituents. A compliant interlayer was found to be beneficial mainly for reducing the tensile residual stresses in the matrix. This result has formed a sound basis for the establishment of the compliant/compensating interlayer concept where the residual thermal stresses could be minimized for a variety of metal matrix composites. The details are presented in Section 7.3.2. The optimum compliant layer for a SiC–Ti₃Al + Nb system was found to have a modulus value about 15% that of the composite without an interlayer (Caruso et al., 1990).

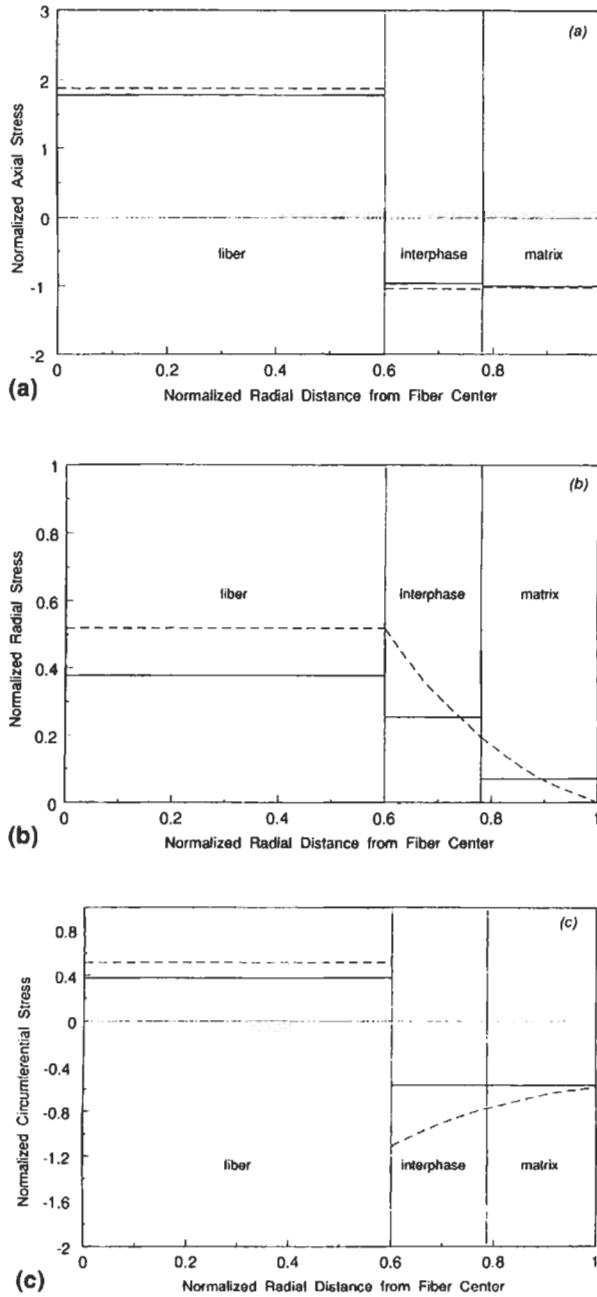


Fig. 7.10. A comparison of (a) axial, (b) radial and (c) circumferential residual stresses in an E-glass-epoxy matrix composites: (- - -) predicted by Jayaraman and Reifsnider (1992);(—) predicted by Gardner et al. (1993a, b).

Finite element analysis has been a popular tool for examining the mechanical response of coated fiber composites (Fan and Hsu, 1992; Daabin et al., 1992; Mital et al., 1993; Daoust et al., 1993; Kim et al., 1994b; Kim and Mai, 1996a; Ho and Drzal, 1995a, b). The use of the finite element method allows a more accurate description of the interactions between neighboring fibers in practical composites containing multiple fibers, and especially of the interface shear stress fields near the singularity. The presence of an elastomeric soft interlayer reduced the shear stress concentration at the fiber ends, and thereby reducing the load transfer efficiency (Daoust et al., 1993), and this effect became more prominent as the interlayer thickness increased. Increasing Young's modulus of the fiber increased the load transfer of the fiber at the expense of increasing shear stress at the interphase; whereas increasing the Young's modulus of the matrix had exactly the opposite effect (Daabin, 1992).

On the contrary, when the interphase is stiffer than the matrix material as for some uncoated carbon–epoxy systems, increasing the interphase modulus does not always increase the efficiency of stress transfer, and there is an optimum Young's modulus ratio of the interphase to the matrix (Ho and Drzal 1995a, b). Increase in the interphase thickness was found to have a much larger effect on the interphase shear stress distribution than on the fiber axial stress for both compliant and brittle interphases. It was also noted that the maximum shear stress at the fiber–coating interface was larger than the coating–matrix interface, which was later confirmed for a carbon–epoxy system (Kim et al., 1994b). Energy distribution within the single fiber composite and the strain energy release rate for interfacial crack propagation has also been analyzed (Di Anselmo et al., 1992) using finite element method. The presence of a compliant interlayer between fiber and matrix resulted in a lower strain energy release rate, an indication of enhanced fracture toughness of the composite. Based on a shear-lag model for CMCs, crack propagation was studied across the fiber as opposed to interfacial debonding (Popejoy and Dharani, 1992). Coating thickness was found to have little effect on crack growth although the interfacial debonding was slightly favored when the thickness was small, an indication of high fracture toughness of CMCs with the thinnest possible coating.

In summary, based on the previous studies as reviewed above, the variables which affect most the mechanical performance of composites have been identified:

- (1) Type and nature of interlayer.
- (2) Modulus, CTE and glass transition temperature of interlayer.
- (3) Thickness of interlayer.
- (4) Modulus of matrix relative to interlayer.
- (5) Interaction at the interface region.

7.3.2. Engineered interface concepts with fiber coating

It is shown in Section 7.2 that the PVAL coating applied onto Kevlar and carbon fibers is potentially beneficial for improving the transverse fracture toughness of the composites made therefrom. Encouraged by this promising result, further studies were conducted on the effects of the compliant interlayer on the stress distributions,

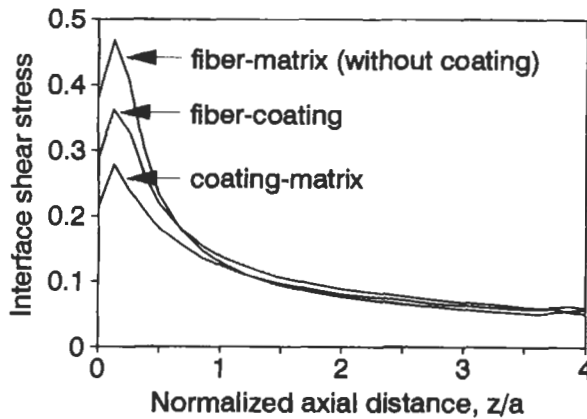


Fig. 7.11. Normalized interface shear stress distributions along the fiber length for composites with and without PVAL coating: coating thickness $t = 5 \mu\text{m}$ and Young's modulus ratio of coating to matrix $E_i/E_m = 0.5$. After Kim et al. (1994c).

based on finite element and micromechanics analyses of the fiber pull-out model (Kim et al., 1994a, c; Kim and Mai, 1996b). The principal results shown in Fig. 7.11 indicate that there is a large shear stress concentration near the fiber entry, followed by a parabolic decay towards a finite value for all interfaces studied. The maximum stress is higher in the order of the fiber/matrix without coating, fiber/coating and coating/matrix interfaces. This has practical implication in that the compliant coating acts as a medium relieving the stress concentration. Further, in the coated fiber composites, debonding would initiate at the fiber-coating interface in preference to the coating-matrix interface if the bond strengths of the two interfaces are identical.

Fig. 7.12 clearly indicates that the maximum interface shear stress increases almost linearly with Young's modulus ratio of coating to matrix, while it decreases with coating thickness and becomes almost constant for coating thickness greater than about $15 \mu\text{m}$. A practical relevance here is that there is an optimum coating thickness for given elastic properties of the composites constituents, which would impart the lowest interface stress concentrations, while minimizing any possible reductions in strength and stiffness due to the presence of the compliant interlayer.

Finite element analysis of the fiber pull-out test was further extended to characterize the residual shrinkage stresses using a similar three-cylinder model with an infinite matrix radius (Kim and Mai, 1996b). Assuming zero resultant stresses in the axial direction when there was no end effect (Hsueh et al., 1988), the residual radial stresses, σ_{ai} , and σ_{ci} , at the fiber-coating and coating-matrix interfaces in the radial direction (see Fig. 7.13) are given for a temperature drop, ΔT , from the processing temperature to ambient:

$$\sigma_{ai} = \frac{[(1 + \nu_i)(\alpha_m - \alpha_i) + s_1 s_3] E_i \Delta T}{s_1 s_2 - \frac{2(1 - \nu_i^2)}{s_4 - 1}}, \quad (7.2)$$

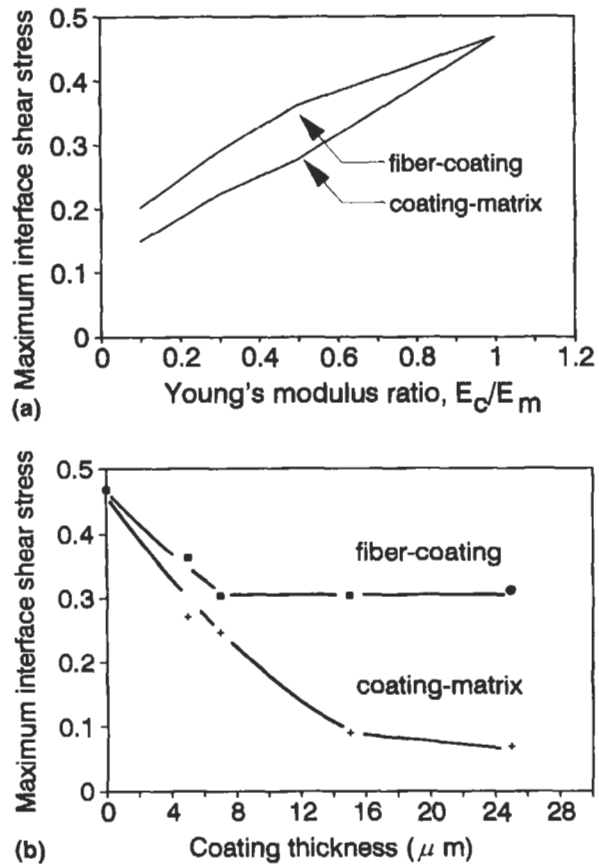


Fig. 7.12. Maximum interface shear stresses plotted (a) as a function of Young's modulus ratio of coating to matrix, E_i/E_m for coating thickness $t = 50 \mu m$, and (b) as a function of coating thickness t for Young's modulus ratio of coating to matrix, $E_i/E_m = 0.5$. After Kim et al. (1994c)

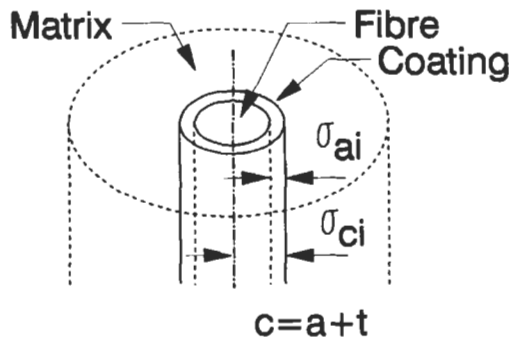


Fig. 7.13. Schematic drawing of a three-cylinder composite model with an infinite matrix radius. After Kim and Mai (1996).

$$\sigma_{ci} = \frac{\left[\frac{s_2(s_4-1)(\alpha_m-\alpha_i)}{2(1-\nu_i)} + s_3 \right] E_i \Delta T}{s_1 s_2 s_4 - \frac{2(1-\nu_i^2)}{s_4-1}}, \quad (7.3)$$

where the coefficients are:

$$s_1 = \frac{1 + s_4(1 - 2\nu_i)}{2s_4(1 - \nu_i)} \frac{(s_4 - 1)(1 + \nu_m) \frac{E_i}{E_m}}{2s_4(1 - \nu_i^2)}, \quad (7.4)$$

$$s_2 = \frac{(1 + s_4 - 2\nu_i)(1 + \nu_i)}{s_4 - 1} + (1 + \nu_r)(1 - 2\nu_r) \frac{E_i}{E_m}, \quad (7.5)$$

$$s_3 = (1 + \nu_i)\alpha_i + (\nu_f - \nu_i)\alpha_m - (1 + \nu_r)\alpha_f, \quad (7.6)$$

$$s_4 = \left(1 + \frac{t}{a}\right)^2, \quad (7.7)$$

E , ν and α are the Young's modulus, Poisson ratio and CTE, respectively, and the subscript i refers to the interlayer or coating. The residual stress at the fiber/matrix interface, σ_{ai} , for the composite without an interlayer can be obtained for $E_i = E_m$, $\nu_i = \nu_m$ and $\alpha_i = \alpha_m$ in Eq. (7.2). Figs. 7.14 and 7.15 present the results which are calculated using the properties of a CFRP given in Table 7.3, and the stresses are normalized with the compressive stress $\sigma_{ai} = -10.7\text{MPa}$ which is obtained without an interlayer. The residual stresses, σ_{ai} and σ_{ci} , decrease parabolically with increasing interlayer thickness when the coating is more compliant than the matrix. Further reductions in these residual stresses were realized with increasing CTE of the interlayer, α_i . This result is explained by the fact that the compressive stress induced by the shrinkage of the stiff matrix is effectively balanced by the greater shrinkage of the compliant interlayer. This means that the thicker the coating layer, the greater is the counterbalance against matrix shrinkage.

When the Young's modulus of the interlayer is the same as the matrix material, i.e., $E_i/E_m = 1$, and α_i is high, σ_{ai} is almost equivalent to that obtained without an interlayer, regardless of the interlayer thickness, t/a . On the contrary, σ_{ci} decreases drastically with increasing interlayer thickness and α_i , becoming negative (i.e. tensile stress) at the right-hand bottom corner of Fig. 7.14(b). It is worth noting that σ_{ai} is always greater than σ_{ci} in absolute terms, regardless of Young's modulus ratio, E_i/E_m , the difference increasing with α_i and t/a . This finding agrees well with the results from finite element analysis shown in Fig. 7.11 such that the interfacial shear stress is always higher at the fiber/coating interface than at the coating/matrix interface for a constant external stress. The Young's modulus of the interlayer is a very important parameter which governs the magnitude of the residual stresses in the composites. Both the residual stresses, σ_{ai} and σ_{ci} , increase significantly within a very small range of low modulus ratio, E_i/E_m , followed by a more gradual increase with further increase in E_i/E_m , depending on CTE and thickness of the interlayer. In

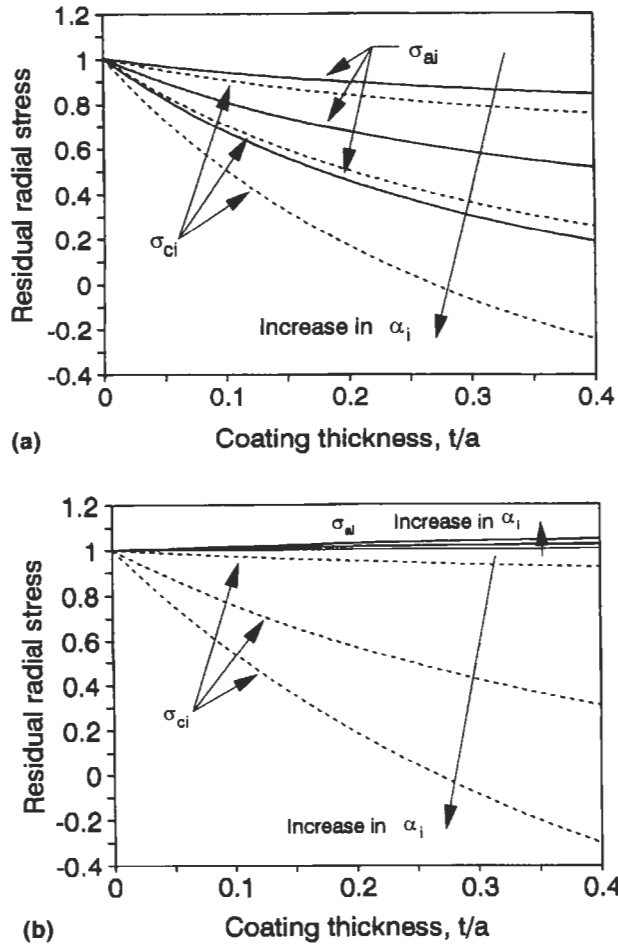


Fig. 7.14. Normalized radial residual stresses as a function of coating thickness, t/a , for varying coefficients of thermal expansion (CTE) of the coating, $\alpha_c = 10, 70, 130 \times 10^{-6}/^\circ\text{C}$: (a) Young's modulus ratio $E_i/E_m = 0.333$; (b) $E_i/E_m = 1.0$. After Kim and Mai (1996a, b).

summary, if the residual stresses at the interfaces are to be reduced substantially, the interlayer material should have a high α_i value, unless its Young's modulus is much lower than that of the matrix (i.e. E_i/E_m less than approximately 0.1 for the CFRP studied). This conclusion is considered to be consistent with the criteria proposed for SiC fiber-Ti₃Al + Nb matrix composites (Arnold and Wilt, 1992).

In the light of the work presented in the foregoing from both the theoretical and experimental viewpoints, three concepts of engineered interfaces have been put forward to explain the roles of the thermoplastic coating, and their physical/chemical requirements for three different functional coatings are proposed by Kim and Mai (1996b):

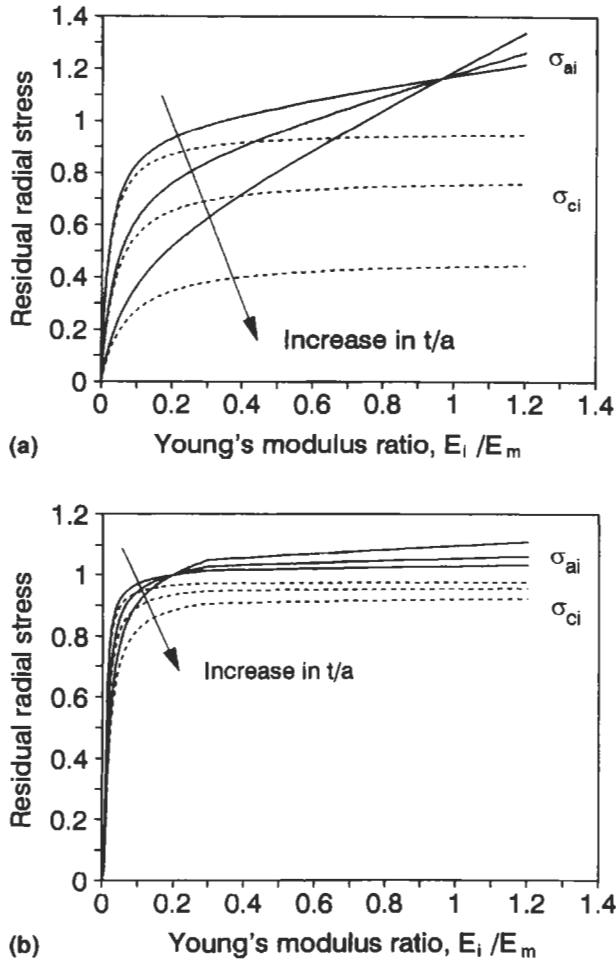


Fig. 7.15. Normalized residual radial stress as a function of Young's modulus ratio, E_i/E_m , for varying coating thickness, $t/a = 0.05, 0.1, 0.2$. Coefficients of thermal expansion (CTE) of the coating: (a) $\alpha_c = 100 \times 10^{-6}/^\circ\text{C}$; (b) $\alpha_c = 20 \times 10^{-6}/^\circ\text{C}$. After Kim and Mai (1996a, b).

Table 7.3
Mechanical properties of carbon fiber-epoxy matrix composites^a.

Composite system	Fiber		Matrix		Interface		
	E_f (GPa)	ν_f	E_m (GPa)	ν_m	G_i (J/m^2)	μ	q_0 (MPa)
Carbon-epoxy	230	0.2	3.0	0.4	37.7	1.25	-9.97

^aAfter Kim et al. (1992).

- (1) weak interface–bond layer;
- (2) microductile/compliant layer;
- (3) compensating layer.

In the weak interface–bond layer concept, the coating layer should provide a weak interface bonding, promoting interface debonding and subsequent fiber pull-out. A coating material which forms a discrete interlayer between the fiber and matrix can readily act as a physical barrier to the chemical bonding between the functional groups present in the composite constituents. To obtain the maximum benefits of high fracture toughness, the coating material should provide a sufficiently high frictional bonding, while maintaining a low chemical bonding at the interface. There must be optimum values for these conflicting requirements.

The microductile/compliant layer concept stems from the early work on composite models containing spherical particles and oriented fibers (Broutman and Agarwal, 1974) in that the stress around the inclusions are functions of the shear modulus and Poisson ratio of the interlayer. A photoelastic study (Marom and Arridge, 1976) has proven that the stress concentration in the radial and transverse directions when subjected to transverse loading was substantially reduced when there was a soft interlayer introduced at the fiber–matrix interface. The soft/ductile interlayer allowed the fiber to distribute the local stresses acting on the fibers more evenly, which, in turn, enhanced the energy absorption capability of the composite (Shelton and Marks, 1988).

A compensating layer concept is based on the interlayer which can reduce the residual thermal stresses, as detailed in Sections 7.3.1 and 7.5.2. This is best achieved when the microductile/compliant layer has a high CTE so that the shrinkage stress in the matrix around the fiber can be effectively balanced by the greater shrinkage of the coating layer, if not completely eliminated. This concept has been originally proposed for advanced metal matrix composites (Vedula et al., 1988; Arnold et al., 1990, 1992; Arnold and Wilt, 1992), such as SiC fiber–Ti₃Al + Nb systems, in which microscopic cracking in the radial and circumferential directions due to high shrinkage stresses was a major concern during the manufacturing process.

Apart from the above three major engineered interface concepts, the ductile coating material may also heal up the surface flaws that are often generated during the fiber manufacturing processes, and protect the brittle fiber surface during subsequent processing.

7.4. Control of laminar interfaces–delamination promoters

Another way of improving the energy absorption capacity of laminate composite in the transverse direction is by promoting controlled delamination when the interlaminar bond strength or interlaminar fracture toughness is weakened. Depending on the orientation of the interface relative to the main crack, the triaxial tension operating at the crack tip causes the main crack to be arrested at the weak laminar interfaces by allowing delamination (Almond et al., 1969). Based on the concept of crack arrest, the transverse fracture toughness of CFRPs has been

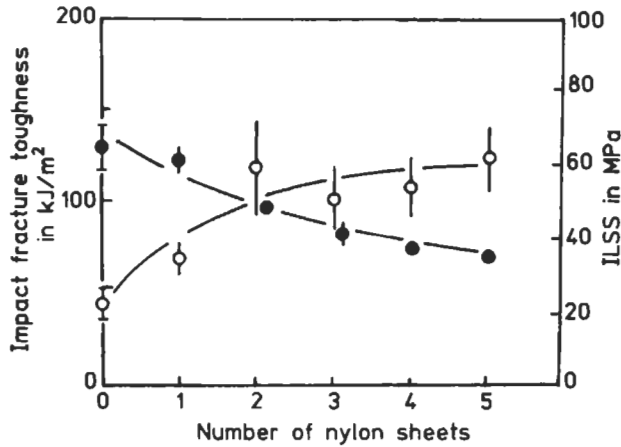


Fig. 7.16. Impact fracture toughness (○) and interlaminar shear strength (ILSS, ●) of carbon fiber–epoxy matrix composites with varying number of nylon sheets as delamination promoters. After Favre (1977).

increased successfully by three times with embedded nylon sheets, at the expense of some 25% reduction in ILSS (Favre, 1977) (Fig. 7.16). Perforated films were found to be more effective than unperforated films because the perforated films could provide both the weak and strong bonding in the regions of film and perforation, respectively, similar to the intermittent interlaminar bond concept (Mai et al., 1982a). The failure mechanisms underlying the delamination promoter concept are schematically shown in Fig. 7.17. In the weak regions, delamination occurred allowing the main crack front to be bifurcated and the sub-cracks to propagate along the laminar interfaces. These mechanisms promote energy absorption, as envisaged from the tensile debonding theory (Cook and Gordon, 1964). However, excessive delamination was effectively discouraged and the shear stress transfer was permitted between laminae in the strong regions, enabling the original bond strength to be maintained. While the tensile strength dropped about 20%, and the Young's modulus remained the same, the transverse fracture toughness of CFRPs increased a

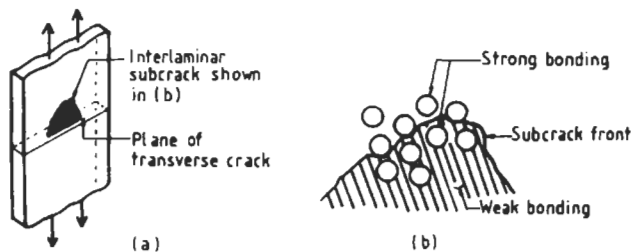


Fig. 7.17. Schematic illustrations of sub-crack propagation along the laminar interface of the composite intermittently bonded with perforated films. After Jea and Felbeck (1980).

remarkable 500% using multi-layers of perforated Mylar films for the best optimum condition (Jea and Felbeck, 1980).

In a similar study using several other type of films, including aluminum foils, bleached papers, polyester textile fabrics and polyimide Mylar, as delamination promoters, it was concluded that the fracture mode and the subsequent energy absorption mechanisms depended strongly on the loading directions relative to the laminar plane and other testing parameters such as loading speed and the span-to-depth-ratio in bending (Jang et al., 1987). The effectiveness of the intermittent interlaminar bonding concept has been further proven for cement mortars with embedded perforated papers as delamination promoters (Mai et al., 1982b). It was noted that the large improvement of 200–800% in transverse fracture toughness was accompanied by a huge 30–50% reduction in flexural strength. In summary, although the delamination promoter concept is quite useful for enhancing the transverse fracture toughness of laminate composites, extreme care must be exercised in its application because delamination and other associated damage are some of the most critical life-limiting failure modes in most engineering structures made from composite materials. Excessive delamination growth may cause unacceptable reduction in the composite stiffness and strength, which, in turn, impair the overall mechanical performance and structural integrity of the composite structure.

7.5. Residual Stresses

7.5.1. Origin of residual stresses

Residual stresses are inherent in almost all fiber composites whether they are based on polymer, metal or ceramic matrices, but they are often ignored or underestimated in both design and analytic modeling. This oversight can lead to incorrect interpretations of material characteristics and mechanical behavior. The primary origins of residual stresses in fiber composites are twofold: thermal and mechanical. The thermal origin is the most prevalent and arises from the different CTE of the composite constituents. Composites in general achieve their structural integrity by being cured or processed at elevated temperatures under pressure and/or in vacuum. This process invariably induces residual stresses to build up in the composite when it is at a temperature different from its process temperature. The resulting residual stresses of thermal origin can be either micro or macroresidual stresses, depending on the geometry and scale of the composites concerned (Chamis, 1971). Favre (1988) has given a review of these residual stresses, the experimental techniques devised to measure them, and of ways to reduce them.

7.5.1.1. Micro-residual thermal stresses

The micro-residual stresses arise from the differential CTE of the fiber and matrix, and the temperature difference. Table 7.4 gives the linear CTE values for various types of reinforcing fibers and matrix materials used widely for composite fabrication. The CTEs of most fibers and ceramic matrices are relatively lower

Table 7.4
Linear coefficients of thermal expansion (CTE) of fibers and matrix materials.

Fibers	CTEs ($\times 10^{-6} K^{-1}$)
Carbon-PAN Based	
HS	$\alpha_L = -0.5 \sim -0.1$ $\alpha_T = 7 \sim 12$
HM	$\alpha_L = -1.2 \sim -0.5$ $\alpha_T = 7 \sim 12$
Aramid	
Kevlar 29	$\alpha_L = -2.26$ $\alpha_T = 59$
Kevlar 49	$\alpha_L = -2$ $\alpha_T = 59$
Kevlar 149	$\alpha_L = -1.49$ $\alpha_T = 59$
Glass	
E-glass	4.7~5.0
S-glass	5.6
Polyethylene	
Spectra 900	$\alpha_L = -10.8$
Boron (B-W)	4.8~8.3
Al ₂ O ₃	3.5~8
SiC	
SCS	4.3~5.7
Nicalon	3.1~4.0
Steel (0.9% C)	12
Stainless steel (18-8)	11.6
Beryllium	11.6
Tungsten	4.5
Molybdenum	6.0

than other materials, and especially are at least one order of magnitude lower than polymeric materials. Unidirectionally oriented fiber composites have two (or sometimes three) CTEs: namely α_{cL} and α_{cT} , in the longitudinal and transverse directions, respectively. The expressions for the effective linear CTEs of unidirectional fiber composites (Schapery, 1968) are derived based on the energy balance method for transversely isotropic fibers, assuming that Poisson ratios of the composite constituents were similar:

$$\alpha_{cL} = \frac{\alpha_m E_m V_m + \alpha_f E_f V_f}{E_m V_m + E_f V_f}, \quad (7.8)$$

$$\alpha_{cT} = (1 + \nu_m)\alpha_m V_m + (1 + \nu_f)\alpha_f V_f - (\nu_f V_f + \nu_m V_m)\alpha_{cL}, \quad (7.9)$$

where the first subscripts, c, f and m refer to composite, fiber and matrix, respectively, while the second subscripts L and T refer to the longitudinal and transverse directions, respectively. For unidirectional fiber composite, the CTEs in the longitudinal direction are normally lower than those in the transverse direction

Table 7.4 (Contd.)

Matrices	CTEs ($\times 10^{-6} K^{-1}$)
Polymers	
Epoxies	55~90
Polyester	50~100
Phenolformaldehyde	26~60
High density polyethylene (HDPE)	150~300
Polypropylene (PP)	100~300
Polytetrafluoroethylene (PTFE)	70~100
Polymethylmethacrylate (PMMA)	54~72
Polyamide (PA, Nylon 6,6)	80~95
Polysulfone (PS)	56
Polyethersulfone (PES)	55
Polyetherimide	62
Polyamideimide	63
Polyphenylenesulfide	54
Polyetherketone	47
Liquid crystal polymer (Vectra)	-5~75
Metals	
Steels (0.9% C)	12
Copper	17
Nickel	13
Aluminum and alloys	22~24
Titanium and alloys	8~9
Ceramics	
Al ₂ O ₃	8.5
SiC	4.3
Borosilicate glass	4.0
Soda glass	8.5
Si ₃ N ₄	3.2
Zr ₂ O ₃	8.0

(i.e. $\alpha_{cL} < \alpha_{cT}$) because fibers in general have lower CTEs than matrix materials. At a low fiber volume fraction, the CTEs of unidirectional fiber composites in the transverse direction, α_{cT} , tend to be even greater than the CTEs of bulk matrix materials, α_m . This is due to the fact that the long stiff fibers prevent the matrix from expanding in the fiber axial direction, forcing the matrix to expand more in the transverse direction.

Three-dimensional distributions of the micro-residual stresses are very complicated, and are affected by the elastic properties, local geometry and distribution of the composite constituents within a ply. Many analytical (Daniel and Durelli, 1962; Schapery, 1968; Harris, 1978; Chapman et al., 1990; Bowles and Griffin, 1991a, b; Sideridis, 1994) and experimental (Marloff and Daniel, 1969; Koufopoulos and Theocaris, 1969; Barnes et al., 1991; Barnes and Byerly, 1994) studies have been performed on residual thermal stresses. A two-dimensional photoelastic study identified that the sign and level of the residual stresses are not uniform within the composite, but are largely dependent on the location (Koufopoulos and Theocaris,

1969). For a single fiber surrounded by a matrix (Fig. 7.18 (a)), shrinkage of the resin matrix causes radial compressive stresses clamping the fiber. For a square array of circular inclusions in a matrix, the residual stresses in the region between adjacent fibers are found to be compressive while they are tensile in the resin pocket region surrounded by the fibers. If the fiber spacing is very small for a high V_f , and the fiber is much stiffer than the matrix material (i.e. $E_m \ll E_f$), the tensile stresses in the resin pocket may become compressive, generating hydrostatic compression around the fibers (Fig. 7.18 (b)). A rough estimate of the compressive residual stress in the radial direction can be obtained by calculating the shrinkage fit (Dugdale, 1968) for an isotropic single fiber embedded in a coaxial cylindrical matrix material (Harris 1978)

$$q_0 = \frac{(\alpha_m - \alpha_f)E_m \Delta T}{(1 + \alpha_f \Delta T)(1 + \alpha_m \Delta T)[(1 - \nu_f)\alpha_m + 1 + \nu_m + 2\gamma]} , \quad (7.10)$$

$$\cong (\alpha_m - \alpha_f)E_m \Delta T$$

which is an approximate form of Eq. (7.2) or Eq. (7.3) when there is no coating or interlayer at the fiber–matrix interface. It is also noted that the magnitude of the residual stress is determined not only by the cure temperature but also by the whole cure cycle (Kim and Hahn, 1989). The differential shrinkage between the fibers and matrix also causes the fibers to be placed under compression along their length, which, in turn, increases the tendency for fiber buckling and produces interface shear stresses leading to interface debonding (Rohwer and Jiu, 1986; Rodriguez, 1989; Hiemstra and Sottos, 1993) and ply cracking (Kim et al., 1989).

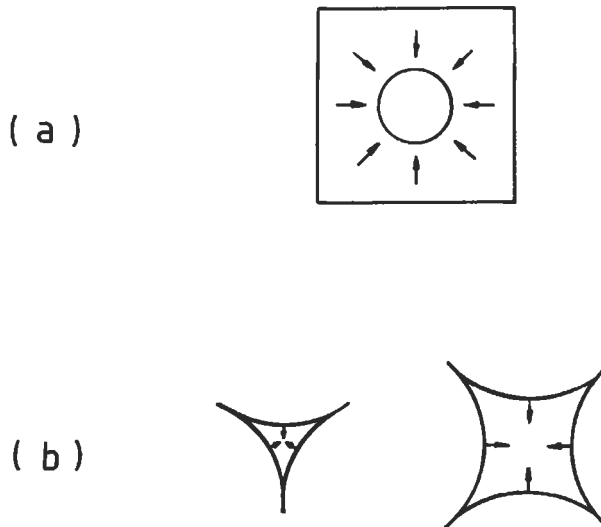


Fig. 7.18. Source of shrinkage stresses: (a) rigid inclusion embedded in a matrix; (b) resin pockets surrounded by fibers in hexagonal and square arrays. After Hull (1981).

The compressive residual stresses in the fiber direction have been measured extensively in recent years for many different combinations of fiber and polymer matrix, e.g. polydiacetylene fiber–epoxy matrix (Galiotis et al., 1984), carbon fiber–PEEK matrix (Galiotis et al., 1988; Young et al., 1989) and Kevlar fiber–epoxy matrix (Jahankhani and Galiotis, 1991), using a technique based on the laser Raman spectroscopy. In the light of the novel observation by Tuinstra and Koenig (1970) that the peak positions of the Raman-active bands in the fiber are sensitive to the magnitude of the applied strain, the fiber residual strain can be estimated from the plots of fiber strain versus composite strain obtained on a model microcomposite containing a single fiber. Further extension of the micro-Raman technique allows the measurements of interfacial shear stress distributions along the fiber length at varying applied strain levels (Jahankhani and Galiotis, 1991), and even during the single fiber pull-out test (Patrikis et al., 1994; Bannister et al., 1995). More details of the findings based on the Raman technique is presented in Section 2.3.3.

7.5.1.2. Macro-residual thermal stresses

Macro-residual stresses, the so-called lamination residual stresses (Doner and Novak, 1969; Chamis, 1971), are present within the individual ply of a laminate consisting of multi-ply of different angles. The residual stresses in the laminate arise from the difference between the ply CTEs in the longitudinal and transverse directions. These residual stresses are integrated averages through the ply thickness, and are typically highest at $[0^\circ/90^\circ]$ or $[+45^\circ/-45^\circ]$ laminate interfaces because a tensile stress develops in the 90° plies with a corresponding compressive stress in the 0° plies (Bowles and Griffin, 1991b). Consider the simple $[0^\circ/90^\circ]_2$ symmetric cross-ply laminate shown in Fig. 7.19. The residual thermal stresses in the plies for a temperature drop, ΔT , is derived based on the RoM (Jones, 1994):

$$\sigma_{90^\circ\text{L}} = \frac{b(\alpha_{cT} - \alpha_{cL})E_L \Delta T}{b + d\frac{E_T}{E_L}}, \quad (7.11)$$

$$\sigma_{90^\circ\text{T}} = -\frac{E_T}{E_L} \sigma_{0^\circ\text{L}}, \quad (7.12)$$

$$\sigma_{0^\circ\text{T}} = \frac{d(\alpha_{cT} - \alpha_{cL})E_L \Delta T}{b\frac{E_T}{E_L} + d}, \quad (7.13)$$

$$\sigma_{0^\circ\text{L}} = -\frac{E_T}{E_L} \sigma_{90^\circ\text{L}}, \quad (7.14)$$

$\sigma_{90^\circ\text{L}}$ and $\sigma_{90^\circ\text{T}}$ are the residual stresses in the longitudinal and transverse directions of the 90° ply lamina, while $\sigma_{0^\circ\text{L}}$ and $\sigma_{0^\circ\text{T}}$ are the residual stresses in the longitudinal and transverse directions of the 0° ply lamina, respectively. b and d are the 90° and 0° ply thickness, and the CTEs of the laminae in the longitudinal and transverse directions, α_{cL} and α_{cT} , are given in Eqs. (7.8) and (7.9). The tensile stresses that develop transversely to the fiber direction, $\sigma_{0^\circ\text{T}}$ and $\sigma_{90^\circ\text{L}}$, are counteracted by the equivalent compressive stresses, $\sigma_{0^\circ\text{L}}$ and $\sigma_{90^\circ\text{T}}$, respectively.

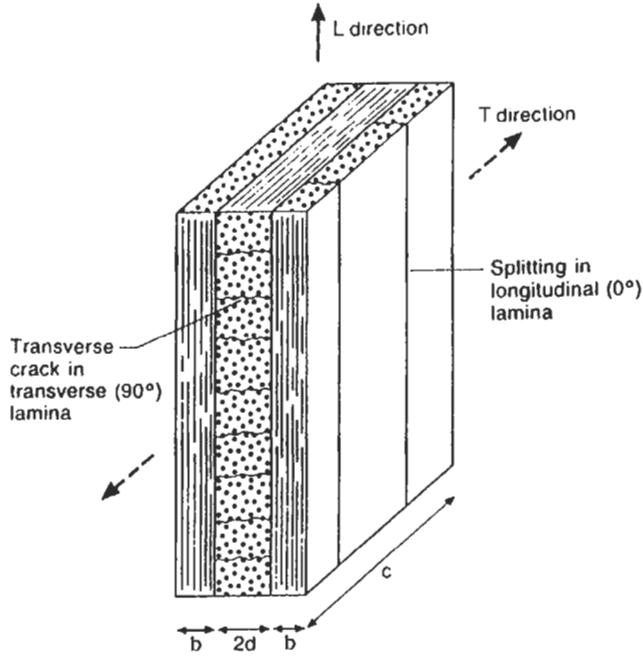


Fig. 7.19. A schematic drawing of a $[0^\circ/90^\circ/0^\circ]$ cross-ply laminate.

These lamination residual stresses promote the onset of transverse layer cracking (Doner and Novak, 1969) and delamination (Jeronimidis and Parkyn, 1988; Tandon and Chatterjee, 1991), and often cause serious warpage in asymmetric laminates even in the absence of external loads (Kim and Hahn, 1989, Jun and Hong, 1990; Crasto and Kim, 1993). Fig. 7.20 shows schematically the change in warpage of an asymmetric $[0_4/90_4]$ laminate with increasing temperature, whereas Fig. 7.21 displays the variation in the maximum deflection at the center of the laminates that are cured at two different temperatures (Crasto and Kim, 1993). There is a steady decrease in the deflection with increasing temperature, with some deflection still present at the

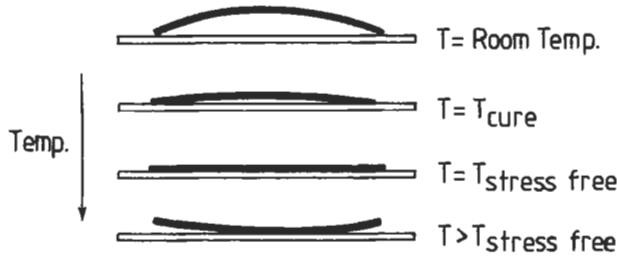


Fig. 7.20. Warpage of a $[0_4^{\circ}/90_4^{\circ}]_s$ AS4 carbon fiber–3501-6 epoxy matrix composite with increasing temperature. After Crasto and Kim (1993).

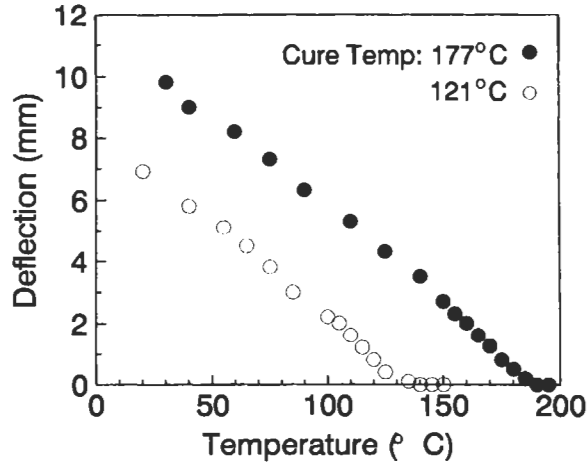


Fig. 7.21. Maximum deflections of $[0_4^o/90_4^o]_s$ AS4 carbon fiber-3501-6 epoxy matrix composites plotted as a function of temperature. After Crasto and Kim (1993).

cure temperature. The laminate returns to a completely flat sheet at a temperature slightly above the cure temperature, and produces a reverse curvature with further increase in temperature. The lamination residual stresses can be reduced, to some extent, within a given temperature range by selecting an optimum stacking sequence and ply orientation (Ishikawa et al., 1989).

7.5.1.3. Other sources of residual stresses

In addition to those induced thermally, there are other sources of residual stresses. These include mechanical residual stresses, and those induced by phase transformation in composites based mainly on ceramics, and crystallization in semi-crystalline thermoplastic composites. Mechanical residual stresses are present mainly in ductile metal matrix composites due to the difference in flow stress between the components (Metcalf, 1974). This type of residual stress becomes important when the composite is highly loaded to plastically deform one or both components. Phase transformation in certain ceramics and ceramic composites accompany significant volume changes, while the transforming component is mechanically restrained. As a result, the surrounding material is locally strained by this volume change. A good example of the phase transformation is partially stabilized zirconia (ZrO_2) which contains small amounts of MgO, CaO or Y_2O_3 , and undergoes a 3.25% volume expansion during cooling below approximately $1000^\circ C$ due to transformation from the tetragonal phase to the monoclinic phase (Porter and Heuer, 1977). A very high fracture toughness can be achieved if the particle size and processing conditions are carefully controlled.

7.5.2. Control of residual stresses

7.5.2.1. Compensating interlayer

Marom and Arridge (1976) were among the early researchers who demonstrated that a soft interlayer present at the interface between the stiff reinforcements and brittle matrix increased the composite strength in the transverse direction. This is attributed to the reduction of the stress concentration around the inclusion, which is influenced by the shear modulus and Poisson ratio of the compliant interlayer. A plasticized epoxy resin and a silicone rubber coating (of thickness less than 10% the reinforcement diameter) on the steel wire produces almost zero shrinkage stresses in the radial and hoop directions, as measured photoelastically. The crack initiated within the soft coating is blunted at the interface region, becoming stable under the applied transverse loading, similar to the observations for other fiber composites (Kardos, 1981).

Apart from PMCs, highly complex residual stresses are also introduced due to thermal mismatch in MMCs during manufacturing. This often causes cracking of the matrix, especially those with brittle matrices (Chou et al., 1985). The tensile residual stresses in the longitudinal and hoop directions are the major cause of the observed matrix cracking (Vedula et al., 1988; Ghosn and Lerch, 1989). Micrographs are shown in Fig. 7.22 of a transverse section with radial cracking at the fiber-matrix interface for a SiC fiber Ti_3Al Nb matrix composite after fabrication and after 1000 thermal cycles. Aiming specifically to tackle the matrix cracking issue, the properties of an interlayer necessary to minimize the local tensile residual stresses in the matrix have been studied extensively (Ghosn and Lerch, 1989; Caruso et al., 1990; Doghri et al., 1990; Morel et al., 1991; Jansson and Leckie, 1992; Arnold et al., 1992). Based on the elastic analysis of a three-cylindrical model with temperature-dependent properties of the fiber and matrix, the following summary is given (Ghosn and Lerch, 1989)

- (1) A well designed interface layer with controlled Young's modulus, CTE and thickness can reduce the tensile residual stresses in a MMC system.

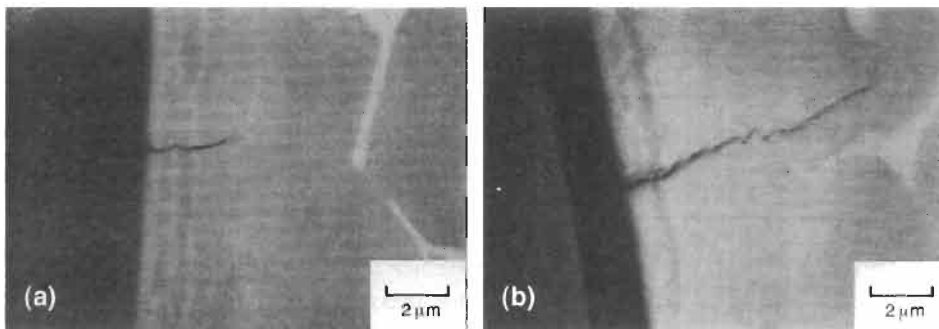


Fig. 7.22. Radial cracking in a SiC fiber/ $Ti-24Al-11Nb$ matrix composite (a) after fabrication and (b) after additional 1000 thermal cycles. After Arnold et al. (1992).

- (2) For a given fiber system, the optimum CTE of the interlayer increases with increasing modulus and CTE of the matrix.
- (3) For a low matrix modulus, the optimum CTE of interlayer can be approximated by the average CTE of the fiber and matrix, whereas for high matrix modulus, the optimum CTE of interlayer approaches the matrix value.

Caruso et al. (1990) further defined the required properties of the compensating interlayer for SCS-6 (SiC) fiber/Ti₃Al + Nb matrix and SCS-6 (SiC) fiber/Ti-15-3 matrix composite systems: the interlayer should have a modulus 15% that of the matrix and CTE approximately equal to that of the composite system without the compensating layer. Although the addition of a recommended interlayer can mitigate the matrix cracking problem, it causes a slight reduction in the composite modulus. Plastic deformation of the matrix is taken into account later (Arnold et al., 1990, 1992; Arnold and Wilt, 1992), proposing the yield point and hardening slope also play a significant role in reducing the stress concentrations within the interlayer. In addition to the above criteria, Arnold et al. (1992) proposed that:

- (1) The interlayer CTE should be greater than the matrix CTE.
- (2) The interlayer thickness to fiber diameter ratio should be as large as other thermo-mechanical considerations would allow.
- (3) The yield point and hardening slope of the interlayer should be low compared to those of the matrix material.

A candidate interlayer consisting of dual coatings of Cu and Nb has been identified successfully for the SiC-Ti₃Al + Nb composite system. The predicted residual thermal stresses resulting from a stress free temperature to room temperature (with $\Delta T = -774^\circ\text{C}$) for the composites with and without the interlayers are illustrated in Fig. 7.23. The thermo-mechanical properties of the composite constituents used for the calculation are given in Table 7.5. A number of observations can be made about the benefits gained due to the presence of the interlayer. Reductions in both the radial, σ_r , and circumferential, σ_θ , stress components within the fiber and matrix are significant, whereas a moderate increase in the axial stress component, σ_z , is noted. The chemical compatibility of Cu with the fiber and matrix materials has been closely examined by Misra (1991).

Similar studies have been reported for CMCs, but with different perspectives regarding the effects of residual stresses (Hsueh et al., 1988; Kuntz et al., 1993). The tensile residual stresses in the hoop direction may cause cracking in the ceramic matrix, especially when combined with external loading. More importantly, the compressive clamping stresses normal to the fiber surface in the radial direction increases the shear stress required for fiber pull-out, and tends to inhibit extensive debonding along the interface. Interfacial debonding, fiber pull-out and associated fiber bridging of cracked surfaces are known to be the major toughening mechanisms for brittle matrix composites containing ceramic matrices. (There is another source of normal stresses at the interface during fiber pull-out, namely the radial strains arising from the fiber roughness, see Chapter 4 (Keran and Parthasarathy, 1991; Jero and Kerans, 1991).) As such, the major purpose of interlayers for CMCs is to minimize the residual thermal stresses at the interface in an effort to improve the fracture toughness, which is considered to be one of the

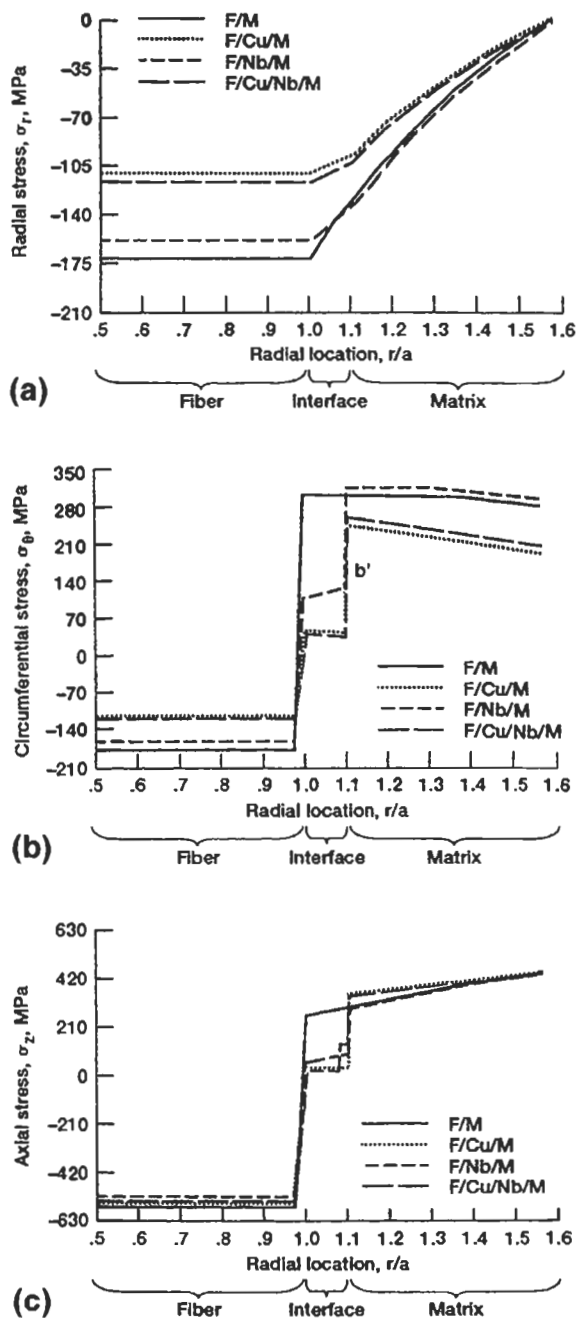


Fig. 7.23. Thermal residual stress distributions in the (a) radial, (b) circumferential and (c) axial directions for a SCS-6 SiC fiber/Ti₃Al + Nb matrix composite with and without Cu, Nb and Cu/Nb coatings. Total coating thickness $t/a = 0.1$. After Arnold and Wilt (1992).

Table 7.5
Thermo-mechanical properties of composite constituents at 25°C^a.

Composite constituents	Young's modulus E (GPa)	Poisson ratio ν	Yield Stress σ_y (MPa)	CTE (10^{-6} K^{-1})
Fiber				
SCS-6	400	0.25	–	3.53
Matrix				
Ti-24Al-11Nb	110	0.26	372	9.0
Coatings				
Nb	98.6	0.38	248	7.13
Cu	78.8	0.34	37.1	16.0

^aAfter Arnold and Wilt (1992).

major concerns associated with CMCs for their wider applications (Tiegs et al., 1987; Ahaim and Heuer, 1987).

7.5.2.2. Control of matrix shrinkage

It is shown in Section 6.1 that fiber pull-out following interface debonding is the predominant failure mechanism responsible for the total toughness of most PMCs containing glass, carbon and aramid fibers. The fracture toughness of composites due to fiber pull-out, R_{po} , has been analyzed, taking into account the residual clamping stress in the radial direction, q_0 , caused by the shrinkage of matrix (Piggott, 1981)

$$R_{po} = \frac{-q_0 V_f d h^2 A^2}{4\mu(\alpha v_f A + q_0)^2}, \quad (7.15)$$

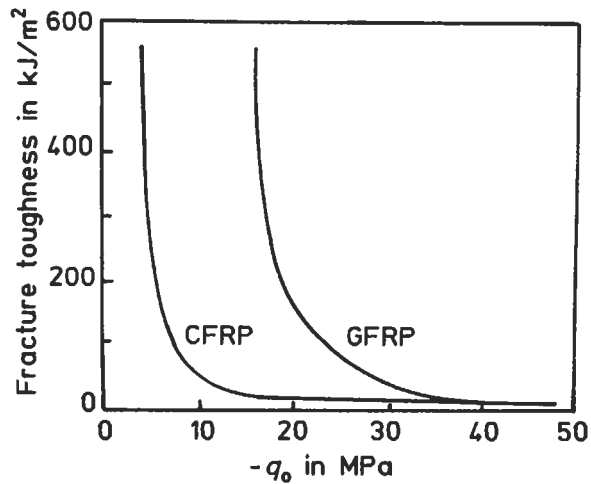


Fig. 7.24. Predicted fracture toughness of carbon and glass fiber-polymer matrix composites (CFRP and GFRP) with varying matrix shrinkage stress, q_0 . After Piggott (1981).

where A and h are parameters determined in the relationship between fiber strength σ_f^* and fiber length l : $\sigma_f^* = Al^{-h}$. In theory, the fracture toughness should be at its maximum when the shrinkage stress can just compensate the Poisson contraction stress, which in turn allows the denominator of Eq. (7.15) to become close to zero. The R_{po} versus q_0 plots for a CFRP and a GFRP given in Fig. 7.24 suggest that the fracture toughness can be improved by reducing q_0 without deteriorating other mechanical properties. Bailey et al. (1977) have been successful in developing special expanding monomers for such applications. Epoxy resins are copolymerized with approximately 5–10% dinorbornene (or tetramethyl) spiro ortho carbonates that balance the shrinkage of resin by expansion through ring opening reactions. In a series of experimental studies (Lim et al., 1984; Lam and Piggott, 1989a, b, 1990), the residual thermal stresses in a CFRP have been reduced successfully with such special expanding monomers. The composites made therefrom have one-third of the usual residual stress with some 50% improvement of Izod impact toughness and a slight reduction in ILSS, as shown in Fig. 7.25. The addition of the expanding monomers also gives improved fatigue properties and better resistance to water absorption of the CFRP.

Unlike carbon fiber composites, the expanding monomers demonstrate little beneficial effect on GFRPs and KFRPs: it actually decreases the toughness by about 30% for GFRP (Lim et al., 1984). It appears that there are many unresolved issues regarding the effects of important parameters, and there must be an optimum value for the fiber clamping stress, q_0 , which would maximize the fiber pull-out toughness. If q_0 is too high, interfacial debonding and subsequent fiber pull-out would be inhibited; whereas if q_0 is too low, only a small frictional energy is dissipated, because q_0 controls directly these failure mechanisms through its influence on the

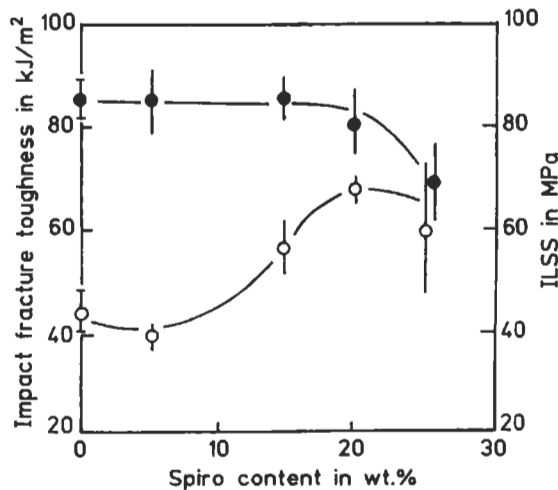


Fig. 7.25. Impact fracture toughness (○) and interlaminar shear strength (ILSS, ●) of unidirectional carbon fiber–epoxy matrix composites as a function of expanding monomer (spiro) content. After Lim et al. (1984).

frictional shear stress (see Section 6.1). The inefficiency of the expanding monomers in composites other than CFRP needs further work to explain the observed results before this technique can be applied widely.

Because the shrinkage stress depends not only on the type of matrix materials used but also on the state of matrix cure (Piggott et al., 1985), it is necessary to specify the optimum cure cycle for a given expanding monomer. In addition to the direct influence of the expanding monomers on fracture toughness, resins which can cure without generating residual stresses are highly desirable for various practical applications, such as high performance adhesives, coatings, precision castings, dental fillings, binders for solid propellants, etc. There are now significant research efforts toward the control of shrinkage stresses in polymers, particularly epoxies (Shimbo et al., 1985; Ochi et al., 1989; He et al., 1989; Sikes and Brady, 1990) and polyesters (Bucknall et al., 1991).

References

- Aboudi, J. (1991). Microfailure criteria for coated fiber composites. *J. Reinforced Plast. Composites* **10**, 146–157.
- Ahaim, R. and Heuer, A.H. (1987). The interface between (Nicalon) SiC fibers and a glass-ceramic matrix. *Adv. Ceram. Mater.* **2**, 154–158.
- Almond E.A., Embury J.D. and Wright E.S. (1969). Fracture in laminated materials. In *Interfaces in Composites*, ASTM STP 452, ASTM, Philadelphia, PA, pp. 107–129.
- Arnold, S.M., Arya, V.K. and Melis, M.E. (1990). Elastic/plastic analysis of advanced composite investigating the use of the compliant layer concept in reducing residual stresses resulting from processing, NASA TM-103204.
- Arnold, S.M., Arya, V.K. and Melis, M.E. (1992). Reduction of thermal residual stresses in advanced metallic composites based on a compensating/compliant layer concept. *J. Composite Mater.* **26**, 1287–1309.
- Arnold, S.M. and Wilt, T.E. (1992). Influence of engineered interfaces on residual stresses and mechanical response in metal matrix composites, NASA TM-105438. (Also in *Composite Interfaces* **1**, 381–402.)
- Arridge, R.G.C. (1975). The effect of interlayers on the transverse stresses in fiber composites. *Polym. Eng. Sci.* **15**, 757–760.
- Atkins A.G. (1974). Imparting strength and toughness to brittle composites. *Nature* **252**, 116–118.
- Atkins A.G. (1975). Intermittent bonding for high toughness/high strength composites. *J. Mater. Sci.* **10**, 819–832.
- Atkins A.G. and Mai Y.W. (1976). Effect of water and ice on strength and fracture toughness of intermittently bonded boron-epoxy composites *J. Mater. Sci.* **11**, 2297–2306.
- Bader M.G., Bailey J.E. and Bell I. (1973). The effect of fiber-matrix interface strength on the impact and fracture properties of carbon fiber-reinforced epoxy resin composites. *J. Phys. D: Appl. Phys.* **6**, 572–586.
- Bailey W.J., Sun R.L., Katsuki H., Endo T., Iwama I., Tsushima R., Saigo K. and Bitritto M.M. (1977). Ring opening polymerization. In *Proc. Am. Chem. Soc. Symp.* (T. Saegusa and M. Goethals, eds.), p. 38.
- Bannister, D.J., Andrews, M.C., Cervenka, A.J. and Young, R.J. (1995). Analysis of the single fiber pull-out test by means of Raman spectroscopy, Part II. Micromechanics of deformation for an aramid/epoxy system. *Composites Sci. Technol.* **53**, 411–421.
- Barnes, J.A., Simms, I.J., Farrow, G.J., Jackson, D., Wostenholm, G. and Yates, B. (1991). Thermal expansion characteristics of PEEK composites. *J. Mater. Sci.* **26**, 2259–2271.
- Barnes, J.A. and Byerly, G.E. (1994). The formation of residual stresses in laminated thermoplastic composites. *Composites Sci. Technol.* **51**, 479–494.

- Beaumont P.W.R. and Phillips D.C. (1972). The fracture energy of glass fiber composites. *J. Mater. Sci.* **7**, 682–686.
- Bell J.P., Chang J., Rhee H.W. and Joseph R. (1987). Application of ductile polymeric coatings onto graphite fibers. *Polym. Composites* **8**, 46–52.
- Benatar, A. and Gutowski, T.G. (1986). Effects of moisture on interface modified graphite epoxy composites. *Polym. Composites* **7**, 84–90.
- Beneveniste, Y., Dvorak, G.J. and Chen, T. (1989). Stress fields in composite with coated inclusions. *Mech. Mater.* **7**, 305–317.
- Bowles, D.E. and Griffin, O.H. (1991a). Micromechanics analysis of space simulated thermal stresses in composites, part I: Theory and unidirectional laminates. *J. Reinforced Plast. Composites* **10**, 504–521.
- Bowles, D.E. and Griffin, O.H. (1991b). Micromechanics analysis of space simulated thermal stresses in composites, part II: Multidirectional laminates and failure predictions. *J. Reinforced Plast. Composites* **10**, 522–539.
- Broutman, L.J. and Agarwal, B.D. (1974). A theoretical study of the effect of an interface layer on the properties of composites. *Polym. Eng. Sci.* **14**, 581–588.
- Bucknall, C.B., Partridge, I.K. and Phillips, M.J. (1991). Mechanics of shrinkage control in polyester resins containing low-profile additives. *Polymer* **32**, 636–640.
- Bucknall, C.B., Partridge, I.K. and Phillips, M.J. (1991). Mechanics of shrinkage control in polyester resins containing low-profile additives. *Polymer* **32**, 636–640.
- Caruso, J.J., Chamis, C.C. and Brown, H.C. (1990). Parametric studies to determine the effect of compliant layers on metal matrix composite system. NASA TM-102465.
- Chamis, C.C. (1971). Lamination residual stresses in cross-ply fiber composites. NASA TM X-52881.
- Chapman, T.J., Gillespie, J.W. and Pipes, R.B. (1990). Prediction of process-induced residual stresses in thermoplastic composites. *J. Composite Mater.* **24**, 616–643.
- Chawla, K.K. (1993). Ceramic Matrix Composites, Chapman & Hall, London.
- Chou, T.W., Kelly, A. and Okura, A. (1985). Fiber reinforced metal matrix composites. *Composites*, **16**, 187–206
- Christensen, R.M. (1979). Effective moduli of cylindrical and lamellar system. In *Mechanics of Composite Materials*, J Wiley, New York, pp. 73–105.
- Cook J. and Gordon J.E. (1964). A mechanism for the control of crack propagation in all-brittle systems. *Proc. Roy. Soc. Lond. A* **282**, 508–520.
- Cooper G.A. and Kelly A. (1967). Tensile properties of fiber-reinforced metals: Fracture mechanics. *J. Mech. Phys. Solids* **15**, 279–297.
- Craddock, J.N. and Savides, I.S. (1994). Modeling elastic-plastic behavior of metal matrix composites with reaction zones under longitudinal tension. *Int. J. Damage Mech.* **3**, 308–311.
- Crasto, A.S., Own, S.H. and Subramanian, R.V. (1988). The influence of the interphase on composite properties: Poly(ethylene-co-acrylic acid) and poly(methyl vinyl ether-co-maleic anhydride) electrodeposited on graphite fibers. *Polym. Composites* **9**, 78–92.
- Crasto, A.S. and Kim, R.Y. (1993). On the determination of residual stresses in fiber-reinforced thermoset composites. *J. Reinforced Plast. Composites*, **12**, 545–558.
- Daabin, A., Gamble, A.J. and Sumner, N.D. (1992). The effect of the interphase and material properties on load transfer in fiber composites. *Composites* **23**, 210–214.
- Daniel, I.M. and Durelli (1962). Shrinkage stresses around rigid inclusions. *Exper. Mech.* **2**, 240–255.
- Daoust, J. Vu-Khanh, T., Ahlstrom, C. and Gerard, J.F. (1993). A finite element model of the fragmentation test for the case of a coated fiber. *Composites Sci. Technol.* **48**, 143–149.
- Dauksys R.J. (1973). Graphite fiber treatments which affect fiber surface morphology and epoxy bonding characteristics. *J. Adhesion* **5**, 211–244.
- de Kok, J.M.M. (1995). Deformation, Yield and Fracture of Unidirectional Composites in Transverse Loading. Ph.D. Thesis, Eindhoven University of Technology, The Netherlands.
- Di Anselmo, A., Accorsi, M.L. and Di Benedetto, A.T. (1992). The effect of an interphase on the stress and energy distribution in an embedded single fiber test. *Composites Sci. Technol.* **44**, 215–225.
- Doghri, H., Jansson, S., Leckie, F.A. and Lemaitre (1990). Optimization of interface layers in the design of ceramic fiber reinforced metal matrix composites. NASA CR-185307.
- Doner, D.R., and Novak, R. C. (1969). Structural behaviour of laminates graphite filament composites. In *Proc. 24th Annual Tech. Conf. Reinforced Plast. Composites*, SPI. Paper 2-D.

- Dugdale, D.S. (1968). Elements of Elasticity. Pergamon Press, Oxford.
- Duvis, T., Papaspyrides, C.D. and Skourlis, T. (1993). Polyamide coating on carbon fibers and potential application in carbon/Kevlar/epoxy hybrid composites. *Composites Sci. Technol.* **48**, 127–133.
- Fan, C.F. and Hsu, S.L. (1992). A study of stress distribution in model composite by finite-element analysis. II fiber/matrix interfacial effects. *J. Polym. Sci. Part B: Polym. Physics* **30**, 619–635.
- Favre J.P. (1977). Improving the fracture energy of carbon fiber reinforced plastics by delamination promoters. *J. Mater. Sci.* **12**, 43–50.
- Favre J.P. (1988). Residual thermal stresses in fiber reinforced composite materials – A review. *J. Mech. Behaviour of Mater.* **1**, 37–53.
- Fila M. Bredin C. and Piggott M.R. (1972). Work of fracture of fiber-reinforced polymers. *J. Mater. Sci.* **7**, 983–988.
- Galiotis C., Melanitis, N., Batchelder D.N., Robinson I.M. and Peacock J.A. (1988). Residual strain mapping in carbon fiber PEEK composites. *Composites* **19**, 321–324.
- Galiotis C., Young, R.J., Yeung, P.H.J. Melanitis, N. and Batchelder, D.N. (1984). The study of model polydiacetylene/epoxy composites: part 1. The axial strain in the fiber. *J. Mater. Sci.* **19**, 3640–3648.
- Gao, Z.J. (1993). Effect of fiber-matrix interfacial shear strength on reliability of composite materials. *Composite Interfaces* **1**, 481–497.
- Gardener, S.D., Pittman, C.U. and Hackett, R.M. (1993a). Residual thermal stresses in filamentary polymer-matrix composite materials incorporating an elastomeric interphase: A mathematical assessment. *Composites Sci. Technol.* **46**, 307–318.
- Gardener, S.D., Pittman, C.U. and Hackett, R.M. (1993b). Residual thermal stresses in filamentary polymer-matrix composites containing elastomeric interphase. *J. Composite Mater.* **27**, 830–860.
- Garg A.C. and Mai Y.W. (1988a). Failure mechanisms in toughened epoxy resin – A review. *Composites Sci. Technol.* **31**, 179–223.
- Garg A.C. and Mai Y.W. (1988b). Failure prediction in toughened epoxy resins. *Composites Sci. Technol.* **31**, 225–242.
- Gatti A., Mullin J.V. and Berry J.M. (1969). The role of bond strength in the fracture of advanced filament reinforced composites. In *Composite Materials: Testing and Design*, ASTM STP 460, ASTM, Philadelphia, PA, pp. 573–582.
- Gerard J.F. (1988). Characterization and role of an elastomeric interphase on carbon fibers reinforcing an epoxy matrix. *Polym. Eng. Sci.* **28**, 173–190.
- Ghosh, L. and Lerch, B.A. (1989). Optimum interface properties for metal matrix composites. NASA TM-102295.
- Hancox N.L. (1981). *Fiber Composite Hybrid Materials*, Appl. Sci. Pub., London.
- Hancox N.L. and Wells H. (1977). The effects of fiber surface coatings on the mechanical properties of CFRP. *Fiber Sci. Technol.* **10**, 9–22.
- Harris B., Beaumont P.W.R. and Moncunill de Ferran E. (1971). Strength and fracture toughness of carbon fiber polyester composites. *J. Mater. Sci.* **6**, 238–251.
- Harris, B. (1978). Shrinkage stresses in glass/resin composites. *J. Mater. Sci.* **13**, 173–177.
- Harris B. (1980). Micromechanisms of crack extension in composites. *Metal Sci.* **14**, 351–362.
- He, P., Zhou Z., Pan, C. and Wu, R.J. (1989). An epoxy resin copolymer with zero shrinkage: part 1. Volume change on cure. *J. Mater. Sci.* **24**, 1528–1532.
- Hiemstra, D.L. and Sottos, N.R. (1993). Thermally induced interfacial microcracking in polymer matrix composites. *J. Composite Mater.* **27**, 1030–1051.
- Ho, H. and Drzal, L.T. (1995a). Non-linear numerical study of the single fiber fragmentation test. part I. Test mechanics. *Composites Eng.* **5**, 1231–1244.
- Ho, H. and Drzal, L.T. (1995b). Non-linear numerical study of the single fiber fragmentation test. part II. Parametric study. *Composites Eng.* **5**, 1245–1259.
- Hsueh, C.H., Becher, P.F. and Angelini, P. (1988). Effects of interfacial films on thermal stresses in whisker-reinforced ceramics. *J. Am. Ceram. Soc.* **71**, 929–933.
- Hughes, J.F. (1984). Electrostatic Powder Coating. Research Studies Press, Letchworth, UK.
- Hull, D. (1981). *An Introduction to Composite Materials*, Cambridge University Press, Cambridge, pp. 81–101.
- Iler, R.K. (1966). Multilayers of colloidal particles. *J. Colloid. Interface Sci.* **21**, 569–594.

- Ishikawa, T., Fukunaga, H. and Ono, K.I. (1989). Graphite–epoxy laminates with almost null coefficient of thermal expansion under a wide range of temperature. *J. Mater. Sci.* **24**, 2011–2017.
- Jahankhani H. and Galiotis C. (1991). Shear stress distribution in model composites. Part I. A Kevlar 49 fiber in an epoxy matrix. *J. Composite Mater.* **25**, 609–631.
- Jang B.Z., Lieu Y.K., Chung W.C. and Hwang L.R. (1987). Controlled energy dissipation in fibrous composites, I. Controlled delamination. *Polym. Composites* **8**, 94–102.
- Jansson, S. and Leckie, F.A. (1992). Reduction of thermal stresses in continuous fiber reinforced metal matrix composites with interface layer. *J. Composite Mater.* **26**, 1474–1486.
- Jao, S.H. and McGarry, F.J. (1992a) On the failure work and modulus of composites reinforced by thin elastomer-coated fibers. *J. Composite Mater.* **26**, 2632–2654.
- Jao, S.H. and McGarry, F.J. (1992b). Interphase bond strength and energy absorption of injection-molded rubber coated glass/nylon composites. *J. Reinforced Plast. Composite* **11**, 811–835.
- Jayaraman, K. and Reifsnider, K.L. (1992). Residual stresses in a composite with continuously varying Young's modulus in the fiber/matrix interphase. *J. Composite Mater.* **26**, 770–791.
- Jayaraman, K. and Reifsnider, K.L. (1993). The interphase in unidirectional fiber reinforced epoxies: effect on residual thermal stresses. *Composites Sci. Technol.* **47**, 119–129.
- Jayaraman, K.L., Reifsnider, K.L. and Swain, R.E. (1993). Elastic and thermal effects in the interphase: Part II. Comments on modelling studies. *J. Composite Technol. Res. (JCTRE)* **15**, 14–22.
- Jea L.C. and Felbeck D.K. (1980). Increased fracture toughness of graphite epoxy composites through intermittent interlaminar bonding. *J. Composite Mater.* **15**, 245–159.
- Jero, P.D. and Kerans, R.J. (1991). Effect of interfacial roughness on the frictional stress measured using push-out tests. *J. Am. Ceram. Soc.* **74**, 2793–2801.
- Jeronimidis, G. and Parkyn, A. (1988). Residual stresses in carbon fiber-thermoplastic matrix laminates. *J. Composite Mater.* **22**, 401–415.
- Jones, F.R. (1994). Laminates-residual thermal and related stresses. In *Handbook of Polymer Fiber Composites* (F.R. Jones, ed.), Longman Scientific & Technical, Essex, England, pp. 254–260.
- Jun, W.J. and Hong C.S. (1990). Effects of residual shear strain on the cured shape of asymmetric cross-ply thin laminates. *Composites Sci. Technol.* **38**, 55–67.
- Kardos J.L. (1981). Strength of oriented short fiber reinforced plastics. In *Proc. 36th Annual Tech Conf. Reinforced Plast. Composites*, SPI, Paper 2E.
- Kelly A. (1970). Interface effects and the work of fracture of a fibrous composites. *Proc. Roy. Soc. Lond. A* **319**, 95–116.
- Keran, R.J. and Parthasarathy, T.A. (1991). Theoretical analysis of the fiber pull-out and push-out tests. *J. Am. Ceram. Soc.* **74**, 1585–1596.
- Kim, J.K. and Mai, Y.W. (1991a). High strength, high fracture toughness fiber composites with interface control – A review. *Composites Sci. Technol.* **41**, 333–378.
- Kim, J.K. and Mai, Y.W. (1991b). The effect of interfacial coating and temperature on the fracture behaviours of unidirectional KFRP and CFRP. *J. Mater. Sci.* **26**, 4701–4720.
- Kim, J.K. and Mai, Y.W. (1993a). Interfaces in Composites. Ch. 6 in *Materials Science and Technology: Vol. 13 - Structure and Properties of Fiber Composites* (T.W. Chou ed.), VCH, Weinheim, Germany, Ch. 6, pp. 229–289.
- Kim, J.K. and Mai, Y.W. (1993b). Fracture of CFRP containing impregnated fiber bundles. *Composites Sci. Technol.* **49**, 51–60.
- Kim, J.K. and Mai, Y.W. (1996a). Micromechanics of fiber–matrix interface and fracture of advanced composites with engineered interfaces. In *Fracture Mechanics: 25th Volume. ASTM STP 1220* (F. Erdogan and R.J. Hartranft, eds.), ASTM, Philadelphia, PA, pp. 125–139.
- Kim, J.K. and Mai, Y.W. (1996b). Modelling of stress transfer across the fiber–matrix interface. In *Numerical Analysis and Modelling of Composite Materials*. (J. Bull ed.), Blackie Academic & Professional, Glasgow, Ch. 10, pp. 287–326.
- Kim, J.K., Mai, Y.W. and Kennedy, B.J. (1992). Surface analysis of carbon fibers modified with PVAL coating and the composite interfaces. *J. Mater. Sci.* **27**, 6811–6816.
- Kim, J.K., Zhou, L.M. and Mai, Y.W. (1994a). Techniques for Studying Composite Interfaces. In *Handbook of Advanced Materials Testing* (N.P. Cheremisinoff ed.), Marcel Dekker, New York, 1994, pp. 327–366.

- Kim, J.K., Zhou, L.M. Bryan, S.J. and Mai, Y.W. (1994b). Effect of fiber volume fraction on the stress transfer in fiber pull-out tests. *Composites* **25**, 470–475.
- Kim, J.K., Lu, S.V. and Mai, Y.W. (1994c). Interfacial debonding and fiber pull-out stresses: Part IV. Influence of interface layer on the stress transfer. *J. Mater. Sci.* **29**, 554–561.
- Kim, K.S. and Hahn, H.T. (1989). Residual stress development during processing of graphite/epoxy composites. *Composites Sci. Technol.* **36**, 121–132.
- Kim, K.S., Hahn, H.T. and Croman, R.B. (1989). The effect of cooling rate on residual stress in a thermoplastic composite. *J. Composites Technol. Res.* **11**, 47–52.
- Kinloch, A.J. (1993). *Toughened Plastics I: Science and Engineering*. American Chemical Society, Washington D.C.
- Koufopoulos T. and Theocaris P.S. (1969). Shrinkage stresses in two-phase materials. *J. Composite Mater.* **3**, 308–320.
- Kuntz, M., Meier, B. and Grathwohl, G. (1993). Residual stresses in fiber-reinforced ceramics due to thermal expansion mismatch. *J. Am. Ceram. Soc.* **76**, 2607–2612.
- Labronici, M. and Ishida, H. (1994). Toughening composites by fiber coating: A review. *Composite Interfaces* **2**, 199–234.
- Lam P.K. and Piggott M.R. (1989a). The durability of controlled matrix shrinkage composites: Part 1. Mechanical properties of resin matrices and their composites. *J. Mater. Sci.* **24**, 4068–4075.
- Lam P.K. and Piggott M.R. (1989b). The durability of controlled matrix shrinkage composites: Part 2. Properties of carbon fiber–epoxy copolymer pultrusion. *J. Mater. Sci.* **24**, 4427–4431.
- Lam P.K. and Piggott M.R. (1990). The durability of controlled matrix shrinkage composites: part 3. Measurement of damage during fatigue. *J. Mater. Sci.* **25**, 1197–1202.
- Lhotellier, F.C. and Brinson, H.F. (1988). Matrix fiber stress transfer in composite materials: elastoplastic model with an interphase layer. *Composite Structures* **10**, 281–301.
- Lim J.T., Piggott M.R. and Bailey W.J. (1984). Toughness of fiber composites with controlled matrix shrinkage. *SAMPE Quarterly* **15**, 25–30.
- Low, B.Y., Gardener, S.D., Pittman, C.U. and Hackett, R.M. (1994). A micromechanical characterization of graphite fiber/epoxy composites containing a heterogeneous interphase region. *Composites Sci. Technol.* **52**, 589–606.
- Low, B.Y., Anderson, K.L., Vincent, M., Gardener, S.D., Pittman, C.U. and Hackett, R.M. (1995a). Toughened carbon fiber/epoxy composites: the relative influence of an elastomer interphase and elastomer dispersed in the matrix. *Composites Eng.* **5**, 437–457.
- Low, B.Y., Gardener, S.D., Pittman, C.U. and Hackett, R.M. (1995b). A micromechanical characterization of residual thermal stresses in carbon fiber/epoxy composites containing a non-uniform interphase region. *Composites Eng.* **5**, 375–396.
- Mai Y.W. (1983). Controlled interfacial bonding on the strength and fracture toughness of Kevlar and carbon fiber composites. *J. Mater. Sci. Lett.* **2**, 723–725.
- Mai Y.W. (1988). Controlled interfacial bonding on the residual strength of fatigue-damaged carbon fiber–epoxy composites. *J. Mater. Sci. Lett.* **7**, 581–582.
- Mai Y.W. and Castino F. (1984). Fracture toughness of Kevlar–epoxy composites with controlled interfacial bonding. *J. Mater. Sci.* **19**, 1638–1655.
- Mai Y.W. and Castino F. (1985). The debonding and pull-out properties of coated Kevlar fibers from an epoxy resin matrix. *J. Mater. Sci. Lett.* **4**, 505–508.
- Mai Y.W., Cotterell B. and Lord R. (1982a). On fiber composites with intermittent interlaminar bonding. In *Proc. ICCM-IV, Progress in science and Engineering of Composites* (T. Hayashi et al., eds.), North-Holland Pub. Amsterdam, pp. 271–277.
- Mai Y.W., Hakeem M. and Cotterell B. (1982b). Imparting fracture resistance to cement mortar by intermittent interlaminar bonding. *Cement Concrete Res.* **12**, 661–663.
- Marloff, R.H. and Daniel, I.M. (1969). Three dimensional photoelastic analysis of a fiber reinforced composite model. *Exp. Mech.* **9**, 156–162.
- Marom, G. and Arridge, G.C. (1976). Stress concentration and transverse modes of failure in composites with a soft fiber–matrix interlayer. *Mater. Sci. Eng.* **23**, 23–32.
- Marston T.U., Atkins A.G. and Felbeck D.K. (1974). Interfacial fracture energy and the toughness of composite. *J. Mater. Sci.* **9**, 447–455.
- Mascia, L. (1989). *Thermoplastics: Materials Engineering*. Elsevier Appl. Sci., London.

- Mascia, L., Dhillon, J. and Harper, J. (1993). Adhesion enhancement of rubbery and ductile polyolefin coatings on glass fibers for epoxy composites and effects on failure mechanisms. *J. Appl. Polym. Sci.* **47**, 487–498.
- Metcalf, A.G. (1974). *Interfaces in Metal Matrix Composites*, Composite Materials, Vol. 1. Academic Press, New York.
- Metcalf, A.G. and Schmitz G.K. (1964). *ASTM Proc.* **64**, 1075.
- Misra, A. (1991). Chemical compatibility issues related to the use of copper as an interfacial layer for SiC fiber reinforced Ti₃Al + Nb composite. NASA CR-187100.
- Mitaka, Y. (1994). Stress field in a continuous fiber composite with a variable interphase under thermo-mechanical loadings. *J. Eng. Mater. Technol.* **116**, 367–377.
- Mitaka, Y. and Taya, M. (1985a). Stress field in a coated continuous fiber composite subjected to thermo-mechanical loadings. *J. Composite Mater.* **19**, 554–578.
- Mitaka, Y. and Taya, M. (1985b). Stress field in and around a coated short fiber in an infinite matrix subjected to uniaxial and biaxial loadings. *J. Appl. Mech.* **52**, 19–24.
- Mitaka, Y. and Taya, M. (1986). Thermal stress in a coated short fiber composites. *J. Appl. Mech.* **53**, 681–689.
- Mital, S.K., Murthy, P.L.N. and Chamis, C.C. (1993). Interfacial microfracture in high temperature metal matrix composite. *J. Composite Mater.* **27**, 1678–1694.
- Morel, M., Saravanos, A. and Chamis, C.C. (1991). Interphase layer optimization for metal matrix composites with fabrication consideration. NASA TM-105166.
- Mullin J.V., Berry J.M. and Gatti A. (1968). Some fundamental fracture mechanisms applicable to advanced filament reinforced composites. *J. Composite Mater.* **2**, 82–103.
- Mullin J.V. and Mazzio V.F. (1972). The effects of matrix and interface modification on local fractures of carbon fibers in epoxy. *J. Mech. Phys. Solids* **20**, 391–400.
- Nairn, J.A. (1985). Thermoelastic analysis of residual stresses in unidirectional high-performance composites. *Polym. Composites* **6**, 123–130.
- Novak R.C. (1969). Fracture in graphite filament reinforced epoxy loaded in shear. In *Composite Materials: Testing and Design*, ASTM STP 460, ASTM, Philadelphia, PA, pp. 540–549.
- Ochi, M., Yamazaki, K. and Shimbo, M. (1989). Internal stress of epoxide resin modified with spiro ortho-ester type resin: part 2. Relation between internal stress and phase structure. *J. Mater. Sci.* **24**, 3189–3195.
- Pagano, N.J. and Tandon, G.P. (1988). Elastic response of multi-directional coated fiber composites. *Composite Sci. Technol.* **31**, 273–293.
- Pagano, N.J. and Tandon, G.P. (1990). Thermo-elastic model for multidirectional coated fiber composites: Traction formulation. *Composites Sci. Technol.* **38**, 247–269.
- Patrikis, A.K., Andrews, M.C. and Young, R.J. (1994). Analysis of the single fiber pull-out test by the use of Raman spectroscopy: part I: Pull-out of aramid fibers from an epoxy resin. *Composites Sci. Technol.* **52**, 387–396.
- Peiffer D.G. (1979). Impact strength of thick interlayer composites. *J. Appl. Polym. Sci.* **24**, 1451–1455.
- Peiffer D.G. and Nielsen L.E. (1979). Preparation and mechanical properties of thick interlayer composites. *J. Appl. Polym. Sci.* **23**, 2253–2264.
- Piggott M.R. (1970). Theoretical estimation of fracture toughness of fibrous composites, *J. Mater. Sci.* **5**, 669–675.
- Piggott M.R. (1981). Fiber length-strength relationships and the fracture of composites. In *Proc. 5th International Conf. Fracture (ICF-5)*, pp. 465–472.
- Piggott M.R., Lam P.K., Lim J.T. and Woo M.S. (1985). The internal pressure, mechanical properties and water absorption of carbon fiber composites with spiro-epoxy copolymer matrices. *Composites Sci. Technol.* **23**, 247–262.
- Piggott, M.G. and Woo, M.S. (1986). Fiber composites with internal stresses under control. *Polym. Composites* **7**, 182–185.
- Popejoy, D.B. and Dharani, L.R. (1992). Effect of fiber coating and interfacial debonding on crack growth in fiber-reinforced composite. *Theor. Appl. Fract. Mech.* **18**, 73–79.
- Porter, D.L. and Heuer, A.H. (1977). Mechanisms of toughening partially stabilized zirconia (PSZ). *J. Am. Ceram. Soc.* **60**, 183–184.

- Rhee, H.W. and Bell, J.P. (1991). Effects of reactive and non-reactive fiber coatings upon performance of graphite/epoxy composites. *Polym. Composites* **12**, 213–225.
- Rodriguez, E.L. (1989). Microdelamination due to resin shrinkage in filament-wound fiberglass composites. *J. Mater. Sci. Lett.* **8**, 116–118.
- Rohwer, K. and Jiu, X.M. (1986). Micromechanical curing stresses in CFRP. *Composites Sci. Technol.* **25**, 169–186.
- Schapery, R.A. (1968). Thermal expansion coefficients of composite materials based on energy principles. *J. Composite Mater.* **2**, 380–404.
- Shelton, C.G. and Marks, P.R. (1988). Failure of ductile interlayer composites: High resolution X-radiographic examination having an opaque penetrant. *J. Mater. Sci. Lett.* **7**, 673–675.
- Shimbo, M., Ochi, M., Inamura, T. and Inoue, M. (1985). Internal stress of epoxide resin modified with spiro ortho-ester type resin. *J. Mater. Sci.* **20**, 2965–2972.
- Sideridis, E. (1994). Thermal expansion coefficients of fiber composites defined by the concept of the interphase. *Composites Sci. Technol.* **51**, 301–317.
- Sikes, A.M., Brady, R.F. (1990). Controlled shrinkage polymers: Characterization of epoxy resins cured with spirobis lactones. *J. Polym. Sci. Part A: Polym. Chemistry* **28**, 2533–2546.
- Skourlis, T., Duvis, T. and Papaspyrides, C.D. (1993). The role of polyamide interphase on carbon fibers reinforcing an epoxy matrix. *Composites Sci. Technol.* **48**, 119–125.
- Subramanian R.V. and Crasto A.S. (1986). Electrodeposition of a polymer interphase in carbon fiber composites. *Polym. Composites* **7**, 201–218.
- Subramanian, R.V., Jakubowski, J.J. (1978). Electro-polymerization on graphite fibers. *Polym. Eng. Sci.* **18**, 590–600.
- Sung N.H., Jones T.J. and Suh N.P. (1977). Strain-rate sensitive tough fiber reinforced composites. *J. Mater. Sci.* **12**, 239–250.
- Tandon, G.P. and Chatterjee, A. (1991). The transverse coefficient of thermal expansion of a unidirectional composite. *J. Mater. Sci.* **26**, 2759–2764.
- Taya, M. and Arsenault, R.J. (1989). *Metal Matrix Composites-Thermomechanical Behavior*, Pergamon Press, Oxford.
- Tetelman A.S. (1969). Fracture process in fiber composite materials. In *Composite Materials: Testing and Design*, ASTM STP 460, ASTM, Philadelphia, PA, pp.473–502.
- Theocaris, P.S. (1984). On the evaluation of adhesion between phases in fiber composites. *Colloid Polym. Sci.* **262**, 929–938.
- Theocaris, P.S. and Demarkos, C.B. (1992). The influence of the elastic properties and dimensions of coatings on the stiffness of encapsulated fiber composites. *Composites Sci. Technol.* **45**, 293–305.
- Tiegs, T.N., Becher, P.F. and Harris, L.A. (1987). The interfaces in alumina-SiC whisker composites. In *Ceramic Microstructures '86, The Role of Interfaces, Materials Science Research*, Vol. 21 (J.A. Pask and A.G. Evans, eds.), Plenum Press, New York, pp. 911–917.
- Tomlinson, W.J. and Barnes, J.A. (1992). Fiber coatings and the mechanical properties of carbon fiber/nylon 6 composites. *J. Mater. Sci. Lett.* **11**, 440–442.
- Tuinstra F. and Koenig J.L. (1970). Characterization of graphite fiber surfaces with Raman spectroscopy. *J. Composite Mater.* **4**, 492–499.
- Van Fo Fy, G.A. (1967). A study of the effect of fiber treatment on stress distribution in glass-reinforced plastic structures. *Prikladnaya Mekanika* **3**, 106–112.
- Vedula, M., Pangborn, R.N. and Queeney, R.A. (1988). Modification of residual thermal stress in a metal matrix composite with the use of a tailored interfacial region. *Composites* **19**, 133–137.
- Walpole, L.J. (1978). A coated inclusion in an elastic medium. *Math. Proc. Camb. Phil. Soc.* **83**, 495–506.
- Waas, A.M. (1992). Effect of interphase on compressive strength of unidirectional composites. *J. Appl. Mech.* **59**, S183–S188.
- Wells J.K. and Beaumont P.W.R. (1985). Crack tip energy absorption processes in fiber composites. *J. Mater. Sci.* **20**, 2735–2794.
- Wicks, J.W., Jones, F.N. and Pappas, S.P. (1992). *Organic Coatings: Science and Technology*, Vol. 2. Applications, Properties and Performances. J Wiley, New York.
- Williams J.H. and Kousiounelos P.N. (1978). Thermoplastic fiber coatings enhance composites strength and toughness. *Fiber Sci. Technol.* **11**, 83–88.

- Wimolkiatisak A.S. and Bell J.P. (1989). Interfacial shear strength and failure modes of interphase modified graphite-epoxy composites. *Polym. Composites* **10**, 162-172.
- Young R.J., Day R.J. Zakikhani M. and Robinson I.M. (1989). Fiber deformation and residual thermal stresses in carbon fiber reinforced PEEK. *Composites Sci. Technol.* **34**, 243-258.
- Zhang, W. (1993). Computation of stress fields in unidirectional n-phase fibrous composite under longitudinal and transverse loads. *Comput. Structures* **34**, 647-653.

Chapter 8

IMPROVEMENT OF INTERLAMINAR FRACTURE TOUGHNESS WITH INTERFACE CONTROL

8.1. Introduction

The superior specific modulus and specific strength along with other unique properties as well as manufacturing advantages and design freedom offered by fine diameter fibers have made polymer matrix composites ideally suited to weight critical applications. Composites are produced normally in the form of layers or laminates which are extremely susceptible to crack initiation and growth preferentially along the laminar interfaces in various failure modes (Kim and Mai, 1991). As reiterated in Section 3.4, delamination is the most prevalent life-limiting crack growth mode in laminate composites. When subjected to complex three-dimensional load paths, delamination may cause severe reduction in in-plane modulus and strength which can possibly lead to catastrophic failure of the whole structure. It has been shown that delamination may be introduced due to the external loading, whether in static tension and bending, in cyclic fatigue or by low-velocity and low-energy impact, during manufacturing and in service. Potential delamination sites are locations with discontinuities in the load path (see Fig. 3.28). These discontinuities give rise to interlaminar stresses even under in-plane loading (Wilkins, 1983).

Much attention has been directed toward fundamental understanding of the root causes and the corresponding failure mechanisms of delamination which are specific to different combinations of fiber and matrix materials and interface characteristics. A number of experimental techniques have also been developed to characterize the interlaminar fracture toughness of various modes (see Section 3.4). Many techniques have been devised to combat the problem of delamination. These techniques involve either material improvement or fiber architecture modification. Material improvement requires the enhancement of fracture toughness of matrix material and fiber-matrix interface bonding because delamination initiates and propagates preferentially in the matrix material and interface region. The use of tough matrix materials, typically rubber-toughened epoxies and high performance engineering thermoplastics have been studied extensively. The interleaving technique is also shown to be very promising where soft, tough strips of adhesive or composite are interleaved

selectively at delamination prone laminar interfaces, particularly at or near free edges. Nevertheless, with an ever-increasing need for large allowable design strains and improved reliability of aerospace structural parts, material improvement alone has proven to be insufficient. Therefore, modification of fiber architecture using through-the-thickness reinforcements has been considered as an alternative solution to the improvement of interlaminar and intralaminar mechanical properties.

In this chapter, the underlying physics and the efficiency of these modifying techniques are critically examined, which have been developed specifically for enhanced interlaminar fracture resistance and damage tolerance of fiber composites. Particular emphasis is placed on the discussion of the advantages achieved and disadvantages induced by the modifications. The property relationships between ductility and toughness of the matrix material, fiber–matrix interface bond strength, composite interlaminar fracture toughness and impact response are specifically discussed.

8.2. Effects of matrix materials on interlaminar fracture resistance

8.2.1. Introduction

The first generation of resins developed for use in high performance carbon fiber composites emphasized high modulus and high glass transition temperature, T_g . Due to the low interlaminar fracture resistance of these resins, in particular under hot and wet conditions, a second generation of matrix materials has been developed with special focus on the resistance to interlaminar fracture of composites.

The development of the second generation resins stems from the early work of McGarry (1969) and Sultan et al. (1971) who found that the fracture toughness of epoxy resins could be improved by adding certain liquid rubber, particularly carboxyl-terminated butadiene acrylonitrile (CTBN) copolymer. In addition to being used as a matrix material for high performance fiber composites, the toughened epoxies have also been used as structural adhesives, tooling compounds, moldings, potting and encapsulating materials.

When epoxy resins are suitably modified to impart optimized composition and microstructure, they possess a balance of desired engineering properties, such as fracture toughness, tensile and flexural strengths and stiffness. Complicated mechanical and fracture properties have been observed for toughened epoxy resins, and significant research efforts have been directed toward disclosing the origins of toughening in these materials. Indebted to many investigators, including especially Bascom et al. (1975), Kinloch and Shaw (1981), Yee and Pearson (1986), various intrinsic (microstructural) and extrinsic (mechanical, thermal and environmental) factors have been identified, which control the fracture properties, deformation and failure processes in toughened epoxies. Besides using rubber as a toughening agent for resins, several inorganic fillers such as alumina, silica, barium titanate, glass beads and aluminum hydroxide have been employed extensively as reinforcements for other applications. Many comprehensive reviews on this topic can be found in

several references (Kinloch and Young, 1986; Kinloch, 1986, 1987; Garg and Mai, 1988a, b; Low and Mai, 1990).

The fracture behavior of toughened polymers, containing rubber or inorganic fillers, may involve several mechanisms, as schematically illustrated in Fig. 8.1 (Garg and Mai, 1988a). These include:

- (1) shear band formation near rubber particle,
- (2) fracture of rubber particle,
- (3) stretching,
- (4) debonding,
- (5) tearing of rubber particles,
- (6) transparticle fracture,
- (7) debonding of hard particle,
- (8) crack deflection by hard particle,
- (9) cavitated or voided rubber particle,
- (10) crazing,
- (11) plastic zone at crack tip,
- (12) diffuse shear yielding,
- (13) shear band/craze interaction.

Several such failure mechanisms may take place simultaneously in a toughened resin, depending on the type of particles, whether liquid rubber or rigid particles, and the matrix material. Each of these mechanisms contributes to the energy absorption of the whole structure.

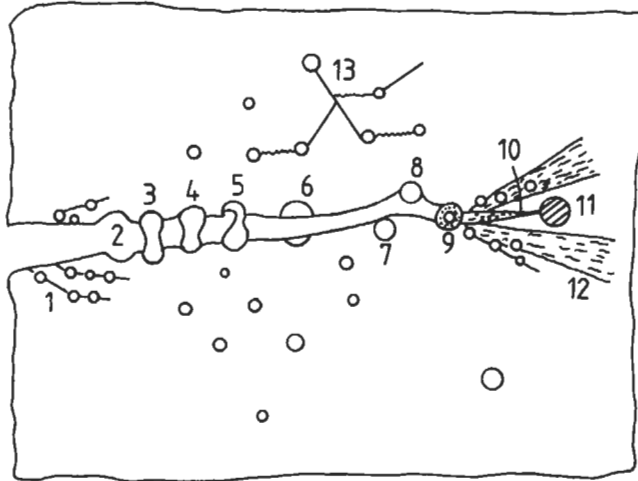


Fig. 8.1. Toughening mechanisms in rubber-modified polymers: (1) shear band formation near rubber particles; (2) fracture of rubber particles after cavitation; (3) stretching, (4) debonding and (5) tearing of rubber particles; (6) transparticle fracture; (7) debonding of hard particles; (8) crack deflection by hard particles; (9) voided/cavitated rubber particles; (10) crazing; (11) plastic zone at craze tip; (12) diffuse shear yielding; (13) shear band/craze interaction. After Garg and Mai (1988a).

8.2.2. Correlations between matrix properties and composite interlaminar properties

Since the development of rubber-toughened epoxy resins, a large volume of information has appeared in the literature, addressing the advantages and drawbacks of these materials as matrices in composites. Carbon fibers of various types have been used as principal reinforcements for composites in aerospace applications. Modification of matrix materials allows the aforementioned failure mechanisms to occur more extensively, which are not present or insignificant in unmodified matrix composites, along with some indirect influences on the fiber-matrix interfacial properties. A comprehensive summary has been presented on the relationship between matrix toughness and composite interlaminar fracture toughness (Bradley, 1989a, b, 1990).

The general observation is that improvement in interlaminar fracture toughness of carbon fiber composites containing such toughened resins has been rather disappointing. Although rubber-modified epoxy shows up to twentyfold increase in fracture toughness of bulk resins, G_{IC}^m , it imparts only a moderate eightfold improvement in mode I interlaminar fracture toughness of composites, G_{IC}^c , with fiber volume fraction V_f greater than 55% (Hunston et al., 1987; Jordan and Bradley, 1987, 1988). This result is in sharp contrast to the fact that for brittle matrices the composite G_{IC}^c is somewhat larger than the resin G_{IC}^m (Hunston et al., 1987). A compilation of the data published for the relationship between the composite mode I interlaminar fracture toughness, G_{IC}^c , and the neat resin fracture toughness, G_{IC}^m , is presented in Fig. 8.2. (Hunston et al., 1987; Russell and Street, 1987; Jordan and Bradley, 1988; Bradley, 1989a; Kim et al., 1992). The composite G_{IC}^c values represent those obtained for the steady-state crack growth rather than for

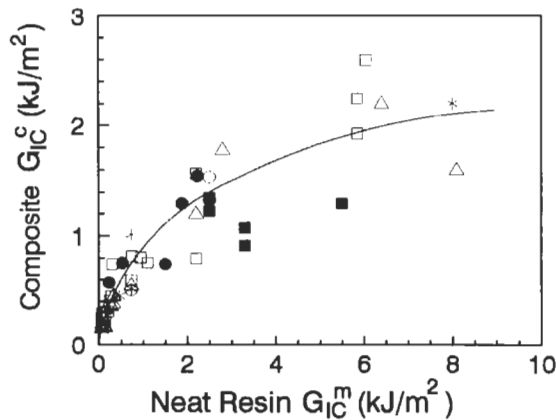


Fig. 8.2. Composite mode I interlaminar fracture toughness, G_{IC}^c , as a function of respective neat resin toughness, G_{IC}^m : (●) Kim et al. (1992); (○) from Russell and Street (1987); (□) toughened thermosets and (■) thermoplastics from Hunston et al. (1987); (Δ) from Bradley (1989a); (*) from Jordan and Bradley (1988).

the crack initiation. Hunston et al. (1987) noted that the composite G_{lc}^c is actually greater than the resin G_{lc}^m for G_{lc}^m values below about 0.5 kJ/m^2 . Further indication from Fig. 8.2 is that as the resin G_{lc}^m increases above this value, the incremental increase in the composite G_{lc}^c is much smaller than the resin G_{lc}^m , and there may be little gain in the composite G_{lc}^c for increase in the resin G_{lc}^m above 2.0 kJ/m^2 . The fact that the composite G_{lc}^c is higher than the resin G_{lc}^m with brittle resins suggests the full development of an intrinsic small plastic deformation zone is possible so that full transfer of the resin G_{lc}^m to the composite can be achieved. In addition, the failure mechanisms, such as interface debonding and fiber bridging, can also contribute significantly to the total energy dissipation in these composites when the matrix materials are brittle (Hunston et al., 1987). For tougher matrices with G_{lc}^m greater than 0.5 kJ/m^2 , the high resin G_{lc}^m is only partly transferred to the composites.

Many investigators have attempted to clarify the relationship between the resin G_{lc}^m and the composite G_{lc}^c with varying degree of success. An established explanation is that for tough resins the poor translation of G_{lc}^m into G_{lc}^c is mainly due to the suppression of the toughening effect in a thin epoxy film between reinforcing fibers which act as rigid fillers and constrain plastic deformation and/or microcracking at the crack tip (Bascom and Cottingham, 1976). This has been confirmed by the strong bond-line thickness dependence of G_{lc}^m in adhesive joints (Scott and Phillips, 1975; Kinloch and Shaw, 1981). Recent work using large deformation finite element analysis carried out by Daghyani et al. (1995a, b, 1996) on rubber-modified epoxies adhesively bonded between two aluminum or carbon fiber composite adherends has confirmed that the adherends impart constraints that have prevented the full toughness of the modified adhesive to be transferred to the joints. The size (or volume) of the crack tip deformation zone can be treated as the ability of the resin to suppress the onset of unstable and rapid crack propagation, which in turn determines the amount of energy dissipated prior to fracture.

Other important parameters for the correlation between G_{lc}^m and G_{lc}^c include the ductility or the failure strain, particularly the non-linear strain (Jordan and Bradley, 1988; Jordan et al., 1989) of the matrix resin, the bond strength of the fiber-matrix interface (Jordan and Bradley, 1987; Bradley 1989a, b), and the fiber V_f and their distributions in the composites (Hunston et al., 1987). A high failure strain promotes the intrinsic capacity of the resin to permit shear deformation, and is shown to increase the G_{lc}^m and G_{lc}^c values almost linearly, the rate of increase being steeper for G_{lc}^m than for G_{lc}^c .

To understand better the relationship between the neat resin fracture toughness and the composite interlaminar fracture toughness, in-situ observations have been made specifically on the crack tip damage zone in interlaminar fracture of carbon fiber composites using scanning electron microscopy (Chakachery and Bradley, 1987; Hibbs et al., 1987). Comparisons between composites containing two different types of epoxy resins with and without rubber modifications, namely T6T145/F155NR ($G_{lc}^m = 167 \text{ J/m}^2$; $G_{lc}^c = 335 \text{ J/m}^2$) and T6T145/F185 ($G_{lc}^m = 6400 \text{ J/m}^2$; $G_{lc}^c = 2000 \text{ J/m}^2$), have been carried out and their major difference in fracture behavior identified in Fig. 8.3. For the unmodified epoxy matrix T6T145/F155NR system, crack extension occurs by void formation in the matrix and interfacial

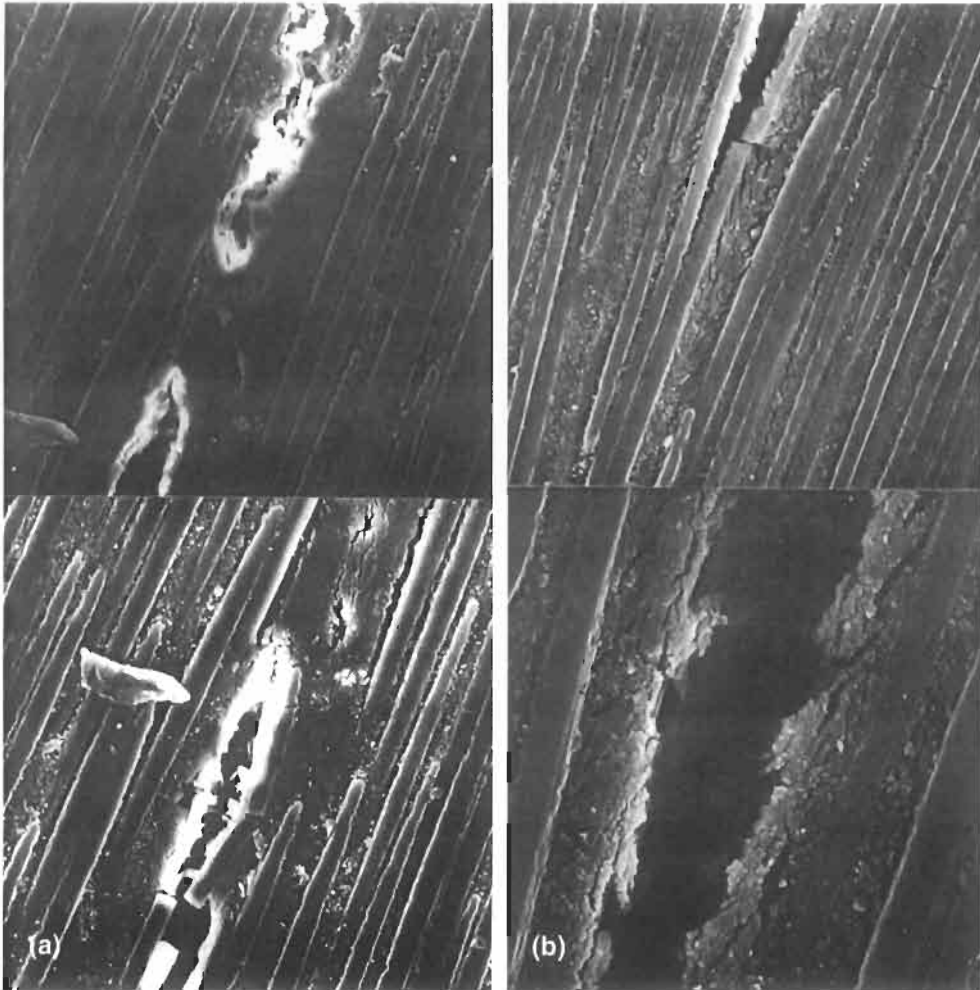
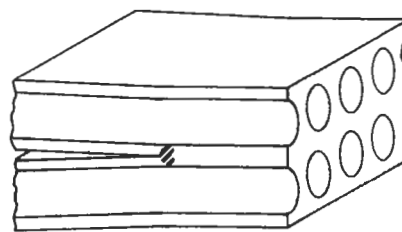


Fig. 8.3. In-situ scanning electron microphotographs of mode I interlaminar fracture of Hexcel T6T145 carbon fiber composites containing (a) F155 unmodified epoxy matrix, and (b) F185 rubber-modified epoxy matrix. Reprinted from Bradley (1989b), with kind permission from Elsevier Science-NL, Sara burger hart straat 25, 1055 KV Amsterdam, The Netherlands.

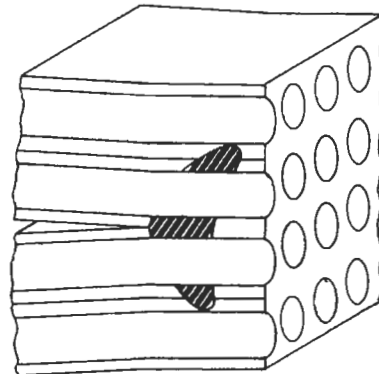
debonding with limited crack tip non-linear deformation both in the transverse and longitudinal directions. In contrast, the deformation zone for the rubber-modified T6T145/F185 system is very large, extending several fiber diameters beyond the resin rich region between plies. It appears that the amount of resin ductility has controlled the degree of crack tip blunting, which in combination with the stress redistribution due to non-linear deformation determine the resistance to crack extension. A strong fiber-matrix interfacial bond is essential to the occurrence of these mechanisms

because the realization of full resistance to delamination provided by the matrix is only possible when the resin deformation is not preempted by interfacial bonding. The crack tip zone sizes in delaminated composites with brittle and ductile matrices are schematically shown in Fig. 8.4, and quantitative data including the corresponding fracture toughness values are given in Table 8.1.

The mode II interlaminar fracture behavior is also very different between the composites with brittle and ductile matrices (Bradley, 1989a; Sue et al., 1993). For the brittle resin system, sigmoidal-shaped microcracks form ahead of the crack tip, and the coalescence of these cracks is much more difficult than that of continuous cracks. The discontinuous crack growth by microcrack coalescence causes the mode II delamination fracture surface to exhibit many hackles, giving rise to a high G_{IIc} value (Hibbs et al., 1987). However, the mode I delamination of brittle resin systems is typified by steady continuous crack propagation. This gives a G_{IIc}/G_{Ic} ratio typically about 3–10. In contrast, for the composites with ductile resins, the fracture process is similar for both mode I and mode II loading, with similar interlaminar fracture toughness values and the G_{IIc}/G_{Ic} ratio is close to unity.



(a) Brittle Resin



(b) Ductile Resin

Fig. 8.4. Schematic illustrations of the formation of a fracture process zone in front of the crack tip for composites containing (a) a brittle resin matrix and (b) a ductile resin matrix. After Bradley and Cohen (1987). Reproduced by permission of ASTM.

Table 8.1

Damage zone size in mode I fracture and corresponding interlaminar fracture toughness values, G_{Ic}^c and G_{IIc}^c , of carbon fiber epoxy matrix composites^a.

System (Fiber/matrix)	V_f (%)	Mode I damage zone size		Fracture toughness (kJ/m^2)		
		ahead of crack (μm)	above/below crack (μm)	G_{Ic}^m	G_{Ic}^c	G_{IIc}^c
AS4/3502	76	20	5	0.07	0.19	0.57
T3T145/F155 NR	54	20	7	0.167	0.335	1.66
T3T145/F155	60	30	20	0.73	1.015	2.06
T3T145/F155	69	20	10	0.73	0.52	1.27
T3T145/F155	71	20	10	0.73	0.615	1.80
T3T145/F185 NR	58	75	35	0.46	0.455	1.05
T3T145/F185	57	200	35	5.0	1.73	2.44

^aAfter Jordan et al. (1989).

V_f , fiber volume fraction; G_{Ic}^m , neat resin fracture toughness; G_{Ic}^c , mode I interlaminar fracture toughness of composite; G_{IIc}^c , mode II interlaminar fracture toughness of composite.

In summary, the mode II composite interlaminar fracture toughness, G_{IIc}^c , is plotted as a function of neat resin toughness, G_{Ic}^m in Fig. 8.5, and the experimental values are given in Table 8.2 with the corresponding mode I interlaminar fracture toughness, G_{Ic}^c . It is clearly seen that the resistance to mode II delamination is an even less sensitive function of neat resin toughness than is the resistance to mode I fracture. This can be explained by the fact that for brittle resin systems, microcracking with hackle formation redistributes, to a certain degree, the load ahead of the crack tip, as for some ductile systems.

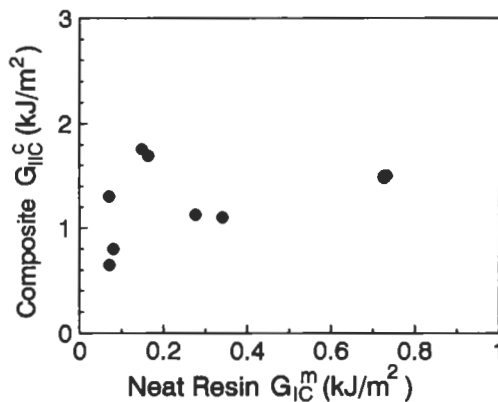


Fig. 8.5. Mode II interlaminar fracture toughness, G_{IIc}^c , as a function of respective neat resin toughness, G_{Ic}^m . After Bradley (1989a).

Table 8.2
Interlaminar fracture toughness of various composite materials^a.

Composite system (fiber/matrix)	Neat resin G_{ic}^m (kJ/m ²)	Mode I G_{ic}^I (kJ/m ²)	Mode II G_{ic}^{II} (kJ/m ²)	G_{IIC}^I/G_{ic}^I
AS4/3501-6	0.07	1.15	8.0	7.0
AS4/Dow P4	0.08	0.8	5.0	6.3
AS4/Dow P6 (Novolac)	0.15	1.75	10.9	6.2
AS4/3502				
T6T145/F155NR	0.07	0.57	3	5.3
T6T145/F155	0.167	1.66	5	3.0
T6T145/F185NR	0.73	1.5	2.7	1.8
T300/BP907	0.34	1.05	2.3	2.2
	0.325			
T6T145/F185				
C6000/HX206	6.4	2.2	1.1	0.5
C6000/HX210	2.2	—	—	—
AS4W6/Lexan	2.8	—	—	—
T6T145/11X205	8.1	1.7	1.06	0.6
	0.34	—	—	—

^aAfter Bradley (1989).

3501-6, 3502, F155NR, F185NR, unmodified epoxies; F155, F185, rubber-modified epoxies; Lexan, polycarbonate.

The effectiveness of the modified matrix on interlaminar fracture toughness is strongly dependent on the fiber–matrix interfacial properties, such as the bond shear strength τ_b , or the interface fracture toughness. It is important to reiterate that the full utilization of the intrinsic toughness of modified resins require a sufficiently strong bond at the fiber–matrix interface so that the resin can be strained to failure before the interface fails (Hibbs et al., 1987; Bradley, 1989a, b). This view is rather different from the beneficial effect of interfacial debonding in brittle matrix composites which may promote fiber bridging of fracture surfaces and thus contribute to the total interlaminar fracture toughness (Hunston et al., 1987). Even in simple compressive or shear loading conditions, the interfacial properties play a decisive role in determining the failure mode during fracture of modified matrix composites (Drzal and Madhukar, 1991), and there is a significant mutual correlation between the properties of the interface and the matrix material (Drzal, 1990). In this regard, the issue of the interface should always be taken into account in the study of matrix modifications.

The local fiber volume fraction, V_f , plays an important role in determining the delamination resistance. The fiber V_f and the distribution across the composite thickness determine the effective thickness of the resin rich region along the crack path, which in turn influences significantly the development of crack tip deformation zone (Kim et al., 1992). Strain energy density (σ_{my}^2/E_m , σ_{my} being the yield strength of the matrix material) and residual stress arising from the matrix shrinkage are also

shown to play an important role for stress distribution at the crack tip which controls the composite G_{Ic}^c (Lee, 1984, 1987).

Addition of rigid fillers along with rubber modification of epoxy resins produce a synergic effect to enhance the interlaminar fracture resistance of carbon fiber composites (Kim et al., 1992). Fig. 8.6 shows the crack growth resistance curves (R-curves) of mode I interlaminar fracture toughness, G_{Ic}^c , for composites containing several different modified matrices, taking into account the residual displacement effect caused by non-elastic deformation. Epoxy resins are modified with combinations of CTBN rubber, Al_2O_3 particles and Al_2O_3 short fibers before being cured with piperidine. The rubber-modified matrix improves the crack growth resistance of the composite about 100% compared to the control. Simultaneous presence of rigid fillers and rubber phase increase the crack growth resistance even further, outperforming the composites with rubber phase only, particularly at large crack extensions. These results have been explained in terms of the compensating effects of rigid fillers (which decrease) and rubber phase (which increases) on the plastic deformation of the matrix material. Toughening mechanisms which occurs in the presence of rigid fillers, such as interfacial debonding and fiber bridging by short Al_2O_3 fibers, pinning by Al_2O_3 particles and increase in fracture surface area due to the irregular crack path, effectively improve the gross crack growth resistance. At the same time, the rigid fillers reduce the matrix non-linear failure strain thus limiting its plastic deformation. However, this loss in toughness is more than compensated by the other toughening mechanisms of the fillers. It is suggested that when both rubber and rigid fillers are present synergism of toughening mechanisms by both these modifiers takes place.

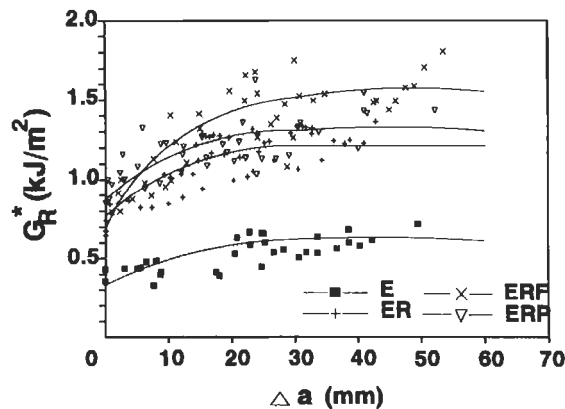


Fig. 8.6. Mode I potential energy release rate, G_R^* , plotted as a function of crack extension, Δa , for carbon fiber composites containing different matrices: E (pure epoxy); ER (rubber-modified epoxy); ERF (short fiber-modified epoxy); ERP (rubber-and particle-modified epoxy). After Kim et al. (1992).

8.2.3. *Impact resistance and tolerance of fiber composites with tough matrices*

Interest in matrix resin fracture toughness in relation to interlaminar fracture toughness of fiber composites is due to their predominant effect on the post-impact residual mechanical properties, particularly the compressive strength-after-impact (CAI), stiffness and fatigue strength. A number of researchers have studied the impact damage resistance and damage tolerance of various thermosets with and without modifications and of thermoplastic resin systems (Williams and Rhodes, 1982; Hirschbuehler, 1987; Evans and Masters, 1987; Sohi et al., 1987; Bowles, 1988; Poon et al., 1990; Recker et al., 1990; Bradley, 1990; Kim et al., 1993; Srinivasan, et al., 1992; Ishikawa et al., 1995). Rubber-modified epoxies in general have better resistance to impact damage than their unmodified counterparts. The CAI test is a standardized test in aerospace industry, which has been developed to characterize the damage tolerance of composite materials. This test has two steps: an impact damaged composite panel is loaded in compression to measure the residual properties. The impact test is largely a mode II high shear rate crack propagation test leading to multiple delamination, while the compression test causes further growth of delamination cracks by macrobuckling in a dominant opening mode I fracture.

Low velocity drop-weight impact tests on laminated panels in the thickness direction have shown that the modified matrix composite system absorbs inelastic energy by a damage process involving delamination and intralaminar transverse shear cracks which produce barely visible impact damage. The characteristic load-displacement records obtained from the test also show that the toughened resin systems absorb much higher elastic energy than unmodified resin systems (Poon et al., 1990). In contrast, for the same input impact energy, unmodified matrix composite systems fails by fiber and matrix fractures which coalesce to form a major through-the-thickness crack with extensive delamination in every ply of the laminate. The damage area is shown to be significantly smaller for the modified resin systems than the baseline epoxy resin system. (Recker et al., 1990; Sohi et al., 1987; Srinivasan, et al., 1992). Fig. 8.7 shows representative C-scan damage area data plotted as a function of impact energy for several different composite systems containing thermosets and thermoplastic resins, clearly indicating the advantages of tough resin systems. Further, the residual CAI strength is also shown to be much higher for the composites with modified epoxies and thermoplastic matrices than the unmodified epoxy system (Hirschbuehler, 1987; Recker et al., 1990; Kim et al., 1993).

One of the most important properties which control the damage tolerance under impact loading and the CAI is the failure strain of the matrix resin (see Fig. 8.8). The matrix failure strain influences the critical transverse strain level at which transverse cracks initiate in shear mode under impact loading, and the resistance to further delamination in predominantly opening mode under subsequent compressive loading (Hirschbuehler, 1987; Evans and Masters, 1987; Masters, 1987a, b; Recker et al., 1990). The CAI of near quasi-isotropic composite laminates which are reinforced with AS-4 carbon fibers of volume fractions in the range of 65–69% has

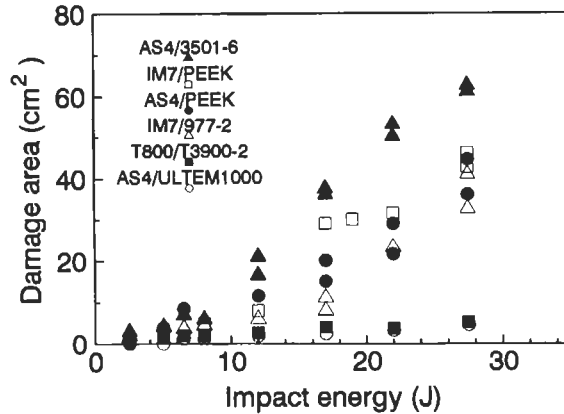


Fig. 8.7. Damage area of 24 ply quasi-isotropic carbon fiber reinforced composite laminates containing different resin matrices. After Srinivasan et al. (1992).

been found to correlate well with the resin toughness G_{Ic}^m (Hirschbuehler, 1987) and the mode I (Masters, 1987a, b) and mode II (Recker et al., 1990) interlaminar fracture toughness of composites. Interestingly enough, all these properties are shown to be approximately linearly proportional to the CAI, as evidenced in Figs. 8.9 and 8.10. Also superimposed in these figures are the results obtained from the laminates containing interleave films as delamination resisters (see Section 8.3). Rubber-modified epoxy resins also have better retainability of stiffness than unmodified epoxy resins, as shown in Fig. 8.11. The mode I interlaminar fracture tests are conducted to measure the compliance and the crack growth resistance curves using the double-cantilever-beam specimens which are prepared from the drop-weight impact-tested composite panels (Kim et al., 1993).

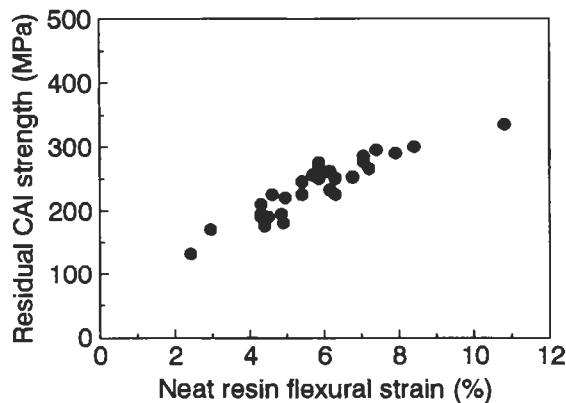


Fig. 8.8. Correlation of residual compression-after-impact (CAI) strength with resin flexural strain to failure. After Hirschbuehler (1987).

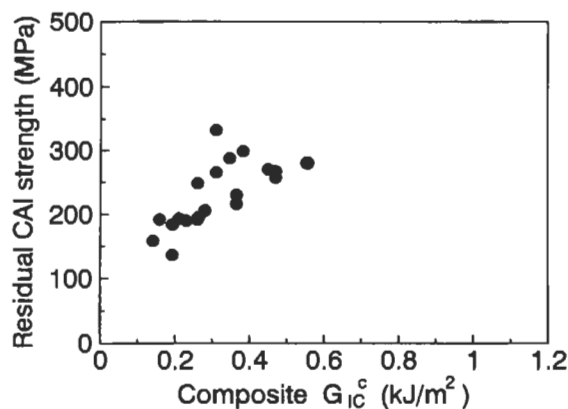


Fig. 8.9. Correlation of residual compression-after-impact (CAI) strength with composite mode I interlaminar fracture toughness, G_{IC}^c . After Hirschbuehler (1987).

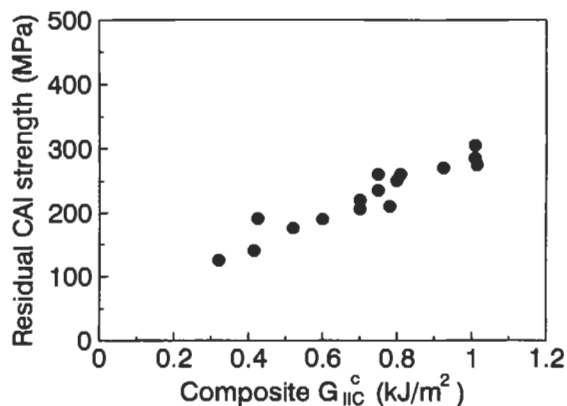


Fig. 8.10. Correlation of residual compression-after-impact (CAI) strength with composite mode II interlaminar fracture toughness, G_{IIc}^c . After Masters (1987a).

The improvement of damage resistance and tolerance in interlaminar fracture and under impact loading for the toughened matrix composites is at the expense of other important mechanical properties, such as inferior stiffness and hot/wet compressive strength (Evans and Masters, 1987). These trade offs appear to be associated with the reduction in matrix modulus and glass transition temperature (Jordan et al., 1989).

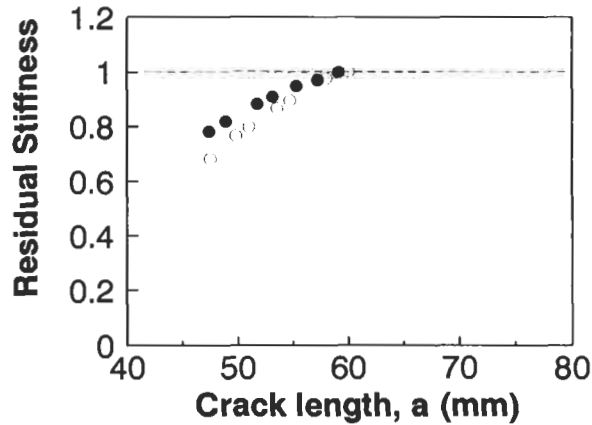


Fig. 8.11. Residual stiffness as a function crack length as measured from double cantilever beam specimens after impact damage: carbon fiber composites containing (○) unmodified epoxy; (●) rubber-modified epoxy. After Kim et al. (1993).

8.3. Delamination resisters

8.3.1. Mechanics of free edge delamination

Delamination along the free edge of composite laminates under in-plane axial loading has been a subject of great importance, and much work has been reported in the literature (Pipes and Pagano, 1970; Pagano and Pipes, 1973; Whitney and Browning, 1973; Hsu and Herakovich, 1977; Pagano and Soni, 1983; Kim, 1989). Typical X-ray radiography and ultrasonic C-scan images are presented in Fig. 8.12 for free-edge delamination occurring in $(\pm 30^\circ/90^\circ)_{ns}$ laminates subjected to in-plane

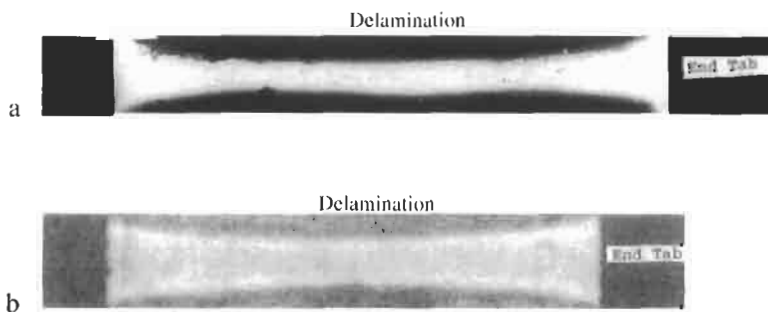


Fig. 8.12. (a) X-ray radiograph and (b) ultrasonic C-scan image, showing edge delamination in the $(\pm 30^\circ/90^\circ)_s$ laminate of T300 carbon-5208 epoxy matrix system which has been subjected to axial tension. Reprinted from Kim (1989), with kind permission from Elsevier Science-NL, Sara Burgerhart straat 25, 1055 KV Amsterdam, The Netherlands.

tension. The testing technique to measure the free edge interlaminar fracture toughness using mode I edge delamination test (EDT, see Fig. 3.34) is schematically shown in Section 3.4.4. Free edge delamination is a direct manifestation of large interlaminar stresses which are highly localized near the free edges. Fig. 8.13 (a) illustrates the stress concentrations, in particular for the tensile stress component through the laminate thickness, taking place near the free edge. The free edge stresses arise from the mismatch in the laminar coefficient of thermal expansion (CTE) and Poisson ratio between the adjoining layers (Herakovich, 1981). If there is no mismatch of these parameters, the interlaminar stresses do not exist even if there is a mismatch in elastic and shear moduli. Even so, delamination between layers of the same orientation can take place if there is an interface moment arising from the neighboring plies of different orientations or elastic properties. For example, delamination at the free edge of a laminate $[\pm 45^\circ/0^\circ/90^\circ]_s$ may occur in the mid-plane, that is at the interface $[90^\circ/90^\circ]_s$ laminae where a large interface moment and tensile stress in the through-thickness direction exist.

The magnitude and distribution of the interlaminar stress components vary widely and depend upon the number of plies for each angle, ply thickness, stacking sequence, the properties of the composite constituents and the nature of loading (Kim, 1989). The lay up sequence, in particular, has a significant effect on the magnitude and the direction of the interlaminar stresses (Pipes and Pagano, 1970; Pagano and Pipes, 1973; Daniel et al., 1974; Wang and Crossman, 1977; Herakovich, 1981, 1982; Wang and Choi, 1982; Kim and Soni, 1984; O'Brien, 1983, 1984; Heyliger and Reddy, 1985; Joo and Sun, 1992; Kim and Hong, 1992; Xu, 1996). For example, the $[90^\circ/45^\circ/0^\circ/-45^\circ]_s$ laminate is less prone to delamination than the $[\pm 45^\circ/0^\circ/90^\circ]_s$ laminate because the through-thickness normal stresses generated at the mid-plane are compressive and tensile, respectively, for the former

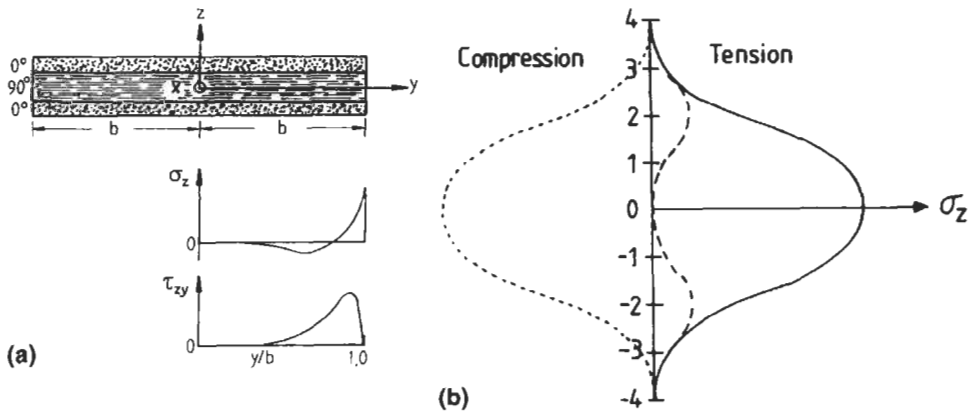


Fig. 8.13. (a) Distribution of interlaminar normal stress, σ_z , and interlaminar shear stress, τ_{zy} , in $[0^\circ/90^\circ]_s$ laminate under axial tension. (b) Effect of stacking sequence on through-the-thickness distribution of interlaminar normal stress, σ_z , near free edge: stacking sequence: (—) $[\pm 15^\circ/\pm 45^\circ]_s$; (—) $[15^\circ/45^\circ/-45^\circ/-15^\circ]_s$; (.....) $[\pm 45^\circ/\pm 15^\circ]_s$. After Pagano and Pipes (1973)

and latter laminates. The tensile normal stress is harmful as it opens up the free edge, leading to delamination.

The presence of $[\pm 15^\circ]$ and $[\pm 45^\circ]$ layers in a laminate also changes drastically the magnitude and sign of the interlaminar normal stress, σ_z , depending on the layer stacking sequence. Typical distributions of the interlaminar normal stress, σ_z , obtained near the free edge when subjected to an uniaxial tension are presented in Fig. 8.13 (b) (Pagano and Pipes, 1971) for the laminates with stacking sequences $[\pm 15^\circ/\pm 45^\circ]_s$, $[15^\circ/\pm 45^\circ/-15^\circ]_s$ and $[\pm 45^\circ/\pm 15^\circ]_s$. It is clearly shown that the $[\pm 15^\circ/\pm 45^\circ]_s$ laminate has the highest tensile stress concentration in the mid-plane, due to the largest difference in the stacking angle. From design considerations, stacking sequence should be selected which can result in low tensile or compressive normal stresses under tension.

The influence of material and stacking sequence on failure of boron fiber–epoxy matrix laminates was studied by Daniel et al. (1974), and is summarized in Table 8.3. It is noted that the ultimate tensile strength depends largely on the stress concentration and the volume fraction of $[0^\circ]$ plies. Laminates with a high fraction of $[0^\circ]$ plies, but with sufficient number of $[45^\circ]$ plies have the highest strength among those studied, due to the low stress concentrations. Laminates without either $[0^\circ]$ or $[45^\circ]$ layers fail prematurely due to the delamination initiated from the free edges: laminates without $[45^\circ]$ plies give the lowest notch strength, whereas those without $[0^\circ]$ layers show the lowest unnotched strength (Daniel et al., 1974). The other parameter which influences the interlaminar stresses is the ply thickness. Thick plies tend to encourage higher interlaminar stresses, thus causing premature delamination. It is shown that the critical strain for the onset of delamination decreases with increase in 90° ply thickness in the laminate, in particular when placed in the mid-plane (O'Brien, 1983).

Table 8.3

Effect of laminate layup and stacking sequence on stress concentration and strength of boron fiber–epoxy matrix composites containing circular holes under uniaxial tension^a.

Layup	Young's modulus (GPa)	Measured stress concentration factor	Predicted stress concentration factor	Notched strength, σ_N (MPa)	Unnotched strength, σ_0 (MPa)	Strength ratio, σ_N/σ_0
$[0^\circ/90^\circ/0^\circ/90^\circ]_s$	115.2	4.82	5.80	194	617	0.314
$[0^\circ_2/\pm 45^\circ/0^\circ]_s$	133.9	3.58	3.68	498	807	0.617
$[\pm 45^\circ/0^\circ_2/0^\circ]_s$	127.3	4.02	3.68	426	807	0.529
$[0^\circ/\pm 45^\circ/0^\circ/90^\circ]_s$	115.2	3.34	3.45	291	669	0.435
$[0^\circ_2/\pm 45^\circ/90^\circ]_s$	116.3	3.15	3.45	291	669	0.435
$[0^\circ/\pm 45^\circ/90^\circ]_s$	79.5	3.08	3.00	180	457	0.394
$[45^\circ/90^\circ/0^\circ/-45^\circ]_s$	81.4	3.1	3.00	213	459	0.465
$[\pm 45^\circ/0^\circ/\pm 45^\circ]_s$	59.3	2.46	2.45	206	378	0.546
$[\pm 45^\circ/\pm 45^\circ]_s$	19.9	2.06	1.84	125	137	0.909
$[45^\circ_2/-45^\circ_2]_s$	20.2	2.55	1.84	115	137	0.833

^aAfter Daniel et al. (1974).

8.3.2. *Interleaving techniques*

Among the several techniques which have been attempted to suppress the onset of free edge delamination, the interleaving technique has received significant attention which uses a soft, tough strip interleaved between delamination-prone layers. The interleaving technique is based on an early study of various crack arrest concepts where integral crack arrester strips were placed at critical damage-prone regions to give a composite structure the ability to carry the limiting load after sustaining the damage (Hess et al., 1977). In a similar study, the use of softening strips made from glass fiber–epoxy matrix composites in place of $[0^\circ]$ carbon fiber–epoxy matrix plies at the center notches reduced significantly the notch sensitivity, thereby improving the laminate strength (Sun and Luo, 1985).

Adhesive layers having low modulus and high elongation were employed successfully at delamination-prone free edges to suppress delamination growth by reducing the interlaminar stresses, particularly the tensile mode I component normal to the laminar interfaces (Chan, 1986, 1991; Chan et al., 1986). The huge reduction in the interlaminar stresses for $[\pm 30^\circ_2/90^\circ_3/- + 30^\circ_2]$ carbon fiber–epoxy matrix composites with interleaves is clearly seen from Fig. 8.14. This, in turn, improved substantially the critical strength before the onset of delamination and the ultimate strength of the laminate in in-plane tension, Fig. 8.15. In uniaxial tension of cross-ply laminates, interfacial delamination was found to be the immediate failure mode associated with transverse cracking, and the presence of soft interleaves could reduce the stresses, and thereby delay the onset of delamination (Altus and Ishai, 1990). Furthermore, it is worth noting that the interleaves effectively eliminated delamination prior to final failure. The edge strips of adhesive had the same effect as the adhesive layer placed over the whole plane.

Although the interleaving technique was originally devised mainly to suppress free edge delamination, this technique has been employed extensively to improve the interlaminar fracture toughness of carbon fiber composites in various fracture modes. The interleaving strips effectively increase the composite mode I interlaminar fracture toughness by almost ten times those without interleaves, depending on the thickness and types of interlayer used (Ishai et al., 1988; Sela et al., 1989; Altus and Ishai, 1990; Chen and Jang, 1991; Sun and Rechak, 1988; Rechak and Sun, 1990; Lagace and Bhat, 1992; Singh and Partridge, 1995). The critical load for mode I delamination crack is substantially higher for the laminates with interleaves, although using adhesive strips may cause a concomitant reduction in in-plane strength and stiffness (Sun and Norman, 1990; Norman and Sun, 1991). Further, the mode II interlaminar fracture toughness of the composites interleaved with thermoset and thermoplastic polymers are also measured experimentally and numerically (Carlsson and Aksoy, 1991; Aksoy and Carlsson, 1992; Sohn and Hu, 1994). Both types of interleaves enhance the fracture toughness significantly, the thermoplastic interleaves being more effective than thermoset counterparts, due to their higher energy absorption capability. The interlaminar fracture toughness in both mode I and mode II fracture increase rapidly with increasing film thickness when the film is relatively thin, whereas it becomes a constant value once the

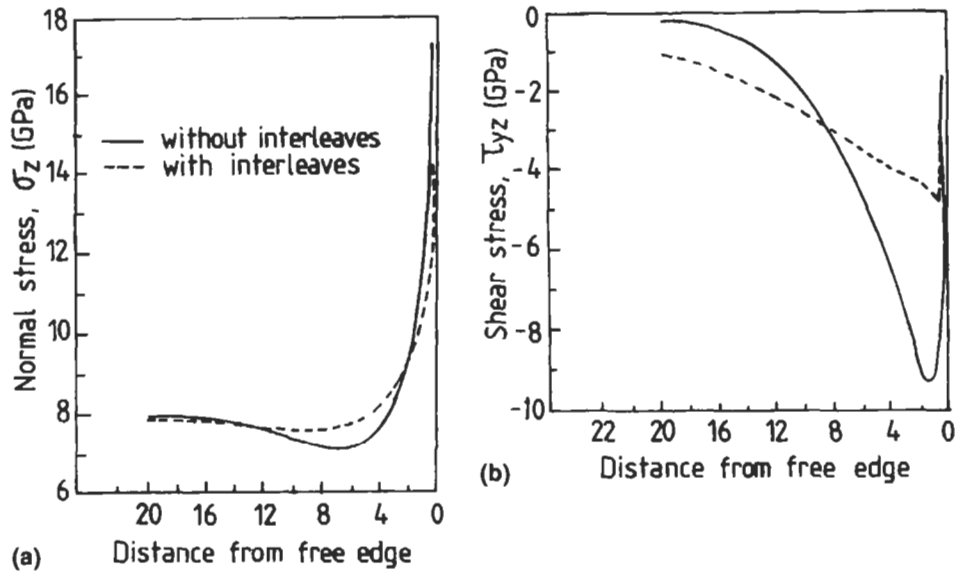


Fig. 8.14. Normalized interlaminar (a) normal stress, σ_z/ϵ_0 , and (b) shear stress, τ_{yz}/ϵ_0 , along the interface between the 90° ply and its adjacent ply of a $[\pm 30^\circ_2/90^\circ_3/-30^\circ_2/+30^\circ_2]_s$ carbon fiber-epoxy matrix laminate. Chan et al. (1986).

film is sufficiently thick. Table 8.4 presents a compilation of data on the improvement of interlaminar fracture toughness with relation to the adhesive film thickness.

Fig. 8.16 illustrates schematically the different configurations of interleaving strips which have been studied (Chan et al., 1986; Chan and Ochoa, 1989; Kim, 1983):

- (1) Adhesive strips interleaved along the free edge.

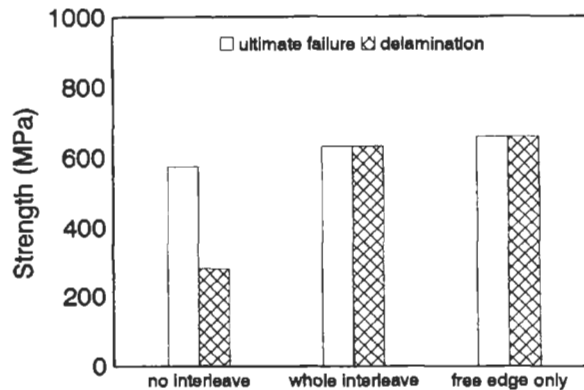


Fig. 8.15. Edge delamination and ultimate strength of $[\pm 35^\circ/0^\circ/90^\circ]_s$ AS4 carbon fiber-3501 epoxy matrix composite laminates with and without interleaves.

- (2) Adhesive strips interleaved at a certain distance away from the free edge.
- (3) Adhesive layers inserted over the whole laminate plane.
- (4) Termination of a critical ply(s) with a tapered end a small distance away from the free edge.
- (5) Wrapping of the laminate edges with edge caps.

In particular, the techniques based on the termination of certain plies within the laminate has also shown promise. Static tensile tests of $[30^\circ/-30^\circ/30^\circ/90^\circ]_s$ carbon-epoxy laminates containing terminals of $[90^\circ]$ layers at the mid-plane show that premature delamination is completely suppressed with a remarkable 20% improvement in tensile strength, compared to those without a ply terminal. Cyclic fatigue on the same laminates confirms similar results in that the laminate without a ply terminal has delamination equivalent to about 40% of the laminate width after 2×10^6 cycles, whereas the laminates with a ply terminal exhibit no evidence of delamination even after 9×10^6 cycles. All these observations are in agreement with the substantially lower interlaminar normal and shear stresses for the latter laminates, as calculated from finite element analysis. A combination of the adhesive interleaf and the tapered layer end has also been explored by Llanos and Vizzini, (1992).

Regarding the use of edge cap reinforcements, Kim (1983) applied a glass fiber cloth, and Howard et al. (1986) used a Kevlar-carbon fiber hybrid composite layer to cap the edges of carbon fiber-epoxy matrix composites. The observed improvement in both static and fatigue strengths in the edge capped laminates is attributed to the reduction in the interlaminar normal stress, similar to the adhesive interleaving technique.

Interleaving strips made from ductile short fibers, notably Kevlar fiber mat, and an adhesive (Browning and Schwartz, 1986) provide extra energy required during delamination crack propagation due to additional toughening mechanisms such as

Table 8.4
Mode I and Mode II interlaminar fracture toughness values, G_{Ic}^c and G_{IIc}^c , of carbon fiber-epoxy matrix composites containing various interleaved adhesive layers.^a

Types of adhesive layer	Adhesive thickness (mm)	G_{Ic}^c (kJ/m ²)	G_{IIc}^c (kJ/m ²)
Control	0	0.193	0.527
Tuff-ply	0.04	0.444	1.15
Tuff-ply	0.08	0.575	1.7
Tuff-ply	0.11	0.754	2.61
FM 73	0.12	0.975	1.84
FM 300	0.1	1.14	1.77
FM 300	0.26	1.47	2.23
FM 300	0.3	1.27	2.01
FM 300	0.68	1.48	2.32
FM 300	1.1	1.78	1.65

^aAfter Sela et al. (1989).

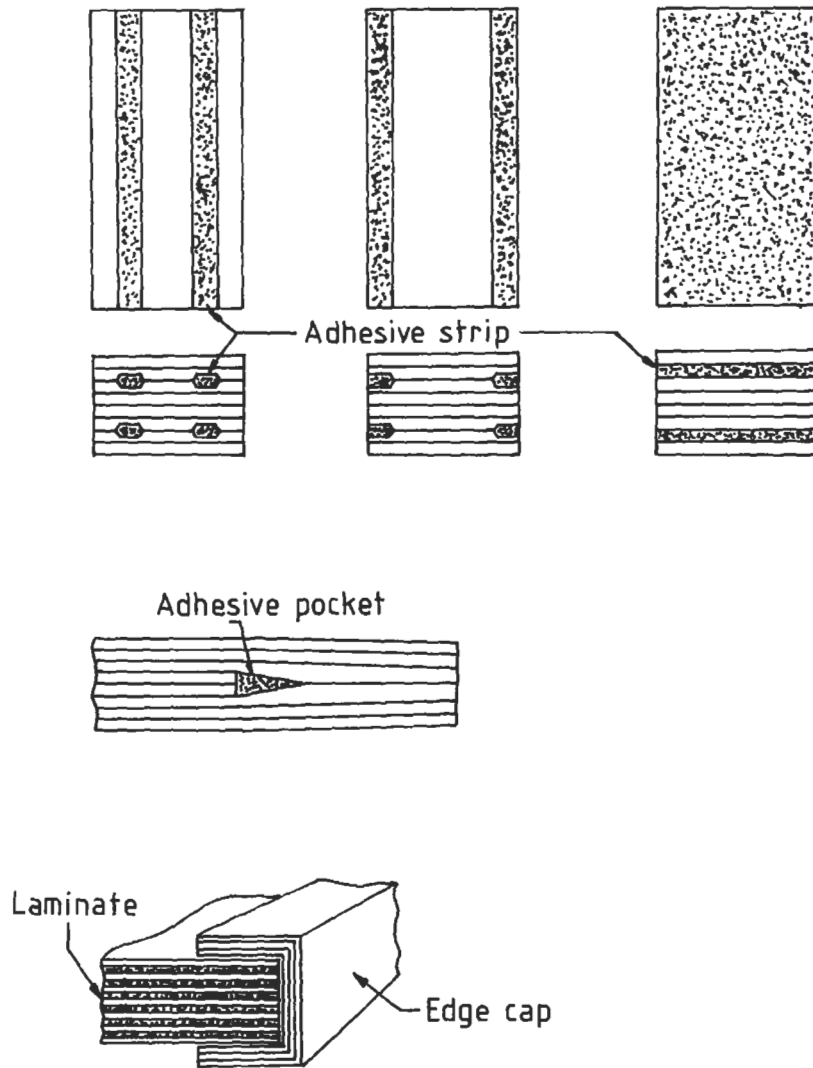


Fig. 8.16. Schematic drawings of different configurations of interleaving strips and the edge cap. After Chan et al. (1986) Chan and Ochoa (1989) and Kim (1983).

interfacial debonding and fiber pull-out which cannot be expected to occur in an interlayer made only with an adhesive. The use of thermoplastic polymers (Carlsson and Aksoy, 1991), polyurethane and CTBN-modified epoxy resin as interleaving layers is also shown to be quite beneficial for improving the mode II interlaminar fracture toughness (Chen and Jang, 1991). The effectiveness of the interleaving technique has also been demonstrated under cyclic fatigue loading (Chan, 1986) and hygrothermal aging conditions (Evans and Masters, 1987; Ishai et al., 1988).

Laminates with interleaves also enhance, to a great extent, the damage resistance and tolerance under impact loading in terms of both damage area and residual CAI (Masters, 1989; Sun and Rechak, 1988; Rechak and Sun, 1990; Lu et al., 1995). The role of the thin discrete ductile resin layer which is placed on one side of standard prepreg tapes is to alter the failure mode by allowing the transverse cracks and delamination to be arrested upon reaching the interleave. Fig. 8.17 shows the cross-sections of AS4/0808 carbon–epoxy laminates with and without thermoplastic interleaves which have been impacted at 3.56 kJ/m and 8.9 kJ/m per unit laminate thickness, respectively. The corresponding plots of delamination size versus impact energy for these laminates are shown in Fig. 8.18 (Masters, 1989). The micrographs clearly indicate that in the laminates without interleaves, a series of transverse cracks occur with extensive delamination, the number of these cracks increasing with impact energy. Delamination appears to have initiated at the intersection of the transverse crack and the laminar interface (Masters, 1987a). A triangular form of no

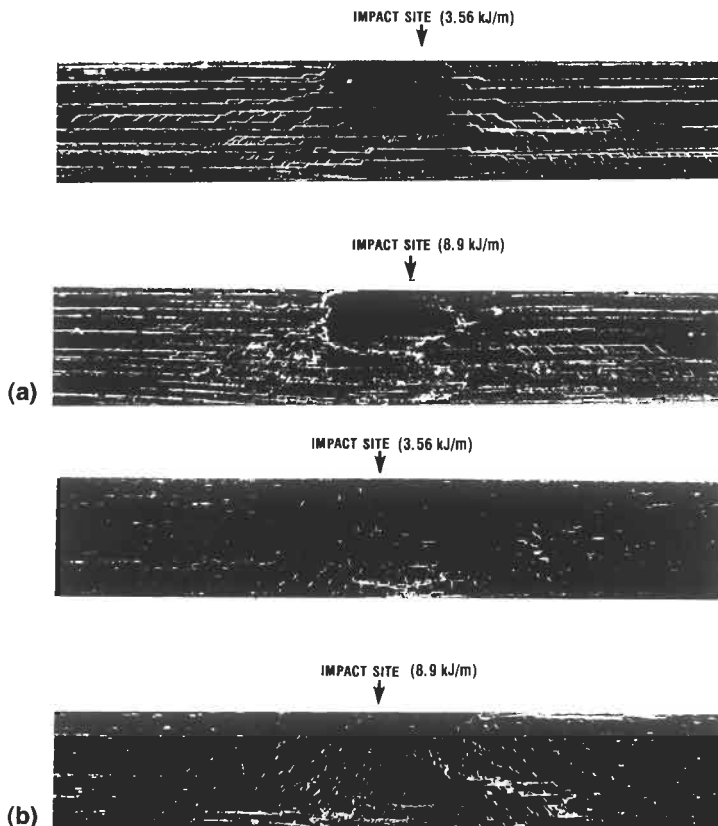


Fig. 8.17. Microphotographs of interply cracking and delamination after impact in carbon fiber epoxy matrix composites (a) without and (b) with interleaving layers. After Masters (1989). Reproduced by permission of Trans Tech Publications Ltd.

damage zone is noted directly below the impact site. In contrast, in the laminates with interleaves near the back face of the laminate, only few delaminations are present although the number of transverse cracks increases at high impact energies.

In summary, the presence of interleaves improves greatly the impact damage resistance of the composites, especially in terms of damage size (Fig. 8.18). A guideline has been proposed (Rechak and Sun, 1990) with regard to the optimal use of interleaves for damage tolerance design:

- (1) Place the adhesive layer at a distance equal to the size of the contact area below the impact face.
- (2) Place an interleaf immediately below the surface layer if the delamination induced by the transverse cracks originating from the impact surface is to be arrested.

It should be reiterated here that the delamination resister concept based on the interleaving technique is not identical to the delamination promoter approach, which is presented in Section 7.4, with regard to both the toughening mechanisms and the primary direction of crack propagation relative to the laminar interfaces. Delamination resisters are intended to improve the *interlaminar* fracture toughness by suppressing delamination growth so that the interleaving layer should have high ductility and low modulus to help reduce the interlaminar stresses. In sharp contrast, delamination promoters are aimed at increasing the *transverse* fracture toughness through extra energy absorption required for the arrest and bifurcation of the transverse cracks at the laminar interface, and hence a weak interlaminar bond is essential for the promotion of delamination. However, both methods are similar in that the modifying layer should be maintained as thin as possible so as not to introduce large losses in in-plane strength and stiffness, although there are optimum thicknesses which would impart balanced mechanical properties.

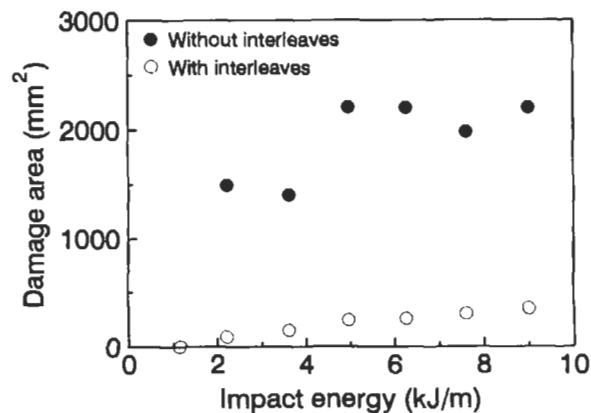


Fig. 8.18. Effect of interleaves on impact delamination area in AS4 carbon fiber-1808 epoxy matrix composites. After Masters (1989).

8.4. Three-dimensional textile composites concept

8.4.1. Introduction

Three-dimensional textile preforms are continuous fiber assemblies which are fully integrated with multi-axial in-plane and through-the-thickness fiber orientations. Ko (1989) and Chou (1992) presented comprehensive reviews on this topic, and a brief summary is given in this section. Composites containing three-dimensional textile preforms display many unique advantages which are absent in traditional two-dimensional laminate composites, and they include:

- (1) Enhanced stiffness and strength in the thickness direction due to the presence of out-of-plane orientation of some fibers.
- (2) Elimination of the interlaminar surfaces through the fully integrated nature of fiber arrangement.
- (3) Feasibilities of near-net-shape design and manufacturing of composite components which, in turn, minimizes the need of cutting and joining of the parts.

Three-dimensional textile preforms may be divided into four groups according to their manufacturing techniques, namely braiding, weaving, stitching and knitting, as shown in Fig. 8.19 (Chou, 1992). A schematic drawing of a set up for the three-dimensional braiding process is given in Fig. 8.20. It is shown that the axial yarns are supplied directly into the braiding structure from the package placed below the track plate, while the braiding yarns are supplied from bobbins mounted on carriers which move with the track plate. The type and microstructure of the braids are controlled by the presence of axial yarns and the pattern of motion of the braiders.

In three-dimensional weaving, a high degree of integration in fiber geometry through the thickness is achieved by modifying the traditional weaving techniques for producing two-dimensional fabrics. Fibers are incorporated at an angle and parallel to the thickness directions, respectively, in two major weaving techniques, namely angle-interlock and orthogonal weaving. Fig. 8.21 schematically illustrates an orthogonal woven fabric with yarns placed in three mutually orthogonal directions. Matrix rich regions are often created in composites containing orthogonal woven fabrics due to the nature of fiber placement.

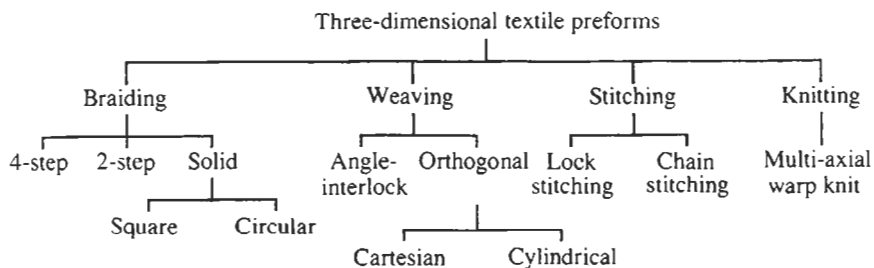


Fig. 8.19. Three dimensional textile preforms. After Chou (1992). Reprinted with kind permission of Cambridge University Press.

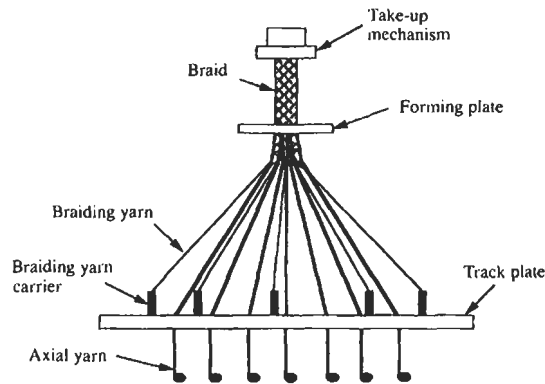


Fig. 8.20. Schematic presentation of three dimensional braiding. After Du et al. (1991).

The process of stitching uses the conventional technology to convert two-dimensional preforms to three-dimensional ones. The types of stitch strand materials, stitch density, the size of the stitch strand, and the types of stitching method determine the final stitch preform. Kevlar fiber strands are among the most popular due to their flexibility which is required to bend into a small curvature in the needle hole. There are two types of stitching methods, namely lock stitch and chain stitch (Fig. 8.22). A lock stitch tends to become unbalanced because of the high tension in the bobbin thread or the needle thread. Fig. 8.23 shows a lock-stitching process for bonding woven fabric layers.

The unlimited variability of the geometric forms which can be obtained using the knitting technique is especially useful for producing preforms with complex shapes.

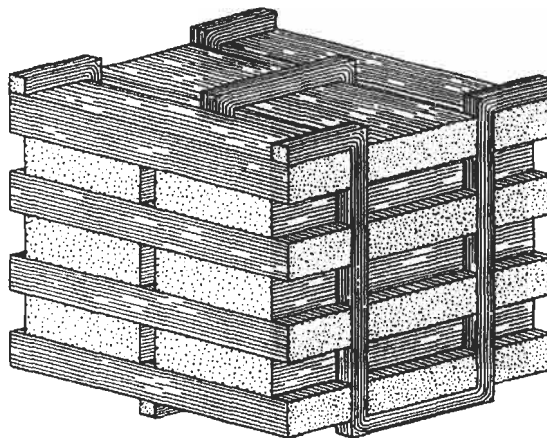


Fig. 8.21. Schematic presentation of an orthogonal woven fabric. After Chou et al. (1986).

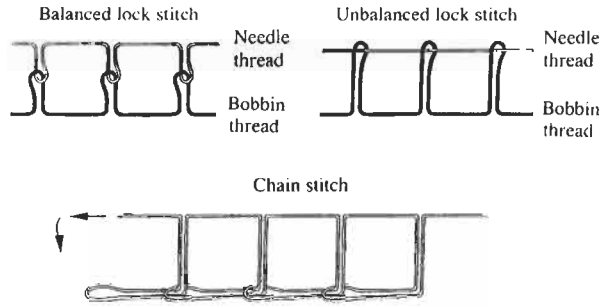


Fig. 8.22. Stitching techniques. After Ogo (1987).

The preforms can be designed for composites subjected to very complex loading conditions, because of the large extensibility and conformability of the preform. A weft knitting or a warp knitting process may be used to produce three-dimensional knitted fabrics. For additional strengthening in the $[0^\circ]$ and $[90^\circ]$ directions, laid-in yarns are often added inside the knitting loops, as illustrated in Fig. 8.24. The major advantages of knitted preforms include enhanced through-the-thickness stiffness and strength with the characteristics of unidirectional laminates (Ko et al., 1986).

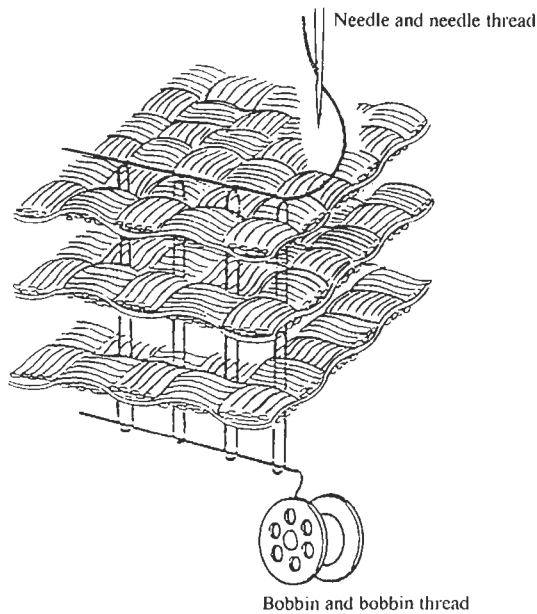


Fig. 8.23. Schematic illustration of the lock stitch process. After Ogo (1987).

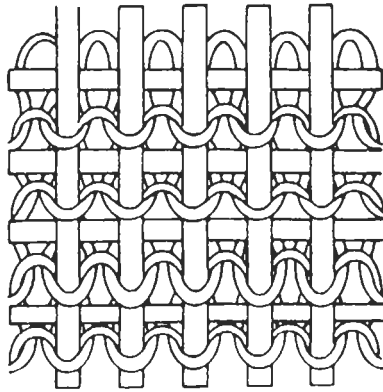


Fig. 8.24. Weft knit with laid-in weft and warp yarns. After Ko (1989).

8.4.2. Improvement of interlaminar fracture toughness

This section examines the advantages and disadvantages of using three-dimensional textile preforms, especially through-the-thickness stitches, as the reinforcements for composites. Their major mechanical properties are compared with those of conventional two-dimensional composites, such as strength, stiffness, interlaminar properties, impact resistance and tolerance, etc. Dransfield et al. (1994) have recently given a useful review on the improvement of interlaminar fracture toughness of stitched composites.

Huang et al. (1978) were among the first researchers who introduced a technique designed to reduce delamination, which, in turn, enhanced the local shear strength of carbon fiber–epoxy matrix composites. Steel wires of 0.33 mm in diameter were placed by hand at an angle of $\pm 45^\circ$ to the laminate surface. Holt (1982) employed the stitching technique in composite joining for aircraft structural components. In a subsequent study by Mignery et al. (1985), Kevlar threads were stitched along the edges of the laminates to mitigate the free edge delamination and ultimately to improve the tensile strength of carbon fiber composites. Stitching along the free edge improves the mode I interlaminar fracture toughness by 85%, while also enhancing the flexural strength by up to 30% for carbon fiber–epoxy matrix composites fabricated from prepregs, as summarized in Table 8.5 (Chung et al., 1989). Stitches also give enhanced interlaminar shear strength (Adanur et al., 1995). The unstitched fiber composites fail normally by interlaminar shear, while the stitched counterparts fail predominantly by tension due to the restriction of shear achieved by the stitches.

The load–displacement curves for the orthogonal interlock fabric composites show a non-linear unloading sequence and an appreciable permanent deformation after unloading, with the crack tip not completely closed (Guenon et al., 1987). These observations are attributed to the crack closure process of the three-dimensional fabric composites where through-the-thickness yarns break near the outer surface of the specimen.

Table 8.5

Effect of through-the-thickness stitches on flexural strength and Mode I interlaminar fracture toughness of carbon fiber-epoxy matrix composites manufactured using unidirectional prepregs^a.

Stitches	Flexural strength (MPa)	Mode I interlaminar fracture toughness G_{Ic}^{∞} (kJ/m ²)
No stitching	226	1.88
6.35 mm at stitch-free center zone	268	2.15
11.1 mm at stitch-free center zone	290	3.45
14.3 mm at stitch-free center zone	217	3.25
19.05 mm at stitch-free center zone	283	2.17

^aAfter Chung et al. (1989).

Among many stitching parameters, stitch density is the most dominant factor determining the efficiency of stitching. It is expected that there is a critical stitch density above which the improvement of interlaminar fracture toughness can be achieved (Dransfield et al., 1994). At the same time, too high a stitch density may not be beneficial as they induce severe misalignment of longitudinal fibers and cause localized in-plane fiber damage resulting from the needle penetration (Mayadas et al., 1985; Morales, 1990; Kang and Lee, 1994). Fig. 8.25 clearly demonstrates that there is an optimum stitch density offering the maximum interlaminar shear strength, after which it decreases drastically because the negative effect of in-plane fiber breakage and misalignment due to the stitch strand penetration dominates the whole fracture process.

In summary, an excessive stitch density causes severe degradation of in-plane strength and stiffness, particularly in bending (Mouritz, 1996) and compression (Farley, 1992). The major reasons for these undesirable effects can be summarized below:

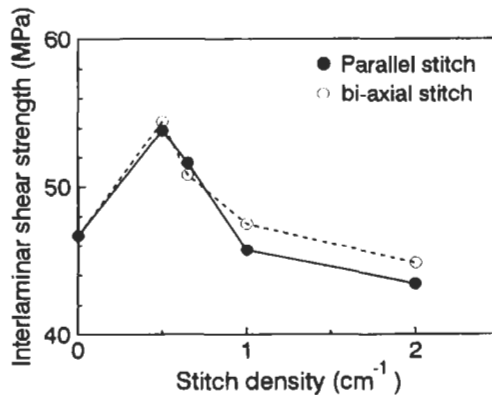


Fig. 8.25. Interlaminar shear strength as a function of stitch density for seven layer off-loom stitched glass fiber-epoxy matrix composites. After Adanur et al. (1995).

- (1) Deleterious effects are introduced during the stitching process, which include the breakage and misalignment of the in-plane reinforcing fibers and the formation of resin rich regions at the stitch holes.
- (2) The stitch knots and holes act as stress concentration sites in the laminate microstructure.

Farley (1992) has made an in-depth study of the negative effect of fiber misalignment. Fig. 8.26 shows the gross in-plane waviness created by through-the-thickness stitches. It is also reported that many microcracks are created around the stitch strands, although the microcracks appear not to have propagated under combined temperature and humidity cycles (Furrow et al., 1996).

The beneficial effects of stitches on interlaminar fracture of composites are fully verified by theoretical predictions. Byun et al. (1990, 1991) and Mai and co workers (Shu and Mai, 1993; Jain and Mai, 1994, 1995) have developed theoretical models to examine the effect of stitches on delamination extension in various modes including edgewise compression, mode I and mode II loading. The parameters studied are stitch density, S_D , matrix stitch thread interfacial bond strength, τ , stitch diameter, d_f , and volume fraction of stitches. Based on the small deflection beam theory for generally anisotropic materials, the crack growth resistance, K_R , curves are established for the intrinsic interlaminar fracture toughness of the composite. The total fracture toughness, K_R , is the sum of the stress intensity factors due to the applied load and due to the closure traction acting across the crack faces arising from the presence of stitches. Fig. 8.27 shows typical K_R curves plotted as a function of crack extension, Δa , for different values of the parameters S_D , τ and d_f . It is shown that the crack growth resistance increases with increasing values of all the above parameters. Improved crack growth resistance by the stitches has a practical implication that the interlaminar fracture can be suppressed, if not completely eliminated. However, there are restrictions which limit the degree to which these parameters can be increased. A very high interfacial shear bond strength may lead to rupture of the stitch strands, instead of interfacial debonding, resulting in limited

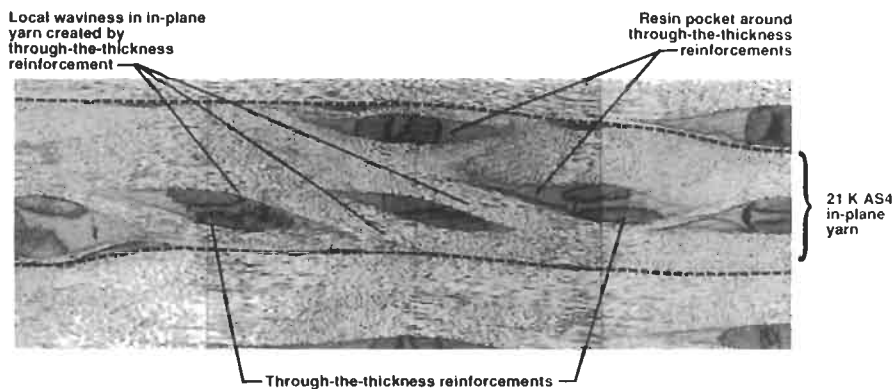


Fig. 8.26. In-plane fiber waviness created by through-the-thickness stitch strands. After Farley (1992).

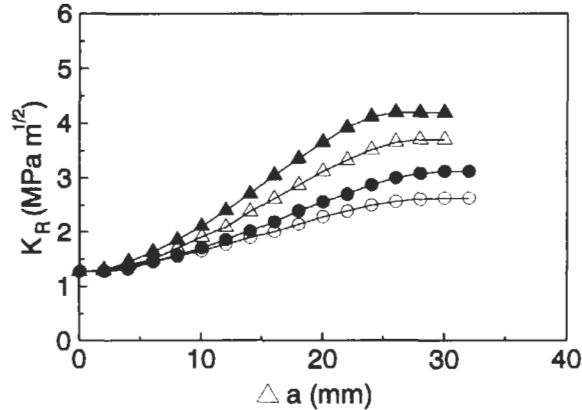


Fig. 8.27. Effects of stitch density, S_D , stitch strand-matrix interface shear stress, τ , and stitch thread diameter, d_f , on the stress intensity factor, K_R , as a function of crack extension, Δa . (▲) $S_D = 1/15 \text{ mm}^{-2}$, $\tau = 5 \text{ MPa}$, $d_f = 0.3 \text{ mm}$; (Δ) $S_D = 1/30 \text{ mm}^{-2}$, $\tau = 7.5 \text{ MPa}$, $d_f = 0.3 \text{ mm}$; (●) $S_D = 1/30 \text{ mm}^{-2}$, $\tau = 5 \text{ MPa}$, $d_f = 0.3 \text{ mm}$; (○) $S_D = 1/30 \text{ mm}^{-2}$, $\tau = 5 \text{ MPa}$, $d_f = 0.2 \text{ mm}$. After Jain and Mai (1994).

efficiency of the stitches. A high stitch density will also lead to interactions between the stitch threads. However, it is noted that under an increasing buckling load, delamination growth may become unstable leading to catastrophic failure, depending on the initial delamination length and stitch density (Shu and Mai, 1993).

The stitching technique has also been applied successfully to joining of laminate composites (Holt, 1982; Sawyer, 1985; Tada and Ishikawa, 1989; Lee and Liu, 1990). In a stitched joint, the stitch strand function as bolts or rivets of a mechanical joint, while the matrix has the same function as that of the adhesive in an adhesive joint. Stitching can be performed either with or without an overlap, the latter method rendering a more smooth surface and uniform thickness with associated weight saving. However, the joint strength without an overlap is always lower than that of the overlap joint. It is argued that the stitched joint is more suitable for woven fabrics than unidirectional prepreg tapes (Lee and Liu, 1990). Tada and Ishikawa (1989) have also shown that the stitches enhance the resistance to damage growth, the ability in crack arrest and deferment of final failure in various loading configurations, such as single lap joint in shear, plates with angle joints in peel tension, T-section stiffness in compression, step lap-joint in four point bending and plate with a hole subjected to compression loading.

8.4.3. Impact response of stitched composites

Composites with stitched reinforcements have been the subject of extensive study under impact conditions in recent years because the damage resistance and damage tolerance of laminate composites are of major concern in a service environment (Liu, 1990; Farley et al., 1992; Farley, 1992; Farley and Dickinson, 1992; Portanova et al., 1992; Caneva et al., 1993; Kang and Lee, 1994; Adanur et al., 1995; Wu and

Wang, 1995; Herszberg et al., 1996; Leong et al., 1996; Furrow et al., 1996). The varying roles of reinforcement architecture including fiber stitching has been reviewed (Bibo and Hogg, 1996; Kim, 1997) on the impact response of the composites. Laminates containing carbon fiber woven fabrics have also shown to provide higher impact damage resistance compared to those made with prepreg cross-ply (Kim et al., 1996). Numerous impact data of stitched and unstitched fiber composites of various constituent combinations consistently show that the extent of damage as measured from the damage area is less and the CAI strength is higher for the stitched fiber composites (Liu, 1990; Kang and Lee, 1994; Adanur et al., 1995; Wu and Wang, 1995). This result is particularly true when the major damage mode during impact and the fracture mode in the subsequent CAI test are induced mainly by delamination. Fig. 8.28 clearly indicates that the decrease of damage area is proportional to the increase in stitch density (Liu, 1990). It appears that the optimum stitch density has not been reached in this particular study. Close examination of the damage surface reveals that some stitching points coincided with the delamination boundary which is indicative of such stitch strands acting as delamination arresters, as shown in Fig. 8.29. Fig. 8.30 also displays the strong dependence of total energy absorbed by stitched laminates on stitch spacing, type of stitches and matrix material.

In some isolated cases, the stitching technique provides no beneficial effects on the impact resistance of carbon fiber–epoxy matrix composites (Herszberg et al., 1996; Leong et al., 1996). When orthotropic laminates are subjected to drop weight impact or projectile impact under tension, the damage area and the CAI are very similar between the composites with and without stitches. This disappointing result is thought to be associated with the excessive stitch density and the unfavorable failure modes, such as transverse shear, of the stitched specimens during impact. The stitched composites containing such transverse shear cracks tend to fail by shear under compression, resulting in a lower CAI strength than the unstitched composites. It should be mentioned here that the residual compressive strength in

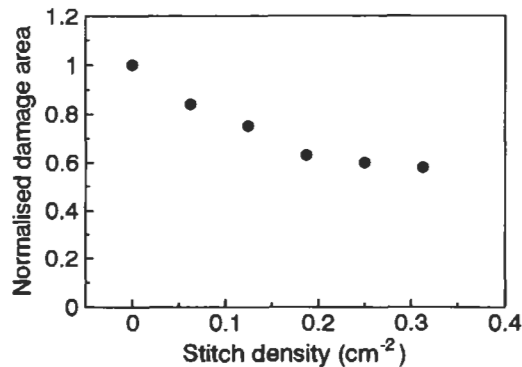


Fig. 8.28. Normalized delamination area due to impact as a function of stitch density for a carbon fiber–epoxy matrix composite. After Liu (1990).

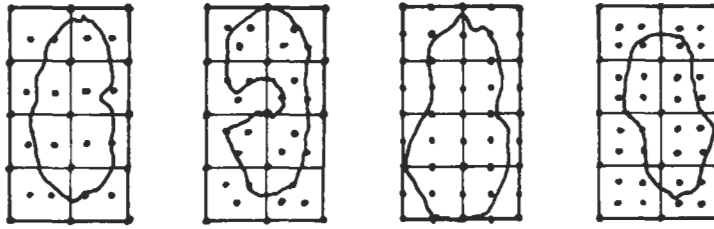


Fig. 8.29. Delamination patterns of a carbon fiber-epoxy matrix composite with varying stitch densities. After Liu (1990).

the CAI test is controlled largely by the damage induced by the impact itself rather than by the failure process during compressive loading. Furthermore, the compressive strength of stitched composites is sometimes lower than the unstitched counterpart even in the undamaged state (Farley et al., 1992; Reeder, 1995). This is attributed to the damage of the in-plane reinforcement fibers and the high stress concentration around the stitch holes, as mentioned before. Although the removal of the surface loops of the stitch strands shows no direct effect on the prominent failure mechanisms, it increases significantly the compressive strength both before and after impact loading (Farley and Dickinson, 1992).

The anomalous behavior of stitched carbon fiber composites with respect to impact damage response mentioned in the above paragraph deserves more attention. Similar observations on Kevlar stitched glass fiber composites show no beneficial effects of stitching in terms of impact damage resistance for thin composite laminates (less than a few mm). However, for thick laminates (~larger than 20 mm) through-the-thickness stitching produces much better damage control than unstitched laminates (Mouritz, 1997). This brings up a “size” effect on stitched

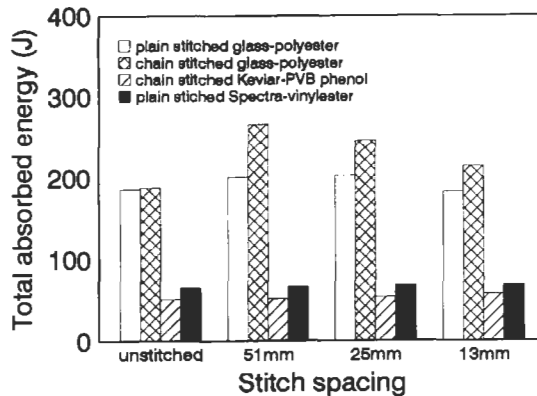


Fig. 8.30. Effect of stitch spacing on total absorbed energy after impact for different stitched composites. After Kang and Lee (1994).

composites which has received little or no attention. It is expected that the damage mechanisms will also be size or laminate thickness dependent.

In summary, it can be said that if through-the-thickness stitching can be effective in improving interlaminar fracture resistance and impact damage tolerance, it is important to identify the optimum stitching conditions, notably the stitch density and stitch strand diameter, so as not to introduce any negative effects. Excessive damage and misalignment of the in-plane reinforcement fibers are the major issues associated with the use of through-the-thickness stitches which must be avoided.

References

- Adanur, S., Tsao, Y.P. and Tam, C.W. (1995). Improving fracture resistance of laminar textile composites by third direction reinforcement. *Composites Eng.* **5**, 1149–1158.
- Aksoy, A. and Carlsson, L.A. (1992). Interlaminar shear fracture of interleaved graphite/epoxy composites. *Composites Sci. Technol.* **43**, 55–69.
- Altus, E. and Ishai, O. (1990). The effect of soft interleaved layers on the combined transverse cracking/delamination mechanisms in composite laminates. *Composites Sci. Technol.* **39**, 13–27.
- Bascom, W.D., Cottingham, R.L., Jones, R.L. & Peyser, P. (1975). The fracture of epoxy and elastomer modified epoxy polymers in bulk and as adhesives. *J. Appl. Polym. Sci.* **19** 2545–2562.
- Bascom, W.D. and Cottingham, R.L. (1976). Effect of temperature on the adhesive fracture behavior of an elastomer-epoxy resin. *J. Adhesion* **7**, 333–346.
- Bibo, G.A. and Hogg, P.J. (1996). A view, the role of reinforcement architecture on impact damage mechanisms and post-impact compression behavior. *J. Mater. Sci.* **31**, 1115–1137.
- Bowles, K.J. (1988). The correlation of low-velocity impact resistance of graphite fiber reinforced composites with matrix properties. In *Composite Materials: Testing and Design (8th Conference)*, ASTM STP 972 (J.D. Whitcomb ed.), ASTM, Philadelphia, PA, pp. 124–142.
- Bradley W.L. (1989a). Understanding the translation of neat resin toughness into delamination toughness in composites. *Key Eng. Mater.* **37**, 161–198.
- Bradley, W.L. (1989b). Relationship of matrix toughness to interlaminar fracture toughness. In *Application of Fracture Mechanics to Composite Materials* (K. Friedrich ed.), Elsevier Science Pub., New York, Ch. 5, pp. 159–187.
- Bradley, W.L. (1990). The effect of resin toughness on delamination toughness and post-impact compression strength. In *Proc. "Benibana" Intern. Symp. How to improve the toughness of polymers and composites-toughness, fracture and fatigue of polymers and composites*, Yamagata, Japan, pp. 221–230.
- Bradley W.L. and Cohen R.N. (1987). Matrix deformation and fracture in graphite-reinforced epoxies. In *Toughened Composites*, ASTM STP 937 (N.J. Johnston ed.), ASTM, Philadelphia, PA, pp. 389–410.
- Browning, C.E. and Schwartz, H.S. (1986). Delamination resistant composite concepts. In *Composite Materials: Testing and Design (7th Conf.)*, ASTM STP 893, (J.M. Whitney ed.), ASTM, Philadelphia, PA, pp. 256–265.
- Byun, J.H., Gillespie, J.W. and Chou, T.W. (1990). Mode I delamination of a three-dimensional fabric composite. *J. Composite Mater.* **24**, 497.
- Byun, J.H., Du, G.W. and Chou, T.W. (1991). Analysis and modelling of 3-D textile structural composites. In *ACA Symposium Series 457*, American Chemical Society, Washington, DC, pp. 22–33.
- Caneva, C., Olivieri, S., Santulli, C. and Bonifazi, G. (1993). Impact damage evaluation on advanced stitched composites by means of acoustic emission and image analysis. *Composite Structures* **25**, 121–128.
- Carlsson, L.A. and Aksoy, A. (1991). Analysis of interleaved end-notched flexural specimen for measuring mode II fracture toughness. *Int. J. Fracture* **52**, 66–77.
- Chakachery, E.A. and Bradley, W.L. (1987). A comparison of the crack tip damage zone for fracture of Hexcel F185 neat resin and T6T145/F185 composite. *Polym. Eng. Sci.* **27**, 33–40.

- Chan W.S. (1986). Delamination arrester-an adhesive inner layer in laminated composites. In *Composite Materials: Fatigue and Fracture*, ASTM STP 907 (H.T. Hahn ed.), pp. 176–196.
- Chan, W.S. (1991). Design approaches for edge delamination resistance in laminated composites. *J. Composites Technol. Res.* **14**, 91–96.
- Chan W.S., Rogers C. and Aker S. (1986). Improvement of edge delamination strength of composite laminates using adhesive layers. In *Composite Materials: Testing and Design*, ASTM STP 893 (J.M. Whitney ed.). ASTM, Philadelphia, PA, 266–285.
- Chan, W.S. and Ochoa, O.O. (1989). Edge delamination resistance by a critical ply termination. *Key Eng. Mater.* **37**, 285–304.
- Chen, S.F. and Jang, B.Z. (1991). Fracture behavior of interlaminar fiber–resin composites. *Composites Sci. Technol.* **41**, 77–97.
- Chou, T.W. (1992). Three dimensional textile composites. In *Microstructural Design of Fiber Composites*, Cambridge University press, Cambridge, Chapter 7, pp. 374–442.
- Chou, T.W., McCullough, R.L. and Pipes, R.B. (1986). Composites. *Sci. Am.* **252**, 192–203.
- Chung, W.C., Jang, B.Z., Chang, T.C., Hwang, L.R. and Wilcox, R.C. (1989). Fracture behaviour in stitched multidirectional composites. *Mater. Sci. Eng.* **A112**, 157–173.
- Daghyani, H.R., Ye, L. and Mai, Y.W. (1995a). Mode I fracture behaviour of adhesive joints. 1. Relationship between fracture energy and bond thickness. *J. Adhesion* **53**, 149–162.
- Daghyani, H.R., Ye, L. and Mai, Y.W. (1995b). Mode I fracture behaviour of adhesive joints. 2. Stress analysis of constraint parameters. *J. Adhesion* **53**, 163–172.
- Daghyani, H.R., Ye, L. and Mai, Y.W. (1996). Mixed mode fracture of adhesively bonded carbon fiber/epoxy composite joints. *J. Composite Mater.* **30**, 1248–1265.
- Daniel, I.M., Rowlands, R.E. and Whiteside, J.B. (1974). Effects of material and stacking sequence on behavior of composite plates with holes. *Exper. Mech.* **14**, 1–9.
- Dransfield, K., Baillie, C. and Mai, Y.W. (1994). Improving the delamination resistance of CFRP by stitching – a review. *Composites Sci. Technol.* **50**, 305–317.
- Drzal, L.T. (1990). The effect of polymeric matrix mechanical properties on the fiber–matrix interfacial shear strength. *Mater. Sci. Eng.* **A126**, 289–293.
- Drzal, L.T. and Madhukar, M. (1991). Fiber–matrix adhesion and its relationship to composite mechanical properties. *J. Mater. Sci.* **28**, 569–610.
- Du, G.W., Chou, T.W. and Popper, P. (1991). Analysis of three-dimensional textile preform for multidirectional reinforcement of composites. *J. Mater. Sci.* **26**, 3438–3448.
- Evans, R.E. and Masters, J.E. (1987). A new generation of epoxy composites for primary structural applications: materials and mechanics. In *Toughened Composites*, ASTM STP 937 (N.J. Johnston ed.), ASTM, Philadelphia, PA, pp 413–436.
- Farley, G.L. (1992). A mechanisms responsible for reducing compressive strength of through-the-thickness reinforced composite materials. *J. Composite Mater.* **26**, 1784–1795.
- Farley, G.L. and Dickinson, L.C. (1992). Removal of surface loop from stitched composites can improve compression and compression-after-impact strengths. *J. Reinforced Plast. Composites* **11**, 633–642.
- Farley, G.L., Smith, B.T. and Maiden, J. (1992). Compression response of thick layer composite laminates with through-the-thickness reinforcement. *J. Reinforced Plast. Composites* **11**, 787–810.
- Furrow, K.W., Loos, A.C. and Cano, R.J. (1996). Environmental effects on stitched RTM textile composites. *J. Reinforced Plast. Composites* **15**, 378–419.
- Garg, A.C. and Mai, Y.W. (1988a). Failure mechanisms in toughened epoxy resin – A review. *Composites Sci. Technol.* **31**, 179–223.
- Garg, A.C. and Mai, Y.W. (1988b). Failure prediction in toughened epoxy resins. *Composites Sci. Technol.* **31**, 225–242.
- Gucnon, V.A., Chou, T.W. and Gillespie, J.W. (1987). Interlaminar fracture toughness of a three-dimensional fabric composites. in *Proc. of the Society of Manufacturing Engineers*, EM87-551, Society of Manufacturing Engineers, Dearborn, MI, pp. 1–17.
- Herakovich, C.T. (1981). On the relationship between engineering properties and delamination of composite materials. *J. Composite Mater.* **15**, 336–348.

- Herakovich, C.T. (1982). Influence of layer thickness on the strength of angle ply laminates. *J. Composite Mater.* **16**, 217–227.
- Herszberg, I., Weller, T., Leong, K.H. and Bannister, M.K. (1996). The residual tensile strength of stitched and unstitched carbon/epoxy laminates impacted under tensile load. In *Proc. 1st Australasian Congress on Applied Mechanics*, Melbourne. pp. 309–314.
- Hess T.E., Huang S.L. and Rubin H. (1977). Fracture control in composite materials using integral crack arresters. *J. Aircraft* **14**, 994–999.
- Heyliger, L.A. and Reddy, J.N. (1985). Reduction of free-edge stress concentration. *J. Appl. Mech.* **52**, 801–805.
- Hibbs, M.F., Tse, M.K. & Bradley, W.L. (1987). Interlaminar fracture toughness and real time fracture mechanisms of some toughened graphite/epoxy composite. In *Toughened Composites*, ASTM STP 937 (N.J. Johnston ed.), ASTM, Philadelphia, PA. pp. 115–130.
- Hirschbuehler, K.R. (1987). A comparison of several mechanical tests used to evaluate the toughness of composites. In *Toughened Composites*, ASTM STP 937 (N.J. Johnston ed.), ASTM, Philadelphia, PA, pp. 61–73.
- Holt, D.J. (1982). Future composite aircraft structures may be sewn together. *Automotive Eng.* **90**, 46–49.
- Howard, W.E., Gossard, T. Jr. and Jones, M.R. (1986). Reinforcement of composite laminate free edges with U-shaped caps. *AIAA Paper*, 89-0972.
- Hsu, P.W. and Herakovich, C.T. (1977). Edge effects in angle ply composite laminates. *J. Composite Mater.* **11**, 422–428.
- Huang, S.L., Richey, R.J. and Deska, E.W. (1978). Cross reinforcement in a GR/EP laminate. Presented at American Society of Mechanical Engineers Winter Annual Meeting, San Francisco.
- Hunston D.L., Moulton R.J., Johnston N.J. and Bascom W.D. (1987). Matrix resin effects in composite delamination: Mode I fracture aspects. In *Toughened Composites*, ASTM STP 937 (N.J. Johnston ed.), ASTM, Philadelphia, PA, pp. 74–94.
- Ishai O., Rosenthal H., Sela N. and Drukker E. (1988). Effect of selective adhesive interleaving on interlaminar fracture toughness of graphite/epoxy composite laminates. *Composites* **19**, 49–54.
- Ishikawa, T., Sugimoto, S. Matsushima, M. and Hayashi, Y. (1995). Some experimental findings in compression-after-impact (CAI) tests of CF/PEEK (APC-2) and conventional CF/Epoxy flat plates *Composites Sci. Technol.* **55**, 349–363.
- Jain, L.K. and Mai, Y.W. (1994). On the effect of stitching on mode I delamination toughness of laminated composites. *Composites Sci. Technol.* **51**, 331–345.
- Jain, L.K. and Mai, Y.W. (1995). Determination of mode II delamination toughness of stitched laminated composites. *Composites Sci. Technol.* **55**, 241–253.
- Joo, J.W. and Sun, C.T. (1992). A failure criterion for laminates governed by free edge interlaminar shear stresses. *J. Composites Mater.* **26**, 1510–1522.
- Jordan W.M. and Bradley W.L. (1987). Micromechanisms of fracture in toughened graphite-epoxy laminates. In *Toughened Composites* (N.J. Johnston ed.), ASTM STP 937, ASTM, Philadelphia, PA, pp. 95–114.
- Jordan W.M. and Bradley W.L. (1988). The relationship between mechanical properties and mode I delamination fracture toughness *J. Mater. Sci. Lett.* **7**, 1362–1364.
- Jordan W.M., Bradley W.L. and Moulton R.J. (1989). Relating resin mechanical properties to composite delamination fracture toughness. *J. Composite Mater.* **23**, 923–943.
- Kang, T.J. and Lee, S.H. (1994). Effect of stitching on the mechanical and impact properties of woven laminate composites. *J. Composite Mater.* **28**, 1574–1587.
- Kim, D.M. and Hong, C.S. (1992). A simple sublaminar approach to the design of thick composite laminates for suppression of free-edge delamination. *Composites Sci. Technol.* **43**, 147–158.
- Kim, J.K. (1998). Methods for improving impact damage resistance of CFRPs. *Key Eng. Mater.* **141–143**, 149–168.
- Kim, J.K. & Mai, Y.W. (1991). High strength, high fracture toughness fiber composites with interface control – A review. *Composites Sci. Technol.* **41**, 333–378.
- Kim, J.K., Baillic, C., Poh, J. and Mai, Y.W. (1992). Fracture toughness of CFRP with modified epoxy resin matrices. *Composites Sci. Technol.* **43**, 283–297.

- Kim, J.K., Leung, L.M., Lee, S.W.R. and Hirai, Y. (1996). Impact performance of a woven fabric CFRP laminates. *Polym. Polym. Composites* **4**, 549–561.
- Kim, J.K., Mackay, D.B. and Mai, Y.W., (1993). Drop weight impact tolerance of CFRP with rubber modified epoxy matrix. *Composites* **24**, 458–494.
- Kim, R.Y. (1983). Prevention of free-edge delamination. in *Proc. of the 28th National SAMPE Symposium*, April 1983.
- Kim, R.Y. (1989). Experimental observations of free-edge delamination. In *Interlaminar Response of Composite Materials* (N.J. Pagano ed.), Elsevier Sci. Pub., Amsterdam, Ch. 3, pp. 111–160.
- Kim, R.Y. and Soni, S.R. (1984). Experimental and analytical studies on the onset of delamination in laminates composites. *J. Composite Mater.* **18**, 70–80.
- Kinloch, A.J. (1986). Rubber toughened thermosetting polymers. In *Development in Resins and Primers* (A.J. Kinloch ed.), Elsevier Appl. Sci. Pub., London.
- Kinloch, A.J. (1987). Adhesion and Adhesives: Science and Technology. Chapman & Hall, London.
- Kinloch A.J. and Shaw S.J. (1981). Fracture resistance of a toughened epoxy adhesive. *J. Adhesion* **12**, 59–77.
- Kinloch, A.J. & Young, R.J. (1986). In *Structural Adhesives: Developments in Resins and primers* (A.J. Kinloch ed.), Elsevier Appl. Sci. Pub., London, p. 127 & 163.
- Ko, F.K. (1989). Three dimensional fabrics for composites. In *Textile Structural Composites* (T.W. Chou and F.K. Ko, eds.), Elsevier Sci. Pub. B.V., Amsterdam, Ch. 5, pp. 129–171.
- Ko, F.K., Oastore, C.M., Yang, J.M. and Chou, T.W. (1986). Structure and properties of multi-layer, multidirectional warp knit fabric reinforced composites. In *Composites '86: Recent Advances in Japan and the United States*, Japan Society for Composite Materials, Tokyo.
- Lagace, P.A. and Bhat, N.V. (1992). Efficient use of film adhesive interlayers to suppress delamination. In *Composite Materials: Testing and Design (10th Volume)*, ASTM STP 1120 (G.C. Grimes ed.), ASTM, Philadelphia, PA, pp. 384–396.
- Lee S.M. (1984). Correlation between resin material variables and transverse cracking in composites. *J. Mater. Sci.* **19**, 2278–2288.
- Lee S.M. (1987). Fracture of adhesive joints and laminated composites. *Polym. Eng. Sci.* **27**, 77–81.
- Lee, C. and Liu, D. (1990). Tensile strength of stitching joint in woven glass fabrics. *J. Eng. Mater. Technol.* **112**, 125–130.
- Leong, K.H., Herszberg, I. and Bannister, M.K. (1996). An investigation of fracture mechanisms of carbon epoxy laminates subjected to impact and compression-after-impact loading. In *Proc. 1st Australasian Congress on Applied Mechanics*, Melbourne, pp. 315–320.
- Liu, D. (1990). Delamination resistance in stitched and unstitched composite plates subjected to impact loading. *J. Reinforced Plast. Composites* **9**, 59–69.
- Llanos, A.S. and Vizzini, A.J. (1992). The effect of film adhesive on the delamination strength of tapered composites. *J. Composite Mater.* **26**, 1968–1983.
- Low, I.M. and Mai, Y.W. (1990). Fracture properties and failure mechanisms of pure and toughened epoxy resins. In *Handbook of Ceramics* (N.P. Cheremisinoff ed.), Marcel Dekker, New York, pp. 105–160.
- Lu, W.H., Liao, F.S., Su, A.C., Kao, P.W. and Hsu, T.J. (1995). Effect of interleaving on the impact response of a unidirectional carbon/epoxy composite. *Composites* **26**, 215–222.
- Masters, J.E. (1987a). Correlation of impact and interleaf delamination resistance in interleaved laminates. In *Proc. 6th Intern. Conf. Composite Mater. (ICCM-VI)* (F.L. Matthews et al., eds.), Elsevier Appl. Sci., London, pp 3.96–3.107.
- Masters, J.E. (1987b). Characterisation of impact damage development in graphite/epoxy laminates. In *Fractography of Modern Engineering Materials: Composites and Metals*, ASTM STP 948, ASTM, Philadelphia, PA, pp. 238–258.
- Masters, J.E. (1989). Improved impact and delamination resistance through interleaving. *Key Eng. Mater.* **37**, 317–348.
- Mayadas, A. Pastore, C, Ko, F.K. (1985). Tensile and shear properties of composites by various reinforcement concepts. In *Proc. 30th Int. SAMPE Symp.* pp. 1284–1293.

- McGarry, F.J. (1969). The fracture of polymers and fiber reinforced polymer composites. In *Proc. AIAA/ASME 10th Structures, Structural Dynamics & Mater. Conf.*, New Orleans, pp. 456–471.
- Mignery L.A., Tan T.M. and Sun C.T. (1985). The use of stitching to suppress delamination in laminated composites. In *Delamination and Debonding*, ASTM STP 876 (W.S. Johnson ed.), ASTM, Philadelphia, PA, 371–385.
- Morales, A. (1990). Structural stitching of textile preforms. In *Proc. 22nd. Int. SAMPE Tech. Conf.* pp. 1217–1230.
- Mouritz, A.P. (1995). The damage to underwater GRP laminates by underwater explosion shock loading. *Composites Sci. Technol.* **55**, 365–374.
- Mouritz, A.P. (1996). Flexural properties of stitched GRP laminates. *Composites Sci. Technol.* **56**, 525–530.
- Mouritz, A.P. (1997). Unpublished discussion, *Workshop on Stitched Composite Laminates*, Sydney University, Sydney.
- Norman, T.L. and Sun, C.T. (1991). Mechanical properties and interlaminar toughness of cross-ply laminates containing adhesive strips. *AIAA J.* **29**, 247–252.
- O'Brien, T.K. (1983). Mixed mode strain energy release rate effects on edge delamination of composites. NASA TR-84592.
- O'Brien, T.K. (1984). *Effects of Defects in Composite Materials*. ASTM STP 836, ASTM, Philadelphia, PA, pp. 125–142.
- Ogo, Y. (1987). The effect of stitching on in-plane interlaminar properties of carbon-epoxy fabric laminates. M.S. Thesis, University of Delaware, Delaware, USA.
- Pagano, N.J. and Pipes, R.B. (1971). The influence of stacking sequence on laminate strength. *J. Composite Mater.* **5**, 50–57.
- Pagano, N.J. and Pipes, R.B. (1973). Some observations on the interlaminar strength of composite laminates. *Int. J. Mech. Sci.* **15**, 679–688.
- Pagano, N.J. and Soni, S.R. (1983). Global-local laminate variational model. *Int. J. Solids Struct.* **19**, 207–228.
- Pipes, R.B. and Pagano, N.J. (1970). Interlaminar stresses in composite laminates under uniform axial extension. *J. Composite Mater.* **4**, 538–548.
- Poon, C., Benak, T. and Gould, R. (1990). Assessment of impact damage in toughened resin composites. *Theor. Appl. Fract. Mech.* **13**, 81–97.
- Potanova, M.A., Poc, C.C., Whitecomb, J.D. (1992). Open hole and post-impact compressive fatigue of stitched and unstitched carbon fiber-epoxy matrix composites. In *Composite Materials: Testing and Design (10th Volume)*, ASTM STP-1120 (G.C. Grimes ed.), ASTM, Philadelphia, PA, pp. 37–53.
- Rechak, S. and Sun, C.T. (1990). Optimal use of adhesive layer in reducing impact damage in composite laminates. *J. Reinforced Plast. Composites* **9**, 569–582.
- Recker, H.G., Altstadt, V., Eberle, W., Folda, T., Gerth, D., Heckmann, W., Itemann, P., Tesch, H. and Weber, T. (1990). Toughened thermosets for damage tolerance carbon fiber reinforced composites. *SAMPE J.* **26**, 73–78.
- Reeder, J.R. (1995). Stitching vs a toughened matrix: compression strength effects. *J. Composite Mater.* **29**, 2464–2487.
- Russell, A.J. and Street, K.N. (1987). The effect of matrix toughness on delamination: static and fatigue fracture under mode I and II shear loading of graphite fiber composites. In *Toughened Composites*. ASTM STP 937 (N.J. Johnston ed.). ASTM, Philadelphia, PA, pp. 257–294.
- Sawyer, J.W. (1985). Effect of stitching on the strength of bonded composite single lap joints. *AIAA J.* **23**, 1744–1748.
- Scott J.M. and Phillips D.C. (1975). Carbon fiber composites with rubber toughened matrices. *J. Mater. Sci.* **10**, 551–562.
- Sela N., Ishai O. and Banks-Sills L. (1989). The effect of adhesive thickness on interlaminar fracture toughness of interleaved CFRP specimens. *Composites* **20**, 257–264.
- Shu, D. and Mai, Y.W. (1993). Effect of stitching on interlaminar delamination extension in composite laminates. *Composites Sci. Technol.* **49**, 105–171.

- Singh, S. and Partridge, I.K. (1995). Mixed mode fracture in an interleaved carbon fiber-epoxy composite. *Composites Sci. Technol.* **55**, 319-327.
- Sohi, M.M., Hahn, H.T. and Williams, J.G. (1987). The effect of resin toughness and modulus on compressive failure modes of quasi-isotropic graphite/epoxy laminates. In *Toughened Composites*, ASTM STP 937 (N.J. Johnston ed.). ASTM, Philadelphia, PA, pp 37-60.
- Sohn, M.S. and Hu, X.Z. (1994). Mode II delamination toughness of carbon fiber/epoxy composites with chopped Kevlar fiber reinforced composites. *Composites Sci. Technol.* **52**, 439-448.
- Srinivasan, K., Jackson, W.C., Smith, B.T., Hinkley, J.A. (1992). Characterization of damage in impact thermoset and thermoplastic composites. *J. Reinforced Plast. Composites* **11**, 1111-1126.
- Sue, H.J., Jones, R.E. and Garcia-Meitin, E.I. (1993). Fracture behavior of model toughened composites under mode I and mode II delamination. *J. Mater. Sci.* **28**, 6381-6391.
- Sultan J.N., Raible R.C. and McGarry F.J. (1971). Microstructure of two-phase polymers. *J. Appl. Polym. Sci.* **6**, 627-634.
- Sun, C.T. and Luo, J. (1988). Failure loads for notched graphite/epoxy laminates with a softening strip. *Composites Sci. Technol.* **22**, 121-133.
- Sun, C.T. and Norman, T.L. (1990). Design of a laminated composite with controlled damage concept. *Composites Sci. Technol.* **39**, 327-340.
- Sun, C.T. and Rechak, S. (1988). Effect of adhesive layers on impact damage in composite laminates in Composite Materials Testing and Design (8th Conf.) ASTM STP 972 (J.D. Whitcomb ed.), ASTM, Philadelphia, PA, pp 97-123.
- Tada, Y. and Ishikawa, T. (1989). Experimental evaluation of the effects of stitching on CFRP laminate specimens with various shapes and loading. *Key Eng. Mater.* **37**, 305-316.
- Wang, S.S. and Choi, I. (1982). Boundary layer effects in composite laminates. Part I: free-edge stress singularities *J. Appl. Mech.* **49**, 541-548.
- Wang, A.S.D. and Crossman, F.W. (1977). Some new results on edge effect in symmetric composite laminates. *J. Composite Mater.* **11**, 92-106.
- Whitney, J.M. and Browning, C.E. (1973). Free edge delamination of tensile coupons. *J. Composite Mater.* **6**, 300-303.
- Wilkins, D.J. (1983). Failure analysis and mechanisms of failure of fibrous composite structures. NASA CP-2278, 67-93.
- Williams, J.G. and Rhodes, M.D. (1982). Effect of resin on impact damage tolerance of graphite/epoxy laminates. In *Composite Materials: Testing and Design (6th Conf.)* ASTM STP 787 (I.M. Daniel ed.), ASTM, Philadelphia, PA, pp 450-480.
- Wu, E. and Wang, J. (1995). Behaviour of stitched laminates under in-plane tensile and transverse impact loading. *J. Composite Mater.* **29**, 2254-2279.
- Xu, L.Y. (1996). Modifying stacking sequence design to delay delamination and matrix cracking in laminated composites - The multi delamination interface design. *J. Reinforced Plast. Composites* **15**, 230-248.
- Yee, A.F. and Pearson, R.A. (1986). Toughening mechanisms in elastomer modified epoxies: part I. Mechanical Studies. *J. Mater. Sci.* **21**, 2462.

APPENDICES

Appendix A

Coefficients B_1 , C_1 and D_1 .

$$B_1 = \left\{ n_2 - \phi(n_2 - n_1 A_1) \left[1 + \frac{A_2}{A_1} \left(1 + \frac{A_2}{A_1} \right) (2 - 2 \cosh \phi + \tanh \phi \sinh \phi) \right] \coth \phi \right. \\ \left. + \left[2n_2 \frac{A_2}{A_1} \left(1 + \frac{A_2}{A_1} \right) - n_3 \left(1 + \frac{2A_2}{A_1} \right) \right] (1 - \cosh \phi) \right\} \operatorname{cosech}^2 \phi - n_4 \quad , \quad (\text{A.1})$$

$$C_1 = \omega \exp(\lambda \ell) \left\{ \lambda F_1 + \left(\frac{dF_1}{d\ell} - \frac{\pi a^2}{E_f} \right) [1 - \exp(-\lambda \ell)] \right\} \quad , \quad (\text{A.2})$$

$$D_1 = \omega^2 \exp(2\lambda \ell) \left\langle [1 - \exp(-\lambda \ell)] \left\{ \frac{\lambda}{\sqrt{A_1}} [(n_2 + n_1 A_1) \cosh \phi \sinh \phi \right. \right. \\ \left. \left. - \phi(n_2 - n_1 A_1)] \right. \right. \\ \left. \left. + [1 - \exp(-\lambda \ell)] [n_2 - \phi(n_2 - n_1 A_1) \coth \phi] \right\} \operatorname{cosech}^2 \phi \right. \\ \left. + n_1 \lambda^2 + n_2 [1 - \exp(-\lambda \ell)]^2 \right\rangle \quad , \quad (\text{A.3})$$

where:

$$\phi = \sqrt{A_1} (L - \ell) \quad , \quad (\text{A.4})$$

$$n_1 = \frac{\pi \gamma (1 + \nu_m)}{2E_m} \left[b^4 \ln \frac{b}{a} - \frac{1}{4} (3b^2 + a^2)(b^2 + a^2) \right] \quad , \quad (\text{A.5})$$

$$n_2 = \frac{\pi a^2}{2E_m} (\alpha + \gamma) \quad , \quad (\text{A.6})$$

$$n_3 = \frac{\pi a^2}{E_m} \left[\frac{A_2}{A_1} (\alpha + \gamma) + \gamma \right] \quad . \quad (\text{A.7})$$

Appendix B

Coefficients B_3 , C_3 and D_3 .

$$B_3 = \frac{A_3}{A_1} \left[\frac{A_3}{A_1} \frac{dF_3}{dl} - n'_3 \sec^2 \phi \right] - n'_4 + \frac{\pi a^2}{2\gamma E_m} , \quad (\text{B.1})$$

$$C_3 = \omega_1 \exp(-\lambda\ell) \left\{ [1 - \exp(\lambda\ell)] \left(2 \frac{A_3}{A_1} \frac{dF_3}{dl} - n'_3 \sec^2 \phi + \frac{\pi a^2}{E_m} \right) - \lambda \left(2 \frac{A_3}{A_1} F_3 + \frac{n'_3}{\sqrt{A_1}} \tanh \phi \right) \right\} , \quad (\text{B.2})$$

$$D_3 = \omega_1^2 \exp(-2\lambda\ell) \left\{ [1 - \exp(\lambda\ell)]^2 \left(\frac{dF_3}{dl} - n_2 \right) - 2\lambda [1 - \exp(\lambda\ell)] F_3 + n'_1 \lambda^2 \right\} , \quad (\text{B.3})$$

where ϕ and n_2 are given in Eqs. (A.4) and (A.6), respectively, and

$$n'_1 = \frac{\pi(1 + v_m)}{2E_m} \gamma^2 \left[b^4 \ln \frac{b}{a} - \frac{1}{4} (3b^2 - a^2)(b^2 - a^2) \right] , \quad (\text{B.4})$$

$$n'_3 = \frac{\pi a^2}{E_m} \left[1 - \frac{A_3}{A_1} (\alpha + \gamma) \right] , \quad (\text{B.5})$$

$$n'_4 = \frac{\pi a^2}{2E_m} \left[\left(\frac{A_3}{A_1} \right)^2 \alpha + \gamma \left(\frac{1}{\gamma} - \frac{A_3}{A_1} \right)^2 \right] , \quad (\text{B.6})$$

$$F_3 = \frac{1}{2\sqrt{A_1}} [(n_2 - n'_1 A_1) \phi \sec^2 \phi + (n_2 + n'_1 A_1) \tanh \phi] . \quad (\text{B.7})$$

Appendix C

Coefficients P_1 , P_2 , P_3 , Q_1 , Q_2 , Q_3 , Q_4 , R_1 , R_2 and R_3 .

$$P_1 = \frac{\alpha v_r + \gamma v_m \beta_2}{v_m (\alpha + \gamma) \lambda} , \quad (\text{C.1})$$

$$P_2 = -\lambda P_1 \quad , \quad (C.2)$$

$$\frac{P_3}{P_2} = \frac{(1 + \gamma)v_m}{\alpha v_f + \gamma v_m} \sigma + \omega \bar{\sigma} \quad , \quad (C.3)$$

$$Q_1 = \frac{1 - \exp(-m_1 \ell)}{\exp(m_2 L) [\exp(-m_1 \ell) - \exp(-m_2 \ell)]} \quad , \quad (C.4)$$

$$Q_2 = -\frac{1 - \exp(-m_2 \ell)}{\exp(m_1 L) [\exp(-m_1 \ell) - \exp(-m_2 \ell)]} \quad , \quad (C.5)$$

$$Q_3 = -\frac{1}{\exp(m_2 L) [\exp(-m_1 \ell) - \exp(-m_2 \ell)]} \quad , \quad (C.6)$$

$$Q_4 = \frac{1}{\exp(m_1 L) [\exp(-m_1 \ell) - \exp(-m_2 \ell)]} \quad , \quad (C.7)$$

where:

$$m_1 = -\frac{P_1 + (P_1 + 4\lambda P_1)^{1/2}}{2} \quad , \quad (C.8)$$

$$m_2 = \frac{-P_1 + (P_1 + 4\lambda P_1)^{1/2}}{2} \quad . \quad (C.9)$$

Also,

$$R_1 = \frac{-m_1 \exp(-m_1 \ell) + m_2 \exp(-m_2 \ell) + (m_1 - m_2) \exp[-(m_1 + m_2) \ell]}{\exp(-m_1 \ell) - \exp(-m_2 \ell)} \quad , \quad (C.10)$$

$$R_2 = \frac{m_1 \exp(-m_1 \ell) - m_2 \exp(-m_2 \ell)}{\exp(-m_1 \ell) - \exp(-m_2 \ell)} \quad , \quad (C.11)$$

$$R_3 = \alpha \lambda (v_m - v_f) + R_2 (\alpha v_f + \gamma v_m) \quad . \quad (C.12)$$

Appendix D

Coefficients A_3 and A_4 .

$$A_3 = \beta_5 \left\{ \alpha + \gamma_2 + \frac{2}{V_f k_2} [(\alpha v_f + \gamma v_m) V_f (\gamma_2 k_3 - \alpha v_f k_1) - \gamma v_m (\gamma_2 k_4 - 2\alpha v_f \gamma)] \right\} \quad , \quad (D.1)$$

$$A_4 = \beta_5 \left\{ 1 - \frac{2}{V_f k_2} [\gamma v_m k_4 - (\alpha v_f + \gamma v_m) V_f k_2] \right\}, \quad (\text{D.2})$$

where:

$$\beta_5 = \frac{1}{a^2 \gamma_2 (1 + v_m) \left[\left(\frac{b}{a} \right)^2 \ln \left(\frac{b}{a} \right) - \frac{1}{2\gamma} \right]}, \quad (\text{D.3})$$

$$k_2 = \frac{1}{V_f} \{ V_f k_1 [\alpha(2 - v_f) + 1 + 2\gamma + v_m] - 4\gamma^2 \}, \quad (\text{D.4})$$

$$k_3 = \frac{2\gamma}{V_f} (v_m - \alpha_1 v_c) - v_m k_1, \quad (\text{D.5})$$

$$k_4 = (v_m - \alpha_1 v_c) [\alpha(1 - v_f) + 1 + 2\gamma + v_m] - 2\gamma v_m. \quad (\text{D.6})$$

SYMBOLS AND ABBREVIATIONS

a	crack length or fiber radius (= half of fiber diameter, $d/2$)
Δa	incremental crack length
b	matrix outermost radius
b	breadth or width
C	compliance
C^*	measured compliance when residual displacements are present
c_0	size of damage zone
d	diameter
d_f	stitch thread diameter
E	elastic modulus (E_f fiber; E_m matrix; E_c composite)
E_{11}	Young's modulus in the first in-plane principal direction (= E_L , longitudinal Young's modulus)
E_{22}	Young's modulus in the second in-plane principal direction (= E_T , transverse Young's modulus)
E'	effective Young's modulus
E	energy (E_k kinetic energy; E_B electron beam energy)
G	potential energy release rate (with units of kJ/m^2)
G_c	critical potential energy release rate
G_e	strain energy release rate in edge notched tension test
G_I	mode I interlaminar fracture toughness (G_{I-II} : mixed mode I & II)
G_{Ic}^c	composite interlaminar fracture toughness
G_{Ic}^m	neat resin fracture toughness
G_{IIc}	mode II interlaminar fracture toughness
G_R^*	total potential energy release rate
G	elastic component of total potential energy release rate
G_{Ic}	interfacial fracture toughness
G	shear modulus
G_{LT}	in-plane shear modulus of laminate
G_m	shear modulus of matrix
h (or t)	height (or thickness)
$h\nu$	total absorbed X-ray photon energy
I	moment of inertia
J_c	composite J integral
K	stress intensity factor (with units of $\text{MPa } \sqrt{\text{m}}$)
K_c	stress intensity factor of composite
K_m	stress intensity factor of matrix material
K_R	crack growth resistance
L	half span

L	embedded fiber length ($= \ell_c$)
L_{\max}	maximum embedded fiber length allowed to pull-out
$(2L)_c$	critical fiber transfer length ($= \ell_c$)
L_a	apparent crystal diameter
m	Weibull modulus
M	microstructural efficiency factor
P	applied force
	P_{\max} maximum applied load
ΔP	driving force for infiltration
q_0	residual shrinkage stress in the radial direction
q^*	radial stress due to Poisson contraction
R	fracture toughness or specific work of fracture (with units of kJ/m^2)
	R_c measured composite fracture toughness
	R_d interfacial debonding
	R_{dr} post-debonding fraction
	R_{fs} plastic shear of fiber
	R_i interfacial fracture toughness (or G_{ic})
	R_L fracture toughness for longitudinal splitting
	R_{ms} plastic shear of matrix material
	R_{po} frictional fiber pull-out
	R_r stress redistribution
	R_s surface energy
	R_T transverse fracture toughness
	R_t predicted total fracture toughness
r_c	radius of capillary
r_f	roughness factor
r_p	half the plastic deformation zone
S_D	stitch density
T_g	glass transition temperature
ΔT	temperature difference
U_t	total strain energy ($= U_b + U_d$, stored in the bonded and debonded regions)
ΔU	area under the load–displacement trace
u	displacement (u_f in the fiber; u_m in the matrix)
V_f	volume fraction of fiber
W_a	work of adhesion
z_{\max}	maximum embedded fiber length for unstable debond process
α	coefficient of thermal expansion (CTE)
	α_c CTE of composite
	α_{cL} CTE of composite in the longitudinal direction
	α_{cT} CTE of composite in the transverse direction
	α_f CTE of fiber
	α_i CTE of interlayer or coating

	α_m	CTE of matrix
γ		volume ratio of fiber to matrix ($= a^2/(b^2 - a^2)$)
δ		displacement
	δ_r	residual displacement
ϵ		(tensile) strain (ϵ_f fiber; ϵ_m matrix; ϵ_c composite)
	$\Delta\epsilon$	differential strain between fiber and matrix
Γ		gamma function
γ		surface free energy
	γ_{SV}	surface free energy at the solid–vapor interface
	γ_{LV}	surface free energy at the liquid–vapor interface
	γ_{SL}	surface free energy at the solid–liquid interface
	γ^d	surface free energy due to dispersion forces
	γ^p	surface free energy due to polar contribution
η		viscosity of fluid
θ		inclined angle of fiber to the applied stress direction
		contact angle (θ_r : change in contact angle due to rough surface)
λ		reciprocal length giving effective shear stress transfer
μ		coefficient of friction
μ		shear modulus
μ_c		effective in-plane shear modulus
ν		Poisson ratio (ν_f fiber; ν_m matrix; ν_c composite; ν_i interlayer or coating)
v_0		velocity of fiber pull-out
π_s		spreading pressure
ρ		density
σ		longitudinal stress or strength
	σ	asymptotic debond stress
	σ_0	frictionless initial debond stress
	σ_{ai}	residual stress at the fiber–coating interface in the radial direction
	σ_b	interface bond strength in tension
	σ_c	composite strength
	σ_{ci}	residual stress at the coating–matrix interface in the radial direction
	σ_d	debond stress
	σ_d^p	partial debond stress
	σ_d^*	maximum debond stress
	σ_f	fiber axial stress
	σ_f^*	fiber tensile strength
	σ_m	matrix axial stress or tensile strength
	σ_{my}	matrix yield strength
	σ_N	net compressive stress
	σ_{od}	external stress for interfacial debonding
	σ_{of}	external stress for fiber fragmentation
	σ_{po}	initial frictional pull-out stress
	σ_{TS}	fiber tensile strength at critical transfer length
	σ_ℓ	crack tip debond stress

τ		shear stress or strength
	τ_a	apparent shear strength at the interphase
	τ_b	interface shear bond strength
	τ_{fr}	frictional shear stress at the interface
	τ_m	matrix shear stress
	τ_y	shear yield stress
v_0		velocity of fiber pull-out
χ		fraction of fibers broken when $l > l_c$
Ω		reinforcing effectiveness parameter
Ψ		phase angle
l		characteristic fiber length
	l_c	critical transfer length
	l_d	fiber debond length
	l_{po}	fiber pull-out length
AES		auger electron spectroscopy
AFMB		asymmetric four-point bending
AFM		atomic force microscopy
AN/MA		acrylonitrile/methyl acrylate
APS		aminopropyl triethoxysilane
BFRP		boron fiber reinforced polymer composites
BMA		polybutadiene-co-maleic anhydride
B/W		boron (tungsten core) fiber
CAI		compressive strength after impact
CBEN		cantilever beam enclosed notch
CC		compliance calibration
CFRP		carbon fiber reinforced polymer composites
CLS		cracked lap shear
CMCs		ceramic matrix composites
CN		center notched
CTBN		carboxyl-terminated butadiene acrylonitrile
CTE		coefficient of thermal expansion
CVD		chemical vapor deposition
DCB		double cantilever beam
DGEBA		diglycidyl ether of bisphenol A
DZM		damage zone model
ELS		end loaded split
ENF		end notched flexure
EP		epoxy
ESCA		electron spectroscopy for chemical analysis
FAS		fiber axial stress
FEM		finite element method
FPZ		fracture process zone
FTIR		fourier transform infrared spectroscopy
GA/MA		glycidyl acrylate/methyl acrylate

GFRP	glass fiber reinforced polymer composites
HDPE	high density polyethylene
HM	high modulus
HMDS	hexamethyl disiloxane
ICCI	international Conference on Composite Interfaces
IFS	interface frictional shear stress
IFM	inherent flaw model
IFT	interlaminar fracture test
ILSS	interlaminar shear strength
IM	intermediate modulus
IPCM	interfacial phenomena in composite materials
IPN	Interpenetrating network
IFSS	interfacial shear stress
ISS	ion scattering spectroscopy
IR	infrared
KFRP	Kevlar fiber reinforced polymer composites
LEFM	linear elastic fracture mechanics
LM	low modulus
MAS	matrix axial stress
MBT	modified beam theory
MCC	modified compliance calibration
MMCs	metal matrix composites
MPS	methacryloxypropyl trimethoxysilane
NPDGE	neopentyl diglycidyl ether
NMR	nuclear magnetic resonance spectroscopy
PA	polyamide
PAN	polyacrylonitrile
PB	polybutadiene
PBT	polybutylene terephthalate
PBT	polyphenylene benzobisthiazole
PC	polycarbonate
PEEK	polyetheretherketone
PET	polyethylene terephthalate
PMCs	polymer matrix composites
PMMA	polymethylmethacrylate
PP	polypropylene
PPS	polyphenylene sulfide
PS	polystyrene
PTC	phase transfer catalytic
PTFE	polytetrafluoroethylene
PUB	polybutyl acrylate
PUV	polyurethane varnish
PVA	polyvinyl acetate
PVAL	polyvinyl alcohol
PVD	physical vapor deposition

RoM	rule of mixture
SALS	small angle light scattering
SAXS	small angle X-ray scattering
SEM	scanning electron microscopy
SEN	single edge notch
SIMS	secondary ion mass spectroscopy
STM	scanning tunneling microscopy
SVF	silicone vacuum fluid
$S/(D-a)$	span-to-depth ratio
UD	unidirectional
UHMPE	ultrahigh modulus polyethylene
UHMW	ultrahigh molecular weight
TEM	transmission electron microscopy
XPS	X-ray photoelectron spectroscopy
WAXS	wide angle X-ray scattering
WTDCB	width tapered double-cantilever-beam

AUTHOR INDEX

[Plain numbers refer to text pages on which the author (or his/her work) is cited.
Boldface numbers refer to the pages where bibliographic references are listed.]

- Abdallah, M.G. 68 **85**
Aboudi, J. 95 **164** 297–298 **320**
Abraham, S. 211 **228**
Abrahams, F.L. 64, 66 **86**
Absolom, D.R. 11 **40**
Accorsi, M.L. 96 **164**
Adams, D.F. 66–68 **85 92** 203 **228**
Adamson, A.W. 6, 8, 17, 21, 34–35 **38**
Adanur, S. 354–355, 358 **360**
Afaghi-Khatibi, A. 271 **273**
Agarwal, B.D. 270 **273** 306 **321**
Ahaim, R. 318 **320**
Aharonov, R. 46 **91**
Ahlstrom, C. 94, 96 **164** 300 **321**
Ait-kadi, A. 199, 203 **236 237**
Aker, S. 345–348 **361**
Aksay, I.A. 226 **228**
Aksoy, A. 345, 348 **360**
Aksoy, S. 218 **232**
Al-khudhauri, D. 34 **41**
Al-Moussawi, H. 178–180 **229 231**
Alam, M.K. 209 **228**
Allassoeur, P. 218 **232**
Albert K, 177 **228**
Alexander, R.M. 268 **273**
Allen, G. 249–250 **277**
Allred, R.E. 51 **90** 196–198, 200 **228 234**
Almond, E.A. 306 **320**
Altstadt, V. 339–340 **364**
Altus, E. 345 **360**
Alwan, J.M. 160 **167**
Amateau, M.F. 8 **38**
Ananth, C.R. 150 **164**
Anderson, K.L. 297 **324**
Andersons, J. 50 **85**
Andreopoulos, A.G. 199 **229**
Andrews, M.C. 312 **320 325**
Angelini, P. 301, 316 **322**
Anstice, P.D. 243, 255 **273 274**
Antoon, M.K. 177 **229**
Argon, A.S. 263, 265 **275**
Arnold, S.M. 220 **229** 304, 306, 315–318
320
Arocho, A.M. 12–13 **41** 94, 150 **168**
Aronsson, C.G. 271 **273**
Arridge, G.C. 280, 291, 306, 315 **324**
Arridge, R.G.C. 126, 135 **168** 291 **320**
Arsenault, R.J. 240 **277** 282 **326**
Arya, V.K. 220 **229** 306, 316 **320**
Asloun El, M. 50–51 **85**
ASTM D 2344 66 **85**
ASTM D 3518 69 **85**
ASTM D 4255 71 **85**
ASTM D 3846 72–73 **85**
ASTM D 3039 72 **85**
ASTM D 5528 79–80 **85**
Atkins, A.G. 240, 243–247, 259 **273 276**
283–284, 294 **320 324**
Atkinson, C. 94, 149 **164**
Avila, J. 94, 149 **165**
Backlund, J. 271 **273**
Bader, M.G. 26 **39** 189, 191 **229** 248, 271
273 274 285 **320**
Bailey, J.E. 248 **274** 285 **320**
Bailey, W.J. 319 **320 324**
Baillie, C. 14, 26 **38** 53–54 **85 89** 108–109,
128, 134–135, **166 169** 191 **229** 354–355
361
Baillie, C.A. 14, 26 **38** 54 **85**
Banbaji 126, 149 **164**
Banks-Sills, L. 345, 347 **364**

- Bannister, D.J. 312 **320**
 Bannister, M.K. 358 **362**
 Bansal, R.C. 186 **231**
 Barczak, V.J. 226 **229**
 Barker, R.M. 94 **167**
 Barnes, J.A. 288, 293, 310 **326**
 Barsoum, M. 53 **86**
 Barthel, R. 252–254, 273 **275**
 Bartos, P. 53 **86**
 Basche, M. 215 **229**
 Bascom, W.D. 45, 50 **86** 175, 186–187 **229**
 330, 333 **360 362**
 Batchelder, D.N. 22 **39** 50 **87** 312 **322**
 Bathias, C. 268 **274**
 Baxevanakis, C. 50 **86**
 Beaumont, P.W.R. 126–127 **168** 243, 246,
 248, 250, 254–256, 268–269 **273–275 277**
 280, 285–286 **321 322 326**
 Becher, P.F. 16 **38** 126, 149–150 **166** 301,
 316, 318 **322 326**
 Bell, I. 285 **320**
 Bell, J.P. 48 **92** 287, 291–295 **321 326**
 Beltzer, A.I. 47 **86**
 Belzunce, F.J. 270 **277**
 Benak, T. 339 **364**
 Benatar, A. 295 **321**
 Bender, B. 222 **229**
 Beneveniste, Y. 298 **321**
 Bennett S.C. 185 **229**
 Benson, R.A. 75 **92**
 Benzeggagh, M.L. 82–83 **86 90**
 Berg, C.A. 64 **86**
 Berg, J.C. 10, 37 **40**
 Berger, E.J. 38 **38**
 Berry, J.M. 282 **322 325**
 Berry, J.P. 79 **86**
 Berthelot, J.M. 95 **164**
 Besio, G.J. 54 **89**
 Betz, E. 94, 149 **164**
 Bhat, N.V. 345 **363**
 Bibo, G.A. 358 **360**
 Birchall, J.D. 228 **229**
 Birger, S. 66 **86**
 Biro, D.A. 54 **86** 205 **229**
 Bishop, P.T. 268 **276**
 Bitritto, M.M. 319 **320**
 Blackburn, L.D. 14 **38**
 Block, A. 175 **235**
 Blue, C.A. 212 **236**
 Boll, D.J. 45 **86**
 Bonifazi, G. 358 **360**
 Boukhili, B. 64 **86**
 Bour, J.S. 217 **233**
 Bourdeux, M. 189 **235**
 Bowles, D.E. 310, 312 **321**
 Bowles, K.J. 339 **360**
 Bradbury, J.A.A. 228 **229**
 Bradley, W.L. 82 **87** 332–333, 335–339, 341
360 362
 Bradshaw, W.G. 189 **234**
 Bradt, R.C. 260 **276**
 Brady, R.F. 320 **326**
 Brandon, D.G. 58 **91**
 Bredin, C. 280 **322**
 Brendle, M. 187 **231**
 Brennan, J.J. 222 **236**
 Breuer, O. 203 **235**
 Brie, M. 189 **235**
 Bright, J.D. 58 **86** 137, 150 **164**
 Brinson, H.F. 95–96 **167** 297 **324**
 Brisbane, A.W. 14 **38**
 Brisson, J. 199 **237**
 Brittain, R.D. 219 **232**
 Brosse, C.R. 220 **234**
 Broutman, L.J. 44 **86** 268 **274** 306 **321**
 Brown, A. 29–30 **39**
 Brown, H.C. 298, 315–316 **321**
 Brown, J.R. 200 **229**
 Browning, C.E. 64, 66 **86 92** 342, 347 **360**
365
 Brun, M.K. 58 **86**
 Brussat, T.R. 83 **86**
 Bryan, S.J. 94, 128, 143, 145–148 **166** 300
324
 Bucher, R.A. 37 **38**
 Bucknall, C.B. 320 **321**
 Buczcck, M.B. 264 **274**
 Butler, E.P. 53 **86** 136 **164**
 Buxton, A. 14 **38**
 Bycrly, G.E. 310 **320**
 Bystry, F.A. 246 **276**
 Byun, J.H. 352, 356 **360**
 Camahort, J. 215 **235 236**
 Camping, J.D. 47–48 **87**
 Camus, G. 220 **235**
 Caneva, C. 357 **360**
 Cano, R.J. 356 **361**

- Cantonwine, P.E. 217 **229**
 Cantor, B. 218 **231**
 Caprino, G. 271 **274**
 Carlsson, L.A. 82 **86** 214 **229** 345, 348 **360**
 Carroll, B.J. 36–37 **38**
 Caruso, J.J. 298, 315–316 **321**
 Carter W.C. 127–128, 157 **164**
 Castino, F. 284, 293–294 **324**
 Castle, J.E. 17, 26–27, 29–30 **38 39**
 Cazeneuve, C. 12, 26–27, 29 **39**
 Cervenka, A.J. 312 **320**
 Chaim, R. 222 **229**
 Chakachery, E.A. 333 **360**
 Chamin, R.A. 75 **92**
 Chamis, C.C. 72–73 **86** 94, 150 **167**, 300,
 308, 312, **321 325**
 Chan, H.M. 53 **86** 136 **164**
 Chan, W.S. 345–348 **361**
 Chandra, N. 150 **164**
 Chang, J. 287, 294 **321**
 Chang, T.C. 189 **232** 354–355 **361**
 Chapman, A.R. 228 **229**
 Chapman, T.J. 310 **321**
 Chappell, P.J.C. 200 **229**
 Charalambides, B. 189 **229**
 Chatterjee, A. 313 **326**
 Chawla, K.K. 217, 221, 224, 226–228 **230**
231, **234–236** 240, 261 **274** 282 **321**
 Chen, E.J.H. 58 **86** 150 **164**
 Chen, R. 213 **230**
 Chen, S.F. 345, 348 **361**
 Chen, T. 297 **321**
 Chen, W.J. 187 **229**
 Chen, X. 126 **165**
 Cheng, T.H. 177, 181 **230**
 Cheung, W.L. 126 **169**
 Chian, K.S. 199 **233**
 Chiang, C.H. 95, 175, 177, 180, 182, **230–**
232
 Chiao, C.C. 70 **87**
 Chiao, T.T. 70 **87**
 Chin, I.J. 178 **236**
 Chitwood, W.E. 200 **236**
 Chiu, S.T. 83 **86**
 Cho, C.R. 205 **230**
 Choi, I. 344 **365**
 Choi, N.S. 248 **277**
 Choksi, G. 62 **90**
 Chou, T.W. 315 **321** 352, 354, 356 **360–363**
 Christensen, R.M. 297 **321**
 Chu, N.J. 54 **87**
 Chua, P.S. 179, 181–182 **230** 268 **274**
 Chuang, S.L. 54 **87**
 Chung, W.C. 308 **323** 354–355 **361**
 Clark, H.A. 174 **230 235**
 Claypool, C.M. 94 **168**
 Clough, R.B. 46 **89**
 Clyne T.W. 58 **92** 208, 219 **230 233** 240 **274**
 Cohen, R.N. 332–333, 336 **360**
 Cook, J. 257–258 **274** 280, 283, 307 **321**
 Cooper, G.A. 244, 247, 257, 259 **274** 280
321
 Corder, L. 45 **86**
 Corleto, C.R. 81 **87**
 Cotterell, B. 6 **39** 59 **87** 102, 127 **165** 240,
 268 **274** 307–308 **324**
 Cotteret, J. 220 **234**
 Cottingham, R.L. 330, 333 **360**
 Cottrell, A.H. 244 **274**
 Courtney, T.H. 47 **89**
 Cox, H.L. 50–51 **87** 93–94, 96–97, 99 **164**
 Craddock, J.N. 298 **321**
 Crasto, A.S. 287, 294, 313–314 **321 326**
 Croman R.B. 58 **86**
 Crossman, F. 215 **235 236** 343 **365**
 Cruse, T.A. 268 **275**
 Cui, W.C. 64–66 **87**
 Culler, S.R. 177 **230**
 Cupcic, A. 95 **164**
 Curtin, W.A. 50 **87** 94 **164**
 Curtis, P.T. 248 **274**
 D'oria, F.J. 175 **235**
 Daabin, A. 94, 96 **164** 300 **321**
 Daghyani, H.R. 333 **361**
 Dagli, G. 189 **230 236**
 Dai, S.R. 179 **230**
 Daly, J.H. 13, 21 **39**
 Danchaivijit, S. 137, 150 **164**
 Daniel, I.M. 95 **167** 310 **321 324** 344 **361**
 Daoust, J. 94, 96 **164** 300 **321**
 Darwish, A.Y. 268, 273 **276**
 Das, H. 189 **232**
 Dauksch, H. 189 **231**
 Dauksys, R.J. 191 **230** 288, 293 **321**
 Davidge, R.W. 240 **274**
 Davidovitz, M. 64 **87**
 Davies, P. 76 **87 90**

- Day, R.J. 22 **39 41**
 de Charentenay, F.X. 81–82 **86 90**
 de Kok, J.M.M. 293 **321**
 de Meester, P. 200 **232**
 DeBolt, H.E. 217 **230**
 Delmonte, J. 186 **230**
 DeLong, J.D. 21 **39**
 Demarkos, C.B. 297 **326**
 Denison, P. 29–30 **39 177, 203 236**
 Derby, B. 218 **231**
 Desaegeer, M. 58 **87 96 166**
 Desarmot, G. 50, 53 **87 98 165**
 Deska, E.W. 354 **362**
 Deslandes, Y. 54 **86 205 229**
 DeVincent, S.M. 212 **230**
 Dharani, L.R. 300 **325**
 Dhillon, J. 287, 293 **325**
 DiAnselmo, A. 96 **164 300 321**
 DiBenedetto, A.T. 96 **164**
 DiCarlo, J.A. 216 **230**
 Dickinson, L.C. 357, 359 **361**
 Dinwoodie, J. 228 **229**
 Diwanji, A.P. 210 **230**
 Dobb, M.G. 196, 198 **230**
 Doble, J.B. 53–54 **90**
 Doghri, H. 298, 315 **321**
 Doner, D.R. 285, 312–313 **321**
 Dong, S. 187 **231**
 Donnellan, M.E. 12–13 **41 217 230**
 Donnet, J.B. 186–189 **231**
 Dow, N.F. 95 **165**
 Dow Corning Corporation 174 **231**
 Doxsee Jr. L. 200 **232**
 Dransfield, K. 354–355 **361**
 Drown, E.K. 178–180 **229 231**
 Drukker, E. 345, 348 **362**
 Drumm, C.A. 32 **39**
 Drzal, L.T. 1–3 **4 36 39 47 48, 51, 54, 58,**
 73–74 **87 89 91 94–96, 150 165 168 178,**
 186, 189, 191, 194–196, 201 **229 231 233**
 234 300 **322 337 361**
 Du, G.W. 352, 356 **360**
 Dugdale, D.S. 311 **322**
 Dugne, O. 220 **234**
 Dundurs, J. 262 **274**
 Durelli 310 **321**
 Duvis, T. 288, 295 **322**
 Dvorak, G.J. 297 **321**
 Dynes, P.J. 36 **39**
 Eberle, W. 339–340 **364**
 Ebert, L.J. 64 **91**
 Eckstein, Y. 38 **38**
 Ehrburger, P. 186, 188 **231**
 Eisenmann, J.R. 75 **92 271 277**
 Ellis, C.D. 268 **274**
 Ellul, M.D. 53 **87**
 Emadipour, H. 175, 182–183, 191 **231 233**
 Embury, J.D. 306 **320**
 Emerson, R.J. 53 **87**
 Endo, T. 319 **320**
 Erdogan, F. 264 **274**
 Erickson, P.W. 175 **231**
 Eshelby, J.D. 95 **165**
 Esnault, R. 268 **274**
 Evans, A.G. 127 **168 223 231 240, 262 274**
 276
 Evans, R.E. 339–341, 349 **361**
 Faber, K.T. 53 **88**
 Fan, C.F. 94 **165 300 322**
 Farley, G.L. 356–359 **361**
 Favre, J.P. 46–47, 50–51, 53 **87 88 91 96,**
 165 307–308 **322**
 Feillard, P. 95, 98 **165**
 Feingold, E. 224 **234**
 Felbeck, D.K. 240, 243, 245–247, 259 **276**
 283, 307–308 **323 324**
 Ferber, M.K. 58 **87 228 235 236**
 Fernando, J. 228 **236**
 Fila, M. 280 **322**
 Filiou, C. 22 **39**
 Filisko, F.K. 259 **276**
 Fischbach, D.B. 260 **276**
 Fisher, S. 64 **87**
 Fitz-Randolph, J. 243 **274**
 Fitzer, E. 213 **231**
 Folda, T. 339–340 **364**
 Francis, D.W. 11 **40**
 Frazier, W.E. 217 **230**
 Friedrich, K. 248, 250, 255–256 **274 275 277**
 Fritz, W. 213 **231**
 Fu, S.Y. 126 **165**
 Fukunaga, H. 314 **323**
 Fuller, E.R. 53 **86 136 164**
 Furrow, K.W. 356 **361**
 Gabayson, S.M. 200 **236**
 Gaddipati, A.R. 219 **235**

- Gadow, R. 213 **231**
 Gaggar, S. 268 **274**
 Galiotis, C. 24–25 **39** 50 **87** 312 **322** **323**
 Gallis, H.E. 37 **41**
 Gamble, A.J. 94, 96 **164** 300 **321**
 Gao, S. 204 **231**
 Gao, Y.C. 59 **87** 102, 127 **165**
 Gao, Z.J. 298 **322**
 Garbassi, F. 187–188 **231**
 Garcia, R. 71 **88**
 Garcia-Meitin, E.I. 335 **365**
 Gardener, S.D. 297–299 **322** **324**
 Garg, A.C. 280 **322** 331 **361**
 Garton, A. 13, 21 **39**
 Gascoigne, H.E. 68 **85**
 Gatti, A. 282 **322** **325**
 Gaur, U. 54–55 **88** **90**
 Gause, L.W. 12–13 **41** 94, 150 **168**
 Gauvin, R. 64 **86**
 Gent, A.N. 53 **88** 126, 149–150 **165**
 Gerard, J.F. 94, 96 **164** 286, 293, 300 **321**
322
 Gershon, B. 244 **274**
 Gerth, D. 339–340 **364**
 Gette, A. 220 **234**
 Ghosn, L. 315 **322**
 Giare, G.S. 270 **273**
 Gilbert, A.H. 10, 37–38 **39**
 Gillespie, J.W. 82 **86** **88** 310 **321** 355–356
360 **361**
 Goan, J.C. 189, 192 **231**
 Goettler, R.W. 53 **88**
 Goldstein, B. 10, 37–38 **39**
 Good, R.J. 11, 34–35 **39** **40**
 Gopalratnam VS 136 **165**
 Gordon, J.E. 257 **274** 280, 283, 307 **321**
 Gould, R. 339 **364**
 Graham, A.L. 263 **277**
 Grande, D.H. 57–58 **88** 94, 150 **165**
 Grap, R.T. 21, 32 **39**
 Grathwohl, G. 316 **324**
 Gray, R.J. 126 **165**
 Greenfield, I.G. 228 **232**
 Greszczuk, L.B. 73 **88** 95, 126 **165**
 Griffin, C.W. 53, 58 **86** **88** 150 **164**
 Griffin, O.H. 310, 312 **321**
 Groves, G.W. 248, 250 **275**
 Gu, M.Y. 211 **237**
 Guenon, V.A. 354 **361**
 Guette, A. 220 **234**
 Guilman, G. 187, 189 **231**
 Gulino, R. 50, **88** 96, 150 **165**
 Guo, Z.X. 218 **231**
 Gupta, V. 263–264 **275**
 Gurney, C. 78 **88** 126 **165**
 Gutowski, T.G. 295 **321**
 Gutowski, W. 10 **39**
 Ha, J.S. 228 **231**
 Hackett, R.M. 297–298 **322** **324**
 Hahn, H.T. 94, 150 **166** 268 **276** 311, 313
324 339 **365**
 Hakeem, M. 308 **324**
 Hall, I.M. 210, 213 **230** **231**
 Halpin, J.C. 271 **274**
 Hamada, H. 182–184 **236**
 Hammer, G.E. 36 **39**
 Hancox, N.L. 279, 286–287, 292–293 **322**
 Hansen, D.H. 58 **87**
 Harper, J. 287, 293 **325**
 Harris, B. 240–244, 246, 248, 250, 254, 259
268 **274** **275** 285–286, 310–311 **322**
 Harris, L.A. 318 **326**
 Harvey, J. 29–30 **39**
 Hasegawa, Y. 216 **237**
 Hashemi, S. 79 **88**
 Hayashi, J. 216 **237**
 He, G.H. 126 **165**
 He, M.Y. 260, 262–263 **275**
 He, P. 320 **322**
 Heckmann, W. 339–340 **364**
 Helfet, J.L. 248, 250, 254 **275**
 Hellmann, J. 226 **234**
 Hellmann, J.R. 94, 150 **166**
 Hener, A.H. 58 **90**
 Henstenburg, R.B. 49 **88**
 Herakovich, C.T. 62 **90** 264 **274** 342–343 **362**
 Herrera-Franco, P. 54–56, 58 **88** **91**
 Herszberg, I. 358 **362**
 Herzog, J.A. 14 **38**
 Hess, T.E. 345 **362**
 Heuer, A.H. 222 **229** 314, 318 **320** **325**
 Heyliger, L.A. 343 **362**
 Hibbs, M.F. 333, 335, 337 **362**
 Hidde, J.S. 62 **90**
 Hiemstra, D.L. 311 **322**
 Hild, D.N. 205 **232**
 Hillerborg, A. 271 **275**

- Hing, P. 248, 250 **275**
 Hinkley, J.A. 37 **38** 339–340 **365**
 Hirai, Y. 358 **363**
 Hirschbuehler, K.R. 339–341 **362**
 Ho, H. 94, 96, 150 **165** 300 **322**
 Hoffmann, A.S. 197 **233**
 Hoffmann, K.R. 174 **235**
 Hogg, P.J. 358 **360**
 Hoh, K.P. 32 **39** 177 **232**
 Holms, S. 205 **232**
 Holt, D.J. 354, 357 **362**
 Homeay, J. 58 **87**
 Hong, C.S. 313 **323** 343 **362**
 Hook, K.J. 21 **39**
 Hooper, R.C. 175 **232**
 Hopfgarten, F. 190 **232**
 Horie, K. 189 **232**
 Howard, W.E. 347 **362**
 Hoysan, S.F. 94, 150 **167**
 Hsu, P.W. 342 **362**
 Hsu, S.L. 94 **165** 300 **322**
 Hsu, T.J. 349 **363**
 Hsueh, C.H. 58–60 **88** 95–96, 126, 149–150
 166 301, 316 **322**
 Hu, X.Z. 79 **88** 345 **365**
 Huang, D.D. 268, 273 **276**
 Huang, S.L. 354 **362**
 Huang, X.N. 79 **88**
 Hubert, P. 64 **86**
 Hughes, J.D.H. 186 **232**
 Hughes, J.F. 293 **322**
 Hull, D. 6, 8 **39** 79 **88** 97 **166** 172–173, 175,
 177 **232** 311 **322**
 Humphrey, P. 29–30 **39**
 Hunston, D.L. 332–333, 337 **362**
 Hunt, J. 77 **88** 126 **166**
 Hutchinson, J.W. 127, 150 **166** **167** 260,
 262–263 **275**
 Hwang, L.R. 189, 219 **232** 308 **323** 354–355
 361

 Imura, M. 216 **237**
 Ikuta, N. 51 **88**
 Iler, R.K. 295 **322**
 Inagaki, N. 201 **232**
 Inamura, T. 320 **326**
 Inoue, M. 320 **326**
 Insley, R.H. 226 **229**
 Iosipescu, N. 66–67 **88**

 Ishai, O. 345, 347–348 **360** **362** **364**
 Ishida, H. 12, 17, 21 **39** **40** 175, 177, 180 **230**
 232 280, 293 **324**
 Ishikawa, T. 314 **323** 339, 357 **365**
 Iskandarni, B. 203 **235**
 Israeli, M. 64 **86**
 Ittemann, P. 339–340 **364**
 Ivens, J. 191 **232**
 Iwama, I. 319 **320**

 Jackson, W.C. 339–340 **365**
 Jacques, D. 51 **87** 96 **165**
 Jahankhani, H. 312 **323**
 Jain, L.K. 356–357 **362**
 Jain, S.C. 210 **228**
 Jakubowski, J.J. 294 **326**
 James, M.R. 12–13 **41**
 James, N.A. 217 **232**
 Jang, B.J. 189 **232**
 Jang, B.Z. 219 **232** 308 **323** 345, 348, 354–
 355 **361**
 Jang, J. 205 **230**
 Janssens, W. 200 **232**
 Jansson, S. 298, 315 **321** **323**
 Jao, S.H. 287, 293, 298 **323**
 Jayaraman, K. 297, 299 **323**
 Jayaraman, K.L. 296–297 **323**
 Jea, L.C. 307–308 **323**
 Jeng, S.M. 218–219 **232**
 Jensen, H.M. 127 **166**
 Jensen, M. 50 **86**
 Jensen, R.M. 45 **86**
 Jerina, K.L. 268 **273**
 Jero, P.D. 127, 157 **166** 316 **323**
 Jeronimidis, G. 313 **323**
 Jeulin, D. 50 **86**
 Jiang, K.R. 127 **166**
 Jiu, X.M. 311 **326**
 Johnson, D.J. 185, 196–198 **230**
 Johnson, S.M. 219 **232**
 Johnston, N.J. 332–333, 337 **362**
 Johnston, W.D. 228 **232**
 Jones, C. 177, 218 **233**
 Jones, F.N. 293 **326**
 Jones, F.R. 26, 29–30 **39** **41** 177, 181, 203,
 230 **233** **236** 312 **323**
 Jones, R.E. 335 **365**
 Jones, R.L. 330 **360**
 Jones, T.J. 285, 291–293 **326**

- Joo, J.W. 343 **362**
 Jordan, W.M. 332–333, 336–337, 341 **362**
 Joseph, R. 287, 294 **321**
 Jouquet, G. 189 **235**
 Jun W.J. 313 **323**
 Jung, T. 50 **88**
- Kaang, S.Y. 53 **88**
 Kaelble, D.H. 36 **39**
 Kahl, A. 178 **236**
 Kajiyama, T. 199 **236**
 Kalanta, J. 51 **88** 201 **233**
 Kaliaguine, S. 177, 203 **236**
 Kallas, M.N. 58 **88** 94, 150 **166**
 Kalnata, J. 21 **39**
 Kamel, I. 203 **235**
 Kamigaito, O. 249 **277**
 Kaminski, B.E. 271 **277**
 Kang, T.J. 355, 358–359 **362**
 Kao, B.G. 68 **91**
 Kao, P.W. 349 **363**
 Karbhari, V.M. 134–135 **166**
 Kardos, J.L. 315 **323**
 Karger-Kocsis, J. 248, 251 **275**
 Katagiri, G. 26 **40**
 Katayama, Y. 36 **41**
 Katayose, T. 199 **236**
 Katsuki, H. 319 **320**
 Katzmann, H.A. 213 **233**
 Kaufman, M.S. 249–250 **277**
 Kawai, H. 201 **232**
 Keily, C.J. 177, 218 **233**
 Keller, T.S. 197 **233**
 Kellogg, D.H. 64 **91**
 Kelly, A. 45, 47, 50 **88** 99, 125 **166** 240, 243–
 245, 247, 257, 259 **274** **275** 280, 315 **321**
323
 Kendall, K. 260 **275**
 Kenig, S. 64 **86**
 Kennedy, B.J. 26 **40** 287, 290, 305 **323**
 Keran, R.J. 127–128, 150, 157 **166** 316 **323**
 Kerans, R.J. 316 **323**
 Keunings, R. 96 **166**
 Kiescheke, R.R. 208, 219 **233**
 Kim, D.M. 332–333, 338–339 **362**
 Kim, J.K. 3 4 5–6, 26 **39** **40** 43, 50, 53–54,
 79–80 **89** 93–96, 98, 114–116, 119–124,
 127–128, 131, 134–135, 140, 143, 145–
 146, 148, 150 **166** **169** 171, 197, 199 **233**
 240–241, 244 **275** 279–281, 285, 287–293,
 300–302, 304–305 **323** **324** 329, 342, 358
362 **363**
 Kim, K.S. 311, 313 **324**
 Kim, R.Y. 83 **89** 268 **275** 313–314 **321** 342–
 344, 347–348 **363**
 Kinloch, A.J. 6, 10 **40** 78 **88** 280 **324** 330,
 331, 333 **363**
 Kirk, J.N. 243 **275**
 Knight, M. 84–85 **92**
 Ko, F.K. 190 **233** 351, 353–355 **363**
 Kodokian, G.K.A. 10 **40**
 Koenig, J.L. 12, 21–22, 32 **39** **41** 175, 177,
 180, 183, 191 **229–233** 312 **326**
 Koenig, M.F. 191 **231**
 Konish, H.J. 268 **275**
 Koss, D.A. 94, 150 **166**
 Koufopoulos, T. 310–311 **324**
 Kousiounelos, P.N. 287 **327**
 Krukonis, V. 214 **233**
 Kunichika, K.T. 34 **38**
 Kuntz, M. 316 **324**
 Kurauchi, T. 249 **277**
- Labronici, M. 280, 293 **324**
 Labrugere, C. 220 **235**
 Lacroix, Th. 50 **89** 95–96 **166**
 Ladizesky, N.H. 203 **233** **236**
 Lagace, P.A. 345 **363**
 Lahaye, M. 217 **234**
 Lai, C.P.Z. 243 **276**
 Lai, J.Y. 187 **237**
 Lam, P.K. 319 **320** 324 **325**
 Lamoreaux, R.H. 219 **232**
 Lancin, M. 217 **233**
 Lau, M.G. 150 **166**
 Lauke, B. 252–254, 273 **275**
 Lawrence, P. 126, 136 **167**
 Lawrence, S. 126, 136 **167**
 Laws, L. 126, 136 **167**
 Laws, V. 126 **167**
 Leckie, F.A. 298, 315 **321** **323**
 Lee, C. 357–359 **363**
 Lee, J.W. 95 **167**
 Lee, L.H. 21 **40**
 Lee, S. 62, 66 **89**
 Lee, S.H. 355, 358–359 **362**
 Lee, S.M. 17–18, 21, 28, 31, 33 **40** 338
363

- Lee, S.W.R. 358 **363**
 Lee, W.J. 10, 37 **40**
 Lee-Sullivan, P. 199 **233**
 Lemaitre 298, 315 **321**
 Leng, Y. 47 **89**
 Leong, K.H. 358 **362**
 Lerch, B.A. 315 **322**
 Lerner, I. 175 **235**
 Leung, C.K.Y. 126, 149–150 **167**
 Leung, L.M. 358 **363**
 Lewis, R.W. 186 **235**
 Lhotellier, F.C. 95–96 **167** 297 **324**
 Lhymn, C. 248, 272 **276**
 Li, P.X. 211 **233** **237**
 Li, Q. 211 **233**
 Li, V.C. 126, 149–150 **167**
 Li, Z. 213 **230**
 Li, Z.F. 46 **90** 205 **234**
 Liang, C. 150 **167**
 Liao, F.S. 349 **363**
 Liao, Y.T. 21 **40** 177, 182 **234**
 Liebowitz, H. 266 **277**
 Lieu, Y.K. 308 **323**
 Lim, J.T. 319–320 **324** **325**
 Limaye, S.Y. 53, 58 **86** **88** 150 **164**
 Lin, K.Y. 271 **276**
 Lin, R.Y. 212 **236**
 Ling, J. 189, 191 **229**
 Ling, S. 50 **89**
 Liu, D. 357–359 **363**
 Liu, G.B. 211 **233**
 Liu, G.L. 149–150 **165**
 Liu, H.Y. 50 **89** 124–125, 128 **167**
 Liu, S.S. 26 **41**
 Liu, W. 211 **237**
 Lloyd, P.F. 1–2 **4** 189, 191, 193 **231**
 Looi, H.C. 199 **233**
 Loos, A.C. 356 **361**
 Lord, R. 307 **324**
 Lovett, D.J. 217 **232**
 Low, B.Y. 297 **324**
 Low, I.M. 331 **363**
 Lowden, R.A. 219, 221–222 **234**
 Lu, G.Y. 59 **89** 96 **167**
 Lu, S.V. 94 **166** 301–302 **324**
 Lu, W.H. 349 **363**
 Lung, C.W. 126 **165**
 Luo, J. 345, 349 **365**
 Ma, Z.Y. 211 **233**
 Mackay, D.B. 340–342, **363**
 Mackin, T.J. 127–128, 157 **168**
 MacLaughlin, T.F. 94 **167**
 Madhukar, M. 3 **4** 73 **87** 337 **361**
 Madhukar, M.S. 73–74 **89** 191, 194–196
 231 **234**
 Maekawa, Z. 182–184 **236**
 Maheshwari, A. 226 **234**
 Mai, Y.W. 3 **4** 5–6, 26 **39** **40** 43, 50, 53–54,
 59, 79 **88** **89** 93–94, 96, 102, 105, 108–
 109, 124–125 127–128, 131, 134–135, 139–
 141, 143, 145–146, 148, 150–151 **166** **167**
 169 171, 197, 199, 206 **233** **234** 240–241,
 244, 253, 268 **274–276** 279–281, 284–285,
 287–294, 300–302, 304–305, 307–308 **320**
 322–324 329, 331–332, 340–342, 354–357
 361–364
 Majumda, B.S. 150 **167**
 Mandell, J.F. 57–58 **88** **89** 94, 150 **165** 268,
 273 **276**
 Manfredo, L.J. 226 **234**
 Manor, A. 46 **89**
 Mans, L. 36 **39**
 Mar, J.W. 271 **276**
 Marchionni, H.J. 246 **276**
 Margolis, W.S. 75 **92**
 Marks, B.S. 189 **234**
 Marks, P.R. 306 **326**
 Marloff, R.H. 310 **324**
 Marom, G. 10, 37–38 **39** 64, 66, 87 **88** 244
 274 280, 291, 306, 315 **324**
 Marotzke, Ch. 94 **167**
 Marshall, D.B. 57, 59 **89** 127, 150 **167** 223
 231
 Marshall, P. 54 **90**
 Marston, T.U. 240, 243, 245–247, 259 **276**
 283 **324**
 Martin, E. 220 **235**
 Martin, R.H. 76, 81 **90**
 Martin, T.W. 192 **231**
 Martineau, P. 217 **234**
 Martinez, D. 263–264, 266 **275**
 Mascia, L. 280, 287, 293 **324** **325**
 Maso, J.C. 6 **40**
 Masters, J.E. 339–341, 349–350 **361–364**
 Mathys, Z. 200 **229**
 Matsuda, H.S. 191 **234**

- Matsui, J. 191 **234**
 Matsuwa, T. 216 **237**
 Maufras, J.M. 95 **164**
 Mauri, R.E. 189 **234**
 Mayadas, A. 355 **364**
 Mazzio, V.F. 282 **325**
 McAlea, K.P. 54 **89**
 McAlea, P.K. 54 **86**
 McCarthy, G. 215 **235**
 McCullough, R.L. 352 **361**
 McElroy, B.J. 197 **233**
 McGarry, F.J. 44 **90** 175 **234** 268, 273 **276**
 287, 293, 298 **323** 330 **364** **365**
 McKee, D.W. 187 **234**
 McNally, R.N. 226 **234**
 McWithey, R.R. 71 **88**
 Meda, G. 94, 150 **167**
 Meier, B. 316 **324**
 Melanitis, N. 50 **87** 312 **322**
 Melis, M.E. 220 **229** 306, 316 **320**
 Merle, G. 50 **89**
 Merrill, E.W. 200 **228**
 Metcalfe, A.G. 1 4 6, 13, 15–16 **40** 215 **234**
 280, 314 **325**
 Meyerer, W.J. 14 **38**
 Michal, G.M. 212 **230**
 Michalske, T.A. 226 **234**
 Mignery, L.A., 354 **364**
 Miller, B. 54–55 **88**
 Miller, J.D. 21 **40**
 Miracle, D.B. 150 **167**
 Misra, A. 316 **325**
 Misra, A.K. 228 **234**
 Mita, I. 190 **232**
 Mitaka, Y. 297–298 **325**
 Mital, S.K. 94, 150 **167** 300 **325**
 Mittelman, A. 64 **87**
 Modeer, M. 271 **275**
 Moncunill de Ferran, E. 244, 246 **275** 285–
 286 **322**
 Monte, S.J. 200 **236**
 Moon, C.K. 54 **90**
 Mooney, R.D. 44 **90**
 Moore, D.R. 76 **87**
 Moore, R.L. 70 **87**
 Morales, A. 355 **364**
 More, K.L. 219 **234**
 Morel, M. 315 **325**
 Morgan, R.J. 51 **90** 196–198 **234**
 Morin, D. 215 **234**
 Morley, J. 243–244 **275**
 Morris, D.H. 268 **276**
 Morris, W.L. 12–13 **41**
 Morscher, G. 58 **90**
 Morton, J. 248 **276**
 Moshonov, A. 64 **86**
 Mostovoy, S. 83 **86**
 Moulton, R.J. 332–333, 336, 341 **362**
 Mouritz, A.P. 356, 359 **364**
 Muki, R. 95 **167** **168**
 Mullin, J.V. 282 **322** **325**
 Munro, M. 62, 66 **89** 243 **275** **276**
 Murai, H. 190 **232**
 Murphy, M.C. 126 **168** 242 **276**
 Murthy, P.L.N. 94, 150 **167** 300 **325**
 Naaman, A.E. 160 **167**
 Nairn, J.A. 95 **168** 261 **276** 297 **325**
 Najm, H.S. 160 **167**
 Nakahara, M. 26 **40** **41**
 Nakayama, Y. 26 **40**
 Namur, G.G. 160 **167**
 Nardin, M. 37 **40** 50 **85** **90**
 Naslain, R. 6, 16 **40** 217, 220 **234**
 Needleman, A. 94 **168**
 Nelson, L.E. 174 **235**
 Netravali, A.N. 46, 49, 58 **90** 205 **234**
 Neumann, A.W. 11, 34 **40**
 Newaz, G.M. 267 **276**
 Ni, S. 178 **236**
 Nicholas, M. 224 **234**
 Nicolais, L. 271 **274**
 Nielsen, L.E. 287, 295 **325**
 Nix, W. 58 **92**
 Noguchi, K. 26 **41**
 Noone, M.J. 224 **234**
 Norita, T. 191 **234**
 Norman, T.L. 345 **364** **365**
 Novak, R. 285, 312–313 **321**
 Novak, R.C. 187 **234**
 Nurse, R.W. 126, 136 **167**
 Nutt, S. 217 **237**
 Nutt, S.R. 222 **236**
 O'Brien, T.K. 76, 80, 82, 85 **90** 343–345 **364**
 Oastore, C.M. 354 **363**
 Occhiello, E. 187–188 **231**
 Ochi, M. 320 **325** **326**

- Ochiai, S. 240, 270, 272 **276**
 Ochoa, O.O. 348 **361**
 Ogata, N. 50 **90**
 Ogo, Y. 353 **364**
 Ohsawa, T. 48 **90**
 Okamura, K. 216 **237**
 Okura, A. 210 **237** 315 **321**
 Oliver, W.C. 59 **89** 150 **167**
 Olivieri, S. 357 **360**
 Omori, M. 216 **237**
 Ono, K.I. 314 **323**
 Outwater, J.D. 126 **168**
 Outwater, J.O. 175 **235** 242 **276**
 Owen, D.K. 11 **40**
 Owen, M.J. 268 **276**
 Own, S.H. 287, 294 **321**
 Ozzello, A.D. 55–56 **91**
- Pagano, N.J. 297–298 **325** 342–344 **364**
 Pai, B.C. 211 **228**
 Pailler, R. 217 **234**
 Pally, I. 127 **168**
 Pan, C. 320 **322**
 Pan, T.Y. 259 **276**
 Pangborn, R.N. 298, 306, 315 **326**
 Papaspyrides, C.D. 288, 295 **322**
 Papirer, E. 189 **231**
 Pappas, S.P. 293 **326**
 Park, W.J. 47–48 **87**
 Parkyn, A. 313 **323**
 Parthasarathy, T.A. 127–128, 150, 157 **166**
 316 **323**
 Partridge, I.K. 320 **321** 345 **365**
 Partridge, P.G. 207 **236**
 Pask, J.A. 226 **228**
 Pastore, C. 355 **363**
 Patrikis, A.K. 312 **325**
 Pawson, D. 177 **233**
 Peacock, J.A. 312 **322**
 Pearson, R.A. 330 **365**
 Peiffer, D.G. 287, 295 **325**
 Pellas, J. 268 **274**
 Penn, L.S. 50, 54 **90** 127 **166** 246 **276**
 Peters, P.W.M. 270, 272 **276**
 Petersson, P.E. 271 **275**
 Petit, P.H. 69 **90**
 Petrovic, J.J. 263 **277**
 Peyser, P. 330 **360**
- Phillips, D.C. 243–244, 246 **274** **275** 285 **321**
 333 **364**
 Phillips, M.J. 320 **321**
 Phoenix, L. 50 **88** 96 **165**
 Phoenix, S.L. 46, 49 **88** **90**
 Piggott, M.G. 280 **325**
 Piggott, M.R. 95, 127 **168** 179 **230** 243, 268
 274 **276** 280, 318–320 **322** **324** **325**
 Pindera, M.J. 62 **90**
 Pipes, R.B. 82 **86** 310 **321** 342–344, 352 **361**
 364
 Pirouz, P. 58 **90**
 Pitkethly, M.J. 53–54, 59, 61–62 **90**
 Pittman, C.U. 297–298 **322** **324**
 Pleizeier, G. 205 **229**
 Plueddemann, E.P. 12, 14 **40** 174–178 **230**
 235
 Pollard, G. 204–205 **236**
 Pompe, W. 252, 273 **276**
 Poon, C. 339 **364**
 Popejoy, D.B. 300 **325**
 Portanova, M.A. 357 **364**
 Porter, D.L. 314 **325**
 Povirk, G.C. 94 **168**
 Prabhakaran, P. 68 **91**
 Prel, Y.J. 82–83 **86** **90**
 Prescott, R. 192 **231**
 Prewo, K.M. 215, 217 **235** **236**
 Price, J. 54 **90**
 Prosen, S.P. 189 **231**
 Prouhet, S. 220 **235**
- Qiu, Y. 55–56 **91** 150 **168**
 Queeney, R.A. 298, 306, 315 **326**
 Quigley, J. 271 **273**
- Raible, R.C. 330 **365**
 Ramsteiner, F. 248 **276**
 Rao, V. 55–56 **91**
 Ratner, B.D. 197 **233**
 Rechak, S. 345, 349–350 **364**
 Recker, H.G. 339–340 **364**
 Reddy, J.N. 343 **362**
 Reeder, J.R. 359 **364**
 Reifsnider, K.L. 296–297, 299 **323**
 Reimanis, I.E. 263 **277**
 Renzow, D. 34 **40**
 Rhee, H.W. 287, 291–295 **321** **325**

- Rhodes, M.D. 339 **365**
 Rich, M.J. 1–2 **4** 21 **39** 47–48 **87** 189, 191, 193 **231**
 Richerson, D.W. 53 **88**
 Richey, R.J. 354 **362**
 Riess, G. 189 **235**
 Riggs, D.M. 186 **235**
 Ripling, E.J. 77 **91**
 Robertson, R.E. 259 **276**
 Robinson, I.M. 22–24 **39–41** 312 **322**
 Rocher, J.P. 220 **234**
 Rochow, E.G. 174 **235**
 Rodriguez, E.L. 311 **326**
 Rogers, C. 345–348 **361**
 Rohwer, K. 311 **326**
 Roman, I. 46, 64 **87** **91**
 Rosen, B.W. 47, 69 **91** 93, 95, 99–100 **168**
 Rosensaft, M. 64, 66 **87**
 Rosenthal, H. 345, 348 **362**
 Rostami, H. 203–204 **235**
 Roulin, A. 76 **87**
 Rovello, R. 67–68 **91**
 Roweliff, D.J. 219 **232**
 Rowlands, R.E. 343–344 **361**
 Roylance, D.K. 200 **228**
 Rubin, H. 345 **362** .
 Rudy, E. 15 **40**
 Ruhle, M. 240 **276**
 Ruoff, S. 49, 58 **90**
 Russel, W.B. 95 **168**
 Russell, A.J. 81–82 **91** 332 **364**
 Ryder, C. 215 **235**
- Sachse, W.H. 46 **90**
 Saigo, K. 319 **320**
 Sakai, M. 260 **276**
 Sakatani, Y. 190 **237**
 Sander, B.A. 268 **273**
 Sandorf P.E. 64 **91**
 Santulli, C. 357 **360**
 Saravanos, A. 315 **325**
 Sarin, V.K. 240 **277**
 Sastry, A.M. 55 **91**
 Sato, N. 248 **277**
 Sato, S. 248 **277**
 Sattar, S.A. 64 **91**
 Satyanarayana, K.G. 211 **228**
 Savides, I.S. 298 **321**
 Saville, B.P. 196–198 **230**
- Sawyer, J.W. 68 **91** 357 **364**
 Schapery, R.A. 268 **273** 309–310 **326**
 Scherf, J. 51 **91**
 Schmitz, G.K. 280 **325**
 Schrader, M.E. 175, 178, 180–181 **235**
 Schreiber, H.P. 199 **237**
 Schultrich, B. 252–254, 273 **275**
 Schultz, J. 50–51 **85** **90**
 Schultz, J.M. 248, 272 **276** **277**
 Schwartz, H.S. 347 **360**
 Schwartz, P. 55–56 **88** **91** 96, 150 **165** **168** 205 **232**
 Scolar, D.A. 6, 15 **40** 186, 188, 190 **235**
 Scott, J.M. 333 **364**
 Scott, V.D. 228 **229**
 Seferis, J.C. 10, 37 **40**
 Sela, N. 345, 347, 348 **362** **364**
 Sevely, J. 220 **234**
 Shafry, N. 58–59 **91**
 Shah, S.P. 126, 136 **165** **168**
 Shaw S.J. 330, 333 **363**
 Shelton, C.G. 306 **326**
 Shetty, D.K. 58 **86** 137, 150–151 **164** **169**
 Shih, G.C. 64 **91**
 Shih, P.T.K. 175 **233**
 Shimbo, M. 320 **325** **326**
 Shimizu, K. 26 **40** **41**
 Shirley, F.P. 34 **38**
 Shishido, T. 216 **237**
 Shu, D. 356–357 **364**
 Shuford, R.J. 186 **235**
 Shyu, S.S. 187 **237**
 Siadati, M.H. 227 **235**
 Sideridis, E. 298, 310 **326**
 Sigety, P. 96 **165**
 Sigl, L.S. 127 **168**
 Sih, G.C. 266 **277**
 Sikes, A.M. 320 **326**
 Silverstein, M.S. 203 **235**
 Sims, D.F. 70 **91**
 Sinclair, J.H. 70 **86**
 Singer, L.S. 184 **235**
 Singh, R.N. 58 **86** 150 **168** 219–220 **235**
 Singh, S. 345 **365**
 Skourlis, T. 288, 295 **322**
 Slepetz, J.M. 67–68 **91**
 Smelser, R.E. 94, 149 **164**
 Smith, B.T. 339–340 **365**
 Snide, J.A. 14 **38**

- Sohi, M.M. 339 **365**
 Sohn, M.S. 345 **365**
 Solar, M.A. 270 **277**
 Somehk, R.E. 208, 219 **233**
 Soni, S.R. 342–343 **363 364**
 Sottos, N.R. 311 **322**
 Spigel, B.S. 68 **91**
 Springer, G.S. 200 **236**
 Srinivasan, K. 339–340 **365**
 Stang, H. 126 **168**
 Stark, G.L. 12 **40 177 235**
 Steif, P.S. 94, 150 **167**
 Sternberg, E. 95 **167 168**
 Stevens, D. 127 **168**
 Stone, D. 49, 58 **90**
 Street, K.N. 81–82 **91 332 364**
 Strife, J. 217 **236**
 Stuhrke, W.F. 14 **38**
 Stumpf, H. 55 **91**
 Su, A.C. 349 **363**
 Subramanian, R.V. 287, 294 **321 326**
 Sue, H.J. 335 **365**
 Sugeran, G. 200 **236**
 Sugihara, T. 182–184 **236**
 Suh, N.P. 285–286, 291–293 **326**
 Sullivan, J.L. 68 **91**
 Sultan, J.N. 330 **365**
 Sumner, N.D. 94, 96 **164 300 321**
 Sun, C.T. 344–345, 349–350, 354 **364 365**
 Sun, E.Y. 222 **236**
 Sun, R.L. 319 **320**
 Sung, C.S.P. 178 **236**
 Sung, N.H. 178, 189 **230 236 285–286, 291–293 326**
 Suo, Z. 263, 265 **275**
 Sutcu, M. 150 **168**
 Sutton, W.H. 224 **234 236**
 Suzuki, Y. 182–184 **236**
 Swain, R.E. 296–297 **323**
 Swedlow, J.L. 268 **275**
- Tada, Y. 357 **365**
 Taguchi, M. 190 **237**
 Takahashi, K. 248 **277**
 Takaku, A. 126, 135 **168**
 Takayanagi, M. 199 **236**
 Takeuchi, S. 260 **277**
 Tam, C.W. 354–355, 357 **360**
 Tamuzs, V. 50 **85**
- Tan, T.M., 354 **364**
 Tandon, G.P. 297–298, 313 **325 326**
 Tasaka, S. 201 **232**
 Taya, M. 240 **277 282, 297–298 325 326**
 Terasaki, M. 58 **91**
 Termonia, Y. 50–51 **91 94 168**
 Tesch, H. 339–340 **364**
 Tetelman, A.S. 243, 247, 259 **274 277 280 326**
 Theocaris, P.S. 296–297, 310–311 **324 326**
 Theysohn, R. 248 **276**
 Thomason, J.L. 13 **41**
 Thibault-desseaux, J. 217 **233**
 Thomas, A.G. 34 **41**
 Tiegs, T.N. 16 **38 318 326**
 Tilmans, B. 96 **166**
 Tirosh, J. 64 **86 257–259, 267 277**
 Tissington, B. 204 **236**
 Tohogo K. 263 **277**
 Tomlinson, W.J. 288, 293 **326**
 Topoleski, L.T.T. 46, 49, 58 **90**
 Tsai, H.C. 12–13 **41 94, 150 168**
 Tsao, Y.P. 354–355, 358 **360**
 Tse, M.K. 333, 335, 337 **362**
 Tsushima, R. 319 **320**
 Tuinstra, F. 312 **326**
 Tuinstra, T. 22 **41**
 Tullock, D.L. 263 **277**
 Tung, I.C. 53 **86**
 Tyson, W.R. 45, 47, 50 **88 99, 125 166 244 275**
- Ulicny, J.C. 32 **39**
- Vaidya, R.U. 228 **236**
 Vaidyan, V.K. 211 **228**
 Valentin, D. 50 **86**
 Van der Zwaag, S. 106 **168**
 Van Fo Fy, G.A. 296 **326**
 Van Oene, H. 68 **92**
 Van Oss C.J. 11 **40**
 Vaughan, D.J. 200 **236**
 Vautey, P. 46–47 **91**
 Vedula, M. 298, 306, 315 **326**
 Verpoest, I. 58 **87 96 166 191, 200 232 236**
 Vidoz, A. 215 **235 236**
 Vincent, M. 297 **324**
 Voss, H. 250, 252 **277**
 Vu-Khanh, T. 83 **92 94, 96 164 300 321**

- Waas, A.M. 298 **326**
 Waddoups, M.E. 271 **277**
 Wadley, HNG 217 **229**
 Wagner, H.D. 37 **41** 50–51 **89 91–92**
 Wake, W.C. 6 **41**
 Walpole, L.J. 298 **326**
 Walrath, D.E. 66, 68 **85 92**
 Wang, A.S.D. 343 **365**
 Wang, D. 26 **41** 177, 181 **230 236**
 Wang, J. 358 **365**
 Wang, Q. 203 **236**
 Wang, S.S. 77–78 **92** 218 **233 343**
 365
 Wang, S.W. 58 **92**
 Wang, Y. 78 **92**
 Ward, I.M. 37 **40** 202–204 **233 236**
 Ward-Close, C.M. 207 **236**
 Waren, P.P. 127, 157 **168**
 Warren, P.D. 127–128, 157 **168**
 Warren, R. 240 **277**
 Warriar, S.G. 212 **236**
 Warwick, C.M. 218–219 **232 233 237**
 Watson, M.C. 58 **92**
 Watts, J.F. 17, 26–27, 29–30 **38 40**
 Wawner, F. 217 **237**
 Wawner, F.E. Jr. 215, 217 **237**
 Weber, T. 339–340 **364**
 Weibull, W. 106 **168**
 Weihs, T.P. 58 **92**
 Weinberg, M. 37–38 **41**
 Weisshaar, T.A. 71 **88**
 Weller, T. 358 **362**
 Wells, H. 286–287, 292–293 **322**
 Wells, J.K. 126–127 **168** 254–256, 268–269
 277 280 326
 Wendt, R.C. 11 **40**
 Wereszczak, A.A. 58 **87**
 Wertheimer, M.R. 199 **237**
 Wevers, M. 191 **232**
 Whiteside, J.B. 344 **361**
 Whitney, J.M. 47, 64–66, 71, 83–85 **86 92 95**
 168 342 365
 Wicks, J.W. 293 **326**
 Wiesel, E. 37 **41**
 Wilcox, R.C. 354–355 **361**
 Wilkins, D.J. 75 **92** 134–135 **166 329 365**
 Williams, J.G. 12–13 **41** 78–79 **88 92 339**
 365
 Williams, J.H. 287 **326**
 Williams, T. 249–250 **277**
 Wilt, T.E. 304, 306, 315–318 **320**
 Wimolkatisak, A.S. 48, **92**, 294, **327**
 Wisnom, M.R. 64–66 **87**
 Withers, P.J. 219 **230 240 274**
 Woo, M.S. 280, 320 **325**
 Wright, E.S. 306 **320**
 Wright, W.W. 186 **237**
 Wu, E. 358 **365**
 Wu, H.F. 46 **90 94 168**
 Wu, J.X. 211 **237**
 Wu, R.J. 211 **237 320 322**
 Xie, M. 50 **89**
 Xu, C.F. 126 **165**
 Xu, L.Y. 343 **365**
 Yabin, B. 48, 50 **92**
 Yajima, S. 216 **237**
 Yamada, S. 190 **237**
 Yamaguchi, Y. 190 **237**
 Yamaki, J. 36 **41**
 Yamamoto, M. 190 **237**
 Yamazaki, K. 320 **325**
 Yang, C.J. 46, 218 **232**
 Yang, J. 127, 158 **167**
 Yang, J.M. 46 **92** 218 **232 353 363**
 Yang, M. 228 **229**
 Ye, L. 59 **89 93**, 128, 108–109 **169 333 361**
 Yee, A.F. 330 **365**
 Yeung, P.H.J. 50 **87 312 322**
 Ying, L. 189 **236**
 Yip, P.W. 26 **41**
 Yokoyama, A. 182, 184 **236**
 Yoon, H.S. 210 **237**
 Young, J.C. 150 **164**
 Young, R.J. 22, 24, 34 **39 41 50 88 312 320**
 322 325 331 363
 Yu, Z. 199 **237**
 Yuan, J. 263–264, 266 **275**
 Yuan, L.Y. 187 **237**
 Yue, C.Y. 126 **169 199 233**
 Zakikhani, M. 22 **39 41**
 Zaper, A.M. 32 **41**
 Zegas, T.F. 67–68 **91**
 Zeng, Y. 204 **231**
 Zhang, G.D. 211 **237 297 327**
 Zhou, B.L. 126 **165**

- Zhou, L.M. 50, 59 **89** 93–95, 102, 105, 108–
109, 124–125, 128, 131, 140–141, 143,
145–146, 148, 150–151, 154, 156, 158,
162–163 **166 167 169** 300–301 **323 324**
- Zhou, Z. 320 **322**
- Zhuang, W.D. 211 **237**
- Zimmerman, R.S. 203 **228**
- Zweben, C. 47 **92**

SUBJECT INDEX

- α -alumina fiber 226
- acetic acid anhydride 199
- acid treated SiC fiber 138
- acidic potassium dichromate 188
- acidic potassium permanganate 188
- acoustic emission 46
- acrylamide 199
- acrylic latex polymer 295
- acrylonitrile copolymers 287
- acrylonitrile/methylacrylate 287
- acrylonitrile/glycidylacrylate 287
- acrylonitrile/methyl acrylate (AN/MA) 291
- active species 187
- adhesion 5, 43, 171
- adhesive joint 72
- adhesive layer 345–350
- adsorbed material 171
- adsorption 5, 7–8, 11, 17
- Al₂O₃, 180, 207
- Al₂O₃ fiber 3, 172, 206, 224, 338
- Al₂O₃ fiber–aluminum matrix composite 228
- Al₂O₃ particle 338
- aldehydes 26
- aligned short fiber 93
- alkyl 175
- alloying element 211
- Almax fiber 224
- alternating stress 164
- alumina fiber–glass matrix composite 227
- alumina whisker–zirconia matrix composite 16
- aluminum hydroxide 330
- aluminum matrix 213–215, 333
- amine 175, 200
- amino 175
- ammonia 200
- ammonium bicarbonate 188
- anhydride copolymer 287
- anionic system 294
- anisotropy 124
- anodic oxidation 188
- anodic treatment 189
- anti-electrostatic 186
- apparent interface bond strength 93, 244
- aramid fiber 22, 124, 171, 187, 196, 279
- aramid fiber–epoxy matrix composite 246
- area method 76, 80
- argon 200, 205
- asperity pressure 128
- asperity wear mechanism 128
- asymmetric laminate 313
- asymmetrical four-point bending (AFPB) 68
- asymptotic debond stress 103
- atomic force microscopy (AFM) 18
- Auger electron spectroscopy (AES) 17, 20, 26, 28, 323
- average fiber length 254
- average fiber tensile strength 48, 96, 106, 113, 115
- average shear strength at the interface 47
- axi-symmetric deformation 101

- B–Al 15
- B–SiC 216
- B/W fiber 3
- backup roller 293
- barium magnesium aluminosilicate (BMAS) matrix composite 222
- barium titanate 330
- basal plane 184
- B₄C coating 216
- BC coating 215
- beam theory 63
- bending moduli 193
- bifurcation 240
- blend of polyester–polyether resins (Estapol) 284
- BN coating 208, 215–216, 219, 222, 228
- BN/SiC coating 222

- boiling water 182
 bolted joint 75
 bond length 108, 120
 bond-line thickness 333
 bond shear strength 44, 336-337
 bonding 5, 7, 190
 boron 172, 206, 210
 boron fiber 214, 282
 boron fiber reinforced epoxy matrix composite 243, 344
 boron fiber-titanium matrix system 14
 braiding 351
 brittle interphase 179
 brittle matrix 247
 buckling 75
 bulk laminate 43
 bundle fiber 280
 butadiene-maleic anhydride 294
- CAI strength 358
 calcium 172
 calorimetric analysis 296
 cantilever beam enclosed notch (CBEN) test 82
 capillary constant 35
 capillary migration 180
 captive bubble method 34
 carbon 124, 139, 187, 206, 294
 carbon coating 216
 carbon crystallite 216
 carbon dioxide 205
 carbon fiber 59, 138, 183, 192, 285, 300, 339
 carbon fiber-aluminium matrix composite 210, 298
 carbon fiber-epoxy matrix composite 13, 47, 73, 97, 104-105, 108, 114, 120, 124, 133, 150, 285-286, 298, 300, 345, 347, 349, 354, 358
 carbon fiber-Mg matrix composite 213
 carbon fiber polymer matrix composite (CFRP) 16, 76, 245, 256, 279, 303-306, 319
 carbon fiber-polyester matrix 286
 carbon fiber-polyetheretherketone (PEEK) matrix composite 37, 46, 312
 carbon fiber woven fabric 358
 C-glass fibers 173
 carbon-Kevlar hybrid composite 287
 carbon-rich surface layer 201
 carbon substrate 214
 carbonization 185
 carbonyl 190
 carbonyl oxygen 26
 carboxyl 190
 carboxyl-terminated butadiene acrylonitrile (CTBN) copolymer 293, 330, 338
 carboxylic acid 26
 cationic system 294
 cavitated 331
 Celanese 202
 cementation process 211
 cementitious fiber composite 240
 cements 250
 ceramic 250
 ceramic matrix composite (CMC) 6, 53, 58
 chain stitch 353
 characteristic length 49, 116
 chemical bonding 5, 14, 137, 175, 190-191, 220, 227, 295
 chemical compatibility 316
 chemical etching/grafting 199
 chemical group 14
 chemical reaction 6, 14
 chemical shift 32
 chemical vapor deposition (CVD) 209, 214
 chemisorbed region 181
 chloro 175
 chromic acid 203
 circular inclusions 311
 CMCs 6, 15, 51, 151, 206, 208, 210, 220, 281-282, 300, 316
 C-O group 287
 coated steel wire-epoxy matrix composite 157
 coating 207
 coating-matrix interface 301-303
 coating thickness 301
 co-cured joint 75
 coefficient of friction 52, 103, 107, 127, 138, 159, 161, 175
 coefficient of thermal expansion (CTE) 208, 210, 222, 296, 306, 343
 cold plasma 187
 colloidal latex particle 287
 compatibility 178

- compensating interlayer 306, 315
- complete debonding 113, 120–121
- compliance method 76, 77, 80, 82
- compliant interlayer 222, 298, 303, 315
- composite strength 247
- compressive residual stress 312, 316
- compressive strength 191
- compressive strength-after-impact (CAI) 339
- condensation polymerization 295
- contact angle 7–8, 17, 34, 212
- continuous fiber 98
- copper matrix composite 45
- corn-cob structure 214, 282
- correction factor 76
- corrugation 16
- Coulomb friction law 93, 121
- counteracting moment 66
- coupling agent 13, 199–201 (also see silane coupling agent)
- Courtaulds XA fibers 59
- covalent bond 190, 200
- Cox's model 95, 100
- crack arrest 241, 306
- crack bridging 79, 257
- crack deflection 78, 240, 331
- crack extension 80
- crack growth resistance 83, 356
- crack tip blunting 240, 257, 280
- crack tip debond stress 103, 112, 133, 152
- cracked lap shear (CLS) test 75, 82
- crazing 331
- critical bond length 135
- critical fiber volume fraction 147–148
- critical transfer length 47, 50, 96, 99, 109, 116, 124, 244
- cross-beam sandwich test
- cross-linking 181
- crushing 58, 68
- crystalline edge 210–211
- crystalline supramolecular sheet 197
- crystallinity 32
- crystallization 314
- CTBN-modified epoxy 349
- Cu coating 211
- cure cycle 320
- curved-neck specimen 44
- cyclic fatigue 157, 161, 329, 345
- cyclic monomer 295
- cylindrical coordinates 101, 129, 152
- cylindrical surface 36
- δ -alumina fiber 224
- damage area 349
- damage tolerance 279, 339
- damage zone 240, 253, 333, 350
- debond area 242
- debond criteria 94, 153
- debond length 58, 107–108, 112, 118, 120, 127, 133, 154, 164, 242, 254
- debond stress 242
- debonding 110, 113, 242, 280, 331
- delamination 74, 329
- delamination promoter 279, 306
- delamination resister 280
- deposition 187
- dichromate permanganate 188
- diepoxide molecule 199
- differential Poisson contraction 104, 123, 243
- differential scanning calorimetry 55
- differential thermal shrinkage 16, 104, 280
- diffusion barrier coating 13, 171
- dimethyl formamide 295
- dimethyl sulfoxide 199, 295
- dinorbornene (or tetramethyl) spiro ortho carbonate 319
- dipolar interaction 191
- dipolychloride solution 295
- direct fracture energy method 77
- dispersion force 36, 191
- displacement method 78
- distilled water 295
- double-cantilever-beam (DCB) test 77, 183, 340
- double-edge notched (DEN) specimen 66
- drop weight impact 358
- droplet aspect ratio method 36
- dry oxidation 187
- dry spinning 224
- ductile fiber 247, 348
- ductile interphase 280
- ductile matrix 125, 247
- duplex SiC/BN coating 228
- duplex Ti–Ni coating 227
- Dupre equation 7
- dynamic loading 253
- Dyneema fiber 202

- E-glass fiber 173
edge cap 347
edge delamination test 83–85
edge plane 185
effective fiber length 124
effective shortening of the beam 78
effective Young's modulus 82, 85
efficiency of stress transfer 94
elastic mismatch 58
elastomer 293, 298
electrochemical deposition 293
electrochemical polymerization 294
electrochemical process 294
electrodeposition technique 293, 294
electroless plating 211–212
electron binding energy 24
electron spectroscopy for chemical analysis (ESCA) 24
electropolymerization 293–294
electrostatic attraction 5–6, 13
electrostatic deposition 293, 295
embedded fiber length 52, 103, 128, 130
end loaded split (ELS) specimen 81–82
end notched cantilever beam (ENCB) specimen 82
end notched flexure (ENF) specimen 81
end rotation 78
energy balance theory 161
energy dispersive spectroscopy (EDS) 212
epoxide group 14, 190
epoxy 175, 177–178, 250, 293, 319
Estepol 291
ester 26, 175, 190
etching 187
ether 190
ethoxy 175
ethylene–acrylic acid copolymer 294
ethylene–propylene elastomer 287
evaporation 210
excessive reaction 207
exchange reaction bonding 56
expanding monomer 280, 319

failure mode transition 64
far field 95
Fe₂O₃ 180
FeAl matrix 228
fiber architecture 330
fiber-avoidance mode 248
fiber bridging 81, 240, 316, 333, 337–338
fiber buckling 200
fiber bundle push-out test 150
fiber/coating interface 303
fiber coating 279–282, 293, 301
fiber damage 355
fiber diameter 254
fiber fracture criterion 124
fiber fragment length 47, 50, 96, 124
fiber fragmentation criteria 107, 110, 113
fiber fragmentation test 44–45, 59, 93–94
fiber–matrix interface (see interface)
fiber orientation 66
fiber protrusion 58
fiber pull-out 240, 243, 253, 280, 282, 301, 316, 348
fiber pull-out length 244, 280
fiber pull-out test 44, 51, 59, 94–95, 125, 312
fiber pull-out toughness 244
fiber push-out 150
fiber push-out (or indentation) test 44, 56, 94
fiber tensile strength model 106, 138
fibril 51, 197
fibrillar structure 203
film 307
finite element (FE) analysis 66, 68, 57, 93–94, 96, 126, 140, 144–145, 147, 149, 300–301
flexural strength 179, 193
Fourier transform infrared spectroscopy (FTIR) 18, 177, 203
four-phase model 297
four-point bending 66
FP fiber 224
fracture mechanics approach 101, 126
fracture process zone (FPZ) 240
fracture toughness 138, 191, 237, 316, 319
fracture toughness map 254
fragmentation of brittle matrix 249
free edge 75, 83, 329, 354
free edge delamination 342
frictional pull-out test 125
frictional resistance 158
frictional shear strength 126
friction stress component 133, 155
frictionally bonded interface 121
full bonding 50, 96, 113

- full debonding/yielding 50
- fully bonded interface 111
- fully unbonded model 96
- functional group 26, 175, 287

- gamma function 48
- γ -aminopropyl 175
- γ -aminopropyl-triethoxysilane (APS) 178
- γ -methacryloxypropyl 175
- γ -methacryloxypropyl trimethoxysilane (γ -MPS) 175
- γ -methylamino-propyltrimethoxysilane (γ -MPS) 177
- gas jet 293
- gas plasma 205
- glass 171, 253, 279
- glass bead 330
- glass fiber 38, 44, 76, 172
- glass fiber–epoxy matrix composite 182, 296, 345
- glass fiber–nylon matrix composite 287, 298
- glass fiber–PC matrix composite 251
- glass fiber–PEEK composite 252
- glass fiber polyester matrix composite 285
- glass fiber reinforced polymer matrix composite (GFRP) 174, 242–243, 256, 279, 319
- glass fiber–PTFE matrix composite 252
- glass transition temperature 178, 287, 330, 341
- glycidyl acrylate/methyl acrylate (GA/MA) copolymer 291
- goniometer scale
- grafting polymerization 187, 203
- graphite 283
- graphite crystal 185
- graphitization 185
- gravimetry 36

- hard particle 331
- hardening slope 316
- Hertzian contact law 128
- homopolymerization 295
- hot plasma 187
- hot/wet compressive strength 341
- hot/wet condition 181
- hybrid fiber composite 279
- hydrogen bonding 6, 11, 191
- hydrogen peroxide 188, 203
- hydrostatic compression 311
- hydroxy 175
- hydroxyl group 14, 190
- hygrothermal aging 181, 255, 284, 349

- immersion 293
- impact damage resistance 346, 338
- impact fracture toughness 192
- ineffective fiber length 47, 95, 100
- infiltration 10
- infinitesimal debond length 139
- infrared spectroscopy (IR) 18, 20
- initial debond stress 107, 129, 134, 154
- initial friction pull-out stress 51, 129, 154
- inorganic filler 330
- in-plane lap-shear test 72
- in-plane shear modulus 69
- in-plane shear strength 61, 62, 195
- instability 135, 139, 154, 157
- instantaneous debond stress 161, 164
- interdiffusion 6, 12, 177, 207
- interface 1, 5, 8, 12, 26, 44, 93
- interface bond strength 44, 52, 62, 94, 116, 254, 330
- interface control 279, 282, 329
- interface debond criterion 104, 106, 131
- interface debonding 52, 125, 240, 242, 253, 280, 311, 316, 333, 337–338, 348 (also see debonding)
- interface fracture toughness 44, 52, 94, 127, 134, 154, 242, 245
- interface-related fracture 279
- interface-related shear failure 257
- interface shear bond strength 44, 94, 115, 191, 246, 279, 356
- interface shear stress (IFSS) 24, 50, 57, 73
- interfacial radial stress 152
- interferogram 18
- interlaminar fracture 75
- interlaminar fracture test 76
- interlaminar fracture toughness 74, 329, 332, 337, 350, 354
- interlaminar normal stress 76, 344
- interlaminar shear strength (ILSS) 37, 61, 63, 179, 287
- interlaminar tension 75
- interlayer 296, 303
- interleaving technique 329, 345

- intermittent bonding concept 280–282, 284
- intermittent interlaminar bond concept 307
- intermolecular dispersion force 7
- interpenetrating network (IPN) 12, 177
- interphase 1, 12–13
- ion plating 209–210
- ion scattering spectroscopy (ISS) 20, 30
- Iosipescu shear test 62, 66, 193
- Izod impact toughness 319
- Kelly–Tyson model 93
- Kevlar 29 197
- Kevlar 49 24, 197
- Kevlar 49–epoxy resin composite 25, 47, 64, 312
- Kevlar 149 197
- Kevlar 51, 196, 197, 253, 294, 300
- Kevlar–carbon fiber hybrid composite 347
- Kevlar fiber mat 348
- Kevlar stitched glass fiber composite 360
- Kevlar threads 354
- kinetic energy 24, 28, 81
- knitting 353
- laminar interface 43
- lamination residual stress 312
- laser Raman spectroscopy 17, 21, 312
- latex coating 287
- lattice 295
- leaching 180
- length to width ratio 71
- linear elastic fracture mechanics (LEFM) 239, 247
- liquid infiltration technique 212
- liquid rubber 331
- lithium aluminosilicate (LAS) 222
- load drop 135, 137
- loading rate 64, 76
- lock-stitching 353
- London dispersion force 11
- longitudinal shear modulus 296
- longitudinal splitting 16, 51, 58, 240–241, 285
- longitudinal striation 189
- low energy impact 280, 329
- low velocity impact 75, 339
- lower-bound transverse strength 72
- LXA500 carbon fiber-epoxy matrix composite 61
- macro-residual stress 312
- magnesium 172
- magnesium matrix 213–214
- matrix-dominant fracture 251
- matrix embrittlement 251
- matrix fracture 240, 251, 253
- matrix plastic deformation 241
- matrix shear yield strength 50, 93, 125
- matrix shrinkage 151
- matrix toughness 332
- maximum debond length 119
- maximum debond stress 51, 126, 129, 137–139, 154
- maximum embedded fiber length 47, 53, 137
- maximum shear strength criterion 242
- mean aspect ratio 49
- mean fiber fragment length 107–108, 110, 116, 120
- mechanical bonding 6, 16, 191
- mechanical residual stress 314
- melting point 210
- mesophase pitch 183
- methacryloyl chloride 199
- methoxy 175
- MgAl₂O₄, 228
- Mg–Li matrix composite 219
- MgO layer 213
- microbuckling 191
- micro-bundle pull-out test 55, 150–151
- microcomposite 43–44, 96
- microcracking 240
- microdebond test 54, 59, 137
- microdroplet 54
- microductile layer 288, 306
- microfailure mechanism 254
- microindentation test 56, 60, 94
- micro-residual stress 310
- micro-residual thermal stress 308
- misalignment 356
- mixed mode 64, 76, 84
- mixed mode test 83
- Metal Matrix Composite (MMC) 6, 13–14, 206, 208, 281–282, 298, 315
- mode I edge delamination test 83

- mode I interlaminar fracture
 - toughness 195
- mode I strain energy release rate 75, 80
- mode II forward shear 75
- mode II interlaminar fracture
 - toughness 196
- mode II strain energy release rate 82
- mode III anti-plane shear
- modified beam theory method 79
- modified compliance calibration
 - method 80
- modified epoxy 339
- modulus 254
- modulus ratio 114, 303
- Moire interferometry 68
- molecular continuity 175
- molecular entanglement 6
- molten glass 173
- molten metal 210
- monoclinic phase 314
- Monte Carlo simulation 49
- multi-layer 295, 297
- multiple fiber composite 93, 99, 141, 150
- multiple fiber composite model 139
- Mylar film 308

- NbC microcrystal 224
- near-net-shape design 351
- Nextel 480 mullite fiber 228
- Nextel 610 fiber 224
- Ni 298
- NiAl 228
- NiAl₃ intermetallic 211
- Ni coating 298
- Ni-Cr alloy 227
- Nicalon 217
- Nicalon fiber-SiC matrix composite 220
- Nicalon SiC fibers-glass matrix
 - composite 222
- nickel coating 211
- nickel wire 254
- nitric acid 188
- nitrogen 205
- nitrogen-rich layer 201
- non-aligned fiber 248
- non-dimensional correction factor 48
- non-linear friction 126
- non-linear plastic deformation 333, 338
- non-linear strain 333

- non-oxidative 187
- non-reactive 15
- non-reactive refractory 207
- non-uniform interphase 296
- non-uniform solid surface 35
- non-wetting 7
- notch geometry 66
- notched rectangular specimen 72
- notched tensile strength 192
- nuclear magnetic resonance (NMR)
 - spectroscopy 21

- off-axis property 193
- oligomeric siloxanol 181
- organic vapor 295
- organofunctional group 175
- organotitanate 201
- organozirconate coupling agent 201
- orientation efficiency factor 253
- orthotropic 66
- out-of-plane stress 75
- overlap joint 357
- oxidative 186-187
- oxide film 15, 215
- oxide layer of Y₂O₃ 219

- PAN-based carbon fiber 183, 185
- parallel-sided specimen 44
- partial debond model 120
- partial debond stress 129, 133, 154-155
- partial debonding 50, 113, 117, 120, 123, 128
- partial yielding 96, 123
- partially debonded interface 96, 108, 111, 118, 130
- partially elastic model 96
- partially embedded fiber 144
- partially stabilized zirconia (ZrO₂) 314
- partially stable 137
- perfect bonding 50
- perfectly bonded (elastic) interface 96
- perforated film 307
- phase transformation 314
- phenolic group 190
- photoelastic technique 46, 54, 66, 68, 306, 310
- physical adsorption 7, 14
- physical attraction 7
- physical vapor deposition (PVD) 209

- physisorbed region 181
 pitch-based carbon fiber 23, 38
 plasma etching 187
 plasma polymerization 187, 189, 295
 plasma treatment 199, 200, 205
 plastic bending 249
 plastic deformation 76, 298, 333
 plastic flow 253
 plastic yielding 124
 plastic zone 331
 plastically shearing 247
 ply cracking 311
 ply orientation 314
 ply terminations 75
 Poisson effect 95, 126, 153, 156, 193
 Poisson ratio 45, 50, 71, 97, 104, 121, 315, 309, 343
 polar component 36
 polar group 205
 polar surface energy 191
 polyacrylonitrile (PAN) 183
 polyacrylonitrile (PAN)-based HMS4 carbon fiber 23
 polyacrylonitrile (PAN) precursor 26
 polyamide (PA) 250, 287–288
 polyamide nylon 6.6 coating 288, 295
 polybutadiene-co-maleic anhydride 287
 polybutyl acrylate 287
 polycarbonate (PC) 250, 288
 polycarbosilane 216
 polycrystalline alpha-alumina yarn 224
 polydiacetylene fiber-epoxy matrix composite 312
 polyester 177, 250
 polyether sulfone (PES) 288
 polyetheretherketone (PEEK) 32, 250
 polyetherimide (PEI) 288
 polyethylene 171
 polyethyl acrylate 287
 polyethylene fiber 37, 187
 polyethylene terephthalate (PET) 252
 polyhedron network 172
 polyimide Mylar 308
 polymer grafting 295
 polymerization 291, 293
 polymethyl methacrylate (PMMA) 288
 polymethylvinylether-co-maleic anhydride 287
 polyphenylene benzobisthiazole (PBT) fiber 22, 51
 polyphenylene sulfide (PPS) 252
 polypropylene (PP) 250, 253
 polysulfone (PS) 287–288
 polytetrafluoroethylene (PTFE) 250
 polytetrafluoroethylene (PTFE) coating 283
 polyurethane 349
 polyurethane coating 291
 polyurethane matrix 149
 polyurethane varnish (PUV) 283
 polyvinyl acetate (PVA) coating 292
 polyvinyl alcohol (PVAL) 287, 291, 300
 post-debonding friction 240, 243, 253, 270, 282
 potassium permanganate 203
 potassium persulfate 188
 p-phenylene diamine 196
 PRD-166 fiber 224
 preferential absorption 175
 pretension 51
 projectile impact 358
 pure shear 66

 R-curve 16, 79
 radial (compressive) stress 104, 127
 radial crack 58
 radio-frequency (RF) plasma 205
 rail shear test 62, 71
 Raman-active band 22
 Raman spectroscopy (RS) 20
 randomly oriented fiber 247
 rayon (cellulose) 183
 reaction barrier coating 207, 214–215, 221
 reaction bonding 5, 14–15
 reaction product 210, 212–213, 218
 reactive coating 291
 reactive functional group 199, 291
 reflective index 33
 reinforcing efficiency 98
 relative displacement 164
 residual clamping stress 16, 52, 75, 84, 103, 127, 138, 156, 159
 residual fiber protrusion 164
 residual relative displacement 159
 residual stress 75, 84, 124, 127, 150, 208, 280, 297, 308

- resin rich region 356
- rigid filler 333
- rigid particle 327
- roll coating 293
- Rosen's model 100
- roughness amplitude 127
- round robin test 76
- rubber coating 298
- rubber-modified epoxy 279, 329, 332–333
- rubber particle 331
- rugosity 189, 287
- Rule of Mixtures (RoM) 212, 239, 283, 312

- S-glass fibers 173
- Saphikon fiber 224
- sapphire fiber 127
- scale factor 106
- scanning Auger microscope (SAM) 29
- scanning electron microscopy (SEM) 18, 193, 197, 208, 333
- scanning tunneling microscopy (STM) 18
- SCS fiber 216
- SCS-6 (SiC) fiber/Ti-15-3 matrix composite 316
- SCS-6 SiC fiber 127, 158, 218
- SCS-8 fiber 217
- secondary ion mass spectroscopy (SIMS) 18, 20, 29
- semicrystalline thermoplastic matrix 199
- shear band 331
- shear deformation 333
- shear-lag model 60, 94, 97, 126, 128, 300
- shear modulus 66, 71
- shear strength 62
- shear strength criterion 110, 126, 147
- shear yield strength 72, 248
- short beam shear test 62, 68, 193
- short fiber composite 98
- shortest bond length 136
- shrinkage 16, 104
- shrinkage fit 311
- shrinkage stress 279
- SiC coating 215–216, 298
- SiC fiber 3, 138, 210, 216
- SiC fiber–glass matrix composite 133, 135, 139, 145, 157
- SiC fiber–Ti₃Al–Nb matrix composite 315
- SiC fiber–Ti₃Al + Nb matrix composite 298, 304, 306, 316
- SiC interlayer 298
- SiC matrix 16, 214
- SiC/BN 222
- sigmoidal-shaped microcrack 335
- silane coupling agent 14, 171–172, 174
- silica (SiO₂) 172, 330
- silicon 287
- silicon carbide (SiC) 189, 206
- silicon nitride (Si₃N₄) 58, 189
- silicone fluid 285
- silicone grease 285
- silicone resin 149
- silicone rubber coating 287, 294, 315
- silicone vacuum fluid (SVF) 283, 291
- silver coating 212
- single fiber 43, 95
- single fiber composite model 95, 97, 142, 149
- single fiber compression test 44
- singularity 94
- SiO₂ coating 213, 216
- size 174, 186
- size effect 360
- slice compression test 44, 58
- small-angle light scattering (SALS) 33
- small-angle X-ray scattering (SAXS) 20, 33
- SnO₂ coating 228
- sodium 172
- sodium ion 172
- sodium silicate glass 172
- soft/ductile interlayer 306
- softening strip 345
- sol–gel method 210, 224
- solid state nuclear magnetic resonance (NMR) spectroscopy 18, 20, 31
- solution concentration 293
- solution dip coating 293
- solvent 293
- span-to-depth ratio 63
- spectra 900 fiber 203, 205
- spectra 1000 fiber 203
- spherulite 34
- spraying 210
- spreading pressure 8
- sputtering 209

- stability 136
- stabilization 185
- stable debonding process 154
- stacking angle 344
- stacking sequence 314
- starter crack 76, 85
- static loading 253
- static tension 329
- steel fiber 138, 254, 354
- steel fiber-epoxy matrix composite 139
- steel fiber-rubber matrix composite 53
- stick slip 137
- stitch 352
- stitch density 355, 357
- stitch diameter 356
- stitch hole 359
- stitch knot 356
- stitched joint 357
- straight-sided tensile specimen 70
- strain energy release rate 77, 104
- strain mapping technique 22
- stress concentration 64, 68
- stress redistribution 240, 243, 282
- stress relief medium 288
- stress transfer 93, 109
- stretching 331
- styrene 175
- sub-critical transfer length 252
- substrate 209
- sub-zero temperature 287
- sulfuric acid 199
- surface area 189
- surface energy 7-10, 175, 226
- surface functional group 189
- surface irregularity 188
- surface roughness 35, 151, 157, 316
- surface rugosity 203
- surface topography 171
- surface treatment 14, 16, 93, 108-109, 171, 186

- tapered layer 347
- tearing 331
- Technora fiber 196
- Tekmilon fiber 202
- tensile debonding mechanism 44, 257, 281
- tensile residual stress 315
- tensile strength 193, 213
- terephthaoyl chloride 196

- tetragonal phase 314
- textile composite 351
- thermal spraying 210
- thermodynamic stability 207
- thermo-mechanics model 95
- thermoplastic coating 288, 291
- thermoplastic matrix 76, 251, 293, 339
- thermoset matrix 178, 293
- thin-walled tube torsion test 62
- three-cylinder composite model 126, 140, 149, 315
- three-dimensional network 172
- three-phase 297
- three point bending 62, 81
- three rail shear test 70-71
- through-the-thickness stitch 351, 354
- Ti alloy matrix 217-218
- Ti coating 228
- Ti matrix composite 216
- Ti-24Al-11Nb intermetallic alloy 217
- Ti-6Al-4V matrix composite 217-219
- Ti-Al intermetallic alloy 218
- Ti-Ni coating 227
- titanium dioxide (TiO₂) 189
- TiB coating 213
- TiB needle 218
- TiB/C duplicate coating 218
- time-of-flight secondary ion mass spectroscopy (TOF SIMS) 177
- tin dioxide 227
- torsion shear test 70
- total fracture toughness 245, 253
- total specific work of fracture 252
- totally unstable 137
- tough matrix material 279, 329
- toughening mechanisms 240, 279
- toughness 237, 242, 254
- transcrystalline 199
- transfer length 120
- translaminar shear strength 61, 69
- transmission electron microscopy (TEM) 18, 214, 222
- transparticle fracture 331
- transverse crack 50, 84, 240
- transverse flexural strength 37
- transverse fracture toughness 279, 306, 350
- transverse tensile modulus 73
- transverse tensile strength 61, 73, 193

- transverse tensile test 62, 72–73
triaxial stress 280
triaxial tension 306
tungsten core 216
tungsten fiber 45
tungsten substrate 214
tungsten wire–copper matrix system 280
turbostratic BN layer 222
Twaron fiber 196
two rail shear test 71
two-way debonding 149
- ultrahigh modulus polyethylene fiber 202
ultrahigh molecular weight (UHMW)
polyethylene 3, 202
ultrasonic C-scan 342
ultrasonic horn 293
uniaxial tension 69
unloading path 80
unstable crack propagation 82
- van der Waal force 6, 14, 184
Vickers microhardness indenter 57
vinyl 14, 175, 295
vinylester matrix composite 200
visco-elastic coating 96
viscosity 8, 285, 293
viscous fluid 285
- warpage 313
water absorption 180
water resistant bond 180
wavelength 21
weak interface–bond layer; 306
weaving 352
Weibull modulus 48, 106
- Weibull probability of failure 106
wet oxidation 187
wet-spinning 196
wettability 5, 7–8, 175, 191, 201, 205, 212,
216, 226
whiskerization 187, 189
wide-angle X-ray diffraction 199
wide-angle X-ray scattering (WAXS) 17,
32
width tapered double-cantilever-beam
(WTDCB) test 77
Wilhelmy balance method 36
Wilhelmy slide technique 34
work hardening 58
work of adhesion 7–8, 50
work of matrix shearing 247
wrapping 347
- X-ray diffraction 212, 214
X-ray monochromator 26
X-ray photoelectron spectroscopy
(XPS) 20, 24, 177, 205, 210, 287
X-ray photon energy 24
X-ray radiography 342
XA 1 fiber 108
XA 100 fiber 104, 108
- yield strength 316, 337
Young–Dupre equation 8
Young’s modulus 45, 66, 303
Young’s modulus ratio 50, 95, 97, 136,
150
- zirconia-based matrix 222
[±45°]_s tensile test 62, 69
[10°] off-axis tensile test 62, 70

ISBN 0-08-042695-6